Electron Transfer and Spin Chemistry in Iridium-Dipyrrin Dyads and Triads

Dissertation zur Erlangung

des naturwissenschaftlichen Doktorgrades der

Julius-Maximilians-Universität Würzburg

vorgelegt von

Johannes Hubert Klein

aus Fulda

Würzburg 2015

Eingereicht bei der Fakultät für Chemie und Pharmazie am

22.07.2015

Gutachter der schriftlichen Arbeit

1. Gutachter: Prof. Dr. Christoph Lambert

2. Gutachter: Prof. Dr. Tobias Hertel

Prüfer des öffentlichen Promotionskolloquiums

1. Prüfer: Prof. Dr. Christoph Lambert

2. Prüfer: Prof. Dr. Udo Radius

3. Prüfer: Dr. Andreas Steffen

Datum des öffentlichen Promotionskolloquiums

28.08.2015

Doktorurkunde ausgehändigt am

Die vorliegende Arbeit wurde in der Zeit von Oktober 2009 bis Juli 2015 am Institut für Organische Chemie der Universität Würzburg angefertigt.

Mein besonderer Dank gilt

Herrn Prof. Dr. Christoph Lambert

dafür, dass ich dieses spannende und vielseitige Thema bearbeiten durfte. Danken möchte ich Ihnen auch für Ihre allzeit offene Bürotür und die geduldige Beantwortung verschiedenster wissenschaftlicher Fragen. Vielen Dank, dass Sie mir die Möglichkeit gegeben haben an diversen Tagungen teilzunehmen und mich bei der Stipendium- und Postdoc-Bewerbung unterstützt haben.

COPYRIGHT

Parts of this thesis have previously been published and are reproduced or adapted with permission from:

1. *Stepwise versus pseudo-concerted two-electron-transfer in a triarylamine–iridium dipyrrin–naphthalene diimide triad*, J. H. Klein, T. L. Sunderland, C. Kaufmann, M. Holzapfel, A. Schmiedel, C. Lambert, *Phys. Chem. Chem. Phys.* **2013**, *15*, 16024–16030. – Reproduced or adapted in part by permission of the PCCP Owner Societies.

2. *A photoinduced mixed-valence state in an organic bis-triarylamine mixed-valence compound with an iridium-metal-bridge*, C. Lambert, R. Wagener, J. H. Klein, G. Grelaud, M. Moos, A. Schmiedel, M. Holzapfel, T. Bruhn, *Chem. Commun.* **2014**, *50*, 11350–11353. – Reproduced by permission of The Royal Society of Chemistry.

3. *Complete Monitoring of Coherent and Incoherent Spin Flip Domains in the Recombination of Charge-Separated States of Donor-Iridium Complex-Acceptor Triads*, J. H. Klein, D. Schmidt, U. E. Steiner, C. Lambert, *J. Amer. Chem. Soc.* **2015**, DOI: 10.1021/jacs.5b04868. Copyright (2015) American Chemical Society.

The following theses contributed also to this work:

4. *Synthese und photophysikalische Untersuchung von Donor-substituierten bis-cyclometallierten Iridium(III)-Komplexen mit unterschiedlichen Nebenliganden*, S. Riese, Graduate thesis (teacher apprenticeship), Julius-Maximilians-Universität (Würzburg), **2012**.

5. *Synthese und photophysikalische Eigenschaften von neutralen Donor- und Akzeptor-substituierten Iridium(III)-Komplexen*, C. Kaufmann, Bachelor thesis, Julius-Maximilians-Universität (Würzburg), **2012**.

CONTENTS

ABBREVIATIONS

ahfc	anisotropic hyperfine coupling
CS	charge separated
CT	charge transfer
ET	electron transfer
EnT	energy transfer
esdi	electron-spin-spin-dipolar interaction
gta	g-tensor anisotropy
GPC	gel permeation chromatography
ihfc	isotropic hyperfine coupling
IV-CT	intervalence charge transfer
LC	Ligand Centred
LEC	light emitting electrochemical cell
MLCT	Metal-to-Ligand Charge Transfer
MV	mixed valence
MRCI	Multi-Reference Configuration Interaction
NDI	1,4,5,8-naphthalene diimide
OLED	organic light emitting diode
SEC	spectroelectrochemistry
sri	spin-rotational interaction
TAA	Triarylamine
TBAHFP	tetrabutylammonium hexafluorophospate
(TD)DFT	(time dependent) density functional theory

1 Introduction

Artificial Photosynthesis

The photoinduced separation of charges is a fundamental process in photosynthesis, where light absorption by an antenna complex is followed by energy transfer (ET) to the so-called special pair which consists of bacteriochlorophyll units. Subsequently, photoinduced electron transfer leads to a charge-separated (CS) state in where the special pair is oxidised and ubiquinone is reduced.[1]

On the way of mimicking the natural charge-separation process, several systems have been developed to transform light energy into useful chemical fuels. For example, in the early 1970s *Fujishima* and *Honda* achieved the splitting of water with the help of anatase TiO_2 in a photoelectrochemical cell with a Pt counter electrode.[2-3] Although there were some earlier reports on the use of TiO_2 as photocatalyst,[2] the beginning of the oil crisis pushed the findings by *Fujishima* and *Honda* strongly. The combination of oil shortage and the development of alternative fuel resources marked the beginning of the era of artificial photosynthesis. The catalytic production of H_2 and O_2 upon irradiation in their experiment is related to the transfer of electrons from water to TiO_2 (O_2 evolution) and from platinum to protons (H_2 evolution).[4-5]

Instead of using a bulk material, e.g. TiO_2, another approach is based on the use of small molecules which absorb the light and then produce charge-separated states. With these CS states reductive or oxidative catalysis of water can be performed. Thereby, it is possible to follow two different strategies. i) The biomimetic approach where the photoactive chromophore consists of a tetrapyrrole pigment in combination with quinone acceptors,[6-10] or ii) the absorption of light is based on transition-metal complexes, whereby d^6 and d^8 metal complexes[8, 11-16] play a leading role in the field of artificial photosynthesis. One important

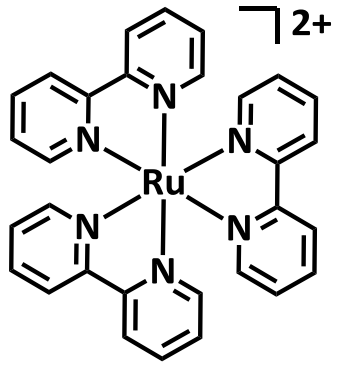

Figure 1 Structure of $Ru(bpy)_3^{2+}$.

example of the latter was introduced by *Meyer et al.* in 1974 who explored the bimolecular quenching of the excited state (ES) of ruthenium *tris*(2,2´-bipyridine) ($Ru(bpy)_3^{2+}$, Figure 1) by methylviologen dication (MV^{2+}) to yield a CS state with the oxidative and reductive equivalents, $Ru(bpy)_3^{3+}$ and MV^{+}, respectively.[17] Thereby, it was shown that the intermolecular ET, controlled by the concentration of the reactants, needed to be faster than the radiative decay or the non-emissive deactivation of the ES of $Ru(bpy)_3^{2+}$.

Design Principle of Multichromophoric Arrays

Mimicking the natural way of using solar energy is not only absorbing sunlight in a broad spectral region, but to do redox chemistry with the collected energy. A successful approach is the use of electron donors and acceptors which are linked to a photoactive metal-complex sensitiser. Figure 2 illustrates various structural designs of donor-photosensitiser-acceptor systems. These are termed triads.[8, 13-14, 18-19]

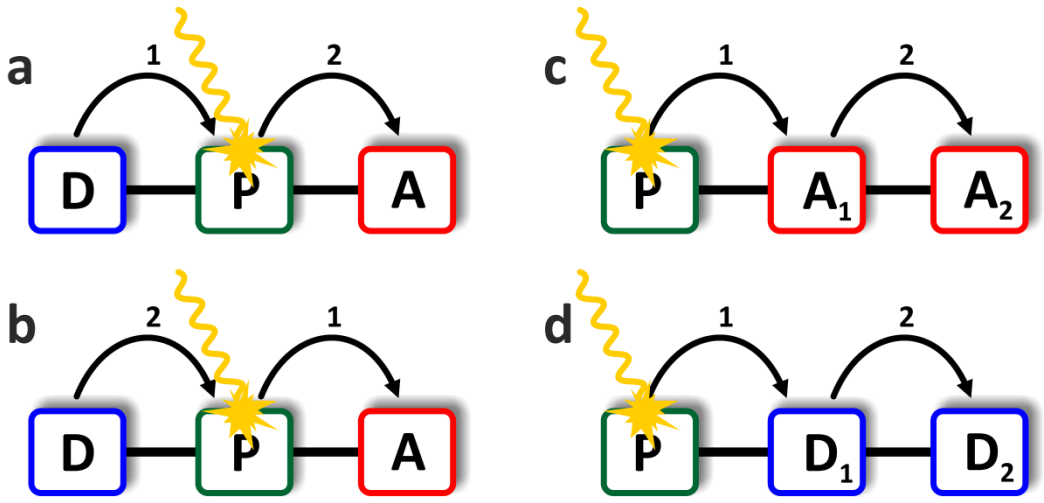

Figure 2 Design principle of (a, b) donor-photosensitiser-acceptor (D–P–A), (c) photosensitiser-acceptor-acceptor ($P–A_1–A_2$) and (d) photosensitiser-donor-donor ($P–D_1–D_2$) systems where in each case just the photosensitiser is excited.

Most design principles of artificial photosynthesis are based on a linear arrangement to realise a directed, long-range electron transfer. The most frequently used strategy is to place a photosensitiser (P) between the donor (D) and acceptor (A) units (Figure 2a, b). In this case,

the photosensitiser acts both as a bridge and as the main chromophore. Besides, in many cases the donor and acceptor units absorb light in the visible spectral regime and are therefore chromophores, too. However, in the D–P–A configuration an electron-transfer sequence can be completed by, first, reductive quenching of the excited state of the photosensitiser (P*) by the donor component (HOMO-HOMO-transfer) leading to the first CS state (CS_1). Second, the fully charge-separated state (CS_2) is formed by the reduction of the acceptor unit by the reduced photosensitiser (LUMO-LUMO-transfer) which is depicted in (Figure 2a). The inverted sequence is displayed in Figure 2b where first the excited photosensitiser is quenched oxidatively and in a second step the donor is oxidised to obtain the CS_2 state.[8, 13] Which mechanism takes place depends on the driving force for each step (= redox properties have to fit) and the electronic communication between the involved redox centres (for HOMO and LUMO-transfer). Other methods to separate charges efficiently over long distances are shown in Figure 2c and d. Here, electron cascades are introduced. These consist either of a P–A_1–A_2 (c) or P–D_1–D_2 (d) framework. The acceptor A_2 is more easily reducible than A_1 and D_2 is more easily oxidised than D_1.[8, 13] In the former examples, the photosensitiser acts as donor, whereas in the latter case it has the functionality of an acceptor.

In the following, important conditions of an ideal donor-photosensitiser-acceptor system are presented. First, the type of linking the redox units to P is a key aspect because it controls amongst others the forward and back electron transfer of intramolecular electron-transfer reactions. Thereby, it can affect the electronic communication between the redox centres and, in addition, influences the redox potentials of donor and acceptor.[20-28] Furthermore, the used systems in artificial photosynthesis have to fulfil the following requirements.[7-8, 10-12, 14, 19, 29-34] As already mentioned it is mandatory to have chromophores which are able to absorb visible-light provided by the sun; that means either the donor, the acceptor or the photosensitiser (can be bridge, redox centre and chromophore at the same time) have to possess absorption features which resemble the sun´s emittance spectrum. The maximum of the sunlight´s spectrum lies in the range of 20 000 cm^{-1} (500 nm) and the matching with the absorbance of the chromophore is of high importance to collect as many photons as possible. If the photosensitiser is a metal complex the absorption is often a charge transfer (CT) excitation whereby the charge is shifted from the metal to one of the ligands.

This is followed by the generation of the CS electron-hole-pair. Further ET lead to an increased electron-hole distance in the CS_2 state. The triads should be designed in such a way that all ET processes to reach the fully charge-separated state are be very fast. In contrast, the electronic communication between the terminal redox centres should be minimised to hamper charge recombination (CR). As a consequence, long-lived, charge-separated states can be achieved with a high efficiency. Furthermore, the photosensitiser should be stable towards thermal and photochemical decomposition and the redox behaviour should be reversible.[8, 11, 32] In addition, the used donors and acceptors and their oxidised and reduced forms should be both photochemically and chemically stable to allow a detailed investigation of the photophysical properties and to enable a long-term performance in potential devices.

In the context of artificial photosynthesis the current work will concentrate on multichromophoric systems, more precise on donor-iridium complex-acceptor arrays, where efficient, photoinduced electron transfer over relatively long distances (> 10 Å) plays a key role. In order to fulfil the above mentioned criteria for a long-lived charge separation a short overview on electron transfer theory and excited state energies in triads will be given in the following.

Electron Transfer

The theoretical description of an electron-transfer event was first deduced by *Marcus* in the 1980s. *Marcus* provided the theoretical basics for an ET from one redox centre to another which can either be expressed as a transition between or motions on free energy surfaces. Thereby, the free energy surface represents the free energy of the whole system (redox centres and solvent environment) in dependence on the degree of freedom of the specific system and can be expressed as the reaction coordinate on which the ET proceeds. It is assumed that the electron is either completely localised on the donor site (initial state) or at the acceptor site (product state). A transition between these two states is then given by the electronic coupling V_{el} which is a measure of the electronic communication between these states. Similar to chemical reactions, thermally induced ET is governed by an activation

barrier while moving on the free energy surface from the initial to the product state. The barrier height $\Delta G^{\#}$ can be determined by eq. (1).[35-36]

$$\Delta G^{\#} = \frac{(\Delta G^{00} + \lambda)^2}{4\lambda} \qquad (1)$$

The difference in *Gibbs* energy ΔG is the energy between the minima of the initial and product states and the reorganisation energy $\lambda = \lambda_o + \lambda_v$ consists of a solvent (λ_o) and a vibrational (λ_v) term. The so called *Marcus* equation (eq. (2)) relates the rate constant of the electron transfer to the aforementioned ET parameters and is only valid in the weak coupling limit ($V_{el} < k_B T$) where the free energy surfaces of ET are treated diabatically.[37-39]

$$k_{ET} = 4\pi^2 hc^2 \frac{1}{\sqrt{4\pi hc\lambda_o k_B T}} V_{el}^2 \exp\left(-\frac{hc(\lambda_o + \lambda_v + \Delta G^{00})^2}{4\lambda_o k_B T}\right) \qquad (2)$$

With these tools at hand it is possible to interpret various electron-transfer events in many donor-acceptor compounds. After *Marcus´* contribution to the field of ET other ET theories were developed, e.g. the semiclassical *Bixon-Jortner* approach which induced the quantumchemical treatment of intramolecular vibrations.[40]

State Energies

Important factors for a successful electron-transfer sequence are the exited-state potentials of P because the photosensitiser needs to have at least either a higher oxidation potential than the attached donor or a lower reduction potential than the attached acceptor. Some photosensitisers are both an excited-state acceptor and donor, whereas other chromophores are either ES donors or acceptors. Other key elements are the ES energies of the respective chromophores (^{1,3}D*, ^{1,3}P* and ^{1,3}A*). They must be higher in energy than the resulting charge-separated (CS) state to exclude energy trapping. In order to verify this, the energy of the ES can be determined by spectroscopy, e.g. by fitting a tangent on the rising edge of the high energy side of the emission band.[41] The ES energy is equal to the energy at the intersection point of the x-axis with the tangent for the singlet or triplet species. If fluorescence is hardly detectable, the procedure can be transferred to the absorption band´s low-energy side, as well.[41] In contrast, the free energy difference of the ground and CS state ΔG_{CS} can be estimated by the difference of the redox potentials of the involved redox units

corrected by *Coulomb* attraction of the charges using the equation derived by *Weller* (eq. 3).[42-43]

$$\Delta G^{00} = \frac{N_A}{1000} ze\left[E_{ox}(\mathrm{D/D^+}) - E_{red}(\mathrm{A/A^-})\right] - \frac{N_A e^2}{1000 \cdot 4\pi e_0}\left[\left(\frac{1}{2r_D} + \frac{1}{2r_A}\right)\left(\frac{1}{\varepsilon_r} - \frac{1}{\varepsilon_s}\right) + \frac{1}{\varepsilon_s d_{DA}}\right] \quad (3)$$

Here, $\left[E_{ox}(D/D^+) - E_{red}(A/A^-)\right]$ reflects the redox-potential difference between oxidation of the donor and reduction of the acceptor. The redox-differences can be derived from cyclic voltammetry (CV) experiments. ε_r is the dielectric constant of the solvent used in the CV and ε_s the one used for spectroscopy. r_D and r_A are the radii of the donor and the acceptor, respectively. d_{AD} is the centre to centre distance of donor and acceptor. However, in many cases the determination of the *Gibbs* energy of the CS state (ΔG_{CS}) lack the *Coulomb* term of eq. (3) and was simplified to the difference of the half-wave potentials ($\Delta E_{1/2}$) of donor and acceptor $\Delta G_{CS} \approx \Delta E_{1/2} = \left[E_{ox}(D/D^+) - E_{red}(A/A^-)\right]$.

1.1 Transition Metal Complexes in Artificial Photosynthesis

In literature, several photosensitisers can be found which satisfy the previously described ideal conditions. The characteristics of $Ru(bpy)_3^{2+}$ will help to explain the important steps of photoinduced ET reactions involving transition-metal complexes. One central feature of $Ru(bpy)_3^{2+}$ (Figure 1) is the relatively intense absorption (blue arrows in Figure 3) in the visible range with an absorption maximum of ca. 22 100 cm^{-1} (452 nm). This band with a molar extinction coefficient (ε_{abs}) of ca. 13 300 M^{-1} cm^{-1} is assigned to a metal-to-ligand-charge transfer (MLCT) where one electron of the occupied metal d-orbitals is excited into a vacant π*-orbital of one of the bipyridine ligands.[44-46] More precisely, after light absorption the metal centre has now an extra positive charge and one of the ligands is negatively charged ($Ru^{II}(bpy)_3^{2+} + h\nu \rightarrow Ru^{III}(bpy)_2(bpy^-)^{2+}$). The next process within the molecule is the internal conversion (IC, upper curly arrow) to its S_1 exited state (^{1}MLCT) followed by intersystem crossing (ISC, grey dashed arrow) to the lowest excited state (^{3}MLCT, T_1)

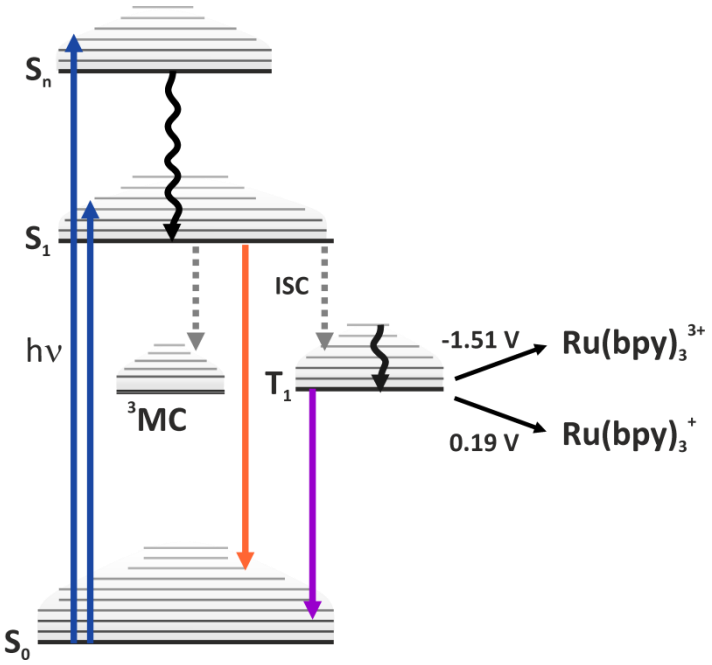

Figure 3 Jablonski diagram of $Ru(bpy)_3^{2+}$ with oxidation and reduction potentials (vs. Fc/Fc^+) of its ES.

which has triplet character and a lifetime of about 600 ns in oxygen-free aqueous solutions with an energy (ΔG^{00}) of 2.12 eV.[16, 44-46] The efficiency of the population of the triplet ES was determined to be unity and makes $Ru(bpy)_3^{2+}$ an attractive candidate as a reference for actinometric measurements of excited state populations.[47] In addition, the easily traceable ES footprint is the ground-state bleaching (GSB) of the MLCT absorption band at around 22 100 cm^{-1} (452 nm). However, the phosphorescence quantum yield of the ^{3}MLCT state is less than 5 % and radiationless deactivation dominates due to low-lying triplet metal-centred (^{3}MC) states. The long lifetime of its triplet ES can be used to perform redox processes with attached or nearby redox partners. This is the reason why metal complexes are advantageous over organic photosensitisers.

The situation of suitable redox potentials makes $Ru(bpy)_3^{2+}$ to both a better excited state reductant and oxidant compared to its ground state (Figure 3).[11, 16, 44-46] The oxidation of the ruthenium complex ES occurs at –1.51 V and the reduction at 0.19 V (all vs. Fc/Fc^+), whereas the corresponding redox reactions originating from the ground state require 0.61 and –1.93 V (vs. Fc/Fc^+), respectively.[44-46] All these promising properties make ruthenium $Ru(bpy)_3^{2+}$ an intensively studied prototype in artificial photosynthesis. However, other complexes were used as photosensitisers in triads which is shown in the following.

Figure 4–5 displays several triads which prove the successful concept to create long-lived, charge-separated states with the use of transition-metal complexes as photosensitiser by applying the design principle in Figure 2a, b.

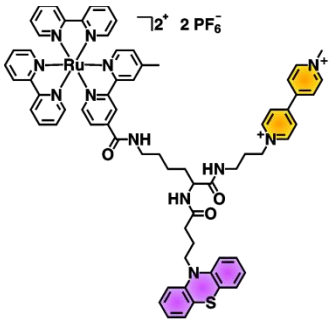

T. J. Meyer et al.[48–50]

A

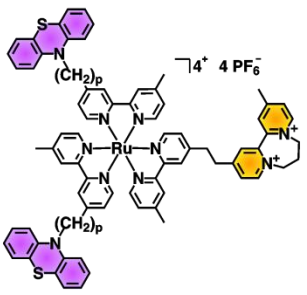

T. J. Meyer et al.[51]

B

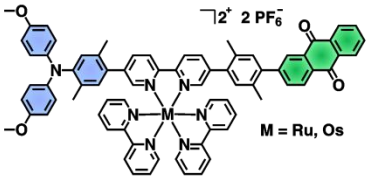

O. Wenger et al.[55–57, 65]

C (Ru), D (Os)

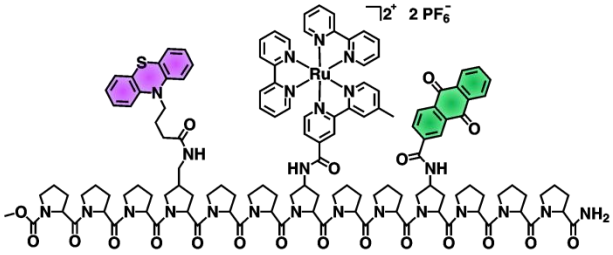

T. J. Meyer et al.[50, 52–53]

E

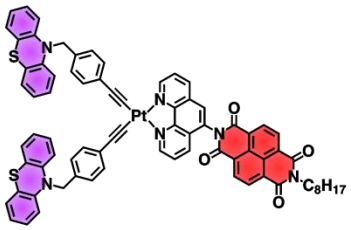

J. Weinstein et al.[58–59]

F

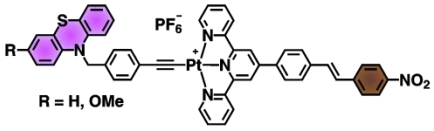

R. Eisenberg et al.[60–62]

G

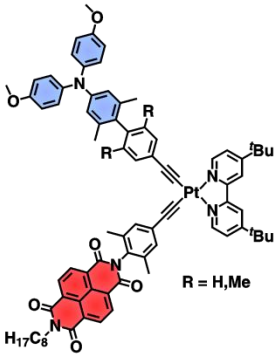

K. Nozaki, K. Akiyama, K. Okada et al.[63–64]

H

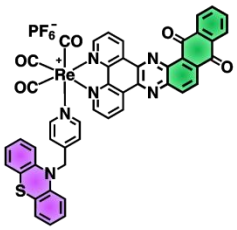

B. Loeb, T. J. Meyer et al.[68]

I

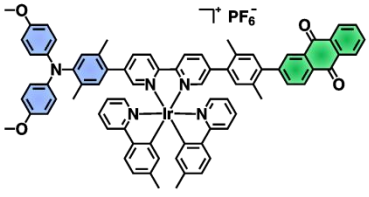

O. Wenger et al.[57]

J

Figure 4 Overview of some successfully studied donor-photosensitiser-acceptor triads: **A–J**.

In Figure 4–5, P is either a ruthenium polyimine complex (**A–C, E, L**)[48-57], a platinum (**F–H**)[58-64], an osmium (**D**)[56-57, 65], an iridium (**J, K**)[57, 66-67] or a rhenium complex (**I**)[68]. Triads **A–L** are constructed with several different donor and acceptor pairs. Phenothiazines (PTZ, purple), triarylamines (TAA, blue) and a dinuclear manganese cluster (Mn_2, light green) are donors, whereas anthraquinons (AQ, green), naphthalene diimides (NDI, red), quaternary bipyridiniums (qBPY, yellow) or a conjugated nitrobenzene (Nb, brown) are used as acceptors.

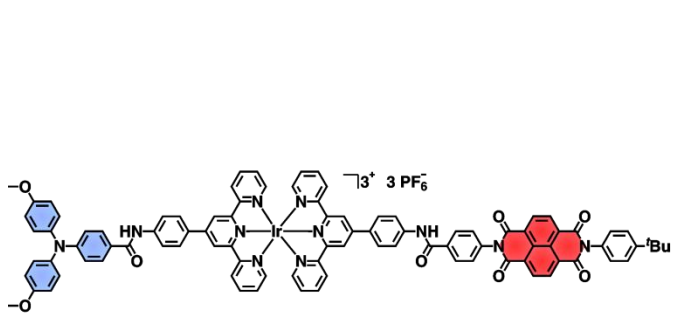

L. Flamingi et al.[66–67]

K

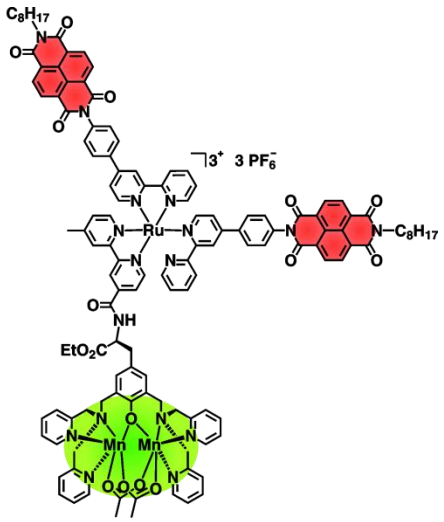

L. Hammaström et al.[54]

L

Figure 5 Donor-photosensitiser-acceptor triads **K** and **L** with extremely long-lived CS state lifetimes.

All triads have the following aspects in common. They possess a relatively rigid structure, that is, the spacers between the different chromophores avoid a close approximation. The donor-acceptor distances are in the range of d_{AD} = 15–37 Å. All photosensitiser complexes show a more or less intense MLCT absorption in the visible spectral region with ε_{abs} = 3000–42 000 M^{-1} cm^{-1}. The energy of the CS states (vide supra) is in the range of 1.04–1.87 eV. However, the lifetimes of the observed charge-separated states vary extremely from 36 ns to 600 µs (see Table 1) just as the quantum yields of the formation of the CS states with ϕ_{CS} = 10–100 % (see Table 1). Thereby, the short-lived CS states (**A–J**,

36 ns–1.3 µs) possess higher quantum yields (25–100 %), whereas the extremely long-lived CS states (**K–L**, 120–600 µs) show rather ineffective CS processes (10–20 %).

This comparison shows that a long lifetime of the CR is compensated by less efficient electron-transfer processes for CS. This may be the consequence of a vanishing electronic coupling (e.g. increased D-A distance) for both CS and CR processes. Furthermore, the long lifetime of some multichromophoric assemblies are explained by a *Marcus* inverted-region effect where a higher driving force for CR results at the same time in a lower rate for the CR process. All other complexes (**A–J**) exhibit higher quantum yields (ϕ_{CS}) and lower lifetimes (τ_{CS}), due to a better electronic coupling between the respective states.

Table 1 Selected triads **A–L** (see Figure 4–5) with specific characteristics: ES lifetime, quantum yield, donor-acceptor distance and stored energy of the CS state.

triad	lifetime / solvent	ϕ_{CS}	D-A-distance / Å	E_{CS} / eV
A[48-50]	147 ns / MeCN	34 %	-[a]	1.14
B[51]	165 ns / CH_2Cl_2	≈26 %	15	1.29
C[55-57]	1.3 μs / MeCN	≈100 %	22	1.57
D[56-57, 65]	80 ns / MeCN	46 %	22	1.58
E[50, 52-53]	175 ns / MeCN	53 %	-[a]	1.52
F[58-59]	36 and 120 ns / CH_2Cl_2	-[a]	17.1 and 20.1	1.2
G[60-62]	230 ns / MeCN	<30 %	28	≈1.6
H[63-64]	839 ns / toluene (Me) 1.34 µs / toluene (H)	>95 %	-[a]	1.87
I[68]	890 ns / MeCN	≈100 %	22	1.56
J[57]	300 ns / 1,2-dichloroethane	-[a]	-[a]	1.04
K[66-67]	120 µs / MeCN	10 %	37	1.26
L[54]	600 µs / *n*PrCN	≈20 %	-[a]	1.07

[a] donor-acceptor distances or quantum yields were not determined.

In conclusion, a precise tuning of the electronic coupling between the redox states is mandatory. Thereby, the electronic coupling needs to be high enough to ensure high quantum yields for the formation of the CS state and low enough to slow down CR.

For application purposes accumulation of charges at an attached catalyst site in multiphoton processes is mandatory because the catalytic reductive or oxidative water splitting includes even (multi-) electron events for the generation of hydrogen or oxygen from water. On the contrary, in photochemistry typically single electron events are observed.[7, 14, 19, 34, 61, 69-71] The catalyst site, e.g. for the reductive water splitting, is in many cases either a cobaloxime[72-73] or diiron carbonyl[74-75] complexes linked to a multichromophoric system.

Possible applications which are driven by sunlight and produce solar fuels are not only related to the development of catalysts which mediate the oxidation or reduction of water. In addition, CO_2 reduction to methanol is a preferable process mankind needs to manage the greenhouse effect.[76-79] This would be a smart and convenient way to use the sunlight´s energy to produce new fuels (H_2 or MeOH) or to consume waste products (CO_2). In this regard, the academic and industrial research has still a lot to do to develop devices which are stable in a long-term performance.

The current work will spot on the electron transfer properties of donor-iridium complex-acceptor triads (chapter 3.1.2) to elucidate ET processes, quantum yields and lifetimes. The effect of an increased donor-acceptor distance is discussed in chapter 3.1.3. The aspect of symmetry breaking will play a leading role in chapter 3.1.4. There, a varying number of quenching events and their influence on the ET processes is studied.

1.2 Iridium Complexes

Metal complexes are widely-used as photosensitisers (Figure 4 and 5) and, especially, iridium complexes play a superior role in the field of photoactive materials compared to other metal complexes due to beneficial properties. Some of these interesting features will be highlighted in following. Moreover, an overview of various complex types (1.2.1) is presented with a detailed analysis of the electrochemical (1.2.2) and photophysical (1.2.3) properties of selected iridium complexes.

Due to their long-lived, emissive triplet states iridium complexes are frequently used in many photonic applications.[80-87] Likewise, they are used as the emitting chromophores in OLEDs[80, 82-83, 88-104] (organic light emitting diode) and light emitting electrochemical cells (LECs),[100, 104-108] as photosensitiser in photocatalytic water splitting,[7, 19, 25, 34, 85, 96-97, 109-114] as well as phosphorescent emitters in biolabeling and -sensing applications.[85, 115-117] In addition, the nonlinear optical (NLO) properties of elongated ligand frameworks coordinated to the iridium centre were studied.[85, 118-122] Typical structures of the complexes used in the aforementioned applications are depicted in Figure 6.

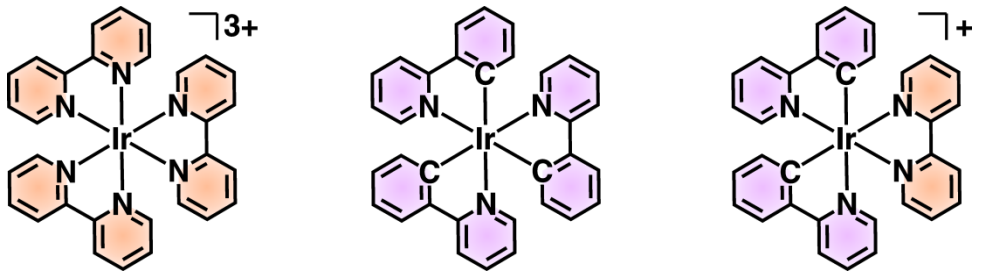

Figure 6 Structures (from left to right) of $Ir(bpy)_3^{3+}$, *fac*-$Ir(ppy)_3$ and $Ir(ppy)_2(bpy)^+$.

Complex $Ir(bpy)_3^{3+}$ (Figure 6, left) is analogous to $Ru(bpy)_3^{2+}$ with neutral 2,2´-bipyridine (bpy) ligands but with an Ir instead of the Ru metal centre (see Figure 1). Concerning *tris*-cyclometalated[1] [82, 85] *fac*-iridium(III) *tris*(2-phenylpyridine) (*fac*-$Ir(ppy)_3$) all bpy ligands are exchanged by 2-phenylpyridine (ppy) ligands (Figure 6, middle). The exchange

[1] Cyclometalated complexes describe a class of complexes where one or two metal-carbon bonds are part of a cyclic structure, e.g. in cyclometalated iridium-complexes the metallacyclus is built of a five- or six-membered ring with the iridium atom on one edge of the ring and the 2-phenylpyridine acts as a bidentate ligand where one carbon atom of the phenyl-ring and the nitrogen atom of the pyridine-ring coordinate to the metal centre.

of only two diamine ligands leads to *bis*-cyclometalated iridium complexes (Figure 6, right), which are used in the present work. The use of two different functionalised ligands, one with a donor and one with an acceptor, is advantageous over the use of three identical ligands, especially for the use as a photosensitiser in triads.

1.2.1 Synthesis of Homoleptic and Heteroleptic Ir(III) Complexes

Before a detailed analysis of the electrochemical and photophysical properties of various iridium complexes is presented, the focus will be on the syntheses of some important complex frameworks with iridium metal centres. The complexes in Figure 6 have an 18-electon configuration in common, as well as a slightly distorted octahedral geometry and a spherical-like structure. The latter makes agglomeration less feasible.[44, 81, 84-85, 87, 123]

The homoleptic, *tris*-cyclometalated complexes (Figure 6, middle) can be prepared with iridium(III)chloride hydrate ($IrCl_3 \cdot nH_2O$) or iridium *tris*(acetylacetonat) ($Ir(acac)_3$) at high temperatures (>200 °C) (Scheme 1, top).[87, 123-124] In contrast, the early attempts to synthesise the *tris*-bipyridine iridium complexes (Figure 6, left) were achieved in a one-pot synthesis, starting with potassium hexachloroiridate(VI) $K_2IrCl_6 \cdot 3\,H_2O$, reducing agents and 2,2´-bipyridine and employing high temperatures (>200 °C) (Scheme 1, bottom).[125-127] Due to the relatively high oxidation state of the iridium metal (+III) and the neutral coordination site of 2,2´-bipyridine $Ir(bpy)_3^{3+}$ the yields are very low. Accordingly, the hard and soft binding concept favours different products. For example, a negatively charged ligand (hard) would preferably coordinate to the harder Ir^{3+} ion (hard) than a neutral *N*-coordinating (soft) binding site. As a result, the carbon atom in 5-position of the 2,2-bipyridine with a formal negative charge binds to the iridium centre in the attempted synthesis of $Ir(bpy)_3^{3+}$. Hence, cyclometalated complexes can be isolated as side products.[128-129] A more recent synthesis of $Ir(bpy)_3^{3+}$ according to *Meyer et al.* used a two-step method with $[Ir(bpy)_2(OSO_2CF_3)_2]^+$ as intermediate.[126-127, 130]

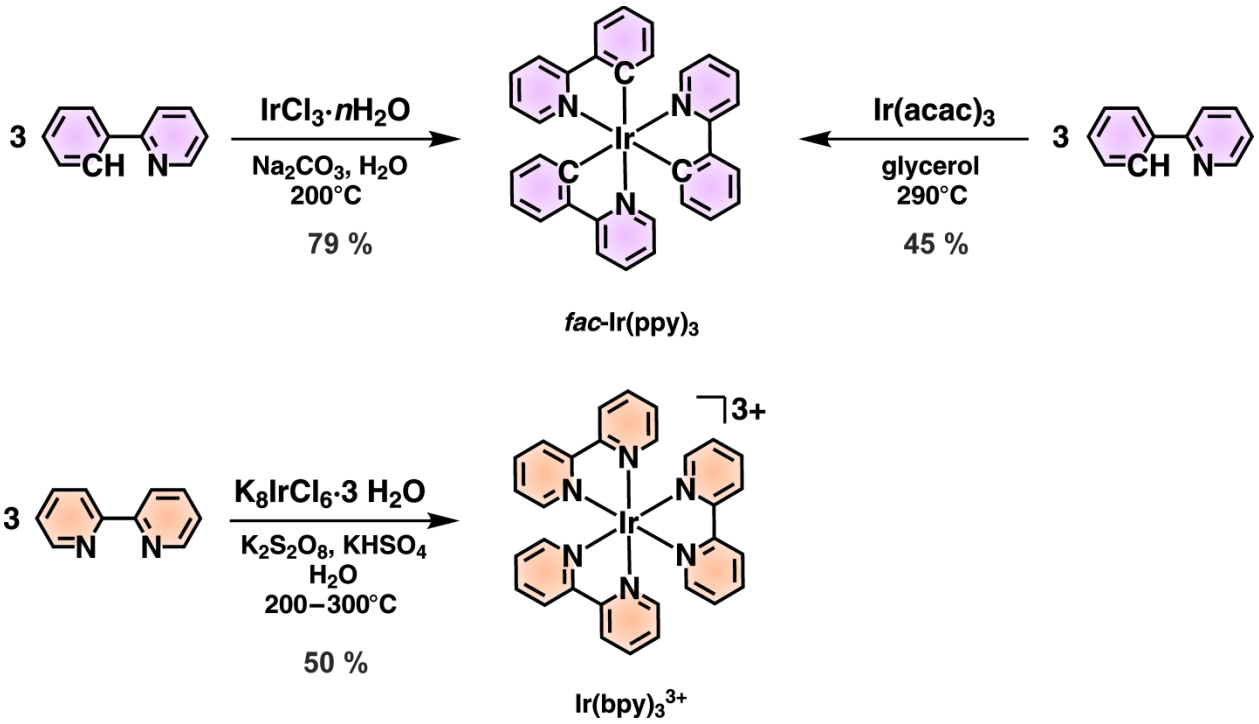

Scheme 1 Syntheses of t*ris*-2-phenylpyridine (top) and *tris*-2,2´bipyridine (bottom) iridium complexes $Ir(bpy)_3^{3+}$ and *fac*-$Ir(ppy)_3$, respectively.

Another access to the *tris*-cyclometalated complexes is provided by the two-step method according to *Nonoyama et al.*[131] as depicted in Scheme 2. In a first step iridium(III)chloride hydrate ($IrCl_3 \cdot nH_2O$) is treated with a cyclometalating ligand (HC^N, Figure 7) while boiling in an aqueous alcoholic solution. These milder conditions lead to the dinuclear iridium μ-chloro bridged dimer $[Ir(C^N)_2Cl]_2$.[81, 85, 87, 105, 132-133] The second step opens several pathways to a variety of new iridium complexes, depending on the ancillary ligand used at that stage. If the same ligand as in the first step is used, the product is a homoleptic complex ($Ir(C^N)_3$) in the *mer*- or *fac*-form, which have slightly different properties. The *mer*-isomer can be converted into the *fac*-isomer upon heating or irradiating with light. The reason for the formation of the themodynamically more stable *fac*-isomer is the higher number of *trans*-C-Ir-N bonds because carbon atoms with strong σ-donor bonds coordinating the iridium centre try to avoid a *trans*-position (cf. trans-effect).[84-85, 87, 124, 134-136]

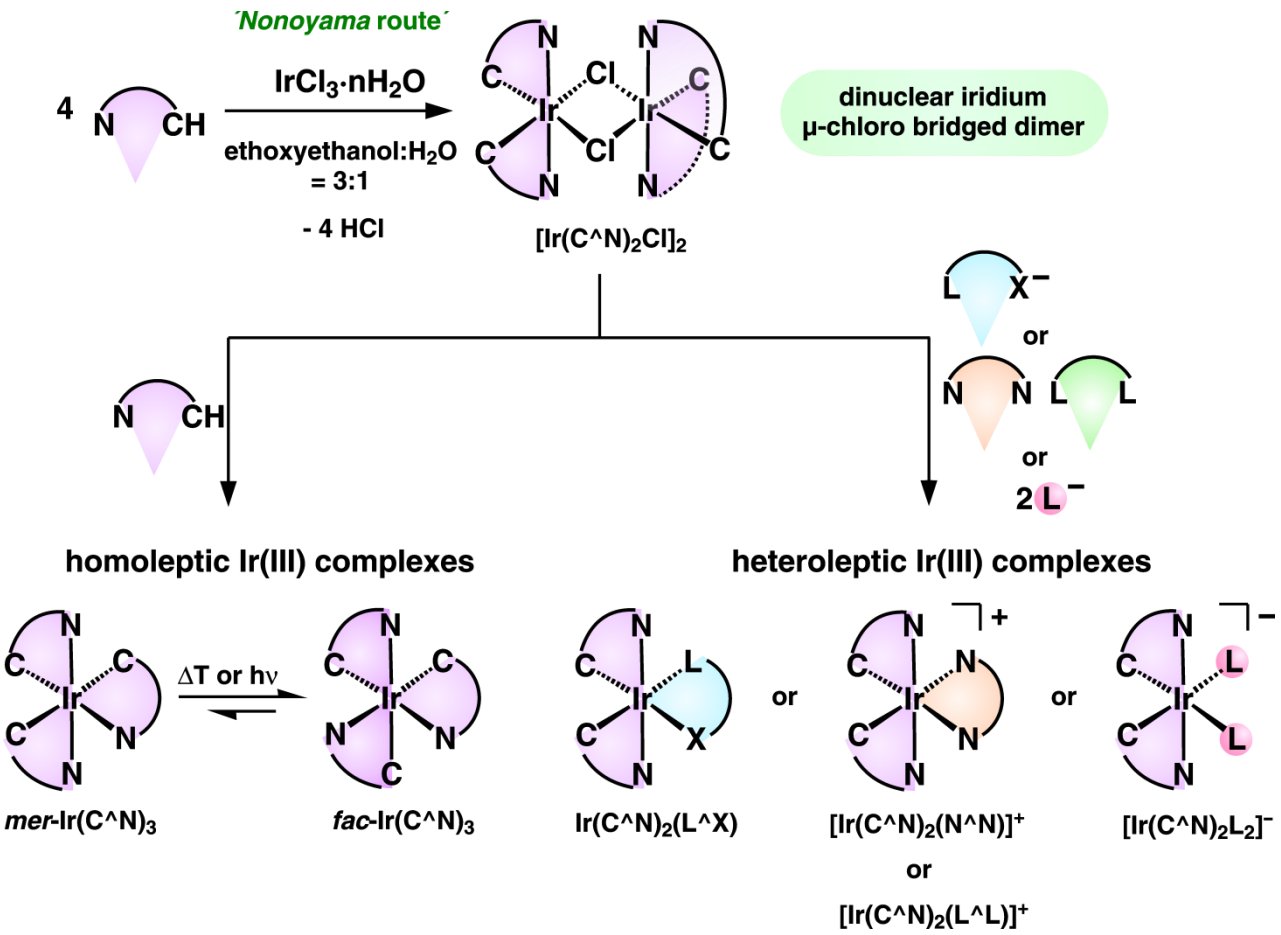

Scheme 2 Syntheses and structures of cyclometalated iridium complexes in neutral, cationic and anionic forms.

Heteroleptic complexes can be prepared when other ligands are involved in the second step to yield neutral $Ir(C^N)_2(X^L)$ (with X = anionic binding site) or $Ir(C^N)_2(C^N')$), cationic $(Ir(C^N)_2(N^N)^+$ or $Ir(C^N)_2(L^L)^+)$ or anionic $(Ir(C^N)_2(L_2)^-)$ complexes. The monocationic complexes are readily synthesised using an ancillary bidentate ligand with non-ionic coordination sites e.g. with 2,2´-bipyridine (see Figure 8 for more examples) in dichloromethane,[80-81, 84-85, 105, 107, 123, 137] whereas the neutral heteroleptic complexes are prepared with a cyclometalating ligand (C^N), different to the first step.[136, 138] Furthermore, similar to the cyclometalating ligands are derivatives of benzyldiphosphine (bz-PPh_2) and *N*-heterocyclic carbene (NHC) containing ligands such as 1-phenyl-3-methylimidazolin-2-ylidene (pmi) (Figure 8), which can build homoleptic complexes of the type $Ir(C^N)_2(L^X)$ and $Ir(L^X)_3$, respectively.[82]

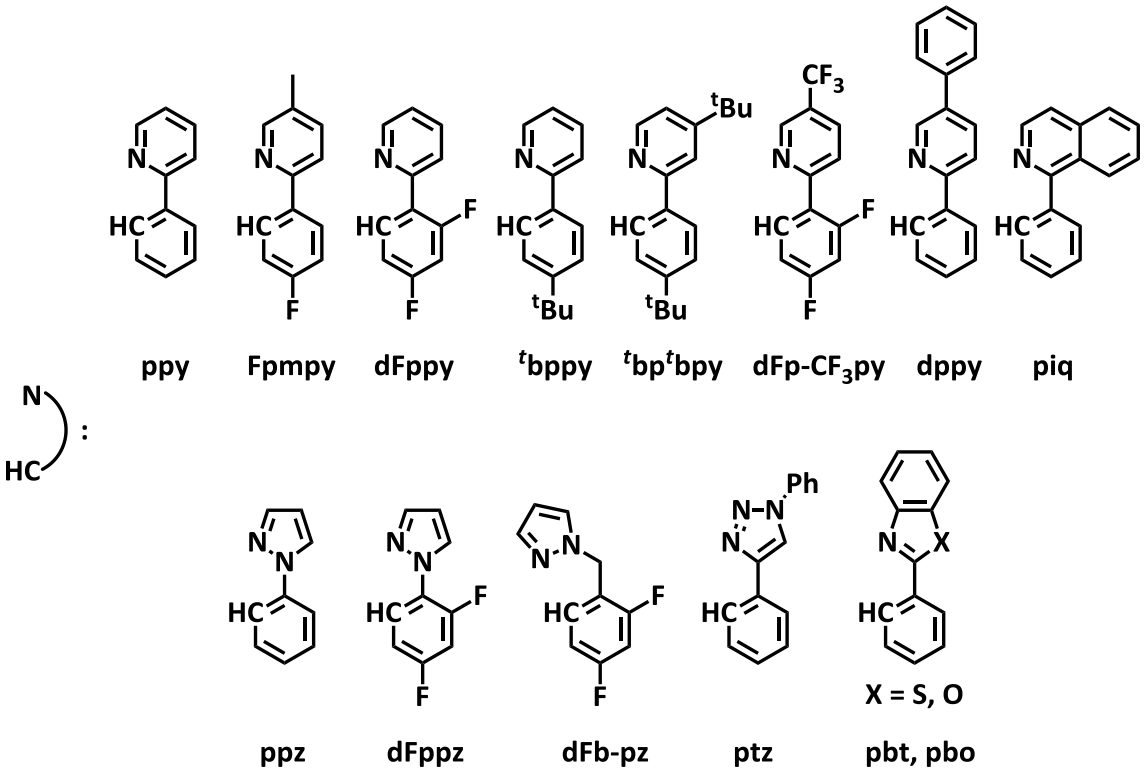

Figure 7 Typical cyclometalating ligands (HC^N) used in the literature.

Another possibility towards neutral heteroleptic complexes is the use of bidentate ligands that possess a neutral and an anionic coordination atom (Figure 9), such like acetyl acetone (acacH), picolinic acid (picH), *N*-methyl salicilimine (salH),[82-84, 86-87, 106, 139] the 2-pyridyl-*C*-linked-triazole (fptzH)[82, 88, 140] and a more recent used ligand, dipyrromethane (dipyH).[141-144] These ligands have to be deprotonated with a base in order to bind the ligand to the metal centre and in the case of dipyH an *insitu* oxidation of the precursor dipyH_2 is necessary.

In principle, the class of heteroleptic complexes can produce isomeric structures, but the already formed configuration in the dinuclear dimer is retained in the mononuclear complexes. The stable configuration is supported by the strong *trans*-effect of the C-Ir-bonds, allowing only C-Ir-N- and not C-Ir-C-bonds *trans* to each other. Nevertheless, the complexes exist as pairs of enantiomers, the *delta*- and *lambda*-isomers (Δ, Λ), which are usually indistinguishable and have identical properties.[106, 131-133, 145]

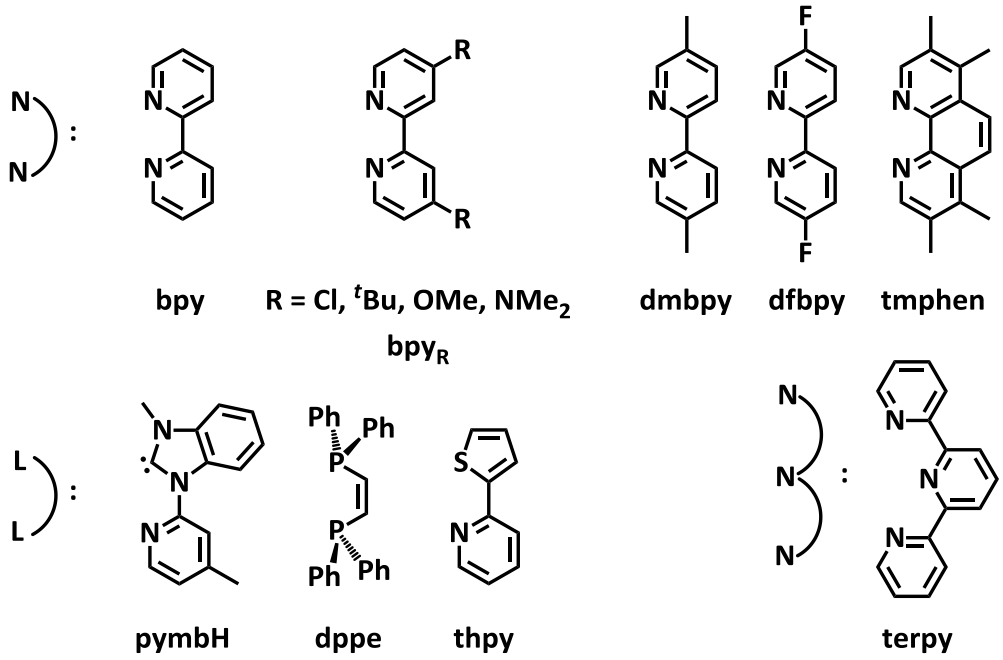

Figure 8 Ancillary ligands to yield monocationic (N^N, L^L) iridium complexes and 2,2´:6´,2´´-terpyridine (terpy) for the preparation of $Ir(terpy)_2^{3+}$ complexes.

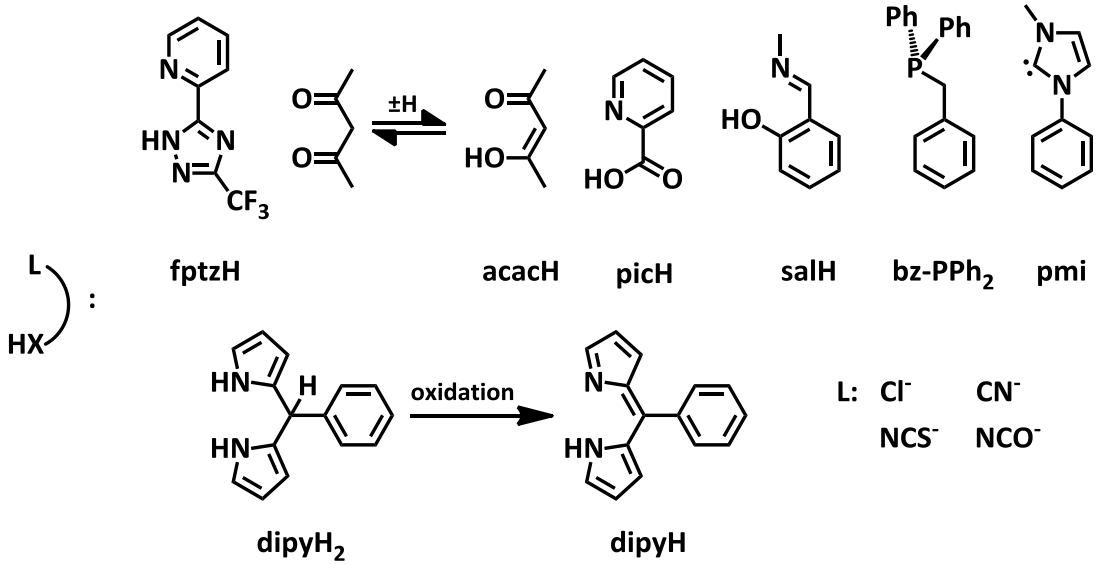

Figure 9 Ancillary ligands for achieving neutral (L^X) or anionic (L_2) iridium complexes.

Anionic complexes are scarce but can be achieved with the use of two monoanionic instead of an ancillary ligand, such as Cl^-, CN^-, NCS^- or NCO^-.[80, 84, 86, 145]

Moreover, the traditional use of the nitrogen and carbon binding sites in the cyclometalated complexes is extended with heteroatoms such as sulphur (thpy, cf. Figure 8) and phosphorus (dppe, cf. Figure 8).[82, 85, 146]

In addition to the bidentate binding motif of the homo- and heteroleptic complexes, several alternatives were developed which use two terdentate ligands (N^N^N (see Figure 8), N^C^N, N^N^C, C^N^C or N^C^C) to yield $Ir(ter)_2^{3+}$ complexes.[8, 66-67, 84-85, 127, 147-151] The use of a terdentate, bidentate and a mono-binding ligand yields, e.g. Ir(N^C^N)(C^N)Cl.[152-153] Further options use other heteroatoms in the terdentate ligands such as C^N^O.[153] Monocyclometalated complexes such as $Ir(ppy)(bpy)_2^{2+}$ are accessible, but are seldom described in literature.[129, 154]

1.2.2 Electrochemical Properties of Selected Iridium(III) Complexes[1]

In this section, characteristics of the oxidation and reduction potentials are highlighted for a series ranging from *tris*-2,2´-bipyridine iridium complexes to *tris*-cyclometalated complexes. The intermediate case, *bis*-cyclometalated complexes, will be discussed in detail, too.

In Table 2 a list of iridium complexes is presented where characteristic trends are illustrated. The selected complexes are built from diverse ligands which can be found in Figure 7–9. The first entry shows the $Ir(bpy)_3^{3+}$ complex with a high value for the first oxidation process (1.76 V),[129, 156] which is in line with the relatively high oxidation state of the metal centre that makes an oxidation process difficult.[84, 129] Conversely, the reduction is achieved more easily (−1.24 V)[129, 156-157] compared to all other complexes. However, this

[1] Due to different references used for electrochemical potentials listed in the literature, the present work follows the IUPAC 'recommendation on reporting electrode potentials in nonaqueous solvents'[155] and all measured electrochemical potentials are referenced against the ferrocen/ferrocenium (Fc/Fc^+) redox couple. Electrochemical potentials which are extracted from the literature are converted to this redox couple with: $V_{Fc/Fc+} = V_{SCE} - 0.41$ V (this value is solvent dependent) and $V_{Fc/Fc+} = V_{NHE} - 0.654$ V.

effect on the reduction is only less pronounced because it is strongly correlated with the reduction potential of the used isolated ligands (*vide infra*).[156]

Table 2 Selected iridium complexes constructed from ligands shown in Figure 7–9, their electrochemical properties ($E_{1/2}$) and the corresponding redox difference $\Delta E_{1/2}$ between each first reductive and oxidative potential. Substitution trends are highlighted with green and blue arrows.

complex	$E_{1/2}$ (ox) / V	$E_{1/2}$ (red) / V	$\Delta E_{1/2}$ / V	ref.
$\mathbf{Ir(bpy)_3^{3+}}$	1.76[i,c]	−1.24[r]	2.88	[129, 156-157]
$\mathbf{Ir(ppy)(bpy)_2^{2+}}$	1.64[r]	−1.61[r]	3.25	[158]
$\mathbf{Ir(ppy)_2(bpy)^{+}}$	0.87[r]	−1.78[r]	2.65	[81]
$\mathbf{Ir(ppy)_2(bpy_{tBu})^{+}}$	0.80[r]	−1.92[r]	2.72	[159]
$\mathbf{Ir(Fpmpy)_2(bpy_{tBu})^{+}}$	0.92[r]	−1.91[r]	2.83	[159]
$\mathbf{Ir(dFp\text{-}CF_3py)_2(bpy_{tBu})^{+}}$	1.28[r]	−1.78[r] / −2.09[r,a]	3.06	[159]
$\mathbf{Ir(ppz)_2(bpy_{Cl})^{+}}$	0.97[r]	−1.54[r]	2.51	[160]
$\mathbf{Ir(ppz)_2(bpy)^{+}}$	0.95[r]	−1.80[r]	2.75	[107]
$\mathbf{Ir(ppz)_2(bpy_{tBu})^{+}}$	0.95[r]	−1.89[r]	2.84	[107]
$\mathbf{Ir(ppz)_2(bpy_{OMe})^{+}}$	0.99[r]	−1.90[r]	2.89	[107]
$\mathbf{Ir(ppz)_2(bpy_{NMe2})^{+}}$	0.77[i] / 1.47[i,b] / 1.57[i,b]	−2.19[i]	2.96	[160]
$\mathbf{Ir(ppy)_3}$	0.31[r]	−2.70[r]	3.01	[84, 134]
$\mathbf{Ir(ppz)_3}$	0.39[r]	-	> 3.39	[134]

All potentials were extracted from the literature and were converted with respect to the ferrocene/ferrocenium redox couple (Fc/Fc^+), see footnote *vide supra*.

[a] reduction of the cyclometalating ligand ($dFp\text{-}CF_3py$), [b] oxidation of the ancillary ligand (bpy_{NMe2}), [c] cathodic peak potential

[r] reversible, [i] irreversible.

The last two entries deal with the *tris*-cyclometalated complexes $Ir(ppy)_3$ and $Ir(ppz)_3$ using 2-phenylpyridine (ppy) and 2-phenylpyrazole (ppz) as cyclometalating ligands (see Figure 7). The potentials for the oxidation is shifted by ca. 1.45 V to more negative potentials (0.31–0.39 eV) compared to $Ir(bpy)_3^{3+}$, because the σ-donating C-atoms push electron density towards the iridium core, facilitating the oxidation process. In contrast, the reduction occurs at more negative potentials (−2.7 V) or, in the case of $Ir(ppz)_3$, cannot be measured under the applied conditions.[84, 134] This observation is again explained by the reductive characteristics of the ligands, especially of the more electron-deficient heterocycles, pyridine and pyrazole.

Substituting one bpy ligand with a ppy ligand results in the *mono*-cyclometalated complex $Ir(ppy)(bpy)^{2+}$ which is slightly easier to be oxidised at an oxidation potential of 1.64 V than $Ir(bpy)_3^{3+}$. Conversely, the reduction is achieved at a more negative potential (−1.61 V).

In line with that are the oxidation and reduction potentials of the *bis*-cyclometalated complex ($Ir(ppy)_2(bpy)^+$) with two 2-phenylpyridines and one 2,2´-bipyridine as cyclometalating and ancillary ligand, respectively. As expected, both reductive and oxidative potentials are in between the *mono*- and *tris*-cyclometalated complexes. Hence, the first reduction can be measured at −1.77 V.[81] Again the reduction value is close to the value found for the Ir-bpy fragment in the $Ir(bpy)_3^{3+}$ complex. Likewise, the *bis*-cyclometalated complexes benefit from the σ-donor ability of the carbon binding site, but compared to the *tris*-cyclometalated complexes the effect is reduced and the oxidation occurs at 0.87 V (vs. 0.31 V in $Ir(ppy)_3$).[81]

The other entries of Table 2 show general trends (green and blue arrows) depending on different functionalisations attributed to either the cyclometalating ligand or the ancillary ligand, here 2,2´-bipyridine, with electron donor or acceptor substituents. Furthermore, the following examples illustrate which fragments/ligands of the complexes are responsible for certain redox properties. The first structure-property relationship concentrates on the variation of the cyclometalating ligands with electron acceptors at the phenyl ring of 2-phenylpyridine. Increasing the acceptor strength on the coordinating phenyl ring results in a reduced electron-donating effect of the carbon atom binding to the iridium metal. Hence, the oxidation potential increases from 0.80 to 1.28 V from 2-phenylpyridine (ppy) to 2-(2,4-diflourophenyl)-5-trifluoromethanepyridine (dFp-CF_3py), displayed by the blue arrow in

Table 2.[159] Whereas the iridium oxidation is harder to realise, the reduction potential of the 4,4´-di-*tert*-butyl-2,2´-bipyridine (bpy_{tBu}) is not affected and therefore stays constant at around −1.8 to −1.9 V. Furthermore, a second reduction of the electron-poor cyclometalating ligand dFp-CF_3py is accessible, too.[159] In conclusion, the tendency of increasing the oxidation potential of the iridium core by adding electron withdrawing substituents on the cyclometalating ligand goes along with a decreased electron density of the phenyl-iridium fragment. Additionally, DFT calculations support the highest occupied molecular orbital (HOMO) character of the phenyl-Ir fragment in a wide range of investigated complexes.[80-81, 85-87, 107, 137, 140, 145, 159, 161-169]

In contrast, regarding the reduction of the *bis*-cyclometalated complexes one has to distinguish between the reduction occurring at the heteroaromatic ring of the cyclometalating ligand and at the ancillary ligand. In other words, the reduction occurs on the fragment with the highest electron deficiency. In most cases, the ancillary ligand (Figure 7) is easiest to reduce. Consequently, the complexes with non-aromatic ancillary ligands, e.g. acetyl acetonate, have very low reduction potentials and therefore the origin of the first reduction is the heteroaromatic fragment of the cyclometalating ligand, as in the *tris*-cyclometalated complexes (*vide supra*).[134, 145, 167]

To demonstrate the electron accepting ability of the ancillary ligand, a comparison of different donor- and acceptor-substituted 2,2´-bipyridine ligands (bpy_R: R = Cl, H, ^{t}Bu, OMe, NMe_2, see Figure 7) are listed in Table 2 with ppz as cyclometalating ligand. The green arrow (Table 2) displays that electron donating substituents result in more difficult reduction potentials (−1.89 to −2.19), compared to the unsubstituted bpy (−1.80 V). On the contrary, electron withdrawing substituents, such as Cl, reduce the electron density on the ligand and make the reduction more feasible (−1.54 V).[107, 160] Analogously, the reduction is centred at the ancillary ligand which is equivalent to the addition of an electron to the lowest unoccupied molecular orbital (LUMO). DFT calculations assist in the visualisation of this observation.[80-81, 85, 87, 107, 137, 140, 145, 159, 161-169] Although, the spatial extent of the LUMO is restricted to the ancillary ligand, the ligand still may influence the HOMO of the complexes by interacting with the Ir *d*-orbital.[87, 100, 145] This can be observed for the $Ir(ppz)_2(bpy_{NMe2})^+$, where a strong electron donor (NMe_2) affects the HOMO energy resulting in an easier

oxidation (0.77 V) compared to the other bpy complexes in this series (*ca.* 0.95 V).[132, 137, 161, 170]

In total, the described electrochemical structure-property relations of the *bis*-cyclometalated complexes open the possibility to easily tune the HOMO and LUMO energies. The big advantage is the individual tuning of either the HOMO energies by reducing or increasing the electron density of the Ir-phenyl fragment with electron withdrawing or donating substituents, respectively. Moreover, substitution of the ancillary ligand with extended π-systems or electron push or pull substituents help to stabilise or destabilise the LUMO. Furthermore, *bis*-cyclometalated iridium complexes show reversible redox behaviour of either reduction or oxidation (Table 2), which is beneficial for application purposes. As a consequence of the electrochemical fine-tuning, the photophysical properties of $Ir(C^N)_2(N^N)^+$ complexes are strongly influenced by attached substituents and will be reviewed in the next paragraph.

1.2.3 General Photophysical Properties of Iridium(III) Complexes

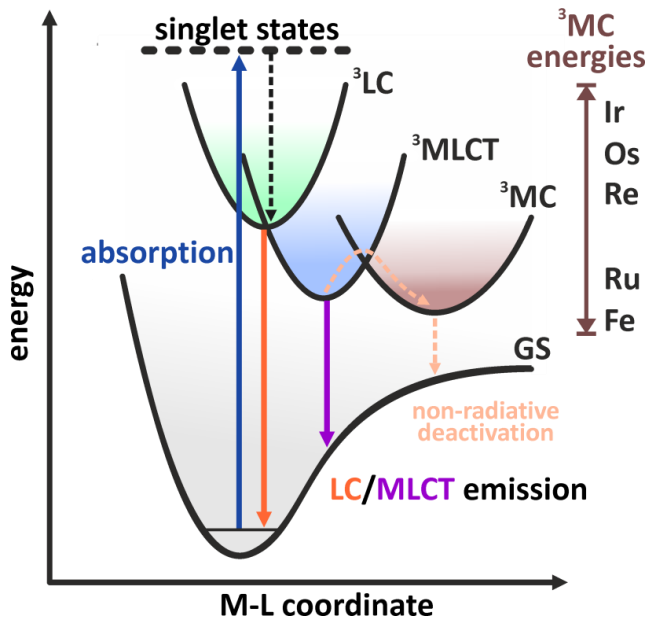

Figure 10 Electronic transitions in transition metal polyimine complexes of Fe, Ru, Re, Os and Ir.

As mentioned in the introduction, despite the big advantages of $Ru(bpy)_3^{2+}$ as a photosensitiser with a unique combination of chemical stability, redox properties and excited-state reactivity, the low-lying triplet metal-centred (^{3}MC) states set limits for several application, e.g. emitting devices.[84] Besides, the change of the metal centre to other d^6-elements such as rhenium (Re(I)), osmium (Os(II)) or iridium (Ir(III)), opens new pathways to novel features. The drawback of low-lying, non-emissive ^{3}MC states in iron (Fe(II)) or ruthenium metal complexes (see Figure 10) can be circumvented using metals with a higher ligand-field

splitting energy (LFSE) in an octahedral ligand field. This is ascribed to the different spatial extension of the involved d-orbitals, where the 6d metals, such as Re, Os and Ir, have the highest expansion. In addition, the LFSE of cyclometalated iridium complexes is further increased compared to the *tris*-diimine complexes, because of the electron pushing Ir-C-bond. Therefore, ^{3}MC states play a minor role in the deactivation of excited states of iridium complexes.[80-81, 84, 88, 138, 159, 171-172]

Absorption Characteristics

Concerning the absorption characteristics of cyclometalated iridium complexes, a look on the involved orbitals seems useful. Thus, in Figure 11, an simplified picture of the orbitals of a *bis*-cyclometalated iridium complex is presented, which shows essential orbitals involved in the light absorption process. First, the LFSE between the t_{2g}(Ir), and e_g(Ir) orbitals is very high and can be neglected (Figure 11, grey arrow). Hence, the discussed complexes all have a low-spin configuration in the ground state.[11, 84, 171] Second, the HOMO consists, in addition to the t_{2g}-orbitals, of π-orbitals of the phenyl ring of the cyclometalating ligand (L) which is in accordance to the electrochemical findings (*vide supra*).[80-81, 85-87, 107, 137, 140, 145, 159, 161-169] Iridium orbital admixture to the ligand orbitals has often been observed in iridium complex orbitals, but there are some important exceptions. In general, the LUMO is composed of orbitals which are located only at the ancillary ligand (L'). This is only true for ancillary ligands with low-lying LUMOs with extended π-systems, such as 2,2´-bipyridine.[80-81, 84-85, 105, 107, 123, 137] Conversely, in *bis*-cyclometalated complexes with e.g. acac as ancillary ligand and in *tris*-cyclometalated complexes the LUMO is extended over the heteroaromatic part of the cyclometalating ligand orbitals (π^*(L)).[82-84, 86-88, 106, 139-140] However, in the vast majority of complexes, the HOMO-LUMO gap is given by the t_{2g}(Ir)-π (L) and π^*(L'). Although DFT calculations demonstrate that the LUMO is solely located at the ancillary ligand,[80-81, 85, 87, 107, 137, 140, 145, 159, 161-169] the inductive effect of the ancillary ligand towards the iridium centre cannot be neglected and affects the HOMO energy as shown by *Nazeeruddin et al.*[100] and *Thompson* and co-workers.[145]

Further accessible orbitals involved in the light absorption are occupied π-orbitals of either the cyclometalating ligand (π (L)) or the ancillary ligand (π (L')). The possible electronic

excitations in cyclometalated iridium complexes are summarised in the following: i) The typical HOMO-LUMO absorptions are metal-to-ligand charge-transfer (ML'CT) transitions (Figure 11, red arrow), where an electron of the t_{2g}(Ir)-π (L)-orbital is promoted to the empty π*(L')-orbital of the ancillary ligand, resulting in a CT state with an oxidised iridium centre (Ir^{IV}) and a reduced ligand framework (L'^{-}). ii) The ligand-centred (L´C) transition is located only on the ancillary ligand and is based on a π-π*(L')-excitation (Figure 11, blue arrow). iii) Further excitations are MLCT transitions between the metal centred orbitals and the cyclometalating ligand, iv) LC transitions within the cyclometalating ligands and v) ligand-to-ligand charge-transfer (LL'CT) transitions between the cyclometalating and the ancillary ligand (the latter three cases are not shown in Figure 11).[11, 80-81, 84-86, 88, 171, 173]

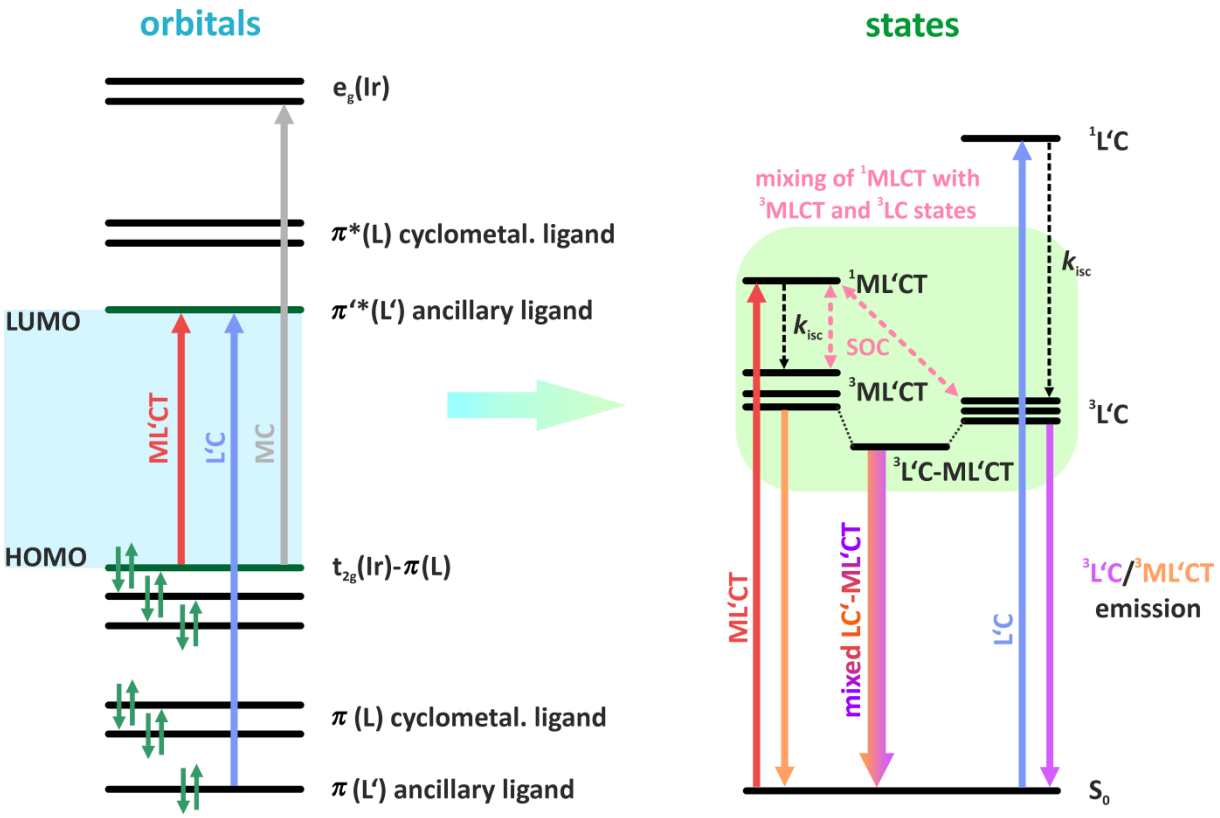

Figure 11 Electronic transitions (e.g. ML'CT and L'C) in cyclometalated complexes are assigned to specific transitions between orbitals (left) and correspond to specific states (e.g. ^{1}MLCT, ^{3}MLCT, ^{1}LC or ^{3}LC, right).

In a next step the orbital picture is transferred to a state picture (Figure 11, right), where transitions between specific orbitals are assigned to specific states, e.g. the HOMO-LUMO transition to the singlet MLCT state. The transformation allows a view on the energetic

situation of the involved states relative to each other. Moreover, states created through spin-orbit coupling (SOC) can be incorporated. Indeed, triplet states have a deep impact on the photophysics of iridium complexes.

The ^{1}MLCT transition, which is correlated to the optical HOMO-LUMO gap, can be estimated roughly by the redox potential difference $\Delta E_{1/2}$ (see Tab. 2). The reason for this is the MLCT character of the transition, where an electron is removed from the metal-phenyl fragment and added to the ancillary ligand, which is equivalent to the ionization potential and the electron affinity of the complex.[107, 132, 145, 159, 161, 174]

In general, the absorption bands corresponding to the HOMO and LUMO transitions (MLCTs) have relatively low extinction coefficients (ε_{abs} = 1000–10 000 M^{-1} cm^{-1}),[81, 83, 106-107, 123, 132, 134, 145, 159, 161, 173, 175-176] which is due to the poor spatial overlap between these orbitals. Interestingly, the formally spin-forbidden triplet ^{3}MLCT gains intensity by mixing with the close-lying ^{1}MLCT transition through spin-orbit coupling (SOC). The SOC is modulated by the iridium core having a very high SOC constant ξ(Ir)[157] = 3909 cm^{-1}. The same is true for the LC absorptions, where ^{1}LC and to a much weaker extend ^{3}LC, resulting from the SOC of iridium, can be observed. Although, the metal participation is less distinct in the ligand-centred absorption, the occurrence of the ^{3}LC transition can be explained by the SOC between the ^{1}MLCT and ^{3}LC states. Thus, SOC is more efficient when the energy difference ($\Delta E_{MLCT-LC}$) between ^{1}MLCT and ^{3}LC states gets smaller (Figure 11). $\Delta E_{MLCT-LC}$ is typically in the range of 1000–5000 cm^{-1} and with small $\Delta E_{MLCT-LC}$ values the ^{3}LC transition gets partially allowed.[86, 145, 173, 176-180] However, the intensities of the singlet LC transitions have a much higher intensity (> 20 000 M^{-1} cm^{-1}) than the MLCT transitions and depend on the ligand framework. Moreover, the absorption intensities reflect more or less the extinction coefficients of the non-bonded ligands.[81, 83, 106-107, 123, 132, 134, 145, 159, 161, 173, 175-176]

The energy sequence of the four transitions is ^{1}LC > ^{1}MLCT > ^{3}MLCT ≈ ^{3}LC.[84-86, 145, 172-173] The energetics can be explained by the higher energy content of the ^{1}LC compared to ^{1}MLCT transitions (Figure 11, left) and by the different exchange energies of the two singlet-triplet pairs ^{1}LC/^{3}LC vs. ^{1}MLCT/^{3}MLCT. Due to the larger spatial extension of the MLCT transition (from Ir-phenyl to L or L') compared to the more localised LC transition in the ligands (π-π*(L or L')) the exchange energy is usually larger for LC transitions than for MLCT transitions.[85-86, 178]

In principle, each of the two triplet states (^{3}LC and ^{3}MLCT) split into three substates in the absence of an external magnetic field which is called zero-field splitting (ZFS). The extent of the splitting is again influenced by the metal. For example, the ZFS energies of ^{3}MLCT states are between 10 and 200 cm^{-1}, whereas pure ^{3}LC states split by less than 1 cm^{-1}, because of less metal admixture of the involved orbitals. Likewise, the latter have similar splitting energies as free organic ligands (approx. 0.01 cm^{-1}).[85, 89, 103, 138, 177-178, 181]

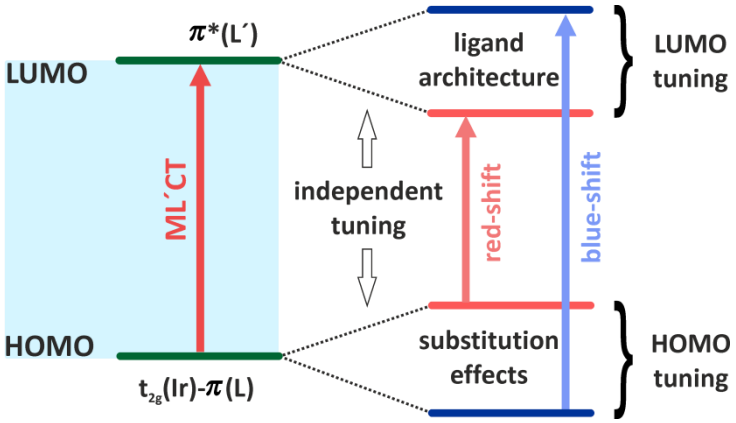

Figure 12 Independent tuning of HOMO and LUMO energies, resulting in a blue- or red-shift of the MLCT transition energy.

Undoubtedly, the big advantage of MLCT transitions of heteroleptic, *bis*-cyclometalated iridium complexes is the control of the MLCT energy by independently modulating either the HOMO and/or the LUMO energies (Figure 12). As already discussed in section 1.2.2, the HOMO energies can be shifted with electron withdrawing or donating substituents. On the other hand, the LUMO energies can be altered with larger π-systems or again by substitution of the ancillary ligand, e.g. bpy with electron push or pull substituents. Hence, the transitions of the MLCT comprise the spectral range from the ultraviolet (UV) to the visible (Vis) by simple synthetic modifications.

Emission Characteristics

The emission properties of cyclometalated iridium complexes are the reason for their popularity and extensive use in diverse applications (*vide supra*). Their high-lying, metal-centred states make them superior to other cyclometalated transition metal complexes.

The absorption characteristics revealed that a deliberate control over the excited states-energies of the discussed complexes can be achieved. The next step is connected to the excited state-dynamics, which can be summarised with the question: what happens after

a complex absorbs a photon? In general, the absorption of a photon is related to the *Franck-Condon* principle, which states that the nuclear configuration is unchanged during an electronic transition.[182-185] However, the electronic configuration after excitation is completely different and the nuclear coordinates respond to this new situation by energy redistribution into diverse vibrational modes and to the environment. The release of energy to e.g. the solvent bath is the general case and is called vibrational energy relaxation (VR).[182] But iridium complexes offer a wide range of deactivation processes, which will be discussed in the following. First, the initial deactivation processes are governed by internal conversion from higher-lying ^{1}LC or ^{1}MLCT states to the lowest ^{1}LC and ^{1}MLCT states with rate constants greater than 10^{13} s^{-1}.[186-188] Second, the outstanding property of iridium complexes is the high spin-orbit coupling constant, permitting facile intersystem crossing (ISC). Thus, the change of the multiplicity of the excited states is very effective in iridium complexes and the correlated rate constant is on the order of 10^{13} s^{-1}.[186-190] The lowest excited state of cyclometalated iridium complexes can either have LC or MLCT character. The more general case is a mixed triplet LC-MLCT state (Figure 11, right) as a consequence from, first, the shared LUMO of both transitions and, second, the similar energies of both triplet states and the ^{1}MLCT state (*vide supra*). Consequently, the mixing between the ^{3}LC and ^{1}MLCT excited states is modulated through spin-orbit coupling (Figure 11). Finally, restoring of the ground state (S_0) is achieved by radiative or non-radiative transitions from the lowest excited state (ES) to S_0. In cyclometalated iridium complexes the spin-forbidden radiative deactivation of the excited state, thus, is phosphorescence.[182] However, the phosphorescence quantum yield depends only on the energy of the emissive state and on the and on the contribution of competing, non-radiative deactivation channels and not on the spin-forbidden nature of these processes because of the strong SOC of the iridium core as discussed above. Concerning the energy of the emissive state, two consequences result: i) with a high-energy excited state, ^{3}MC levels are thermally more accessible[138, 191] (Figure 10) and ii) in the opposite case a low-lying ES is governed by the energy-gap law which means that the rate of internal conversion increases with decreasing energy gap of the involved states.[86, 107, 137, 145, 192-193] Accordingly, blue and red emitting chromophores may favour non-radiative deactivations. For a quantitative description of the competing processes the phosphorescence quantum yield (φ_{phos}) helps to distinguish between radiative (k_{phos}) and non-radiative ($k_{non\text{-}rad.}$) relaxation: $\varphi_{phos} = k_{phos} / (k_{phos}$

+ $k_{non\text{-}rad.}$). In general, cyclometalated iridium complexes possess a k_{phos} value of 10^4–10^5 s^{-1} and phosphorescence quantum yields of up to 100 %.[83-87, 105, 107, 134-139, 145, 159, 169-170, 175, 191, 194-195]

Coming back to the mixed LC-MLCT nature of the emission of the discussed complexes, only qualitative features how to distinguish between a more LC or MLCT character are available. These are based on the different properties of the more extended MLCT transition compared to the more localised LC transition. First, the spectral features of a 100 % LC-emission appear as structured spectra with vibrational fine-structure (purple and blue spectra, Figure 13) and have smaller rate constants (longer lifetimes) than the MLCT transitions. In addition, for LC emission solvatochromic and rigidochromic[1] behaviour is observed in rare cases because excited and ground state potential surfaces do not differ extremely. On the other side, pure MLCT emissions show broad and structureless spectra (red, yellow, green, and cyan spectra, Figure 13) typically arising with a large *Stokes*-shift. The increased metal character of the emission results in a faster SOC, resulting in shorter lifetimes for the excited state. Furthermore, solvatochromism and rigidochromism[1] are classical associates of MLCT phosphorescence, due to the charge transfer character (*vide supra*).[83-86, 105, 107, 142, 173, 175-177, 191] The magnitude of iridium participation to the mixed LC/MLCT emission is difficult to specify and in many cases only a rough estimate is possible. For example, many phosphorescence spectra of cyclometalated iridium complexes show a broad emission feature typically observed for MLCT transitions. But upon cooling to 77 K (in a solid matrix of 2-MeTHF) a hypsochromically shifted, structured LC emission appears, due to the destabilisation of the MLCT state.[39, 84, 107, 136, 145, 173, 175-177] Further indicators for the mixed nature and a significant metal contribution are the polarisation, intensity, lifetime and zero-field splitting of the LC emission compared to the emission of the isolated ancillary ligand. Usually, the polarisation of the π-π^* emission of non-coordinated ligands can be characterised by an out-of-plain polarisation, which changes to an in-plain polarised transition when coordinated to the metal.[177] Furthermore, the lifetime of the excited state

[1] While going from room-temperature to a glassy matrix, polar solvent molecules are more and more hindered to align their dipoles to the new electronic situation of the excited chromophore and consequently more polar excited states cannot be stabilised by the surrounding solvent at lower temperatures anymore. The excited state is therefore higher in energy and the emission maximum is shifted hypsochromically.[107, 138, 145, 148, 193, 196]

decreases and the intensity of the transition increase due to a more spin-allowed process. Finally, in comparison to the pure organic ligands the ZFS is larger for the LC states and increases with increasing metal participation.[89, 103, 173, 177-178, 181, 197] In conclusion, an absolute classification in pure LC or MLCT transition can hardly be achieved because many aspects come into play. Despite the difficulty of assigning the character of the phosphorescence, tuning the HOMO-LUMO gap is a powerful tool to control the emission energy of the cyclometalated iridium complexes as demonstrated in Figure 13 where the concept of colour tuning was successfully applied.[105]

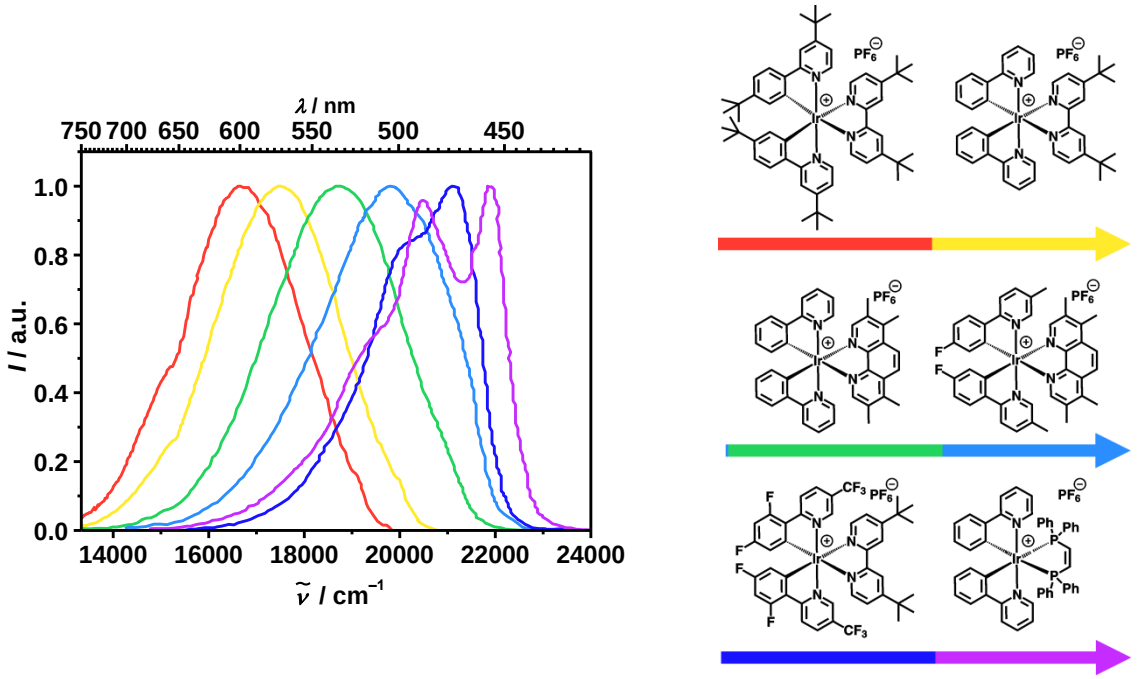

Figure 13 Demonstration of the emission tuning of cyclometalated iridium complexes by a series of six examples applying the concept of independent HOMO-LUMO tuning. The colours of the spectra correspond to the complexes with the same underplayed colour (Spectra were extracted with DigitizeIt from lit.[105]).

The used complexes illustrate the above mentioned strategy of independently varying the HOMO and LUMO energies. As a consequence of different absorption energies, the excited-state energies change, too. As a result a wide colour versatility is obtained. The structures in Figure 13 (right) have, e.g. electron withdrawing substituents (F, CF_3) at the phenyl ring of the cyclometalating ligand to stabilise the HOMO energy which shifts the absorption into the UV and results in blue emission. Furthermore, electron donating groups

(^{t}Bu) at the ancillary and cyclometalating ligands cause low-energy absorption and, consequently, red phosphorescence is observed.

The 'colourful' versatility of the iridium complexes make them attractive for optoelectronic devices, such as OLEDs (*vide supra*). However, in the current work neutral iridium complexes with dipyrrin ligands are used which proved to be weak emitters.[142] Therefore, the emissive aspect of the iridium complexes is not important within this project aim. Even more, the focus lies on the use of the absorption features (photosensitation) and the follow-up reactions of the long-lived, excited states (reductive or oxidative exited state quenching) of the iridium complexes.

1.3 Magnetic Field Effects on the Kinetics of Charge-Separated States

An electron transfer (ET) event is often followed by the formation of a charge-separated (CS) state (e.g. a radical pair (RP)) where one redox centre is oxidised and the other one is reduced. Thus, a radical pair is obtained. While ET reactions of donor-bridge-acceptor compounds have widely been explored,[24-28] their spin state often is ignored.[198-199] The involved radical pairs may form equilibria between singlet and triplet species which are sensitive to an external magnetic field. This aspect may be used to control photophysical[10, 199-214] and photochemical[198, 215-224] processes in general but also has an impact on optoelectronic device performance as in OLEDs[225-228] and photovoltaics.[229-234] Magnetic field effects are also discussed as the origin of avian navigation under the influence of both light and the earth magnetic field ("magnetic compass") or in context of magnetoreceptors in other living organisms.[235-240] The *in vivo* investigation of the navigation process is very complex and almost impossible. Therefore magnetic-field effects (MFEs) on charge-recombination kinetics in isolated proteins such as cytochrome[241] but also in artificial model systems gained more attention quite recently.[242-243] Clearly, as the geomagnetic field is quite weak (~50 μT) one aims at finding and investigating processes that are sufficiently pronounced at very low fields.

In this chapter the basic principles of MFEs on the kinetics of CS states will be introduced which help to understand under which conditions MFEs can occur and how they can be influenced. Some of the studied complexes in this work are investigated under magnetic field dependent transient absorption spectroscopy in the nanosecond time range (chapter 3.1.5) and their interpretations are based on the principles explained in this introductory chapter.

1.3.1 Basic Principles of Linked Radical Pairs

First of all, the basic principles of linked radical pairs at zero-magnetic field will be sketched. In systems with unpaired electrons, as in a radical pair, the two electrons are located in different orbitals of a molecule and are separated by a given distance. The resulting spin situation is always accompanied with the creation of singlet and triplet

configurations. The quantum mechanical treatment of the spin wave function of two unpaired spins result in a total spin S of zero (S = 0) for the singlet state and S = 1 for the triplet configuration. The latter arrangement can further be divided into three sublevels according to their orientation in space[1], based on the spin quantum number M_s = +1, 0, −1.[223, 244-250]

In general, singlet and triplet states are characterised by an energy difference (^{1}LE vs. ^{3}LE, Figure 14). Triplet states often are lower in energy because of a higher orbital angular momentum compared to the singlet states (*Hund´s* rule). This energy difference $\Delta E_{S\text{-}T}$ can be expressed by 2J (J = electron spin-spin exchange energy) and decreases when the distance of the two parallel spins increases.[22, 205, 223-224, 244, 246, 251-256]

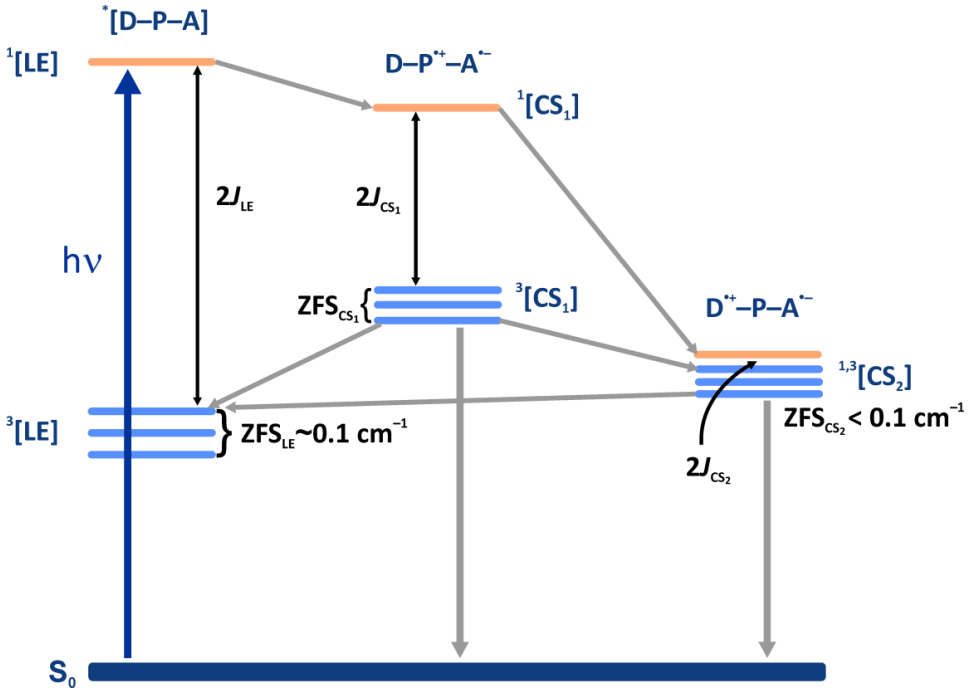

Figure 14 Simplified energy state diagram of an organic triad containing a photosensitiser (P), a donor (D) and an acceptor (A) unit. The separation (CS_1 and CS_2) of the unpaired electrons increases from the left to the right side, while the electron-electron exchange energy (2J) and the zero-field splitting (ZFS) decrease. Note that the spin conservation rule is strictly maintained during the electron transfer processes (grey arrows). LE = local excited.

[1] The four spin states consist of an αα and ββ alignment (triplet spins with S = 1 and M_s = +1, −1) and a linear combination of α and β, that is, αβ + βα and αβ − βα. The former linear combination results in the triplet state with S = 1 and M_s = 0 and the latter is the singulet configuration with S = 0 and M_s = 0. The spins of triplet states have a parallel and the singulet an anti-parallel orientation in a vector model for spin half particles.

In addition, a vanishing coupling between these two spins yields quasi-degenerate states with a negligible 2*J*-value at long spin-spin distances (> 10 Å), e.g. in $^{1,3}[CS_2]$ (Figure 14). The triplet sublevels deviate in energy due to electron-electron dipolar interaction and/or spin-orbit coupling. The contribution to the energetic splitting in the former case is in the range of 10^{-3}–10^{-1} cm^{-1} for e.g. organic radicals, whereas the latter can possess very large values of 1–200 cm^{-1} if transition metals are involved.[89] This splitting is called zero-field splitting because it appears even without an applied magnetic field. Charge separation (CS_1, CS_2) further decreases the ZFS, if spin-orbit coupling is omitted.[223, 255-256] The energy diagram in Figure 14 only shows processes which are based on the spin conservation rule,[22] but other singlet-triplet transition mechanism are possible in the case of negligible $\Delta E_{S\text{-}T}$. These will be discussed in the following.

Various population and depopulation channels are presented in Figure 15, which are typically observed in linked donor-acceptor radical pairs ($D^{\bullet+}\cdots A^{\bullet-}$) with little or no electron spin-spin exchange interaction (J < 0.008 cm^{-1}).[257-258] In general, the CS states under investigation are formed by photoinduced ET from locally excited (LE) states. Consequently, the spin situation in the CS states is initially dependent on the total spin of these precursor states (^{1}LE vs. ^{3}LE). In purely organic D···A systems only singlet RPs are formed as spin-orbit coupling is negligible and the spin conservation rule holds true ($\Delta S = 0$). On the contrary, the occurrence of precursors with sufficient SOC assistance, due to transition metal participation, may induce the population of triplet states. Once the radical pair has formed, the spin-crossover between both singlet and triplet RP states is mediated by isotropic hyperfine coupling (ihfc), which is explained in more detailed in this chapter (*vide infra*). Depending on the precursor state ^{*1,3}LE there exist several paths concerning the radical pair dynamics and yield of products (e.g. S_0 or local triplets (LT)) of the RP.[22, 198, 221, 223]

First (1), in case of an exclusively generated ^{1}RP, the ^{3}RP may only be observed due to a spin flip caused by ihfc. Hence, the rate constant for the deactivation to the ground state ($k_{1RP\text{-}S0}$) must be lower than for the isotropic hyperfine coupling driven spin flip (k_{ihfc}). Otherwise, if $k_{1RP\text{-}S0} >> k_{ihfc}$, the triplet state (^{3}RP) is not populated. However, k_{ihfc} is typically in the range of 10^7–10^8 s^{-1} [22, 221, 252, 255-256, 259] and therefore a competing process should be in the range of 10^9–10^{10} s^{-1} in order to circumvent the formation of a triplet RP. Second (2), in an initially formed ^{1}RP, where ihfc guarantees an efficient spin-flip process to ^{3}RP, one can think of two

subcases: 2i) A relaxation from ^{3}RP to local neutral triplet states (LT) of either donor or acceptor sites ($^*[^3$A···D] or *[A···^{3}D]) may be observed if these local triplet states lie energetically below the ^{3}RP state. This was intensively studied with rod-like donor-acceptor systems by *Wasielewski* and co-workers.[10, 206-212] However, these D-A-systems usually have a significant exchange interaction contribution and *Wasielewski´s* group could observe the so called *J*-resonance. This *J*-resonance occurs at an applied magnetic field when one of the triplet sublevels (T_+ or T_-) crosses the S state (at $\Delta E = 2J$) resulting in an enhanced singlet-triplet coupling. 2ii) If no such low-lying triplet traps are available and the ihfc rate is comparable to $k_{1RP\text{-}S0}$, the ^{3}RP acts as a delay buffer because charge-recombination ($k_{3RP\text{-}S0}$) to the ground state is forbidden. The only deactivation path is via back spin flip to the ^{1}RP and further by singlet recombination to S_0 resulting in an overall lower recombination rate.[260-262] Following the same train of thought, if a pure ^{3}RP is formed (3), the recombination kinetics are likewise influenced by 3i) the presence of low-lying triplet states and the competition between the rates for the triplet formation and the ISC to ^{1}RP. 3ii) If these triplets are not available, only recombination via the singlet pathway will proceed. Finally, the population of singlet and triplet RP states in a certain ratio (4) occurs if precursor states allow a mixing of spin states due to SOC.[221, 223, 263-264] In conclusion, the recombination of RPs to the neutral ground or excited state species is strongly affected by the spin dynamics of the degenerate singlet and triplet energy levels of the RPs. The effect of an applied magnetic field to this spin dynamics is further discussed in the next part with the help of the relaxation mechanism introduced by *Hayashi and Nagakura*.[198, 252]

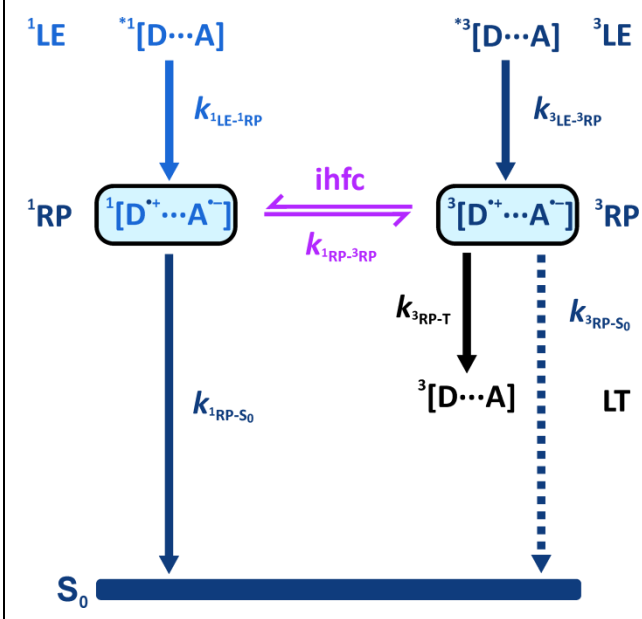

Figure 15 Population and depopulation channels of linked donor-acceptor (D···A) systems and corresponding rate constants (k) for the interconversion between singlet and triplet states (^{1,3}[]). Isotropic hyperfine coupling (ihfc) modulates the spin-flip of the radical pair (RP).

1.3.2 The Radical-Pair Model – Coherent and Incoherent Mechanism

In this section a closer look on the interconversion of singlet and triplet radical pairs is presented and the influence of a magnetic field on the dynamics of this interconversion is presented. Subsequently, only charge-separated states with very small 2*J* values ($^{1,3}[CS_2]$ in Figure 14) are discussed and therefore the singlet and triplet charge-separated states are quasi-degenerate. In 1984, *Hayashi* and *Nagakura* proposed the relaxation mechanism describing the change of dynamics between singlet and triplet radical-pair states upon applying a magnetic field.[198, 252, 265] This mechanism is based on the radical-pair mechanism developed earlier by *Closs* and *Kaptein*.[266-267] The magnetic field induced splitting of the triplet sublevels is based on the *Zeeman* effect, where states with $M_s \neq 0$ are affected by an external magnetic field. The interaction between S, T_0 on one side and $T_\pm$ on the other side is hampered, because the increasing energy separation of the triplet states reduces the rate of interconversion with the inverse of the magnetic field. Consequently, S-T_0 is the only effective singlet-triplet channel at high magnetic field.[22, 198, 223-224, 244-247, 252, 255-258, 268-270]

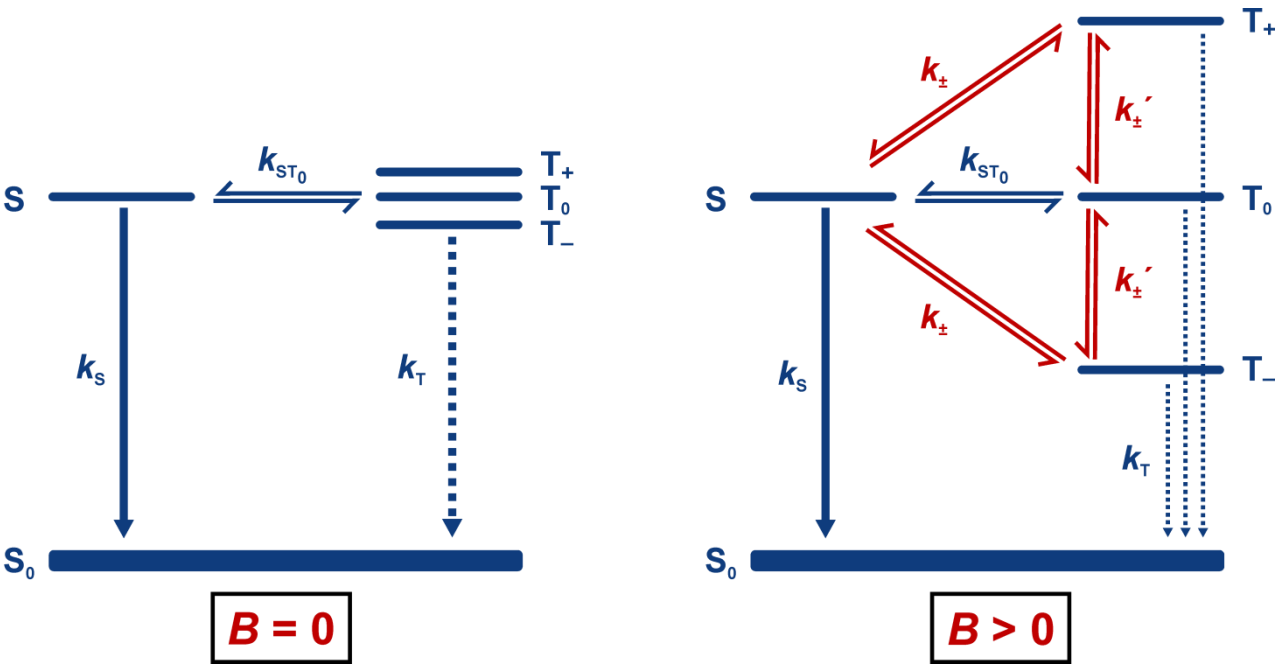

Figure 16 State diagram of the CS state including the zero (left) and non-zero (right) magnetic field case.

Figure 16 shows a state diagram of the singlet-triplet radical pair at zero-field $B = 0$ and at $B > 0$, where all population and depopulation processes (k_S, k_T) of the CS states (S_0, T_+, T_0 and T_-) are sketched. In the following low-lying triplet states are omitted for simplification. At zero-magnetic field only coherent processes (blue equilibria, k_{ST_0}) between the degenerate triplets and the singlet CS state can be observed, whereas at non-zero fields also incoherent relaxation processes (red equilibria, $k_\pm$ and $k_\pm'$) can occur either within the triplet manifold or between singlet and triplet CS states. *Hayashi et al*. showed that both rate constants $k_\pm$ and $k_\pm'$ can be merged together to one constant which will be denoted as $k_\pm$.[198-199, 214, 224, 252]

In the following, several effects will be presented which can result from the *Zeeman* splitting and affect the RP kinetics. The possible mechanisms are either of coherent or incoherent nature.

Coherent Relaxation Mechanism

i) Isotropic Hyperfine Coupling[1]

Hyperfine coupling is caused by the interaction of the magnetic field resulting from the spin moment of an unpaired electron with the magnetic fields induced by the magnetic dipoles of the non-zero nuclear spin atoms. As the donor and acceptor radical centres do not interact with each other, due to a large distance between the two spins and therefore a low coupling, both radicals can be treated as isolated species.[10, 22, 198, 223-224, 244, 254-255, 258-259, 268-272] Consequently, the specific magnetic fields B_i for the individual radicals *I* can be described in terms of the isotropic hyperfine coupling constant a_{ik} (determined by EPR measurements) and the corresponding nuclear spin quantum number I_{ik} of the involved nuclei *k* (eq. (4)).[198, 205, 223, 269-270, 273]

$$B_i = \sqrt{\sum_{ik} a_{ik}^2 I_{ik}(I_{ik}+1)} \qquad (4)$$

[1] The spin chemical literature is based on the electromagnetic cgs-system (cm-gram-second), where the magnetic induction constant is set to $1/4\pi$. Therefore, derivation of equations will be maintained in the Gaussian system and later on, if needed, transformations to the MKSA-system (meter-kilogram-second-ampere) from Gauss (G) to Tesla (T) is performed. (see p. 3 of lit.[223])

Although both radicals are isolated, a simple relation between B_1 (radical 1, e.g. donor site), B_2 (radical 2, e.g. acceptor site) and the magnetic half-field $B_{1/2}$ of the radical pair is shown with equation (5) (cf. pp. 37–39 of lit.[223]):

$$B_{1/2}{}^2 = 3\left(B_1{}^2 + B_2{}^2\right) \tag{5}$$

Isotropic hyperfine coupling (ihfc) mediates the magnetic field independent coherent spin-flip of the singlet and the degenerate triplet CS states. In the following, the time evolution of a triplet born radical pair is shown on the basis of the classical and semiclassical approach. Within these two approaches a zero-field and a high-field case are discussed. Starting with the classical way, one may consider three equilibria (k_{hfc}) between the degenerate singlet and triplet states at zero-field (Scheme 3),

$$\mathrm{S} \underset{k_{hfc}}{\overset{k_{hfc}}{\rightleftharpoons}} \mathrm{T}_0$$
$$\mathrm{S} \underset{k_{hfc}}{\overset{k_{hfc}}{\rightleftharpoons}} \mathrm{T}_{\pm} \qquad \text{(Scheme 3)}$$
$$\mathrm{T}_0 \underset{k_{hfc}}{\overset{k_{hfc}}{\rightleftharpoons}} \mathrm{T}_{\pm}$$

whereas at high fields only S-T_0 mixing is effective for the spin interconversion (Scheme 4):

$$\mathrm{S} \underset{k_{hfc}}{\overset{k_{hfc}}{\rightleftharpoons}} \mathrm{T}_0 \qquad \text{(Scheme 4)}$$

At zero field equal population of all three triplet states (^{T}) marks the beginning of the spin motion. The time dependent population of the singlet state $p_{s,zf}(t)$ can then be expressed by equation (6), whereas at high field equation (7) is obtained. Both equations result from the solution of the differential equations based on Scheme 3 and 4.

$${}^{T}p_{S,zf}(t) = \frac{1}{4}\left(1 - \exp\left[-4k_{hfc}t\right]\right) \tag{6}$$

$${}^{T}p_{S,hf}(t) = \frac{1}{6}\left(1 - \exp\left[-2k_{hfc}t\right]\right) \tag{7}$$

With ${}^{S}p_T = 3\cdot{}^{T}p_S$ the situation analogously can be described by a radical pair which is initially in a pure singlet state (^{S}) and the time evolution results in increasing triplet ($_T$) concentration.

Furthermore, the classical behaviour is contrasted to the semiclassical spin motion at zero- and high-field derived by *Schulten* and *Wolynes*.[259, 271, 274] According to these authors

the isotropic hyperfine coupling situation in each radical is reduced to a characteristic time constant τ_i for each radical *i* by the relation:[224, 259, 271, 273-274]

$$\frac{1}{\tau_i^2} = \frac{1}{6}\sum a_{ik}^2 I_{ik}\left(I_{ik}+1\right) \tag{8}$$

$$\tau_i = \frac{\sqrt{6}}{B_i} \tag{9}$$

For the singlet probability (p_S) of an initial triplet (^{T}) radical pair *Schulten and Wolynes* derived expressions for the zero- and high-field case, eq. (10) and (11), respectively.[224, 259, 274]

$${}^T p_{S,zf}(t) = \frac{1}{4}\left\{1-\frac{1}{9}\left[1+2\exp\left(-\frac{t^2}{\tau_1^2}\right)\left(1-\frac{2t^2}{\tau_1^2}\right)\right]\left[1+2\exp\left(-\frac{t^2}{\tau_2^2}\right)\left(1-\frac{2t^2}{\tau_2^2}\right)\right]\right\} \tag{10}$$

$${}^T p_{S,hf}(t) = \frac{1}{6}\left[1-\exp\left(-t^2/\tau_1^2\right)\exp\left(-t^2/\tau_2^2\right)\right] \tag{11}$$

In equation (11) the two individual time constants can be contracted to a single one by using the definition

$$\frac{1}{\tau^2} = \frac{1}{\tau_1^2}+\frac{1}{\tau_2^2} \tag{12}$$

With this definition, equation (11) is simplified to

$${}^T p_{S,hf}(t) = \frac{1}{6}\left[1-\exp\left(-t^2/\tau^2\right)\right] \tag{13}$$

For a fixed relation between τ_1 and τ_2: $\frac{1}{\tau^2} = \text{const.} = \frac{1}{\tau_1^2}+\frac{1}{\tau_2^2}$. Thereby, the dependency of the spin motion on the individual τ-values calculated by eq. (10) and (13) can be studied. In Figure 17 the singlet probability of the radical pair is plotted against the ratio of $t\tau^{-1}$.

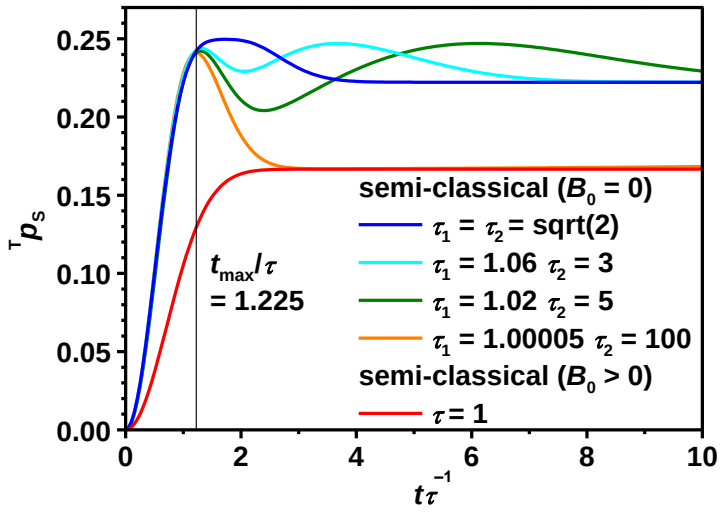

Figure 17 Spin motion due to isotropic hyperfine coupling of a radical pair starting with triplet character. The evolution of singlet probability $^{T}p_S$ is calculated by eq. (10) with different combinations of τ_1 and τ_2 at zero field which obey the relation $\frac{1}{\tau^2} = \text{const.} = \frac{1}{\tau_1^2} + \frac{1}{\tau_2^2}$. The high field limit is obtained by eq. (13). Values for τ_1, τ_2 and τ are given in the legend.

For short delay times all zero-field curves are identical until a first spin equilibrium is reached at ca. 0.25. Thereafter, one can observe a crossover to the high-field curve and an oscillatory return to equilibrium conditions, except for the orange curve which stays at the high-field limit of $^{T}p_S \approx 0.17$. The latter value is caused by the initially triplet concentration which removes the triplet sublevels $T_{\pm}$ from the coherent spin motion at high magnetic fields (Scheme 4). Both triplet sublevels comprise a concentration of 2/3 and do not participate at the coherent equilibrium situation. The remaining 1/3 is further affected by the statistical ratio of T_0/S = 1:1 and allows a maximum value of $^{T}p_S \approx 0.17$ under equilibrium conditions.[223] Furthermore, the progress of the zero-field curves (blue, cyan, green and orange) clearly shows that the maximum of the first spin equilibrium is for all curves at the same ratio of $t/\tau \approx 1.225$. Obviously, the spin evolution is not dependent on the individual radical times (τ_1 and τ_2), but on the overall lifetime τ. Therefore, the ratio t_{max}/τ is universal for all radical pairs and the factor 1.225 has to be multiplied with τ to get the t_{max} time for different radical pairs.

In the following, equations will be presented to estimate a hyperfine coupling limit τ_{hfc}. To get a rough estimate for the spin dynamics, the hfc limit can be calculated by equation (14).[223-224]

$$\tau_{hfc} = \frac{1}{\gamma_e B_{1/2}} \approx \frac{60\ \text{ns}}{B_{1/2}/G} \tag{14}$$

In this equation $\gamma_e = 1.76 \cdot 10^7\ s^{-1}\ G^{-1}$ is the gyromagnetic ratio of an electron and the magnetic half-field $B_{1/2}$ is defined in eq. (5).

Alternatively, τ_{hfc} can be calculated by a semiclassical approach. Thereby, eq. (14) is modified by eq. (15) by taking into account the factor of 1.225 for reaching the spin equilibrium and eq. (16) is obtained.

$$\frac{1}{\tau_i} = \frac{\gamma_e B_i}{\sqrt{6}} \tag{15}$$

$$\tau_{hfc} = \frac{1.225}{\gamma_e \sqrt{\frac{1}{6}(B_1^{\,2} + B_2^{\,2})}} = \frac{1.225 \times 3\sqrt{2}}{\gamma_e B_{1/2}} \approx \frac{300\ \text{ns}}{B_{1/2}/\text{G}} \tag{16}$$

Expression (16) results in prolonged hfc times compared to eq. (14) giving a more realistic picture of the kinetics.

The final approach to evaluate the hyperfine coupling limit combines the classical and the semiclassical spin motion picture. For that reason, the semiclassical spin motion is plotted for a fictive radical pair for the zero and high field case with $\tau_1 = \tau_2 = 1.0 \cdot 10^{-8}$ s in Figure 18 (solid curves). The transformation according to eq. (12) yields $\tau = 7.07 \cdot 10^{-9}$ s. Conversely, for the classical motion picture (dashed curves in Figure 18) the rate constant is chosen such that the total integral over the classical and the semiclassical high-field curves are equal ($k_{hfc} = 7.98 \cdot 10^7\ s^{-1}$). The resulting relation between these two high-field cases then can be expressed as follows:

$$k_{hfc} = \frac{1}{\tau_{hfc}\sqrt{\pi}} \tag{17}$$

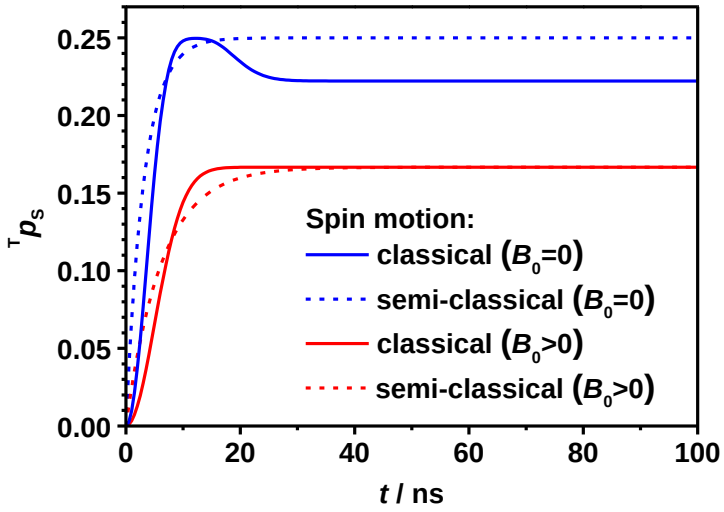

Figure 18 Spin motion due to isotropic hyperfine coupling of a radical pair starting with triplet character resulting in the evolution of singlet probability ${}^{T}p_S$. Solid curve: semiclassical model for a radical pair with $\tau_1 = \tau_2 = 1.0 \cdot 10^{-8}$ s (for the zero-field curve, blue) and thus $\tau = 7.07 \cdot 10^{-9}$ s (for the high-field curve, red). Dashed curves: classical description of spin motion with $k_{hfc} = 7.98 \cdot 10^{7}$ s^{-1} (see text for derivation of k_{hfc}).

Equation (12) is used in the following as starting point and τ_i is substituted by eq. (15). Furthermore, $B_{1/2}$ is used to simplify the resulting expression to obtain eq. (18) and with the help of eq. (17) the final equation for the rate constant of the hyperfine coupling (eq. (19)) is obtained, which is only dependent on the $B_{1/2}$ value.

$$\frac{1}{\tau^2} = \frac{\gamma_e B_1^2}{6} + \frac{\gamma_e B_2^2}{6} = \frac{1}{6}\gamma_e (B_1^2 + B_2^2) = \frac{1}{18}\gamma_e B_{1/2}^2 \qquad (18)$$

$$k_{hfc} = \frac{1}{\tau_{hfc}\sqrt{\pi}} = \frac{\gamma_e B_{1/2}}{3\sqrt{2\pi}} \qquad (19)$$

The advantage of eq. (19) is the fact that its derivation is easily accessible (only ESR parameters are necessary) and it combines both the semiclassical with the classical model. Moreover, the latter is the basis of the relaxation model in Figure 16 and therefore equation (19) will be used in the present work for the estimation of the hfc limit of radical pairs (see section 3.1.5).

ii) Δg-*mechanism*

Additionally, the singlet-triplet interconversion can be influenced by the coherent Δg-mechanism.[198, 223-224, 247, 253, 274] This type of coherent spin evolution usually is neglected in the case of aromatic radicals because their g-values only differ by less than 0.001 from the typical value of 2.0023.[247, 253] The difference in the g-values, however, may have a strong effect on the radical pair evolution for radicals where atoms with a high SOC contribution are involved, especially at higher magnetic fields. This can be explained by a vanishing *Zeeman* term ($\Delta g \cdot \mu_B \cdot B$) at low magnetic field. As a consequence eq. (10) remains unchanged. On the contrary, eq. (13), describing the semiclassical spin-motion at high-field, is modified by the *Zeeman* term giving eq. (20).[274]

$$^{T}p_{S,hf}(t) = \frac{1}{6}\left[1 - \exp\left(-t^2 \,/\, \tau^2\right)\cos\left(\Delta\omega t\right)\right] \tag{20}$$

where

$$\Delta\omega = \frac{\left(g_1 - g_2\right)\mu_B B}{\hbar} = \frac{\left(\Delta g\right)\mu_B B}{\hbar} \tag{21}$$

At low fields the hyperfine coupling is dominating, while the Δg-mechanism gains more importance at higher fields as the hfc is limited to a certain extent.

Incoherent Relaxation Mechanism

In general, incoherent processes only contribute significantly at $B > 0$ and are the reason for the magnetic-field effect. More important, the limiting equilibrium conditions (going from Scheme 3 to 4) of the coherent mechanism at high fields are a key factor for the change of the observed kinetics which is caused by the *Zeeman* splitting of the triplet sublevels (T_+ and T_-). Consequently, the analysis of the magnetic field-dependent rate constants, termed $k_\pm$ and $k_\pm'$ in Figure 16, reveal key information on the type of the MFE. Usually, anisotropic hyperfine coupling (ahfc) is dominating. In addition, g-tensor anisotropy (gta), spin-rotational interaction (sri) and electron-spin-spin-dipolar interaction (esdi), may also contribute to MFEs. All four mentioned relaxation mechanisms are due to longitudinal spin relaxations T_1 and are caused by stochastic modulation of the electron spin *Hamiltonian*.

An expression for the relaxation time T_1 is presented in eq. (22) where anisotropic hyperfine coupling (A) and g-tensor (g) anisotropy contributions are included.[275]

$$\frac{1}{T_1} = \frac{2}{5}\left[\begin{array}{l}\left(\frac{\Delta g^2}{3} + \delta g^2\right)\mu_B^2 B^2 \\ +\frac{1}{8}\left(\Delta A_\omega^2 + \delta A_\omega^2\right)\left(7I\,(I+1) - m_I^2\right) \\ -\left(\Delta g\,\Delta A_\omega + 3\,\delta g\,\delta A_\omega\right)\mu_B B m_I\end{array}\right]\frac{\tau_c}{1+\omega_0^2\tau_c^2} \qquad (22)$$

with $\Delta g = g_{zz} - \frac{1}{2}(g_{xx} + g_{yy})$ and $\delta g = \frac{1}{2}(g_{xx} - g_{yy})$, $\Delta A = A_{zz} - \frac{1}{2}(A_{xx} + A_{yy})$ and $\delta A = \frac{1}{2}(A_{xx} - A_{yy})$ and finally m_I is the orbital angular momentum quantum number according to $m_I = 2I + 1$ (with I = 0, 1/2, 1, 3/2, 2… for the nuclear angular momentum quantum number).

The orange coloured term represents the g-anisotropy modulation of the relaxation, the blue term is equal to the hyperfine anisotropy and the green part is a cross-term coming from a combination of g- and hyperfine anisotropy. Furthermore, the red term contains the correlation time (τ_c) due to rotation and translation of the involved radicals. The correlation time for organic radicals is typically in the range of 10^{-10}–10^{-9} s.[199, 223, 276] The electron *Larmor* frequency $\omega_0 = \gamma_e B$ includes the strength of the magnetic field B. The last term reflects the *Lorentzian* type behaviour of rotational diffusion.[275]

If, however, the difference of the g-values of the involved radicals vanishes, eq. (22) can be reduced to eq. (23). The latter is a pure hyperfine anisotropy modulation, where the system can be found in an axial orientation with $\delta A = 0$.

$$\frac{1}{T_1} = \frac{1}{20}\left[\Delta A_\omega^2\left(7I\,(I+1) - m_I^2\right)\right]\frac{\tau_c}{1+\omega_0^2\tau_c^2}\,^1 \qquad (23)$$

In addition, the relaxation time T_1 is correlated to the rate constant $k_\pm$ in the kinetic model of Figure 16 by eq. (24):[223]

$$k_\pm(T_1) = \frac{1}{4T_1} \qquad (24)$$

Hence, eq. (23) is transformed to eq. (25).

[1] The $1/\hbar$ factor in the equation used in lit.[275] is omitted in eqs. 22–23 and 25 because multiplication with $\hbar$ yields rate constants instead of angular frequencies.

$$k_{\pm}(T_1) = \frac{1}{80}\left[\Delta A_{\omega}^2\left(7I\ (I+1) - m_I^2\right)\right]\frac{\tau_c}{1+\omega_0^2\tau_c^2} \qquad (25)$$

The effect of hyperfine anisotropy results in a decreasing $k_{\pm}$ value while the magnetic field increase due to a B^{-2} dependence.

A very similar expression for the spin-lattice relaxation is given by eq. (26).[277]

$$\frac{1}{T_1} = \frac{2}{9}I(I+1)\sum_i (A_{ii} - A_{iso})^2 \frac{\tau_c}{1+\omega_0^2\tau_c^2} \qquad (26)$$

with the sum of the squared difference between isotropic ($A_{iso} = \frac{A_{xx}+A_{yy}+A_{zz}}{3}$) and anisotropic ($A_{ii} = A_{xx}, A_{yy}$ and A_{zz}) parts of the spin anisotropy of a given radical nucleus. Assuming axial symmetry ($A_{\perp} = A_{xx}, A_{yy}$ and $A_{II} = A_{zz}$) eq. (26) can be simplified with $\sum_i (A_{ii} - A_{iso}) = \frac{2}{3}\Delta A^2$ to eq. (27) which will be used in the chapter 3.1.5. Within eq. (27) the relation according to eq. (24) is included.

$$k_{\pm}(T_1) = \frac{1}{27}I(I+1)\Delta A^2 \frac{\tau_c}{1+\omega_0^2\tau_c^2} \qquad (27)$$

In general, this *Lorentzian* behaviour is often attributed to the rotational motion of the molecule and τ_c can be compared with the *Debye* correlation time $\tau_{c,Debye}$,[199, 214, 223, 275]

$$\tau_{c,Debye} = \frac{4\pi \cdot r^3}{3 \cdot k_B T}\eta \qquad (28)$$

where r (in m) is the hydrodynamic radius of the molecule of interest and η is the solvent viscosity in Pa·s.

The gta mechanism, on the other side, causes an increase of the $k_{\pm}$ value with increasing magnetic field. But this term only gains intensity at very high magnetic fields and if the difference in the g-factors of the individual radicals is significant (e.g. $\Delta g > 0.01$).

The electron-spin-spin-dipolar interaction (esdi) is caused by the $T_{\pm} \rightarrow T_0$ relaxation, while S-$T_{\pm}$ interconversion is not included, because esdi occurs mainly through direct (contact) interactions of the radical moieties. This interaction is also present in the exchange term correlated to the ZFS (*vide supra*). Similar to the anisotropic hyperfine coupling (ahfc), the esdi mechanisms is effective at low fields. On the contrary, the spin-rotational interaction (sri) and g-tensor anisotropy (gta) interaction are only observed at very high fields, beyond

that applied in this work. The spin-rotational interaction, as well as the gta, are based on SOC effects modulating the g-tensor of the radicals.[214, 223]

Which of the aforementioned interactions dominate or act concomitantly in the radical-pair mechanism depends on the rate determining step or the type of radicals which are produced after the electron transfer process (i.e. different g-values of the individual radicals). In many cases only a qualitative description of the MFE is possible, because multiple interactions cannot be separated from each other. In addition, a reason of misleading identifications of MFEs is the indirect determination of the $k_{\pm}$ parameter and the extraction of reliable values is only possible with intense MFEs and a very good signal-to-noise ratio of the kinetic traces. Magnetic field dependent transient absorption measurements (3.1.5) were performed in the scope of the current work and were analysed in terms of an extended relaxation mechanism based on the work on *Hayashi* and *Nagakura* (*vide supra*).

2 Scope of the Work

The aim of the present work is the synthesis of donor-iridium complex-acceptor triads (**T1–T4**) with the general structure shown in Figure 19, where an iridium dipyrrin complex (green) acts as a photosensitiser. After excitation of that unit a photoinduced electron transfer sequence will result in oxidised and reduced redox equivalents of the donor (blue) and acceptor (red) site, respectively, generating a charge-separated (CS) state ($D^{\bullet+}$–P–$A^{\bullet-}$). Triarylamines (TAA) and naphthalene diimide (NDI) serve as donor and acceptor units. After discussing the synthetic work, the electrochemical and photophysical characteristics will be presented to clarify the electron transfer (ET) processes in this donor-iridium-acceptor family.

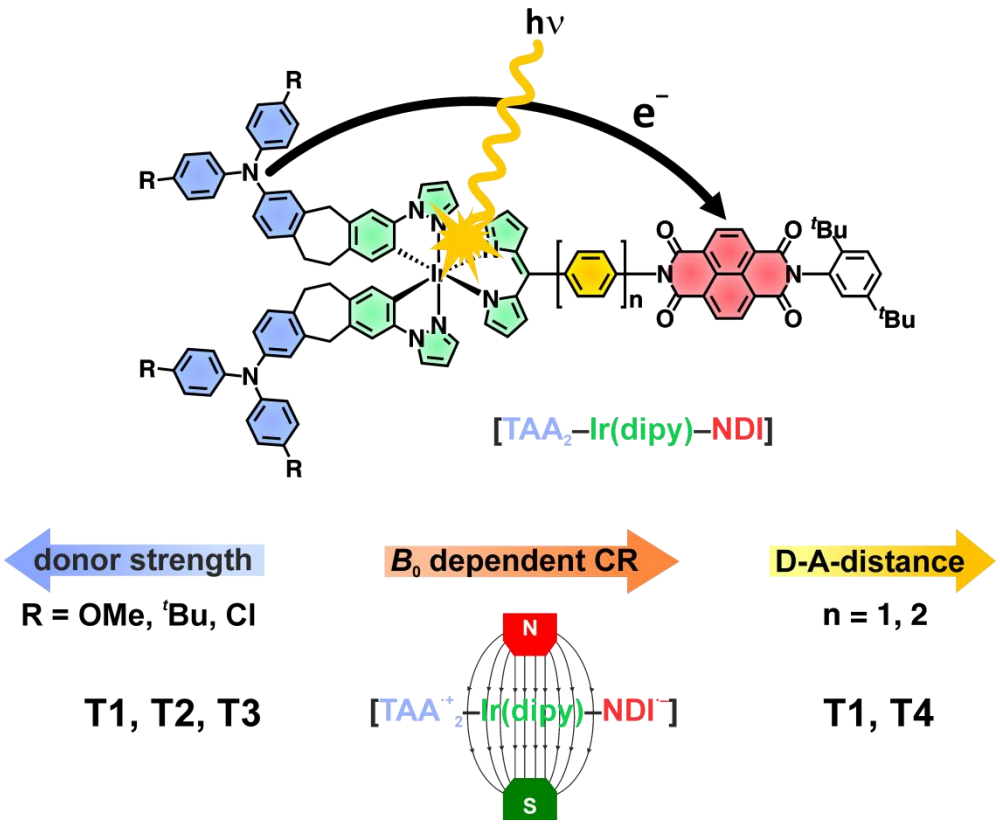

Figure 19 Architecture of the investigated donor-iridium complex-acceptor triads giving rise to charge-separated (CS) states. The kinetics of charge separation and recombination (CS, CR) will be analysed by the donor strength (blue arrow), magnetic field (orange arrow) and donor-acceptor distance (yellow arrow) dependence.

The generated CS states of the synthesised triads (**T1**–**T3**) will be influenced (Figure 19) by changing the donor strength of the donor unit with chloro, *tert*-butyl and methoxy substituents (R = Cl, ^{t}Bu, OMe) yielding a lower driving force for the charge recombination (CR) in the series from chloro to methoxy. The change of the substituents in addition to different solvents polarities will elucidate whether the CR process lies in the *Marcus* normal or inverted region.

A second approach focuses on the change of the CS distance. An increased donor-acceptor distance will induce a prolongation of the lifetime of the CS state. This will be done by inserting an additional phenyl unit (n = 2 (R = OMe), **T4** in Figure 19) between the iridium complex and the NDI acceptor.

Furthermore, the CS state of some triads will be influenced by an applied magnetic field (*B*) to detect possible magnetic field effects (MFEs) on the kinetics of CR. These experiment will clarify the spin nature of the CS states.

The triad family, **T1**–**T4**, will further be extended with complexes where the number of amines donors varies (**T5** and **T6** in Figure 20). The change from one amine donor (**T5**) to two and four donor units (**T1** and **T6**, respectively) is a feasible way to investigate the aspect of symmetry breaking which might have an effect on the overall electron transfer rate.

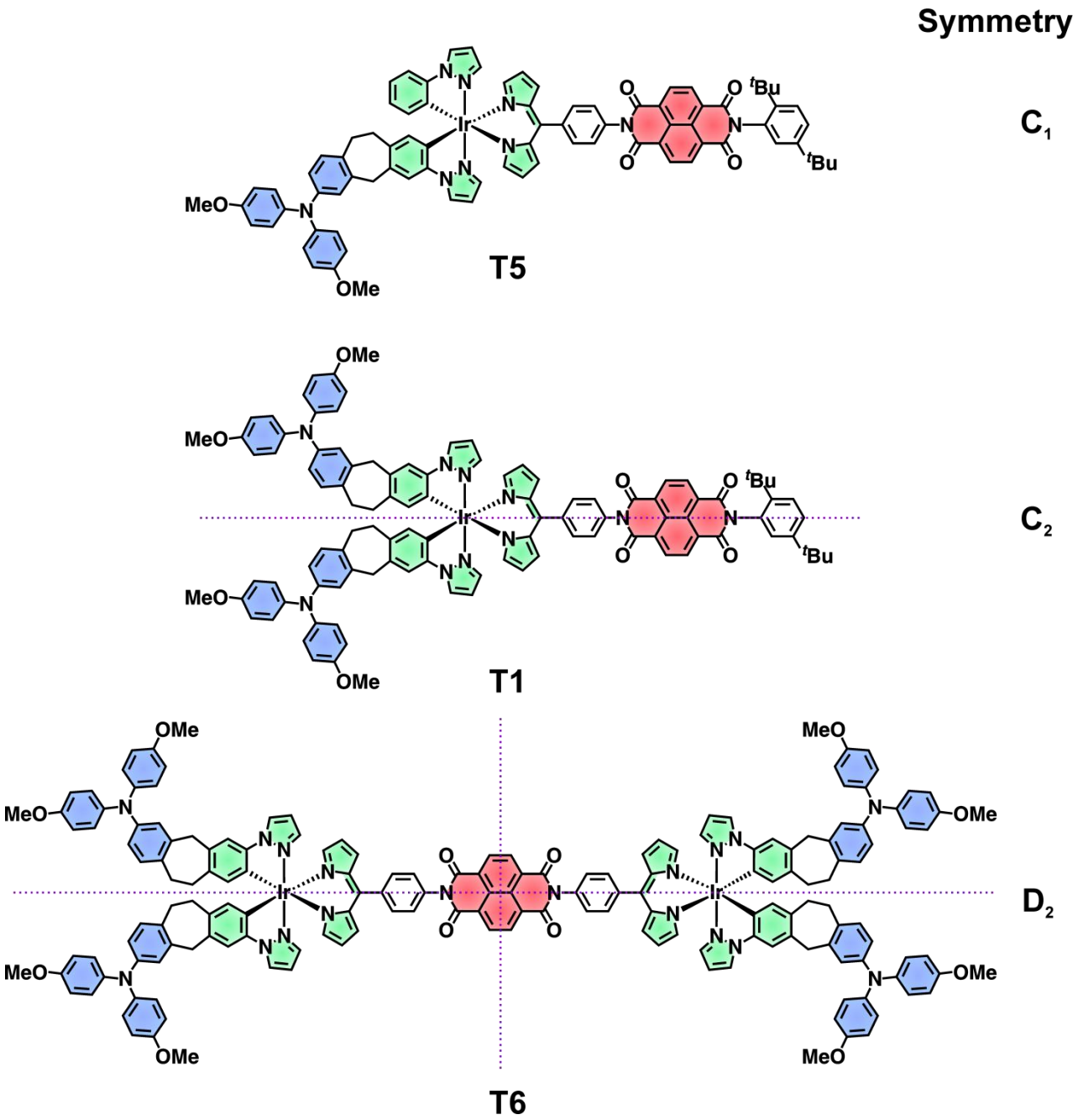

Figure 20 The issue of symmetry breaking will be investigated with triads **T1**, **T5** and **T6**.

The last two members of the triad family (**pMV1** and **mMV1**, Figure 21) were synthesised within the scope of the Master thesis of *R. Wagener*. In this work the TAA donor groups were fused with the ligand framework of the cyclometalating ligands. To realise this, two ways are in principle possible. On one side the, the *para*-position towards the iridium centre was functionalised with *bis*(*p*-methoxyphenyl)amines (**pMV1**) and on the other side the *meta*-connected complexes were synthesised (**mMV1**). It was supposed that **pMV1**, in contrast to **mMV1**, generates a mixed-valence character within the excited state upon photoexcitation. Thus, the positive charge of the amine donor in the CS state is delocalised over the iridium bridge to the other nearby donor site. In the present thesis (chapter 3.2) the interpretation of the photophysical properties will be complemented with ultrafast pump-probe spectroscopy and TD-DFT calculations.

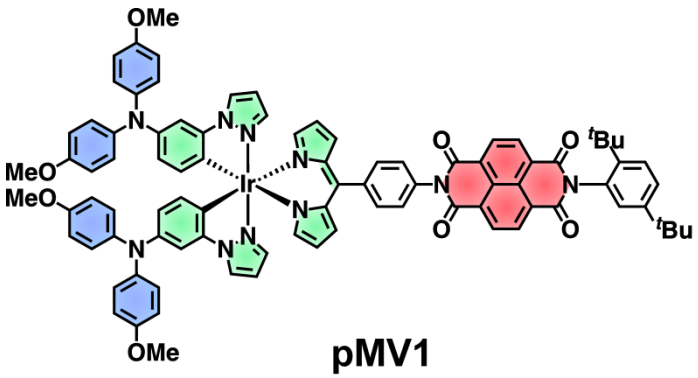

pMV1

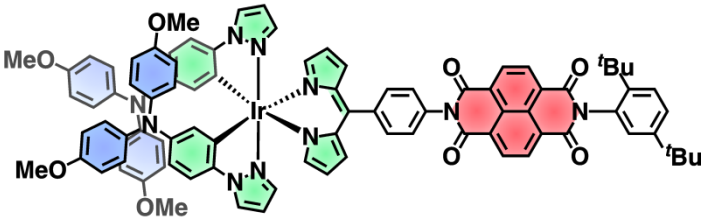

mMV1

Figure 21 A mixed-valence in the excited state is proposed for **pMV1** but not for **mMV1**.

The last chapter of the present work deals with the synthesis of iridium dyads and their electrochemical and photophysical features. The ancillary ligand attached to the iridium core is modified with electron withdrawing substituents (**D1**–**D4**, Figure 22). This might result in a CS state where the donor unit will still be oxidised but the dipyrrin ligand is now the reduced unit.

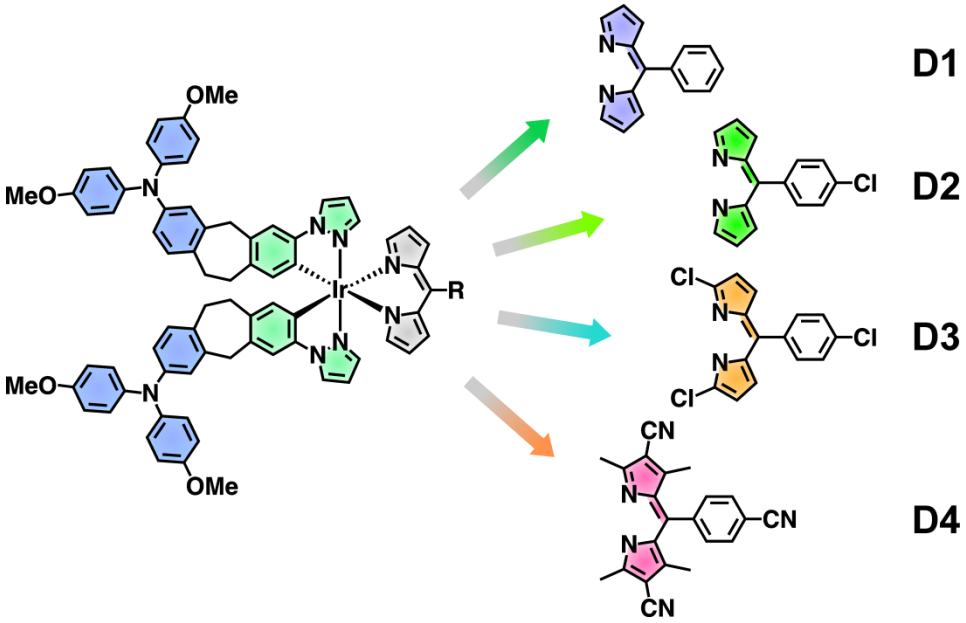

Figure 22 Dyad complexes where the acceptor strength of the dipyrrin ligand increases from green and blue to orange (**D1**–**D4**).

3 Results and Discussion

3.1 Triads T1–T6[1]

3.1.1 Introduction to the Electrochemical and Photophysical Properties of T1–T6

As mentioned in section 1.2.1 today's standard approach for the synthesis of iridium complexes follows the tow-step *Nonoyama* procedure[131] (Scheme 5). Thus, the use of the μ-chloro bridged dimer is an easy way to introduce two different functionalities, which result in *bis*-cyclometalated iridium complexes with two identical ligands, bearing e.g. the donor functional group (DF). The other functional group, e.g. the acceptor (AF, Scheme 5), can be linked to the ancillary ligand. With both different donor and acceptor ligands it is possible to have a building-block set of different ligands resulting in a variety of donor-iridium complex-acceptor triads. In addition to the triad complex synthesis, it is inevitable to have reference complexes with only one or no DF or AF functionality which help to elucidate the electrochemical and spectroscopic properties of the fully functionalised complexes.

All complexes prepared have in common that the basic structure of the iridium complexes is constructed of 2-phenylpyrazole as cyclometalating ligands and a dipyrrin ligand as an ancillary ligand (Figure 19–21). Furthermore, the donor units are differently substituted triarylamines and the acceptor moiety is a naphthalene diimide.

This introductory chapter highlights the basic electrochemical and photophysical features of the synthesised complexes. The presented measurements include steady-state absorption and emission spectroscopy as well as cyclic voltammetry and

[1] Reproduced or adapted in part with permission from a) *Stepwise versus pseudo-concerted two-electron-transfer in a triarylamine–iridium dipyrrin–naphthalene diimide triad*, J. H. Klein, T. L. Sunderland, C. Kaufmann, M. Holzapfel, A. Schmiedel, C. Lambert, *Phys. Chem. Chem. Phys.* **2013**, *15*,16024-16030. - Reproduced or adapted in part by permission of the PCCP Owner Societies; b) *Complete Monitoring of Coherent and Incoherent Spin Flip Domains in the Recombination of Charge-Separated States of Donor-Iridium Complex-Acceptor Triads,* J. H. Klein, D. Schmidt, U. E. Steiner, C. Lambert, *J. Amer. Chem. Soc.* **2015**, DOI: 10.1021/jacs.5b04868. Copyright (2015) American Chemical Society.
Parts of this chapter have been investigated in a Bachelor thesis and a Graduate thesis (teacher apprenticeship) under the supvervision of J. H. Klein: C. Kaufmann, Bachelor thesis, Julius-Maximilians-Universität (Würzburg), **2012** and S. Riese, Graduate thesis (teacher apprenticeship), Julius-Maximilians-Universität (Würzburg), **2012**.

spectroelectrochemistry. These analytic methods are the basis for all further interpretations e.g. the ns-laser flash experiments, which will be discussed in the current chapter, too. Mechanistic studies on the selected electron transfer properties and advanced theoretical discussions will be presented in separated chapters. Thereby, the results and analysis of the fs-pump-probe spectroscopy will be a decisive aspect. For that reason, experimental details of the fs-pump-probe set-up are introduced at the end of the current chapter but are necessary for the better understanding of the following three chapters.

3.1.1.1 Synthesis

Nonoyama-Procedure

In Scheme 5 the retrosynthesis of a *bis*-cyclometalated iridium complex is shown, which consists of two 2-phenylpyrazole cyclometalating ligands and a dipyrrin ligand. The advantage of using the two-step strategy by *Nonoyama* is that the donor and acceptor units are established consecutively in the final two steps. At the same time the complex framework is adopted and both functional groups can be prepared individually without dragging one unit all the way during the synthesis of the other one. The cyclometalating ligands and their configuration in the dinuclear complex are retained in the target complex avoiding a *trans*-position of the coordinating C-atoms. The dinuclear complex reacts easily with the *in situ* oxidised dipyrromethane (oxidised form is named dipyrrin) while exchanging the chloro ligands in refluxing THF and in the presence of a base (e.g. K_2CO_3). The dinuclear complex in the precursor step is prepared with $IrCl_3 \cdot nH_2O$, as the iridium source, and two equivalents of the cyclometalating ligand in a mixture of 2-ethoxyethanol and water (3:1) at 110°C.

The synthesis of the dinuclear complex usually is obtained in quantitative yield. For the smaller ligand frameworks, the yield of the second step is satisfying with up to 70 %. Unfortunately, the yield drops when the steric hindrance of substituents in the 2- and 9-position of the dipyrromethane increases or the ligand structures get bigger. A fundamental characteristic of the synthetic strategy in Scheme 5 is that there are always two donor-functionalities compared to one acceptor functionality because the ligand ratio is 2:1 for the cyclometalating and ancillary ligand, respectively.

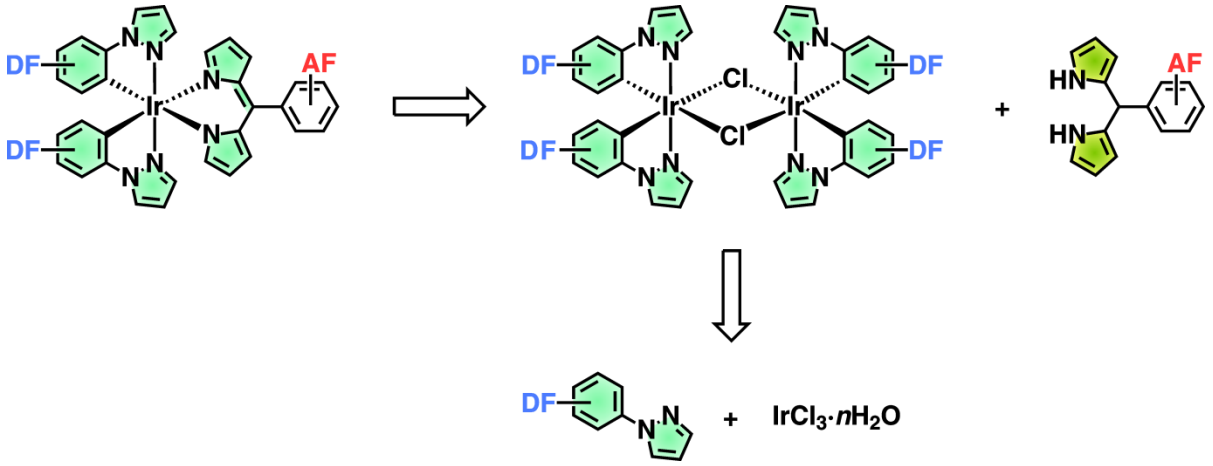

Scheme 5 Retrosynthetic strategy towards *bis*-cyclometalated iridium complexes with 2-phenylpyrazole and dipyrrin, as cyclometalating and ancillary ligands, respectively. The donor functionality (DF) is attached to the 2-phenylpyrazole ligand and the acceptor functionality (AF) is linked to the dipyrrin.

A convenient but also material consuming way to synthesise a 1:1 ratio of donor and acceptor functionalities is depicted in Scheme 6. The synthesis using two different cyclometalating ligands (L and L'), where one bears the donor functionality (DF → L'), and iridium(III)chloride hydrate ($IrCl_3 \cdot nH_2O$) were performed with the same conditions as mentioned above. The resulting mixture of dinuclear complexes, with the general formula $[(L)_{4-n}(L')_nCl_2Ir]_2$, contains five compounds with different molecular formulas which are built of seven different ligand combinations. More precise, there are two compounds each with four times the same ligand (with (n = 4) and without DF (n = 0)), two complexes each with three times the same ligand and another ligand (n = 3 and 1) and finally three isomers of the complex with a ligand ratio of 1:1 (n = 2). In this regard, the presence of diastereomers, which result from Λ- and Δ-isomers (cf. introduction section 1.2.1), is ignored for simplicity. These mixed-ligand complexes are not separable, but the second step in the *Nonoyama* route reduces the number of resulting products. Treating the mixed-ligand complexes with the ancillary ligand yields only three well separable *bis*-cyclometalated iridium complexes with no, one and two donor functionalities.

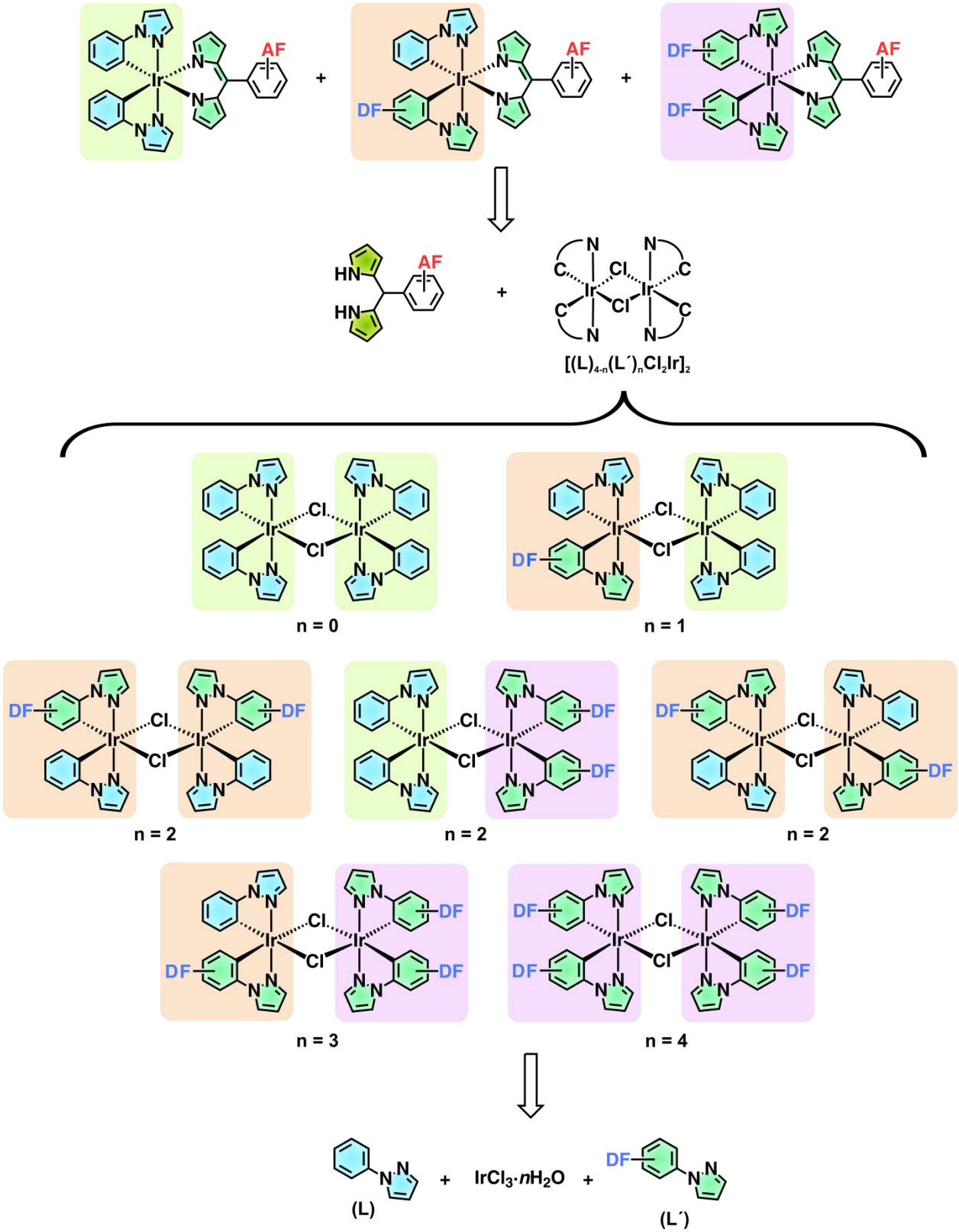

Scheme 6 Retrosynthetic strategy towards unsymmetrical *bis*-cyclometalated iridium complexes with two different 2-phenylpyrazole ligands and one dipyrrin ligand, as cyclometalating and ancillary ligands, respectively. The donor functionality (DF) is attached to one of the two 2-phenylpyrazole ligands and the acceptor functionality (AF) is linked to the dipyrrin.

The drawback of this method is the lower yield of the unsymmetrical complex (one DF group) because the two symmetrical complexes (with no and two DFs) are always part of the synthesis. However, if these complexes are desirable, too, one ends up in a win-win-situation because the side products are now additional target compounds. The different products can easily be isolated by recycling gel permeation chromatography (GPC).

Donor-functionalised and Unfunctionalised Phenylpyrazoles (Cyclometalating Ligands)

In the following the synthesis of the diverse ligands is presented, beginning with the triarylamine donor substituted phenylpyrazoles **4, 6, 8** and **9**, having methoxy, *tert*-butyl, chloro and cyano groups attached to the TAA, respectively (Scheme 7). The methoxy substituted TAA ligand with the saturated ethylene and methylene linker was already synthesised by *M. Holzapfel*[278-279] and *B. Geiss*,[160, 262] but the procedure could be further improved, avoiding harsher conditions and omitting three steps due to direct bromination of dibenzosuberone giving **1** in 23 % yield.

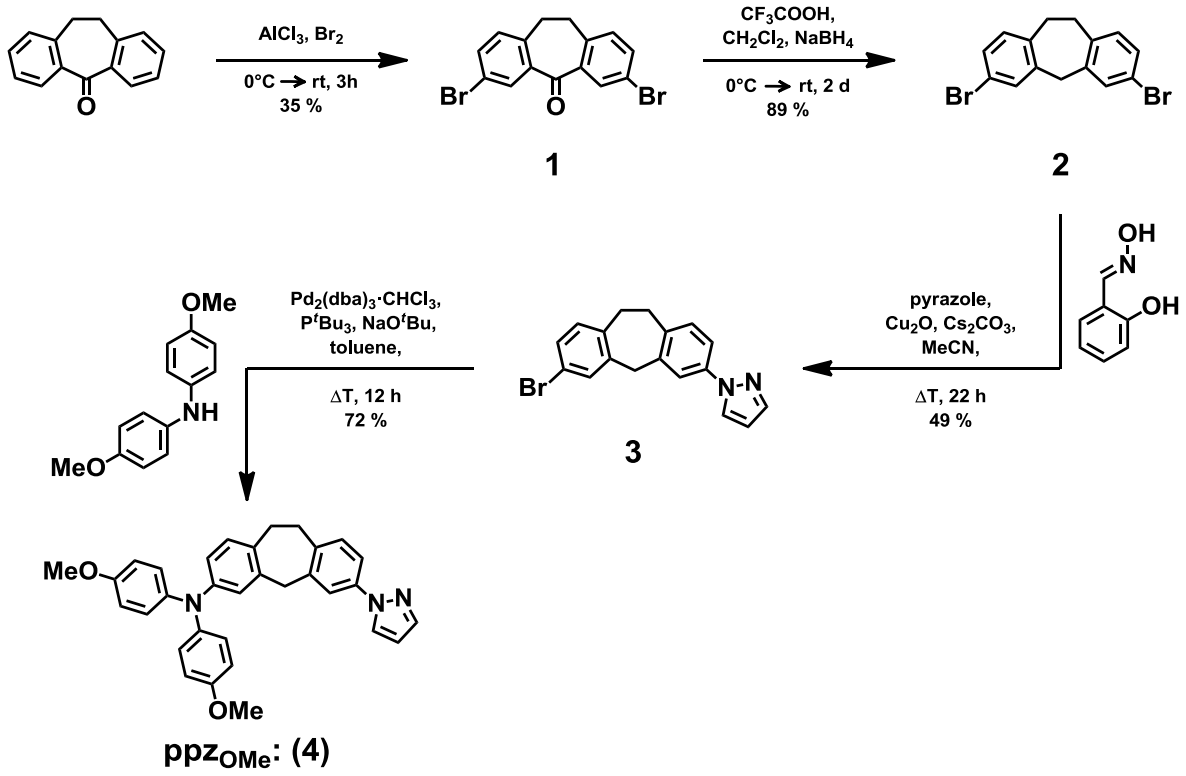

Scheme 7 Synthesis of the TAA-substituted phenylpyrazole **4**.

In the next step the brominated dibenzosuberone is reduced with sodium borohydride yielding **2** in 90 %. Furthermore, the next two steps are transition metal catalysed C-N-couplings. The first one is a copper-catalysed *Ullmann* coupling[280-282] with pyrazole to yield **3**. The resulting 2-phenylpyrazole motif represents the binding site in the iridium complex. The second palladium-catalysed *Buchwald-Hartwig* coupling[283-284] with *bis*(*p*-methoxyphenyl)amine results in the triarylamine substituted phenylpyrazole ligand ppz_{OMe} (**4**).

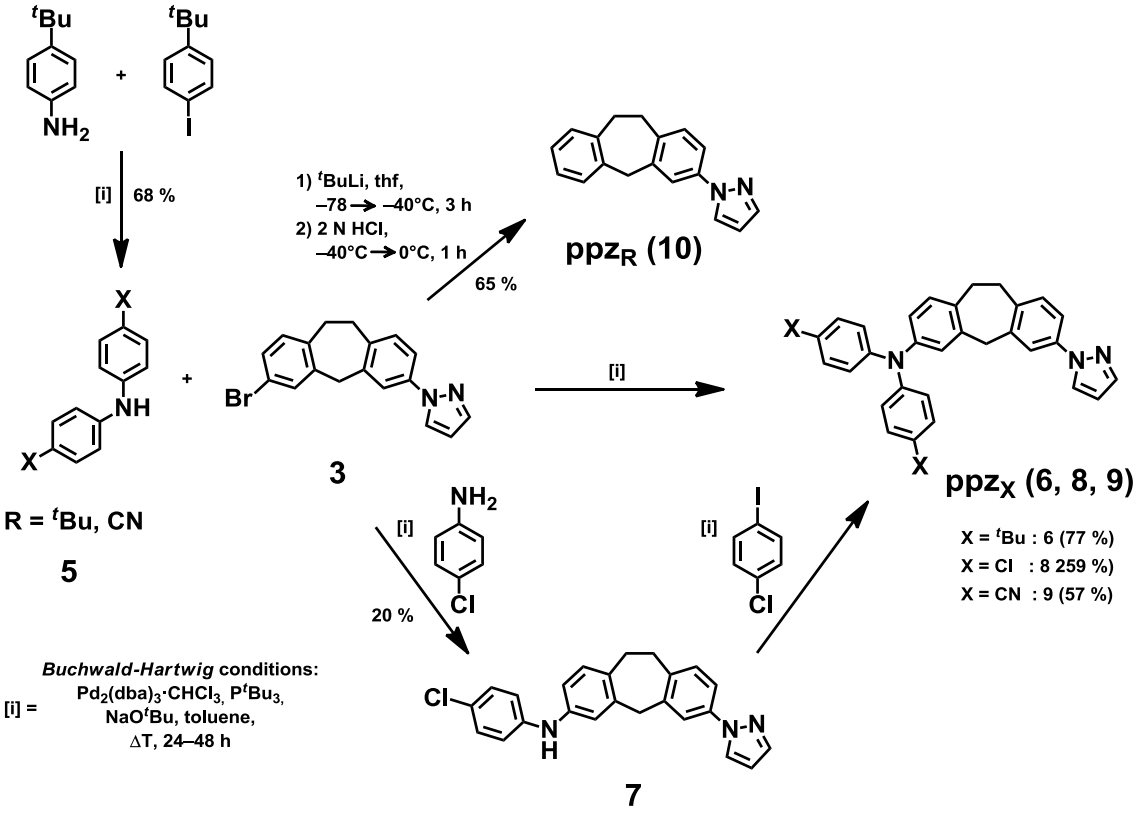

Scheme 8 Synthesis of the TAA-substituted phenylpyrazoles **6, 8** and **9** via *Buchwald-Hartwig* couplings, and the unsubstituted ligand **10**.

The triarylamine ligands **6** and **9** (ppz_X: X = ^{t}Bu and CN, respectively) were obtained in the same manner as **4** (Scheme 8) using the diarylamines with ^{t}Bu- and CN-substituents. The *bis*(*p-tert*-butylphenyl)amine (**5**) could be prepared from 4-*tert*-butylaniline and 1-*tert*-butyl-4-iodobenzene and the cyano *bis*-arylamine was available from the stock of Dipl. Chem. *A. Heckmann*. Unfortunately, the chloro compound was not readily synthesised and an additional step was introduced. Thus a twofold *Buchwald-Hartwig* coupling, first with 4-

chloroaniline and second with 1-chloro-4-iodobenzene, was performed to obtain the diarylamine **7** and finally the triarylamine **8** (ppz_{Cl}). All phenylpyrazole ligands could easily be isolated with flash-column chromatography with good yields ranging from 56 to 77 %.

In addition to the donor substituted ligands, also unsubstituted ligands were used to synthesise dinuclear complexes in the first step of the *Nonoyama* rout in Scheme 5, namely the commercially available bare 2-phenylpyrazole and the debrominated phenylpyrazole **10** (ppz_R in Scheme 8), which results from **3** after lithiation and subsequent treatment with aqueous HCl at low temperatures.

Dinuclear μ-Chloro Bridged Iridium Dimer Synthesis

The four different substituted cyclometalating ligands (**4**, **6**, **8**–**9**, ppz_X: X = OMe, ^{t}Bu, Cl and CN, respectively) and the two ligands without any functionality (ppz_R (**10**) and ppz) can be further used in the reaction with iridium(III)chloride hydrate yielding the dinuclear complexes **34**–**39** (Scheme 9).

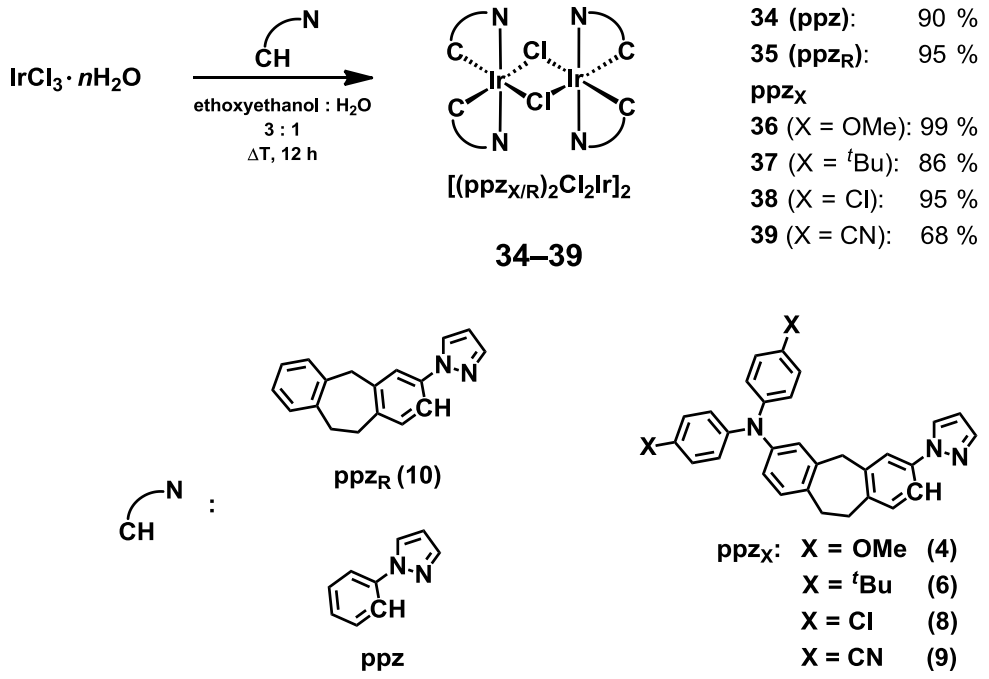

Scheme 9 Synthesis of the dinuclear cyclometalated *μ*-chloro bridged iridium(III) complexes without (**34**–**35**) and with donor substituents (**36**–**39**).

The mixed-ligand dinuclear complexes **40** (Scheme 10) were obtained by mixing 2-phenylpyrazole and ligand **4** in a 1:1.2 ratio together with $IrCl_3 \cdot nH_2O$ resulting in different, not separable complexes (for details see Scheme 6). Thus, it is impossible to determine a yield for the individual compounds and therefore the mixture was employed for further reactions as such.

In general, a bright grey or yellow cloudy solid precipitated during heating of the reaction mixture and the collected solids were washed with water and used without further purification for step two of the *Nonoyama* route. Concerning the yield of the different complexes, only the cyano-substituted triarylamine containing complex gave lower yields (70 %), whereas the others are close to 90 % or above.

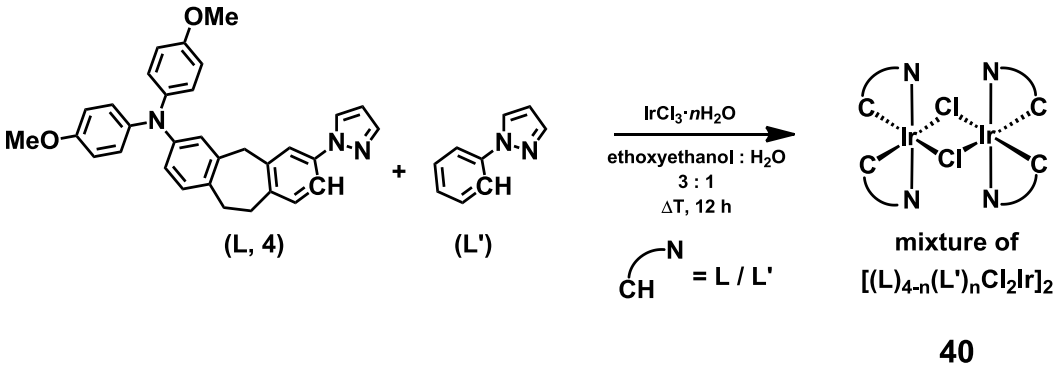

Scheme 10 Synthesis of the mixed-ligand dinuclear cyclometalated μ-chloro bridged iridium(III) complexes (**40**). For the variety of different complexes in the mixtures see Scheme 6.

Dipyrromethane Synthesis (Ancillary Ligands)

In general, a simple synthetic access to *meso*-(phenyl)dipyrromethanes (Scheme 11) is known since the early works of *Lindsey et al.*[285] where triflouroacetic acid (TFA) or a *Lewis* acid, e.g. $BF_3 \cdot OEt_2$, was used to activate an aldehyde group for a nucleophilic attack of pyrrole. Recently, a microwave assisted reaction with iodine as *Lewis* acid was developed to readily synthesise dipyrromethanes from various aldehyde precursors.[286] In the present work the iodine method is preferred to prepare the desired *meso*-(phenyl)dipyrromethanes **11** and **12** which substitute R in Scheme 11 with H and NO_2, respectively. The nitro-

compound **12** is further reduced with palladium on activated carbon resulting in the *meso*-(aminophenyl)dipyrromethane **13**.[287]

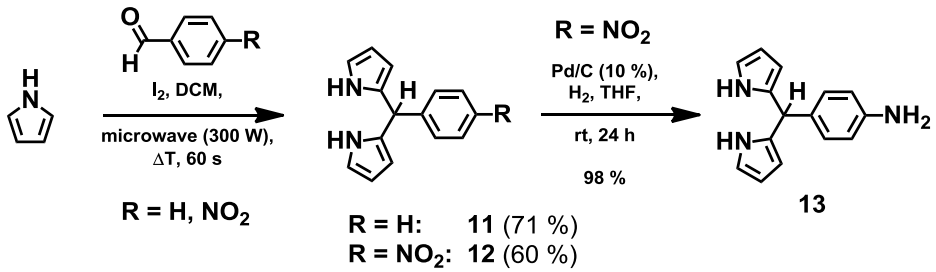

Scheme 11 Dipyrromethane synthesis with different substituted phenyl units in *meso*-position (**11**–**13**).

The amino-functionalised dipyrromethane **12** was the starting point of the hitherto unknown naphthalene diimide (NDI) compounds **18** and **19** (Scheme 12). Naphthalene-1,4,5,8-tetracarboxylic dianhydride was transformed to compounds **18** and **19** with either two different or identical amines, respectively, in a condensation reaction under microwave irradiation. Similarly, reference compound **17** without dipyrromethane functionality, was synthesised in a one-pot synthesis in refluxing DMF. Although, the one-pot synthesis was accompanied with low yields for the diimides, this procedure was beneficial over a step by step strategy because an easier isolation of the diimides compared to the naphthalene monoimide (NMI) compounds was achieved.

Reference compound **17** was synthesised to identify transitions and excited state behaviour localised solely on the acceptor unit. The 2,4-di-*tert*-butylaniline was chosen to increase the solubility of the target complexes. Naphthalene bisimide **19** was also detected as a side product in the reaction of **18**. Likewise, the naphthalene bisimide with twice 2,4-di-*tert*-butylaniline attached (not shown) could be identified, as well. Thus, the unsymmetrical naphthalene diimide is always accompanied with the two symmetrical bisimides which explains the lower yield of **17**–**18**. Nevertheless, the symmetrical bisimide **19** could be prepared in refluxing pyridine in a microwave oven with high yields because less side products were possible.

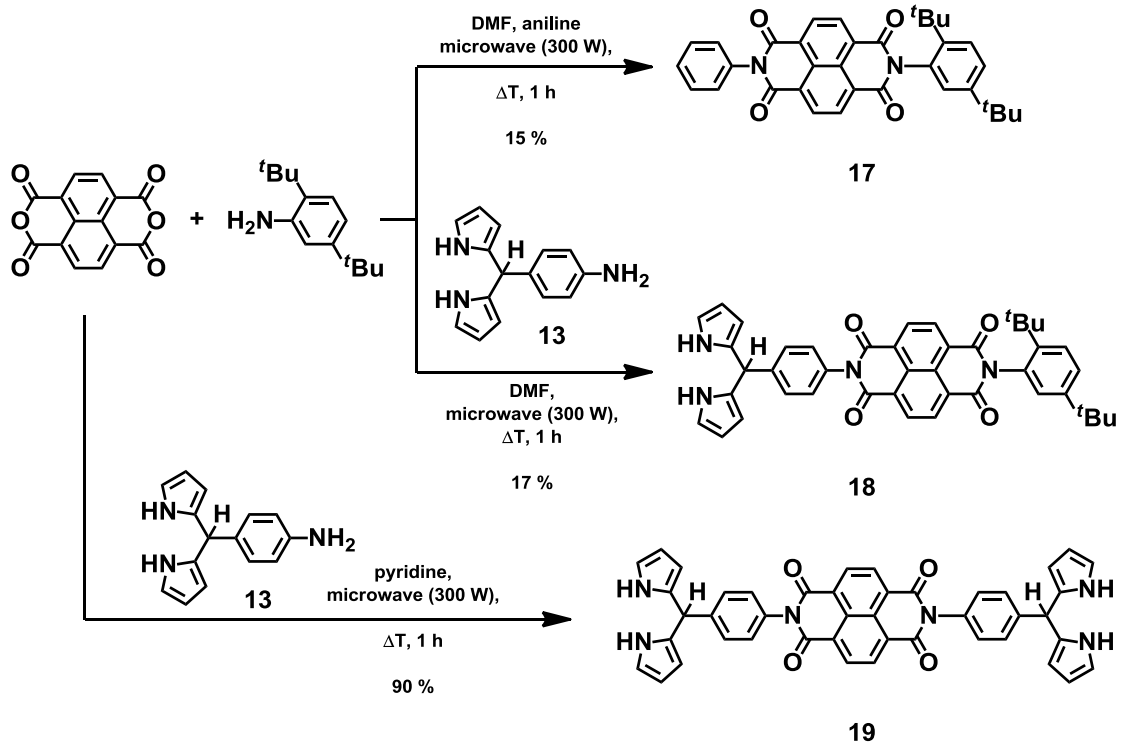

Scheme 12 Unsymmetrical (**17**–**18**) and symmetrical (**19**) naphthalene diimides in a one-pot synthesis.

Extending the unsymmetrical dipyrromethane-functionalised naphthalene diimide **18** with an additional phenyl spacer (**25**), provided a synthetically longer reaction sequence starting with 4-bromobenzaldehyde (Scheme 13). The aldehyde group was protected with ethylene glycol[288] (**20**) before treating with *n*BuLi and *tris*-diisopropyl boronic ester resulted in a bromo-boron exchange, followed by the cleavage of the protecting group with 2 N HCl yielding **21**.[289] After this, the biphenyl spacer **22** was synthesised by a *Suzuki-Miyaura* coupling.[290] Next, the free aldehyde was converted to the dipyrromethane **23** by a microwave assisted reaction with iodine.[286]

Likewise, having **18** as an example, the synthesis of the unsymmetrical naphthalene diimide **25** was completed with the reduction of the nitro group[287] and the one-pot protocol for the condensation reaction in refluxing DMF. Finally, the unsymmetrical naphthalene diimide **25** was obtained with relatively low yields but the synthesis was uncomplicated and the different di- and bisimides were even better separable as it was the case for ligand **18** and its side products.

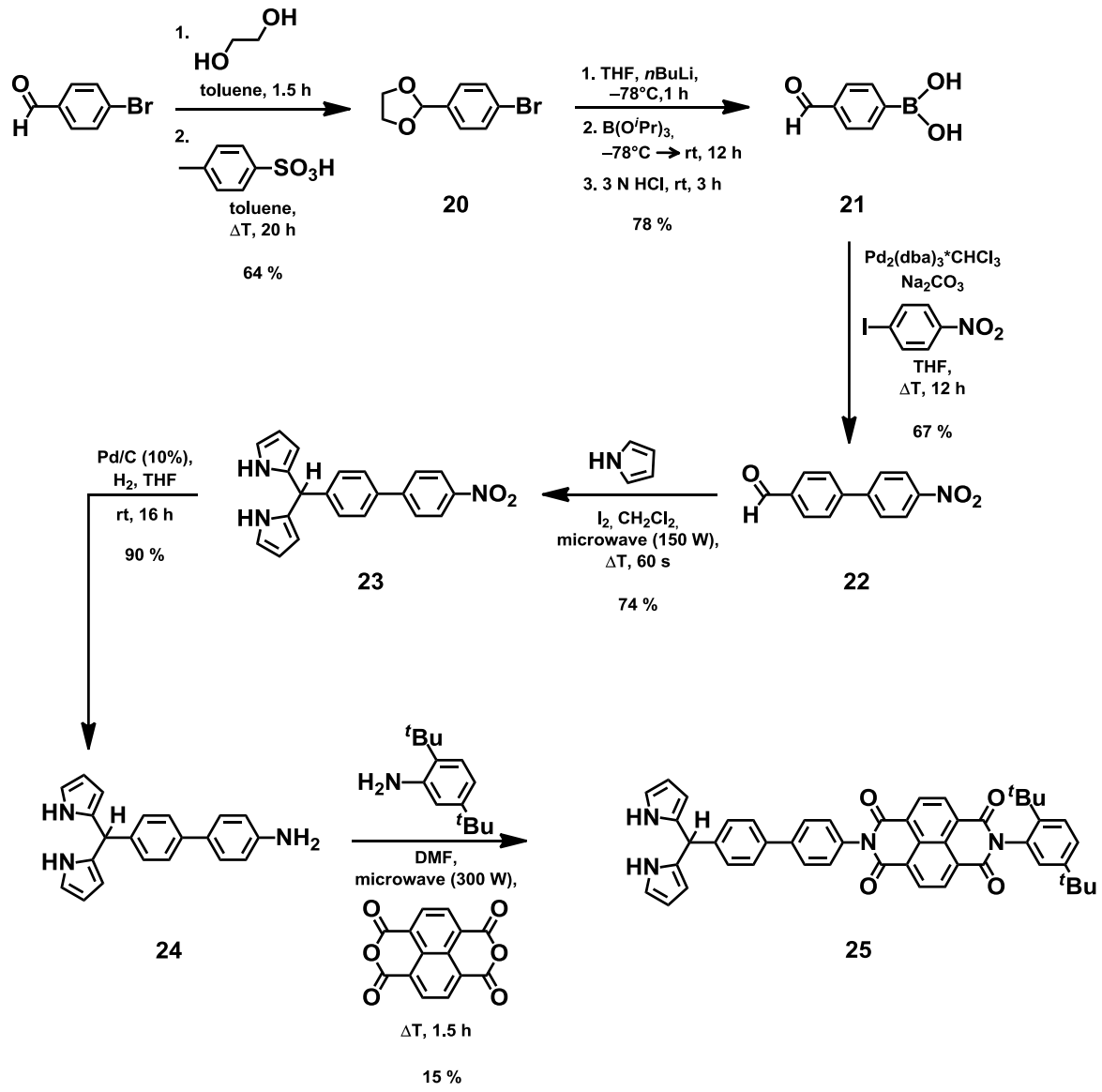

Scheme 13 Reaction sequence yielding the unsymmetrical naphthalene diimide **25**, respectively.

After completing the synthesis of the cyclometalating ligands (**4, 6, 8–10**), the corresponding dinuclear complexes (**34–40**), and the ancillary ligands (**11, 18–19, 25**) a set of different *bis*-cyclometalated complexes was achieved, which will be discussed in the following.

Synthesis of Neutral Bis-Cyclometalated Iridium(III) Complexes

The second step of the Nonoyama synthesis towards *bis*-cyclometalated iridium complexes with the above prepared cyclometalating and ancillary ligands is presented in Scheme 14 giving the triad complexes **T1–T6** and the reference complexes **Ref1** and **Ref$_{NDI}$**. The triad complexes and **Ref1** and **Ref$_{NDI}$** are shown in Figure 23.

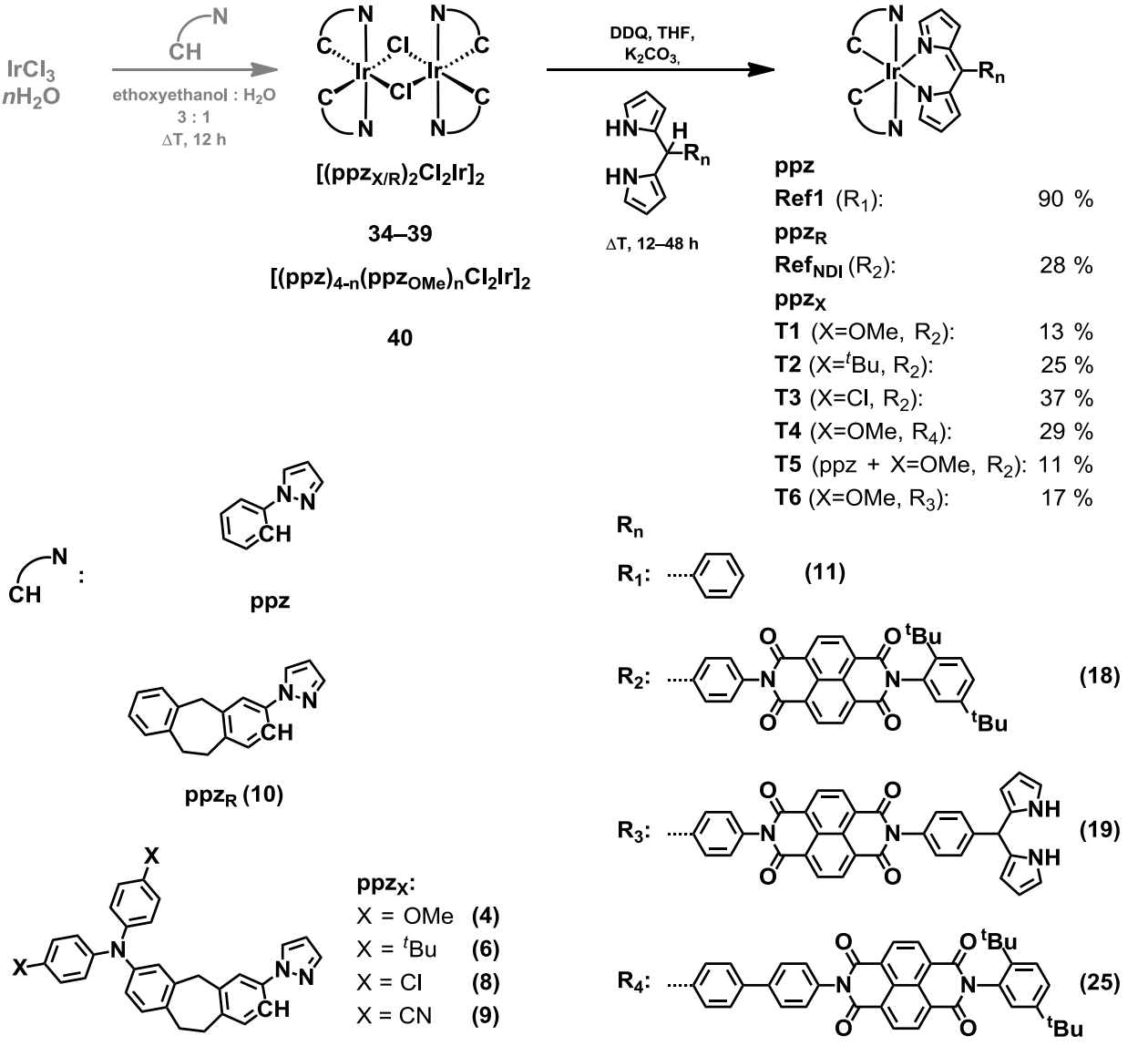

Scheme 14 Synthesis of *bis*-cyclometalated iridium complexes giving triads **T1–T6**, **Ref1** and **Ref$_{NDI}$** in the second step of the *Nonoyama* rout (black). The first step is displayed in grey and is discussed in detail in Scheme 9 and 10.

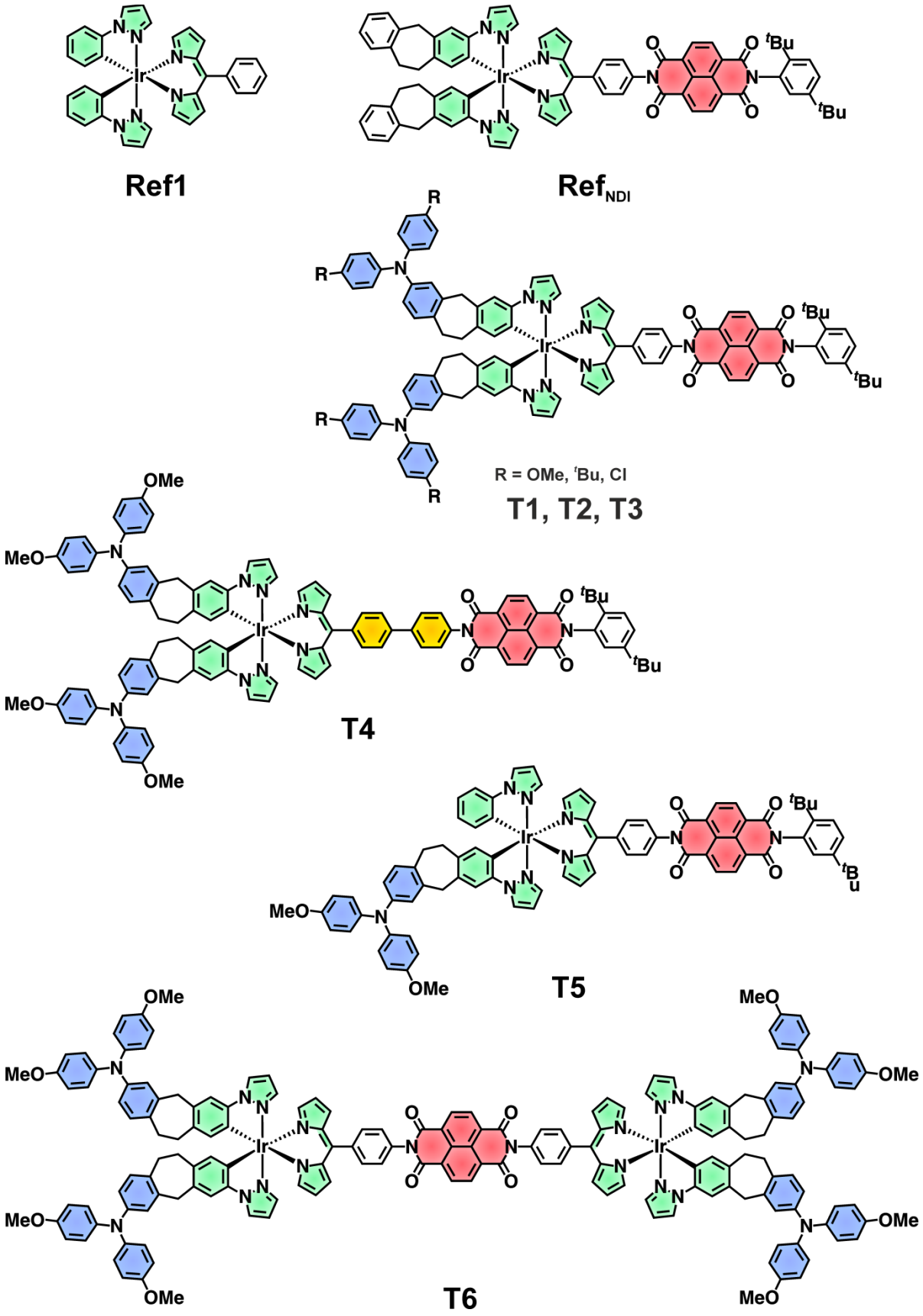

Figure 23 Complexes **Ref1**, **Ref$_{NDI}$** and **T1–T6**.

An important feature characterising the *Nonoyama* rout to the dipyrrin-containing *bis*-cyclometalated complexes is the in situ oxidation of the dipyrromethanes to dipyrrins as was shown by *Thompson* and co-workes[142] (Scheme 15). Here, the oxidation with 2,3-dichloro-5,6-dicyano-1,4-benzoquinone (DDQ) in THF creates a significantly extented π-system of the ligand combined with an anionic binding site on one pyrrole of the dipyrrin after deprotonation with K_2CO_3. The anionic charge is conjugated to the nitrogen of the other pyrrole ring (Scheme 15) making both nitrogens equivalent for the coordination of the iridium centre.

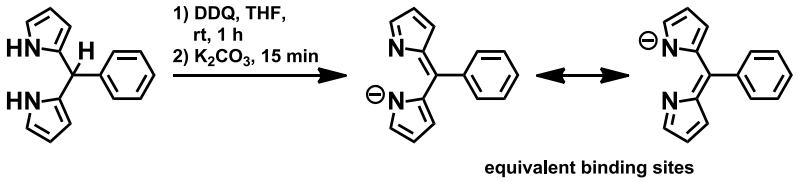

Scheme 15 Oxidation and deprotonation of dipyrromethanes to dipyrrins illustrating the equivalent binding motive of the nitrogen atoms.

The oxidation of the dipyrromethane usually is completed within one hour giving a dark yellow-green colour. Thereafter, the dinuclear complex is added to react with the in situ prepared dipyrrin ligand to a dark red-brown solution after refluxing for 12–48 h. **Ref1** could be easily purified by flash-column chromatography on silica gel, whereas the NDI containing complexes were first filtered through a pad of silica gel and then injected into a recycling gel permeation chromatography (GPC) system for final purification. All iridium dipyrrin complexes were obtained as deep red solids with yields of 11–37 % for the triads and 27 and 90 % for the reference complexes. The complexes were characterised with proton- and carbon-NMR, high-resolution mass spectrometry (HRMS) and microanalysis (CHN). The analytic results (see experimental part) were all in line with a required purity for publication. In addition, specific information on the molecular geometry of compound **T1** was obtained by single crystal X-ray diffraction (see Figure 24). Single crystals of **T1** were grown by liquid/liquid diffusion of hexane into a solution of **T1** in dichloromethane.

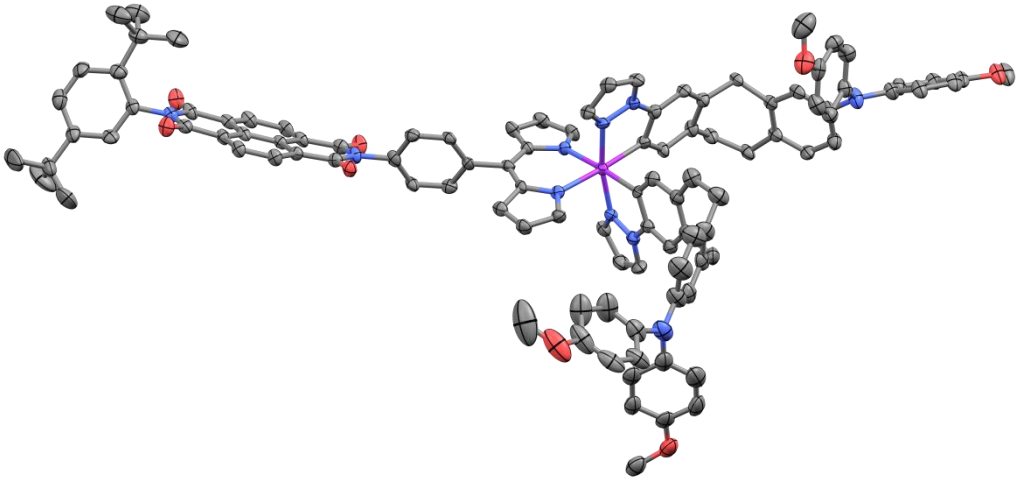

Figure 24 Molecular structure of **T1** in the *Λ*-configuration obtained from single crystal X-ray diffraction (see Appendix for details of the X-ray analysis). The ellipsoids indicate a probability level of 50 %).

The structure analysis revealed a distorted octahedral iridium complex configuration with a slightly bent dipyrrin ligand, similar to the observed values for **Ref1** in literature.[142] Besides, the expected *trans*-configuration of the pyrazolyl groups is present and likewise the *Δ*- (not shown) and *Λ*- (Figure 24) configuration can be seen in the unit cell. Furthermore, the dihedral angle between the phenylene ring and the neighbouring NDI, on the one side, and the dipyrrin fragment on the other side are 121.7° and 86.1°, respectively. The fact that two different conformers of the TAAs relative to the iridium complex are present in the solid state structures indicates that this may also be the case in solution. The donor-acceptor distances between the centre of the carbon-carbon bond of the central carbon atoms of the NDI core and the two nitrogen atoms of the TAA units are for the two possible TAA conformers 19.1 Å and 22.9 Å.

It has to be mentioned that not all synthetic possible complexes were investigated because elementary structure-property relationships already can be achieved with selected examples. Besides, complexes with the cyano-functionalised donor ligand resulted in low yields and were therefore not investigated further. Other donor substituted complexes with either ligand **11** or other functionalised dipyrrins will be discussed in chapter 3.3.

3.1.1.2 Steady-State Absorption Spectroscopy

The absorption characteristics of all triads (**T1**–**T6**) in CH_2Cl_2 are presented in Figure 25, including the absorption spectra of the donor-substituted cyclometalating ligands **4**, **6** and **8** TAA references), compound **17** (NDI reference) and **Ref1** (Ir(dipy) reference) for clarifying the origin of bands in the triads. In addition, $\mathbf{Ref_{NDI}}$ is shown for completeness, too. All important features are listed in Table 3.

Starting with the reference compounds in Figure 25a, one can identify the typical broad π-π*-absorption of the triarylamine[291] containing ligands (**4**, **6**, **8** in grey, light green and orange, respectively) with a maximum absorption energy of ca. 33 000 cm^{-1} (303 nm) with a maximum molar absorption coefficient (ε_{max}) of 23 000–28 000 M^{-1} cm^{-1}. In a series from the chloro- to the methoxy-substituted TAA the absorption maximum is slightly shift hypsochromically by 500 cm^{-1}. Furthermore, the intensity decreases by ca. 3500 M^{-1} cm^{-1} within the same series. Conversely, the second band of the TAAs at ca. 37 700 cm^{-1} gains intensity in the methoxy-substituted TAA compared to the chloro and *tert*-butyl derivatives. The blue shift and a reduced intensity is reproduced in the triad molecules **T1**–**T3**, too. The overall extinction coefficient for the TAA bands in **T1**–**T4** are by a factor of at least two higher in the triads, because there are two donor ligands present in the complex geometry. In contrast, **T6** exhibits four identical TAA units and **T5** just one, therefore the intensity is increased by a factor of four in **T6** and remains the same for **T5**. Besides, the absorption of the Ir(dipy) unit adds to the overall absorption in this spectral region, too.

The NDI (**17**) shows a vibronic fine-structure of the absorption with a first maximum at ca. 26 300 cm^{-1} (380 nm) with ε_{max} = 28 100 M^{-1} cm^{-1} followed by two maxima with a peak separation of each ca. 1500 cm^{-1} between the neighbouring peaks.[292-294] The fine-structure of this π-π*-transition can be seen in the NDI-containing complexes, too. The ^{1}NDI state energy was estimated by fitting a tangent to the rising edge of the low energy side of the absorption spectra of **17** and the intersection point with the x-axis giving 3.21 eV.

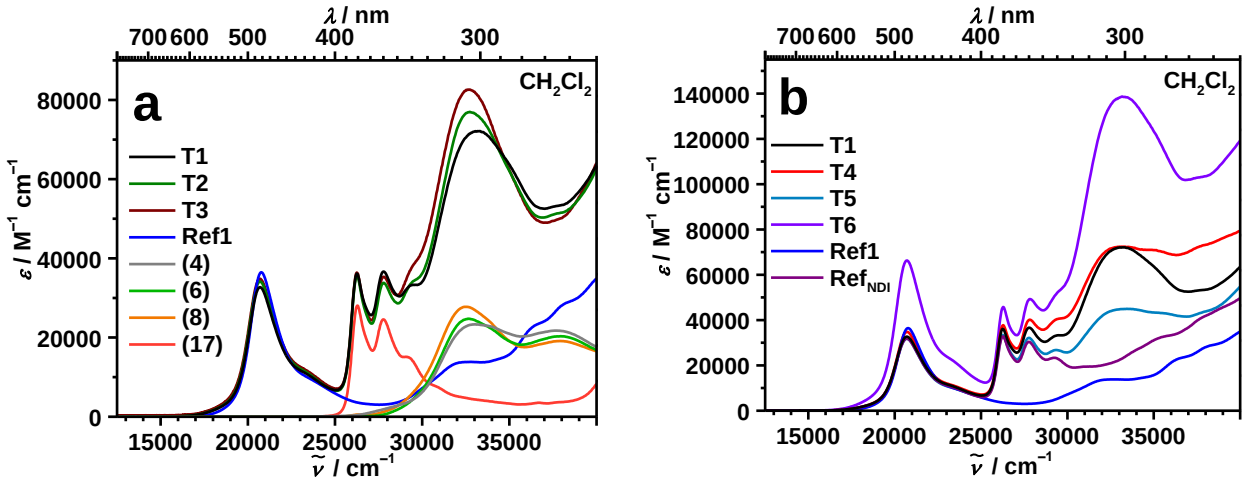

Figure 25 Absorption spectra of (a) triads **T1–T3**, ligands **4**, **6**, **8** and compound **17** and (b) **T1**, **T4–T6**, **Ref1** and $\mathbf{Ref_{NDI}}$ in CH_2Cl_2. For comparison **T1** and **Ref1** are displayed in both figures.

For the determination of the absorption features of the naked iridium dipyrrin complex, **Ref1** was used. The most important absorption band of **Ref1** is located at 20 800 cm^{-1} (481 nm) with ε_{max} = 36 500 M^{-1} cm^{-1} displaying a broad band with a shoulder at ca. 23 600 cm^{-1} (424 nm). Further absorption characteristics towards higher energies can be found at 32 300 cm^{-1} (309 nm), 36 600 cm^{-1} (273 nm) and 38 200 cm^{-1} (262 nm). According to *Thompson* and co-workers, the low-energy absorption band represents the π-π*-absorption of the dipyrrin ligand framework within the complex similar to BODIPYs (boron-dipyrromethene, Figure 26), where the cyclometalated iridium part is replaced by a BF_2 group. In addition, the high-energy absorption features correspond to ligand-centred (LC) and metal-to-ligand charge transfer (MLCT) transitions related to the cyclometalating phenylpyrazole ligands.[142] The origin of the ligand-centred transition could be well reproduced in a Master thesis by J. Föller in the group of *C. Marian* (Düsseldorf) with DFT/MRCI-calculations.[295] The shoulder at 23 600 cm^{-1} (424 nm) is based on an MLCT transition, equivalent to the promotion of an electron from the $Ir(ppz)_2$ unit to the dipy-ligand, which is correlated to the redox potential difference $\Delta E_{1/2}$ [107, 132, 145, 159, 161, 174] given by ca. 2.91 eV (23 500 cm^{-1}, cf. 3.1.5). Furthermore, a comparison of the rise of the low-energy side of the LC-band between the BODIPY chromophore and the iridium dipyrrin complexes

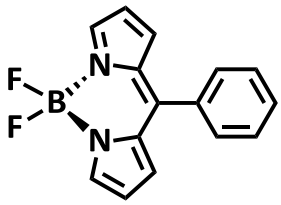

Figure 26 Structure of a BODIPY.

displays a foot to lower energies for the iridium complexes. This foot, between 17 000–19 000 cm^{-1} (588–526 nm), may be caused by spin-forbidden transitions to LC triplets, which gain in intensity due to the heavy-atom effect of the iridium atom. Consequently, all complexes exhibit this LC absorption features, but in particular for **T6** there is an increase of this band by a factor of two, compared to all other complexes, corresponding to a second iridium dipyrrin unit in this compound (Figure 25b). Concerning the excited state energy of the iridium complex singlet state (^{1}Ir) a tangent was fitted on the rising edge of the low energy side of the absorption band[41] of **Ref1** and the intersection point with the x-axis yielded $E(^1\text{Ir})$ = 2.42 eV. Besides, the group of Prof. Dr. *M. Chergui* (Lausanne) was able to record a fluorescence spectrum of **Ref1** by fs-resolved fluorescence up-conversion and fitting a tangent on the high energy side of the obtained emission band yielded $E(^1\text{Ir})$ = 2.58 eV for the ^{1}Ir state energy.[296] The former value of 2.42 eV is used in the following for the singlet state energy of all iridium complexes.

In general, the absorption features of the three different chromophoric moieties (donor, iridium complex and acceptor) sum to an overall absorption spectra for the triads (including reference complex $\mathbf{Ref_{NDI}}$) taking into account the total number of the different chromophores. Moreover, the band intensities and maxima of the individual units do not change significantly when linked together in the complexes architecture, which indicates that the three different building blocks are well decoupled.

The reasons for the efficient decoupling of the chromophores are threefold: i) the saturated bridge between TAA and the iridium complex,[262, 279] ii) orbital nodes of HOMO and LUMO along the long axis of the NDI chromophore which minimises orbital overlap to the bridging phenylene or biphenyl (in **T4**) spacer[297-298] and iii) both spacers exhibit an almost 90° dihedral angle to the *meso*-position of the dipyrrin ligand[141-142] (see molecular structure of the single crystal X-ray diffraction, Figure 24). Besides, the three different spectroscopic features are well separated in energy, allowing a detailed analysis of a wavelength dependent behaviour of the excited state properties (*vide infra*).

Table 3 Absorption maxima and extinction coefficient of the characteristic absorption bands (iridium complex = Ir(dipy), NDI and TAA) of triads **T1–T6**, ligands **4**, **6** and **8** (TAA-references), compound **17** and **Ref$_{NDI}$** (NDI-references) and **Ref1** (Ir(dipy)-reference).

	solvent	**Ir(dipy)** $\tilde{\nu}_{max}$ (λ_{max}) / ε_{max}[2] / cm^{-1} (nm) / cm^{-1} M^{-1}	**NDI (1st peak)[1]** $\tilde{\nu}_{max}$ (λ_{max}) / ε_{max}[2] / cm^{-1} (nm) / cm^{-1} M^{-1}	**TAA** $\tilde{\nu}_{max}$ (λ_{max}) / ε_{max}[2] / cm^{-1} (nm) / cm^{-1} M^{-1}
Ref1	CH_2Cl_2	20 800 (481) / 36 500	-	-
	THF	20 800 (481) / 35 300	-	-
	MeCN	20 900 (478) / 33 200	-	-
Ref$_{NDI}$	CH_2Cl_2	20 700 (483) / 31 900	26 200 (382) / 32 800	-
	MeCN	20 900 (478) / 29 600	26 500 (377) / 34 400	-
T1	CH_2Cl_2	20 700 (483) / 32 700	26 200 (382) / 36 100	33 200 (301) / 72 100
	THF	20 700 (483) / 33 600	26 400 (379) / 33 500	33 400 (299) / 77 700
	MeCN	20 900 (478) / 31 100	26 500 (377) / 37 200	33 700 (297) / 70 600
T2	CH_2Cl_2	20 700 (483) / 34 200	26 200 (382) / 35 600	32 700 (306) / 77 000
	MeCN	20 900 (478) / 29 000	26 500 (377) / 34 700	33 200 (301) / 72 200
T3	CH_2Cl_2	20 700 (483) / 34 800	26 200 (382) / 36 400	32 600 (307) / 82 600
T4	CH_2Cl_2	20 700 (483) / 34 800	26 300 (380) / 37 800	33 200 (301) / 72 400
	MeCN	20 900 (478) / 31 100	26 500 (377) / 38 600	35 300 (283) / 72 100
T5	CH_2Cl_2	20 700 (483) / 31 800	26 200 (382) / 33 500	33 400 (299) / 45 000
	THF	20 700 (483) / 32 300	26 400 (379) / 31 800	33 800 (296) / 48 300
	MeCN	20 900 (478) / 30 000	26 500 (377) / 35 300	34 100 (293) / 44 600
T6	CH_2Cl_2	20 700 (483) / 66 400	26 300 (380) / 45 800	33 200 (301) / 139 000
	THF	20 700 (483) / 64 900	26 500 (377) / 43 500	33 600 (298) / 147 000
(4)	CH_2Cl_2	-	-	33 000 (303) / 23 300
(6)	CH_2Cl_2	-	-	32 600 (307) / 24 700
(8)	CH_2Cl_2	-	-	32 500 (308) / 27 800
(17)	CH_2Cl_2	-	26 300 (380) / 28 100	-

[1] 2nd and 3rd peak of the NDI absorption are located at ca. 27 800 and 29 300 cm^{-1}, respectively, in CH_2Cl_2 (ΔE(peak-separation) = 1600 and 1500 cm^{-1}). For MeCN: 28 000 cm^{-1} and 29 600 cm^{-1} and for THF: 27 900 cm^{-1} and 29 500 cm^{-1}.

[2] the error of ε_{abs} lies in the range of ±3 %

In the following, the solvatochromic behaviour of selected complexes will be discussed (Figure 27). However, not all complexes permit the use of polar solvents due to solubility reasons, e.g. **T3** and **T6** were not sufficiently soluble in MeCN.

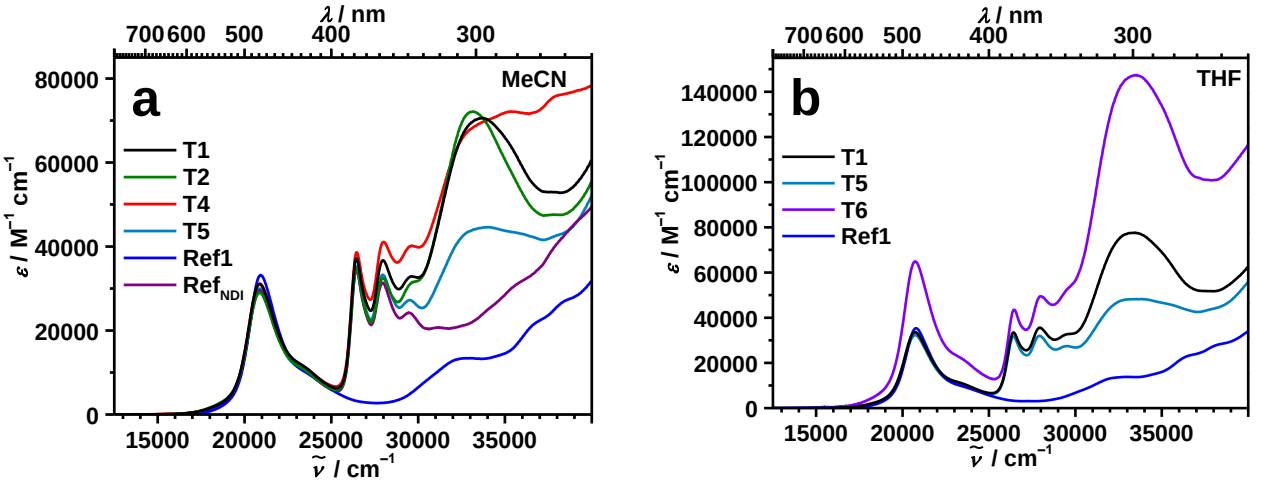

Figure 27 Absorption spectra of (a) triads **T1**, **T2**, **T4** and **T5**, reference complexes **Ref1** and **Ref$_{NDI}$** in MeCN and (b) triads **T1**, **T5** and **T6**, as well as **Ref1** in THF.

A detailed picture of the solvent dependency is only possible with the help of Table 3 because at a first sight no obvious changes can be detected. The reason for that is the little change of the absorption features in the different solvents. Despite, the important aspects going from dichloromethane to acetonitrile are: i) The π-π*-transition of the NDI is most affected by the solvent with a change of ca. 300 cm^{-1}, whereas the other bands are less shifted, ii) the maxima of the dipy absorption bands in one specific solvent are the same for all compounds, except **Ref1** which shows a little hypsochromic shift in CH_2Cl_2 and THF. iii) Furthermore, the maximum of the molar extinction coefficient for the LC-band of the Ir(dipy)-fragment in **Ref1** is always higher in intensity compared to the other complexes where the ligand framework is substituted with either donor and/or acceptor moieties. iv) Concerning ε_{max} for specific bands in different solvents, there is no general trend present, but can be summarised as follows: the dipyrrin (except **Ref1**) and TAA bands are more intense in THF, whereas the NDI features have the highest absorption in MeCN.

In conclusion, the spectroscopic features are dominated by the transitions of the three chromophoric units which are: ligand-centred absorption of the iridium dipyrrin fragment in the middle of the visible spectrum (15 400–25 000 cm^{-1}) and in the UV the vibronic transition of the NDI (25 000–31 000 cm^{-1}) and the structureless band of the TAA (29 000–37 000 cm^{-1}). The different units are well separated and, in addition, there is less to no communication between the three moieties. Finally, little solvatochromism can be observed.

3.1.1.3 Emission- and Excitation-Spectroscopy

As was already shown by *Thompson et al.* iridium dipyrrin complexes are weak emitters (with low quantum yields, cf. Table 4). However, their emission features are extended into the NIR (near-infrared) spectral region with a *Stokes*-shift of more than 6000 cm^{-1} between the ^{1}LC absorption and the ^{3}LC emission maximum and a lifetime of several microseconds. These properties are strong indicators of a spin-forbidden process, i.e. phosphorescence.[142] The results in the present work confirm the findings of the *Thompson* group. As displayed in Figure 28 the emission spectra of **Ref1** (blue) in 2-MeTHF exhibit a structured band with at least three peak maxima at 14 500 cm^{-1} (690 nm), 13 400 cm^{-1} (746 nm) and 12 300 cm^{-1} (813 nm). On the contrary, the highly fluorescent BODIPY dyes (Figure 26) possess fluorescence quantum yields up to 100 %, a *Stokes*-shift of less than 700 cm^{-1} and fluorescence lifetimes in the range of some ns or less.[299-301]

In general, the comparison of pure organic triplet emission with iridium complex phosphorescence reveals a shortening of the lifetime for the transition metal complexes due to the SOC effects. Accordingly, these transitions are partially allowed. However, for the iridium dipyrrin complexes only low quantum yields were detected probably as a result of the energy-gap law and the indirect spin-orbit coupling ^{1}MLCT onto the ^{3}LC state. For that reason, non-radiative deactivation of the lowest excited state is increased when the energy content of that state decreases. Low quantum yields can be also explained by a distorted dipyrrin ligand framework in the coordination sphere of the iridium metal. The π-plain of the dipyrrin (cf. X-ray structure in Figure 24) is slightly bent and may favour non-radiative pathways.[141]

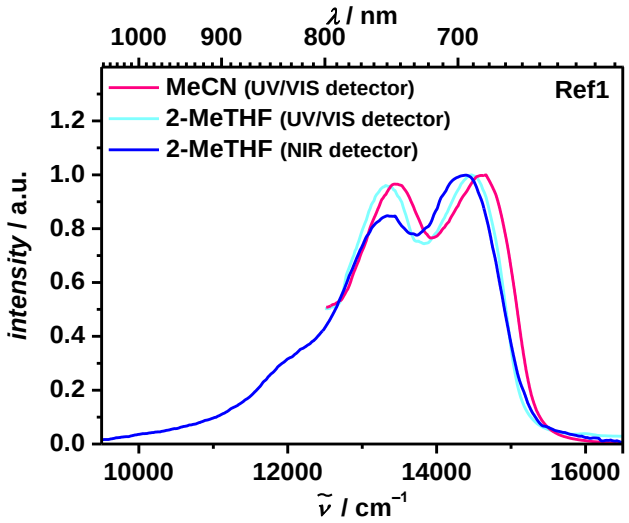

Figure 28 Emission spectra of reference complex **Ref1** in 2-MeTHF (blue and cyan) and in MeCN (red). The cyan and red spectra are recorded with a photomultiplier (R928P) for the UV/Vis and the blue spectrum with an InGaAs-detector for the NIR spectral region.

An important aspect of the emission analysis is the choice of the emission detector. The phosphorescence spectra of **Ref1** in 2-MeTHF and MeCN are plotted in Figure 28. Using 2-MeTHF it was possible to record the spectra with two different detectors i) a InGaAs-diode which covers the complete emission band and ii) a photomultiplier (R928P, Hamamatsu) which is only sensitive up to 12 500 cm^{-1} (800 nm). Although the detection range of the photomultiplier is limited, the first two peak maxima of the emission can be compared resulting in a higher intensity for the second peak and a shift of the emission maxima by ca. 100 cm^{-1}. This can be explained by the limited sensitivity of the photomultiplier at the end of the detection range at 12 500 cm^{-1} (800 nm). Thus, the difference in the emission spectra may be caused by an erroneous correction of the emission band by the spectrometer software due to a limited sensitivity of the detector in that spectral region.

Nevertheless, the use of the InGaAs-diode was limited because the overall sensitivity of the diode is reduced compared to the photomultiplier and spectra of the complexes in MeCN could not be recorded because of a reduced quantum yield in that solvent (cf. Table 4). Thus, the photomultiplier had to be used for all complexes at rt. Furthermore, a decrease of the emission quantum yield in polar solvents for **Ref1**, like MeCN, and a further reduced emission intensity of the triads, which show only minor features, was observed. For that reason, the access to reliable quantum yields and band shapes was limited. However, for

Ref1 it was possible to determine the quantum yield in MeCN with a calibrated integrating sphere using a CCD array (Ocean Optics).

Table 4 Emission maxima, quantum yields and lifetimes of **Ref1** and emission maxima of **Ref_{NDI}**, **T1**, **T2** and **T4**. Emission data of **Ref1** and **T1** at 77K in a 2-MeTHF glassy matrix.

	solvent	$\tilde{\nu}_{max}$ (λ_{max})[1] / cm^{-1} (nm)	Φ_{em}	τ_{em} / µs
Ref1	2-MeTHF (rt)	14 500 (690) 13 400 (746) 12 300 (813)	0.06[2]	5.3[2]
	2-MeTHF (77 K)	14 800 (676) 13 500 (741) 12 200 (820) 11 100 (901)	–	17.8[3]
	MeCN (rt)	14 700 (680) 13 400 (746)	0.016[4]	1.68[3]
Ref_{NDI}	MeCN (rt)	14 300 (699) 13 300 (752)	–	–
T1	2-MeTHF (rt)	only minor features	–	–
	2-MeTHF (77 K)	14 800 (676) 13 500 (741) 12 200 (820) 11 100 (901)	–	10.3[3]
	MeCN (rt)	only minor features	–	–
T2	MeCN (rt)	only minor features	–	–
T4	MeCN (rt)	14 200 (704) 13 400 (748)	–	–

[1] all complexes were excited at 20 800 cm^{-1} (480 nm), [2] according to ref.[142], [3] see Appendix for decay profiles, [4] determined by a calibrated integrating sphere, – could not be determined

Despite the limited analytical description of the emission properties of the presented triads and reference complexes, some important features could be assessed which are outlined in the following.

One central outcome of the phosphorescence measurements is the fact that the emission band can be clearly assigned to a ligand-centred transition of the iridium dipyrrin fragment, because of band shape, lifetime and solvatochromic behaviour of these spectra. The lifetimes of LC emissions are typically in the range of one microsecond or higher, whereas the lifetime of MLCT dominated emission is shortened and the bands are broad and structureless and show strong solvatochromism. Conversely, the difference of the emission maxima of complex **Ref1** in different solvents, e.g. in 2-MeTHF and MeCN, is with 300 cm^{-1} relatively small. Furthermore, the rigidochromic[107, 138, 145, 148, 193, 196] (see introduction section 1.2.3) behaviour of **Ref1** in a 2-MeTHF matrix at 77 K (Figure 29) resulted in a minor hypsochromic shift of the emission maxima of 400 cm^{-1} which is a strong indicator for the LC emission. Accompanied with that, the emission intensity is strongly increased and a fourth emission peak in the vibronic progression can be detected which was not visible at rt. Moreover, for triad **T1** a very similar emission band appears and the lifetime of the phosphorescence is strongly increased for **Ref1** and **T1** with 17.8 and 10.3 µs, respectively.

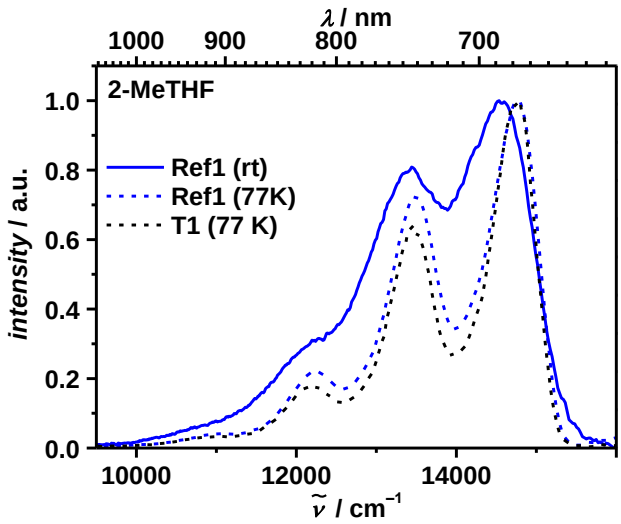

Figure 29 Emission spectra of **Ref1** (blue) and **T1** (black) in 2-MeTHF at rt and 77 K (solid and dashed lines, respectively).

As already mentioned, the triad complexes show only minor or no emission, even at high concentrations of up to $4 \cdot 10^{-5}$ M. Hence, the low intensity phosphorescence only was detected with the photomultiplier and therefore the emission band shapes and maxima differ compared to **Ref1**. For example, the second maxima of the emission peak is sometimes more intense than the first one (Figure 30b) due to an inaccurate correction of the emission signal (*vide supra*) and in general, the signal-to-noise ratio is strongly decreased (Figure 30a).

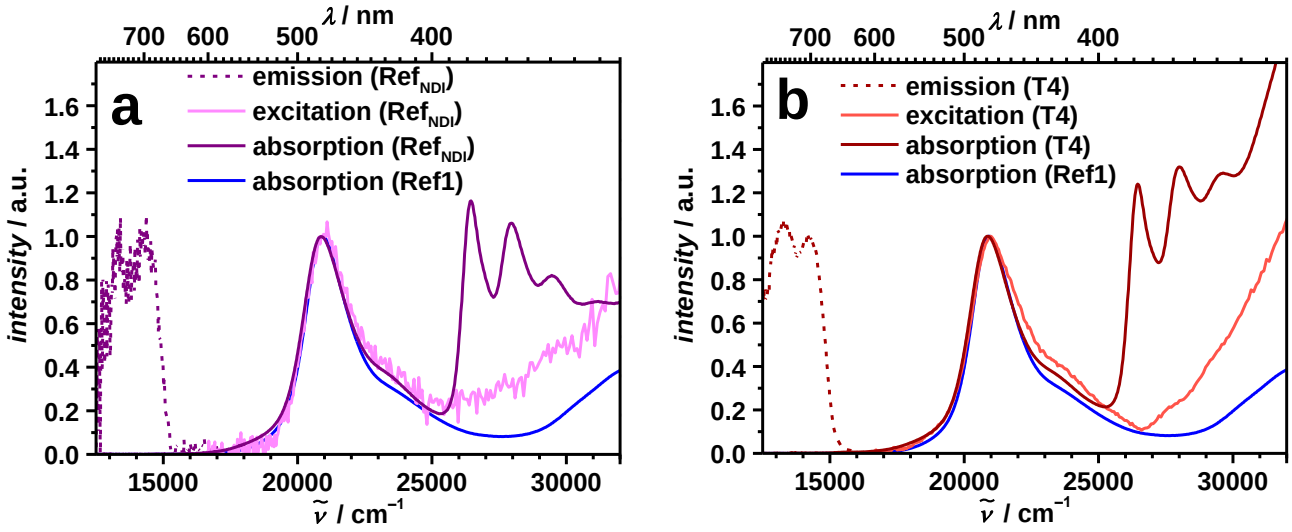

Figure 30 Emission, excitation and absorption spectra of (a) **Ref$_{NDI}$** and (b) **T4** in MeCN at rt.

However, the emission and excitation spectra of **Ref$_{NDI}$** and **T4** in MeCN were obtained by exciting the samples at $\tilde{\nu}_{ex}$ = 20 800 cm^{-1} (480 nm) and detecting the emission at $\tilde{\nu}_{em}$ = 14 500 cm^{-1} (690 nm), respectively. The excitation features in the visible spectral region fit quite well to the LC absorption band of both complexes. Conversely, at higher energies the excitation and absorption spectra of **Ref$_{NDI}$** and **T4** differ noticeably. Interestingly, the difference occurs as the NDI absorption is involved above ca. 25 000 cm^{-1} (400 nm). Thus, it seems to be obvious that there is limited energy transfer from higher-lying states, in this case NDI excited states, to the emitting state which is located on the iridium dipyrrin fragment. This supports the assumption of weak coupling between the iridium dipyrrin complex and the NDI unit (*vide supra*).

The strength of this coupling was further investigated by emission spectroscopy of the reference NDI **17**. Two theories may adopt for this, the *Dexter* and the *Förster* energy-

transfer (EnT).[302-304] *Dexter* energy transfer (EnT) between NDI and the dipyrrin can be ruled out because a direct orbital overlap is not present. The NDI nodes and the 90° and 120° orientation of the bridging phenyl ring reduce the orbital overlap to zero. The alternative, the *Förster* EnT is dependent on the overlap integral of the fluorescence of the energy donor, i.e. the NDI, and the absorption spectrum of the energy acceptor, i.e. the iridium complex, and the rate constant of the fluorescence, including quantum yield and radiative lifetime. Hence, the fluorescence in MeCN and CH_2Cl_2 was investigated by exciting into the NDI absorption band at 29 400 cm^{-1} (340 nm). Unfortunately, the fluorescence in MeCN could not be determined which is a sign for a very low quantum yield and, thus, the subsequent experiments were performed solely in CH_2Cl_2. In Figure 31 the absorption spectrum and emission spectrum are displayed. The absorption spectrum shows the typical structured NDI transition (*vide supra*), whereas the emission is characterised by a broad band with an emission maximum at 19 000 cm^{-1} (526 nm). The broad band is representative for a CT transition coming from a charge shift from one *N*-substituted phenyl unit to the NDI core. The emission from the π-π*-excited state, often observed for *N*-alkylated NDIs,[292, 294, 305-306] is only present to a minor extend between 22 000–26 000 cm^{-1}.

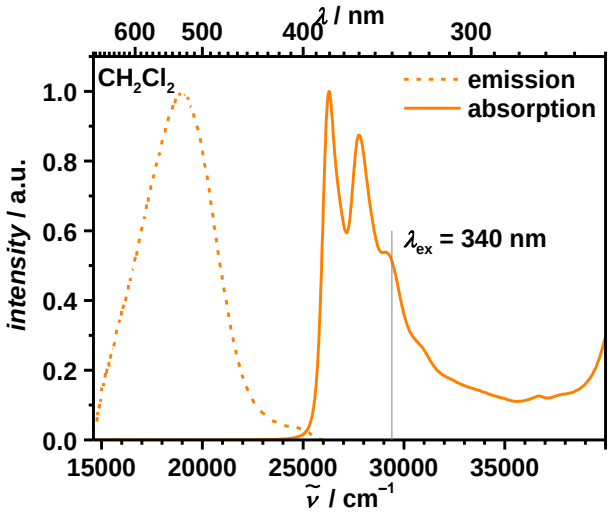

Figure 31 Emission and absorption spectra of **17** in CH_2Cl_2 at rt. Flourescence spectrum was recorded at $5 \cdot 10^{-6}$ M and the absorption spectrum at $1 \cdot 10^{-5}$ M.

Although there is an excellent overlap of the emission spectra with the absorption of the iridium dipyrrin transition under 25 000 cm^{-1} (above 400 nm), the quantum yield

(Φ < 1 %)[292] and lifetime (τ < 100 ps)[305] of the NDI emissions are in general too low/short to allow for an efficient *Förster* EnT to the iridium complex. Consequently, the observations in Figure 30, where the excitation spectra of **Ref$_{NDI}$** and **T4** lack of the NDI absorption band, may be explained by a very inefficient *Dexter* or *Förster* EnT. The energy of the NDI-CT state is determined by the intersection point of a tangent at the high energy side of the CT emission band with the x-axis[41] yielding 2.76 eV for the emission in CH_2Cl_2. However, the energy of the CT fluorescence in MeCN may be lower due to a distinct stabilisation of that state in a more polar solvent.

In conclusion, the NIR emission of the iridium complexes, **Ref1** is only weak (Φ_{em} = 1.6 %) and for the triads it is hardly detectable (Φ_{em} << 1 %). On the contrary, at 77 K in 2-MeTHF strong phosphorescence is observed, even now for triad **T1** (Figure 29). In general, the lifetime of the radiative transition, their band shape and solvatochromic behaviour are strong indicators for their dipyrrin ligand-centred nature. Finally, energy transfer from the NDI to the iridium dipyrrin is inefficient which was shown by excitation spectroscopy and, in addition, rationalised by slow energy transfer mechanisms (*Dexter* and *Förster* mechanism).

3.1.1.4 Cyclic Voltammetry (CV)

In order to investigate the electrochemical properties of the triad complexes **T1–T6** and the reference complexes **Ref1** and **Ref$_{NDI}$** and to determine the energy of CS states (CS_1 and CS_2), cyclic voltammetry (CV) was performed in CH_2Cl_2 with tetrabutylammonium hexafluorophosphate ([*n*Bu_4][PF_6], 0.2 M) as supporting electrolyte. Moreover, for complexes, for which solubility in MeCN was sufficient, cyclic voltammetry (CV) measurements were carried out in that solvent, too. For these measurements the same electrolyte salt was used but in the case of the more polar MeCN with a lower concentration (0.1 M).[307] The overall solubility of the complexes was lower in MeCN and therefore only the voltammograms measured in CH_2Cl_2 are displayed in Figures 32–33, whereas the CV data of both solvents are listed in Table 5. All CVs were referenced against the ferrocen/ferrocenium (Fc/Fc^+) redox couple.

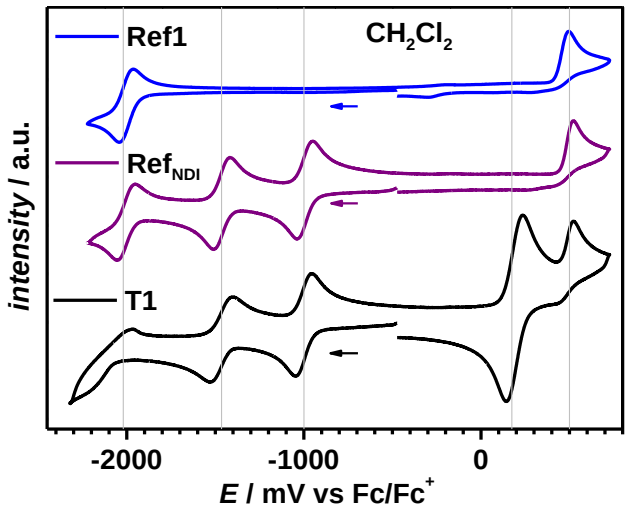

Figure 32 Cyclic voltammograms of **Ref1** (blue), **Ref$_{NDI}$** (purple) and **T1** (black) in CH_2Cl_2/[*n*Bu$_4$][PF$_6$] (0.2 M) at a scan rate of 250 mV s^{-1}. All voltammograms are referenced against (Fc/Fc$^+$), normalised and recorded by first scanning into the reductive direction. The grey lines highlight potentials at −2020, −1465, −1000, 175 and 510 mV, respectively, for an easier comparison.

First, the redox properties of **Ref1** will be discussed (Figure 32, blue). Whereas for the first reduction potential at −2005 mV in CH_2Cl_2 (−1880 mV/MeCN) a reduction wave could be observed, the first oxidation shows only an anodic peak potential at ca. 500 mV in CH_2Cl_2 (530 mV/MeCN). However, not only the oxidation is irreversible but the reduction tested by multi-thin-layer experiments and measurements at different scan rates (10–1000 mV s^{-1}) turned out to be irreversible, too. Both redox events are located at the dipyrrin fragment of the iridium complex,[142] because reduction of the *bis*-phenylpyrazole iridium fragment is according to Table 2 at much lower potentials (<−3000 mV) and the oxidation occurs at ca. 900 mV.[160] As can be seen in Table 5 this situation is similiar for all complexes in this section and averaged potentials of ca. −2020 and 500 mV for reduction and oxidation, respectively, are highlighted with grey lines in Figure 32 and 33b. Triads **T2–T3** have a slightly lower potential for the reduction process of the iridium dipyrrin part at ca. −2090 mV (Figure 33a).

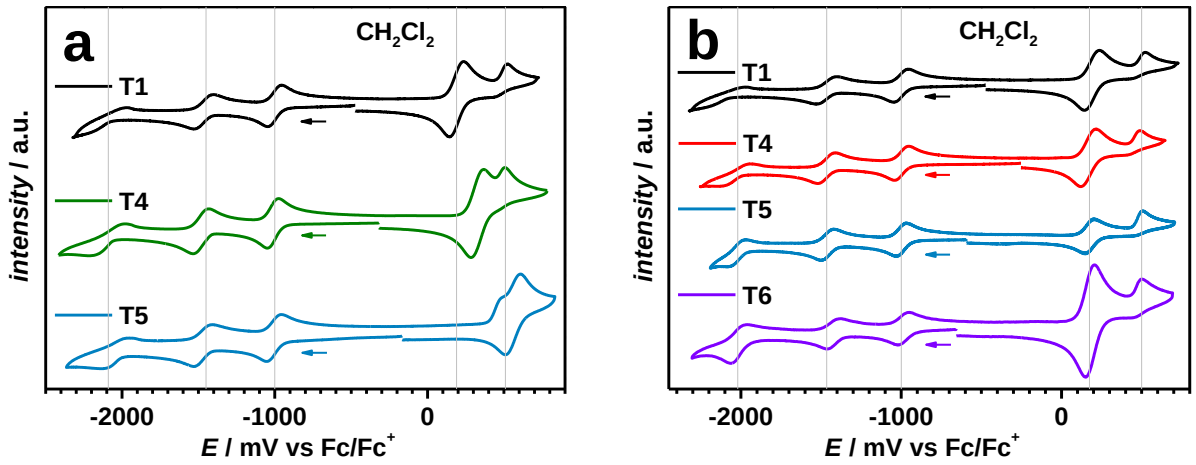

Figure 33 Cyclic voltammograms of (a) **T1**–**T3** and (b) **T1**, **T4**–**T6** in CH_2Cl_2/[nBu$_4$][PF_6] (0.2 M) at a scan rate of 250 mV s^{-1}. All voltammograms are referenced against (Fc/Fc^+), normalised and recorded by first scanning into the reductive direction. The grey lines highlight potentials at −2090 (left) and −2090 (right) and for both figures at −1465, −1000, 175 and 510 mV, respectively, for an easier comparison.

If an NDI is attached to the iridium complex, as in **Ref$_{NDI}$**, two additional reversible reduction waves appear at ca. −1000 and −1465 mV in CH_2Cl_2 (ca. −950 and −1410 mV/MeCN) which correspond to the first and second reduction of the NDI core.[71, 293-294, 297, 306, 308-311]

In a next step linking the TAA donor groups to the complex architecture results in a reversible oxidation of two identical methoxy-substituted TAAs at 190 mV in CH_2Cl_2 (225 mV/MeCN) for **T1**.[262] The oxidation potential is increased when the donor strength of the TAA is reduced, e.g. with the *tert*-butyl and chloro-substitutions in **T2** and **T3**, respectively. Thus, the oxidation occurs at 325 and 560 mV in CH_2Cl_2 for **T2** and **T3**, respectively, while all other redox properties are unchanged (Figure 33a). Moreover, the oxidation potential of the TAAs in **T3** is higher than the oxidation of the iridium dipyrrin which remains at ca 500 mV.

The cyclic voltammograms in Figure 33b correspond to the already discussed triad **T1**, the triad with a biphenyl bridge between the iridium dipyrrin and the NDI (**T4**) and complexes with a different number of amine donors (**T5**, **T6**). The comparison with **T1** shows that there is almost no difference between **T1** and **T4** because the intensity and position of the redox processes are unaltered. This is not true for the other two triads, where the intensity of the first oxidation at around 170 mV (CH_2Cl_2) changes according to the number of present TAA units, increasing from **T5** (1 TAA) via **T1**/**T4** (2 TAAs) to **T6** (4 TAAs). In addition, the intensity

of the dipyrrin reduction and oxidation is increased by the factor of two in **T6**. A second iridium complex is responsible for the increased intensity. However, the half-wave potentials of the TAAs and all the other redox events are very similar except the second reduction of the NDI in **T6** which is shifted by ca. 50 mV to lower potentials.

Table 5 Redox potentials[1] ($E_{1/2}$) and potential difference between the first reduction and oxidation ($\Delta E_{1/2}$) of **Ref1**, **Ref$_{NDI}$** and **T1–T6** in CH_2Cl_2 and MeCN. The concentration of the solute was either 1–5 mM in CH_2Cl_2 or 0.5–1 mM in MeCN.

	solvent[2]	Ir(dipy) $E_{1/2}^{red}$ / mV	NDI $E_{1/2}^{red}$ / mV	TAA $E_{1/2}^{ox}$ / mV	Ir(dipy) E_{pa}^{ox} / mV	$\Delta E_{1/2}$ / mV
Ref1	CH_2Cl_2	-2005^{i}			495^{i}	2500
	MeCN	-1880^{i}			530^{i}	2410
Ref$_{NDI}$	CH_2Cl_2	-2005^{i}	-995^{r} (-1465^{r})		520^{i}	1515
	MeCN	-1945^{i}	-960^{r} (-1405^{r})		550^{i}	1510
T1	CH_2Cl_2	-2065^{i}	-1005^{r} (-1460^{r})	190^{r}	520^{i}	1195
	MeCN	-1945^{i}	-960^{r} (-1425^{r})	225^{r}	565^{i}	1185
T2	CH_2Cl_2	-2100^{i}	-1015^{r} (-1485^{r})	325^{r}	505^{i}	1340
	MeCN	-1910^{i}	-940^{r} (-1410^{r})	410^{r}	575^{i}	1350
T3	CH_2Cl_2	-2100^{i}	-1005^{r} (-1470^{r})	560^{r}	500^{i}	1505
T4	CH_2Cl_2	-2015^{i}	-995^{r} (-1460^{r})	170^{r}	490^{i}	1165
	MeCN	-1870^{i}	-945^{r} (-1390^{r})	225^{r}	545^{i}	1170
T5	CH_2Cl_2	-2015^{i}	-1000^{r} (-1455^{r})	165^{r}	500^{i}	1165
	MeCN	-1905^{i}	-955^{r} (-1420^{r})	230^{r}	575^{i}	1185
T6	CH_2Cl_2	-2020^{i}	-985^{r} (-1415^{r})	175^{r}	510^{i}	1160

[1] all potentials are referenced against Fc/Fc^{+} and were measured at a scan rate of 250 mV s^{-1}

[2] tetrabutylammonium hexafluorophosphate ([nBu$_4$][PF_6]) was used as supporting electrolyte with a concentration of 0.2 M and 0.1 M for CH_2Cl_2 and MeCN, respectively.

E_{pa} = anodic peak potential, ^{r} reversible, ^{i} irreversible

Another important aspect of the electrochemical analysis is the negligible shift of the redox features which do not change significantly from one complex to the other, except if the electronic situation, e.g. of the TAAs, is altered (Table 5). This is again a consequence of the

low electronic coupling between the three redox units. Even for the extended π-system of the biphenyl bridge in **T4** there is neither a change of the redox behaviour of the NDI nor of the iridium dipyrrin. The use of the more polar solvent MeCN shifts the redox potential to higher potential which has almost no effect on the redox difference ($\Delta E_{1/2}$) of the first reduction and oxidation.

The $\Delta E_{1/2}$ values of the triads **T1–T6** and **Ref$_{NDI}$** offer the possibility to estimate the *Gibbs* free energy (ΔG_{CS}) of a potential charge-separated state (Table 6) according to the *Weller* approach (eq.(3)).

$$\Delta G_{CS} = \frac{N_A}{1000} ze\left[E_{ox}(D/D^+) - E_{red}(A/A^-)\right] - \frac{N_A e^2}{1000 \cdot 4\pi e_0}\left[\left(\frac{1}{2r_D} + \frac{1}{2r_A}\right)\left(\frac{1}{\varepsilon_r} - \frac{1}{\varepsilon_s}\right) + \frac{1}{\varepsilon_s d_{DA}}\right] \quad (3)$$

In eq. (3) $\Delta E_{1/2} = \left[E_{ox}(D/D^+) - E_{red}(A/A^-)\right]$ reflects the redox-difference between oxidation of the donor and reduction of the acceptor (cf. Table 5). ε_r is the dielectric constant of the solvent used in the CV and that used in the transient absorption (ε_s) measurements. r_D and r_A are the radii of the donor and the acceptor, respectively. d_{AD} is the centre to centre distance of donor and acceptor.

In all potential CS states NDI is reduced. In case of the CS state of Ref$_{NDI}$, the iridium dipyrrin is oxidised (CS_1), whereas in all other cases the triarylamine donors are oxidised to yield the fully charge-separated state (CS_2). One exception is **T3** where both possible CS states, the one with the oxidised iridium complex and the alternative with the oxidised TAA, were calculated because the oxidation processes of TAA and Ir(dipy) are strongly overlapping. The used donor-acceptor centre-to-centre distances (d_{DA}) and radii (r_D, r_A) of the redox units were based on a molecular model obtained from DFT calculations[1]. The radii $r_{D,A}$ were determined by calculating the surface of the afore calculated redox units with the "Connolly Molecular Area" tool of the ChemBioDraw Ultra 12.0 software and performing a back calculation to a radius of an ideal spherical molecule with the same surface.

[1] *Gaussian09* with *PBE1PBE* functional and a 6-31G* basis set for C, H and N and pseudo potentials (SDD) for the Ir atom was used.[312]

Table 6 Energy content (ΔG_{CS}) of charge-separated (CS) states of **Ref_{NDI}**, **T1–T6** in different solvents determined with the oxidative and reductive redox potential (E^0(A,D)), the donor-acceptor distance (d_{DA}) and the radii of the redox centres ($r_{A,D}$) according to eq. (3).

	solvent	E^0(A) / mV	E^0(D) / mV	d_{DA} / 10^{-10} m	r_D / 10^{-10} m	r_A / 10^{-10} m	ΔG_{CS} / eV
Ref_{NDI}[2]	MeCN THF[4]	−960[r,2]	535[i,1]	10.0	5.32	3.97	1.47 1.65
T1[2]	MeCN THF[4]	−960[r]	225[r]	20.1	4.81	3.97	1.17 1.44
T2[2]	MeCN	−940[r]	410[r]	20.1	5.48	3.97	1.33
T3[3]	THF[4]	−1005[r]	500[i,1] 560[r]	20.1	5.32 4.74	3.97	1.39 1.54
T4[2]	MeCN	−945[r]	225[r]	14.6 24.2	5.32 4.81	3.97	1.16 (CS_1) 1.51 (CS_2)
T5[2]	MeCN THF[4]	−1000[r]	165[r]	20.1	4.81	3.97	1.17 1.44
T6[3]	THF[4]	−985[r]	175[r]	20.1	4.81	3.97	1.41

[1] anodic peak potential, [2] CV experiments performed in MeCN/[nBu$_4$][PF_6] (0.1 M) with ε_r(MeCN) = 35.49, [3] CV experiments performed in CH_2Cl_2/[nBu$_4$][PF_6] (0.2 M) with ε_r(CH_2Cl_2) = 8.93, [4] ε_s(THF) = 7.58.

All calculated CS states (CS_1 and CS_2) are in the range of 1.16–1.65 eV in a MeCN or THF environment and thereby below the emissive iridium dipyrrin triplet excited state (^{3}Ir) for which the state energy was determined to be 1.91 eV. A possible ET from a TAA chromophore to the iridium complex (similar to the ET 1 in Figure 2a) is omitted in Table 6 because this state is at least 2.14 eV energetically uphill compared to the emissive iridium complex excited state. Thus, from an energetical viewpoint the formation of charge-separated states is downhill when exciting the complexes. But, this conclusion is drawn without knowing the energies of activation ($\Delta G^{\#}$) for each ET process. This will be part of the discussion later on.

In conclusion, the redox characteristics of the investigated complexes can be clearly assigned to the individual chromophores. In the accessible electrochemical window the reduction and oxidation of the iridium dipyrrin complex, the first and second reduction of the NDI and the first oxidation of the TAA are noticeably separated from each other, except the oxidation of the *tert*-butyl and chloro-substituted TAAs overlap with the iridium dipyrrin oxidation. The number of amines and iridium complexes are well correlated to the intensities of the specific redox units which show a vanishing coupling between each other.

3.1.1.5 Spectroelectrochemistry (SEC)

The reversible first reductions and oxidations of the triad complexes **T1–T6** are perfect requirements for the investigation by spectroelectrochemistry, where a successive increase of a negative or positive electrochemical potential induces changes of the UV/Vis spectroscopic properties of the sample/electrolyte solution. Triad **T1** will serve as an example for other triads and the measurements were performed in MeCN with the same electrolyte as in the CV experiments. Figure 34 shows the evolution of the radical anion (left) and cation (right) features when reducing or oxidising **T1**. Here, only the first oxidation and reduction are shown, because they proved to be reversible in the electrochemical investigations. The resulting features for oxidative and reductive species will help to interpret the transient absorption spectra and to understand possible ET pathways.

Upon stepwise reduction of **T1** one can see in Figure 34a the rise of five peaks at 12 900 cm^{-1} (775 nm), 14 300 cm^{-1} (699 nm), 16 500 cm^{-1} (606 nm), 21 100 cm^{-1} (474 nm) and 36 800 cm^{-1} (272 nm) (see Table 7) and a decrease of the characteristic vibronic NDI absorption between 25 000 and 31 000 cm^{-1}. Whereas the first three sharp peaks have relatively low intensities, the peak at 21 100 cm^{-1} (474 nm) strongly grows on top of the Ir(dipy) absorption at 20 800 cm^{-1} (474 nm). The evolution of the anion spectra showed one isosbestic point at 25 600 cm^{-1} (391 nm) indicating that one species turns into another which excludes the presence of further species. The decrease of the typical NDI absorption band (25 000–31 000 cm^{-1}) together with the growth of the characteristic radical anion peaks of the NDI in the visible[71, 293-294, 305, 310-311, 313-315] are strong indicators for the formation of the

$NDI^{\bullet-}$ in the first reductive process. This is in line with the CV measurements (see previous section).

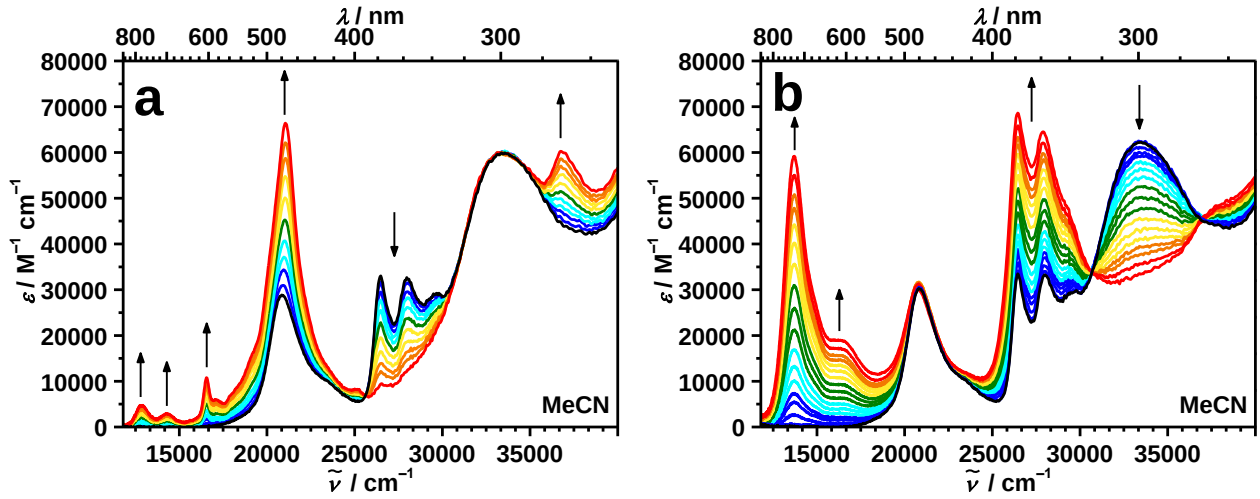

Figure 34 Spectroelectrochemistry of each the first (a) reduction and (b) oxidation of **T1** in MeCN/[nBu$_4$][PF$_6$] (0.1 M). In black: spectrum of the neutral species which acts as calibration for ε_{abs}. Early spectra in blue–green and late spectra in orange–red colours. Black arrows illustrate which bands increase or decrease.

The progress in Figure 34b represents the successive first oxidation of **T1** which is characterised by an intense signal at 13 700 cm^{-1} (730 nm) with a shoulder at 16 300 cm^{-1} (614 nm).[262, 291] Furthermore, a broad band overlapping with the NDI absorption between 25 000 and 31 000 cm^{-1} (see Table 7) and the drop of the TAA transition between 31 000 and 37 000 cm^{-1} is visible. The last two wavenumbers reflect the two isosbestic points during the oxidation process. Thus, one can clearly observe the rise of the radical cation band of the TAA which is in accordance to the CV experiment. In the CV the two TAAs are electronically equivalent and show an oxidation wave with twice the intensity.

In Figure 35 the spectra of the monoradical cation and of the anion (in blue and red) generated in the SEC measurement are plotted together with the sum of both monoradical spectra (green) and the spectrum of **T1** (black). The individual monoradicals were obtained by subtracting the spectrum of maximum intensity of either the first reduction or oxidation by the neutral ground state spectrum. In case of the monoradical cation the resulting spectrum was divided by the number of oxidised TAAs, here, by the factor 2. The resulting green spectrum should be an ideal prediction of the transient absorption spectrum, when one TAA

is oxidised and the NDI is reduced. This comparison is done in the next section. The negative signals below 25 000 cm^{-1} (400 nm) are due to a missing absorption of either the anion or the cation which is a hint for a possible ground-state bleaching in the transient absorption measurements. Table 7 summarises the characteristic radical anion and cation peaks with their molar extinction coefficients obtained in comparison the known intensity of the Ir(dipy) absorption of the neutral ground-state spectrum.

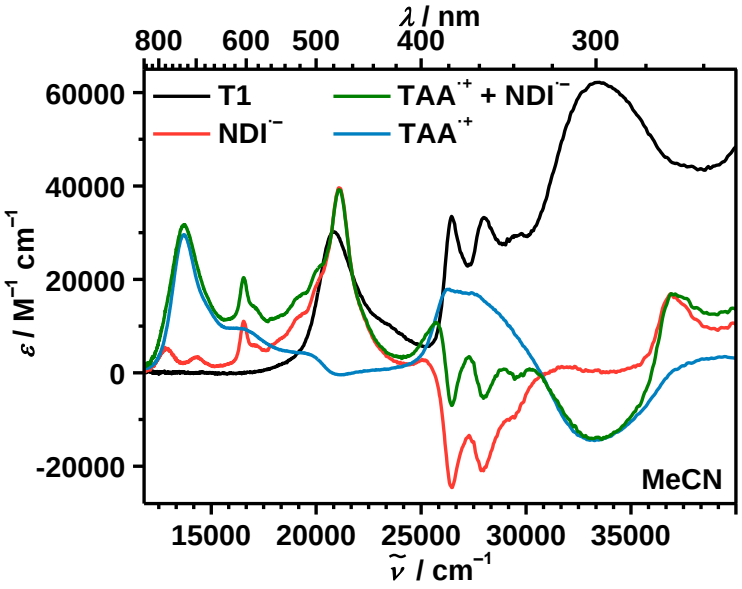

Figure 35 UV/Vis spectra of the neutral triad **T1** (black), monoradical anion (red) and cation (blue) and the sum of the latter two (green) in MeCN/[nBu$_4$][PF$_6$] (0.1 M).

Table 7 Spectroelectrochemistry data of **T1** in MeCN/[nBu$_4$][PF$_6$] (0.1 M). For the origin of the monoradical and sum spectra see text.

	solvent	NDI$^{\bullet-}$ $\tilde{\nu}_{max}$ (λ_{max}) / ε_{max} / cm^{-1} (nm) / cm^{-1} M^{-1}	**TAA$^{\bullet+}$** $\tilde{\nu}_{max}$ (λ_{max}) / ε_{max} / cm^{-1} (nm) / cm^{-1} M^{-1}	**TAA$^{\bullet+}$ + NDI$^{\bullet-}$** $\tilde{\nu}_{max}$ (λ_{max}) / ε_{max} / cm^{-1} (nm) / cm^{-1} M^{-1}
T1	MeCN	12 900 (775) / 5070 14 300 (699) / 3350 16 500 (606) / 11 000 21 100 (474) / 39 600	13 700 (730) / 29 600 14 300 (614) / 9520 26 200 (382) / 17 900	13 700 (730) / 31 700 16 500 (606) / 20 400 21 100 (474) / 39 200

3.1.1.6 Transient Absorption Spectroscopy

The formation and detection of charge-separated states is the central aim of this theses and transient absorption spectroscopy is the predominant technique allowing the detection of time-dependent charge separation or recombination in the excited states. Whereas charge recombination usually can be resolved within the ns-time domain, for the separation process a higher time resolution is necessary, e.g. fs- and ps-transient absorption spectroscopy. Furthermore, the well separated absorption band of the triads (cf. 3.1.3) permit a wavelength dependent analysis of the triads by exciting either the Ir(dipy) at 20 800/24 000 cm^{-1} (480/416 nm) or the NDI at 26 500/28 200 cm^{-1} (378/355 nm) with the fs-/ns-laser set-up, respectively.

On one side, the early processes of charge separation will be investigated with a pump-probe set-up consisting of a Helios transient spectrometer from Ultrafast Systems which is driven by a Solstice CPA femtosecond laser from Newport Spectra Physics having a pulse duration of 100 fs. The experiments were performed under magic angle conditions. The pump wavelengths used in the experiments with 20 800 cm^{-1} (480 nm) and 26 500 cm^{-1} (378 nm) excitation were generated by a TOPAS-C with a pulse duration of about 140 fs. For probing the excited sample the fundamental wavelength of 12 500 cm^{-1} (800 nm) is used to generate a white light continuum with a CaF_2 crystal from 12 500–25 000 cm^{-1} (800–400 nm).

On the other side, the longer charge recombination kinetics were investigated by ns-laser flash spectroscopy measured with an Edinburgh LP 920 Laser Flash spectrometer. The samples were excited with 5 ns laser pulses either at 24 000 cm^{-1} (416 nm) and/or 28 200 cm^{-1} (355 nm). The excitation pulse was produced by a Continuum Minilite II Nd:YAG laser operating at 10 Hz and the white light was provided by a pulsed Xe flash lamp. For experiments at 24 000 cm^{-1} the THG (third harmonic generation) of the fundamental of 9400 cm^{-1} (1064 nm) was shifted to lower energy by means of a 50 cm Raman shifter which was charged with hydrogen (∼50 bar). The corresponding energy was selected by a Pellin-Broca prism. A drawing of the set-up is shown in the experimental section. The transient maps were obtained by measuring the temporal decay profiles in 4 nm steps between 12 500 and 24 900 cm^{-1} (402–800 nm). The raw data were analysed with the data slicing tool of the software

package (LP900) yielding transient spectra at different times. In most cases the start of the slicing was set at the maximum of the obtained decay curves.

The spectra of the monoradical cation and anion derived from the SEC experiments together with the state energies of several states serve as the basis for the interpretation of the ET processes. Thus, the state diagrams were constructed taking all information from the previous section to achieve a complete picture of what happens upon light excitation in the compounds of interest.

ns-Laser Flash Spectroscopy

In the previous section the characteristic signals of the monoradical anion and cation were extracted from spectroelectrochemistry experiments. The ultimate proof if photoinduced charge separation is successful within the synthesised triads, was provided by ns-laser flash spectroscopy. The excites-state absorption of the CS state, where the NDI is reduced and one TAA is oxidised, will be the sum of both radical ion absorptions. The spectra of the monoradical ions and its sum are displayed in Figure 36. This spectral region (12 500–25 000 cm^{-1}) is essentially an enlargement of Figure 35 which match with the spectral window of the laser flash experiment for a better comparison.

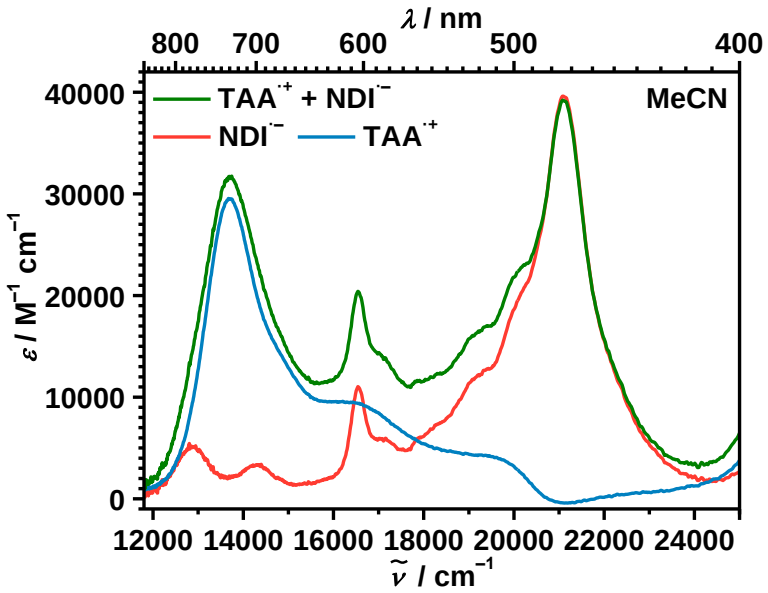

Figure 36 Spectra of monoradical anion (red) and cation (blue) and the sum of both (green) in MeCN/[nBu$_4$][PF$_6$] (0.1 M).

However, the reference complexes will be discussed first. The time-dependent transient absorption spectra of **Ref1** at 24 000 cm^{-1} (416 nm) in MeCN and THF shown in Figure 37a and b, respectively, are dominated by an intense ground-state bleaching (GSB) signal at 20 800 cm^{-1} (480 nm). A comparison with the ground-state absorption spectra (Figure 25 and 26) of all complexes in this spectral region explains the origin of the corresponding state. The iridium dipyrrin fragment obviously possesses only a weak excited-state absorption (ESA) at $\tilde{\nu}$ < 18 000 cm^{-1} (556 nm) and the population of the iridium excited state results in a "dark" state behaviour with a strong bleaching band. The recovery of the ground state can be fitted with a single time constant of 1.86 and 3.79 µs in MeCN and THF, respectively. These lifetimes are in good agreement with the emission lifetimes of the phosphorescence (1.68 and 5.3 µs in MeCN and 2-MeTHF, respectively) corroborating the assumption that the decay of the iridium dipyrrin triplet excited state to the ground state is monitored.

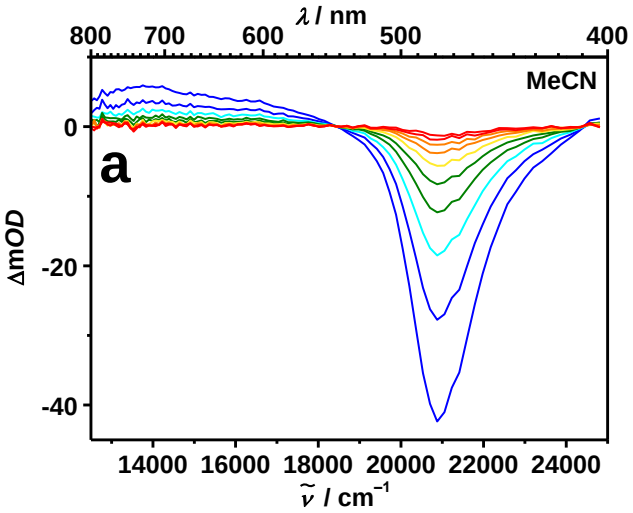

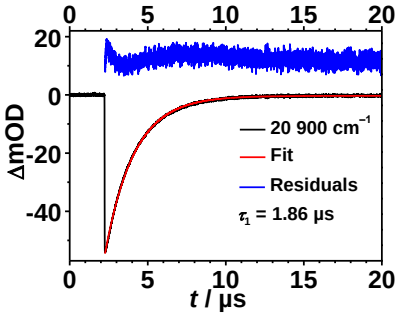

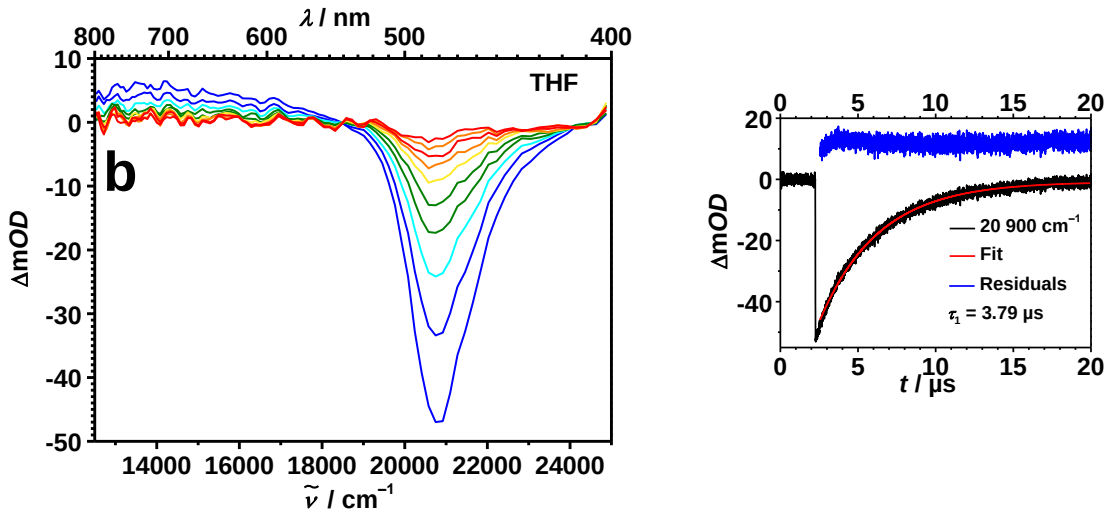

Figure 37 ns-Transient absorption spectra of **Ref1**: (a) in MeCN (0–6.5 µs) and (b) THF (0–11.4 µs) and corresponding time scans and fits at 20 900 cm^{-1} (480 nm). Early spectra are shown in blue/green and spectra at later times in yellow/orange/red colours.

On the contrary, the transient absorption measurements of $\mathbf{Ref_{NDI}}$ at 24 000 cm^{-1} (416 nm) suffer from too short-lived transient species in MeCN and THF making it difficult to detect any kinetic traces. Therefore, the measurements were performed in *tert*-butyl methyl ether (^{t}BME) and are shown in Figure 38. In this relatively nonpolar solvent it was possible to record a very short-lived component with a lifetime of τ_1 = 4.3 ns after deconvolution with the instrument response function (IRF of ca. 8 ns). But these traces have a low signal-to-noise ratio. The observed component exhibits a bleaching signal at 20 600 cm^{-1} (486 nm) and an additional excited-state absorption peak with minor intensity at 16 500 cm^{-1} (606 nm) with the same decay profile (not shown). The latter peak can be correlated to the NDI radical anion (cf. Figure 36, red) but missing the intense signal at 21 100 cm^{-1} (474 nm) which is located in the same spectral region as the GSB of **Ref1** at 20 800 cm^{-1} (480 nm). Overlaying both spectra, GSB and radical anion, results in a reduced GSB signal with a shift of the maximum by ca. 500 cm^{-1} because the monoradical anion absorption steals intensity at the high energy side of the GSB. At this point it has to be mentioned that the measured lifetime is within the lower limit of the time resolution of the TA set-up. For that reason, the rise of the transient absorption in Figure 38 from blue to cyan and the following recovery of the ground state (cyan to red) is not further interpreted because fitting a rise and a decay time with this short lived species is not reliable. Consequently, this will be matter of discussion in the fs-

pump probe experiment (*vide supra*) but this time in MeCN. The take home massage from the current observation is the fact that a reduced NDI in combination with a GSB of the Ir(dipy) may be caused by a charge-separated state (CS_1) where the positive charge is located at the Ir(dipy) unit.

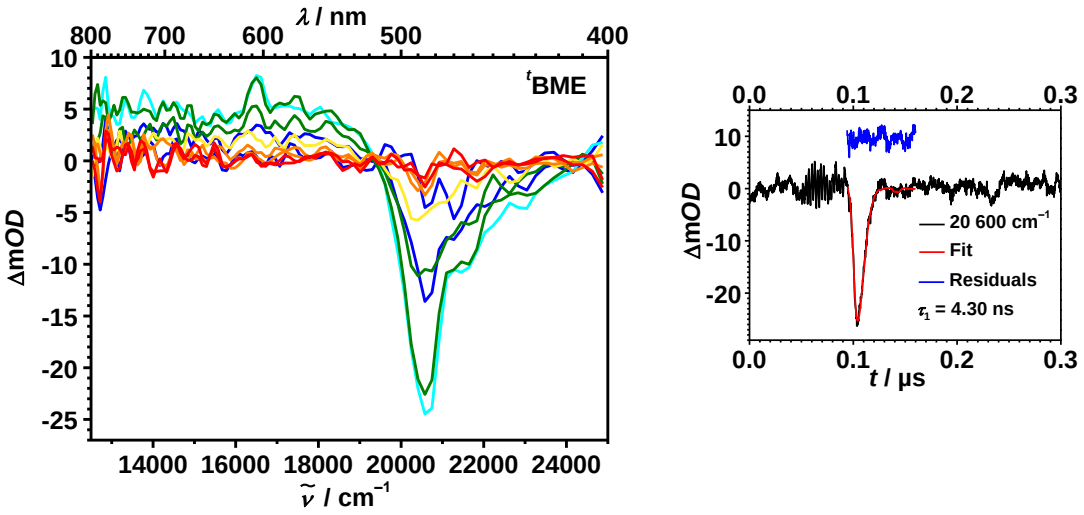

Figure 38 ns-Transient absorption spectra of **Ref_{NDI}** in ^{t}BME (0–32 ns) and corresponding time scan and fit at 20 600 cm^{-1} (480 nm). Early spectra are shown in blue/green and spectra at later times in yellow/orange/red colours.

In the following, the transient spectrum of the triads will be analysed. In principle, the presence of the triarylamine donors added to the phenylpyrazole framework permit a second ET from a TAA to the complex, whereas in **Ref_{NDI}** only the first ET to CS_1 was possible (cf. Figure 2b). The second ET will result in the fully charge-separated state CS_2.

First, **T1** was excited at 24 000 cm^{-1} (416 nm) in MeCN and THF. The TA spectra in both solvents (Figure 39) are identical in shape showing three ESA peaks at 13 700 cm^{-1} (730 nm),[262, 291] 16 500 cm^{-1} (606 nm) and 21 100 cm^{-1} (474 nm)[71, 293-294, 305, 310-311, 313-315] and, thus, resemble to the sum of spectra of the monoradicals in Figure 36 (green).[64, 66] Accordingly, the formation of a charge-separated state with the TAA radical cation and the NDI radical anion was confirmed. The decay time measured at all peak maxima was identical and is shown for the kinetic profile at 21 100 cm^{-1} (474 nm) as an example. Fitting the decay curves yielded monoexponential lifetimes of τ_1 = 580 and 160 ns in MeCN and THF, respectively. Besides, the longer lifetime of 580 ns in a more polar solvent (MeCN) provides further information of the nature of the fully charge-separated state. The estimation of the

energy content of the CS_2 state (Table 6) yielded 1.17 and 1.44 eV in MeCN and THF, respectively. This argument in combination with the shorter lifetime of the CS_2 state with higher energy in THF is proof for the recombination taking place in the *Marcus* normal or optimum situation. The polar CS state is better stabilised within polar solvents, such as MeCN. Consequently, the CS state with the higher energy content (1.44 eV in THF) has a higher driving force for the recombination process, which in turn should be faster (160 vs. 580 ns).

Furthermore, the laser flash experiments were performed with a laser energy of 28 200 cm^{-1} (355 nm) where predominantly the NDI is excited, yielding exact the same transient absorption spectra (not shown) with similar lifetimes.

The energies of activation for the different charge separation and recombination steps will be discussed at the end of the fs-pump-probe section (Table 8).

Finally, the quantum yield of the formation of the CS state at 24 000 cm^{-1} (416 nm) and 28 200 cm^{-1} (355 nm) was estimated by actinometry with $Ru(bpy)_3Cl_2$ (in H_2O)[47] and benzophenone (in benzene)[316], respectively. The results were 100 % for the 24 000 cm^{-1} (416 nm) and 47 % for the 28 200 cm^{-1} (355 nm) excitation. The following equation $\Phi_{CS} = \Phi_{ref} \times ((\Delta OD_{CS} \times \varepsilon_{ref}) / (\Delta OD_{ref} \times \varepsilon_{CS}))$[260, 317] was used to calculate these yields. Here, Φ_{Ref} is the quantum yield of the population of the triplet state of the reference compounds ($Ru(bpy)_3Cl_2$ or benzophenone) which are according to literature[318-320] set to one. The ΔOD values were obtained from the ns-TA measurements and the extinction coefficient for maxima of certain bands were extracted from literature (see Experimental Section)[47, 316] or were determined by spectroelectrochemistry (cf. Table 7). Interestingly, excitation at two different chromophores results in a different efficiency of the ET in this triad. The NDI excitation is less efficient than the iridium dipyrrin excitation which will be discussed in more detail in the next section. In the following the quantum yields are expected to be similar for a specific excitation energy but in different solvents.

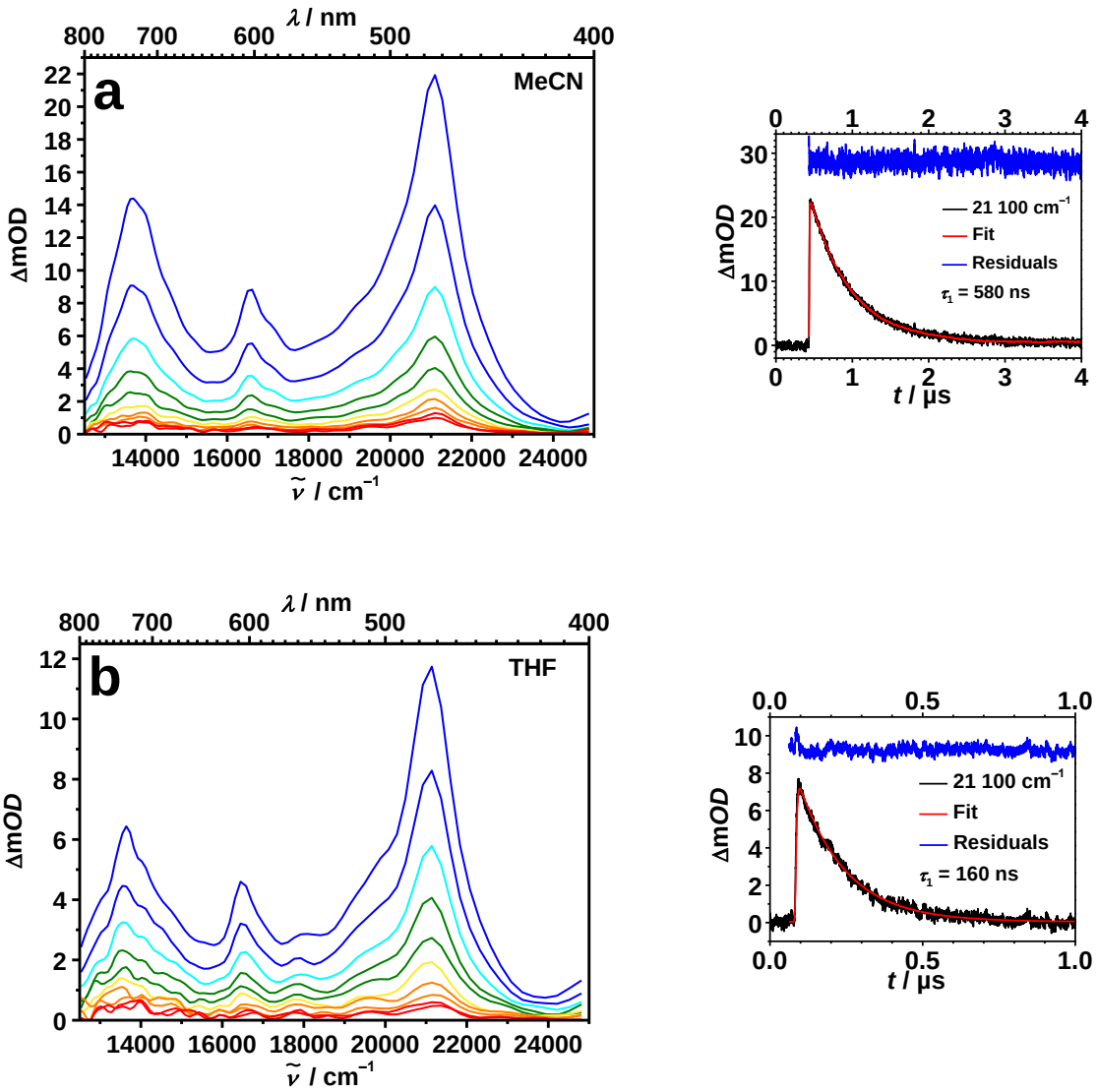

Figure 39 ns-Transient absorption spectra of **T1**: (a) in MeCN (0–2.1 µs) and (b) THF (0–0.5 µs) and corresponding time scans and fits at 21 100 cm^{-1} (474 nm). Early spectra are shown in blue/green and spectra at later times in yellow/orange/red colours.

The next analysis deals with the TA spectra of **T5** and **T6**. Both complexes should form the same CS state, due to identical donor-acceptor distances and equal redox properties, differing only in the number of amines. Indeed, the TA spectra of both triads (Figure 40) look very similar to those of **T1**. However, because of the low solubility of **T6** in MeCN only measurements in THF were performed. Therefore, measurements of **T5** in MeCN and those of **T6** in THF are shown in Figure 40a and b, respectively.

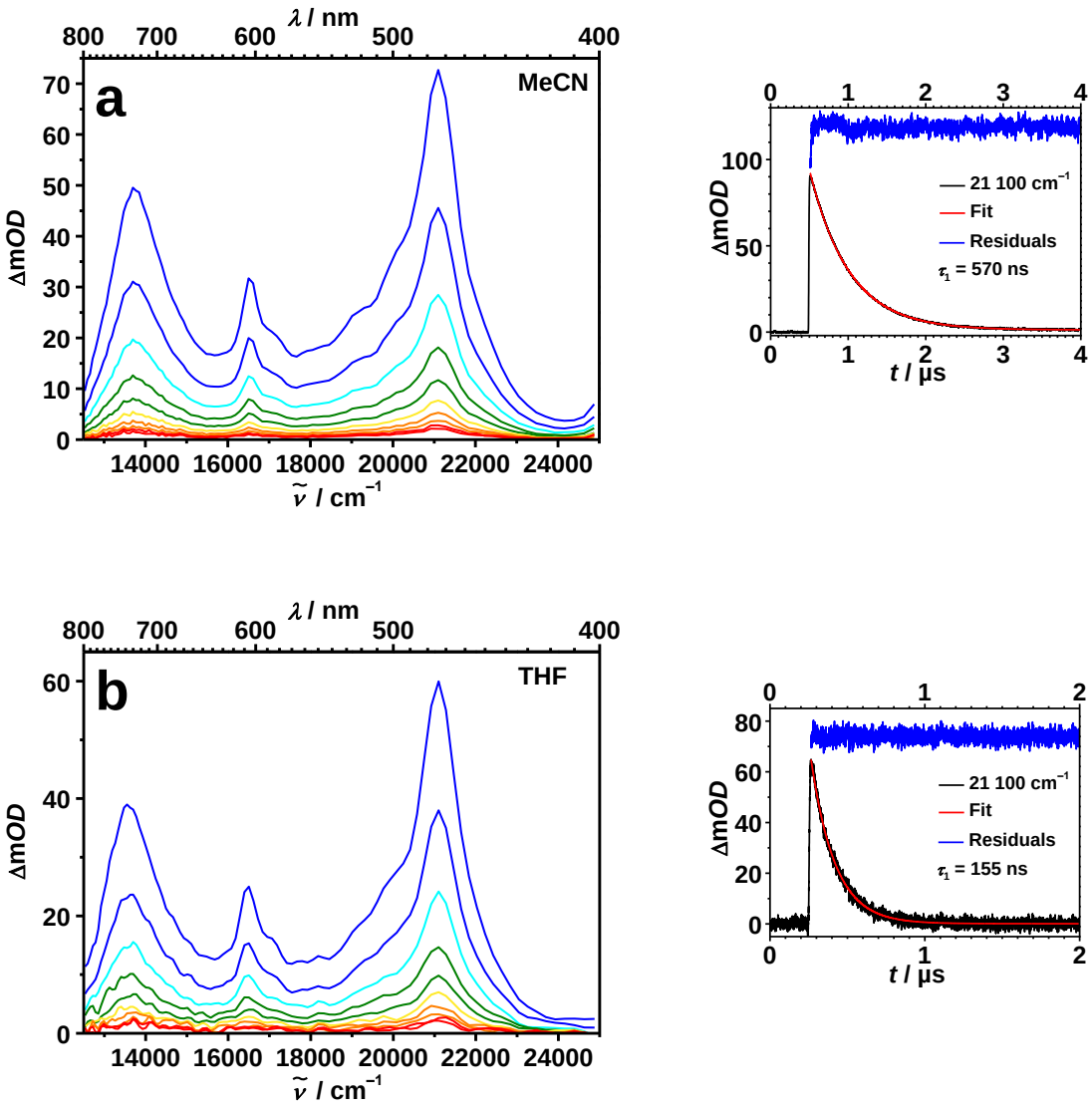

Figure 40 ns-Transient absorption spectra of **T5**: (a) in MeCN (0–2.5 µs) and (b) of **T6** in THF (0–0.74 µs) and corresponding time scans and fits at 21 100 cm^{-1} (474 nm). Early spectra are shown in blue/green and spectra at later times in yellow/orange/red colours.

The corresponding time constants found in MeCN for **T5** and in THF for **T6** (570 and 155 ns, respectively) are very similar to the lifetimes of **T1** in MeCN and THF (580 and 160 ns, respectively). The ns-TA spectra of **T5** in THF (not shown) exhibit almost identical transient spectra with a slightly increased lifetime of τ_1 = 185 ns. The experiments with **T5** and **T6** at 28 200 cm^{-1} (355 nm) laser energy were not conducted because they are expected to show the same behaviour as **T1**. Consequently, the number of amines has no effect on the charge recombination kinetics. But the number of donor sites probably will influence the charge separation process in these triads, which will be investigated in detail in chapter 3.1.4.

Triad **T4** with an additional phenyl unit between the Ir(dipy) and the NDI fragment was excited at both laser energies (24 000 cm^{-1} (416 nm) and 28 200 cm^{-1} (355 nm)) to investigate the effect of the longer bridge on the charge recombination.

In order to cover the details of rise and decay processes, the analysis was performed for two time windows (460–622 ns, Figure 41a and 42a). Hence, excitation of triad **T4** produces a series of ΔOD spectra shown in Figure 41a and b (24 000 cm^{-1} (416 nm)) and 42a and b (28 200 cm^{-1} (355 nm)) which reflect the dynamics quite well.

First, excitation at 24 000 cm^{-1} (416 nm) starts with a strong bleaching signal in Figure 41a and the spectra further evolve to an overall positive transient spectrum. The strong bleaching signal with a minimum at ca. 20 800 cm^{-1} (480 nm) proves the initial population of ligand centred iridium complex states (cf. Figure 37). A kinetic trace corresponding to the short time window which reflects the rise of the signal is shown in Figure 41. The rise time of the excited-state absorption could be fitted with τ_1 = 35 ns, which seems to be much longer than in the case of all other triads. The CS_2 state of **T1**, **T5** and **T6** were always completely developed within the instrument response. Consequently, the prolonged distance between iridium complex and NDI (ca. 14.6 Å in **T4** vs. ca. 10.0 Å in all other triads) may cause the relatively long rise time because the ET has to proceed via the biphenyl spacer. The final ΔOD spectrum in Figure 41a shows the characteristic peaks of the TAA radical cation at 13 700 cm^{-1} (730 nm)[262, 291] and of the NDI radical anion at 21 100 cm^{-1} and 16 600 cm^{-1} (474 and 602 nm)[71, 293-294, 305, 310-311, 313-315] which proves charge separation in **T4**. Its transient spectrum decays without further changes of spectral shape (cf. Figure 41b). Its decay characteristics are biexponential comprising a component of τ_2 = 12.3 µs (66 %) and a component of τ_3 = 79 µs (34 %). The determination of the quantum yield by actinometry (*vide supra*) at 24 000 cm^{-1} (416 nm) exhibited a value of 97 % which is little less compared to the findings of **T1** with a shorter donor-acceptor distance, but still very efficient.

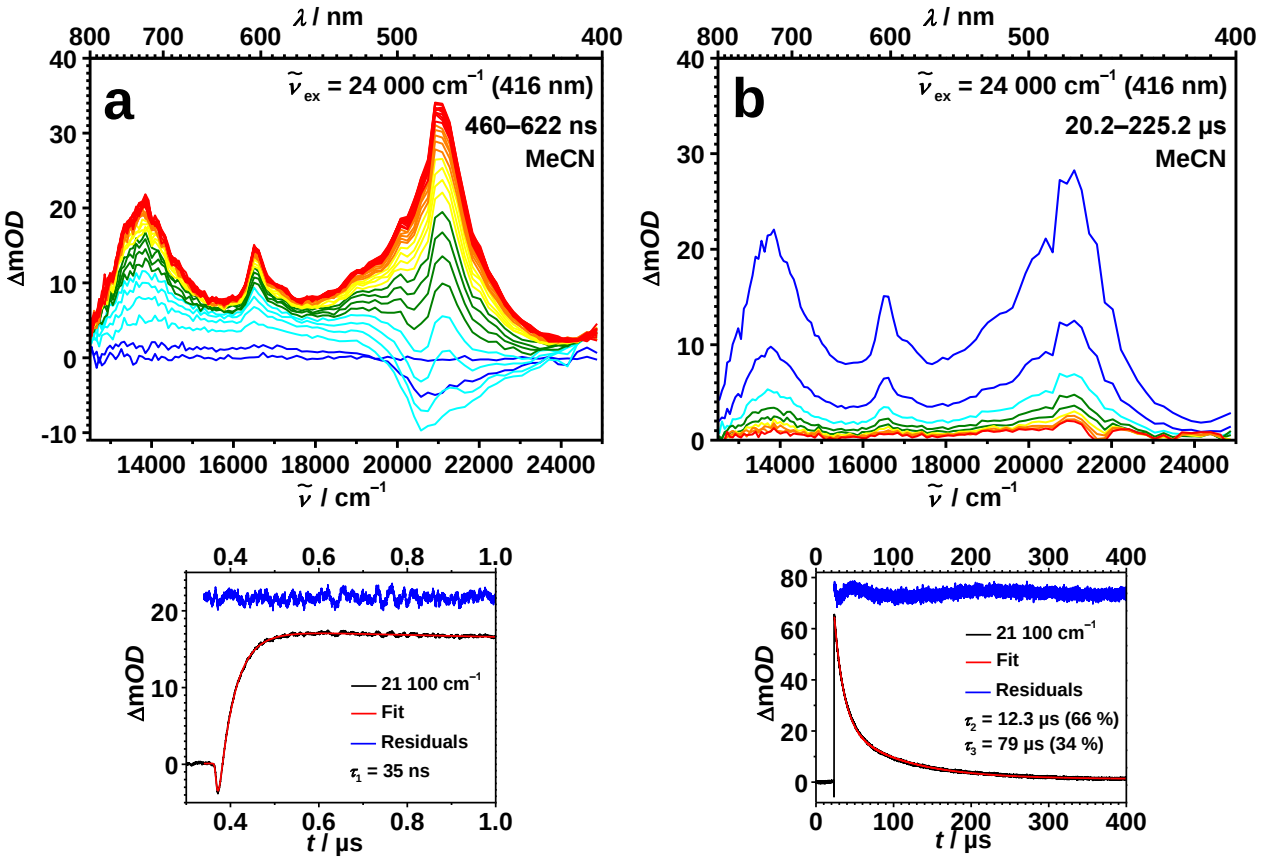

Figure 41 ns-Transient absorption spectra (excitation at 24 000 cm^{-1} (416 nm)) of **T4** in MeCN: (a) (460–622 ns) and (b) (20.2–225.2 µs) and corresponding time scans and fits at 21 100 cm^{-1} (474 nm). Early spectra are shown in blue/green and spectra at later times in yellow/orange/red colours.

On the other side excitation at 28 200 cm^{-1} (355 nm) produces very similar spectra (Figure 42) which differ only in the short time window (460–622 ns) from those in Figure 41a when the Ir(dipy) unit is excited. The evolution of the exited state absorption does not exhibit any bleaching characteristics, but forms the fully charge-separated state starting from zero. Besides, the rise of the CS_2 state was monitored (Figure 42a) which is correlated to a time constant of τ_1 = 31 ns similar to the former experiment. Besides, the formation of the CS_2 was with Φ_{CS} = 37 % less efficient compared to triad **T1** which can be correlated to the longer ET distance in **T4** making the first ET less efficient. Likewise, the full decay (cf. Figure 42b) was biphasic with one component of τ_2 = 17 µs (66 %) and a second component of τ_3 = 72 µs (34 %), as well. Hence, both experiments provide an identical picture of the rise and the full decay of the charge-separated state (CS_2). However, comparing Figures 41a and 42a there is a small but interesting difference. The precursor of the CS_2 state seems to be different in both

experiments because on one side the bleaching signal (Figure 41a) is a hint for the excited iridium complex and on the other side excitation at 28 200 cm^{-1} (355 nm) gives no further information on the precursor state. But both are formed within the same time range (τ_1 = 30–35 ns). A detailed analysis of the charge-separation processes will be matter of debate in the fs-pump-probe section (*vide infra*).

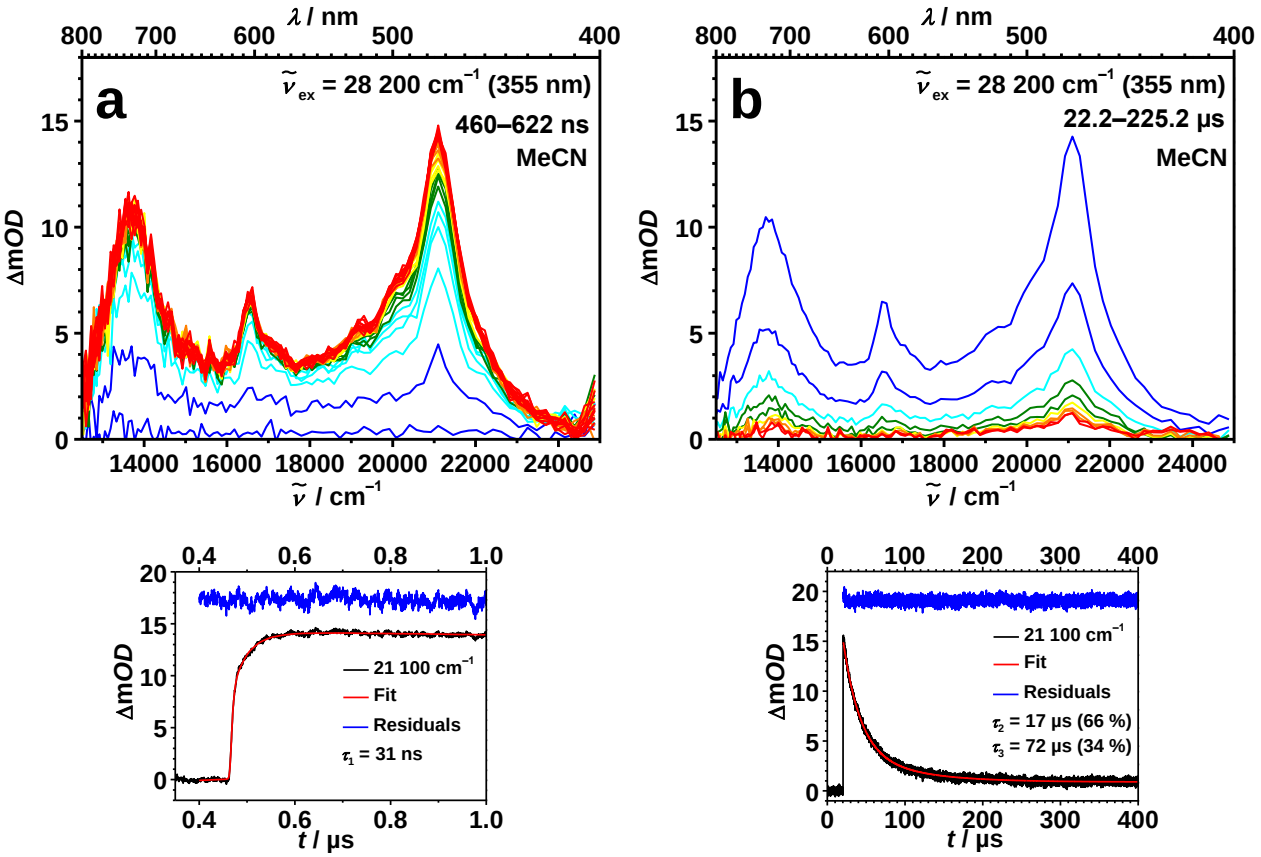

Figure 42 ns-Transient absorption spectra (excitation at 28 200 cm^{-1} (355 nm)) of **T4** in MeCN: (a) (460–622 ns) and (b) (20.2–225.2 µs) and corresponding time scans and fits at 21 100 cm^{-1} (474 nm). Early spectra are shown in blue/green and spectra at later times in yellow/orange/red colours.

For the observation of a second decay time, in principle two explanations may be offered: the first is the possibility of a bimolecular deactivation, which can be excluded, because the two lifetimes of the CS_2 state do not change significantly with different concentrations of $8.5 \cdot 10^{-6}$–$4.6 \cdot 10^{-5}$ mol L^{-1} and pulse energies of 0.2–1.0 mJ in the ns-time regime. The second explanation may be related to an additional degree of freedom of triad **T4** concerning conformational changes, due to the extra phenylene ring between the NDI and

the iridium complex. One can estimate that in order to observe a biphasic decay from two different excited conformers with the given amplitudes and lifetimes, the rate for interconversion of these conformers must not exceed 2000 s^{-1}. However, this appears to be much too slow for isomerization around a biphenyl axis.

Another aspect related to a biphasic decay of a charge-separated state which was not yet discussed is the solvent dependence. The CS_2 state of **T4** should be located in the normal *Marcus* region as it was observed for **T1** (*vide supra*). For that reason the charge recombination kinetics were investigated in THF (Figure 43), too, but this time solely with excitation energies of 24 000 cm^{-1} (416 nm).

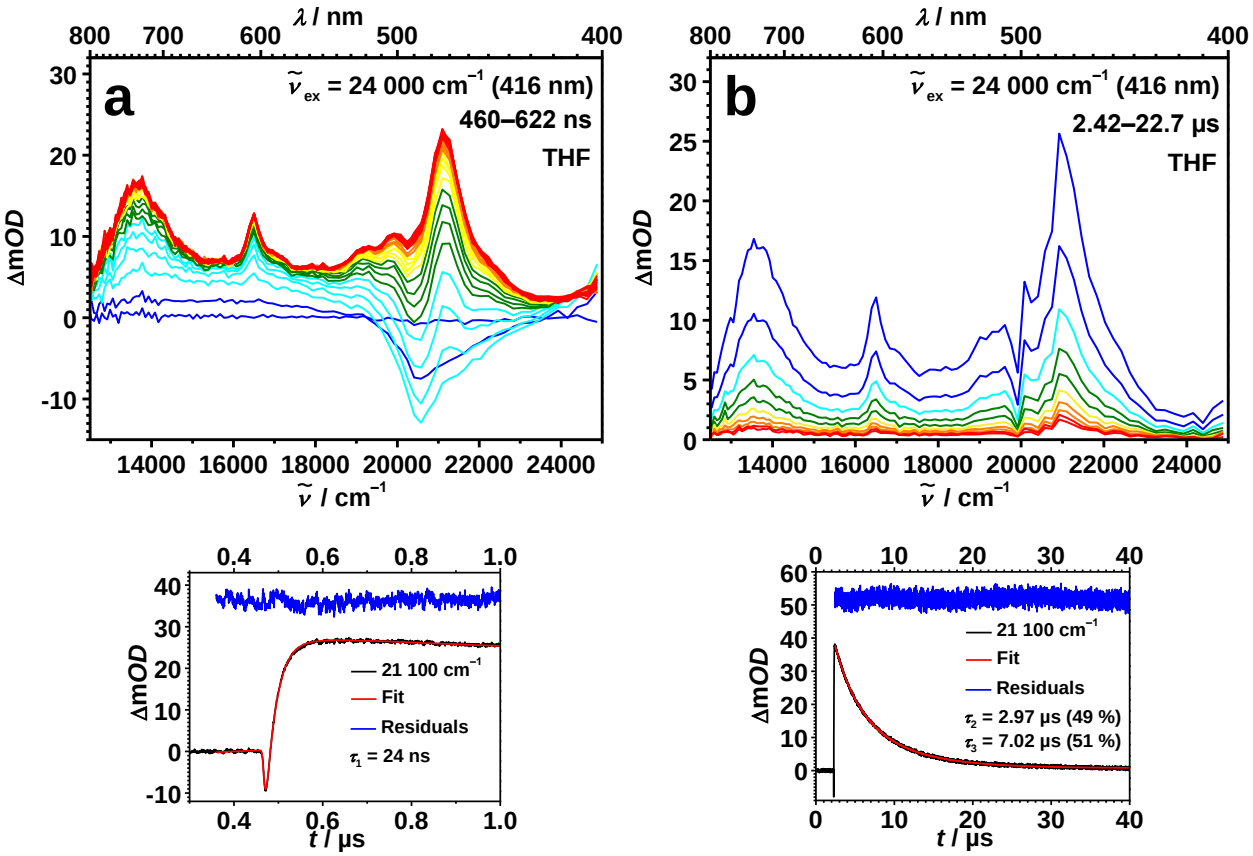

Figure 43 ns-Transient absorption spectra (excitation at 24 000 cm^{-1} (416 nm)) of **T4** in THF: **a** (460–622 ns) and **b** (2.42–22.7 µs) and corresponding time scans and fits at 21 100 cm^{-1} (474 nm). Early spectra are shown in blue/green and spectra at later times in yellow/orange/red colours.

The results in Figure 43 (**T4** in THF) are very similar to those in Figure 41 for **T4** in MeCN, except charge separation and recombination kinetics are different from the findings

for **T1**, as expected. In the time range of 460–622 ns (Figure 43a) a shorter rise time from the initial bleaching signal to the CS_2 state was detected (τ_1 = 24 ns) compared to the MeCN experiment (τ_1 = 35 ns). Next, the complete evolved CS_2 signal with TAA cation and NDI anion peaks decays without any spectral change with two time constants. The first component has a lifetime of τ_2 = 2.97 µs (49 %) and the second of τ_3 = 7.02 µs (51 %). Consequently, the change of the solvent not only shortens the rise and decay times, it additionally influences the ratio of the amplitudes of both decay times (from 66/34 in MeCN to 49/51 in THF). Obviously, the change of the solvent is accompanied with the change of the ratio of both involved species which may point to a slow equilibrium between two species. Thus, at the time being, there is no reasonable explanation for this observation. It has to be emphasised, though, that both lifetimes, τ_2 = 12.3–17 µs and τ_3 = 72–79 µs in MeCN and even those found in THF (τ_2 = 2.97 µs and τ_3 = 7.02 µs), are exceptionally long for the recombination of a CS state in such a small triad in fluid solution at rt. Moreover, the relatively small change in the donor-acceptor distance by just one phenylene unit (from 20.1 Å in all other triads to 24.2 Å in **T4**) is responsible for a drastic increase of the charge-recombination lifetime (from ns to µs by a factor of at least 100).

Finally, triads **T2** and **T3** are the last members of the triad family and their discussion will follow now. The strength of the donors in these two triads is reduced and as a consequence the CS_2 state is lifted up in energy (Table 6) slowing down charge separation processes and increasing the rate for charge recombination. Both complexes were excited at the iridium dipyrrin chromophore (at 24 000 cm^{-1} (416 nm)) where charge separation in all triads discussed before was achieved. Unfortunately, triad **T3** could not be measured because the decay of the signals was too short for the time resolution of the ns-laser set-up. But this was already expected from the CV data, where the chloro-substituted TAA is harder to oxidise than the Ir(dipy) unit which is equivalent to an energetically uphill ET (1.39 to 1.54 eV in THF, Table 6) from the first to the second charge-separated state in this complex. If population of the first charge-separated state is possible in this triad, will be discussed in the fs-pump-probe section (*vide infra*).

The *tert*-butyl-substituted triad **T2** was measured in MeCN and the results can be observed in Figure 44. The recorded spectra show the already mentioned radical anion peaks

at 21 100 cm^{-1} and 16 600 cm^{-1} (474 and 602 nm)[71, 293-294, 305, 310-311, 313-315] but the radical cation peak is shifted by 900 cm^{-1} to 14 600 cm^{-1} (685 nm) compared to the methoxy-substituted complexes. This effect is caused by a changed electronic situation in the TAA when going from OMe to ^{t}Bu which shifts the radical cation band to higher energies. The lifetime of the charge-separated state is relatively short with τ_1 = 32 ns, because the driving force for charge recombination is increased from 1.17 eV in the OMe-complexes up to 1.33 eV in the ^{t}Bu-substituted complex (Table 6). This behaviour is again a proof for being in the *Marcus* normal situation. Thus, the increased CS_2 state energy (1.33 eV) causes a lower energy of activation and therefore the stored energy can more easily relax to the ground state and a shorter lifetime can be observed.

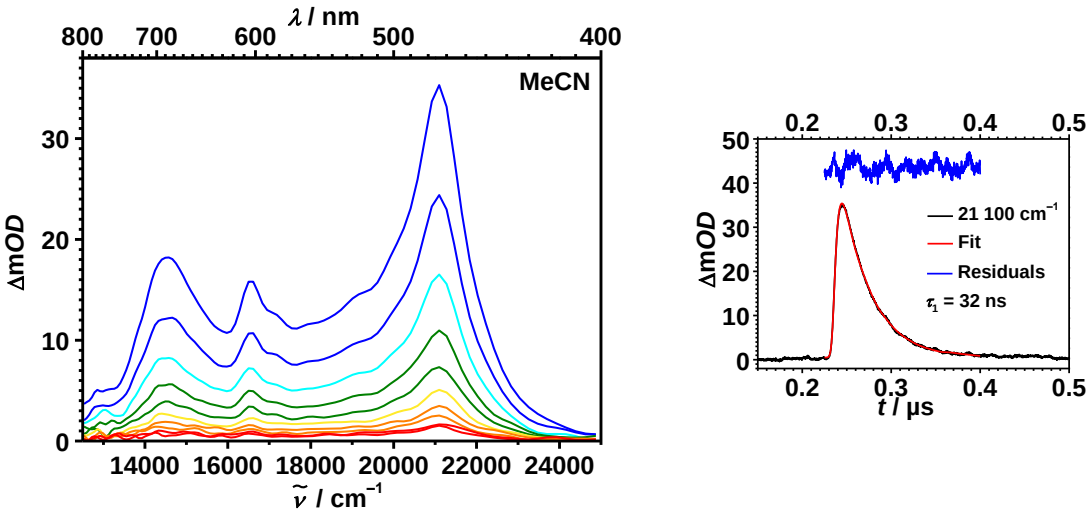

Figure 44 ns-Transient absorption spectra (excitation at 24 000 cm^{-1} (416 nm)) of **T2** in MeCN (445–567 ns) and corresponding time scans and fits at 21 100 cm^{-1} (474 nm). Early spectra are shown in blue/green and spectra at later times in yellow/orange/red colours.

In conclusion, the results show that in almost all triads, except **T3**, a CS state was efficiently (Φ_{CS} up to 100 %) generated. This was achieved by exciting the iridium dipyrrin or the NDI chromophore with 24 000 cm^{-1} (416 nm) and 28 200 cm^{-1} (355 nm), respectively. Even in the reference complex **Ref$_{NDI}$** charge separation was successful. This observation points to the existence of the first CS state (CS_1) in the triads, following the ET sequence in Figure 2b. The same situation as in **Ref$_{NDI}$** may hold for **T3** where the lowest excited state is

expected to be identical. A detailed analysis of the charge-separation processes in **T3** is given in chapter 3.1.2.

The lifetimes of the fully charge-separated states of triads **T1**, **T5** and **T6** in MeCN are with $\tau_1 \approx 580$ ns very similar and are relatively long compared to those of the triads presented in the introduction (see Table 1). Moreover, being in the *Marcus* normal region of the ET potential surfaces the lifetimes decrease from 580 ns to i) 160 ns in less polar solvents, i.e. THF and ii) 32 ns by using donors with an increased redox potential, i.e. TAA_{tBu}. On the contrary, little increase of the donor-acceptor distance (phenylene vs. biphenyl) in triad **T4** prolongs the lifetime by a factor of more than 100 compared to the former three triads (79 µs vs. 580 ns). Interestingly, the formation of the CS state is hardly affected by the long rise time of τ_1 = 35 ns in MeCN (τ_1 = 24 ns in THF) and is with nearly 100 % efficiency in a comparable order to triad **T1** (ca. 100 %). Moreover, the lifetimes of the final CS_2 states of the different triads do not change significantly in aerated MeCN.

fs-Pump-Probe Spectroscopy

Next, a short introduction of the ultrafast transient absorption experiments will be given. The ultrafast pump-probe spectra are the central basis of the interpretation of the charge-separation dynamics in the synthesised triads. The subsequent chapters (3.1.2, 3.1.3 and 3.1.4) have many aspects in common which can be summarised as follows. i) The transient maps (time × wavelength) obtained by exciting at the NDI moiety at 26 500 cm^{-1} (378 nm) and second by exciting the iridium dipyrrin unit at 20 800 cm^{-1} (480 nm) were deconvoluted by global fitting with GLOTARAN[321] employing a sequential or a target model (i.e. branched model) taking into account the IRF (ca. 150–300 fs), the white light dispersion (chirp), and the coherent artifact (the model used has the time characteristics of the IRF) at time zero. The sequential and target model yield evolution associated difference spectra (EADS) and species associated difference spectra (SADS), respectively.[321] In addition, the corresponding time constants and efficiencies for the formation of the SADS based on the assumption of reasonable extinction coefficients at selected wavelengths were obtained. The number of components was estimated by singular value decomposition. Lifetimes of states marked with “infinite” are longer than the maximum time delay (8 ns) of the fs-pump-probe

set-up and the state diagrams will also be complemented with the fitted times from the ns-laser-flash experiments because both set-ups overlap in the time window between 4 and 8 ns.

In the subsequent chapter complexes **Ref1**, **Ref$_{NDI}$** and the NDI (**17**) serve as reference compounds to evaluate common excited state properties of the used chromophores. Besides, the results of **T1–T6** will be presented in the same way but are split into discrete chapters where different aspects of selected triads will be discussed. For example, chapter 3.1.2 gives a general view on the excited state properties of the reference compounds together with the charge-separation dynamics in triad **T1** and **T2** in MeCN and **T3** in THF. These triads differ in their redox strength of the donor site (OMe, ^{t}Bu and Cl, respectively) but comprise the same acceptor chromophore (NDI). The dynamics will be further investigated at different pump energies to see if a different excited state behaviour can be induced in these triads.

On the contrary, chapter 3.1.3 covers the ET aspects of **T4** where the donor and acceptor strength is identical to **T1**. However, these two complexes differ in the distance between the NDI and Ir(dipy) chromophore. Whereas **T1** consists of a phenylene spacer between both chromophores, a biphenyl bridge determines the distance of these chromophores in **T4**. In the ns-transient absorption section an increase of the charge recombination and separation was already observed. Hence, the chapter 3.1.4 will highlight the ET characteristics of the changed bridging unit. Furthermore, the additional degree of freedom due to the biphenyl bridge will be evaluated.

The last chapter, including fs-pump-probe spectroscopy of the synthesised triads, will concentrate on the concept of symmetry breaking in the charge-separation process of triads **T1**, **T5** and **T6**. The structural requirements for this purpose are given by the different number of quenching events equal to the number of amine donors in **T5**, **T1** and **T6**, respectively. In addition a second iridium complex in **T6** is present, too.

A last remark to the structure of the following three chapters is related to the way of presenting the experimental data. The EADS/SADS (Figure Xa) and corresponding transient absorption evolution (Figure Xb) plus decay kinetics at selected wavelengths (Figure Xc) are presented for each molecular structure. Furthermore, the rate constants for the different

energy or electron transfer steps are listed in the Appendix and the state diagrams provide a detailed overview of the photophysics in these compounds.

3.1.2 Stepwise versus Concerted Two-Electron Transfer

Introduction

This section will focus on the electron transfer properties of triads **T1–T3** which are investigated with the help of **Ref1** and **Ref$_{NDI}$** and **17**. First, both reference complexes and **17** will be studied, whereas **Ref1** is just excited at the maximum of the Ir(dipy) absorption band at 20 800 cm^{-1} (480 nm). Additionally, **17** is solely pumped at 26 500 cm^{-1} (378 nm) laser energy. All other complexes will be pumped at both laser energies (Figure 45). Thereafter, a detailed summary is given whether the ET mechanism is governed by a stepwise or concerted two-electron transfer.

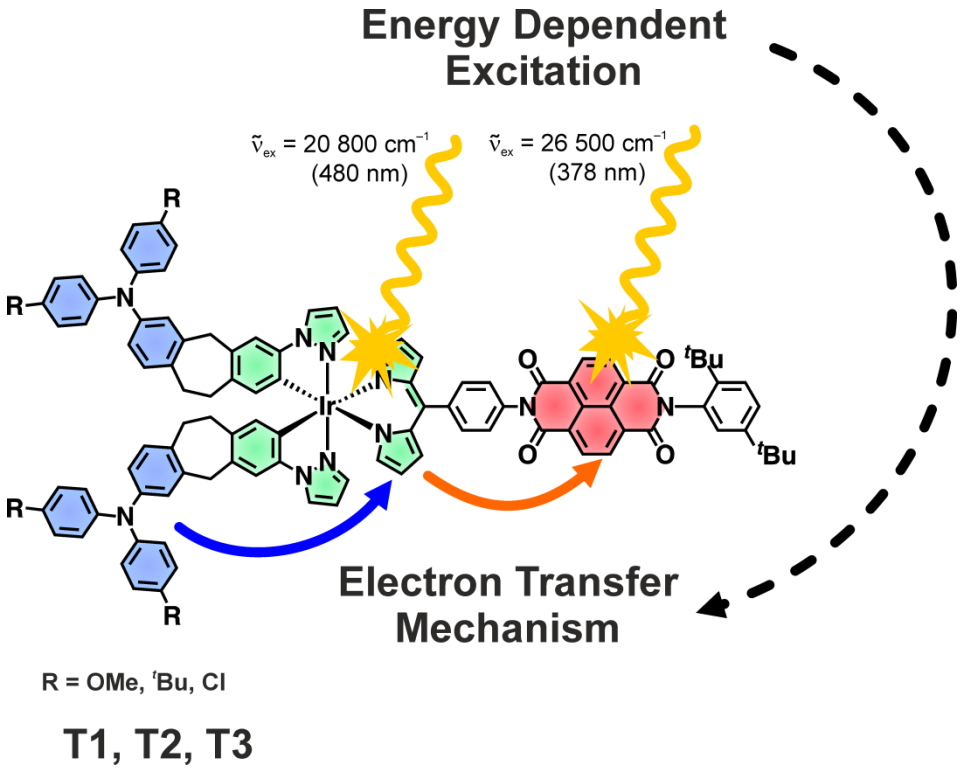

Figure 45 Excitation of the iridium complex and the NDI in triads **T1–T3** at different laser energies affects the mechanism of the electron transfer in these triads.

Reference Compounds

The experiments with **Ref1** were performed in MeCN (Figure 46) and at an excitation wavenumber of 20 800 cm^{-1} (480 nm) which excites the Ir(dipy) unit. Within the instrument

response time a strong ground-state bleaching (GSB) at 20 800 cm^{-1} (480 nm) is observed, indicating the formation of an excited iridium complex as this exhibits only little excited-state absorption but otherwise GSB. The identical spectrum was already obtained in Figure 37 for the same complex. The first EADS ($^3Ir_{initial}$ = ^3Ir_i) has a lifetime of τ_1 = 51 ps and is followed by an almost identical spectrum (corresponding to a transition from ^3Ir_i to ^3Ir) with a slightly lower intensity. The lifetime of this spectrum could not be determined within the time window of the employed set-up and is therefore set as infinite. Hence, the state diagram is labelled with the fitted time of 1.86 µs from the ns-experiment. Emission measurements revealed a similar lifetime of 1.68 µs (*vide supra*).

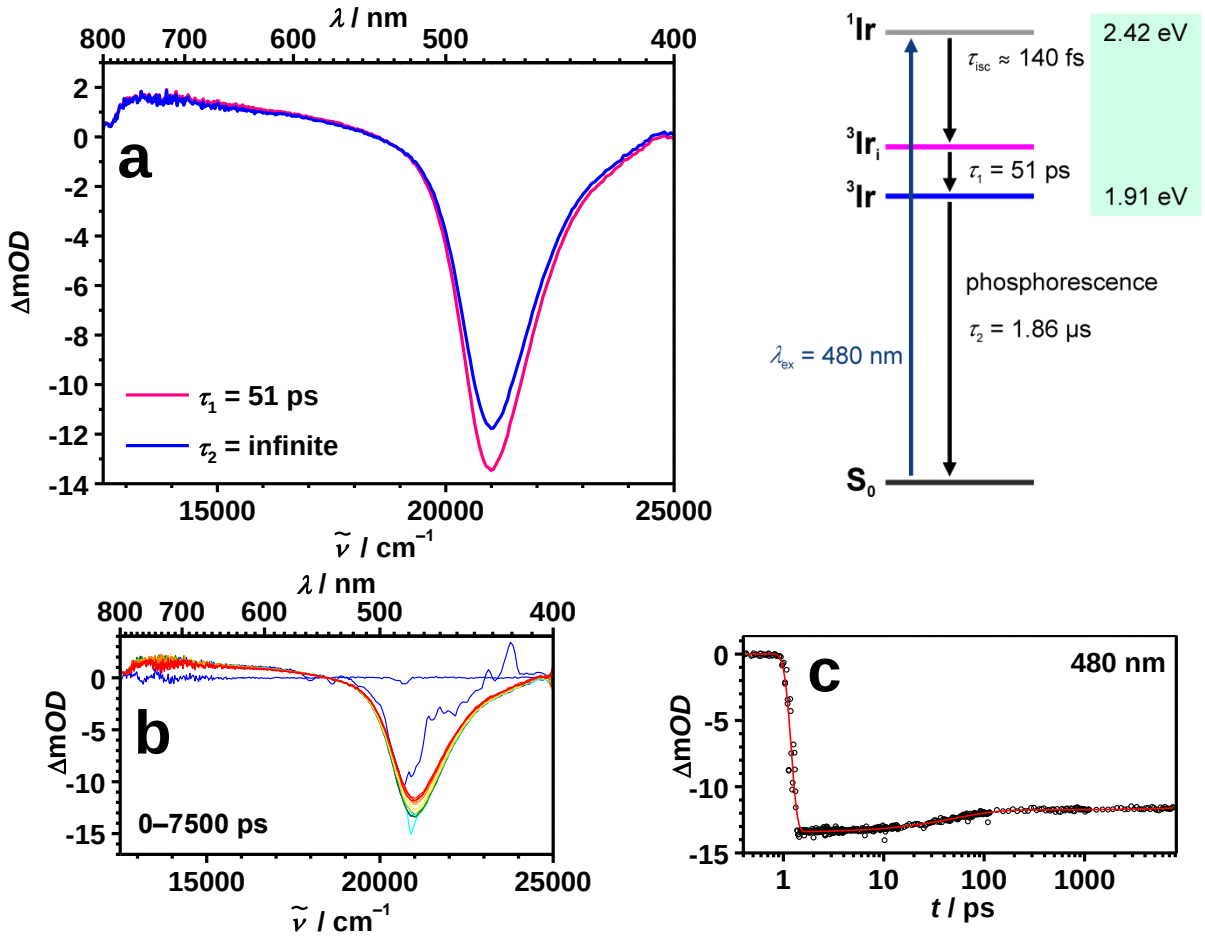

Figure 46 (a) Evolution associated difference spectra (EADS) of **Ref1** obtained from a global analysis of a transient map. The colours of the EADS refer to the states in the corresponding state diagram (right). (b) fs-Transient absorption data corrected for chirp and scattered pump light. Early spectra are depicted in blue to green and at later times in orange to red colours. (c) Decay profiles at selected wavelengths for which the zero time delay was set arbitrarily. Excitation at 20 800 cm^{-1} (480 nm) in MeCN.

Identical spectral features of consecutive spectra may be an indication of intersystem crossing but for metal complexes often a very faster ISC (< 100 fs) is observed.[186-190] The ISC is usually as fast as or even faster than the time resolution of the used laser set-up of ca. 50 fs after deconvolution with the instrument response. From the transient absorption measurements no ISC could be observed for **Ref1**. Besides, the group of Prof. Dr. *M. Chergui* (Lausanne) was able to determine an ISC lifetime of ca. 140 fs by fs-resolved fluorescence up-conversion.[296] The longer lifetime (infinite) clearly reflects the phosphorescence deactivation (see emission and ns-laser flash section) whereas for the shorter one (51 ps) a solvent reorganisation can be excluded as the average solvent reorganisation time of MeCN is about 0.5 ps.[322] One possible explanation for the ps lifetime may be a conformational change of one part of the molecule, e.g. the rotation of the phenyl ring in the *meso*-position of the dipyrrin ligand.

The second transient-absorption analysis of the NDI reference **17** will help to explain the photophysics of the NDI unit at 26 500 cm^{-1} (378 nm) excitation (Figure 47 and 48). From the target evaluation of the global fit six SADS were obtained which indicates a complex excited state behaviour. The first SADS within the instrument response shows the prominent features of the NDI singlet excited state (^{1}NDI) with a peak at 16 900 cm^{-1} (592 nm)[305] with a lifetime of τ_1 = 89 fs (Figure 48a, black). For the following state an intense signal at ca. 21 200 cm^{-1} (472 nm) and a weaker one at 16 600 cm^{-1} (602 nm) are observed (see Figure 48a, light blue) which are both typical of the NDI radical anion ($NDI^{\bullet-}$)[71, 292, 294, 305, 310-311, 313-315] and were already observed in the SEC and ns-laser flash experiments. The subsequent spectrum (formed with τ_2 = 219 fs) looks very similar to the one before but has somewhat sharper signals due to vibrational relaxation. It is assumed that in these two states the positive charge is located at one phenyl ring nearby the NDI subunit.[305] Thus, the first of the two species is termed a 'hot charge transfer' (hot-CT, cyan) state which 'cools' down with τ_2 = 219 fs to the relaxed CT state (orange).[323-326] On this time scale, vibrational relaxation (VR) may be accompanied by solvent reorganisation.[322] The relaxed CT state has a lifetime of τ_3 = 14 ps (Figure 48a, orange).

Next, the assignment of the following two SADS (Int_1 and Int_2) is much more complicated because their broad unstructured spectral shape combined with small amplitudes makes a classification difficult. But both spectra had to be taken into account due to unsatisfying global fits when omitting these SADS which possess lifetimes of τ_4 = 39 and τ_4 = 538 ps. The origin of these states is speculative at the moment and may be related to excimer formation of two NDIs.[292, 327] Finally, the grey spectra represented by a broad band at 22 100 cm^{-1} (452 nm) with a lifetime of τ_6 = 10 ns is attributed to the NDI triplet state (^{3}NDI)[305-306, 328] and completes the complex excited states behaviour of that small molecule. The formation of the triplet state from its singlet precursor was set to 10 % (see state diagram in Figure 47).

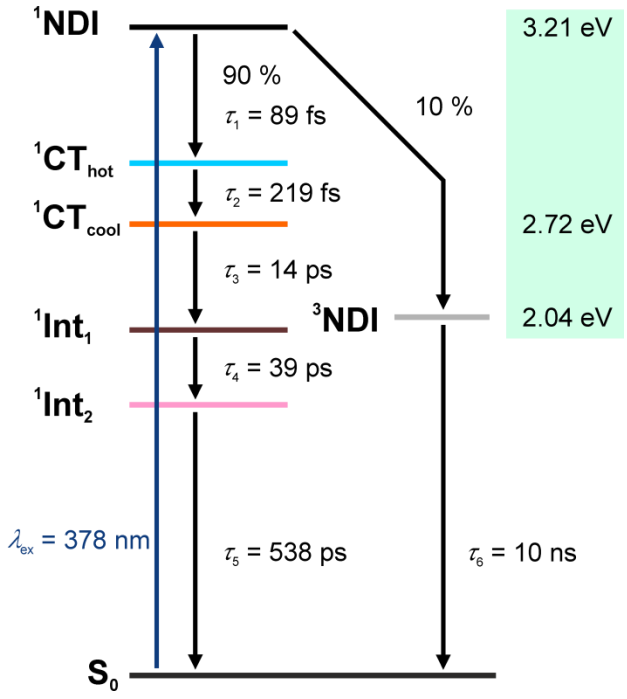

Figure 47 State diagram for **17** in MeCN at 26 500 cm^{-1} (378 nm) excitation. The colours of the states are the same as used in Figure 48a for the SADS.

The central outcome of the excited state analysis of **17** is the detection of the singlet and triplet species of the NDI, vibrationally excited and relaxes CT states and two further states whose origin is presently unclear. The latter two can be ignored for the further investigations, but all others will be considered again in the interpretation of the NDI excited at 26 500 cm^{-1} (378 nm).

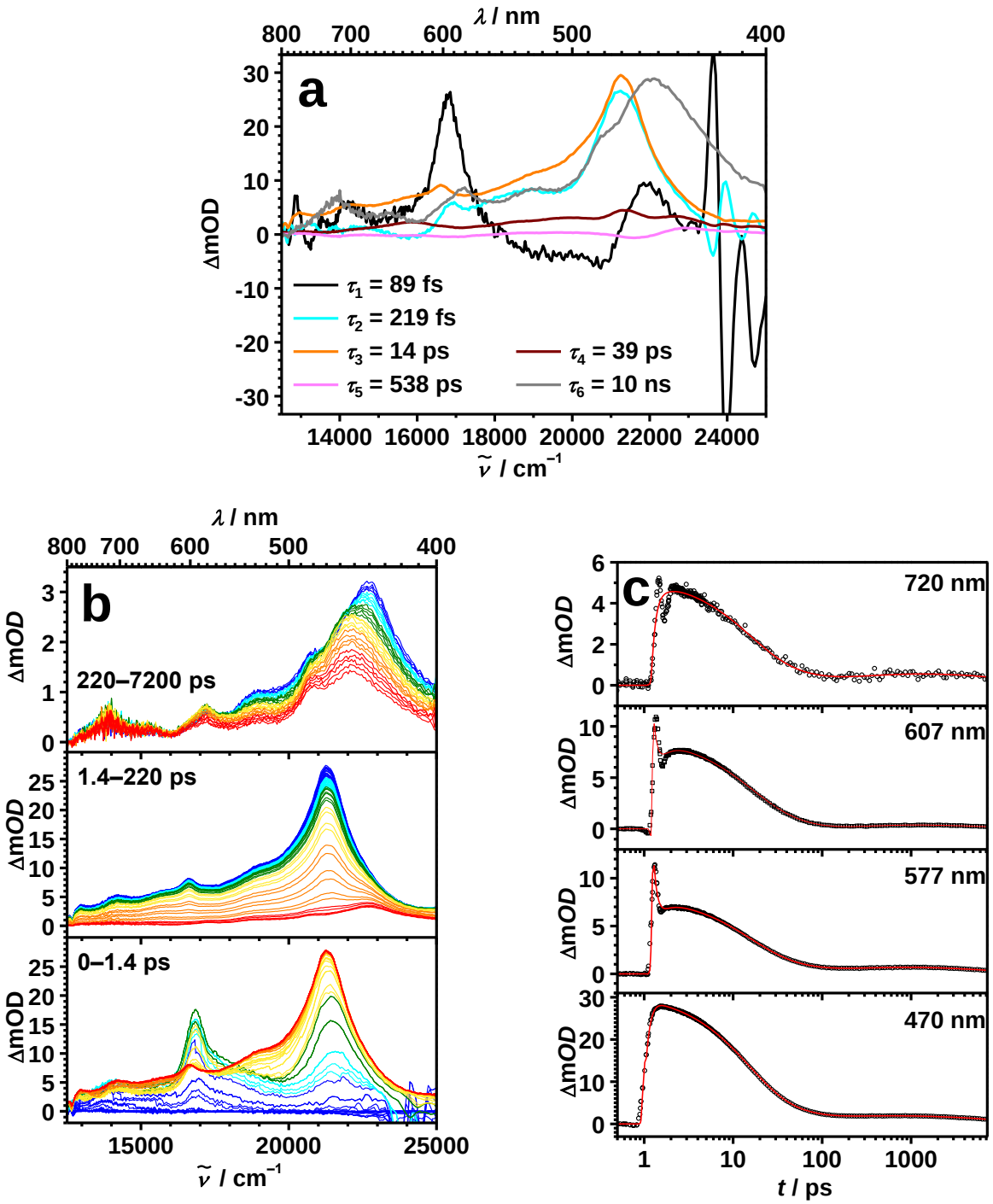

Figure 48 (a) Species associated difference spectra (SADS) of **17** obtained from a global analysis of a transient map. The colours of the SADS refer to the states in the corresponding state diagram in Figure 47. (b) fs-Transient absorption data corrected for chirp and scattered pump light. Early spectra are depicted in blue to green and at later times in orange to red colours. (c) Decay profiles at selected wavelengths for which the zero time delay was set arbitrarily. Excitation at 26 500 cm^{-1} (378 nm) in MeCN.

With the help of the already discussed compounds **Ref1** and **17** the further analysis of complex **Ref$_{NDI}$** will illuminate the interplay of the NDI linked to the iridium complex. The six SADS obtained by the global analysis (Figure 49 and 51) show a combined picture of the photophysics of both chromophores. Excitation at 26 500 cm^{-1} (378 nm) results in the spectrum of ^{1}NDI ($\tilde{\nu}_{max}$= 16 900 cm^{-1} (592 nm), τ_1 = 120 ps in black) followed by the sequence of hot and cool CT ($\tilde{\nu}_{max}$= 21 200 cm^{-1} (472 nm) and 16 600 cm^{-1} (602 nm), with τ_2 = 730 fs in cyan and τ_3 = 14 ps in orange, respectively) as already observed for the NDI (**17**) without the dipyrromethane unit. The relaxed CT species is followed by an SADS (green) with the typical features of a NDI radical anion (strong absorption at 21 200 cm^{-1} (472 nm) and a significant peak at 16 600 cm^{-1} (602 nm)).

However, compared to the CT states described before, there is less transient absorption intensity at around 20 000 cm^{-1} (500 nm). This is caused by the overlaid ground-state bleaching (GSB) in this spectral region. This state, thus, is a charge-separated state (CS_1) which may form an equilibrium between singlet and triplet states. The spin multiplicity is unknown and, consequently, this state is labelled $^{1,3}CS_1$. This state in turn decays back to the ground state with τ_4 = 170 ps. In order to get a reasonable global fit a fifth component with τ_5 = 720 ps (blue) had to be added. The associated SADS only shows GSB and, thus, is attributed to the dipyrrin centred excited state (^{3}Ir) which is generated with 15 % efficiency parallel to the excitation of the ^{1}NDI state at 26 500 cm^{-1} (378 nm). This ^{3}Ir then directly decays to the CS_1. A sixth component with infinite lifetime (τ_6, grey) shows a broad transient absorption ($\tilde{\nu}_{max}$= 22 200 cm^{-1} (450 nm)) and is assigned to the localised triplet state of the NDI. The ^{3}NDI is formed with 10 % efficiency from the initially excited ^{1}NDI state. Unfortunately, the NDI triplet state was not detected in the ns-experiments because its concentration of about 10 % is probably too low for its detection in these measurements.

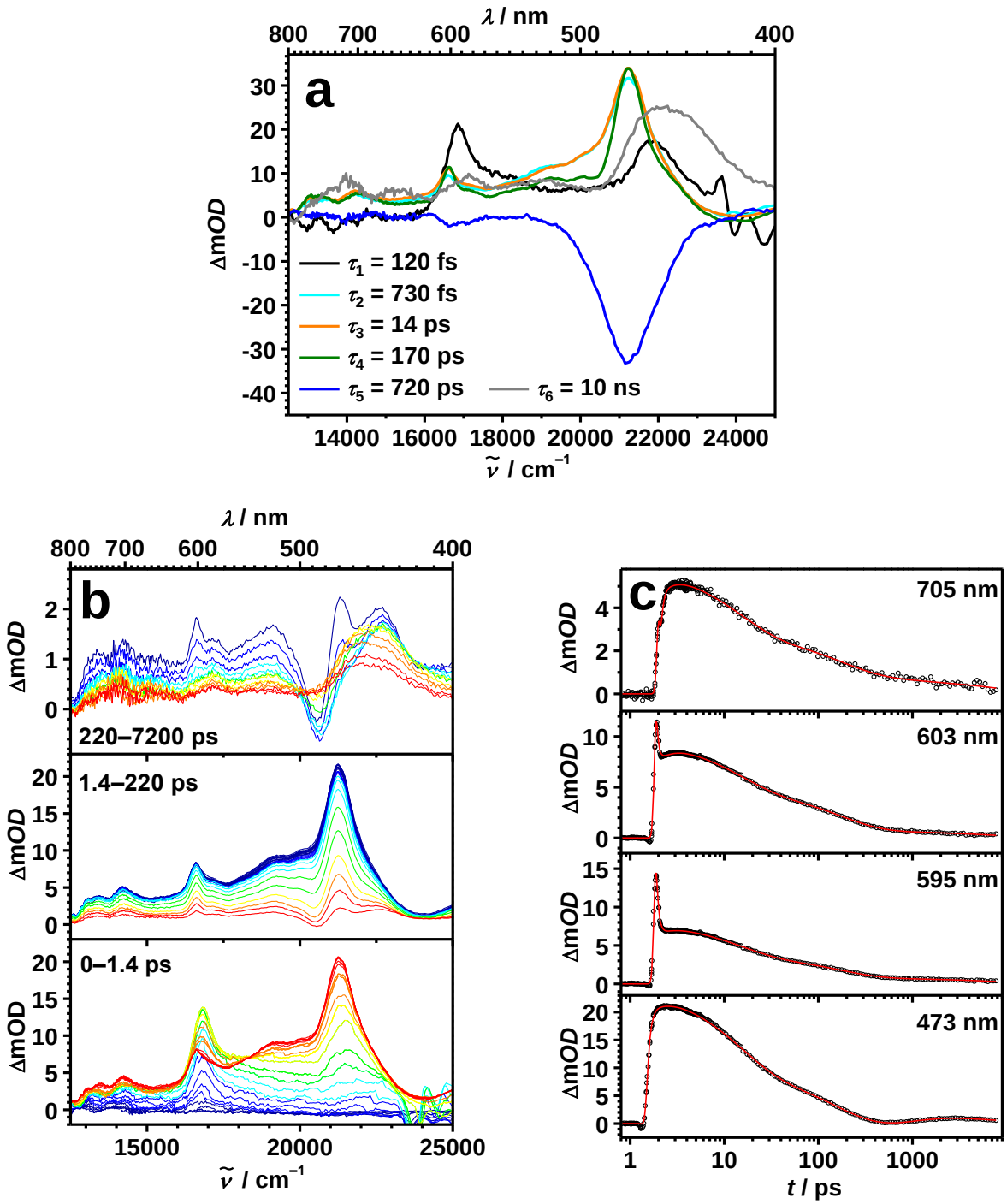

Figure 49 (a) Species associated difference spectra (SADS) of **Ref$_{NDI}$** obtained from a global analysis of a transient map. The colours of the SADS refer to the states in the corresponding state diagram in Figure 50. (b) fs-Transient absorption data corrected for chirp and scattered pump light. Early spectra are depicted in blue to green and at later times in orange to red colours. (c) Decay profiles at selected wavelengths for which the zero time delay was set arbitrarily. Excitation at 26 500 cm^{-1} (378 nm) in MeCN.

Excitation of **Ref$_{NDI}$** at 20 800 cm^{-1} (480 nm) gives a much simpler picture. The global fit only requires two components (see Figure 51a). The first transient spectrum (blue) refers to the ^{3}Ir excited state and only shows GSB around 20 800 cm^{-1} (480 nm). It is therefore essentially identical to the blue spectrum in Figure 46 and 49. Interestingly, a second bleaching spectrum was not observed which may be the initial triplet excited state (^{3}Ir$_i$) of the iridium complex as it was detected for **Ref1** (magenta spectrum in Figure 46). A possible explanation may be a hampered rotation of the phenyl ring in the *meso*-position of the dipyrrin because the bigger NDI moiety makes a conformational change more difficult. Nevertheless, the ^{3}Ir state relaxes almost exclusively into the ^{1,3}CS$_1$ state (green) which shows both features of the NDI radical anion with a sharp absorption at 16 600 cm^{-1} (602 nm) and an intense peak at 21 200 cm^{-1} (472 nm). Moreover, the overlaid signal of the transient absorption of the NDI radical anion at 21 200 cm^{-1} (472 nm) and GSB of the positively charged iridium complex at 20 800 cm^{-1} (480 nm) can be observed. These features attributed to the green SADS differ somewhat from that in Figure 49a for the same state.

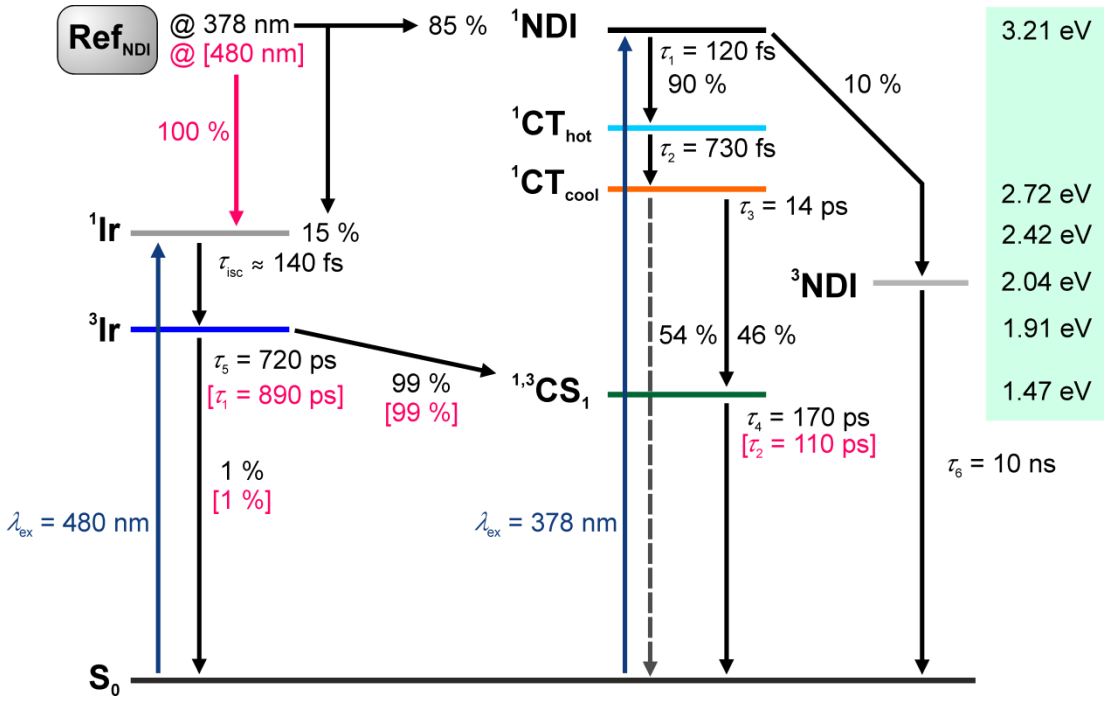

Figure 50 State diagram for **Ref$_{NDI}$** in MeCN. Lifetimes for excitation at 26 500 cm^{-1} (378 nm) are given in black, those for 20 800 cm^{-1} (480 nm) excitation in pink. The colours of the states are the same as used in Figure 49a and 51a for the SADS. The ISC lifetime of 140 fs was estimated from the fs-fluorescence up-conversion measurements of **Ref1** (cf. Figure 46).

However, analysis of several measurements have shown that this spectrum is variable to some extent because of the superpositional character of the two effects. The ^{3}Ir and CS_1 state possess similar lifetimes (890 and 110 ps) as was observed for the 26 500 cm^{-1} (378 nm) excitation (720 and 170 ps). This clearly shows that the CS_1 state additionally suffers from an inversion of the observed time constants. That is, the lifetime of the ^{3}Ir state is longer than for the subsequent CS_1 state. Moreover, the ns-measurement of $\mathbf{Ref_{NDI}}$ in ^{t}BME (Figure 38) showed that the GSB dominates the superposition of both states but the analysis suffers from the short-lived CS_1 state.

Remarkably, the reaction dynamics concerning charge separation and recombination strongly differ comparing both excitation energies. An ET sequence can be clearly observed at 26 500 cm^{-1} (378 nm) excitation which starts from ^{1}NDI, via the CT states (CT_{hot}, CT_{cool}) and results in the CS_1 state. All lifetimes subsequently increase from 120 fs to 170 ps. Conversely, this is not the case at 20 800 cm^{-1} (480 nm), where an inversion of lifetimes can be observed (890 ps for ^{3}Ir and 110 ps for CS_1). Thus, the formation of the CS_1 state is slower than charge-recombination to the ground state and consequently the concentration of that state is reduced which explains its noisy shape.

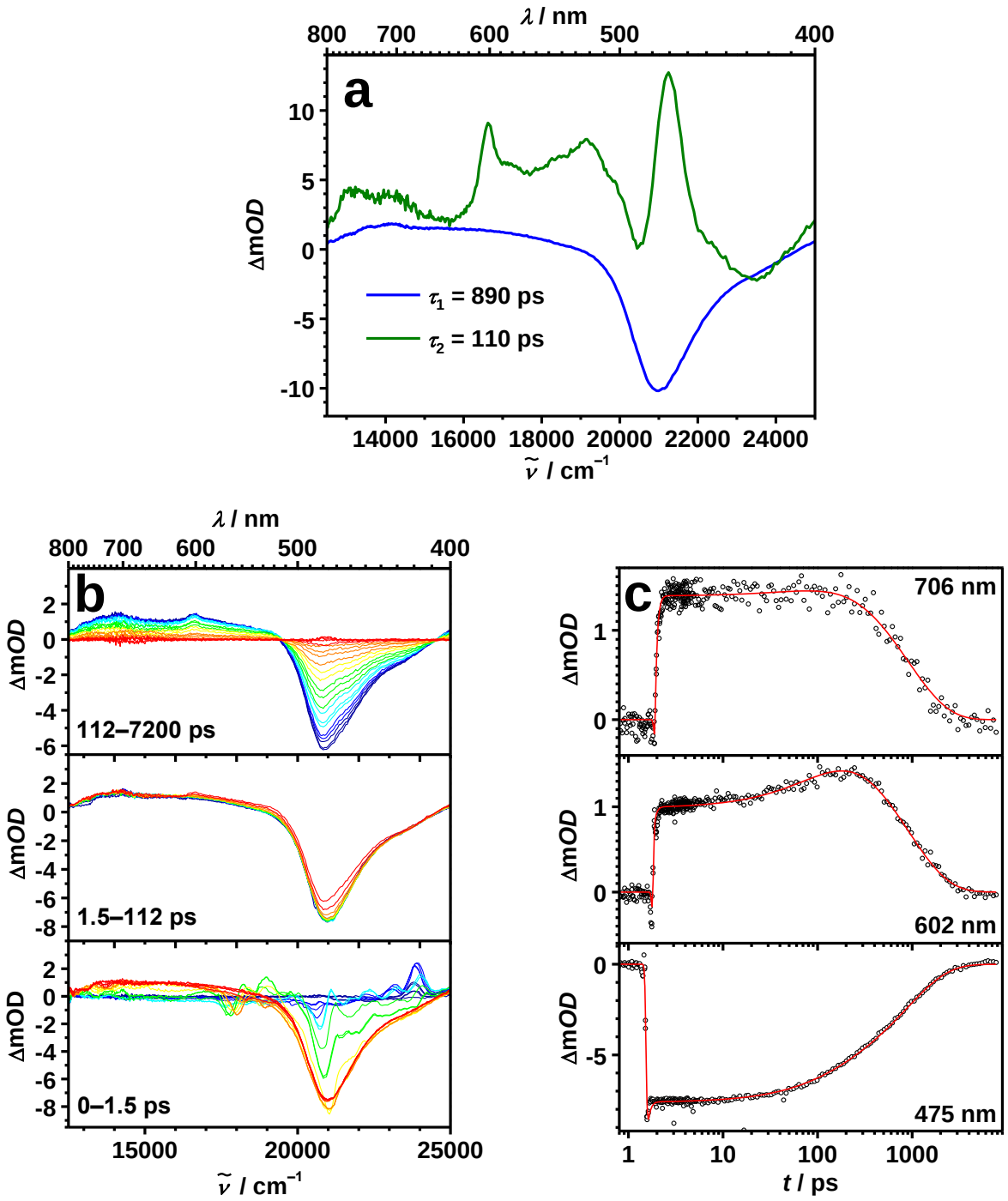

Figure 51 (a) Species associated difference spectra (SADS) of **Ref$_{NDI}$** obtained from a global analysis of a transient map. The colours of the SADS refer to the states in the corresponding state diagram in Figure 50. (b) fs-Transient absorption data corrected for chirp and scattered pump light. Early spectra are depicted in blue to green and at later times in orange to red colours. (c) Decay profiles at selected wavelengths for which the zero time delay was set arbitrarily. Excitation at 20 800 cm^{-1} (480 nm) in MeCN.

Triads T1–T3

Photoexcitation of triad **T1** will elucidate how charge separation in the synthesised donor-iridium complex-acceptor systems is mechanistically working. For the 26 500 cm^{-1} (378 nm) excitation of **T1** the global target fit yielded six SADS (Figure 52a and Figure 53) with six decay times: the first three processes are essentially the same as in **Ref_{NDI}** which can be seen by very similar spectral features and lifetimes. Thus, formation of the ^{1}NDI state is followed with τ_1 = 110 fs by the hot CT and with τ_2 = 630 fs by the relaxed CT state. Contrary to **Ref_{NDI},** the CT of **T1** decays with 13 ps to give rise to an SADS with the typical features of a NDI radical anion (strong absorption at 21 200 cm^{-1} (471 nm) nm and a significant peak at 16 600 cm^{-1} (601 nm))[71, 293-294, 305, 310-311, 313-315] and the triarylamine radical cation $TAA^{\bullet+}$ (strong absorption at 13 800 cm^{-1} (725 nm)).[262, 291] This spectrum is in excellent agreement with that obtained by spectroelectrochemistry (see Figure 36). Thus, it can be concluded that a charge-separated state CS_2 is formed.[64, 66]

Nanosecond time-resolved pump-probe measurements (Figure 39a) show that this CS_2 state has a lifetime of ca. 580 ns. It is assumed that all states possess singlet multiplicity as the singlet NDI excited state. For triad **T1** the state in-between the CT state and CS_2 state as in **Ref_{NDI}** in which the iridium complex is oxidised and the NDI is reduced is hardly visible in the transient map of **T1** for reasons outlined below. Excitation at 26 500 cm^{-1} (378 nm) induces another path where the ^{3}Ir state of the iridium complex is excited via the ^{1}Ir state followed by fast ISC. The iridium complex contributes only 12 % to the total absorption at 26 500 cm^{-1} (378 nm) excitation. This path leads directly to the population of the CS_2 as will be discussed in more detail in the next paragraph.

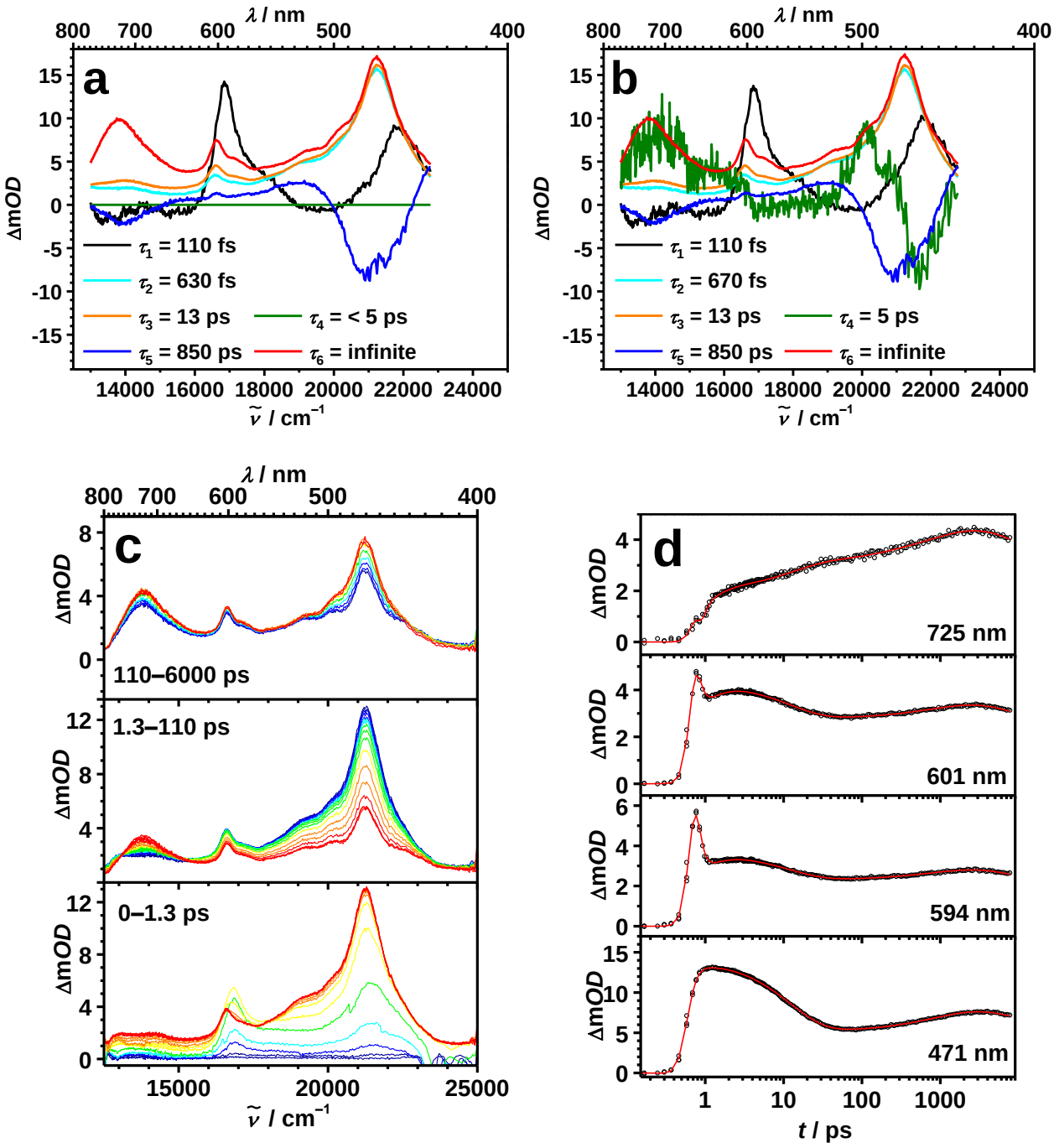

Figure 52 (a) Species associated difference spectra (SADS) of **T1** obtained from a global analysis of a transient map. For the green spectrum the amplitude was set $A = 0$, whereas in (b) the CS_1 species was explicitly included as the green SADS. The state diagram in Figure 53 includes all SADS. (c) fs-Transient absorption data corrected for chirp and scattered pump light. Early spectra are depicted in blue to green and at later times in orange to red colours. (d) Decay profiles at selected wavelengths for which the zero time delay was set arbitrarily. Excitation at 26 500 cm^{-1} (378 nm) in MeCN.

Excitation at the NDI at 26 500 cm^{-1} (378 nm) clearly induces a stepwise ET starting from the ^{1}NDI state to the relaxed CT state and then via the intermediate CS_1 state to the final $^1CS_2$ state. In the final $^1CS_2$ state the NDI is reduced and one TAA unit is oxidised. A quantum yield of n approx. 47 % for the CS_2 state formation was estimated by actinometry with benzophenone (*vide supra*) at 28 200 cm^{-1} (355 nm) laser energy using ns-laser flash spectroscopy. For comparison, the target model of the fs-data independently yields 47 %. The loss is clearly caused by direct relaxation of the CT state to the ground state. Moreover, the stepwise ET process of **T1** is corroborated by pump-probe measurements of **Ref$_{NDI}$** at 26 500 cm^{-1} (378 nm) pump energy which shows essentially the same SADS (see Figures 49 and 50) for ^{1}NDI, hot CT and CT, along with a ^{3}NDI state which is simultaneously formed to a minor extent (10 %) but which was not observed for **T1**. For **Ref$_{NDI}$** the formation of the CS_1 state in which the iridium complex is oxidised and the NDI is reduced is clearly visible. For the oxidised iridium complex one can only see a strong ground-state bleaching (GSB) around 20 800 cm^{-1} (480 nm) which superposes with the strong absorption of $NDI^{\bullet-}$ at 21 200 cm^{-1} (472 nm) which then leads to a decreased absorption in this spectral region. The CS_1 state is the final state in **Ref$_{NDI}$** which decays with a lifetime of τ_4 = 170 ps (Figure 49 and 50) to the ground state by charge recombination. The comparatively long lifetime of the CS_1 state is the reason why CS_1 is present in **Ref$_{NDI}$** but not in **T1** where a very fast follow-up reaction (< 5 ps) decreases its intermediate concentration drastically. It has to be mentioned that in the fits of triad **T1** the ^{3}Ir state as well as the CS_1 state are associated with major uncertainties concerning both, lifetime and spectral shape. This is caused by the low amplitude (< 5 %) of these contributions to the transient map and the fact that the spectroscopic signatures of the different species are highly overlapping between 20 000–25 000 cm^{-1} (500–400 nm). Thus, the spectrum of the CS_1 state was forced to have zero spectral intensity during the fit. The spectral shape of these states can better be estimated from the global fit of dyad **Ref$_{NDI}$** (see Figure 49a). In addition, a global fit which includes the noisy spectra of the CS_1 state for comparison is presented in Figure 52b.

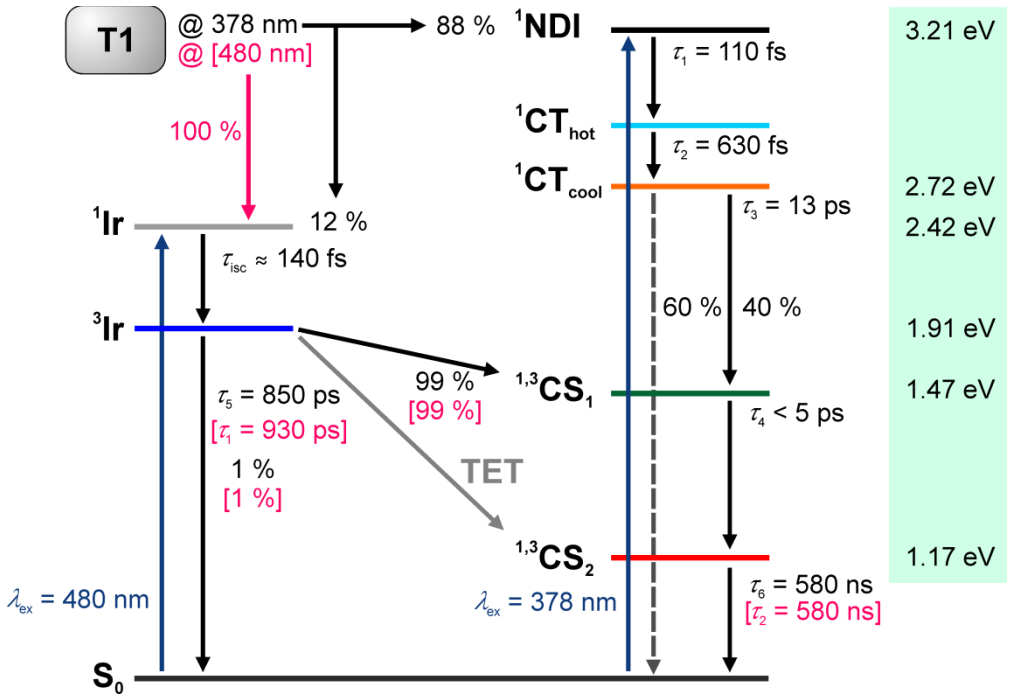

Figure 53 State diagram for **T1** in MeCN. Data for excitation at 26 500 cm^{-1} (378 nm) are given in black, those for 20 800 cm^{-1} (480 nm) excitation in pink. The colours of the states are the same as used in Figure 52a and 54a for the SADS. The ISC lifetime of 140 fs was estimated from the fs-fluorescence up-conversion measurements of **Ref1** (cf. Figure 46).

A much contrasting behaviour to the experiments at 26 500 cm^{-1} (378 nm) excitation was observed when the ^{3}Ir states of the iridium complex of **T1** were populated at 20 800 cm^{-1} (480 nm) excitation, see Figure 54. Within the instrument response time a strong GSB at 20 800 cm^{-1} (480 nm) is observed which indicates the formation of an excited iridium complex as this shows almost no excited-state absorption but only GSB. The assumption that this iridium state has triplet character still holds. In addition, a second triplet state is not observed as it was in **Ref1** because the NDI fragment may slow down the rotation of the phenyl ring in the *meso*-position of the dipyrrin ligand. Due to a faster follow-up reaction in **T1** the lowest energy excited ^{3}Ir state with a natural lifetime of ca. 1.86 µs in MeCN shows a reduced lifetime of τ_1 = 930 ps. Moreover, within these 930 ps the transient spectrum of the CS_2 state, identical to that described in the ns-laser flash section, is formed without any trace of an intermediate species. This is the process that runs simultaneously to the stepwise mechanism outlined above but with a minor efficiency of 12 % at 26 500 cm^{-1} (378 nm) excitation. For the CS_2 state a spin equilibrium is always established between the singlet and

the three triplet states (cf. 3.1.5). Consequently, both CS states ($^{1,3}CS_2$) decay with an infinite lifetime (τ_2 = 580 ns from the ns-experiment, Figure 39a) to the ground state after a spin interconversion to a $^1CS_2$ state occurred because the spin conservation rule only permits singlet-singlet deactivation to the ground state.[213] This spin interconversion is probably mediated by hyperfine coupling interactions and is in the range of 10^7–10^8 s^{-1}.[22, 221, 252, 255-256, 259]. The spectra of $^3CS_2$ and $^1CS_2$ are practically identically as shown in a comprehensive study for this spin interconversion in chapter 3.1.5 where magnetic field dependent ns-laser flash spectroscopy experiments will be described which will elucidate the effect on the recombination kinetics of the CS states.

As already mentioned actinometric experiments with $Ru(bpy)_3Cl_2$ at 24 000 cm^{-1} (416 nm) excitation show a quantum yield of almost unity. These observations are very startling, even more in view of the slow kinetics of charge separation. Additionally, the findings of **T1** at 20 800 cm^{-1} (480 nm) excitation raise questions because the first CS state was not detected. This opens the way to two mechanistic scenarios. The first is a stepwise ET including CS_1 but with a vanishing concentration for this state due to a very fast follow-up reaction. A second possibility may be offered if a concerted two-electron transfer (TET, grey arrow in Figure 53) is taken into account. Both ways will be discussed after the experimental results of triad **T2** and **T3** have been presented.

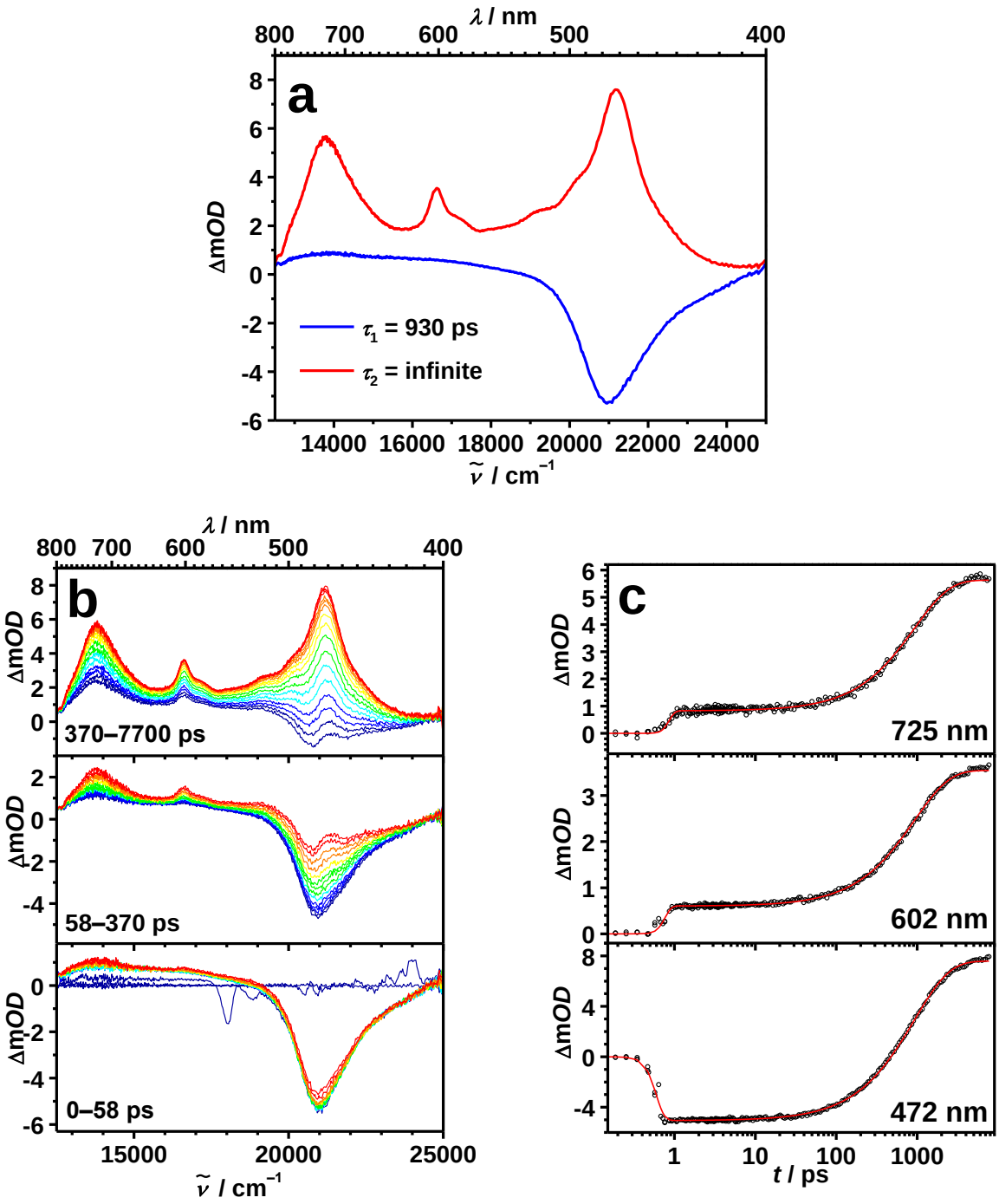

Figure 54 (a) Species associated difference spectra (SADS) of **T1** obtained from a global analysis of a transient map. The colours of the SADS refer to the states in the corresponding state diagram in Figure 53. (b) fs-Transient absorption data corrected for chirp and scattered pump light. Early spectra are depicted in blue to green and at later times in orange to red colours. (c) Decay profiles at selected wavelengths. Decay profiles at selected wavelengths for which the zero time delay was set arbitrarily. Excitation at 20 800 cm^{-1} (480 nm) in MeCN.

Similarly, triad **T2** was investigated in the same way as it was done for **T1**. First, the transient spectra produced by a pump energy of 26 500 cm^{-1} (378 nm) are shown in Figure 55. Here, six SADS were necessary to reproduce the transient map starting with the peak for the ^{1}NDI at 16 800 cm^{-1} (595 nm), followed by the hot and cooled CT (cyan and orange spectra in Figure 55). The first three species all have almost identical lifetimes compared to **T1** with 88 fs, 250 fs and 11 ps, respectively. The noisy bleaching signal (in blue) is also present with a lifetime of τ_5 = 980 ps. The only difference between triad **T1** and **T2** within the ultrafast dynamics at 26 500 cm^{-1} (378 nm) excitation can be seen in the green spectrum which was associated with uncertainties concerning spectral shape and intensity for **T1**. For triad **T2** the shape of this spectrum is characterised by the small peak at 16 600 cm^{-1} (602 nm) and the band at 21 200 cm^{-1} (472 nm) very similar to a CT state. However, this green spectrum lacks intensity in the spectral region between 19 000–23 000 cm^{-1} (435–526 nm) which is again a strong indication for a superposition of a bleaching and radical anion peaks as was already found for **Ref$_{NDI}$**. Accordingly, the more distinct CS_1 spectrum was fitted with a lifetime of τ_4 = 41 ps and is clearly assigned to the CS_1 state which proves the stepwise formation of the fully charge-separated state for **T2** at 26 500 cm^{-1} (378 nm) excitation. A further difference to the **T1** results is the shift of the radical cation peak to higher energy as was already observed in the ns-measurements (Figure 44).

The contrasting behaviour of the CS_1 species is present at the 20 800 cm^{-1} (480 nm) excitation, as well. The iridium-dipyrrin excitation yields the blue spectrum (Figure 56), corresponding to GSB at 20 800 cm^{-1} (480 nm) with a lifetime of τ_1 = 870 ps. An additional lifetime had to be added to the global fit which yielded the green spectrum with characteristics for the radical anion. Contrary to the other compounds the radical anion peak at 21 000 cm^{-1} (476 nm) was fully developed and a superposition of the bleaching signal is missing. However, until now the shape of this spectrum differs to a certain degree for several fits. The bleaching is sometimes more or less pronounced and, consequently, this spectrum is ascribed to the CS_1 state. This indicates the stepwise character of this excitation path. The green spectrum decays with 88 ps, slower than for **T1** (< 5 ps), to the CS_2 state which is formed with the same time constant. Likewise, an inversion of lifetimes was also found for **T2**.

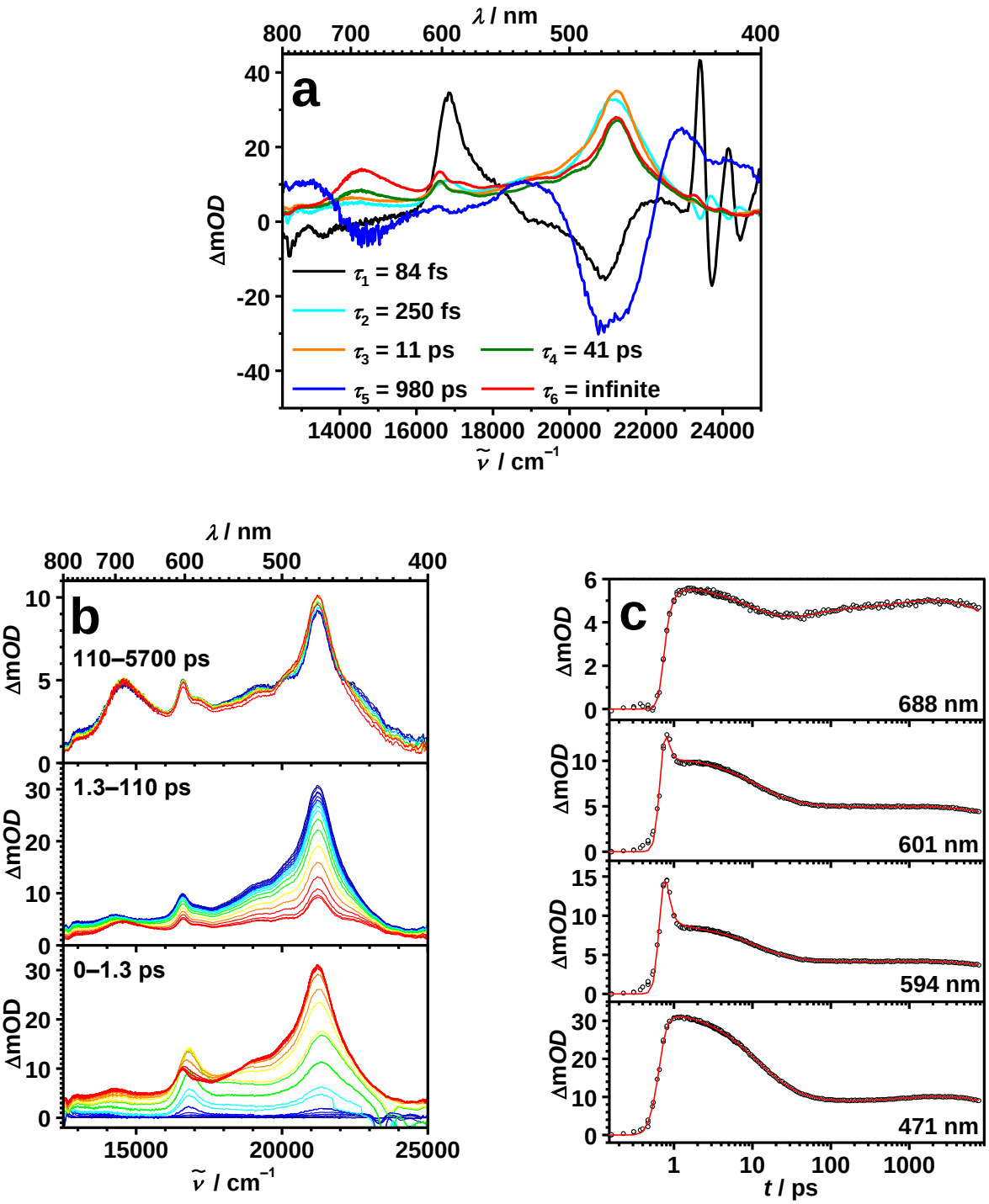

Figure 55 (a) Species associated difference spectra (SADS) of **T2** obtained from a global analysis of a transient map. The colours of the SADS refer to the states in the corresponding state diagram in Figure 57. (b) fs-Transient absorption data corrected for chirp and scattered pump light. Early spectra are depicted in blue to green and at later times in orange to red colours. (c) Decay profiles at selected wavelengths for which the zero time delay was set arbitrarily. Excitation at 26 500 cm^{-1} (378 nm) in MeCN.

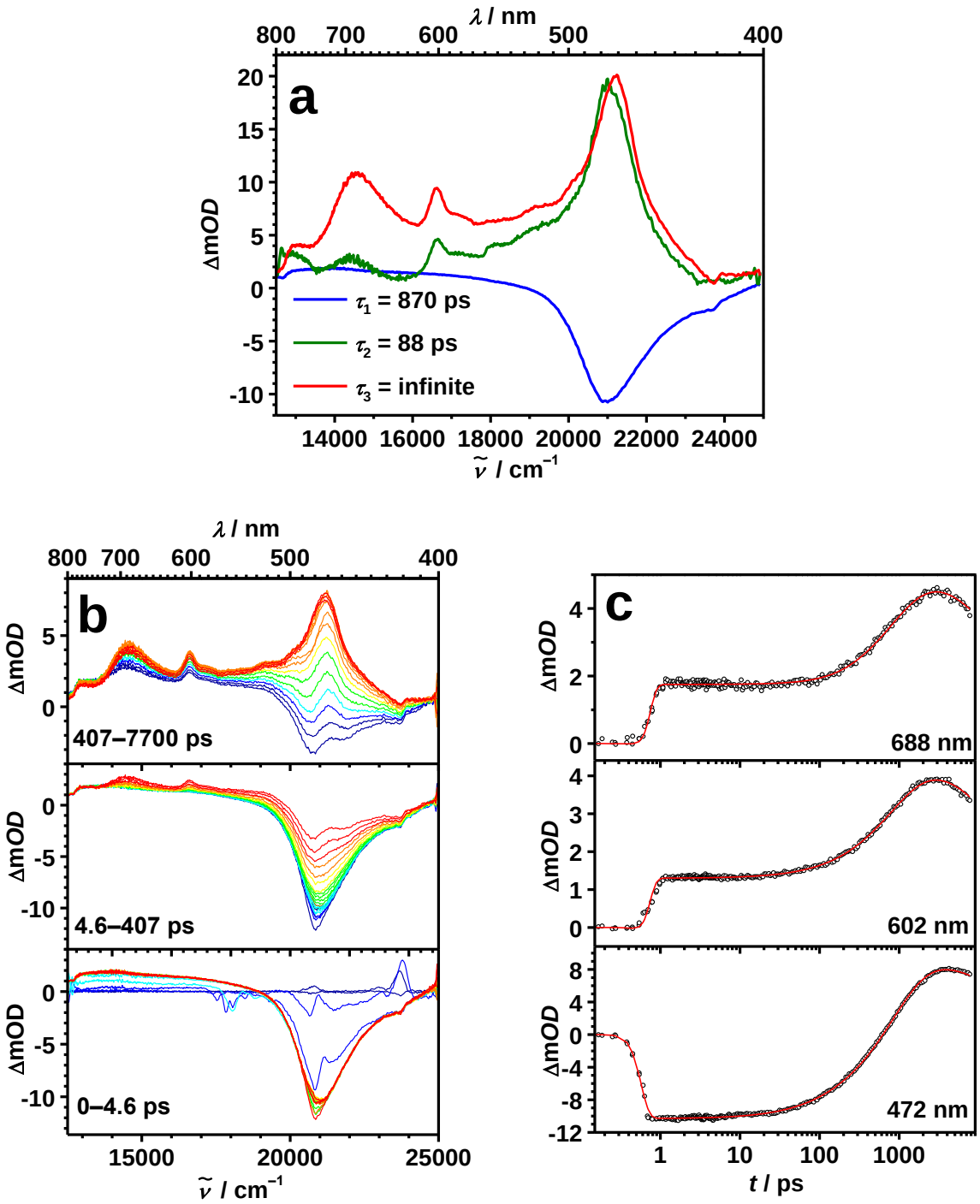

Figure 56 (a) Species associated difference spectra (SADS) of **T2** obtained from a global analysis of a transient map. The colours of the SADS refer to the states in the corresponding state diagram in Figure 57. (b) fs-Transient absorption data corrected for chirp and scattered pump light. Early spectra are depicted in blue to green and at later times in orange to red colours. (c) Decay profiles at selected wavelengths for which the zero time delay was set arbitrarily. Excitation at 20 800 cm^{-1} (480 nm) in MeCN.

The formation of the CS_1 state is slower than the follow-up process which explains the low concentration of this species. Next, the following state (CS_2) comprises all characteristics of radical cation and anion peaks. Hence, it is identical to the CS_2 state found in the ns-transient absorption section for **T2** with a lifetime of 32 ns. The quantum yield in this case was determined by the relative intensities of the GSB at early (t = 0) times and the ESA at later times (t = 5.4 ns) for the radical anion peak at 21 100 cm^{-1} (472 nm) and was with approx. 50 % less efficient compared to **T1** (~100 %). In addition, the efficiencies of the target model of the global fit independently yielded 53 % (Figure 57).

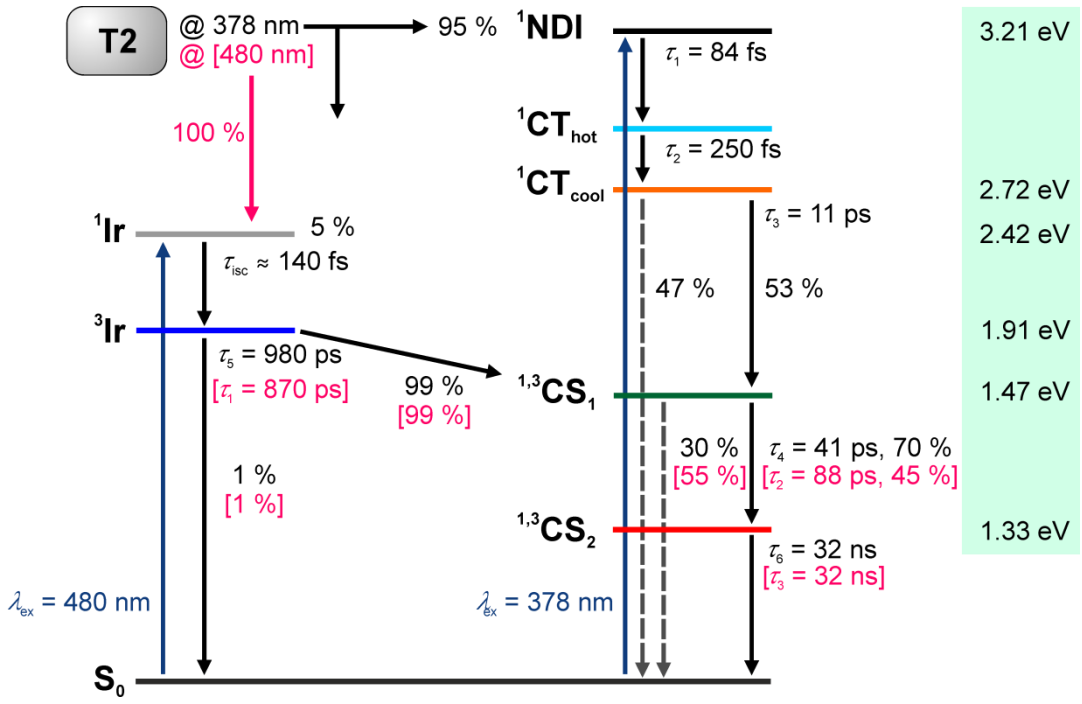

Figure 57 State diagram for **T2** in MeCN. Data for excitation at 26 500 cm^{-1} (378 nm) are given in black, those for 20 800 cm^{-1} (480 nm) excitation in pink. The colours of the states are the same as used in Figure 55a and 56a for the SADS. The ISC lifetime of 140 fs was estimated from the fs-fluorescence up-conversion measurements of **Ref1** (cf. Figure 46).

Finally, the ultrafast transient absorption experiments of triad **T3** in THF will be presented. Unfortunately, MeCN could not be used as solvent because the solubility of the complex was too low and a comparison with **T1** and **T2** investigated in MeCN, may be impossible or misleading. The analysis of **T3** will focus on the aspect whether charge

separation will occur in this triad or not. The estimated *Gibbs* free energy of the first and second CS state in THF according to eq. (3) resulted in 1.39 and 1.54 eV, respectively (cf. 3.1.1.4). Hence, the ET from the first to the second CS state is by 0.06 eV higher in energy and no CS_2 formation is expected.

The global analysis of the transient map of **T3** at 26 500 cm^{-1} (378 nm) excitation in THF resulted in four SADS. The first SADS (black line in Figure 58) has a lifetime of τ_1 = 173 fs and shows features for a ^{1}NDI absorption at 16 900 cm^{-1} (592 nm).[305] The subsequent SADS with a lifetime of τ_2 = 4.8 ps possesses characteristics of a CT state with the NDI radical anion peaks at 16 500 and 21 200 cm^{-1} (606 and 471 nm, respectively). However, the corresponding spectrum lacks intensity at ca. 20 000 cm^{-1} (500 nm) compared to the CT states of triads **T1** and **T2** in MeCN. In addition, the next state which was obtained by the global analysis is not another vibrationally relaxed CT state. The subsequent state, however, shows a peak at 16 500 cm^{-1} (606 nm) corresponding to a NDI anion but the intensity of the second radical anion peak at 21 200 cm^{-1} (471 nm) is reduced. This spectral behaviour was already observed for **Ref$_{NDI}$** in MeCN and can be attributed to the CS_1 state. The CS_1 state has a lifetime of τ_3 = 1.1 ns and, thus, lives longer than the same state in MeCN (ca. 170 ps). The fourth SADS has minor absorptions with a very low amplitude and a lifetime of τ_4 = 6.0 ns could be obtained. Only a broad absorption feature is found in the spectral region from 20 000 and 24 000 cm^{-1} (500–416 nm) and is very similar to the ^{3}NDI absorption, which was detected in **Ref$_{NDI}$** and in **17**, as well. In addition, this state is populated by only 20 % from its singlet precursor (see state diagram in Figure 59) which explains the low amplitude.

Concluding, **T3** shows similar dynamics as **Ref$_{NDI}$** (Figure 48 and 49) where the donor groups are missing. Indeed, the CS_1 state (green state in Figure 58) was determined as the lowest excited state from the global analysis. However, the different solvents (MeCN for **Ref$_{NDI}$** and THF for **T3**) make a comparison of the involved intermediates difficult.

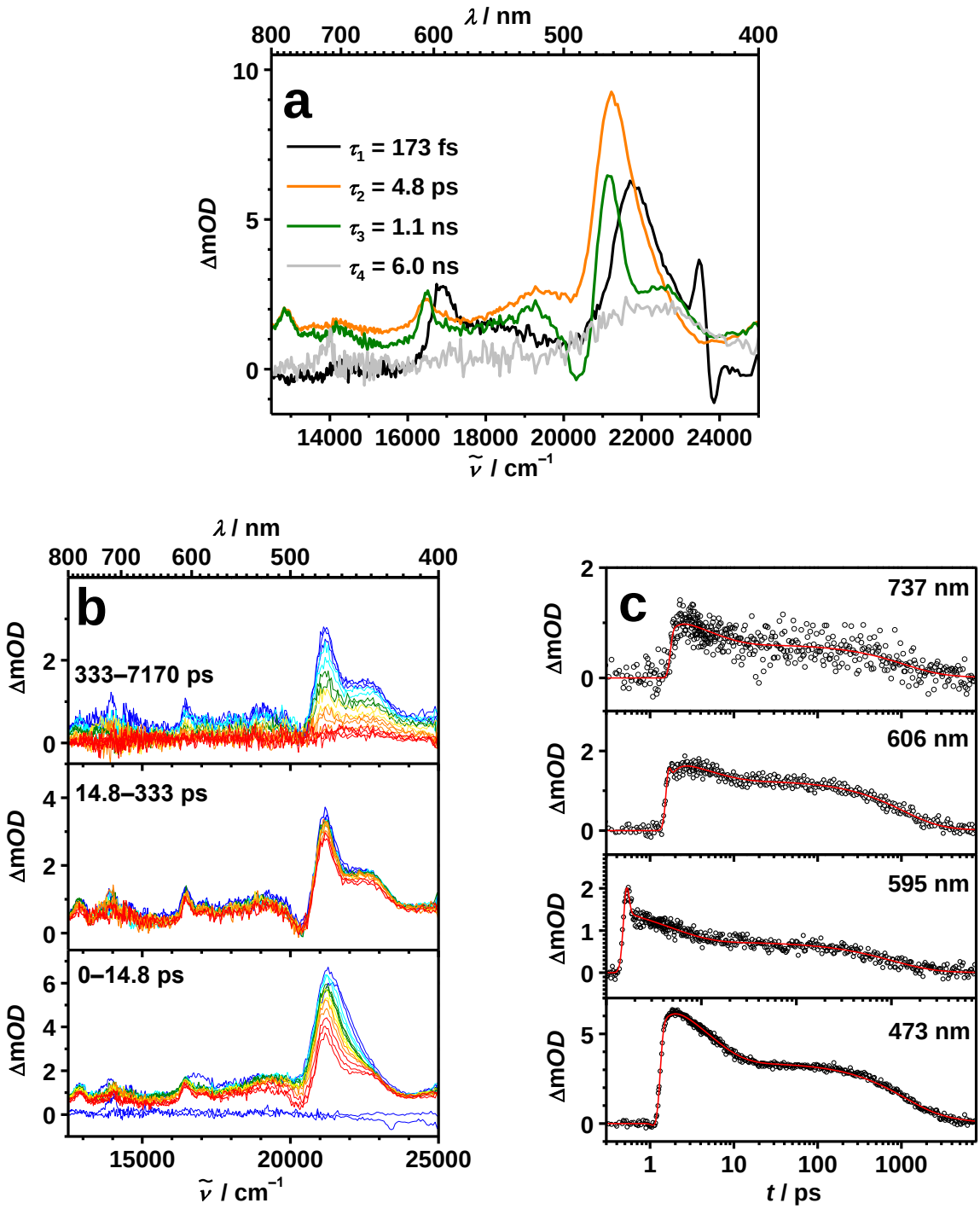

Figure 58 (a) Species associated difference spectra (SADS) of **T3** obtained from a global analysis of a transient map. The colours of the SADS refer to the states in the corresponding state diagram in Figure 59. (b) fs-Transient absorption data corrected for chirp and scattered pump light. Early spectra are depicted in blue to green and at later times in orange to red colours. (c) Decay profiles at selected wavelengths for which the zero time delay was set arbitrarily. Excitation at 26 500 cm^{-1} (378 nm) in THF.

Common aspects for **Ref$_{NDI}$** and **T3** are: i) The ^{3}NDI is populated in both cases with 10–20 % from its singlet precursor. ii) A CT state is formed, having the negative charge on the NDI and the positive on a neighbouring phenyl unit. From that CT the CS_1 state is generated which then relaxes to the ground state. Contrary to that, discrepancies are as follows: i) No vibrationally excited CT is obtained from the global analysis of **T3** whereas such a state is present in the **Ref$_{NDI}$** analysis. ii) A parallel population of the CS_1 state from an excited iridium triplet state as it was confirmed by a bleaching signal in **Ref$_{NDI}$** is missing in **T3**, as well. iii) The lifetimes of common states differ to a certain extent. The lifetime of the ^{1}NDI and the CT are longer in THF compared to MeCN which may be explained by the different solvent polarity.[329] The lifetime of the CS_1 state is different, too. The MeCN measurements revealed lifetimes of 170 ps for that state, whereas the lifetime is with ca. 1 ns significant longer in THF.

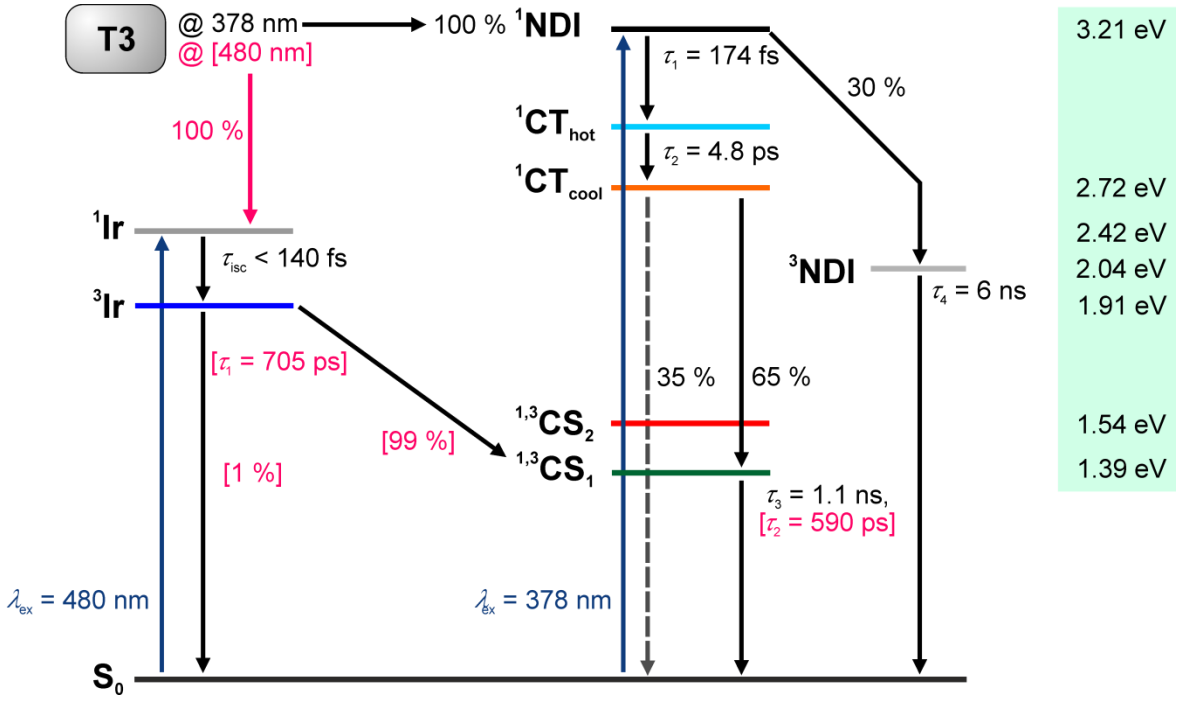

Figure 59 State diagram for **T3** in THF. Data for excitation at 26 500 cm^{-1} (378 nm) are given in black, those for 20 800 cm^{-1} (480 nm) excitation in pink. The colours of the states are the same as used in Figure 58a and 60a for the SADS. The ISC lifetime of 140 fs was estimated from the fs-fluorescence up-conversion measurements of **Ref1** (cf. Figure 46).

A further experiment deals with the excitation of the Ir(dipy) unit at 20 800 cm^{-1} (480 nm). Although there are some discrepancies between **Ref_{NDI}** and **T3** at an excitation energy of 26 500 cm^{-1} (378 nm), the global analysis of the current experiment in THF is very similar to the one of **Ref_{NDI}** in MeCN (Figure 60). Likewise, the GSB at ca. 20 800 cm^{-1} (480 nm) is a sign for the ^{3}Ir state with a corresponding lifetime of τ_1 = 706 ps (890 ps in the **Ref_{NDI}** experiment). The subsequent state shows features of the NDI radical anion at 16 500 cm^{-1} (606 nm) and less distinct at 21 100 cm^{-1} (474 nm). The latter peak is formed by a superposition of the ESA of the radical anion and a GSB of the radical cation in that specific spectral region. Consequently, these features can be assigned to the CS_1 state which has a lifetime of τ_2 = 590 ps (110 ps for **Ref_{NDI}**).

Interim Conclusion and Interpretation

To sum up, the experimental outcomes are collected and plotted in a simplified energy state diagram (Figure 61) where the efficiencies of the different energy or electron transfer processes are omitted and a range of similar lifetimes of identical involved intermediates is presented. This will help to highlight some important details of the results so far. The essential question is correlated to the role of the CS_1 state in triad **T1** upon 26 500 cm^{-1} (378 nm) excitation. First, excitation of the NDI produces the following sequence: i) NDI singlet species (84–120 fs), ii) hot (219–739 fs) and cool (11–14 ps) CT which differ only little in spectral shape. Second, at the same laser energy the iridium dipyrrin complex is excited. This chromophore is electronically decoupled from the NDI states (cf. emission section) and absorbs to a certain extent (5–15 %) at 26 500 cm^{-1} (378 nm). Thus, a GSB signal (blue spectrum, Figure 52 and 54), corresponding to the ^{3}Ir state, can be observed with less intensity at 20 800 cm^{-1} (480 nm) and lifetimes of 720–980 ps. Third, the fully charge-separated state is populated, except for **Ref_{NDI}** and **T3**. In the former, the donor site is missing and the latter exhibits a higher lying CS_2 state compared to the CS_1 state. Fourth, the quantum yields of 47 and 39 % for **T1** and **T2**, respectively, are very similar for 26 500 cm^{-1} (378 nm) excitation but the radical cation band of the TAAs is located at different energies due to the different electronic situation in the TAAs (OMe vs. ^{t}Bu). The reduced quantum yield is caused by direct relaxation of the CT state to the ground state.

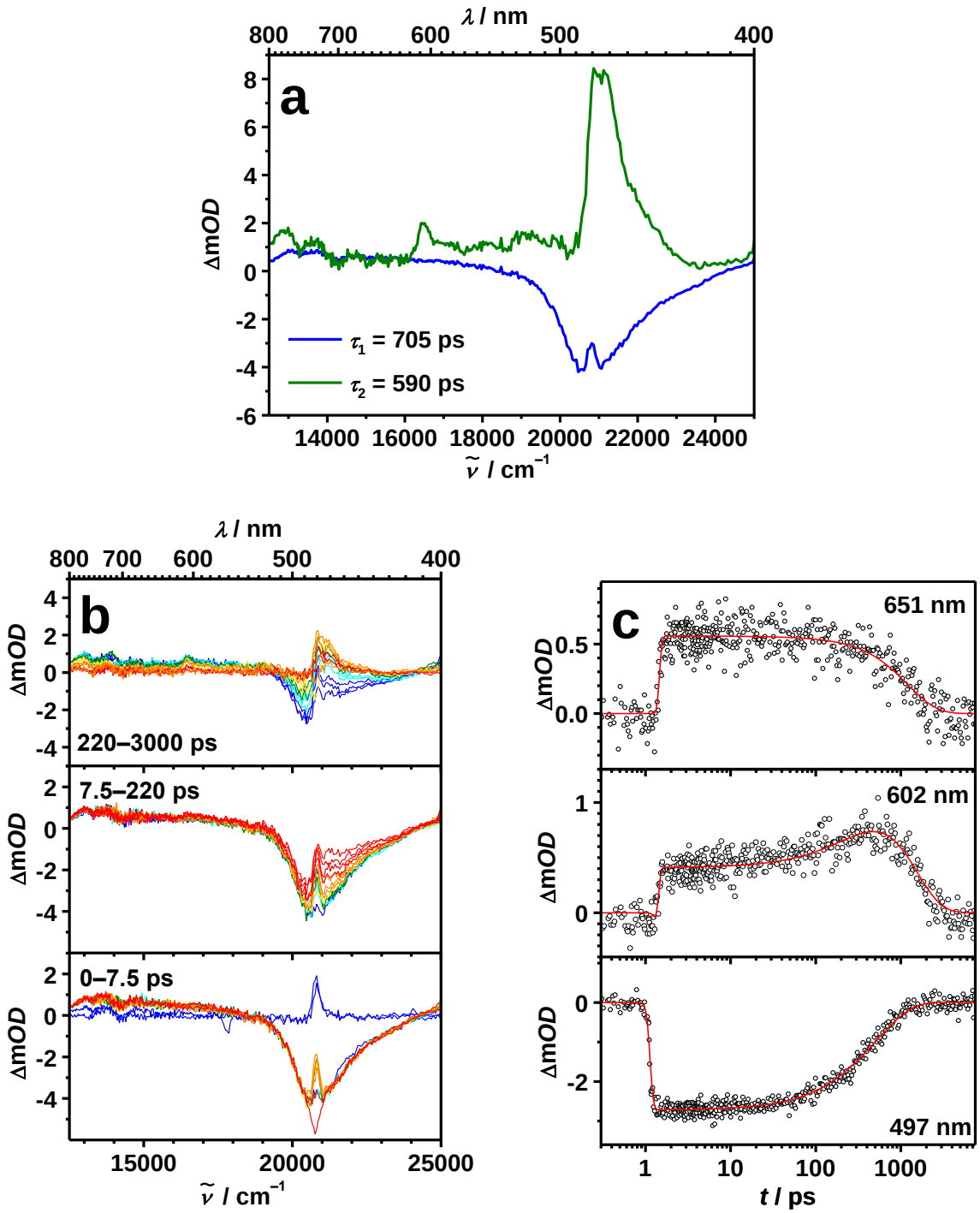

Figure 60 (a) Species associated difference spectra (SADS) of **T3** obtained from a global analysis of a transient map. The colours of the SADS refer to the states in the corresponding state diagram in Figure 59. (b) fs-Transient absorption data corrected for chirp and scattered pump light. Early spectra are depicted in blue to green and at later times in orange to red colours. (c) Decay profiles at selected wavelengths for which the zero time delay was set arbitrarily. Excitation at 20 800 cm^{-1} (480 nm) in THF.

Finally, the most interesting point is related to the CS_1 state which i) has always a low concentration because of inverted lifetimes, ii) is caused by a superposition of two opposed effects (GSB of Ir(dipy) and ESA of NDI radical anion) which strongly influences the shape of this spectrum in the overlapping area (19 000–23 000 cm^{-1} (435–526 nm) and iii) is the crucial factor of proving a stepwise ET mechanism involving the positively charged iridium complex as an intermediate. Whereas for **Ref_{NDI}**, **T2** and **T3** strong indications were found for the existence of this state, triad **T1** suffers from a vanishing concentration of CS_1. As a consequence this state is postulated to be active in the ET process on the basis of reliable arguments coming from the comparison of **Ref_{NDI}** with **T2** and **T3**.

On the contrary, the findings for **T1** upon direct excitation of the iridium complex are even more impressive as the global fit is satisfactory without taking the CS_1 state into account. The lifetimes of the GSB and of the fully charge-separated state are almost identical to what is found for the NDI excitation, because this pathway is involved there, too. Besides, the missing of the higher lying NDI states, like ^{1}NDI and CT states, is not surprisingly. In the following, the fate of the first charge-separated state is investigated in more detail.

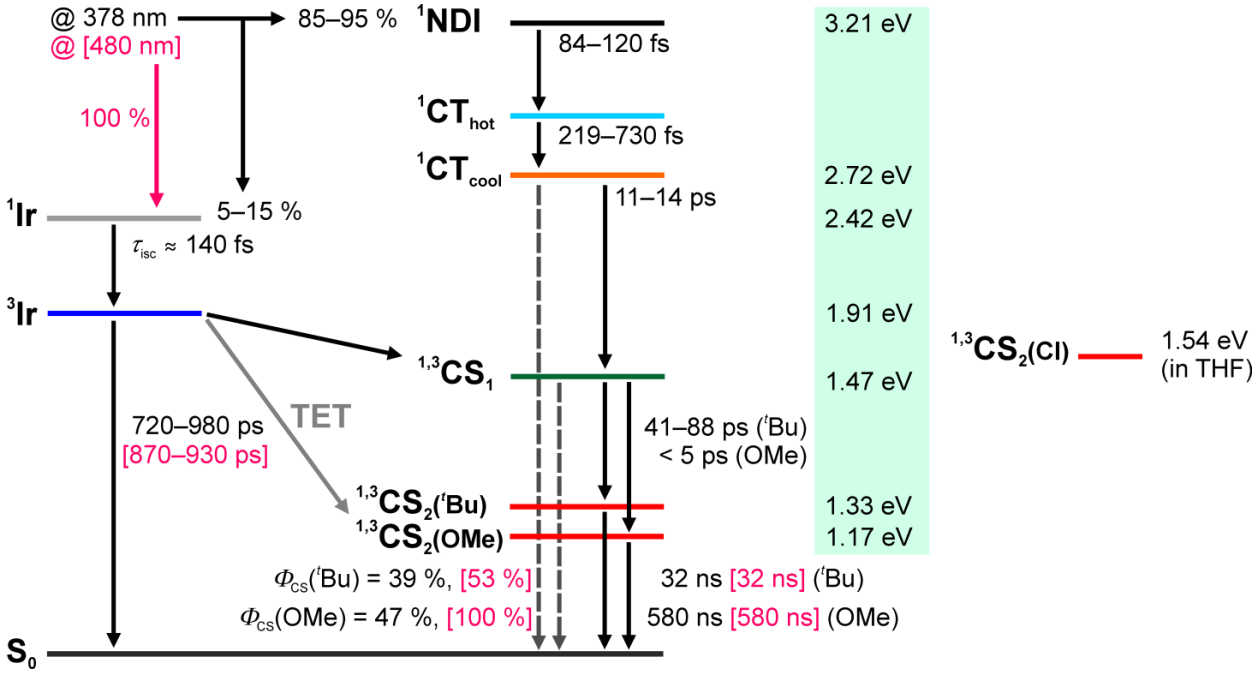

Figure 61 Generalised state diagram of donor-acceptor substituted triads including **Ref_{NDI}** in MeCN. **T3** was measured in THF and is omitted for simplicity but shows similar features. Data for excitation at 26 500 cm^{-1} (378 nm) are given in black, those for 20 800 cm^{-1} (480 nm) excitation in pink. The colours of the states are the same as used for the SADS.

In principle two scenarios may explain the experimental findings concerning the absent CS_1 state: The first is a stepwise process with a first slow ET step leading from the ^{3}Ir state to the $^3CS_1$ followed by a very fast ET process to the final CS_2 state. As outlined above, the CS_1 state is postulated from the results of **Ref$_{NDI}$** and **T2**. An even faster follow-up process in **T1** would then lead to a vanishing concentration of the intermediate CS_1 state which thus, cannot be detected by transient absorption spectroscopy. This process is also induced at 26 500 cm^{-1} (378 nm) excitation to ca. 15 % because at this wavelength higher lying Ir-complex states also absorb. The alternative explanation would be a concerted TET (two-electron transfer) from the ^{3}Ir state directly to the $^3CS_2$ state as indicated by a grey arrow in Figure 53 and 61. In order to evaluate the possibility for these two conceivable mechanisms, the discussion will be based on both electronic and kinetic aspects.

The first argument for a stepwise mechanism is the observation that the lifetime of ^{3}Ir of **Ref$_{NDI}$** does not change upon attaching the TAA donors in **T1**. This supports the formation of an intermediate CS_1 state in the rate limiting step as no TAA is involved in this process. The natural lifetime of CS_1 is ca. 110–170 ps as determined for **Ref$_{NDI}$**. Thus, it can be assumed that the lifetime of CS_1 in **T1** must be shorter by a factor of 10 so that its amplitude is too small to be detected. In fact, including this state in the target fit of **T1** at 26 500 cm^{-1} (378 nm) yields a very small lifetime of < 5 ps (Figure 52a and b).

For the kinetic interpretation of the different ET-pathways ET barriers were estimated with eq. (1) (Table 8).[38-39]

$$\Delta G^{\#} = \frac{(\Delta G + \lambda)^2}{4\lambda} \qquad (1)$$

The ΔG_{CS} values were already calculated in the CV section and are listed in Table 6. Reorganisation energies for the self-exchange (λ_v) which are required for these calculations were either extracted from literature for $NDI^{\bullet-}$ (0.39 eV)[330] and $TAA^{\bullet+}$ (0.12 eV)[331] or calculated via the NICG (neutral in cation geometry, cf. 5.1.10 for detailed information) method[35, 332-333] for the Ir(ppz)$_2$(dipy) cation (0.25 eV). Besides, the outer reorganisation (λ_o) energy for a specific ET process was calculated as the average of the self-exchange reorganisation energy of the constituting molecular units. The solvent reorganisation energies (λ_o) were estimated by the *Born* equation (eq. (29)).[35, 334-335]

$$\lambda_o = \frac{e^2}{4\pi \cdot e_0}\left(\frac{1}{2r_D}+\frac{1}{2r_A}-\frac{1}{d_{DA}}\right)\left(\frac{1}{n_D{}^2}-\frac{1}{\varepsilon_s}\right) \qquad (29)$$

Here, n is the refractive index and ε_s the static dielectric constant of the used solvent. The resulting free energies of activation $\Delta G^{\#}$ for an ET processes between different states including ^{3}Ir, CS_1, CS_2 and S_0 states are listed in Table 8.

Table 8 Outer reorganisation energies (λ_o) calculated by the *Born* equation (29) for the CS (^{3}Ir→CS_1, ^{3}Ir→CS_2, CS_1→CS_2) and CR (CS_2→S_0, CS_1→S_0) processes of triads **T1–T3** and **Ref_{NDI}**, as well as corresponding λ_v and $\Delta G^{\#}$ values.

		^{3}Ir⟶CS_1, (CS_1⟶S_0)			CS_2⟶S_0, (^{3}Ir⟶CS_2)			CS_1⟶CS_2		
	solvent	λ_o	λ_v	$\Delta G^{\#}$	λ_o	λ_v	$\Delta G^{\#}$	λ_o	λ_v	$\Delta G^{\#}$
		/ eV			/ eV			/ eV		
Ref_{NDI}	MeCN	0.91	0.32	0.12 (0.01)						
	THF	0.64	0.32	0.14 (0.12)		-			-	
	^{t}BME	0.54	0.32	0.17 (0.26)						
T1	MeCN	0.91	0.32	0.13 (0.01)	1.36	0.26	0.03 (0.12)	0.88	0.19	0.14
	THF	0.64	0.32	0.14 (0.12)	0.97	0.26	0.01 (0.13)	0.63	0.19	0.11
T2	MeCN	0.91	0.32	0.13 (0.01)	1.36	0.26	0.01 (0.17)	0.88	0.19	0.20
T3	THF	0.64	0.32	0.06 (0.05)	0.97	0.26	0.02 (0.16)	0.63	0.19	0.15

The static dielectric constants for the specific solvents are as follows: ε_r(MeCN) = 35.49, ε_s(THF) = 7.58 and ε_r(^{t}BME) = 4.50. The refractive indices are: n_D(MeCN) = 1.3441, n_D(THF) = 1.4072 and n_D(^{t}BME) = 1.370. The distances (d_{AD}) and radii (r_A, r_D) of the molecular structures were extracted from DFT calculations (see 5.1.10).

First, the ET step from the iridium complex to the NDI (^{3}Ir⟶CS_1) in **Ref_{NDI}** which is identical within triads **T1–T3**, and the recombination process (CS_1⟶S_0) are analysed. $\Delta G^{\#}$ for the charge recombination increases from a vanishing activation barrier of 0.01 eV in MeCN to 0.12 and 0.26 eV in THF and ^{t}BME, respectively. On the other hand, the barrier for the charge-separation process also increases but to a minor extent from 0.12 to 0.17 eV. The low energy barrier for the charge recombination gives an explanation why no kinetic traces were detected in the ns-transient absorption experiments in MeCN and THF. Moreover, in ^{t}BME it was possible to measure short-lived signals (cf. Figure 38). The energy barrier for the back

electron transfer increases and at the same time the lifetime of the CS_1 state is prolonged and allows detection with the ns-laser flash set-up.

On the contrary, the electrochemical experiments of **T3** were performed in CH_2Cl_2 and as a result the estimated state energies (ΔG_{CS}) for CS_1 in THF change significantly (1.39 eV measured in CH_2Cl_2 vs. 1.65 eV in MeCN), while the $\Delta E_{1/2}$ value corresponding to CS_1 stays constant compared to the CV of $\mathbf{Ref_{NDI}}$ in MeCN. For that reason, the energy barriers of **T3** are not suitable for a comparison with the other complexes. However, the increase of the energy barrier of the $CS_1 \longrightarrow S_0$ process can be reproduced in **T3**, as well, but the effect is less pronounced (0.05 eV). If a higher barrier for charge recombination from CS_1 to S_0 is assumed in THF compared to MeCN this may explain the higher time constant of the CS_1 state in **T3** (0.6–1 ns) than in $\mathbf{Ref_{NDI}}$ (170 ps).

Coming back to the CS_1 issue of **T1**, the energy barriers for the different ET steps will be discussed. A value of $\Delta G^{\#}$ = 0.14 eV is calculated for the ET process $CS_1 \longrightarrow CS_2$ of **T1**, while for the charge-recombination steps $CS_2 \longrightarrow S_0$ and $CS_1 \longrightarrow S_0$ the barriers are much lower with $\Delta G^{\#}$ = 0.03 eV and 0.01 eV, respectively. Conversely, the associated lifetimes for the both ET processes are much longer. This indicates that electronic coupling effects are the decisive aspect rather than kinetic barriers when comparing these rates.[22] The large distance of charges in CS_2 and CS_1, the decoupling effect of the nodal plane in the NDI's LUMO, the almost 90° twist of the phenyl-ring of the dipyrrin, and the saturated methylene and ethylene bridges between the Ir-complex and the TAAs all will certainly lead to very small electronic couplings and, thus, slow down ET processes. In particular, the back electron-transfer of CS_2 shows a lifetime of 580 ns although being in the *Marcus* normal region. For the same reason, the ET from ^{3}Ir to CS_1 might be slow because of the low electronic coupling between ^{3}Ir and CS_1: the electronic coupling can be estimated by the *Hush*-equation (30).[336]

$$V_{el} = \frac{\mu_{eg}\tilde{\nu}_{max}}{er} \qquad (30)$$

Here, μ_{eg} is the projection of the transition moment of the ^{3}Ir-LUMO (*b* symmetry)⟶NDI-LUMO (*a* symmetry) transition with energy $\tilde{\nu}_{max}$, onto the effective ET distance vector e × *r*. From the LUMO and $LUMO_{-1}$ (cf. Figure 62) one can see that the transition moment for this LUMO⟶LUMO transfer is perpendicularly polarised to the ET vector ($b \times a = b$) which thus yields a vanishing coupling. In order to support all these arguments, consideration of the

energies of activation of **T2** with less donating substituents on the TAA raise the energy of the CS_2 state by ca. 0.16 eV (all other states are unchanged) might be helpful. fs-Transient absorption spectroscopy of **T2** essentially shows the same spectral and kinetic features as **T1** with two exceptions: indeed it was possible to find a state corresponding to CS_1 with a lifetime of 41 ps at 26 500 cm^{-1} (378 nm) excitation and 88 ps at 20 800 cm^{-1} (480 nm) excitation. The prolonged lifetime of CS_1 in **T2** compared to the upper limit of 10 ps in **T1** can easily be explained by the higher kinetic barrier which is 0.20 eV (cf. 0.14 eV in **T1**) which would change the rate by a factor of 11 which is reasonable. The other point concerns the lifetime of CS_2 in **T2** which is now reduced to 32 ns because of the CS_2 state 0.16 eV higher in energy in the *Marcus* normal region. The experimental ratio of lifetimes τCS_2(**T1**) / τCS_2(**T2**) = 18 is in good agreement with the factor estimated above.

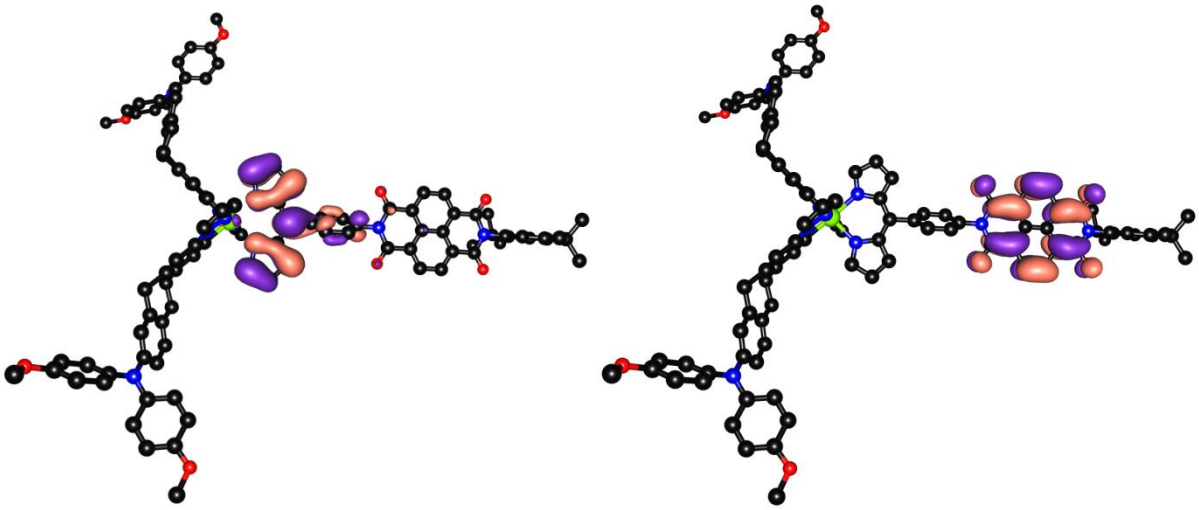

Figure 62 Orbital pictures of the LUMOs involved in the ET process $^3Ir \longrightarrow CS_1$. $LUMO_{-1}$ (b symmetry, left) and LUMO (a symmetry, right) of complex **T1** calculated at DFT level of theory (see experimental part).

Despite the overwhelming arguments for a stepwise ET in **T1** at 20 800 cm^{-1} (480 nm) excitation, a concerted TET cannot be fully excluded, particularly in view that a direct observation of the intermediate CS_1 in **T1** is missing. Moreover, the twofold difference between the quantum yield in **T2** (53 %) compared to the 100 % in triad **T1** may not only be caused by the reduced barrier (0.14 in **T1** vs. 0.20 in **T2**) for the HOMO-HOMO transfer in **T1**.

The orbital diagram for a concerted TET (see Figure 63) clearly resembles that for *Dexter* energy transfer[71] and the electronic coupling can thus be approximated by eq. (31).

$$V_{cTET} = \left\langle \phi_{LUMO\text{-}Ir}(1)\phi_{LUMO\text{-}NDI}(1) \middle| \hat{V} \middle| \phi_{HOMO\text{-}TAA}(2)\phi_{HOMO\text{-}Ir}(2) \right\rangle \qquad (31)$$

This integral will be small but non-negligible, because of weak orbital overlap between donor HOMO and Ir-complex HOMO, as well as between Ir-complex LUMO and NDI LUMO. Along with the fact that the barrier for this TET is estimated to be the same[1] as for the rate limiting ^{3}Ir⟶CS$_1$ step in the stepwise process, it remains possible that a concerted TET may be involved, at least in parallel.

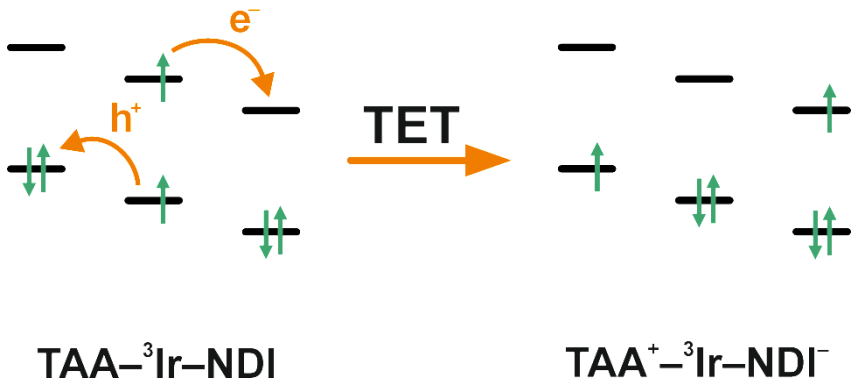

Figure 63 HOMO-LUMO diagram of triad **T1** with a hypothetical concerted TET.

Conclusion

The electron transfer properties of triads **T1–T3**, which differ in the redox strength of the used TAAs (**T1** = OMe, **T2** = ^{t}Bu and **T3** = Cl), were investigated systematically with fs-pump-probe spectroscopy at two different laser excitation energies (26 500 cm^{-1} (378 nm) and 20 800 cm^{-1} (480 nm)). The NDI is excited with the first laser energy, whereas the Ir(dipy) complex is pumped at 20 800 cm^{-1} (480 nm). The reference compounds **Ref1**, **Ref$_{NDI}$** and **17** were studied, as well, as they help to identify processes which are solely occurring in one of the used chromophores. Due to a low solubility of **T3** in MeCN the measurement were performed in THF, whereas all other complexes were sufficiently soluble in MeCN.

[1] One expects a concerted TET to have the fourfold reorganisation energy compared to a SET as the reorganisation energy scales with the square of charge transferred.[337] This is not the case here as on the donor and the acceptor only a single charge is created.

Remarkably, the global analysis with GLOTARAN[321] of all investigated complexes show a very consistent picture of the ET events in these triads. SADS of identical states and their corresponding lifetimes are all very similar. This is even more surprising as all complexes consist of different substituted TAAs. Of course, the lifetimes are different for ET processes in which the changed electronic environment influences ET barriers or the state order is affected due to the omission of certain chromophores. Besides, the complexes benefit from a low electronic coupling between the TAA, Ir(dipy) and NDI chromophores. Finally, a comparison of the ET barriers unravelled the electron transfer mechanisms at different excitation energies.

In all NDI containing compounds, excitation of the NDI produces a ^{1}NDI followed by vibrationally excited and relaxed CT states (CT_{hot}, CT_{cool}). Thereafter, a charge shift from the CT to a first CS state (CS_1) is observed in **T2**, **T3** and **Ref_{NDI}**. This intermediate state is depopulated from a very fast follow-up ET to the CS_2 state in **T1** for which the CS_1 state shows an almost negligible concentration. However, the resulting CS_2 state in **T1** and **T2** clearly show the characteristic features of the TAA radical cation and the NDI radical anion which proves that charge separation actually occurs in these triads.

On the contrary, excitation of the iridium complex at 20 800 cm^{-1} (480 nm) displays a completely different picture of the ET in the triads under investigation. After fast ISC (∼140 fs) the ^{3}Ir state shows only GSB. In case of **T2**, **T3** and **Ref_{NDI}** the following state is attributed to the CS_1 state which shows only a small intermediate concentration due to inverted time constants. In a next step, **T2** generates the fully charge-separated state. The GSB and monoradical ESA are present in **T1**, as well, whereas a SADS for the CS_1 state is completely missing. The explanation for this can be found in the higher driving force and reduced ET barriers for the ET from CS_1 to CS_2 in **T1** compared to **T2**. Consequently, the vanishing concentration of the CS_1 state in **T1** let this state escape from the detection limit, contrary to **T2**, whereas this state can be observed. The higher CS_1 concentration in **T2** is in line with a *Marcus* normal situation of the observed ET.

For **Ref_{NDI}** and **T3** charge separation at both laser energies is observed, too. However, in **Ref_{NDI}** the structural requirements for the formation of the CS_2 state are missing because the TAAs are not present. On the contrary, **T3** exhibits both donor and acceptor units but suffers from a changed state order. The oxidation of the chloro-substituted TAA (**T3**) is now

associated with higher potentials compared to the methoxy-TAA (**T1**), *tert*-butyl-TAA (**T2**) and the Ir(dipy) oxidation. Consequently, the CS_1 state is energetically below the CS_2 state which makes a detection of the latter impossible.

Two different ET mechanism were discussed for **T1** which may explain the absence of the CS_1 state. On the basis of kinetic and electronic aspects, a stepwise ET and a concerted two-electron transfer were discussed. Both mechanisms may be involved in the case of **T1**, at least in parallel.

Multichromophoric assemblies incorporating the above mentioned iridium complex as photosensitiser, where the NDI is substituted against a proton reduction catalyst, e.g. different cobaloxim complexes or dithiolate-bridged hexacarbonyl diiron(I) complexes, are currently under investigation in the group of Prof. Dr. *C. Lambert*. Thereby, the efficient charge separation in these complexes is used to achieve high quantum yields for the reduction process from protons to molecular hydrogen (H_2) in water or in organic solvent-water mixtures. These contributions to the field of photocatalytic water splitting seems promising because the use of light to produces solar fuels, such as hydrogen, is an important step towards an economy which uses exclusively renewable energies.

3.1.3 Combination of Slow and Efficient ET – Both are Possible

Introduction

In the following paragraph solely **T4** is discussed concerning its fs-transient absorption data. The previous section discussed the characteristics of the first charge separation in the model complex (**Ref$_{NDI}$**) and all triads **T1–T3** influenced by different follow-up reactions (restoring of the ground state or formation of the CS_2 states). Conversely, the first charge separation step in **T4** has to proceed from the Ir(dipy) fragment to the NDI via the longer biphenyl (biph) spacer compared to the phenylene bridge in **Ref$_{NDI}$** and **T1–T3** (Figure 64). However, the second ET step is equivalent to that in **T1** because all ET parameters (electronic coupling, donor-acceptor distance and redox potentials) are identical. Likewise, triad **T4** was excited with the same pump energies as it was for the complexes in the previous chapter.

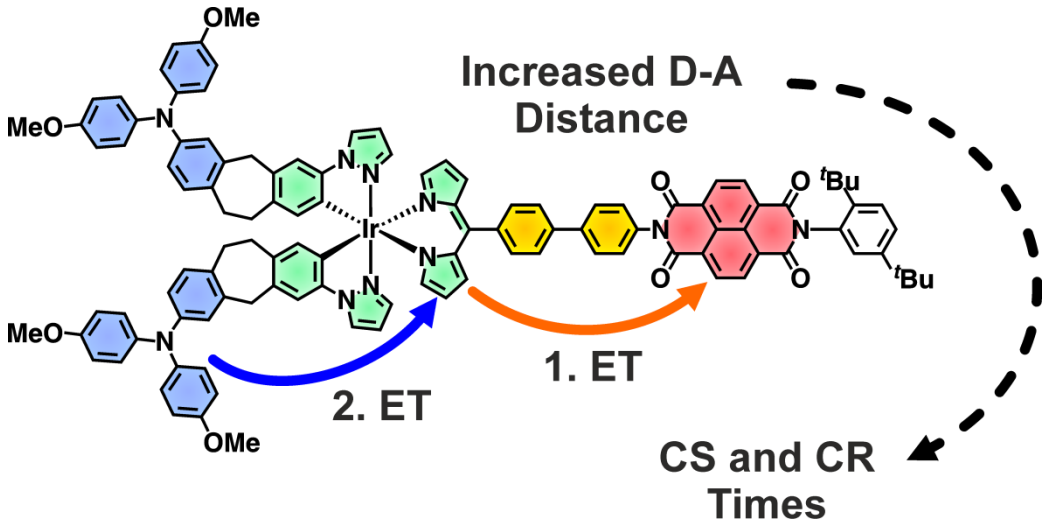

Figure 64 Prolonged ET distance for the first ET in **T4** affect charge separation and charge recombination.

fs-Pump-Probe Spectroscopy

As already shown in the preceding chapter excitation of the NDI unit at 26 500 cm^{-1} (378 nm) produces the excited ^{1}NDI species (black curve, Figure 65a) with its prominent peak at 16 800 cm^{-1} (593 nm) for **T4**.[305] This state transforms into a hot charge-transfer (CT) state (CT_{hot}, cyan) and relaxes to the cooled CT state (CT, orange) which can be seen by the typical

signals for the NDI radical anion at 16 600 cm^{-1} (602 nm) and 21 200 cm^{-1} (472 nm)[71, 293-294, 305, 310-311, 313-315] and the little sharpening of signals on going from CT_{hot}, to CT. This CT state has the positive charge at the bridging biphenyl unit (which does not display any significant spectroscopic signature in the transient spectra) and the negative one on the NDI. The observed dynamics possess almost the same rate constants as those for triad **T1**–**T2** and **Ref_{NDI}** (see Figure 61).

Unlike in case of **T1**, the global analysis of **T4** reveals an additional SADS with a lifetime of 900 ps which shows similar spectroscopic signatures as the CT state of the biph-NDI fragment. The origin of that state is not completely clear but may be assigned to a conformational change of the biphenyl unit (CT_{biph}, magenta).[338-343] The following intermediate state is not visible in the transient spectra as its concentration is very low because of a very fast follow-up reaction. This state is postulated in analogy to **T1** for which additional spectroscopic information from model compound **Red_{NDI}** and triad **T2** is available. Likewise, the SADS of this state is forced to have zero intensity with a lifetime of less than $\tau_5 <$ 1.4 ps. As in **T1** this state is assigned to the CS_1 state (green), where the NDI is reduced and the iridium dipyrrin complex is oxidised. This CS_1 state is populated from two different precursor states, the first one is the CT state and the second one is the conformationally relaxed CT state (CT_{biph}) which populates the CS_1 state with 60 % and 80 % efficiencies, respectively (see Figure 66). The very short-lived CS_1 state is followed by the fully charge-separated state (CS_2, red) with its typical signatures for the TAA radical cation at 13 800 cm^{-1} (723 nm)[262, 291] and for the NDI radical anion (16 600 cm^{-1} (602 nm) and 21 200 cm^{-1} (472 nm)).[71, 293-294, 305, 310-311, 313-315] Yet, the relative intensities of the monoradicals, especially those at 13 800 cm^{-1} (723 nm) and 21 200 cm^{-1} (472 nm), differ compared to all observed CS_2 spectra so far. The latter peak lacks intensity in the region where typically the GSB of the ^{3}Ir or CS_1 state occurs and additionally the signal-to-noise ratio is very low. This observation fits perfectly with the slow rise time of 35 ns found in the ns-laser flash section because the CS_2 state evolution exceeds beyond the time resolution of the fs-laser set-up. The CS_2 state obviously is populated from a state where an excited iridium species (either cation (CS_1) or just triplet species (^{3}Ir)) is involved which explains the missing intensity in the region of 19 000–23 000 cm^{-1} (435–526 nm). However, the bleaching of the ^{3}Ir state which is always visible at 26 500 cm^{-1} (378 nm) excitation at least to a minor extend of ca. 10 %, is missing

and with that a comparable rise time for the CS_2 state (35 ns were found in the ns-experiments).

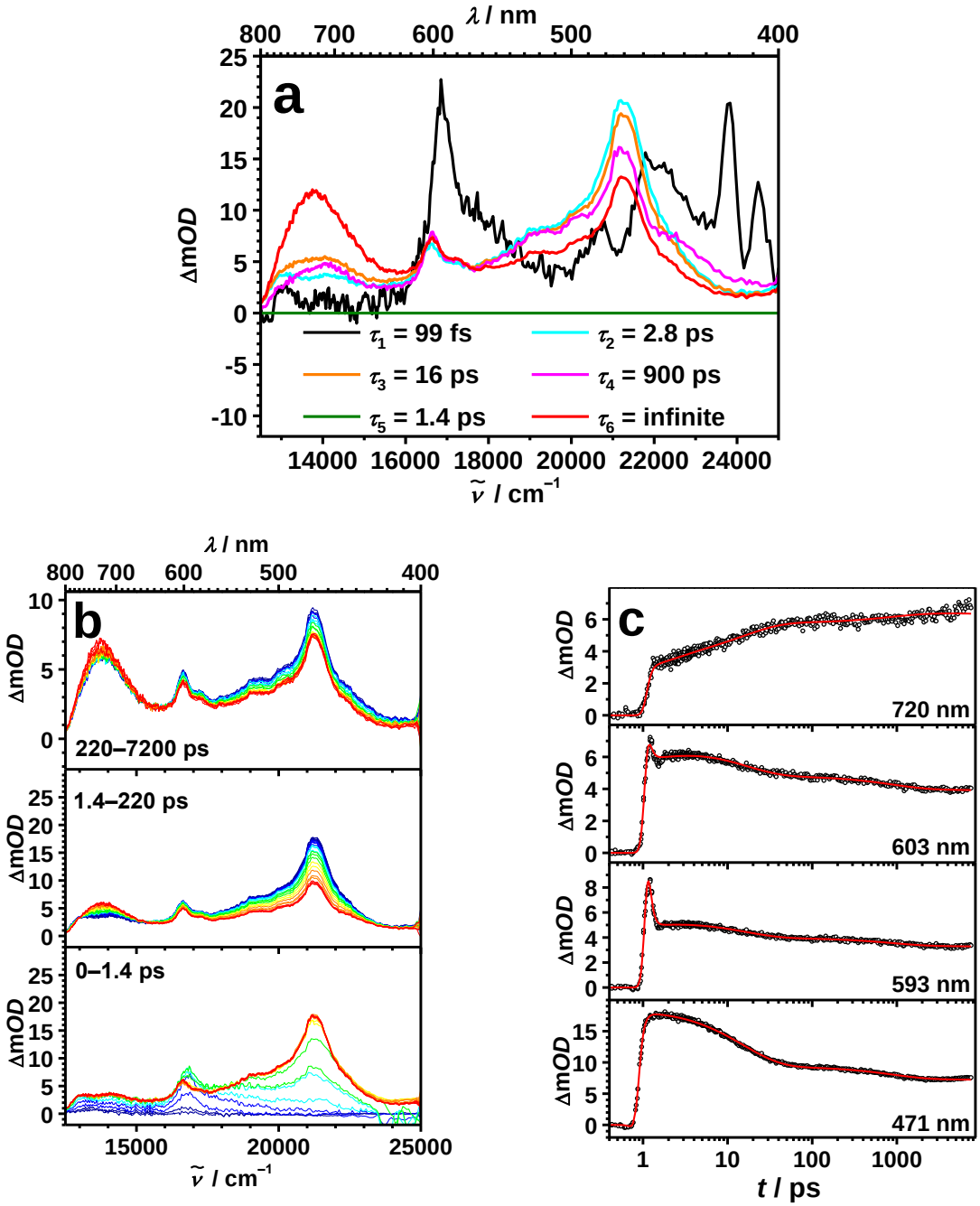

Figure 65 (a) Species associated difference spectra (SADS) of **T4** obtained from a global analysis of a transient map. The colours of the SADS refer to the states in the corresponding state diagram in Figure 66. (b) fs-Transient absorption data corrected for chirp and scattered pump light. Early spectra are depicted in blue to green and at later times in orange to red colours. (c) Decay profiles at selected wavelengths for which the zero time delay was set arbitrarily. Excitation at 26 500 cm^{-1} (378 nm) in MeCN.

But several tested deconvolutions with different efficiencies in the highly branched model describing the energy and electron transfer pathways did not show a spectrum where a GSB was visible. This might be explained by the low concentration of that state as it is the case for the CS_1 state. Although the complete mechanism is to a certain extent speculative it is very striking that the quantum yield of the formation of the CS_2 state of 37 % is in the same order than for **T1** (47 %), even taking into account that the ET distance in the first step is extended because of the biphenyl bridge.

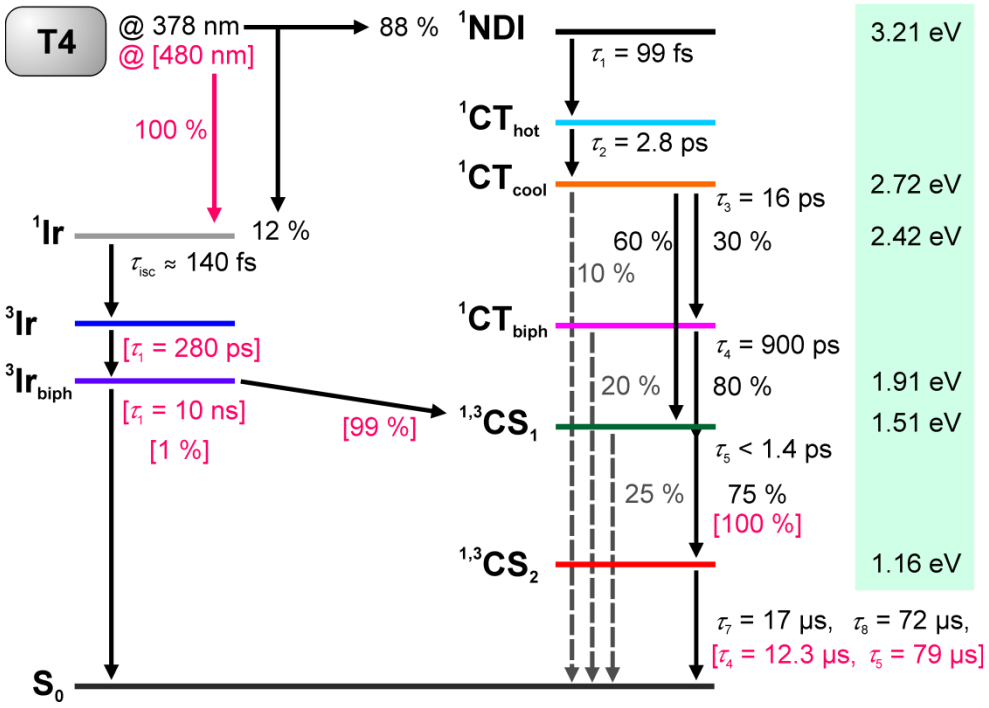

Figure 66 State diagram for **T4** in MeCN. Data for excitation at 26 500 cm^{-1} (378 nm) are given in black, those for 20 800 cm^{-1} (480 nm) excitation in pink. The colours of the states are the same as used in Figure 65a and 67a for the SADS.

A second experiment covers the excitation of the iridium dipyrrin unit at 20 800 cm^{-1} (480 nm) and is somehow easier to interpret. The first SADS (Figure 67a) is characteristic for the excited state of the triplet iridium dipyrrin complex (^{3}Ir, blue) with a pronounced ground-state bleaching at around 20 900 cm^{-1} (478 nm) but almost no excited-state absorption elsewhere. This state evolves within the instrument response and is caused by very fast intersystem crossing (ISC, approx. τ_{ISC} = 140 fs, *vide supra*) from the initially excited singlet iridium dipyrrin complex (in grey). From this state with a lifetime of 280 ps another one is

formed whose SADS can again be assigned to an excited triplet iridium dipyrrin state ($^3Ir_{biph}$, purple) because it looks almost identical to the first one (^3Ir, blue). Again this is different to what was investigated in the preceding chapter. Consequently, this behaviour may be explained by different conformers of the biphenyl bridge.[338] According to the global fit the conformationally relaxed state $^3Ir_{biph}$ has a lifetime on the order of 10 ns. The last SADS which rises with the decay time of the former (~10 ns) shows the beginning rise of the spectra of the fully charge-separated state (CS_2, red) without giving the pronounced signatures of the CS_2 state as it was observed for excitation at 26 500 cm^{-1} (378 nm). This is caused by the slow rise time which exceeds the delay time-limit of the fs-set-up (8 ns) given by the length of the delay stage. Nevertheless, the rise time of the CS_2 state was determined to be 35 ns by ns-transient absorption spectroscopy which is in very good agreement with the 10 ns found here.

Comparing the last SADS with infinite lifetime (red spectra in Figure 65a and 67a) of both excitation energies, it is obvious that the spectra of the CS_2 state at 26 500 cm^{-1} (378 nm) excitation is more intense than the one at 20 800 cm^{-1} (480 nm) excitation. From the fs-pump-probe data a fast stepwise ET (ca. 900 ps) is postulated when the NDI is excited where the spectra for the GSB is missing, whereas excitation of the iridium dipyrrin moiety points to a slow rise (> 10 ns) of the CS_2 state. Indeed, a similar time (35 ns) could be fitted for the rise of the fully CS state. Remarkably, the slow charge-separation process has a high quantum yield for the CS of 97 %. Compared to what is found in literature (Table 1) **T4** exhibits at the same time very efficient charge-separation processes and its fully charge-separated state has an extremely long lifetime (79 µs). Both aspects combined in one metal complex sensitised donor-acceptor triad is quite unique.

In the following, some kinetic aspects according the slow charge separation in **T4** at 20 800 cm^{-1} (480 nm) are discussed. First, the CS_2 state in **T4** (ΔG_{CS} = 1.16 eV) has a similar energy as that in **T1** (ΔG_{CS} = 1.17 eV), whereas the difference of the CS_1 state energy is more pronounced with 1.47 vs. 1.51 eV (Table 6) for **T1** and **T4**, respectively. Furthermore, CS is by a factor of approx. 35 slower in **T4** than in **T1** (35 ns vs. 0.93 ns) and the kinetic barrier ($\Delta G^{\#}$) increase in the same series from 0.13 to 0.19 eV (Table 9). However, the predicted factor for the change of the rate constants of that specific process is 11. Although, the difference

between the ratios of the measured time constants and the calculated ET barriers is threefold, the higher electron barrier in **T4** may be responsible for the slower CS process.

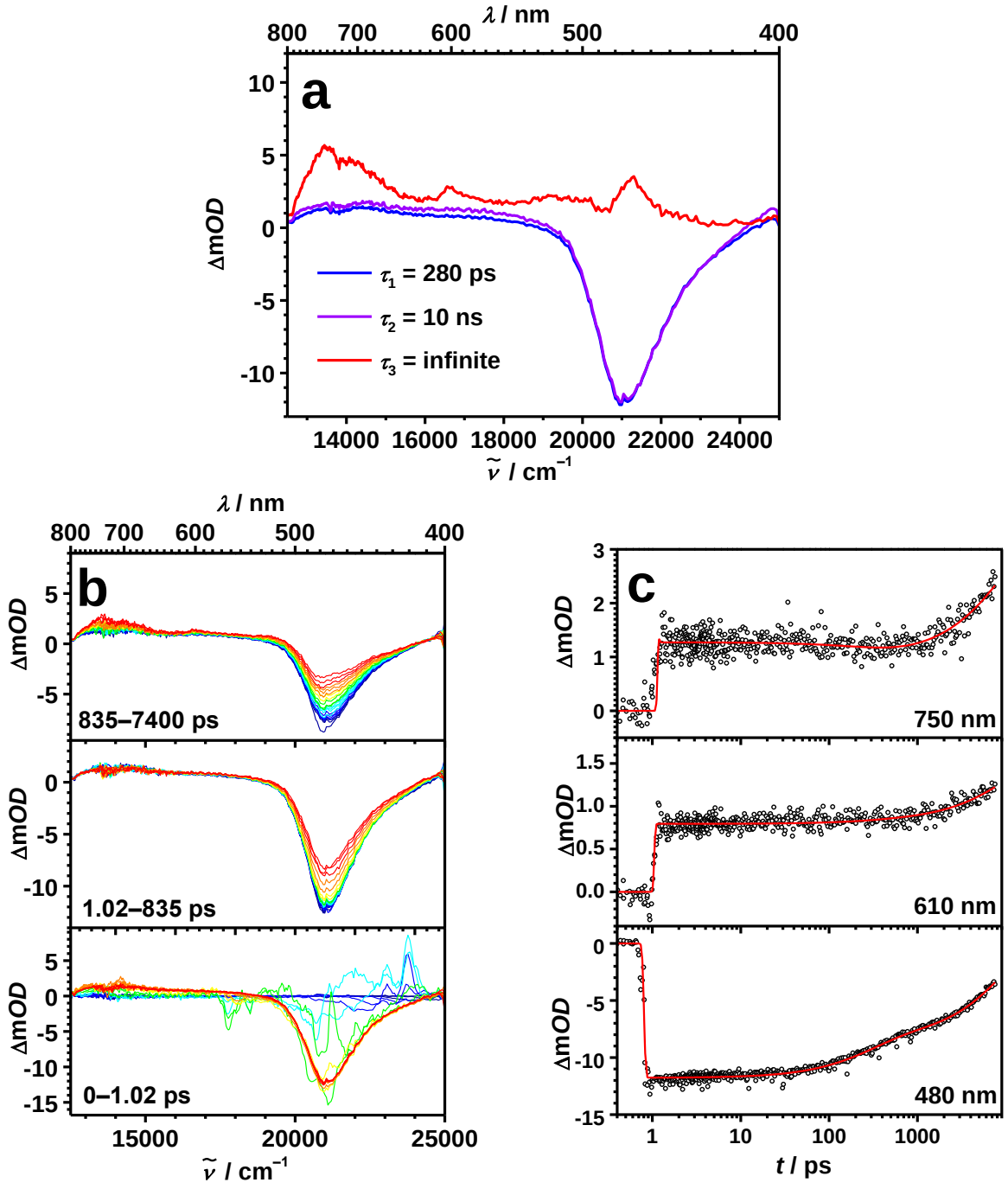

Figure 67 (a) Species associated difference spectra (SADS) of **T4** obtained from a global analysis of a transient map. The colours of the SADS refer to the states in the corresponding state diagram in Figure 66. (b) fs-Transient absorption data corrected for chirp and scattered pump light. Early spectra are depicted in blue to green and at later times in orange to red colours. (c) Decay profiles at selected wavelengths for which the zero time delay was set arbitrarily. Excitation at 20 800 cm^{-1} (480 nm) in MeCN.

Table 9 Reorganisation energies (λ_o) calculated by the *Born* equation (eq. (3)) for the CS (^{3}Ir→CS_1, ^{3}Ir→CS_2, CS_1→CS_2) and CR (CS_2→S_0, CS_1→S_0) processes of triads **T1** and **T4** and corresponding λ_v and $\Delta G^{\#}$ values.

		^{3}Ir⟶CS_1, (CS_1⟶S_0)			CS_2⟶S_0, (^{3}Ir⟶CS_2)			CS_1⟶CS_2		
	solvent	λ_o	λ_v	$\Delta G^{\#}$	λ_o	λ_v	$\Delta G^{\#}$	λ_o	λ_v	$\Delta G^{\#}$
		/ eV			/ eV			/ eV		
T1	MeCN	0.91	0.32	0.13 (0.01)	1.36	0.26	0.03 (0.12)	0.88	0.19	0.14
T4	MeCN	1.15	0.32	0.19 (<0.01)	1.43	0.26	0.04 (0.13)	0.88	0.19	0.12

The static dielectric constant and the refractive index of MeCN used is ε_r(MeCN) = 35.49 and n_D(MeCN) = 1.3441, respectively. The distances (d_{AD}) and radii (r_D, r_A) of the molecular structures were extracted from DFT calculations (see 5.1.10).

Conclusion and Future Outlook

To sum up, only a little change in the donor-acceptor distance, i.e. the use of a biphenyl instead of a phenyl bridge between the Ir(dipy) and the NDI chromophores in **T4**, causes a dramatic change of the CS and the CR dynamics compared to triad **T1**. Excitation of the NDI fragment in **T4** at 26 500 cm^{-1} (378 nm) yielded similar features and lifetimes as those for **T1**. First, the spectra of ^{1}NDI and the subsequent CT states (hot and cool) are visible. Furthermore, the CS_1 state with a vanishing concentration is included into the global fit. Contrary to the findings in **T1**, an additional spectrum similar to a CT absorption is present in the global analysis which is assigned to a conformational change of the biphenyl unit with a lifetime of 900 ps. The complete rise of the CS_2 state was limited by the time window of the fs-set-up. Finally, the simultaneously excitation of the iridium complex at 26 500 cm^{-1} (378 nm) was absent in this experiment.

A comparison of the pump-probe experiments for **T1** and **T4** at 20 800 cm^{-1} (480 nm) shows that both experiments differ in the number of SADS. Whereas for **T1** only one GSB was observed, the transient data of **T4** shows two SADS characterised by GSB. Both spectra are attributed to a ^{3}Ir state, whereas the second GSB is caused by a conformational change of the biphenyl bridge in the direct vicinity of the iridium complex in **T4**. The evolution of the CS_2 state was fitted with 10 ns which is in good agreement to the 35 ns from the ns-laser flash

experiment (*vide supra*). Consequently, the transient absorption spectra of the CS_2 state at later times was not fully developed due to the slow CS.

The charge separation kinetics were already discussed in section 3.1.1.6 and showed a very long lifetime of approx. 79 µs for the charge recombination at 24 000 and 28 200 cm^{-1} (416 and 355 nm, respectively) which is seldom found for this type of triads (cf. Table 1).

Actinometric measurements revealed a low quantum yield (37 %) for the CS_2 state formation at 26 500 cm^{-1} (378 nm). On the contrary, the quantum yield is almost unity at 20 800 cm^{-1} (480 nm) excitation.

In total, the very efficient charge separation is quite unique for donor-acceptor substituted metal complex photosensitisers taking into account the slow CS kinetics. In addition, the low electronic coupling between donor and acceptor site causes a very long CS_2 lifetime of nearly 100 µs compared to approx. 0.6 µs if the biphenyl unit is exchanged by a phenyl unit (=**T1**).

To find out whether the second lifetime of the fully CS state (12 and 79 µs, 3.1.1.6) and the additional CT and ^{3}Ir SADS are based on a conformational change of the biphenyl spacer, future projects may incorporate the following structural changes: i) The rotation may be easily blocked by methyl substituents at the *ortho*-positions of the C-atoms building the biphenyl axis. ii) The use of a fluorene, phenanthrene or 9,10-dihydrophenanthrene spacer will break down rotation around the biphenyl axis, as well.

3.1.4 Symmetry Breaking in Donor-Iridium Dipyrrin-Acceptor Triads

Introduction

Symmetry breaking (SB) as a result of photoinduced charge-separation processes can be found in multichromophoric assemblies where an excited chromophore has several apparently equivalent donor (or acceptor) sites in its direct vicinity quenching the excited state. As a consequence, a reduced (or an oxidised) chromophore and an oxidised donor (a reduced acceptor) moiety can be obtained.[344-345] The resulting CS state has now a reduced symmetry because only one quenching event is involved in the ET process. A similar situation also resembles the situation in the excited states of $Ru(bpy)_3^{2+}$ or $Ir(piq)_3$ where the MLCT excited state is postulated to be located on one ligand rather be delocalised over all three ligands.[345-348] Moreover, the general concept of SB-CS often is hard to realise because synthetic access of attaching a second donor or acceptor group onto a certain chromophore is not easily feasible and often goes along with a reduced symmetry. This in turn breaks down the idea of symmetry breaking because one ET pathway is then more favoured compared to another. For that reason, in literature are only few examples of SB-CS systems.[345, 349-352] Although some multichromophoric systems possess the requirements for SB-CS,[54] the necessary experiments to confirm this were omitted.[345]

A second case concerning symmetry breaking is the quenching of an excited state where two identical molecular units are linked to each other while one of them is excited, e.g. in the reaction centre of photosynthetic purple bacteria[353] or in purely artificial systems.[344-345, 352, 354-356]

In this section the attempt towards photoinduced SB will be investigated with three triads (**T1**, **T5** and **T6**) which are schematically shown in Figure 68. The main difference in these triads is the number of amines (1, 2 and 4, respectively) and in case of **T6** the number of iridium complex units (2). From the CV (Figure 33) and ns-transient absorption spectroscopy (Figure 39 and 40) their properties are identical, whereas their steady-state absorption spectra differ taking their different number of chromophoric units into account (Figure 27). Besides, they are perfect candidates for the investigation of SB-CS because either the first ET (orange arrow in Figure 68) from the iridium complex to the NDI or the second ET from the TAA to the complex (blue arrow) can in principle be studied considering a different

number of quenching events. On one side, **T5** and **T1** will have identical rate constants for the first ET, because there is only one iridium quencher available. Conversely, **T6** with two iridium complexes may have a reduced time constant. On the other side, **T1** and **T6** will have similar kinetics due to two TAAs which participate in the second ET step. At the same time, **T5** may have a reduced time constant, because only one TAA unit present. Another advantage of the complexes is the unchanged energetic architecture which was proved (by UV/Vis- and ns-TA spectroscopy and CV measurements) to be identical within all triads due to a low electronic coupling between the different chromophores.

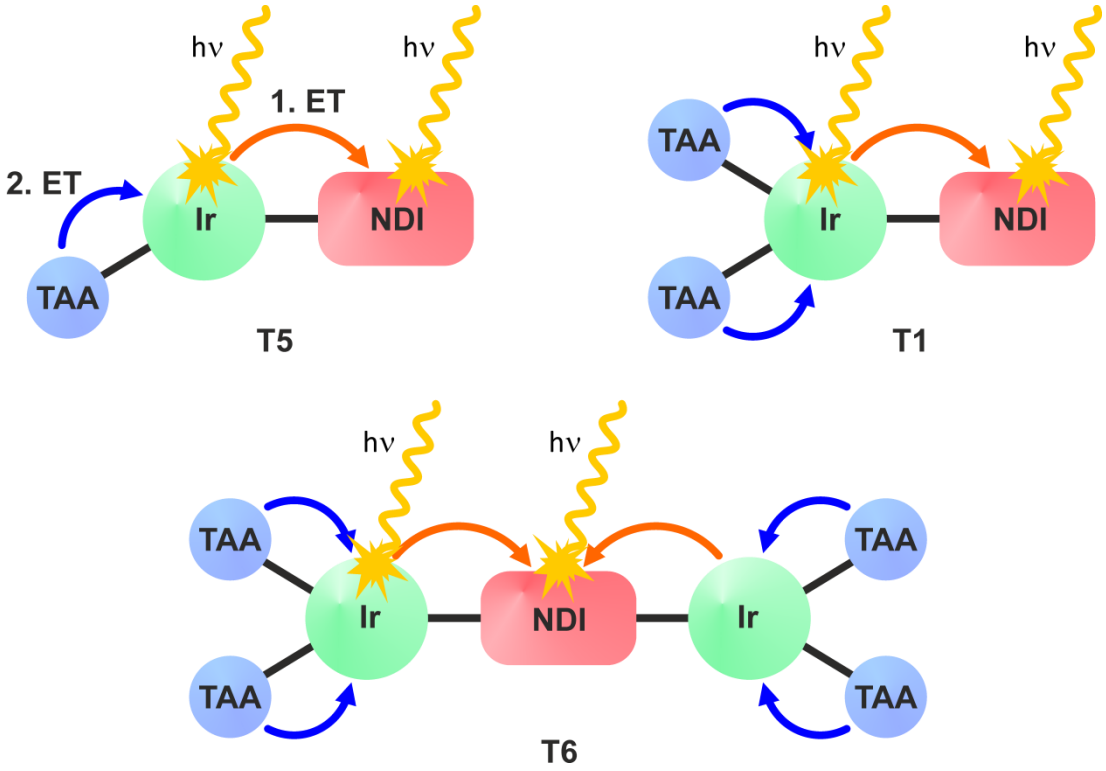

Figure 68 Schematic visualisation of the SB-CS effect in triads **T1**, **T5** and **T6**. First ET from the Ir complex (green) to the NDI (red) (orange arrow) and second ET from the TAA (blue) to the Ir complex (blue arrow) indicate the probability of the ET events.

fs-Pump-Probe Spectroscopy

The predominant technique to investigate the SB-CS phenomenon of weakly coupled systems is ultrafast pump-probe spectroscopy. Therefore, all multichromophoric systems were pumped at the same energy as it was conducted for the triads in the previous section (at 26 500 cm^{-1} (378 nm) and 20 800 cm^{-1} (480 nm)). This time the experiments were performed in THF as solvent because the solubility of triad **T6** in MeCN is too low.

Figure 69 illustrates the SADS (a, c and e) and EADS (b, d and f) of triads **T5**, **T1** and **T6** (top, middle and bottom, respectively) according to their number of amines. First of all, the SADS will be compared with each other and with the measurements of **T1** in MeCN (Figure 53). Likewise, the ^{1}NDI signal at 16 900 cm^{-1} (592 nm) appears as SADS (black) but is less pronounced compared to the MeCN experiments. The lifetimes of the ^{1}NDI is slightly slowed down in THF (140–218 fs) but differs within the same range as for the MeCN measurements (84–120 fs) due to major uncertainties (chirp correction and coherent artifact) in the subpicosecond time range. Furthermore, a CT state (cyan) can be observed where the NDI is negatively charged and a phenyl ring attached to the NDI bears the positive charge. Likewise, for **T1** in MeCN vibrational cooling (2.7–4.2 ps) is visible, too, accompanied with the solvent relaxation of some ps.[357] Accordingly, the observed vibrational cooling times in MeCN are with 219–730 fs clearly faster due to a higher polarity of MeCN which influences the energy of the involved state. The resulting relaxed CT (CT_{cool} in orange) is populated with 100 % only in case of triad **T6**, whereas for the other triads direct relaxation with ca. 30 % to the ground state has to be incorporated into the target model to yield reasonable SADS intensities. However, the CT states of the three triads decay directly into the CS_1 state equivalent to the orange arrow in Figure 68. Here, the effect of SB should be manifested displaying different lifetimes of the CT state. Unfortunately, the lifetimes for that state are very similar, but slightly slower for **T6** (26 ps) as for **T5** and **T1** (31 and 30 ps, respectively).

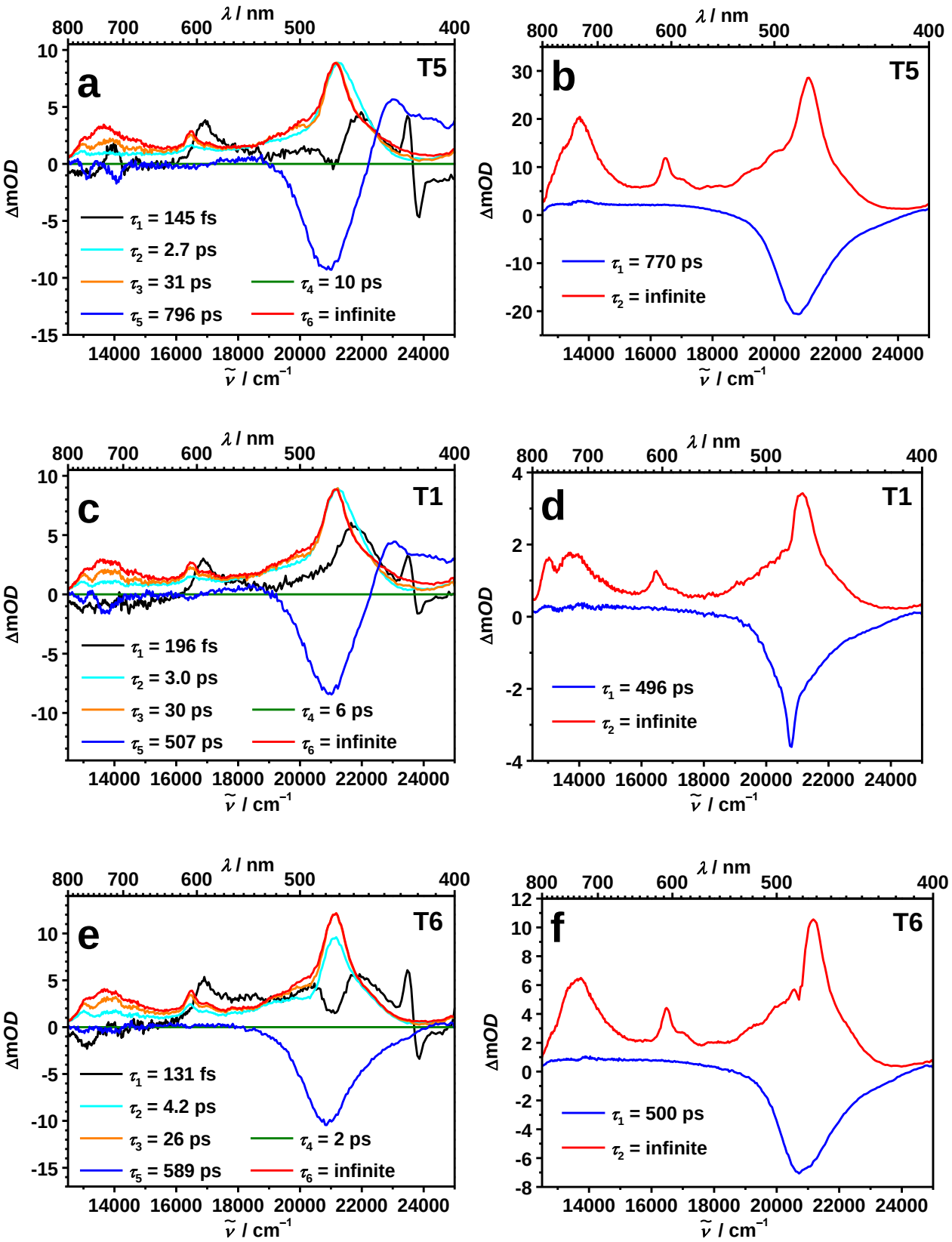

Figure 69 Species associated difference spectra (SADS, left) and evolution associated difference spectra (EADS, right) of **T5** (a, b), **T1** (c, d) and **T6** (e, f) from a global analysis of a transient map obtained by both 26 500 cm^{-1} (378 nm) (a, c and e) and 20 800 cm^{-1} (480 nm) (b, d and f) excitations in THF. The spectra on the right side (especially d and f) suffer from remaining stray light of the pump beam after the global analysis.

The CS_1 state furthermore comprises two superpositional effects, that is i) the radical anion excited-state absorption (ESA) of the NDI with a distinct peak at 16 500 cm^{-1} (606 nm) and an intense band with a maximum at 21 100 cm^{-1} (473 nm)[71, 293-294, 305, 310-311, 313-315] and ii) the GSB of the radical cation located at the iridium dipyrrin chromophore at 20 800 cm^{-1} (480 nm) (*vide supra*). In addition to the strongly overlapping spectral region between 19 000–23 000 cm^{-1} (435–526 nm) a reduced intermediate concentration of that state due to inverted time constants is assumed. The MeCN experiments revealed the same trend and a zero line for the CS_1 state (green) was introduced for both solvents because the resulting SADS is afflicted with major uncertainties concerning shape and a vanishing intermediate concentration.

Next, the successive ET from the CS_1 to the CS_2 state with fixed lifetimes between 2 and 10 ps yields the red SADS which clearly show the formation of the radical anion and radical cation peaks of the NDI and TAA, respectively. To obtain a reasonable fit result the latter lifetimes corresponding to the CS_1 state were fixed. Consequently, an interpretation of the differing lifetimes of that state is not serious. Additionally, a second population pathway of the CS_1 state (Figure 69) has to be mentioned where higher iridium complex excited states are involved due to a minor absorption (15–23 %) at the excitation energy of 26 500 cm^{-1} (378 nm). This path runs in parallel and the intermediate iridium complex triplet ES (^{3}Ir) shows the characteristic GSB at 21 000 cm^{-1} (476 nm) with lifetimes of 796, 507 and 589 ps for **T5**, **T1** and **T6**, respectively. Additionally, the contribution of a second iridium complex in **T6** to the overall absorption at the pump energy of 26 500 cm^{-1} (378 nm) is increased. A closer look on the differences of these lifetimes will be performed later on.

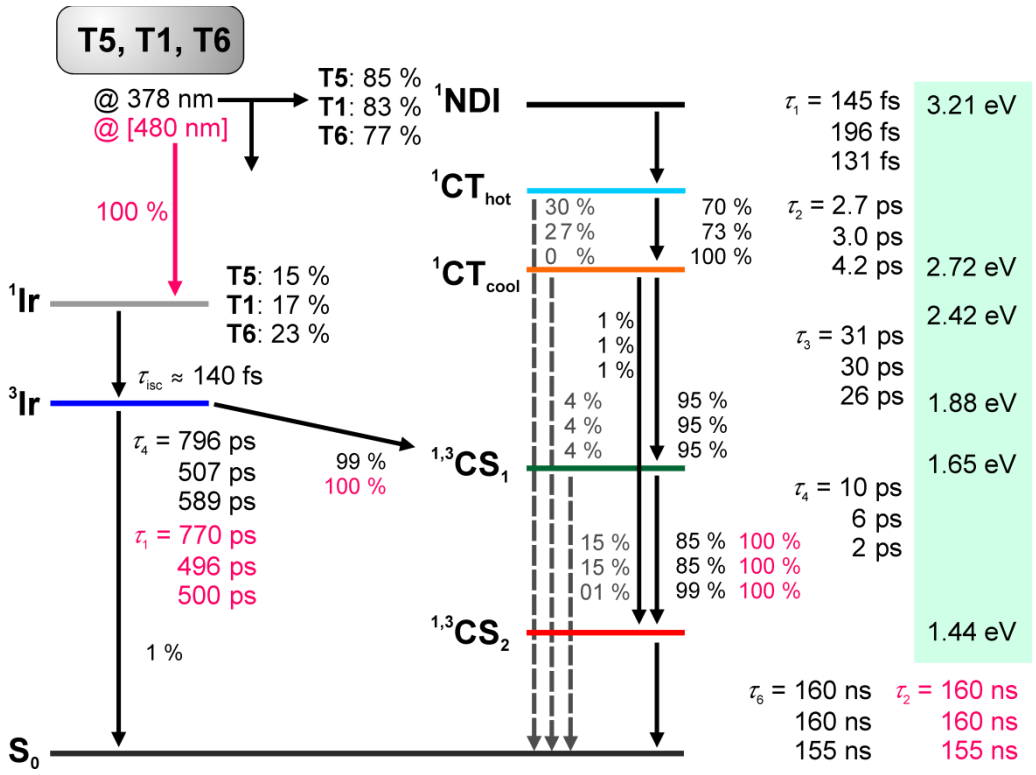

Figure 70 State diagram for **T5**, **T1** and **T6** in THF. Data for excitation at 26 500 cm^{-1} (378 nm) are given in black, those for 20 800 cm^{-1} (480 nm) excitation in pink. The colours of the states are the same as used in Figure 69 for the SADS and EADS.

A final aspect of the 26 500 cm^{-1} (378 nm) excitation in THF is the lower driving force for the generation of the CS_1 state by a charge shift from CT_{cool} to CS_1 as in MeCN (roughly estimated to 1 eV in THF vs. 1.25 eV in MeCN). Both charge shifts occur nearly without an activation barrier and hence are governed by the low electronic coupling between the chromophores (*vide supra*). At the same time the activation barrier for the ET step from ^{3}Ir to CS_1 is with 0.12 eV in the same order compared to those in MeCN (0.14 eV). Interestingly, the energy barrier for the direct relaxation of the CS_1 state to the ground state is by a factor of 10 lower in MeCN compared to THF (Table 10). Finally, the evolution of the transient spectra in the time window between 1.4 and 220 ps (shaded area in Figure 71, top) and in the decay profiles at selected wavelengths (shaded area in Figure 71, bottom) clearly reflect the difference between **T1** and **T5** on one side and **T6** on the other side. As already mentioned, pronounced differences already were present in the efficiencies of the different processes (Figure 70) which had to be taken into account for reasonable SADS intensities. Besides, the time range at early (0–1.4 ps) and at later times (0.2–7.4 µs) are practically identical, whereas

the middle part (1.4–220 ps) shows a pronounced difference especially in the spectral region between 20 000–23 000 cm^{-1} (500–435 nm). At the beginning triads **T5** and **T1** lose intensity in this region and at later times start to rise. On the contrary, **T6** gains intensity over the whole time range in this spectral region. This aspect is present in the decay profiles (shaded area in Figure 71, bottom), as well.

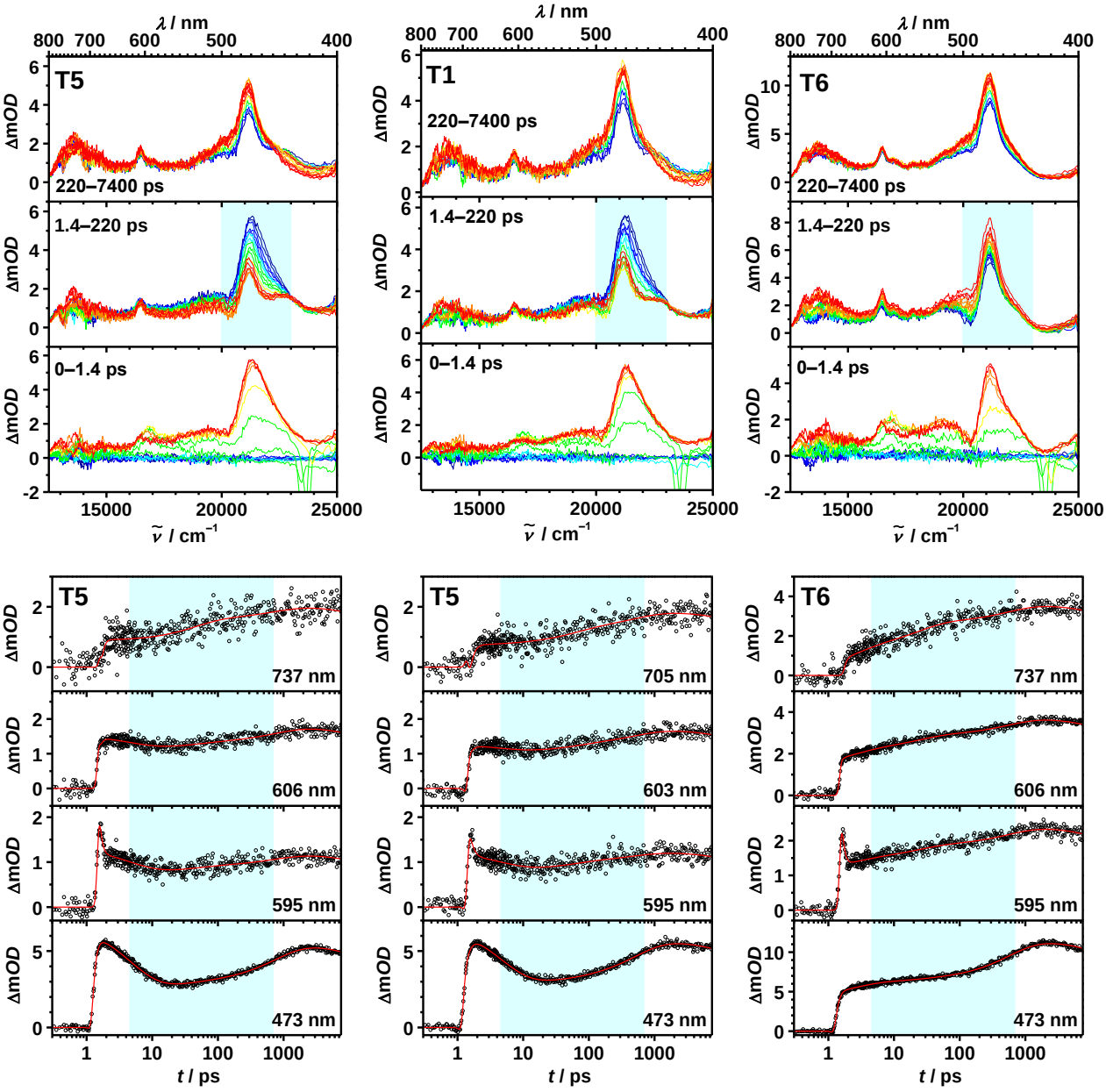

Figure 71 Top: fs-Transient absorption data of **T5**, **T1** and **T6** (from left to right) corrected for chirp and scattered pump light. Early spectra are in blue to green and at later times in orange to red colours. Bottom: Decay profiles at selected wavelengths for which the zero time delay was set arbitrarily. Excitation at 26 500 cm^{-1} (378 nm) in THF.

However, once creating the CS_1 state it is immediately quenched by the ET from one TAA to the iridium complex (blue arrow in Figure 68) yielding the fully CS state. As expected all three triads end up with the same state characterised by the monoradical ion features for the TAA cation at 13 600 cm^{-1} (735 nm)[262, 291] and the NDI anion band at 21 200 cm^{-1} (472 nm) and at 16 500 cm^{-1} (606 nm)[71, 293-294, 305, 310-311, 313-315] which in turn is identical in all triads. More important, the CS_2 state in all triads decays with the same time constant (ca. 160 ns) to the ground state proven by the ns-TA measurements. In the following, some requirements to obtain reasonable SADS from the global analysis will be discussed. First, the target model yields quantum yields of the CS_2 state of 63, 66 and 85 % for triads **T5**, **T1** and **T6**, respectively. The loss of quantum yield for **T5** and **T1** is based on the direct relaxation of the CT_{hot} state to the ground state. The fixed efficiencies for this energy loss is physically contradictable but were necessary to get realistic SADS signatures. Unfortunately, comparative values from actinometric measurements are at the moment not available and will be subject to future work. Second, the CS_1 state had to be incorporated in the global fit as a zero line (green line in Figure 69a, c and e) with fixed lifetime of 2–10 ns. This was done because the ordering of states with the CT_{hot}, CT_{cool} and CS_1 sequence and corresponding lifetimes of 131–145 fs, 2.7–4.2 ps and 26–31 ps, respectively, fit very good to the MeCN results. Moreover, the solvent relaxation times are well reflected for the CT_{hot} to CT_{cool} process[357] and are shorter within the THF compared to the MeCN measurements.

Table 10 Reorganisation energies (λ_o) calculated by the *Born* equation (3) for the CS (^{3}Ir⟶CS_1, ^{3}Ir⟶CS_2, CS_1⟶CS_2) and CR (CS_2⟶S_0, CS_1⟶S_0) processes of triads **T1**, **T5** and **T6** and corresponding λ_v and $\Delta G^{\#}$ values.

		^{3}Ir⟶CS_1, (CS_1⟶S_0)			CS_2⟶S_0, (^{3}Ir⟶CS_2)			CS_1⟶CS_2		
	solvent	λ_o	λ_v	$\Delta G^{\#}$	λ_o	λ_v	$\Delta G^{\#}$	λ_o	λ_v	$\Delta G^{\#}$
		/ eV			/ eV			/ eV		
T1	MeCN	0.91	0.32	0.12 (0.01)	1.36	0.26	0.03 (0.12)	0.88	0.19	0.14
	THF	0.64	0.32	0.14 (0.12)	0.97	0.26	0.01 (0.13)	0.63	0.19	0.12
T5	THF	0.64	0.32	0.14 (0.12)	0.97	0.26	0.01 (0.13)	0.63	0.19	0.12
T6	THF	0.64	0.32	0.14 (0.12)	0.97	0.26	0.01 (0.12)	0.63	0.19	0.12

The static dielectric constants for the specific solvents are as follows: ε_s(MeCN) = 35.49 and ε_s(THF) = 7.58 and the refractive indices are: n_D(MeCN) = 1.3441 and n_D(THF) = 1.4072. The distances (d_{AD}) and radii (r_D, r_A) of the molecular structures were extracted from DFT calculations (see 5.1.10). Although the electrochemical analysis of **T6** were solely performed in CH_2Cl_2, the same values for the state energies as for **T1** (CVs in MeCN) are assumed for **T6** in THF.

Excitation at 26 500 cm^{-1} (378 nm) causes a stepwise electron transfer process and shows a significantly different behaviour for **T6** where a second iridium complex quencher is attached to the NDI. Now, a closer look on the excitation of the Ir(dipy) unit (at 20 800 cm^{-1} (480 nm)) will be done, reflecting the same pathway which runs in parallel to a minor extent in the former ET at 26 500 cm^{-1} (378 nm) excitation. The corresponding EADS of complexes **T5**, **T1** and **T6** are shown in Figure 69b, d and f, respectively (see Figure 72 for evolution of the transient spectra and decay profiles). Global fits of all complexes yield two EADS where the first can be described by a GSB at 20 800 cm^{-1} (480 nm) and the second is characteristic for the CS_2 state. According to the global fit the quantum yield is in all triads the same (100 %). A comparison with actinometric measurements is not available at the moment and will be subject to future work. Likewise, the same situation is present in **T1** in MeCN (Figure 54). The MeCN experiments support the explanation that the first and second ET step towards the fully charge-separated state possesses inverted time constants resulting in a vanishing intermediate concentration of the CS_1 state. The same is assumed for the THF measurements because almost identical spectra for ^{3}Ir and CS_2 and additionally similar lifetimes, e.g. 500–770 ps for the GSB could be obtained. Consequently, the CS_1 state is not

part of the global analysis in the THF experiments, as well. Similar lifetimes for the ^{3}Ir state (530–786 ps) were already present at an excitation energy of 26 500 cm^{-1} (378 nm).

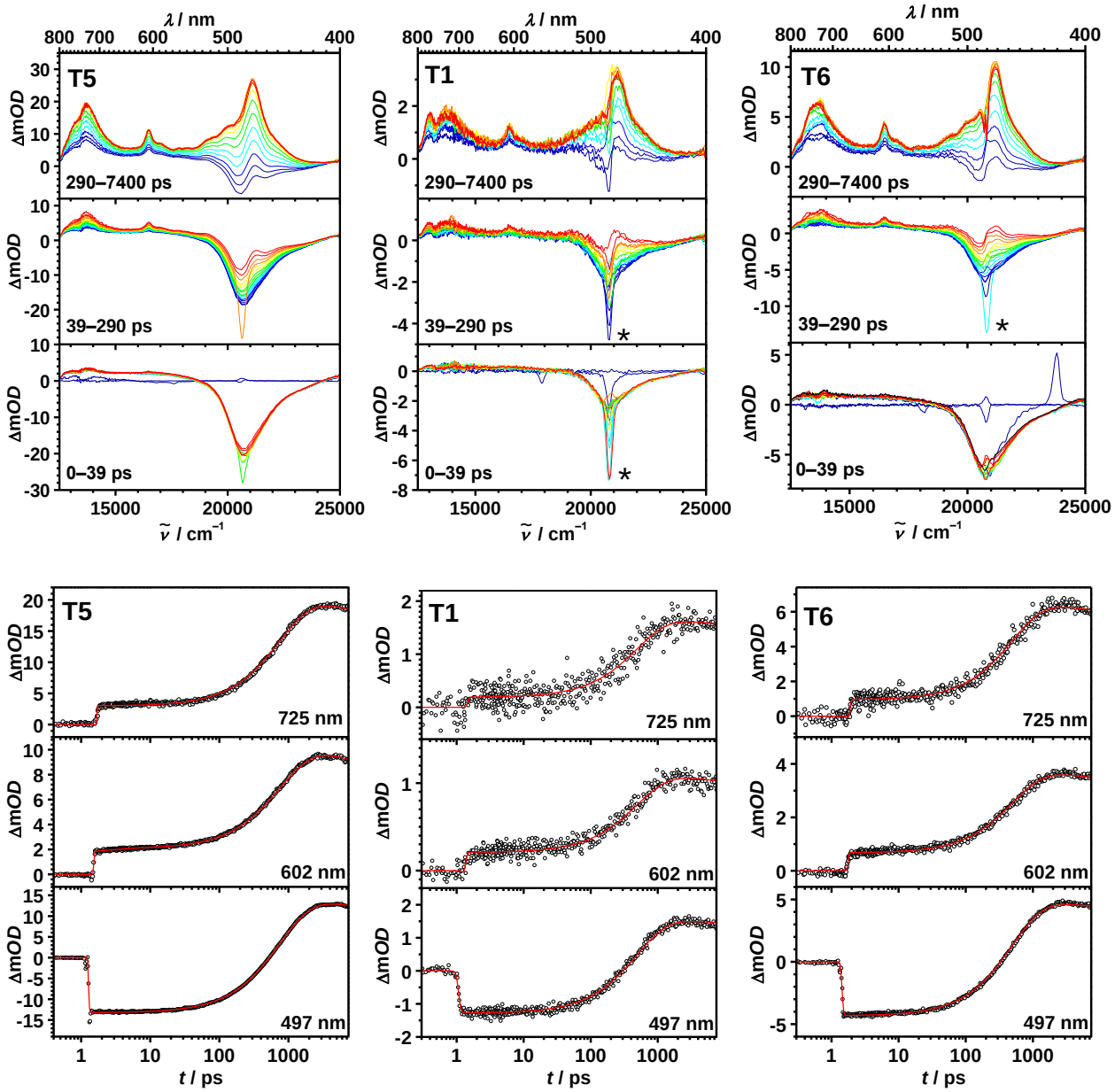

Figure 72 Top: fs-Transient absorption data of **T5**, **T1** and **T6** (from left to right) corrected for chirp and scattered pump light. Early spectra are in blue to green and at later times in orange to red colours. Bottom: Decay profiles at selected wavelengths for which the zero time delay was set arbitrarily. Excitation at 20 800 cm^{-1} (480 nm) in THF. * remaining stray light.

Moreover, the transient spectra within different time windows and the selected decay profiles look all the same pumping the three triads at an energy of 20 800 cm^{-1} (480 nm)

which is different to the former experiment at 26 500 cm^{-1} (378 nm). However, the GSB of triad **T5** with just one TAA unit was fitted with a longer lifetime (786 and 770 ps at 26 500 cm^{-1} (378 nm) and 20 800 cm^{-1} (480 nm), respectively) at both laser energies compared to the other triads **T1** and **T6** (530, 496 ps and 584, 500 ps, respectively). The occurrence of shorter lifetimes for the latter two complexes only may be feasible if the number of amines in the quenching process of the CS_1 state is taken into account. At the moment, this explanation needs more experimental evidence, e.g. the fs-transient absorption measurements of **T5** in MeCN are missing and could verify the present findings.

Conclusion

In principle, the requirements necessary for SB-CS are present in **T5**, **T1** and **T6** and are schematically sketched in Figure 68. For that reason, fs-pump-probe spectroscopy of all triads was performed to clarify if a SB effect occurs upon photoexcitation. Unfortunately, the measurements revealed contradictory and less-founded results. First, excitation of the NDI chromophore at 26 500 cm^{-1} (378 nm) shows clearly a stepwise formation of the CS_2 state in all triads. But the analysis of the energy and electron transfer steps, following the same sequence within all triads, is based on different efficiencies of the target model for **T5** and **T1** compared to **T6**. Especially the direct relaxation from the CT_{hot} state to the ground state with ca. 30 % in **T5** and **T1** (Figure 70) is very speculative. However, to obtain reasonable SADS these efficiencies were incorporated into the model. On the contrary, the lifetimes for the vibrational relaxation in all triads (ca. 3 ps from CT_{hot} to CT_{cool}) are slower in the less polar solvent THF compared to MeCN (ca. >220 fs from CT_{hot} to CT_{cool}) which supports the state order of the used target model. From an energetic view point both the CS_1 and CS_2 states are raised in energy (1.65 and 1.47 eV, respectively) in the more nonpolar solvent THF compared to MeCN. As a consequence, the lifetime of the fully CS state is reduced in THF (160 ns) than in MeCN (580 ns). Within the latter solvent the CS_2 state energy is with 1.17 eV lower in energy due to a *Marcus* normal behaviour. Similar lifetimes of the CS state are obtained for the excitation of the Ir(dipy) unit at 20 800 cm^{-1} (480 nm). Besides, GSB followed by an invisible CS_1 state due to a very fast follow-up reaction into the CS_2 state is accompanied with lifetimes of the ^{3}Ir state of ca. 500 ps for **T1** and **T6**. Conversely, **T5** exhibits somewhat longer lifetimes (ca. 800 ps) which are in a similar order of the MeCN measurements. The difference

between these lifetimes may be related to the different number of amines equivalent to an enhanced quenching process in **T1** and **T6**, but this calls for further investigations. Unfortunately, the SB concept applied to **T5**, **T1** and **T6** is still contradictable and future work is necessary to determine e.g. the quantum yield of the CS_2 state by actinometric experiments to verify or reject the efficiencies of the used target model. Furthermore, triad **T5** in MeCN could be pumped with both excitation energies to check if there is a prolonged lifetime of the ^{3}Ir state compared to **T1**.

3.1.5 Spin-Chemistry of Charge-Separated States

Introduction

In this section the focus lies on magnetic-field effects (MFE) of charge-separated states in **T1**, **T4** and **T5** and in particular on the transition from coherent to incoherent spin-flip which has hitherto never been observed. Moreover, it was possible to evaluate the spin nature of the lowest excited states of the triads. In chapter 3.1.2 the different excitation pathways (26 500 cm^{-1} (378 nm) and 20 800 cm^{-1} (480 nm)) result in a singlet and a triplet precursors (^{3}Ir vs. $^1CT_{cool}$) which populate the CS_2 state of the investigated triads. For that reason, both spin configurations of the CS_2 state were assumed. Furthermore, similar lifetimes of the CS_2 state indicate a fast spin interconversion between both singlet and triplet states.

The work in this chapter is an outcome of the cooperation with Prof. Dr. U. E. Steiner (University of Konstanz) who is an expert in the field of spin-chemistry.[223-224] He supported the presented work with a comprehensive fitting procedure using MATHEMATICA and assisted with the estimation of error widths for the fitted parameters.

The complete zero-field characterisation (steady-state absorption, cyclic voltammetry and ns-transient absorption spectroscopy) of the three triads was already presented in chapter 3.1.1 and will be summarised in the following. Thereafter, the non-zero magnetic field dependent ns-transient absorption kinetics of the CS states will be analysed with the help of a kinetic model derived by *Hayashi* and *Nagakura* (cf. 1.3.2). This model is the basis of the a global fit with the experimental decay curves. At the end of this chapter the MFEs will be interpreted and future plans will be sketched.

The basic features of triads **T1**, **T4** and **T5** are displayed in Figure 73. These are steady-state absorption spectra (Figure 73a) of all investigated triads and a transient spectrum of the CS_2 state (Figure 73b) reflecting the situation of all triads and decay profiles for **T1** (c) and **T4** (d). The cyclometalated iridium complex with a dipyrrin ligand absorbs between 17 000 cm^{-1} (588 nm) and 25 000 cm^{-1} (400 nm) and acts as photosensitiser in the photoinduced ET pathway. The attached redox units, the TAA donors and the NDI acceptor, absorb at higher energies with a characteristic vibrational fine structure for the NDI transition (25 000–30 000 cm^{-1} (333–400 nm)) and a broad band related to the TAA units (29 000–37 000 cm^{-1} (345–

270)). The absorption of complexes **T1** and **T4** differ only at higher energies (34 000–40 000 cm^{-1} (294–250 nm) due to the use of a biphenyl bridging unit in **T4** compared to a phenylene spacer in **T1**. Due to the absence of one TAA unit in complex **T5** the extinction coefficient is reduced in the spectral region of the triarylamine transitions in that complex.

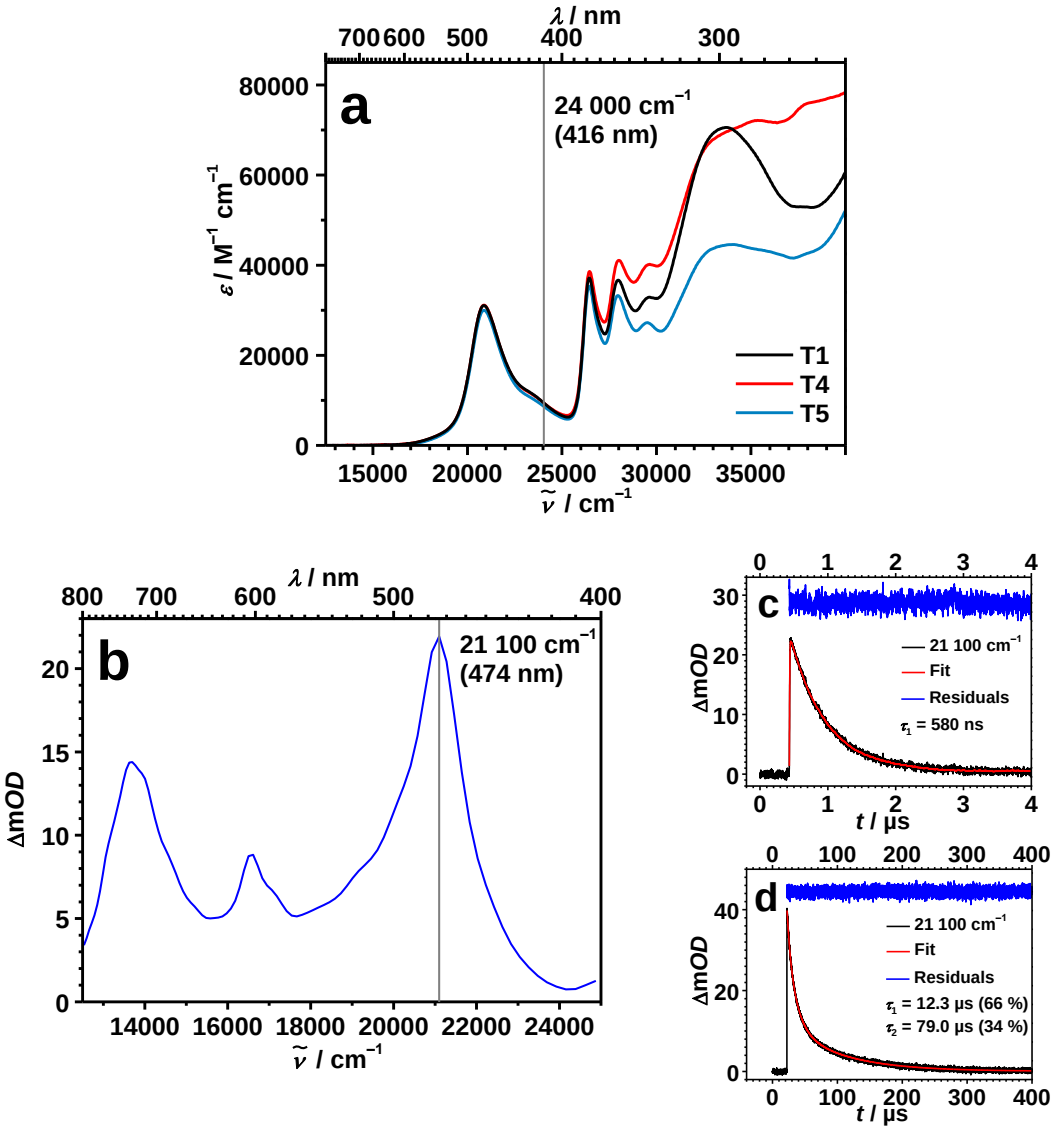

Figure 73 a) Steady-state absorption spectra of **T1**, **T4** and **T5** in MeCN. b) Representative transient absorption spectrum of all triads upon excitation at 24 000 cm^{-1} (416 nm) in MeCN corresponding to the CS_2 state. c) Decay profile at 21 100 cm^{-1} (474 nm) exemplary for **T1** and **T5**. d) Decay profile at 21 100 cm^{-1} (474 nm) for **T4**.

The ns-TA experiments show that photoinduced electron transfer generates long-lived, charge-separated states with almost quantitative quantum yields in these triads. While

triad **T1** and **T5** with a single phenylene bridge between the dipyrrin ligand and the NDI acceptor possess CS lifetimes of ca. 0.6 μs, triad **T4**, with a biphenyl instead of the phenylene bridge, shows a biphasic, extremely long-lived CS state lifetime of 12.3 (66 %) and 79 μs (34 %). The electrochemical properties do not change because of the low electronic coupling between the different chromophores. However, the multiplicity of the lowest excited state (ES) cannot be deduced from the aforementioned excited state behaviour and from the energy dependent ultrafast pump-probe experiments (cf. 3.1.2). The CS_2 state equivalent to a radical pair (RP) with a NDI radical anion and one TAA radical cation can in principle adopt either singlet or triplet spin configurations. Due to a vanishing exchange energy between singlet and triplets, their spectral shape and their energy of the CS_2 state should be identical. However, the spin relaxation of excited state biradicals are often influenced by rotational diffusion of the whole molecule or parts of it (see chapter 1.3.2). Since **T5** is somewhat smaller than **T1**, this difference will help to differentiate effects of rotational diffusion on the spin chemistry of these triads. These aspects shall be investigated by the following experiments.

Magnetic-Field Effects

In order to gain insight into the spin-chemistry of the radical pairs of the CS states of triad **T1**, **T4** and **T5** magnetic-field dependent transient absorption measurements in the ns-time regime were performed. For these measurements, the optical set-up was changed such that the 24 000 cm^{-1} (416 nm) pump beam and the white light probe beam overlap perpendicularly in the cavity of an electromagnet (0–1.8 T) (details of the set-up can be found in the experimental section). The photoinduced dynamic behaviour at magnetic zero-field of complex **T5** in MeCN is essential the same as that of triad **T1** (cf. Figure 39 and 40) because the electronic coupling and the distance between the redox centres are identical within both complexes.

Figure 74 shows transient absorption kinetic traces of (a) **T1** and (b) **T5** in MeCN at varying magnetic fields. The change of the CS state kinetics from 0–1.8 mT shows a strong MFE which can be divided into two parts for both complexes. The first part covers the low-magnetic field range from 0–50 mT, where the MFE is most pronounced. In the second part from 50–1800 mT the MFE saturates. The low field case also can be divided into two regimes.

At very low fields (0–10 mT) the kinetic traces can be fitted with a single exponential function. From there on to higher magnetic field two exponential functions are needed to fit the decay curve whereby the additional, shorter time constant has a constant value of about 300 ns. The longer decay component – corresponding to the monoexponential decay at very low field – has a lifetime of 2.2 µs for triad **T1** and *ca.* 3.9 µs for triad **T5** at very high fields. This is a 3.8-fold (triad **T1**) and 6.6-fold (triad **T5**) increase compared to the zero-field lifetime of *ca.* 0.6 µs for both complexes. The ratio of the amplitudes of the high-field curves is roughly 1:1.8 and 1:2.4 for compound **T1** and **T5**, respectively, with smaller contribution for the shorter lifetime. It has to be stressed, that a carfule deoxygenation of the samples is crucial, since the MFE is not observed or strongly reduced, if there are traces of O_2 in the solution.[199, 214, 266]

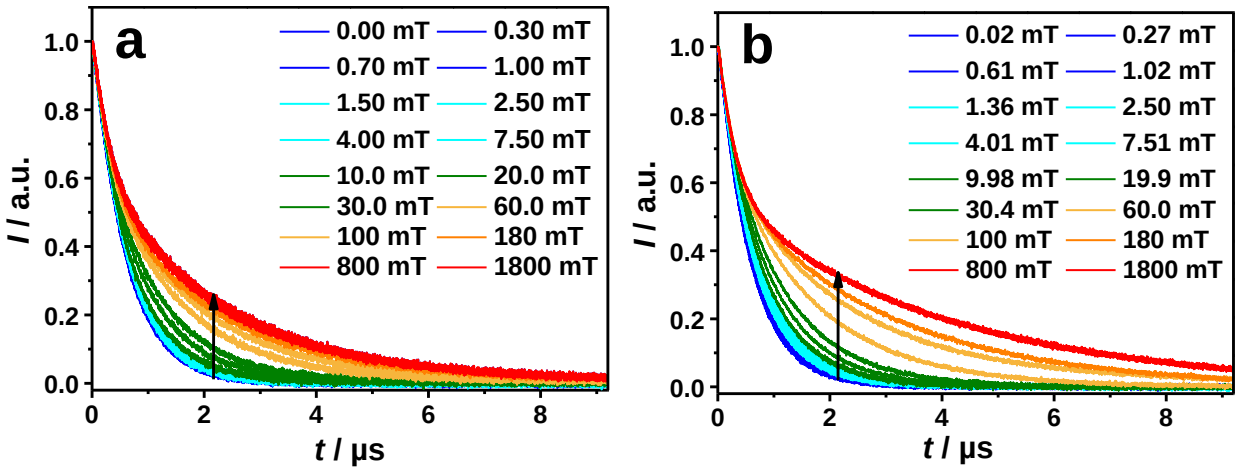

Figure 74 Selected transient absorption decay curves at 21 100 cm^{-1} (474 nm) at specified magnetic fields for complex **T1** (a) and **T5** (b) in MeCN. The experimental data have been normalised after correction for the finite width of the laser pulse and an offset at very long decay times (for details cf. experimental part).

For compound **T4**, for which the zero-field lifetime of CS_2 state is on the order of 79 µs, a magnetic-field effect is hardly detectable (Figure 75).

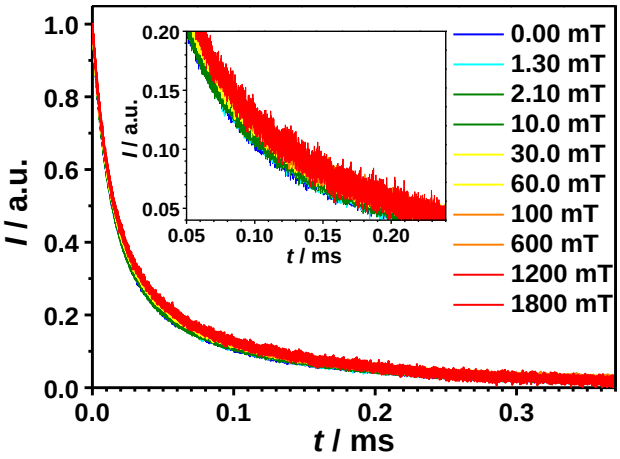

Figure 75 Experimental transient absorption decay curves for triad **T4** in MeCN at various magnetic fields observed at 21 100 cm^{-1} (474 nm). The experimental data are corrected for an offset at very long decay times. Inset: Magnification of the decay curves between t = 0.05–0.24 ms.

As already discussed in chapter 1.3 a theoretical description of RPs is given by the reaction scheme derived by *Hayashi* and *Nakagura* (Figure 76) where the radicals are separated over relatively large distances (ca. 20 Å).[252] This scheme addresses the reaction dynamics of a RP with a relatively fast S/T_0 equilibration (10^7–10^8 s^{-1})[22, 221, 252, 255-256, 259] driven by isotropic hyperfine interactions. Furthermore, the transition between the central *Zeeman* and outer *Zeeman* levels (S, T_0 and T_+, T_-, respectively) are assumingly governed by spin relaxation of the individual radicals, e.g. incoherent processes. In the present case the kinetic scheme is expanded to cover coherent processes which participate in the interconversion of the four spin configurations. In addition, the following simplifications are made: i) $k_\pm = k_\pm'$, if spin dipolar interactions are neglected due to the large spin-spin separation in the present RPs. ii) The rate constants k_{ST_0}, k_S, k_T and the initial spin configuration p_S are considered to be field independent (global parameters). iii) Due to the spin conservation rule, the k_T parameter is set to zero (k_T = 0) due to the spin conservation rule. Hence, $k_\pm$ is the only field dependent parameter and the investigation of this rate constant will be the decisive factor of a MFE analysis.

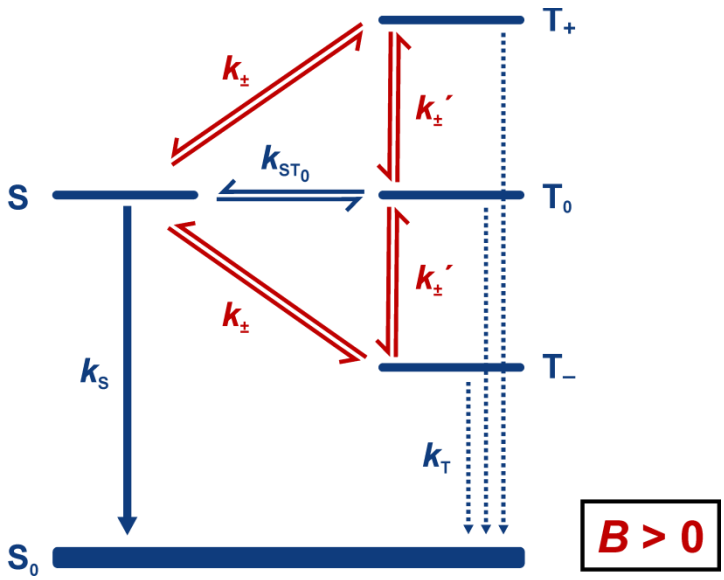

Figure 76 Reaction and spin conversion processes of a radical pair. The situation refers to a finite *Zeeman* splitting of the triplet levels and negligible exchange interaction. The rate processes connecting the spin sublevels may be either of coherent or incoherent nature, depending on the magnitude of the *Zeeman* splitting in relation to the isotropic hyperfine couplings.

The time dependent population and depopulation of the involved states (S, T_+, T_0, T_-) can be described by differential rate equations eq. (32) with four rate constants k_{ST_0}, k_S, k_T and $k_\pm$. The experimental data represent the superposition of concentrations of all spin substates of the CS_2 state. For a numerical solution of eq. (32) assumptions for the initial concentrations of each state are necessary ($[S]_0$, $[T_+]_0$, $[T_0]_0$, $[T_-]_0$). In a next step, 16 selected experimental decay curves monitored at different magnetic fields (MatLab script attached to the Appendix).

$$
\begin{aligned}
d[S]/dt &= -\left(k_S + 2k_\pm + k_{ST_0}\right)[S] + k_{ST_0}[T_0] + k_\pm([T_+] + [T_-]) \\
d[T_0]/dt &= k_{ST_0}[S] - \left(k_T + 2k_\pm + k_{ST_0}\right)[T_0] + k_\pm([T_+] + [T_-]) \\
d[T_+]/dt &= k_\pm[S] + k_\pm[T_0] - \left(k_T + 2k_\pm\right)[T_+] \\
d[T_-]/dt &= k_\pm[S] + k_\pm[T_0] - \left(k_T + 2k_\pm\right)[T_-]
\end{aligned}
\qquad (32)
$$

The fitting strategy was further simplified by assuming k_{ST0} to be field-independent. A semiclassical model by *Schulten* and co-workers[259, 271] was used to predict the coherent hyperfine-driven motion k_{ST0} of the electron spins in a RP. In this model, the hyperfine coupling constants a_{ik} for the individual radicals sum up to a classical vector by $I_i = \sum_k a_{ik} I_{ik}$ and are given as follows: for NDI[358] $2 \times \alpha_N$ = 0.095 mT, $4 \times \alpha_H$ = 0.190 mT; for TAA[359] $4 \times \alpha_H$ = 0.055 mT, $4 \times \alpha_H$ = 0.203 mT, $6 \times \alpha_H$ = 0.084 mT, $2 \times \alpha_H$ = 0.160 mT, $2 \times \alpha_H$ = 0.094 mT, $1 \times \alpha_N$ = 0.921 mT, $1 \times \alpha_H$ = 0.210 mT. With these hyperfine coupling constants and eq. (19) a specific value for the hyperfine coupling (hfc) time can be obtained for each radical. This is further used to plot the evolution of the spin character of the RP based on the semiclassical model by *Schulten* and *Wolynes*.[259] In Figure 77 the zero and high field case (blue and red, respectively) are displayed as solid curves according to eq. (10) and (13) whereas the classical kinetic evolution is given with dashed lines for k_{ST_0} = $5 \cdot 10^7$, $4 \cdot 10^7$ and $3 \cdot 10^7$ s^{-1}. The latter values are obtained by eq. (6) and (7) and their limiting values of $5 \cdot 10^7$ and $3 \cdot 10^7$ s^{-1} match quite well either the zero field (higher dashed red curve with k_{ST_0} = $5 \cdot 10^7$ s^{-1}) or the high field case (lower dashed blue curve with k_{ST_0} = $3 \cdot 10^7$ s^{-1}).

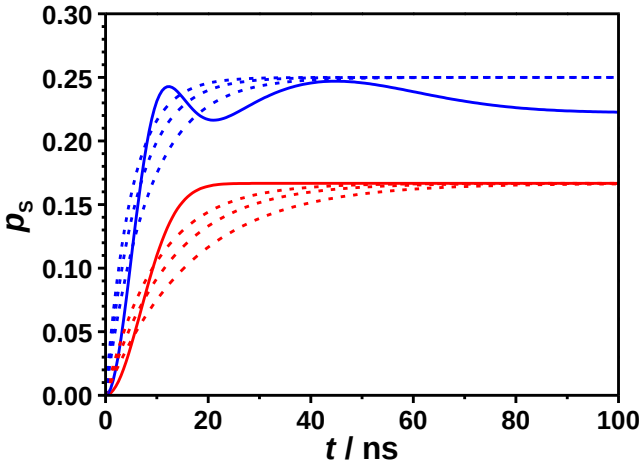

Figure 77 Evolution of singlet probability p_S in a CS_2 state starting from a pure triplet spin configuration. Solid lines (blue: zero field, red: high field) calculated according to the semiclassical model by *Schulten* and *Wolynes*.[259] Dashed lines from top to bottom represent classical kinetic behaviour according to equations (6) and (7), with k_{ST_0} = $5 \cdot 10^7$ s^{-1}, $4 \cdot 10^7$ s^{-1} and $3 \cdot 10^7$ s^{-1}. For details see text.

The values for k_{ST_0} = 5·10^7 and 3·10^7 s^{-1} were used for the global fit as trial values to determine a preliminary k_S parameter which was globally fitted. The rate constant k_s was forced to have the same value for all 16 curves to retain its field independent character. Furthermore, several initial populations were tested to find the best fit (Table 11 and 12 for **T1** and **T5**, respectively). Additionally, the field-independent parameter $k_\pm$ was freely optimised and its resulting values are not further interpreted at this step of the fitting procedure. It turned out that for both trial values of k_{ST_0} (5·10^7 and 3·10^7 s^{-1}) the total minimum was centred around an initial singlet population of $p_{S,0}$ = 0.25, i.e. full equilibrium between the spin substates of the RP. The rout mean square deviation (rms-dev.) serves as criterion for the fit result (Table 11 and 12). Consequently, $p_{S,0}$ = 0.25 is set as constant factor in all following fits. The preliminary k_s values from the aforementioned fits are very similar for both complexes which proves its field independence.

In a next step, k_{ST_0} = 4·10^7 s^{-1} was set as global parameter in the MatLab fit because the somewhat higher and lower values of k_{ST_0} = 3·10^7 and 5·10^7 s^{-1} showed very similar results for k_s (Table 11 and 12) and $k_\pm$ (not shown). Furthermore, the k_s parameter was fitted globally with the restriction of being constant for all field cases. Hence, only $k_\pm$ values were freely optimised during the fitting procedure. Thus, the optimised values are: k_S = 6.7·10^6 s^{-1} for triad **T1** and 6.97·10^6 s^{-1} for triad **T5**, if $p_{S,0}$ = 0.25 and k_{ST_0} = 4·10^7 s^{-1}.

Table 11 The rout mean square deviation (rms-dev.) over all data points in the fits of decay curves of CS_2 for triad **T1** at 16 characteristic magnetic fields[(a)] for various sets of global kinetic parameters $p_{S,0}$, k_{ST_0}, k_S and $k_{\pm}$. In each case $k_T = 0$.

$p_{S,0}$	k_{ST_0} / s^{-1}	k_S / s^{-1}	rms-dev.
0.00	$3.0 \cdot 10^7$	$1.22 \cdot 10^7$	0.0094
0.20	$3.0 \cdot 10^7$	$7.59 \cdot 10^6$	0.0070
0.25	$3.0 \cdot 10^7$	$6.83 \cdot 10^6$	0.0066
0.30	$3.0 \cdot 10^7$	$6.50 \cdot 10^6$	0.0067
0.50	$3.0 \cdot 10^7$	$5.90 \cdot 10^6$	0.0154
0.00	$5.0 \cdot 10^7$	$1.13 \cdot 10^7$	0.0096
0.20	$5.0 \cdot 10^7$	$7.27 \cdot 10^6$	0.0069
0.25	$5.0 \cdot 10^7$	$6.66 \cdot 10^6$	0.0062
0.30	$5.0 \cdot 10^7$	$6.70 \cdot 10^6$	0.0074
0.50	$5.0 \cdot 10^7$	$6.70 \cdot 10^6$	0.0208

[(a)]magnetic field values (mT): 0, 0.3, 0.7, 1.0, 1.5, 2.5, 4.0, 7.5, 10, 20, 30, 60, 100, 180, 800, 1800.

Table 12 The rout mean square deviation (rms-dev.) over all data points in the fits of decay curves of CS_2 for triad **T5** at 16 characteristic magnetic fields[(a)] for various sets of global kinetic parameters $p_{S,0}$, k_{ST_0}, k_S and $k_{\pm}$. In each case $k_T = 0$.

$p_{S,0}$	k_{ST_0} / s^{-1}	k_S / s^{-1}	rms-dev.
0.00	$3.0 \cdot 10^7$	$1.22 \cdot 10^7$	0.0124
0.20	$3.0 \cdot 10^7$	$7.12 \cdot 10^6$	0.0058
0.25	$3.0 \cdot 10^7$	$6.69 \cdot 10^6$	0.0052
0.30	$3.0 \cdot 10^7$	$6.45 \cdot 10^6$	0.0067
0.50	$3.0 \cdot 10^7$	$5.65 \cdot 10^6$	0.0236
0.00	$5.0 \cdot 10^7$	$1.18 \cdot 10^7$	0.0133
0.20	$5.0 \cdot 10^7$	$7.16 \cdot 10^6$	0.0063
0.25	$5.0 \cdot 10^7$	$6.62 \cdot 10^6$	0.0054
0.30	$5.0 \cdot 10^7$	$6.41 \cdot 10^6$	0.0081
0.50	$5.0 \cdot 10^7$	$6.00 \cdot 10^6$	0.0248

[(a)]magnetic field values (mT): 0, 0.3, 0.7, 1.0, 1.5, 2.5, 4.0, 7.5, 10, 20, 30, 60, 100, 180, 800, 1800.

The fitting procedure with 16 selected kinetic decay curves yielded global parameters ($p_{S,0}$, k_S and k_{ST_0}) which are identical for all experimental traces. For that reason, all experimental decay curves were separately fitted to obtain the $k_\pm$ values for each field case. The resulting field dependence of $k_\pm$ for **T1** and **T5** is plotted in Figure 78 (a table of all values can be found in the Appendix) with error bounds for each $k_\pm$ value calculated with the MATHEMATICA program.

The behaviour of $k_\pm$ can qualitatively be understood as follows. On one side, at zero-field (B = 0) the rate limiting process is the deactivation from the S state to the ground state under spin conservation ($k_S \approx 7\cdot10^6$ s^{-1} vs. $k_\pm \approx 5\cdot10^7$ s^{-1}) while $k_{ST_0} = 4\cdot10^7$ s^{-1}. In contrast, the triplet sublevels split at non-zero field into three non-degenerated states due to the *Zeeman* splitting and $k_\pm$ becomes smaller than $k_{ST_0} = 4\cdot10^7$ s^{-1} with increasing magnetic field. At fields B ≥ 10 mT $k_\pm$ is even smaller than k_S and, thus, becomes the rate determining constant ($k_S \approx 7\cdot10^6$ s^{-1} vs. $k_\pm \approx 2\cdot10^5$ s^{-1}). Hence, the field dependent parameter $k_\pm$ is well established over 2–3 orders of magnitude and the error margins are higher at low fields where $k_\pm$ is not rate determining and becomes well defined at higher magnetic field where $k_\pm$ is the limiting rate constant.

A quantitative analysis of Figure 78 was performed with a mathematical model which was fitted to the data. In contrast to the simple model presented in the introduction section (eq. (27)), a reasonable fit of the data points with a single *Lorentzian* is impossible. Thus, a sum of two *Lorentzians* and a constant factor $k_{rel,\infty}$ for infinitely high magnetic fields was used (eq. (33)).

$$k_\pm(B) = \frac{k_{hfc,0}}{1+\left(B_0 / B_{1/2,hfc}\right)^2} + \frac{k_{rel,0}}{1+\left(B_0 / B_{1/2,rel}\right)^2} + k_{rel,\infty} \qquad (33)$$

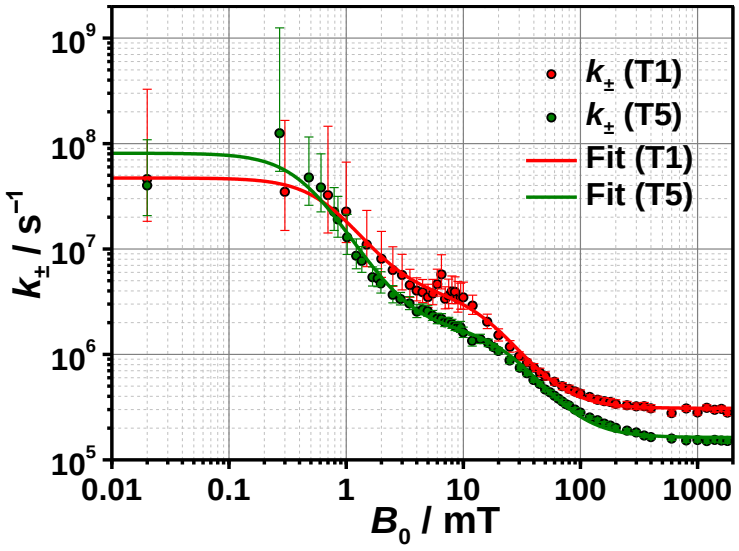

Figure 78 Magnetic-field dependence of $k_\pm$ with error bars obtained by fitting the CS_2 decay curves. triad **T1** (red) and triad **T5** (green). The solid lines represent best fits of the double *Lorentzian* function of eq. (33) to the data. The parameters are given in Table 13.

Table 13 Magnetic field effect parameters obtained by fitting $k_\pm(B)$ curves in Figure 78 according to eq. (33).

	$k_{hfc,0}$/ 10^7 s^{-1}	$B_{1/2,hfc}$ / mT	$k_{rel,0}$ / 10^6 s^{-1}	$B_{1/2,rel}$ / mT	$k_{rel,\infty}$ / 10^5 s^{-1}
T1	4.3±0.4	0.69±0.07	3.6±0.25	15±1	3.1±0.1
T5	7.9±1.1	0.44±0.04	1.6±0.1	25±2	1.64±0.08

In the following, the various parameters of the double *Lorentzian* fit will be correlated to inherent properties of either triad **T1** or **T5**. Although both triads show similar transient absorption spectra, their fitted MFE parameters (Table 13) differ significantly. However, the initial (t = 0) ratio of singlet to triplet state concentration $p_{S,0}$ = $[S]_0$ / ($[T_+]_0$ + $[T_0]_0$ + $[T_-]_0$ + $[S]_0$) yielded a minimum at 0.25 (Table 11 and 12) for both complexes. It may be assumed that the strong spin-orbit coupling of the iridium atom (ξ_{Ir} = 3909 cm^{-1})[157] leads to a mixing, or better, a smearing out of singlet and triplet character[199, 360-361] for species where the iridium complex is directly involved as a formally oxidised iridium (d Ir^{+IV} = d^5 or CS_1). Charge separation from these states will then lead to a statistical mixture of pure spin states $^3CS_2$ and $^1CS_2$ because the purely organic radical-pair character does not allow a mixed spin

multiplicity. The same is known for Ru and Fe complexes with d^5 configuration which have very short spin relaxation times (10^{10}–10^{11} s^{-1}) supporting the observed initial spin population of $p_{S,0} = 0.25$.[362-363]

Coherent Spin-Flip Regime

The first term of equation (33), is an empirical description of the field dependence of the coherent spin-flip with the two parameters $k_{hfc,0}$ and B_{hfc}. The former is $k_{hfc,0}$ = (4.3±0.4)·10^7 s^{-1} for **T1** and (7.9±1.1)·10^7 s^{-1} for **T5** (see Table 13). The estimation of $k_{hfc,0}$ via eq. (19) yields 5.85·10^7 s^{-1} which is in good agreement to the fitted values, given the high error bars of the experimental values. However, the deviation of the experimental $B_{1/2,hfc}$ (0.69±0.07 and 0.44±0.04 mT for triad **T1** and **T5**, respectively, cf. Table 13) from the theoretical $B_{1/2}$ values estimated by eq. (5) (2.50 mT) is quite substantial.

$$B_{1/2} = \sqrt{3(B_1^2 + B_2^2)} \tag{5}$$

with the individual B_i given by the following sum over the nuclei *k* in either radical,

$$B_i = \sqrt{\sum_{ik} a_{ik}^2 I_{ik}(I_{ik}+1)} \tag{4}$$

a_{ik} representing the isotropic hyperfine coupling constant of nucleus *k* in radical *i*.

The difference between the theoretically and experimentally determined $B_{1/2,hfc}$ may be explained by the assumptions used for the derivation of the theoretically value which will be described in the following. The first magnetic field dependent experiments in the early 1970s[223-224] were performed on freely diffusing RPs where spin-evolution and re-encounter probabilities are present at the same time. Whereas the lifetime of such RPs is located on the timescale of a few ns, the linked radical pairs in the present case (**T1** and **T5**) possess lifetimes of more than 500 ns. Thus, lower magnetic fields are sufficient to achieve the same MFE with linked RPs compared to free radical pairs.

Moreover, the observed $B_{1/2,hfc}$ are not only smaller than the theoretically determined ones, but are different for both triads (0.69 and 0.44 mT for **T1** and **T5**, respectively). The smaller value for **T1** may be assigned to the presence of a second TAA unit in the complex

architecture which allows for an electron hopping in the CS_2 state between both energetically equal TAAs. As a consequence, spin motion of the RP is affected by such an additional perturbation so that $k_{hfc,0}$ is reduced in **T1** compared to **T5** ($4.3 \cdot 10^7$ vs. $7.9 \cdot 10^7$ s^{-1}). Consequently, the aforementioned values for $B_{1/2,hfc}$ differ, too. An estimation of the degenerate hole transfer rate is given by eq. (34).[271, 364-365]

$$k_{exch} \approx \gamma_e \Delta B_{1/2} \tag{34}$$

Here, the gyromagnetic ratio of the electron γ_e = $1.76 \cdot 10^{11}$ rad·s^{-1} T^{-1} together with the difference of the $B_{1/2,hfc}$ values ($\Delta B_{1/2}$ = 0.25 mT) yields an exchange rate of $k_{exch} \approx 4.4 \cdot 10^7$ s^{-1}. This is in good agreement with results from EPR measurements on intramolecular hole exchange in organic mixed-valence compounds based on symmetric *bis*(triarylamine)paracyclophane redox systems with similar electron hopping distances as in **T1**.[366] In contrast, in a further donor-iridium dipyrrin-acceptor triad (**pMV1**, chapter 3.2), where the triarylamine donors are fused with the phenylpyrazole framework of the iridium complex, the coupling between the oxidised and the neutral TAA via the iridium d-orbital is so strong that this interaction is manifested by an intervalence charge-transfer band in the NIR spectral region (*vide infra*).

In conclusion, the coherent spin-flip regime is well fitted with the first *Lorentzian* branch and illuminates structure-property relations on the interconversion between the S and T states (T⇌S) with a reduced $k_{hfc,0}$ rate due to electron hopping between the TAAs in **T1**. Above all, the coherent spin-flip region is observed for the first time taking into account that classical kinetics were used to evaluate the experimental data. However, MFEs of another donor-acceptor triad with $Ru(bpy)_3^{2+}$ as photosensitiser indicated a similar behaviour of the coherent transition but the interpretation lacked on reduced data points at low magnetic fields where this effect is dominant.[199] Consequently, the interpretation of that work was not able to substantiate the present findings.

Incoherent Spin-Flip Regime: 10 mT < B < 1 T

The second term of eq. (33) describes the incoherent spin-relaxation of the individual radicals which is dominated by the anisotropic hyperfine coupling of the nitrogen nucleus in the TAA radical cation. Phenomenologically, this is described with the two parameters $k_{rel,0}$

and $B_{1/2,\mathrm{rel}}$ (see Table 13). From the latter the correlation time τ_c is estimated via eq. (14) (Table 14).

$$\tau_c = \frac{1}{\gamma_e B_{\mathrm{rel}}} \tag{14}$$

Table 14 Correlation times determined by eq. (14) and (28).

	$B_{1/2,\mathrm{rel}}$ / mT	τ_c / ns	r_{hydro} / 10^{-10} m	$\tau_{c,Debye}$ / ns
T1	15±1	0.38	10.6	0.42
T5	25±2	0.23	9.54	0.30

An independent estimate of τ_c via eq. (28) correlating the hydrodynamic radius[1] (**T1** r = $1.06\cdot10^{-9}$ m and **T5** r = $9.54\cdot10^{-10}$ m) and the solvent viscosity of acetonitrile (η = 0.343 m Pa·s) gives $\tau_{c,Debye}$ (**T1**) = 0.42 ns and $\tau_{c,\,Debye}$ (**T5**) = 0.30 ns.

$$\tau_{c,\,\mathrm{Debye}} = \frac{4\pi r^3}{3k_B T}\eta \tag{28}$$

This is in excellent agreement with the values evaluated above and supports the fact that diffusional rotation is the origin of the modulation of the hyperfine interaction for both molecules.

The longitudinal relaxation time T_1 can be correlated to the $k_{\mathrm{rel},0}$ parameter by eq. (24), (27) and (35).

$$k_{\mathrm{rel}}(T_1) = \frac{1}{4T_1} \tag{24}$$

[1] The hydrodynamic radii in eq. (28) were based on a molecular model obtained from DFT calculations using *Gaussian09* with *PBE1PBE* functional and a 6-31G* basis set for C, H and N and pseudo potentials (SDD) for the Ir atom.[312] The hydrodynamic radius r is determined by calculating the surface of the afore calculated structure with the "Connolly Molecular Area" tool of the ChemBioDraw Ultra 12.0 software and performing a back calculation to a radius of an ideal spherical molecule. The area of triad **T1** was determined to be A(**T1**) = 1411.18 Å^2 and hence, r = $1.06\cdot10^{-9}$ m. The same was done for triad **T5** resulting in A(**T5**) = 1143.24 Å^2 and r = $9.54\cdot10^{-10}$ m.

Assumptions for eq. (27) are as follows: i) Due to a large radical-separation distance negligible g-tensor anisotropy is expected and ii) the anisotropy of the dominating hyperfine interaction is axially oriented.

$$k_{\mathrm{rel}}(T_1) = \frac{1}{T_1} = \frac{4}{27} I(I+1)\Delta A^2 \frac{\tau_c}{1+\omega_0^2\tau_c^2} \qquad (27)$$

where the hyperfine coupling anisotropy is defined as $\Delta A = A_{\parallel} - A_{\perp}$, I is the nuclear angular momentum quantum number, ω_0 is the Lamor frequency and τ_c is the rotational correlation time. Combining equations (24) and (27) and substituting I = 1 for a ^{14}N nucleus yields:

$$k_{\mathrm{rel}} = \frac{2}{27}\Delta A^2 \frac{\tau_c}{1+\omega_0^2\tau_c^2} \qquad (35)$$

A further transformation results in eq. (36).

$$\Delta A^2 = \frac{27 \cdot k_{\mathrm{rel}}}{2} \frac{1+\omega_0^2\tau_c^2}{\tau_c} \qquad (36)$$

The resulting ΔA values are ΔA = 3.6 10^8 rad·s^{-1} (2.04 mT) for **T1** and ΔA = 3.1·10^8 rad·s^{-1} (1.75 mT) for **T5** using the fitted parameters form Table 13 (k_{rel} = 3.6·10^6 s^{-1} and 1.6·10^6 s^{-1} for **T1** and **T5**, respectively) and the corresponding correlation times (τ_c = 0.38 and 0.23 ns, respectively).

Unfortunately, appropriate ΔA values, equivalent to the anisotropy value of the nitrogen atom at the TAA donor, are not accessible from literature. However, quantum chemical calculations of another nitrogen containing donor, a phenothiazine,[367] revealed an 2.7 times higher value for ΔA compared to its isotropic value of 0.92 (*vide supra*). A similar ratio between the isotropic and anisotropy values for the nitrogen nucleus was found in $N(SO_3)_2^{\bullet 2-}$ and $NH(SO_3)^{\bullet -}$.[368] Assuming the same ratio in the present case ($TAA^{\bullet +}$) would lead to a value of ΔA = 2.7 × 0.92 mT ≈ 2.5 mT which is in satisfactory agreement with the found values (2.04 mT and 1.75 mT for **T1** an **T5**, respectively). Besides, the group of Prof. Dr. *Kaupp* (TU Berlin) was able to calculate the hyperfine tensors of TAA monoradical cations with and without methoxy groups at the three *para*-positions of the TAA (*tris*-(*p*-methoxyphenyl)amine radical cation ($N(Ph_{OMe})_3^{\bullet +}$) and triphenylamine radical cation ($NPh_3^{\bullet +}$)).[369]

Table 15 Calculated[1] values for isotropic (A_{iso}) and anisotropic hyperfine tensors (T_{xx}) for two different TAA units.

	A_{iso} / MHz	T_{11} / MHz	T_{22} / MHz	T_{33} / MHz	ΔA	$\Delta A/A_{iso}$
$N(Ph_{OMe})_3^{\bullet+}$	28.98	-21.88	-21.88	43.76	65.64	2.27
$NPh_3^{\bullet+}$	25.33	-19.31	-19.29	38.60	57.88	2.28

[1] Calculations were performed at BLYP35/IGLO-II//B3LYP35/TZVP level of theory.

The ratio $\Delta A/A_{iso} \approx 2.28$ is slightly smaller than for the inorganic nitrogen radicals ($\Delta A/A_{iso}$ = 2.7) and results in $\Delta A = 2.28 \times 0.92$ mT ≈ 2.10 mT. This value fits even better to the observed ΔA values of the triads (2.04 mT for **T1** and 1.75 mT for **T5**).

Incoherent Spin-Flip Regime: B > 1 T

The major difference in the magnetic field dependence of $k_{\pm}$ between **T1** and **T5** is the limiting value at high field, $k_{rel,\infty} = 3.1 \cdot 10^5$ and $1.64 \cdot 10^5$ s^{-1} for **T1** and **T5**, respectively. In the already mentioned donor-ruthenium(II)-*tris*bipyridine-acceptor triad, investigated by *Steiner et al.*, a similar value for $k_{rel,\infty} = 5 \cdot 10^5$ s^{-1} has been found.[214, 367] A possible explanation for this observation may be a "local mode mechanism" caused by modulation of spin-orbit coupling as has been described for trityl radicals.[370-371]

MFE in T4

Finally, for complex **T4** the magnetic-field dependent measurements showed no significant effect (Figure 75) at magnetic fields up to 1.8 T. This clearly shows that the charge recombination is the rate-determining step even at high magnetic fields. This is plausible as the smallest rate constant of **T4** at very high field ($k_{rel,\infty} = 3.08 \cdot 10^5$ s^{-1}) is still one order of magnitude higher than the shortest lifetime of the CS_2 state ($1/\tau_1 = 4.8 \cdot 10^4$ s^{-1}, see Figure 43a). Thus, the lack of a MFE in **T4** support the general decay and spin-interconversion mechanisms assumed for all triad.

Conclusion and Future Outlook

In this chapter the MFE on the recombination kinetics of charge-separated states of three triads (**T1**, **T4** and **T5**) were investigated in the magnetic field range of 0–1.8 T. Whereas **T4** shows no significant MFE, the triads **T1** and **T5** exhibit a pronounced MFE with prolonged lifetimes by a factor of 3.8 and 6.6, respectively, at high magnetic fields. This is in line with a change of the rate determining process. At zero and low fields (<10 mT) k_S is the limiting factor but at higher fields (>10 mT) the field-dependent $k_\pm$ rate constant becomes rate determining. The MFEs were analysed with a modification of the *Hayashi-Nagakura* scheme describing both the incoherent spin relaxation (T_1) at higher field and coherent interconversion (S, $T_0 \leftrightarrow T_\pm$) at low field. Even more surprising is the observation of a change of mechanism for the spin interconversion. At low fields, the spin flip is a coherent process mediated by the isotropic hyperfine coupling while at high field the spin-flip is a stochastic relaxation process governed by the anisotropic hyperfine coupling. The similar correlation times derived from the *Debye* equation (eq. (28)) and from the double *Lorentzian* fit to the field dependence of $k_\pm$ are a strong support for this suggested mechanism. Triad **T4** does not show a similar MFE because k_s is always the rate-limiting factor.

Further insight into the spin-chemistry of these triads could probably be provided by time-dependent electron paramagnetic resonance (tEPR) spectroscopy. These measurements perfectly fit to the scope of the Research Training School 2112: 'Molecular Biradicals: Structure, Properties and Reactivity' and might be performed by the group of Prof. Dr. *V. Dyakonov*.

The transition from the coherent to incoherent spin-flip regime of the recombination kinetics of charge-separated states is reported for the first time in such donor-metal complex-acceptor arrays. The observed $B_{1/2,hfc}$ values of 0.69 and 0.44 mT for **T1** and **T5**, respectively, are only one order of magnitude away from the earth magnetic field value (~0.050 mT). Consequently, future projects may deal with the variation of the radical bearing units to reduce the effective magnetic moment. The contribution of the TAA radical to the total $B_{1/2,hfc}$ value is dominating, whereas the NDI radical has less influence on this parameter. This can be explained by the small hyperfine coupling constants (a_{ik}) of the involved N-atoms in $NDI^{\bullet-}$, whereas the TAA nitrogen bears a very high a_{ik} value because the free electron is

located mainly on this atom. Therefore, a substitution of the TAA donor against, e.g. a tetrathiafulvalene (TTF) donor group would be reasonable, because the sulphur atoms, which probably bear the radical upon oxidation, do not contribute to the total magnetic moment due to a zero angular momentum (I = 0). In addition, the redox properties are quite similar to those of the TAA donor unit and it can be easily attached to compound **3** by a *Stille*-coupling (Scheme 16).[372]

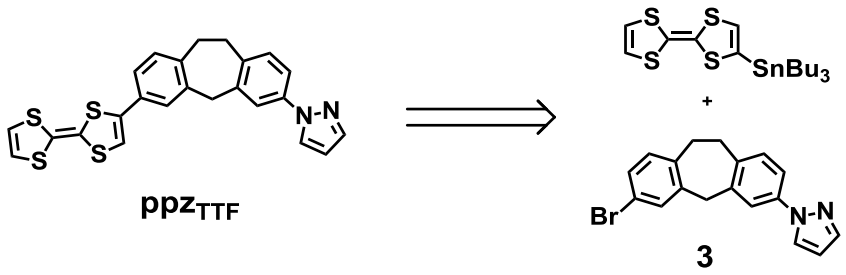

Scheme 16 Retrosynthesis of the TTF-substituted phenylpyrazole **ppz$_{TTF}$**.

3.2 Mixed-Valence Complexes[1]

Introduction

In this chapter, the photoinduced generation of a mixed-valence (MV) state between two TAA units are reported which are fused with the ligand framework of an iridium complex. While the acceptor site of the investigated complexes is unchanged (cf. **T1**–**T6**), the connection of the TAAs to the iridium complex is varied (Figure 79). That is, *bis*-(*p*-methoxyphenyl)amines (blue shaded units in Figure 79) were directly attached to the phenylpyrazole ligand in *para*- and *meta*-position at the phenyl ring relative to the iridium centre (**pMV1** and **mMV1**).

The synthesis of complexes **pMV1** and **mMV1** and the reference complexes **pMV2** and **mMV2** were described in the Master thesis of *R. Wagener*[373]

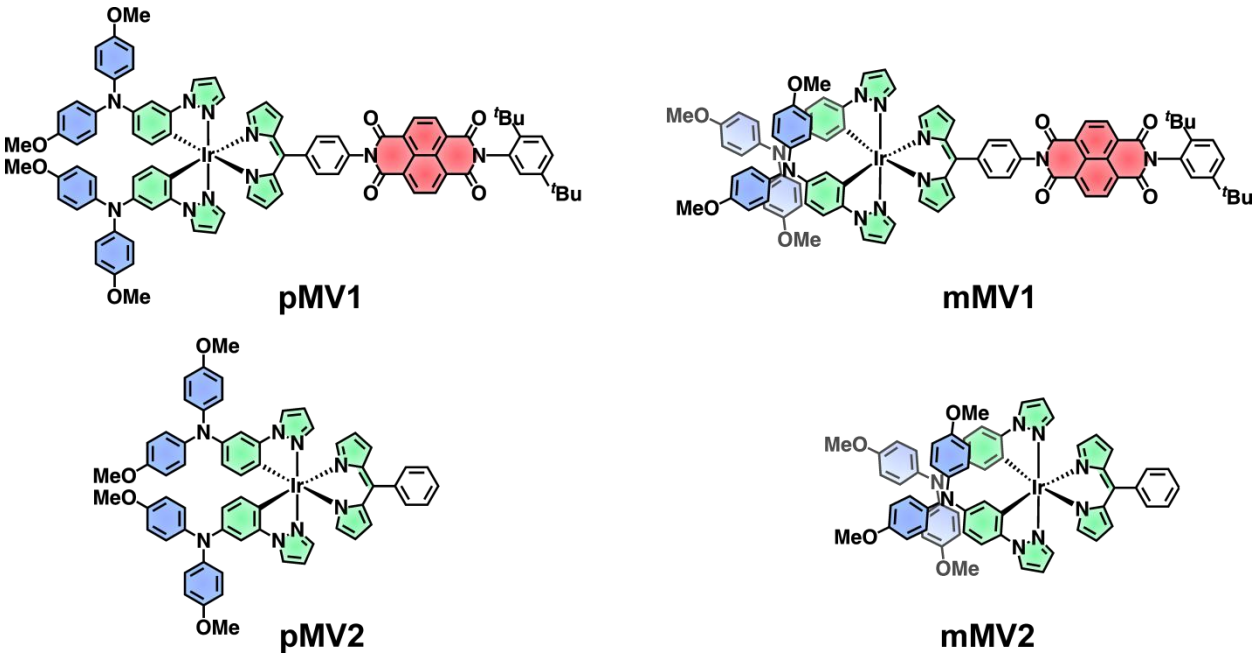

Figure 79 Triads (**pMV1** and **mMV1**, top) and dyads (**pMV2** and **mMV2**, bottom) under investigation. **pMVx** and **mMVx** (x = 1, 2) only differ by their position of the amine donor relative to the iridium centre (*para* and *meta*).

[1] Reproduced or adapted in part with permission from *A photoinduced mixed-valence state in an organic bis-triarylamine mixed-valence compound with an iridium-metal-bridge*, C. Lambert, R. Wagener, J. H. Klein, G. Grelaud, M. Moos, A. Schmiedel, M. Holzapfel and T. Bruhn, *Chem. Commun.* **2014**, *50*, 11350–11353. – Reproduced by permission of The Royal Society of Chemistry.

Additionally, UV/Vis-spectroscopy, cyclic voltammetry and spectroelectrochemistry were reported. *R. Wagener* also investigated the triad complexes by ns-TA spectroscopy in MeCN. In the following, a short introduction to the field of MV will be given followed by a summary of *R. Wagener´s* experimental results. Thereafter, the contributions of the current work, fs-pump-probe spectroscopy and TD-DFT calculations, will be discussed.

The concept of MV is strongly connected to donor-acceptor (D-A) systems, because both MV and D-A compounds consist of at least two redox centres where an electron transfer (ET) or charge transfer (CT) can occur between both redox moieties. Hence, one redox centre acts as an electron donor and the other as acceptor.[35, 374-376] A CT is often accompanied by an optical transition and can theoretically be described by the *Jortner* approach.[40] Thereby, characteristic parameters of the CT event, e.g. the *Gibbs* free energy (ΔG^{00}), the averaged molecular vibration mode ($\tilde{\nu}_v$) and the inner and outer reorganisation energy (λ_v and λ_o, respectively) can be obtained. Although MV and D-A systems have a donor-acceptor architecture in common, their electronic configuration is different. A mixed-valence system is characterised by an open-shell configuration. This is usually achieved by oxidation or reduction of one redox centre either by chemical processes or by electrochemical methods in equilibrium. On the contrary, organic donor-acceptor frameworks are closed-shell systems in the ground state. Moreover, an important feature, which characterises MV and D-A systems, is the bridge connecting both redox units. Usually, two redox centres are bridged by a saturated or unsaturated spacer which serves to keep the redox centres in a fixed distance and to mediate CT and ET events. Thereby, the bridge can also change the redox properties of the used redox centres and their spectroscopic features if a sufficient electronic coupling is present. In most cases, the bridge is a π-conjugated organic compound such as benzene, stilbene, tolan or pyrazine etc.[20-21, 24, 26-28, 35]

Figure 80 shows examples of both a MV (left) and a D-A (right) compound with a butadiyne bridge connecting either both TAAs (left) or the TAA and the NDI (right) unit. Optically induced charge transfer by direct excitation into the CT or in case of the MV compound in the intervalence (IV-) CT absorption yields either a change of the redox states in the MV compound or a charge-separated (CS) state in the D-A compound.

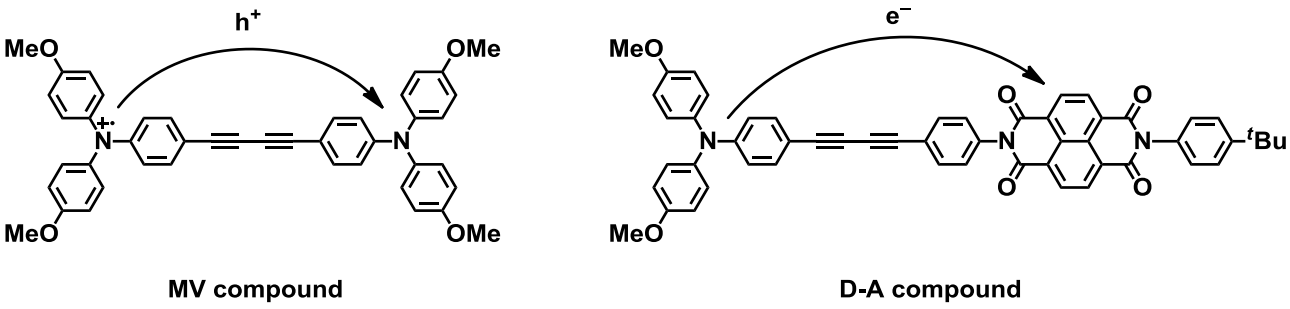

Figure 80 Examples of a MV and a D-A compound synthesised in the group of Prof. Dr. C. Lambert.[260, 377] Arrows indicate an ET between the redox centres upon photoexcitation.

The general concept of the present MV compounds is sketched in Figure 81 whereby the iridium atom (green) mediates the electronic communication between both TAA (blue) units and the iridium complex acts as the main chromophore. Additionally, a NDI acceptor (red) is attached to the iridium complex.

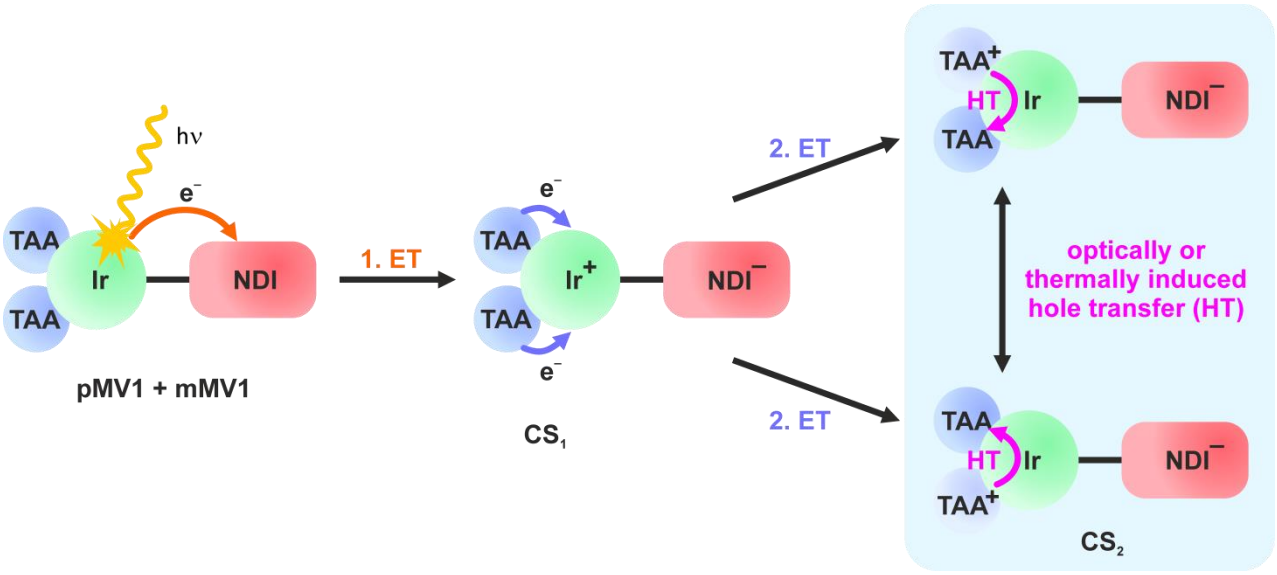

Figure 81 Concept of photoinduced MV state formation in triads of the type mMV and pMV.

Upon excitation of the iridium complex, a photoinduced ET can be observed yielding a CS_1 state where the iridium complex is oxidised and the acceptor is reduced. The positive charge is then transferred to the better electron donor (neutral TAA unit). The resulting CS_2 state can alternatively be described as a MV state where one TAA is oxidised and the other one is

neutral. Between these redox centres, a hole transfer (HT) can proceed either optically induced by irradiation into a IV-CT band or thermally activated via an ET barrier. Finally, charge recombination between TAA^+ and NDI^- restores the ground state.

In the following, a short summary of important properties of the MV compounds is given. Thus, not all complexes will be discussed and the interested reader is referred to the Master thesis of *R. Wagener*.[373]

The UV/Vis spectra of **pMV1** and **mMV1** in CH_2Cl_2 (Figure 82) display similar features as those for **T1–T6**. The absorption of the dipyrrin fragment in the spectral region between 15 400 and 25 000 cm^{-1} possesses almost identical extinction coefficients (32 800 M^{-1} cm^{-1} at 20 700 cm^{-1} (483 nm)) for **pMV1** compared to **T1–T5** (Table 3). Furthermore, the NDI absorption features are in all cases located between 25 000 and 31 000 cm^{-1} with a structured band. The typically absorption characteristics of the TAA transitions in **pMV1** can be observed between 29 000 and 37 000 cm^{-1} and are similar to the already discussed triads **T1–T6**. On the contrary, the altered connection of the TAAs in **mMV1** causes different absorption features when compared with that of **mMV1**. The TAA absorption band of **mMV1** shifts to lower energies and overlaps with the NDI absorption. This shift can be rationalised by an electronic interaction of the electron withdrawing pyrazole unit linked in *para*-position relative to the TAA in the **mMV** complexes. Due to the *meta*-linkage the electronic communication in the **pMV** complexes is hampered.

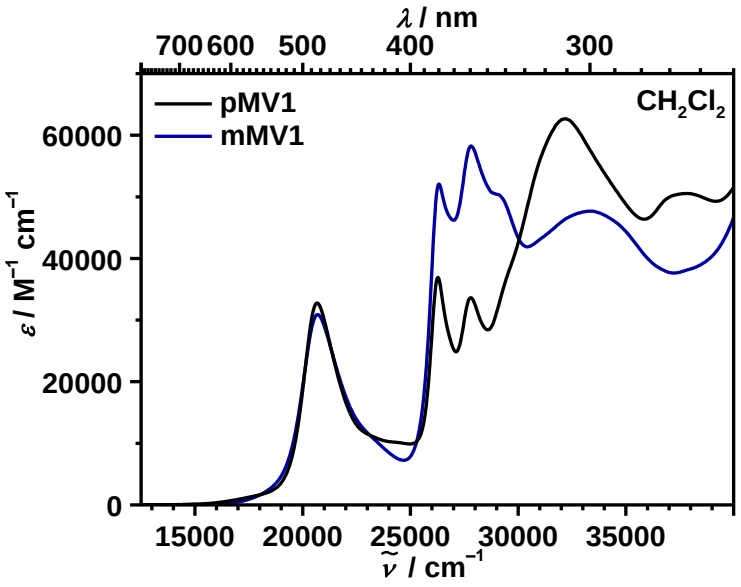

Figure 82 Absorption spectra of triads **pMV1** and **mMV1** in CH_2Cl_2.

Effects of the *meta*- and *para*-architecture of the attached donor groups are also visible in the cyclic voltammograms (only shown for **mMV1** and **pMV1** in Figure 83). Both complex types show a splitting of the first oxidation which is in contrast to the already known triads **T1**, **T4**–**T6** where the oxidation is achieved at the same potential for the TAAs. The splitting is more pronounced in the pMV complexes where completely separated redox potentials are observed. Whereas the second oxidation of both complexes (at ca. 160 mV) is in the same potential range as those of the complexes **T1**, **T4**–**T6** in CH_2Cl_2 (cf. Table 5), the first oxidation of both complexes occurs at much lower potentials (8 and 72 mV for **pMV1** and **mMV1**, respectively). These findings indicate a stronger electronic coupling between the *para*-connected TAAs than in the *meta* ones. Conversely, this coupling is not observed in the triads **T1**–**T6** because the saturated bridges of the suberone fragment diminish a similar electronic communication between both TAA branches and, therefore, both TAAs are oxidised at the same potential.

All other redox potentials (Table 16) reflect more or less the situation in triads **T1**, **T4**–**T6**, except the oxidation of the iridium dipyrrin fragment which can be observed at slightly higher oxidation potentials for pMV and mMV compounds.

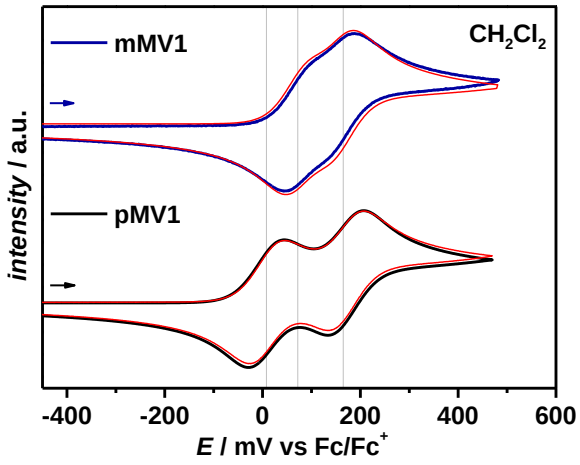

Figure 83 Cyclic voltammograms (black) and corresponding fits (red) of **pMV1** and **mMV1** (1–5 mM) in 0.2 M [nBu$_4$N][PF$_6$]/CH_2Cl_2. All potentials are referenced against Fc/Fc$^+$ and were measured at a scan rate of v = 250 mV s^{-1}. The grey lines highlight potentials at 8, 72 and 160 mV, respectively, for an easier comparison.

Table 16 Redox potentials[1] ($E_{1/2}$) and potential difference between the first reduction and oxidation ($\Delta E_{1/2}$) of **mMV1** and **pMV1** in CH_2Cl_2.

	solvent[2]	Ir(dipy) $E_{1/2}^{red}$ / mV	NDI $E_{1/2}^{red}$ / mV	TAA $E_{1/2}^{ox}$ / mV	Ir(dipy) E_{pa}^{ox} / mV	$\Delta E_{1/2}$ / mV
mMV1	CH_2Cl_2	-1995^{i}	-1010^{r} (-1485^{r})	$72^{r,f}$ ($161^{r,f}$)	660^{i}	1023
pMV1	CH_2Cl_2	-2035^{i}	-1015^{r} (-1485^{r})	$8^{r,f}$ ($163^{r,f}$)	650^{i}	1082

[1] all potentials are referenced against Fc/Fc^+ and were measured at a scan rate of v = 250 mV s^{-1}
[2] tetrabutylammonium hexafluorophosphate ([nBu$_4$][PF_6]) was used as supporting electrolyte with a concentration of 0.2 M and 0.1 M for CH_2Cl_2 and MeCN, respectively.
E_{pa} = anodic peak potential, ^{r} reversible, ^{i} irreversible

The different redox potential separations are assumed to be caused by a varying electronic communication between two TAA units mediated by the iridium centre. Accordingly, the stronger electronic communication of the *para*-linked TAAs in the pMV complexes leads to a more pronounced potential splitting. To support this assumption, spectroelectrochemistry (SEC) measurements were performed. Thereby, only the model complexes **mMV2** and **pMV2** were examined, because the attached acceptor unit has little influence on the oxidation potentials of the TAAs. The results of the SEC are shown in Figure 84.

The superposition of the redox events, shown in the CV experiments, required a deconvolution of the SEC spectra by a single value decomposition (SVD) / global analysis[378] procedure in order to obtain the spectra of the "pure" radical cations and dications. The monocations of **mMV2** and **pMV2** are MV compounds in the electronic ground state (see Figure 81). When oxidising **mMV2** the signature of a triarylamine radical cation absorption can be observed at ca. 14 000 cm^{-1} (see Figure 84a).[262, 291, 379-380] In addition, less intense transitions are visible in the NIR spectral region which are assigned to bridge bands (*vide supra*). The dication spectrum of **mMV2** shows the same features as the monocation spectrum but with an increased intensity for the transitions localised at the TAA radical cation and for the bridge bands.

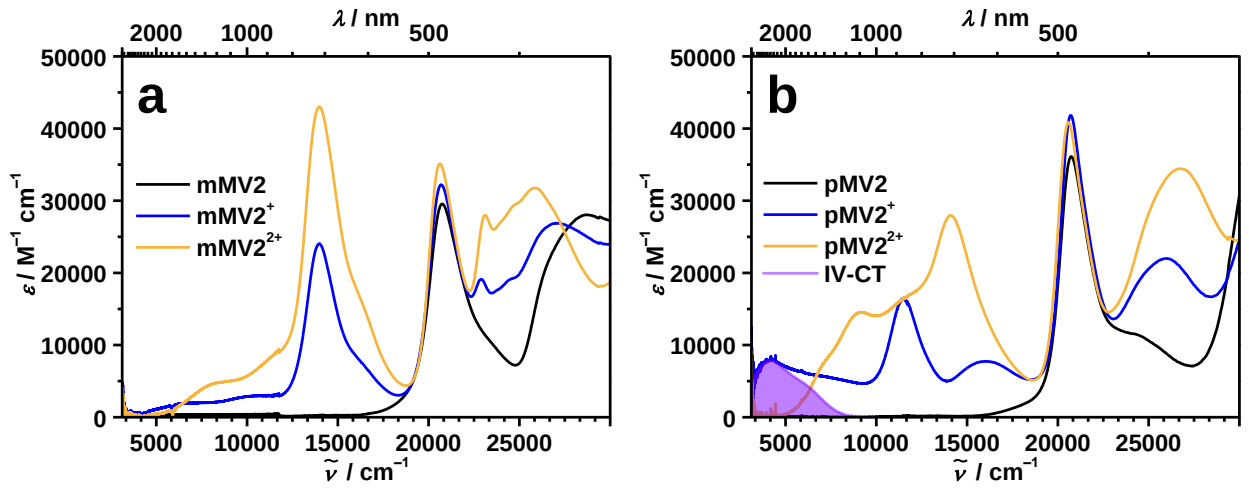

Figure 84 Spectra of the neutral, cation and dication species obtained by UV/Vis/NIR spectroelectrochemistry experiments of **mMV2** (a) and **pMV2** (b) in CH_2Cl_2/0.2 M [*n*Bu_4][PF_6]. The purple shaded area in (b) is a deconvolution of the IV-CT band with two *Gaussian* functions and extends beyond the measured range of 3000 cm^{-1} (cf. text *vide infra*).

In contrast, the TAA radical cation band in **pMV2** (Figure 84b) is weaker and shifted to ca. 11 000 cm^{-1} which indicates a strong change of its electronic environment compared to that of **mMV2**$^{+}$. Interestingly, a strong and broad NIR absorption for **pMV2**$^{+}$ can be observed which extends beyond the accessible range of the used spectrometer (> 3000 cm^{-1}) and has a maximum at 4200 cm^{-1}. This band shows characteristics of an IV-CT band and the analysis of this band is discussed *vide infra*. On the contrary, the IV-CT band is absent or strongly reduced in the dication spectrum of **pMV2**. Moreover, the spectrum of **pMV2**$^{2+}$ displays similar features as that of the oxidised **mMV2** species with a band maximum for the TAA localised transition at 14 100 cm^{-1} and further bridge bands at lower energies.

Finally, the ns-TA measurements in MeCN (not shown) proofed a CS state formation for **mMV1** with the typical TAA$^{\bullet+}$ and the NDI$^{\bullet-}$ absorptions as already discussed for triad **T1** and **T4**–**T6**. This was in line with the SEC results in Figure 84a. Conversely, in the nanosecond transient absorption measurements of **pMV1** the TAA radical cation band was not visible, so that the NDI radical anion absorption was the only hint for a CS formation. The SEC experiment showed a bathochromical shift of the TAA$^{\bullet+}$ band in **pMV2** which may explain the absence of that band in the detector window of the set-up ($\tilde{\nu}_{min}$ = 11 800 cm^{-1}). For that reason, fs-pump-probe spectroscopy in the Vis- and NIR-spectral region (6800–25 000cm^{-1}

(1470–400 nm)) were performed with both triads to support the MV character in the NIR region. In addition, TD-DFT calculations were carried out in order to substantiate the experimental findings by the theoretical modelling. Both aspects will be discussed in the following.

fs-Pump-Probe Spectroscopy

The fs-transient absorption spectra of **pMV1** and **mMV1** in CH_2Cl_2 were obtained by exciting at 20 800 cm^{-1} (480 nm) and probing in the visible range between 11 800–25 000 cm^{-1} (847–400 nm) and in the NIR range between 11 800–6820 cm^{-1}. Evolution associated difference spectra (EADS) of both triads, transient raw data and selected decay profiles can be seen in Figure 85–86.

Excitation of **mMV1** resulted in two EADS. The first EADS is characterised by a strong ground-state bleaching (GSB) at the ligand-centred (LC) band region. The following EADS shows an excited-state absorption (ESA) at 21 100 cm^{-1} (474 nm), 16 500 cm^{-1} (606 nm) and 14 100 cm^{-1} (710 nm). The former two are typical of the NDI radical anion,[71, 292, 294, 305, 310-311, 313-315] while the latter can be attributed to a triarylamine radical cation.[262, 291] This proves the formation of a charge-separated state where one triarylamine is oxidised and the NDI is reduced. This result is in very good agreement with the ns-TA measurements of **mMV1** in MeCN (*vide supra*). The global fit of the data yields two time constants, 90 ps for the photoinduced formation of the CS state and 6.9 ns for the charge recombination to the ground state. Similarly, these spectral features were present for **T1** in MeCN but with different time constants (cf. 3.1.2, Figure 54).

In the NIR spectral region only band signatures with very low intensities can be observed which is in accordance with the SEC measurements of **mMV2** (*vide supra*).

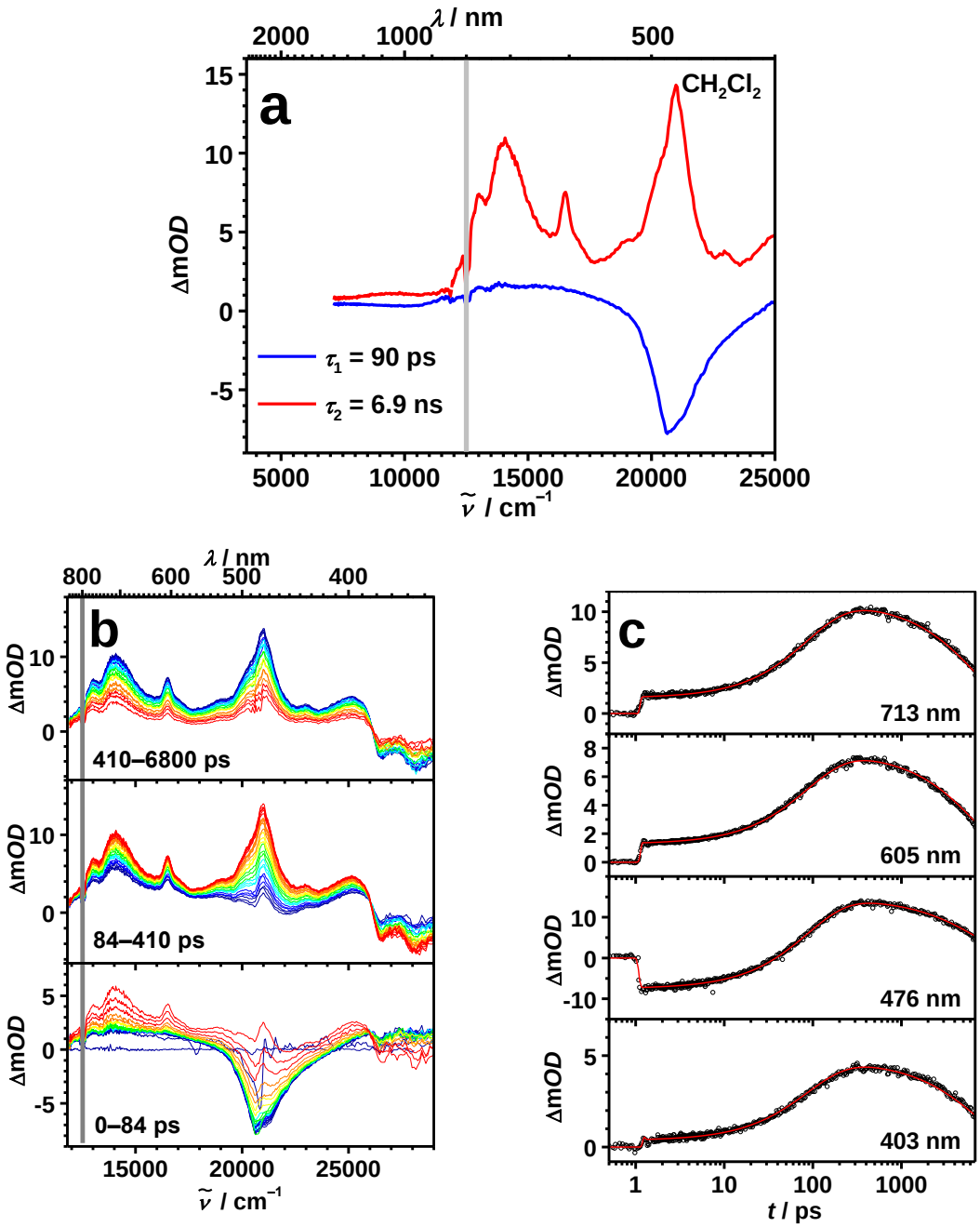
a
CH2Cl2
τ1 = 90 ps
τ2 = 6.9 ns
ΔmOD
λ / nm
ν̃ / cm−1
b
410–6800 ps
84–410 ps
0–84 ps
c
713 nm
605 nm
476 nm
403 nm
t / ps

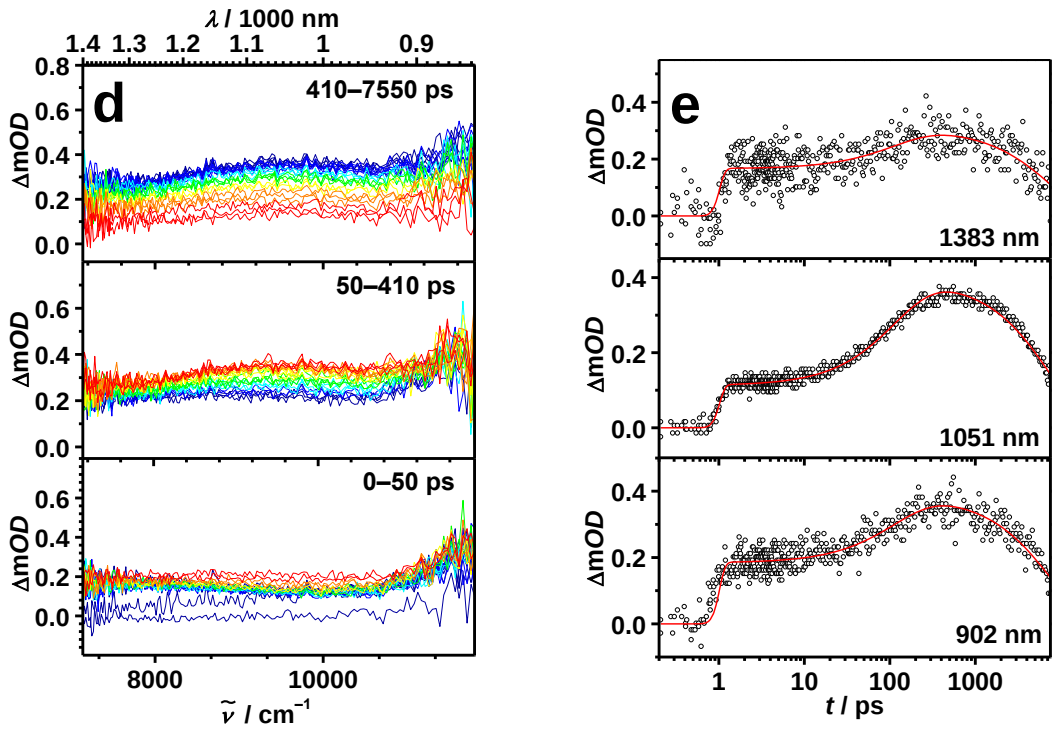

Figure 85 (a) Evolution associated difference spectra (EADS) of **mMV1** in the visible and NIR spectral range obtained in a global analysis of a transient map. (b) and (d): fs-Transient absorption data of the Vis and NIR region, respectively, were corrected for chirp and scattered light. The grey bar in the Vis spectral region marks the fundamental laser energy at 12 500 cm^{-1} (800 nm). Early spectra are in blue to green and at later times in orange to red colours. (c) and (e): Decay profiles at selected wavelengths for which the zero time delay was set arbitrarily. Excitation at 20 800 cm^{-1} (480 nm) in MeCN.

Excitation of **pMV1** at 20 800 cm^{-1} (480 nm) in CH_2Cl_2 results in an EADS with a GSB similar to that observed for **mMV1** (blue EADS, Figure 85a). The second EADS with NDI radical anion features at 21 100 cm^{-1} (474 nm) and 16 500 cm^{-1} (606 nm) are in agreement with the ns-TA measurements in MeCN. In addition, a band appears at 11 900 cm^{-1} (840 nm) which matches to the SEC measurements (Figure 84b, blue spectra) where a TAA^+ band was observed at lower energy (11 500 cm^{-1} (870 nm)) and with a lower intensity as that of **mMV1**. In the NIR transient spectra a transient absorption between 6820 and 11 100 cm^{-1} (1466–900 nm) is detected. This is the onset of the IV-CT band (cf. Figure 84b) which cannot be entirely monitored due to experimental limitations of the pump-probe set-up.

In both cases, **mMV1** and **pMV1**, the quantum yield of the MV-state formation is essentially quantitative as judged from the relative intensity of the ground-state bleaching at

early delay times (t = 0) and the ESA at later times (t = 400 and 80 ps for **mMV1** and **pMV1**, respectively) at 21 000 cm^{-1} (476 nm).

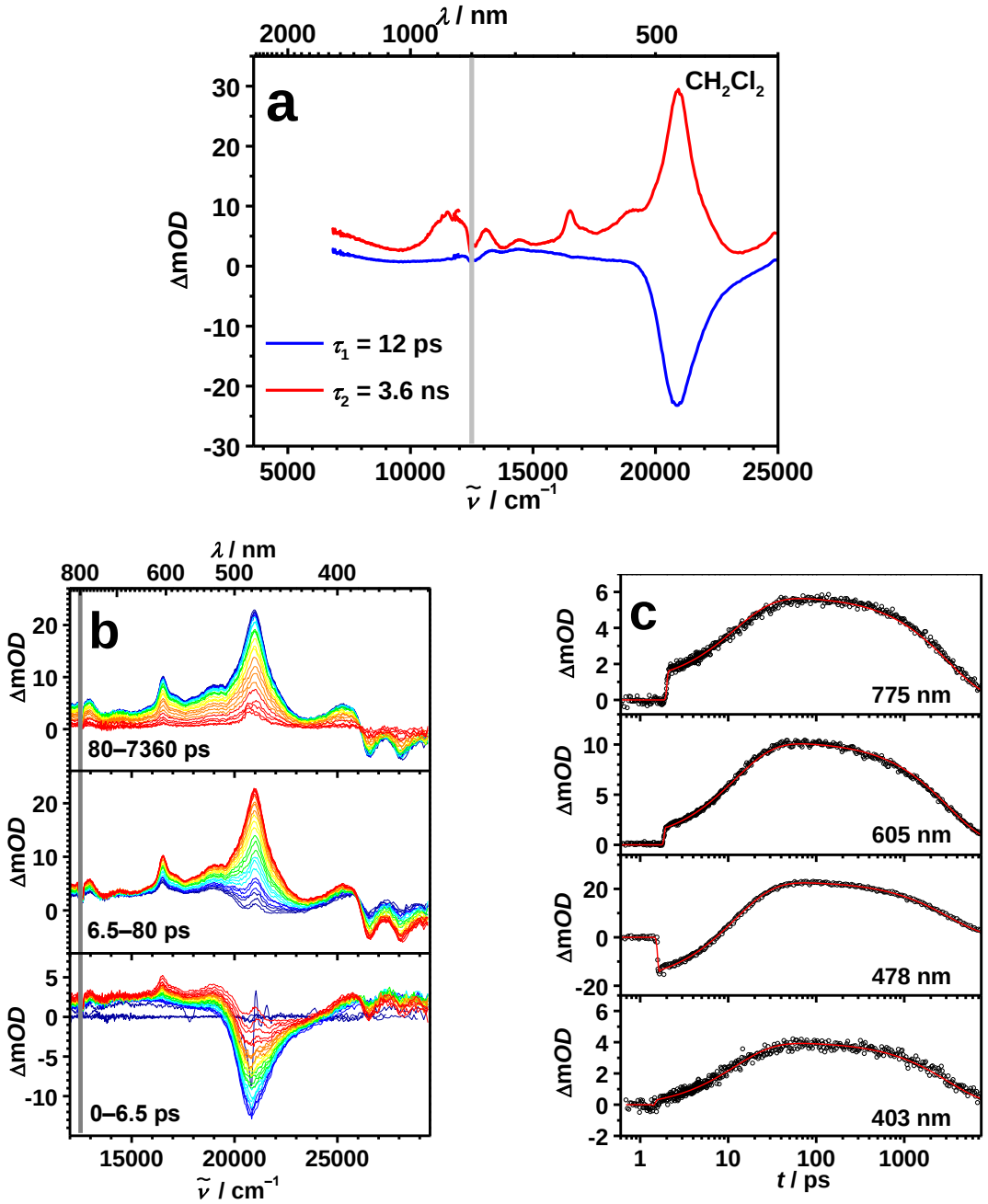

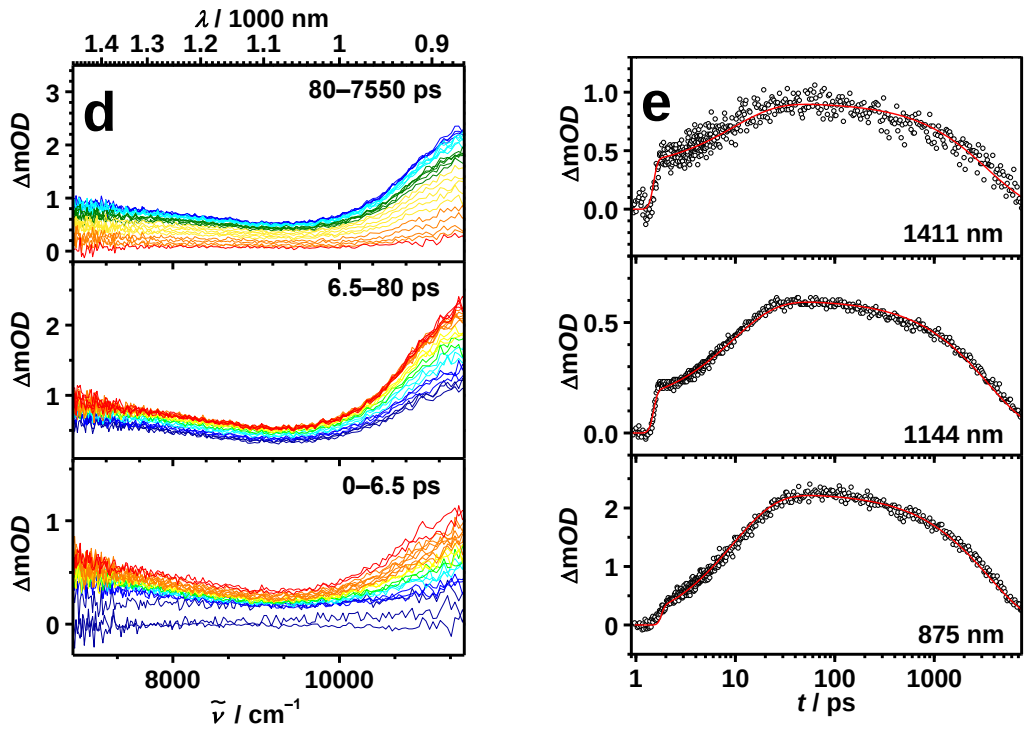

Figure 86 (a) Evolution associated difference spectra (EADS) of **pMV1** in the visible and NIR spectral range obtained in a global analysis of a transient map. (b) and (d): fs-Transient absorption data of the Vis and NIR region, respectively, were corrected for chirp and scattered light. The grey bar in the Vis spectral region marks the fundamental laser energy at 12 500 cm^{-1} (800 nm). Early spectra are in blue to green and at later times in orange to red colours. (c) and (e): Decay profiles at selected wavelengths. Decay profiles at selected wavelengths for which the zero time delay was set arbitrarily. Excitation at 20 800 cm^{-1} (480 nm) in MeCN.

Finally, the transient spectra of the CS states of **mMV1** and **pMV1** are compared to the sum of the spectroelectrochemistry spectra of each **mMV2**$^{+}$ and **pMV2**$^{+}$ and a reduced naphthalene diimide parent compound (**17**). The monoradical cation and anion spectra, their sum, and the transient absorption spectra are plotted in Figure 87. The sums of the cation and anion features (green spectra) are in very good agreement with the fs-experiment reflecting the fully CS state (black spectra). Thus, the second EADS can be rationalised as a $TAA^{\bullet+}$–$NDI^{-\bullet}$ CS state.

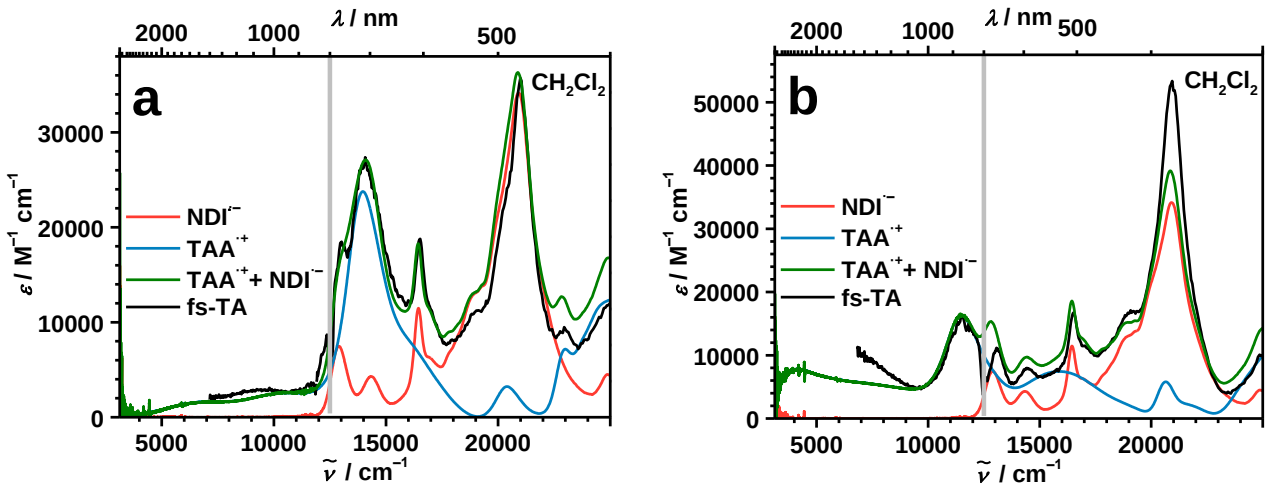

Figure 87 UV/Vis spectra of the monoradicals cations of (a) **mMV2** and (b) **pMV2** (in blue), monoradical anion of **17** (red) and the sum of the anion and cation (green) in CH_2Cl_2/[*n*Bu_4][PF_6] (0.2 M). The black curve comprises the Vis and NIR spectra of the fs-pump-probe measurement. The grey bar marks the fundamental laser energy at 12 500 cm^{-1} (800 nm).

(TD)-DFT Calculation

The a comparison of the calculated electronic transitions, obtained by time-dependent (TD-) DFT, between ground and excited state and the steady-state absorption can help to elucidate the electronic structure of the MV compounds. Furthermore, solvent effects can be simulated with a conductor-like screening model (COSMO) where the solvent-molecule interaction is approximated with the electrostatic effect of a continuum solvation towards the calculated molecule. Thereby, the key parameter is the permittivity ε of the used solvent. A pronounced solvent effect often is observed if the molecular structure possesses a significant dipole moment which is the case for CS states.

Consequently, DFT was used to simulate the charge-separated states in both triads **mMV1** and **pMV1** with a CH_2Cl_2 solvent model. As discussed for the SEC experiments the calculations were performed for the single oxidised model complexes **mMV2**$^+$ and **pMV2**$^+$, instead of the triads. The Structure optimisations were conducted analogously to the method described by *Kaupp et al.* for MV compounds with *bis*(triarylamine) motifs.[381-382] They set the Hartree Fock (HF) exchange contribution in the BHandHLYP[383] (*Becke*-Half-and-Half *Lee Yang*

and *Parr*) functional to 35 % and achieved satisfactory results for the simulation of MV transition energies (see experimental part).

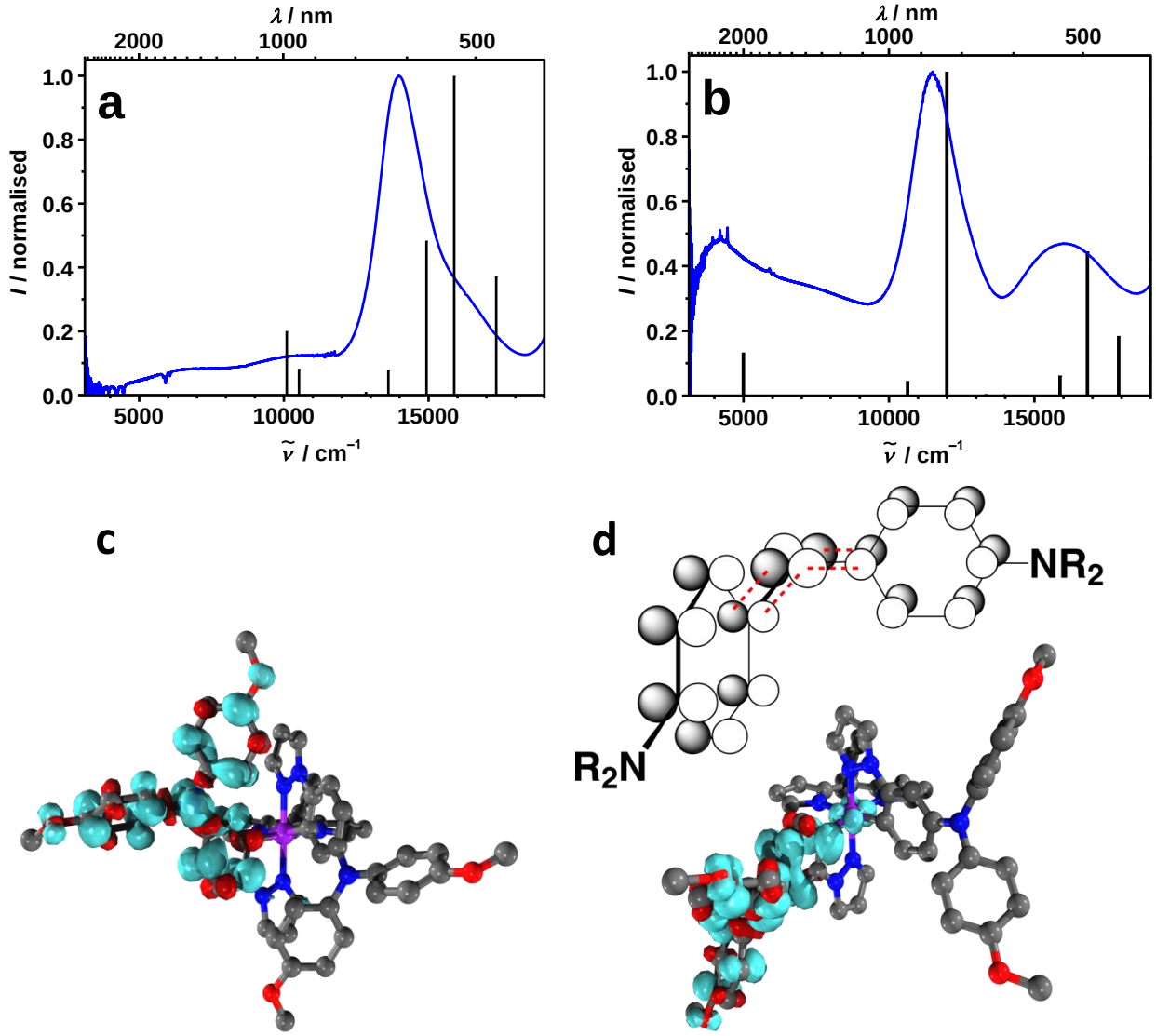

Figure 88 Absorption spectrum and stick diagram of the computed transitions of the monocation of (a) **mMV2** and (b) **pMV2** (see Table 17 for exact energies and oscillator strengths). Spin densities (isovalue ±0.002) for the ground-state structures of (c) **mMV2**$^{+}$ and (d) **pMV2**$^{+}$.

To elucidate the origin of the low energy transitions, the difference of electron density between the ground and excited state were calculated for both model complexes. This is visualised in electron density difference (EDDs) plots. (Figure 89 and 90). In these plots an increase (green) or decrease (yellow) of electron density is visible for a certain transition.

Table 17 Transition energies ($\tilde{\nu}$) and oscillator strengths (*f*) of the computed transitions of the single oxidised complexes **mMV2** and **pMV2**. For the blue shaded transitions electron density differences (EDDs) were calculated (Figure 89 and 90).

mMV2	$\tilde{\nu}$ (λ) / cm^{-1} (nm)	*f* /a.u.	**pMV2**	$\tilde{\nu}$ (λ) / cm^{-1} (nm)	*f* /a.u.
	23 440 (426.6)	0.0026		21 880 (457.1)	0.0002
	23 060 (433.6)	0.0000		21 850 (457.6)	0.0013
	23 040 (434.0)	0.0009		21 760 (459.6)	0.0012
	22 900 (436.6)	0.0116		21 610 (462.7)	0.0004
	22 530 (443.8)	0.0000		20 310 (492.4)	0.0086
	22 470 (445.0)	0.0004		19 250 (519.6)	0.0098
	22 080 (452.9)	0.0043		17 900 (558.6)	0.0686
	21 460 (466.1)	0.0000		16 820 (594.4)	0.1656
	21 090 (474.1)	0.0000		15 880 (629.7)	0.0232
	18 750 (533.4)	0.0005		13 950 (716.7)	0.0000
	18 590 (538.0)	0.0003		13 340 (749.7)	0.0018
	17 340 (576.8)	0.1047		12 780 (782.7)	0.0004
	15 890 (629.5)	0.2806		11 990 (833.9)	0.3717
	14 930 (669.8)	0.1358		10 640 (939.7)	0.0169
	14 000 (714.5)	0.0001		4998 (2000.7)	0.0496
	13 610 (734.7)	0.0221			
	12 840 (779.1)	0.0028			
	10 520 (950.2)	0.0231			
	10 100 (990.2)	0.0564			
	5219 (1916.0)	0.0005			

The calculated transitions corresponding to the absorption of the oxidised model complexes **mMV2** and **pMV2** are in satisfactory to very good agreement to the absorption spectra of the monoradicals of both complexes obtained by SEC (cf. Figure 88, Table 17). This holds true especially for the transition at ca. 5000 cm^{-1} in **pMV2**.

The spin density of the unpaired electron in **mMV2**$^{+}$ (Figure 88c) is totally localised at one TAA branch, whereas in **pMV2**$^{+}$ (Figure 88d) the spin density extends to the iridium atom. This delocalisation is caused by a significant overlap of an iridium d-orbital with the p-orbital of the *ipso*-carbon of neighbouring TAA phenyl groups. The spin-density which is extended to

the iridium centre is observed for both TAA branches and indicate an electronic communication between the TAAs centres.

Three transitions will be investigated in the following. These are the two lowest calculated transitions at 5219 cm^{-1} (1920 nm) and 10 100 cm^{-1} (990.2 nm) for **mMV2**$^{+}$ and at 4998 cm^{-1} (2001 nm) and 10 640 cm^{-1} (839.7 nm) for **pMV2**$^{+}$ (Figure 89a, b and 90a, b, respectively). A third transition, at the energy where the transition of the monoradical is localised, was chosen, that is, at 15 890 cm^{-1} (629.5 nm) for **mMV2**$^{+}$ and 11 990 cm^{-1} (839.7 nm) for **pMV2**$^{+}$.

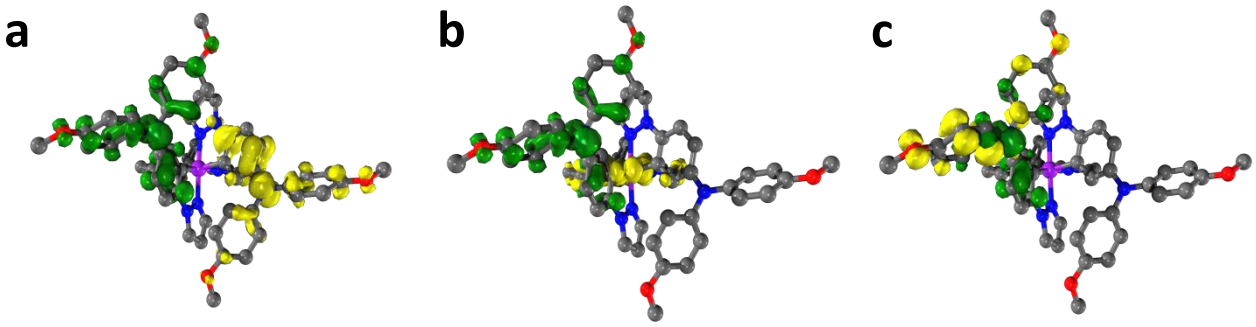

Figure 89 Electron density difference plot (isovalue: ±0.002, yellow = lowered electron density, green = increased electron density) of calculated transitions of **mMV2**$^{+}$ at (a) 5219 cm^{-1} (1920 nm) with f = 0.0005, (b) 10 100 cm^{-1} (990.2 nm) with f = 0.0564 and (c) 15 890 cm^{-1} (629.5 nm) with f = 0.2806.

For both MV compounds the first transition (Figure 89a and 90a) represents an electron density shift from one TAA branch to the neighbouring one. This strongly supports a MV character, but the oscillator strength is by a factor of 100 lower for the **mMV2** complex where the TAAs are in *meta*-position to the iridium centre. Accordingly, the occurrence of an IV-CT band is more pronounced in pMV than in mMV complexes which reflects different electronic coupling strengths between both configurations.

The other two EDDs show a very similar picture for the chosen transitions within both complexes. The transition at ca. 10 500 cm^{-1} (952 nm) causes an electron transfer from the dipyrrin fragment to the oxidised TAA unit and may be the origin of the aforementioned bridge band. The TAA localised transitions in the monoradicals are located at 15 890 cm^{-1} (629.5 nm) for the mMV and 11 990 cm^{-1} (833.9 nm) for the pMV complexes. Accordingly, the TAA localised transition of **mMV2**$^{+}$ was calculated to be at a slightly higher energy

compared to the experimental value of ca. 14 000 cm^{-1} (714 nm). However, the theoretical findings for the model complexes are very satisfactory and can be assumed to be valid for the triad complexes **mMV1** and **pMV1**, as well.

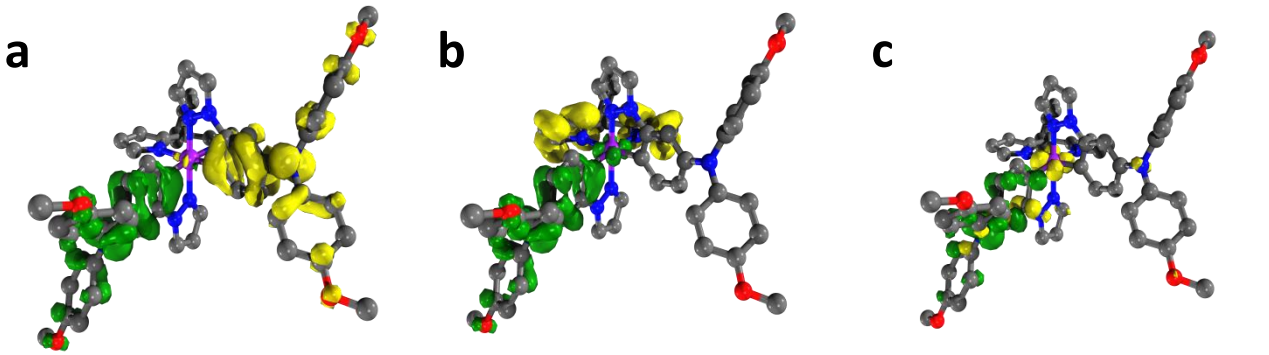

Figure 90 Electron density difference plot (isovalue: ±0.002, yellow = lowered electron density, green = increased electron density) of calculated transitions of **pMV2$^+$** at (a) 4998 cm^{-1} (2001 nm) with f = 0.0496, (b) 10 640 cm^{-1} (839.7 nm) with f = 0.0169 and (c) 11 990 cm^{-1} (833.9 nm) with f = 0.3717.

IV-CT Analysis

In the following, a detailed analysis of the IV-CT band in the NIR region for the pMV complexes will be performed. This will be done within the *Marcus-Hush* approach.[384-385] An IV-CT band is caused by an optically induced HT from an oxidised donor unit, here a triarylamine, to a neutral donor site (the second TAA) and its spectral position is governed by the total *Marcus* reorganisation energy λ associated with this process.[386] While symmetric *Gaussian* shaped IV-CT bands are expected for the limit of weak electronic coupling, the strong asymmetry of this band in **pMV$^+$** indicates a strong coupling. Deconvolution of the NIR absorption with five *Gaussian* bands (two for the triarylamine radical cation band at 11 000 cm^{-1}, one for the "bridge-band" at ca. 8400 cm^{-1} and two for the IV-CT band at 4000 and 5900 cm^{-1}) yields an asymmetric IV-CT band (shaded in purple in Figure 84b) whose integration gave a transition moment of μ_{ab} = 6.74 D. Following the *Marcus-Hush* approach[384-385] the electronic coupling is evaluated by eq. (37) and yields V_{12} = 823 cm^{-1} with the maximum of the IV-CT band $\tilde{\nu}_{max}$ = 4200 cm^{-1} and the DFT computed dipole moment difference of the ground and excited state of $\Delta\mu_{ab}$ = 31.66 D.

$$V_{12} = \frac{\mu_{ab}\tilde{\nu}_{max}}{\sqrt{\Delta\mu_{ab}^2 + 4\mu_{ab}^2}} \quad (37)$$

This coupling V_{12} which is distinctly smaller than the IV-CT band maximum classifies **pMV2$^+$** in the *Robin-Day* class II valence localised regime.[387]

In the dications of **mMV2^{2+}** and **pMV2^{2+}** and in the monocation of **mMV2$^+$** there are also NIR bands visible which have their maxima at higher energies (ca. 7 000 cm^{-1}). The second EDD plot (Figure 89b, and 90b) shows that these bands are bridge bands. That is, they are caused by the excitation of the hole at TAA$^{\bullet+}$ to the bridging unit (iridium complex).[388]

Contrary to the IV-CT band analysis of **pMP2$^+$**, it was not possible to identify an IV-CT band in the SEC spectrum of **mMV2$^+$** (Figure 84a). However, the electronic coupling could be calculated from the projection of the transition dipole moment (μ_{ab}) derived by the TD-DFT calculations. In addition, the TD-DFT calculations of the monocation of **mMV2$^+$** show a reduced oscillator strength for the IV-CT band (*vide supra*). The lowest energy transition is located at 4889 cm^{-1} (μ_{ab} = 4.255 D) for **pMV2$^+$** and at similar energy (5219 cm^{-1}) for **mMV2$^+$** but with an almost negligible transition moment (μ_{ab} = 0.421 D). Consequently, a low electronic coupling of V_{12} = 85.8 cm^{-1} between both TAAs is present in the mMV complexes, if $\Delta\mu_{ab}$ = 29.41 D (from the DFT results) and $\tilde{\nu}_{max}$ = 6000 cm^{-1} are assumed for the calculation. This is a approx. ten-fold reduced electronic coupling compared to **pMV2$^+$**. In addition, there are also much stronger bridge bands in the NIR spectral region, which may overlap with the weak IV-CT band. As mentioned above, DFT calculations of **mMV2$^+$** and **pMV2$^+$** clearly support this interpretation (*vide supra*). Therefore, **mMV2$^+$** can be assigned as a border case between a class I and II MV compound according to the classification of *Robin* and *Day*.

Conclusion

In this chapter the MV properties of triad **mMV1** and **pMV1** upon photoexcitation and their oxidised model complexes **mMV2** and **pMV2** were investigated. The CV measurements already indicated an electronic interaction between both donor moieties which results in a splitting of their oxidation potentials. Additionally, the splitting is more pronounced in the case of **pMV1**. The occurrence of an intense IV-CT band for the oxidised **pMV2** complex in the SEC experiments supports this observation. The broad IV-CT band extends up to 3125 cm^{-1} (3200 nm). The fs-pump-probe experiments in the Vis and NIR spectral range verified the SEC

findings with a shifted radical cation peak to lower energies and the onset of an IV-CT band up to ca. 6700 cm^{-1} (1500 nm) for the triad **pMV1**. On the contrary, **mMV1** exhibits less pronounced band features in the NIR spectral region and shows similar characteristics as for **T1** and **T4–T6**. However, both triads form a fully charge-separated state proven by comparison of the transient spectrum to the SEC data.

The DFT performance yielded stick diagrams of the absorption spectra and spin density plots of the oxidised model complexes **mMV2** and **pMV2**. The stick diagrams are in very good agreement with the absorption spectra of the monoradical cations of both model complexes. **mMV2**$^{+}$ and **pMV2**$^{+}$ show a low energy absorption at ca. 5000 cm^{-1} (2000 nm) but with an strongly increased oscillator strength in the **pMV2**$^{+}$ complex. Furthermore, the spin density situation in **pMV2**$^{+}$ clearly shows a participation of the iridium atom, whereas this is not the case for **mMV2**$^{+}$. The nature of the first transition at 5000 cm^{-1} (2000 nm) in each model complex could be verified with EDDs to be an IV-CT.

The IV-CT analysis of the low energy band in **mMV2**$^{+}$ and **pMV2** showed a weak transition dipole moment for the former (V_{el} = 85.8 cm^{-1}), while for the *para*-compound the electronic coupling was estimated to be V_{el} = 823 cm^{-1} (according to a *Marcus-Hush* approach). Accordingly, the MV complexes **mMV2**$^{+}$ and **pMV2**$^{+}$ can be attributed to the classification based on *Robin* and *Day* as class I+II and II MV compounds, respectively.

The use of metal bridges are only seldom found in organic MV compounds[382, 389-390] and more important the rectangular mediating mode of electronic communication of the iridium atom is totally unique and opens a new way using such metals as bridges in MV systems. Moreover, the MV-compounds are generated by a photoinduced electron transfer (PET) and not with the typically used methods, such as chemical or electrochemical oxidation processes.

3.3 Dyads D1–D4[1]

The main focus of this thesis is on the charge separation in donor-iridium complex-acceptor triads but also donor-iridium complex structures have been prepared to investigate charge separation. Those structures are termed dyads.

The main difference compared to the triads in chapter 3.1 is the omission of the NDI acceptor linked to the dipyrrin, whereas the donor site (TAA) is unchanged (Figure 91). In this chapter, the relatively electron rich dipyrrin ligand is functionalised with electron withdrawing substituents to make an oxidation of this ligand more feasible.

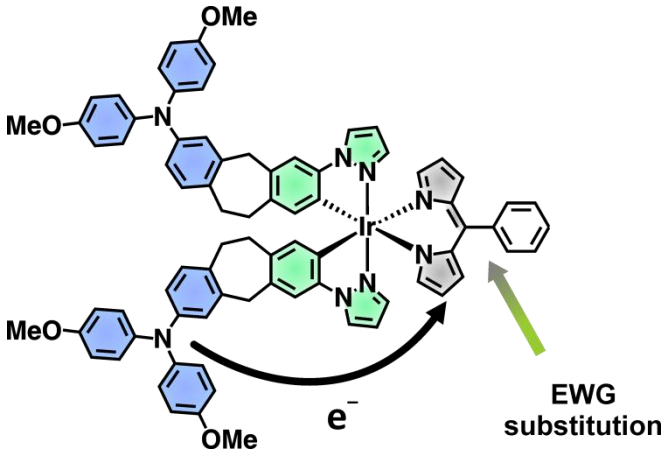

Figure 91 Schematic representation of the project aim of the current chapter. The NDI chromophore is omitted and charge separation will occur by substituting the dipyrrin ligand with electron withdrawing groups (EWG).

Three strategies were used to achieve an increased reduction potential of the dipyrrin ligand attached to the iridium complexes. First, the phenyl ring in *meso*-position was substituted with electron withdrawing groups (EWGs), e.g. Cl and CN in **15** and **31**, respectively. Second, the pyrrole core was functionalised with EWGs, e.g. cyano groups in case of **31**–**33** and Cl in **15**. Finally, an extended π-system in the *meso*-position of the dipyrromethane was chosen to increase delocalisation of electron density in the ligands and thereby producing electron deficient dipyrromethanes **16**, **32** and **33**.

[1] Parts of this chapter have been investigated in a Graduate thesis (teacher apprenticeship) under the supvervision of J. H. Klein: S. Riese, Graduate thesis (teacher apprenticeship), Julius-Maximilians-Universität (Würzburg), **2012**.

3.3.1 Synthesis

Dipyrromethane Synthesis

The synthesis of the donor ligand (**4**) and the dinuclear μ-chloro bridged dimers (**34** and **36**) is already discussed in section 3.1.1.1. For that reason, the synthesis of various dipyrromethanes and the resulting complexes (Figure 92) is the focus of the present discussion. The experimental procedure of dipyrromethane **14** was carried out in the same way as it was for the unsubstituted dipyrromethane **11** (Scheme 17). A microwave assisted reaction with pyrrole, *p*-chlorobenzaldehyde and iodine as *Lewis* acid yielded the desired chloro-substituted dipyrromethane in 42 %.[286] In a next step, **14** was treated with *N*-chlorosuccinimide (NBS) at low temperatures to obtain **15** in 52 %.[391] Flash chromatography was successful but had to be carried out under the exclusion of light because the compound was somewhat light sensitive. In addition, *Lindsey´s*[285] method was used to synthesise **16** with trifluoro acetic acid (TFA) and the commercially available 3-phenylpropioaldehyde.

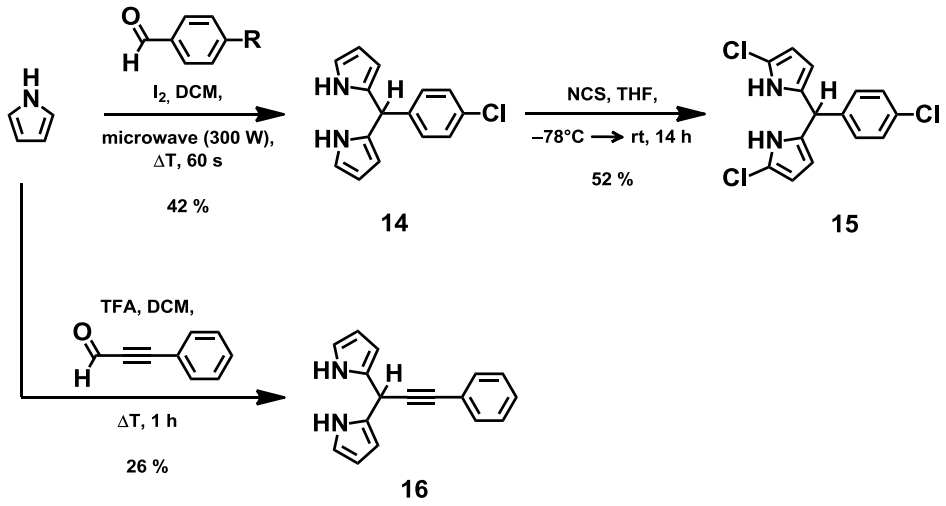

Scheme 17 Synthesis of dipyrromethanes **14**–**16**.

The advantage of the preceding dipyrromethane syntheses was the easy access of the starting material, the unsubstituted pyrrole. The limited commercial availability of core-substituted pyrroles with e.g. cyano (CN) and chloro (Cl) substituents with an unfunctionalised 2- and/or 5-position was the motivation to synthesise pyrrole **29** via a *Hantzsch*-like pyrrole synthesis (Scheme 18).[392-394] The reaction sequence started with an

amino-protected *N*-methoxy-*N*-methylglycinamide which was deprotected with aqueous HBr (48 %) to give **26** in almost quantitative yield. The resulting compound **26** served as a synthon of the α-haloketone in the *Hantzsch* pyrrole synthesis and is further treated with 3-aminocrotonitrile. The latter compound was the second synthon in the pyrrole synthesis according to *Hantzsch*. The main difference between the typical *Hantzsch* synthesis and the current one is the nucleophilic attack of the amine on the carbon which is bonded to the ammonium group. Conversely, in the classical *Hantzsch* procedure the amine attacks the carbon atom of the keto group. Of course, the keto group of the amide in **26** is not electrophilic enough compared to the carbon with a positively charged leaving group. Hence, the nucleophilic attack of 3-aminocrotonitril yielded **27** in high yields (82 %). The next step was a *Grignard* reaction with methyl magnesium bromide to transfer the amide function into a keto group which resulted in **28** (92 %). In the last step of the synthesis the ring closure reaction was conducted in which the carbon atom of the enamine attacks the keto group, followed by dehydration and formation of the aromatic system. This last step in the synthesis of 3-cyano-2,4-dimethyl-1*H*-pyrrole (**29**) resulted in a satisfactory yield of 80 %. The electron deficient pyrrole was used in the following synthesis as building block for the dipyrromethane synthesis.

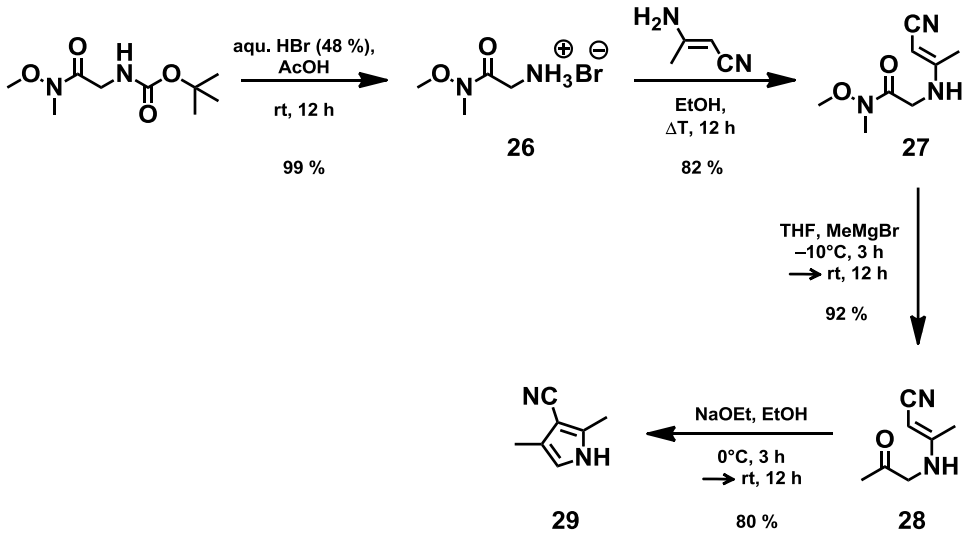

Scheme 18 Reaction sequence of a modified *Hantzsch* pyrrole synthesis yielding 3-cyano-2,3-dimethyl-1*H*-pyrrole (**29**).

Dipyrromethane **31** (Scheme 19) was prepared following the standard procedure according to *Lindsey* and co-workers.[285] TFA, pyrrole (**29**) and *p*-cyanobenzaldehyde reacted in high yields to the dipyrromethane **31** which bears three cyano substituents. In addition, for compound **32** the microwave assisted reaction was used because cleavage of the trimethylsilyl group could be excluded under acid free conditions. In the following step, the planed cleavage was performed with potassium fluoride (KF) in a mixture of THF and MeOH to get dipyrromethane **33** (92 %).

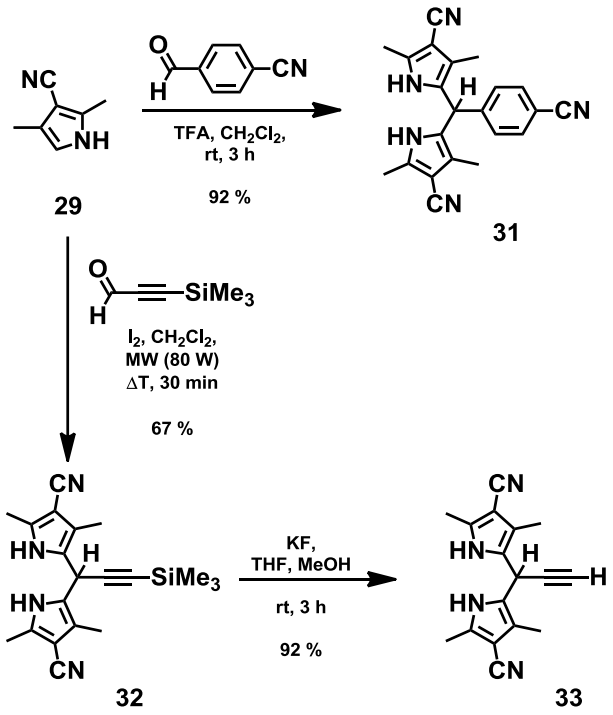

Scheme 19 Synthesis of the dipyrromethanes **31**–**33** starting with the core-substituted pyrrole **29**.

A dipyrromethane synthesis with 2-cyano-1*H*-pyrrole (**30**, see Experimental Part) and benzaldehyde was also tested with several *Bronsted* and *Lewis*-acids but no product could be isolated. This may be explained by the too electron withdrawing cyano group in 2-position which hampers the nucleophilic attack of the pyrrole to the aldehyde.

Dyad Synthesis

In the following, the complex synthesis will be presented. The reference complexes **Ref1**–**Ref4** resulted from the dimer complex **34** with the dipyrromethanes **11**, **14**–**15** and **31**. The same dipyrromethanes in combination with the dinuclear iridium complex **36** with the methoxy-TAA substituted phenylpyrazole ligand yielded the dyads **D1**–**D4**. Additionally, **D5** resulted from the reaction of **37** and **11**. All successfully performed syntheses towards the cyclometalated iridium complexes are displayed in Scheme 20 and the complexes are shown in Figure 92.

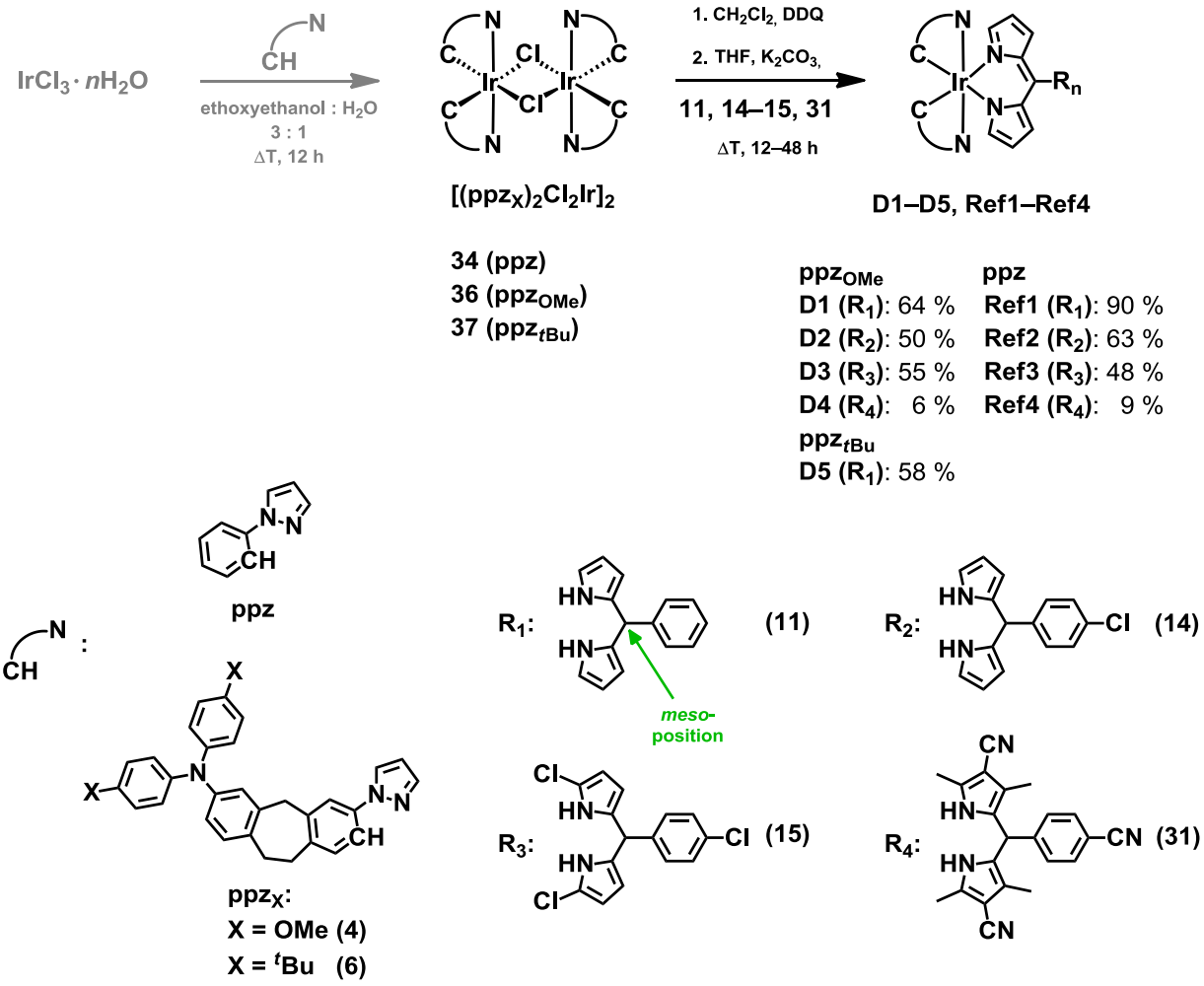

Scheme 20 Synthesis of *bis*-cyclometalated iridium complexes giving dyads **D1**–**D5** and **Ref1**–**Ref4** in the second step of the *Nonoyama* route (black). The first step is displayed in grey and has been already discussed in section 3.1.1.1.

Almost all complexes were obtained in satisfying yields. The synthesis of the complexes with a cyano-dimethyl substitution pattern (**Ref4** and **D4**) gave low yields of 6–9 %. A possible explanation may be a sterically increased demand of the methyl substituent in 2- and 9-position compared to the unsubstituted or chloro-bearing dipyrromethanes.

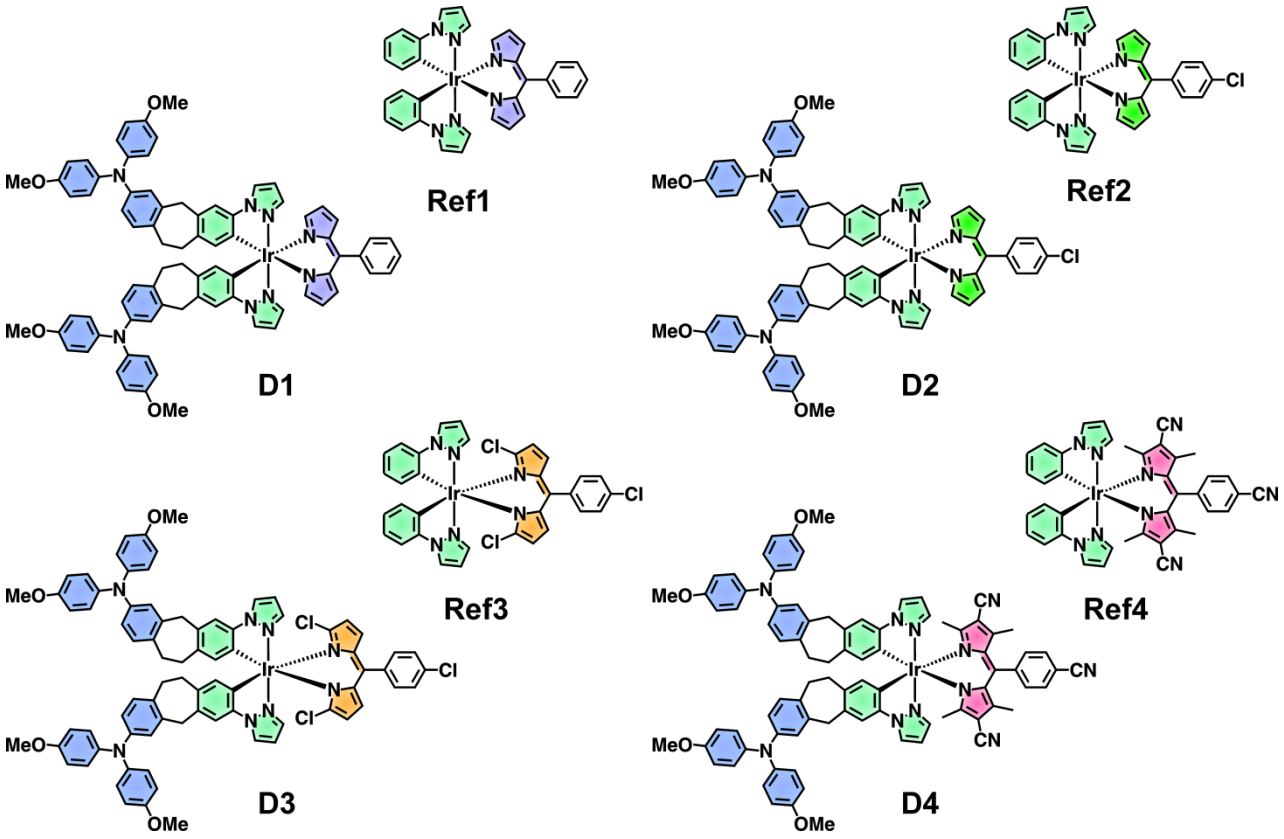

Figure 92 Dyads **D1**–**D4**.

Unfortunately, no complexes were obtained in the synthesis using the ligands **16** and **32** with the triple bond attached to the *meso*-position (cf. Scheme 20) of the dipyrromethanes. When ligand **33** was used the desired complex was only obtained in traces. A mass spectrometry analysis of various tested reactions indicated a cleavage of the triple bond in the complex synthesis. This result may be explained by coordination of the ligand´s triple bond to the iridium complex dimer with a follow-up reaction where the triple bond was destroyed. Future projects will be necessary to verify this assumption. Moreover, different reaction conditions, e.g. change of solvent, base or reaction temperature may be tested to circumvent this unwanted side reaction.

3.3.2 Steady-State Absorption Spectroscopy

The absorption features of the reference complexes **Ref1**–**Ref4** and dyads **D1**–**D5** are displayed in Figure 93a and b in MeCN, respectively. The model complex **Ref1** (blue line in Figure 93a) was already discussed in chapter 3.1.1.2 and the main characteristics can be summarised as follows: i) The ligand-centred (LC) iridium dipyrrin transition is visible in the spectral region between 17 000 and 26 000 cm^{-1} (588–385 nm) with a maximum absorption at 20 900 cm^{-1} (478 nm) and the corresponding absorption coefficient of ε_{abs} = 33 200 cm^{-1} M^{-1}. ii) A shoulder at lower energies is located at ca. 19 000 cm^{-1} (526 nm) and indicates a triplet absorption of the iridium complex. iii) The LC absorption is accompanied with a high energy shoulder at ca. 24 500 cm^{-1} (408 nm) which was assigned to a metal-to-ligand charge-transfer (MLCT) transition including the dipyrrin ligand. iv) At higher energies (> 27 000 cm^{-1} (< 370 nm)) the transitions with extinction coefficients of 12 000–30 000 M^{-1} cm^{-1} correspond to the iridium phenylpyrazole ($Ir(ppz)_2$) fragment including π-π*- and further MLCT-transitions.[142] The following reference complexes (**Ref2**–**Ref4**) all have the $Ir(ppz)_2$-fragment in common and differ only by the used dipyrrin ligand.

Thus, reference complex **Ref2** shows almost no change in the absorption behaviour compared to **Ref1** which indicates that chloro-substitution in the *meso*-position of the dipyrrin has little effect on the absorption features (Table 18). This may be explained by the almost 90° twist of the phenyl ring in *meso*-position which is evident from the molecular structure obtained by single crystal X-ray diffraction of **T1**. Thus, the effect of EWGs linked to the phenyl ring is hampered.

In contrast, the chloro functionalisation of the pyrrole core in **Ref3** induces a shift of the absorption maximum of ca. 800 cm^{-1} to lower energies. In addition, the change of the absorption band maximum indicates a narrower band shape in combination with a higher absorption cross section of the absorption maximum (ε_{abs} = 39 600 M^{-1} cm^{-1}). However, the transitions at higher energies are almost unchanged compared to **Ref1** and **Ref2**. The absorption shift to lower energies can be clearly assigned to the now more electron deficient pyrrole core.

The last reference complex consists of the $Ir(ppz)_2$-fragment and the dipyrromethane (**31**) with the cyano-dimehtyl substitution at the pyrrole rings. Likewise, to **Ref3**, the

absorption shift of **Ref4** in MeCN is about 900 cm^{-1} compared to **Ref1** and **Ref2**. However, the intensity of the absorption maximum is strongly increased up to ε_{abs} = 64 900 M^{-1} cm^{-1}. Thus, the extinction coefficient of the Ir(dipy) absorption band is higher by a factor of ca. two compared to **Ref1** and **Ref2**. In addition, the absorption intensity is also increased in the spectral region of 33 000–40 000 cm^{-1} (303–250 nm). This may be related to the absorption of the nitrile groups which cause an additional absorption of that complex at higher energies. A comparison of **Ref3** and **Ref4** revealed a similar absorption maximum but with a more pronounced extinction coefficient for **Ref4** (see Table 18).

As shown in Figure 93c, the shoulder at the high energy side of the Ir(dipy) absorption at ca. 23 500 cm^{-1} (426 nm) in **Ref1** and **Ref2** seems to shift into the main absorption peak in the other complexes and causes an increased absorption for **Ref3** and **Ref4**. This shoulder was attributed to an MLCT transition (cf. 3.1.1.2) where the dipy ligand is involved. However, this effect occurs in addition to the changed electronic situation of the ligand-centred absorption.

The absorption intensities increase in a series from **Ref1**/**Ref2** to **Ref3** and **Ref4** as a result of the EWG functionalisation of the pyrrole core within the dipyrromethane framework. On the contrary, the substituents in *para*-position of the phenyl ring have no or little influence on the Ir(dipy) absorption in the visible spectral region.

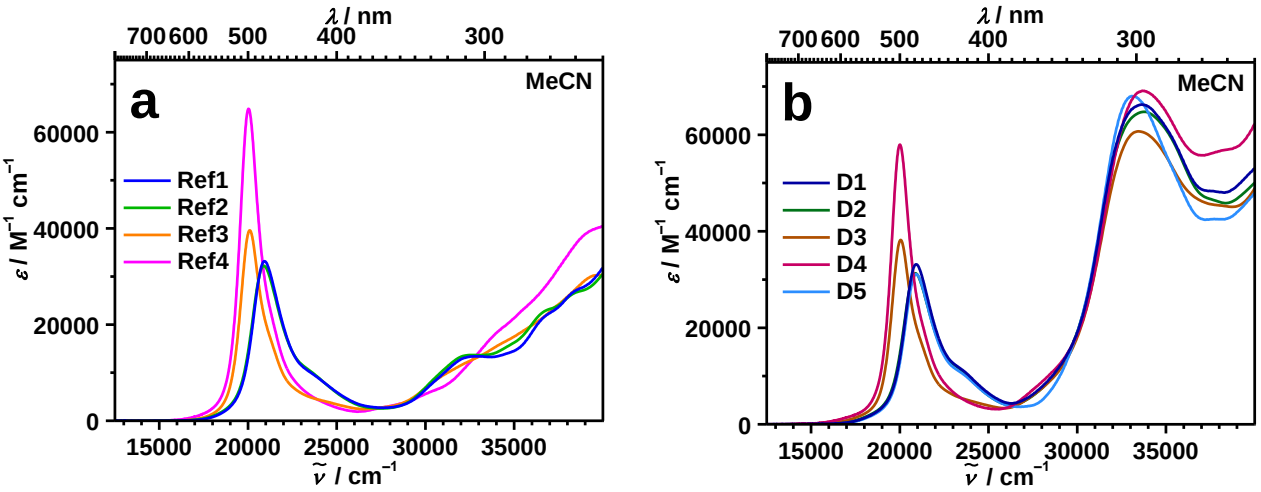

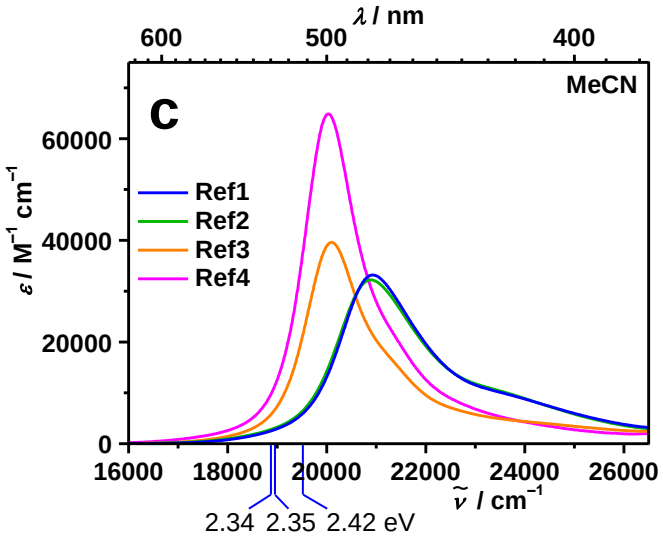

Figure 93 Absorption spectra of (a) reference complexes **Ref1**–**Ref4**, (b) dyads **D1**–**D5** and (c) mangification of the absorption features in the visible spectral region of **Ref1**–**Ref4** in MeCN. The energies in eV in (c) belong to the iridium singlet energies determined by fitting a tangent on the absorption band.

The analysis of the reference complexes is followed by the discussion of the absorption features of the dyad complexes **D1**–**D5** in MeCN which are presented in Figure 93b and listed in Table 18. First, it has to be mentioned that the numbering of the dyads correspond to the one used in the references, that is **Ref1** and **D1** form a pair of complexes, where the dipy ligand is the same and the ppz-ligand is different. Hence, **D1** consists of the unsubstituted dipyrrin ligand and the donor functionalised phenylpyrazole (**4**). The other pairs are **Ref2**-**D2**, **Ref3**-**D3** and finally **Ref4**-**D4**. Conversely, **D5** is the only exception because the used donor ligand is the *tert*-butyl substituted TAA (**6**) together with the unsubstituted dipyrromethane **11**. Hence, the corresponding reference is **Ref1**.

The main difference within the reference-dyad pairs is the additional broad absorption band of the TAA donors located at 30 000–38 000 cm^{-1} (333–357 nm) with ε_{abs} > 60 000 cm^{-1} M^{-1} (cf. Table 18). The absorption maxima and extinction coefficients of the TAAs slightly differ between the complexes. The following reasons may account for this: i) In case of **D5** the shift of the TAA band maximum can be explained by a different electronic situation of the *tert*-butyl substituted TAA which was already discussed in chapter 3.1.1.2. ii) The increased absorption intensity of **D4** in the spectral region > 30 000 cm^{-1} (< 333 nm) is not caused by the TAA traits because they are already present in **Ref4** (see Figure 93a) and extend further

to higher energies. However, the TAA absorption features of **D1**–**D3** should differ only to a minor extent due to almost identical intensities of the reference complexes. **D3** shows a somewhat lower intensity compared to **D1** and **D2**. At the moment, an explanation for that effect is not present. However, a comparison of the absorption spectra of **D2** and **D3** in THF (not shown) shows equal intensities of the TAA bands.[395]

The absorption traits of the ligand-centred transition are in all dyads very similar, except for complex pair **Ref4**–**D4**. In **D4** the absorption intensity is reduced by about 11 % compared to its reference partner **Ref4** (cf. Table 18). The results were tested several times with analytically pure samples according to micro analysis. Further tests in different solvents may be necessary to verify or reject this outcome. Unfortunately, at the moment no sound explanation can be given for this difference.

The energy levels of the singlet LC transition of each reference-dyad pair were determined by fitting a tangent on the rising edge of the low energy side of the absorption band of the reference complexes.[41] The intersection point with the x-axis yielded the ^{1}Ir state energies of $E(^1\text{Ir})$ = 2.42, 2.35 and 2.34 eV for **Ref1**/**Ref2**, **Ref3** and **Ref4** (Figure 93c), respectively and reflect quiet well the shift of the absorption maximum of the LC bands. The same values are assumed for the dyad complexes.

Table 18 Absorption maxima and extinction coefficients of the characteristic absorption bands (iridium complex = Ir(dipy) and TAA) of references **Ref1**–**Ref4** and dyads **D1**–**D5** in MeCN.

	Ir(dipy) $\tilde{\nu}_{max}$ (λ_{max}) / ε_{max}[1] / cm^{-1} (nm) / cm^{-1} M^{-1}	**TAA** $\tilde{\nu}_{max}$ (λ_{max}) / ε_{max}[1] / cm^{-1} (nm) / cm^{-1} M^{-1}
Ref1	20 900 (478) / 33 200	-
Ref2	20 900 (478) / 32 200	-
Ref3	20 100 (498) / 39 600	-
Ref4	20 000 (500) / 64 900[2]	-
D1	20 900 (478) / 33 200	33 600 (298) / 66 300
D2	20 900 (478) / 31 300	33 800 (296) / 64 800
D3	20 100 (498) / 38 200	33 400 (299) / 60 700
D4	20 000 (500) / 58 000[2]	33 700 (297) / 69 100
D5	20 900 (478) / 31 100	33 100 (302) / 68 000

[1] the error of ε_{abs} lies in the range of ±3 %

[2] difference in ε_{abs} of ca. 11 % between **Ref4** and **D4** were tested several times with analytical pure samples according to CHN analysis

3.3.3 Emission Spectroscopy

Emission spectroscopy was performed for all reference and dyad complexes in MeCN in order to obtain an overview of the excited state behaviour of **Ref1**–**Ref4** and **D1**–**D4**. Going from **Ref1**-**D1** to **Ref4**-**D4**, a shift of the emission maxima is expected which should reflect the steady-state behaviour of the complexes (*vide supra*). The emission characteristics of **Ref1** were already investigated in chapter 3.1.1.3 and can be summarised as follows. For the weak NIR emission (Figure 94b) of the iridium complex **Ref1** with a large *Stokes* shift of approx. 6000 cm^{-1} an emission quantum yield of Φ_{em} = 1.6 % could be determined at rt. On the contrary, at 77 K in 2-MeTHF strong phosphorescence could be observed. The lifetime of the radiative transition, its band shape and solvatochromic behaviour are strong indicators for its dipyrrin ligand-centred nature.

In general, the emission properties within all reference-dyad pairs are very similar. The already depicted limitations of the used UV/Vis-emission detector (cf. 3.1.1.3) in combination with a low quantum yield of the radiative deactivation makes a detailed analysis of the emission spectra impossible. Therefore, the reference complexes **Ref1**–**Ref4** will be solely discussed and stand exemplarily for the dyad complexes which always have a lower emission intensity. Additional non-radiative rates probably cause the reduced emission compared to the reference complexes which may be related to the larger molecular size of the dyads. Moreover, no emission was detected for the **Ref4**-**D4** pair at rt. However, the emission spectra were recorded for the three other pairs (**Ref1**-**D1**, **Ref2**-**D2** and **Ref3**-**D3**) in MeCN (Figure 94a). For all complexes a structured band shape can be observed which extends further into the NIR spectral region but cannot be covered by the UV/Vis detector (limited to 12 500 cm^{-1} (800 nm)). The **Ref2**-**D2** pair is slightly shifted (100 cm^{-1}) to lower energies compared to the **Ref1**-**D1** pair. The shift of the emission maximum is with about 300 cm^{-1} even more pronounced for the **Ref3**-**D3** pair. The limited detection range of the former detector was bypassed with a less sensitive NIR detector. For that reason, the emission spectra were recorded in 2-MeTHF because the phosphorescence quantum yield in these complexes is higher in less polar solvents (Table 4). Unfortunately, emission was only detectable for the complex pairs including **Ref1** and **Ref2** (Figure 94b). The full spectra extending up to ca. 10 000 cm^{-1} (1000 nm) show a vibronic progression with three peaks at ca. 14 500 cm^{-1} (690 nm), 13 400 cm^{-1} (746 nm) and 12 300 cm^{-1} (813 nm). The spectrum of **Ref2** is slightly shifted (ca. 100 cm^{-1}) to lower energies but is otherwise identical to **Ref1**.

If the samples were cooled in 2-MeTHF to 77K the solvent forms a glassy matrix. As the complexes are imbedded in the matrix, the resulting emission spectra show a higher resolution of the vibrational progression combined with a strong emission intensity. In addition, the peak maxima shift to higher energies (see introduction for rigidochromism)[107, 138, 145, 148, 193, 196] because an excited state is better stabilised in liquid solvents (Table 19). Moreover, the relatively small shift of ca. 300 cm^{-1} between the rt and 77K spectra are a strong evidence of the LC nature of the phosphorescence. The lifetimes of the ^{3}Ir state increase strongly with 17.8 and 12.2 µs for **Ref1** and **Ref2**, respectively. Furthermore, **Ref3** and **Ref4** show an intense phosphorescence emission at low temperature, too (Figure 94c). Both complexes have very similar features but compared to **Ref1** and **Ref2** they differ

significantly concerning their spectral shape and energetic position. First, the energetically lowest maxima are located at lower energies by around 600 cm^{-1}. Second, the relative intensities of the progression are changing, too. The second maxima are more intense than the first ones. This effect points to a changed relative position of the ground and excited state potential surfaces in **Ref3** and **Ref4** compared to **Ref1** and **Ref2**. The exited triplet state possesses lifetimes of 6.5 and 52 µs for **Ref4** and **Ref3**, respectively. Although both complexes have a similar shape, their lifetimes differ by a factor of approx. 8.

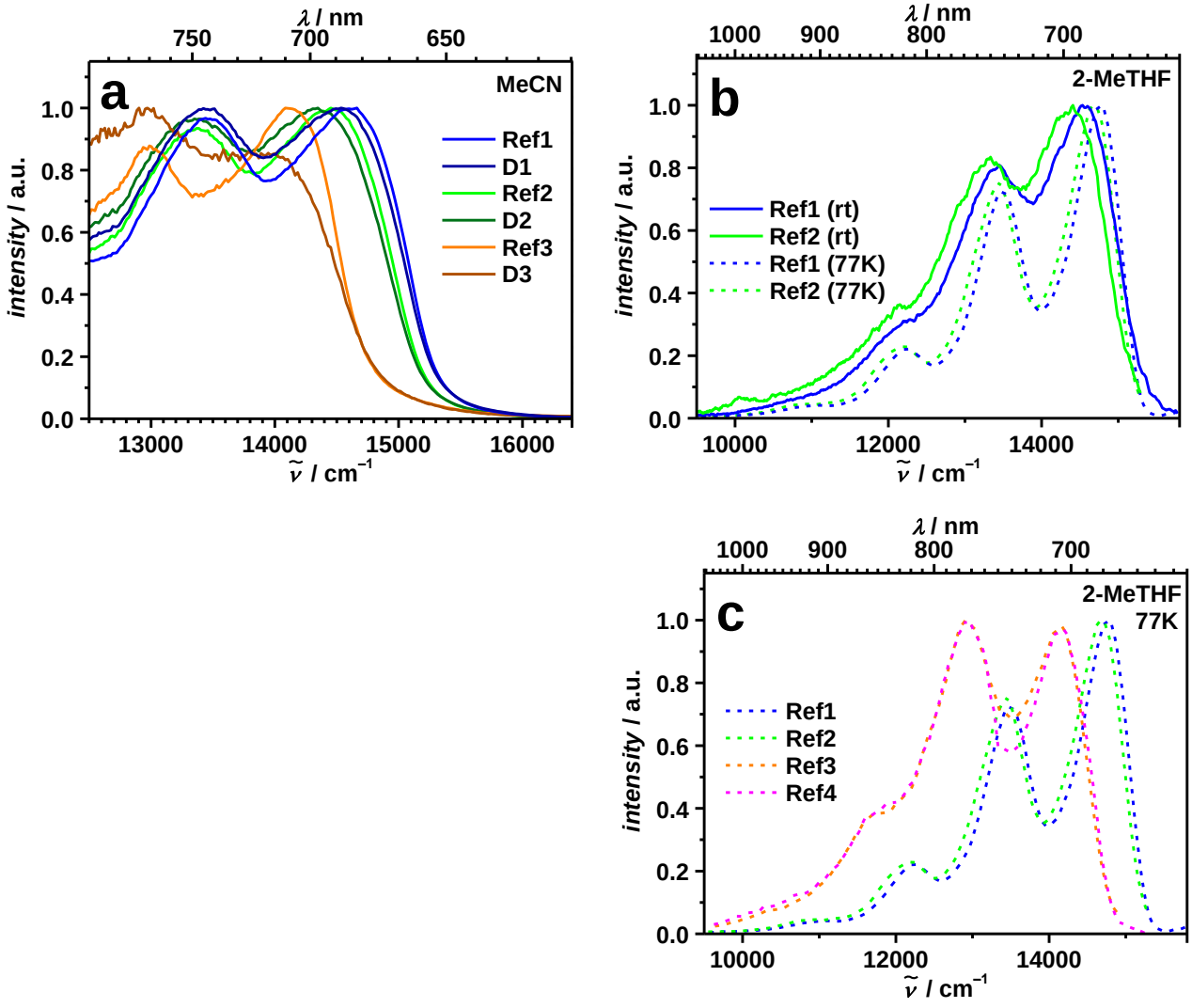

Figure 94 Emission spectra of reference complexes and dyads (a) **Ref1–Ref3** and **D1–D3** in MeCN, (b) **Ref1–Ref3** and **D1–D2** in 2-MeTHF at rt and 77K and (c) **Ref1–Ref4** in 2-MeTHF at 77K. A photomultiplier (R928P) was used to record the UV/Vis spectra in MeCN whereas an InGaAs-detector recorded the NIR spectra in 2-MeTHF.

The energy content of the iridium dipyrrin triplet state associated with the phosphorescence emission was determined by fitting a tangent on the rising edge of the high energy side of the emission spectra. The intersection with the x-axis yielded $E(^3\text{Ir}) = 1.91$, 1.89 and 1.83 eV for **Ref1**, **Ref2** and **Ref3**, respectively, in MeCN. These values will be used later on for the energy of the ^{3}Ir state.

The emission characteristics of all complexes can be described as very weak LC phosphorescence which is located at the dipyrrin ligand. Hence, the emission energy changes within the different dipyrrins. For the unsubstituted ref-dyad pair **Ref1**-**D1** the highest excited state energy was estimated to 1.91 eV, whereas the **Ref2**-**D2** pair has a slightly lower energy with 1.89 eV. Although the absorption data show no discrepancy between **Ref1** and **Ref2**, the emission features indicate little influence of the chloro-group in *para*-position of the phenyl ring in *meso*-position of the dipyrromethane. The energetic shift is further increased within **Ref3**-**D3** where two chloro-substituents are linked to the pyrrole cores. In addition, the observed shifts for the emission bands are similar to the shifts of the absorption maxima (Table 18). Unfortunately, no emission spectra of the **Ref4**-**D4** pair at rt could be recorded. However, the EWG functionalisation of the dipyrrins seems to affect the HOMO-LUMO gap. Hence, either the LUMO or the HOMO are influenced by the EWGs which results in a lower emission energy. DFT calculations may be a helpful tool to investigate this aspect in more detail in the future.

Interestingly, all reference complexes strongly emit in a glassy matrix at 77K. **Ref1** and **Ref2** look the same but differ in their maxima by ca. 100 cm^{-1}, whereas **Ref3** and **Ref4** are stronger influenced by the EWG substituents (larger shift and changed relative intensities). The lifetimes of the 77K emissions are in a typical range for LC emissions with several µs.

Table 19 Emission data of **Ref1**–**Ref4** in MeCN at rt and in 2-MeTHF at rt and 77K. The reference complexes stand exemplarily for the dyads.

	solvent	$\tilde{\nu}_{max}$ (λ_{max}) / cm^{-1} (nm)	Φ_{em}	τ_{em} / µs
Ref1[1]	MeCN	14 700 (680) 13 400 (746)	0.016[5]	1.68[4]
	2-MeTHF (rt)	14 500 (690) 13 400 (746) 12 300 (813)	0.06[3]	5.3[3]
	2-MeTHF (77K)	14 800 (676) 13 500 (741) 12 200 (820) 11 100 (901)	×	17.8[4]
Ref2[1]	MeCN	14 500 (690) 13 400 (746)	–	×
	2-MeTHF (rt)	14 400 (690) 13 300 (746) 12 200 (813)	×	×
	2-MeTHF (77K)	14 700 (680) 13 400 (746) 12 100 (826) 11 000 (909)	×	12.2[4]
Ref3[2]	MeCN	14 100 (709) 13 000 (769)	–	×
	2-MeTHF (rt)	×	×	×
	2-MeTHF (77K)	14 200 (704) 12 900 (775) 11 800 (847)	×	51.9[4]
Ref4[2]	MeCN	×	–	×
	2-MeTHF (rt)	×	×	×
	2-MeTHF (77K)	14 200 (704) 12 900 (775) 11 900 (840)	×	6.5[4]

[1] complexes were excited at 20 800 cm^{-1} (480 nm) or at [2] 20 000 cm^{-1} (500 nm), [3] according to ref.[142], [4] see Appendix for decay profiles, [5] determined by a calibrated integrating sphere, – was estimated to be <1 %, × could not be determined.

3.3.4 Cyclic Voltammetry (CV)

After evaluation of the absorption and emission characteristics of the dyads and their reference complexes, the electrochemical properties will be discussed. In Figure 95 the cyclic voltammograms measured in MeCN are displayed and separated in their oxidative (b, d) and reductive (a, c) parts. The reference complexes are shown on top and the dyads on the bottom. All potentials are listed in Table 20. Similarly, the same analytical procedure can be used as in the emission measurements. First, the reference-dyad pairs can be treated as being identical, except the additional oxidation of the TAAs in the dyads. Second, the **Ref1**-**D1** pair serves as starting point for the discussion and shifts will be given relative to that pair.

The oxidation potentials of the dipyrrin oxidation of **Ref2**-**D2** are almost identical to the first reference-dyad pair, whereas their reductive potential is shifted by ca. 50 mV to higher potentials. The different reduction may be explained by the chloro-substituent in the **Ref2**-**D2** pair which has an influence on the reduction potential but not on the oxidation. An inductive effect may only be responsible for the little change in the reduction potential because the 90° twist (*vide supra*) of the phenyl ring in *meso*-position reduces an effective π-conjugation. In line with that are the findings of the *Thompson* group who calculated HOMO and LUMO orbitals of **Ref1**. According to them, the phenyl ring has a significant contribution on the LUMO, whereas the HOMO is solely located on the dipyrrin ligand.[142] These results may explain the stronger effect on the reduction which is strongly correlated to the LUMO.

On the contrary, the effect of EWGs at the core positions of the pyrrole is more pronounced for the reduction as well as for the oxidation process. A shift of the reduction peaks of ca. 190 mV can be observed for the **Ref3**-**D3** pair, whereas nearly 400 mV were found for the last pair (**Ref4**-**D4**). Consequently, the opposite electronic effects of the cyano group on one side and the dimethyl groups on the other side still results in a more electron deficient dipyrrin framework compared to the chloro-substitution in the **Ref3**-**D3** pair. At this point it has to be mentioned that all reductions in MeCN discussed before seem to be reversible redox processes but under multiple thin layer conditions only **Ref4** and **D4** exhibited perfectly reversible redox waves. This may be related to the blocked pyrrole positions by cyano and methyl substituents, whereas all other dipyrrins have at least two positions available to undergo further reactions in the reduced form.[396]

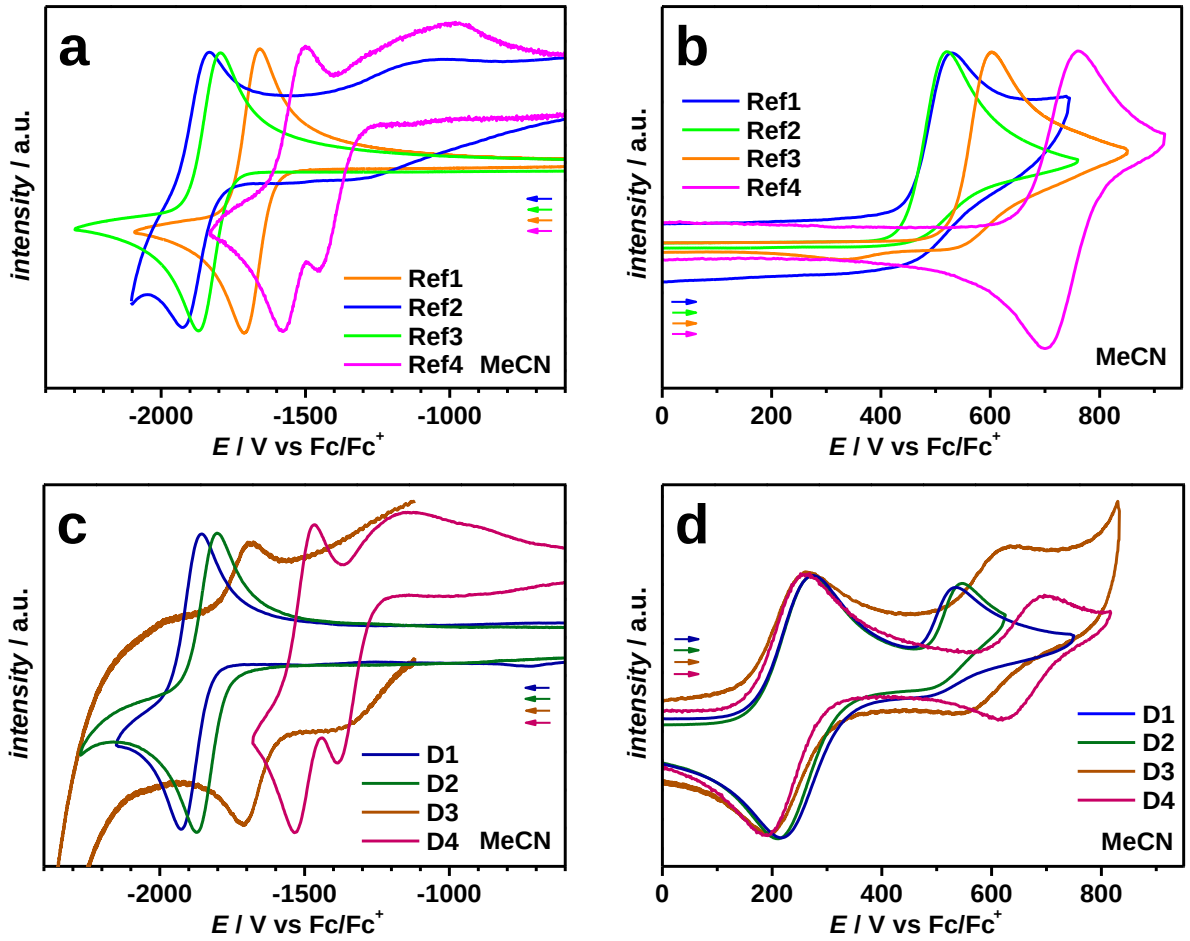

Figure 95 (a) Reduction and (b) oxidation part of **Ref1–Ref4** and (c) reduction and (d) oxidation part of **D1–D4** in MeCN/[nBu$_4$][PF$_6$] (0.1 M) at a scan rate of 250 mV s^{-1}. All voltammograms are referenced against (Fc/Fc$^+$), normalised.

The **Ref4**-**D4** pair shows an additional reduction at higher potentials with a delayed back-oxidation at ca. –1145/–965 mV. It can be excluded that the additional reduction is caused by the Ir(ppz)$_2$-fragment and its donor part because this group is identical to all other dyads and the reduction is missing there. Furthermore, the cyanophenyl moiety in *meso*-position is relatively isolated because of the nearly 90° twist relative to the π-plain of the dipyrrin. In addition, the methyl-groups manifest this orientation and hamper a possible rotation of the phenyl group.[141] For that reason, the attached phenyl ring is more or less equal to a benzonitrile moiety which can be oxidised at ca. –2.8 eV[157] vs. Fc/Fc$^+$ and can be excluded as the origin of the additional reduction. BODIPYs show only one reduction wave when they are formed from a dipyrromethane with a hydroxy methylene instead of a

cyanophenyl group in *meso*-position of the otherwise identical dipyrromethane **31**.[393] Thus, at the moment the origin of the second reduction process with a back oxidation at much higher potentials is speculative. A structural change e.g. the omission of the CN-group on the phenyl unit or the use of another solvent in the CV experiment may help to elucidate the origin of that redox process.

Next, the oxidation processes (Figure 95b and d) are discussed. The reference complexes show one oxidation process whereas for the dyads an additional one is detected. The oxidation above 500 mV found in **Ref1–Ref4** is present in the dyad complexes **D1–D4**, too, and is assigned to the oxidation of the Ir(dipy) moiety. The second redox process in the dyads which occurs at lower potentials corresponds to the TAA units at 230–245 mV. Similar, the oxidation is influenced more strongly by the core substitutions than by the substitution on the phenyl ring (*vide supra*). The oxidation of the dipyrrin units of the first two pairs (**Ref1**-**D1**, **Ref2**-**D2**) occur almost at the same potential (cathodic peak potential ca. 530 mV), whereas **Ref3**-**D3** and **Ref4**-**D4** are shifted by 75 and at least 120 mV, respectively. Hence, the oxidation is less affected by the core substitution than the reduction. It has to be stressed that for the first three pairs only cathodic peak potentials were measured, whereas for the **Ref4**-**D4** pair a reversible redox wave was obtained. This would lead to a higher cathodic peak potential and a larger shift of the latter two complexes if one compares only the peak potentials. In addition, a further oxidation could be detected in **Ref4** (at ca. 1030 mV, not shown) which is irreversible and can be assigned to an oxidation of the $Ir(ppz)_2$-fragment. Interestingly, after scanning the oxidation of the dipyrrin and $Ir(ppz)_2$-moieties the back-reduction of the dipyrrin gets irreversible, too. This may be a result of a follow-up reaction during the second irreversible oxidation of the $Ir(ppz)_2$-fragment.

The redox potentials of the first oxidation and reduction provide the possibility to calculate the state energy of the charge-separated states within the dyads where the TAA is oxidised and the iridium dipyrrin is reduced. The approach according to Weller (eq. (3)) was used to determine these values (Table 21) in MeCN.

$$\Delta G^{00} = \frac{N_A}{1000} ze\left[E_{ox}(D/D^+) - E_{red}(A/A^-)\right] - \frac{N_A e^2}{1000 \cdot 4\pi e_0}\left[\left(\frac{1}{2r_D} + \frac{1}{2r_A}\right)\left(\frac{1}{\varepsilon_r} - \frac{1}{\varepsilon_s}\right) + \frac{1}{\varepsilon_s d_{DA}}\right] \quad (3)$$

MeCN will also be used in the transient absorption spectroscopy (see next section). The obtained values for the CS state energy of E_{CS} = 2.14, 2.05, 1.89 and 1.70 eV subsequently

decrease from dyad **D1** to **D4**. The decrease in energy is exclusively caused by the changed reduction potentials, while all other parameters stay constant. Although the radii of the acceptor change for the different dipyrrin ligands, the changes were neglected for simplification. No significant effect is expected for slightly larger radii for the dipyrrin chromophore in **D3** and **D4**.

In addition, the energy of the excited triplet state of the dyads was estimated by fitting a tangent on the rising edge of the emission band of the reference complexes and are listed in Table 20.

Table 20 Redox potentials[1] ($E_{1/2}$) and potential difference between the first reduction and oxidation ($\Delta E_{1/2}$) of **Ref1**–**Ref4** and **D1**–**D4** in 0.1 M [*n*Bu$_4$][PF$_6$]/MeCN.

	Ir(dipy) $E^{red}_{1/2}$ / mV	E^{red}_{pc} (E^{red}_{pa}) / mV	TAA $E^{ox}_{1/2}$ / mV	Ir(dipy) E^{ox} / mV	$\Delta E_{1/2}$ / mV
Ref1	−1880^{i}			530^{pa,i}	2410
Ref2	−1830^{i}			520^{pa,i}	2350
Ref3	−1700^{i}			605^{pa,i}	2305
Ref4	−1515^{r}	−1385^{i} (−1145)^{i}		720^{r} 1035^{i,3}	2245^{2} 2115
D1	−1895^{i}		245^{r}	535^{pa,i}	2140
D2	−1840^{i}		240^{r}	545^{pa,i}	2080
D3	−1690^{i}		230^{r}	630^{pa,i}	1920
D4	−1500^{r}	−1450^{i} (−965)^{i}	230^{r}	660^{r}	1730^{3} 1680

[1] all potentials are referenced against Fc/Fc^{+} and were measured at a scan rate of 250 mV s^{-1}
[2] $\Delta E_{1/2}$ between the dipy reduction and oxidation, [4] Ir(ppz)$_2$ oxidation.
E_{pa} = anodic peak potential, E_{pc} = cathodic peak potential ^{r} reversible, ^{i} irreversible

Dyads **D1**–**D3** exhibit CS state energies which lie above the emissive ^{3}Ir state as can be seen from Table 21. The energy separation (ΔE(CS-^{3}Ir)) between these two states decreases gradually from 0.23 to 0.06 eV in **D1** to **D3**. On the contrary, for **D4** a change of the state

order can be observed. The corresponding CS state is estimated to be 0.13 eV below the ^{3}Ir state because the cyano-dimethyl substitution has a stronger effect on the electrochemical than on the spectroscopic properties compared to the chloro-functionalisation. Besides, the origin of the additional irreversible reduction process at higher potentials is not yet clarified and may disturb the ET in **D4**.

Table 21 Energy content (ΔG_{CS}) of charge-separated (CS) states of **D1–D4** in MeCN determined with the oxidative and reductive redox potential (E^0(A,D)), the donor-acceptor distance (d_{DA}) and the radii of the redox centres ($r_{A,D}$) according to eq. (3).

	solvent	E^0(A)[1] / mV	E^0(D)[1] / mV	d_{DA} / 10^{-10} m	r_D / 10^{-10} m	r_A / 10^{-10} m	ΔG^{00} (CS) / eV	ΔG^{00} (^{3}Ir) / eV
D1	MeCN	−1895[i]	245[r]	12.3	4.81	5.32	2.14	1.91
D2	MeCN	−1840[i]	240[r]	12.3	4.81	5.32	2.05	1.89
D3	MeCN	−1690[i]	230[r]	12.3	4.81	5.32	1.89	1.83
D4	MeCN	−1500[r]	230[r]	12.3	4.81	5.32	1.70	1.83[a]

[1] CV experiments performed in MeCN/[nBu$_4$][PF$_6$] (0.1 M) with ε_r(MeCN) = 35.49.
[r] reversible, [i] irreversible, [a] is expected to be in the order of the ^{3}Ir state energy of the **Ref3**-**D3** pair, because of almost identical 77K spectra and similar steady-state maxima.

3.3.5 Transient Absorption Spectroscopy

In the preceding sections the electrochemical and photophysical aspects of the dyads (**D1–D4**) and their reference complexes (**Ref1–Ref4**) revealed the state energies of the singlet and triplet excited states of the different iridium complexes. Furthermore, the iridium triplet state was contrasted with the CS state energies. From that the following prediction was made: Charge separation will only be expected for **D4**, whereas all other dyads possess a energetically lower lying ^{3}Ir state, which will act as a trap for the CS process. To clarify this, **Ref1**-**D1**, **Ref2**-**D2** and **Ref3**-**D3** will be investigated with ns-laser flash spectroscopy and for **Ref4**-**D4** fs-pump probe spectroscopy will be carried out.

The analysis of **Ref1** was already carried out in section 3.1.1.6 and can be summarised as follows: i) The LC triplet state (^{3}Ir) of the iridium dipyrrin complex shows almost no excited-state absorption. Consequently, a bleaching of the absorption band in the visible spectral region (maximum at 20 800 cm^{-1} (480 nm)) is detected (cf. Figure 37). ii) The lifetime τ_1 = 1.86 µs of the ground state recovery reflects quiet well the emission lifetime of the LC emission (τ_{em} = 1.68 µs).

Likewise, the dyad complex **D1** shows ground-state bleaching (GSB) but with a somewhat shorter lifetime of τ_1 = 810 ns (Figure 96). The shorter lifetime may be caused by a larger molecular structure of the dyad in comparison to the reference complex **Ref1**. The larger structure may increase the non-radiative deactivation of that complex. This is in line with a reduced quantum yield of the LC emission in **D1** of Φ_{em} = 1.0 % compared to **Ref1** (Φ = 1.6 %). The CS state energy E_{CS} = 2.14 eV in **D1** is energetically higher than the emissive ^{3}Ir state energy E_{3Ir} = 1.91 eV (Table 21). For that reason, a CS state is energetically not favoured and was not involved in the ET processes described in chapter 3.1.

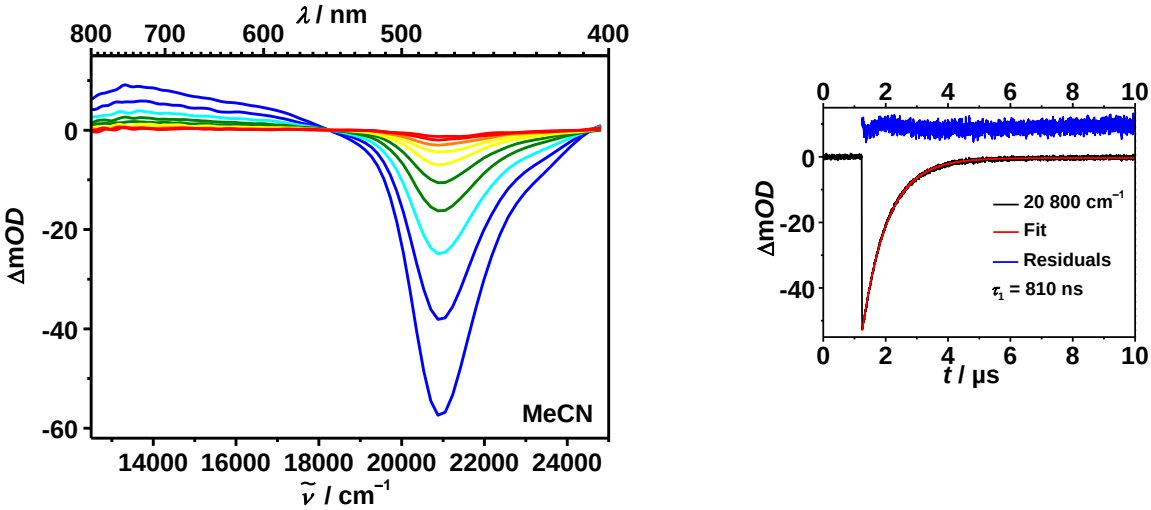

Figure 96 ns-Transient absorption spectra of **D1** in MeCN (0–0.95 µs) and corresponding time scans and fits at 20 800 cm^{-1} (480 nm). Early spectra are shown in blue/green and spectra at later times in yellow/orange/red colours.

For **D1** no ET could be observed because of the high lying CS state. The same is predicted for the pairs **Ref2**-**D2** and **Ref3**-**D3**. Indeed, all complexes exclusively show GSB as can be seen in Figure 97 and 98. Due to similar absorption features the transient absorption

spectra of the **Ref2**-**D2** pair are identical to the **Ref1**-**D1** pair. In addition, the lifetime of the ^{3}Ir state of **Ref2** (τ_1 = 1.02 µs) is longer as that of **D2** (τ_1 = 395 ns).

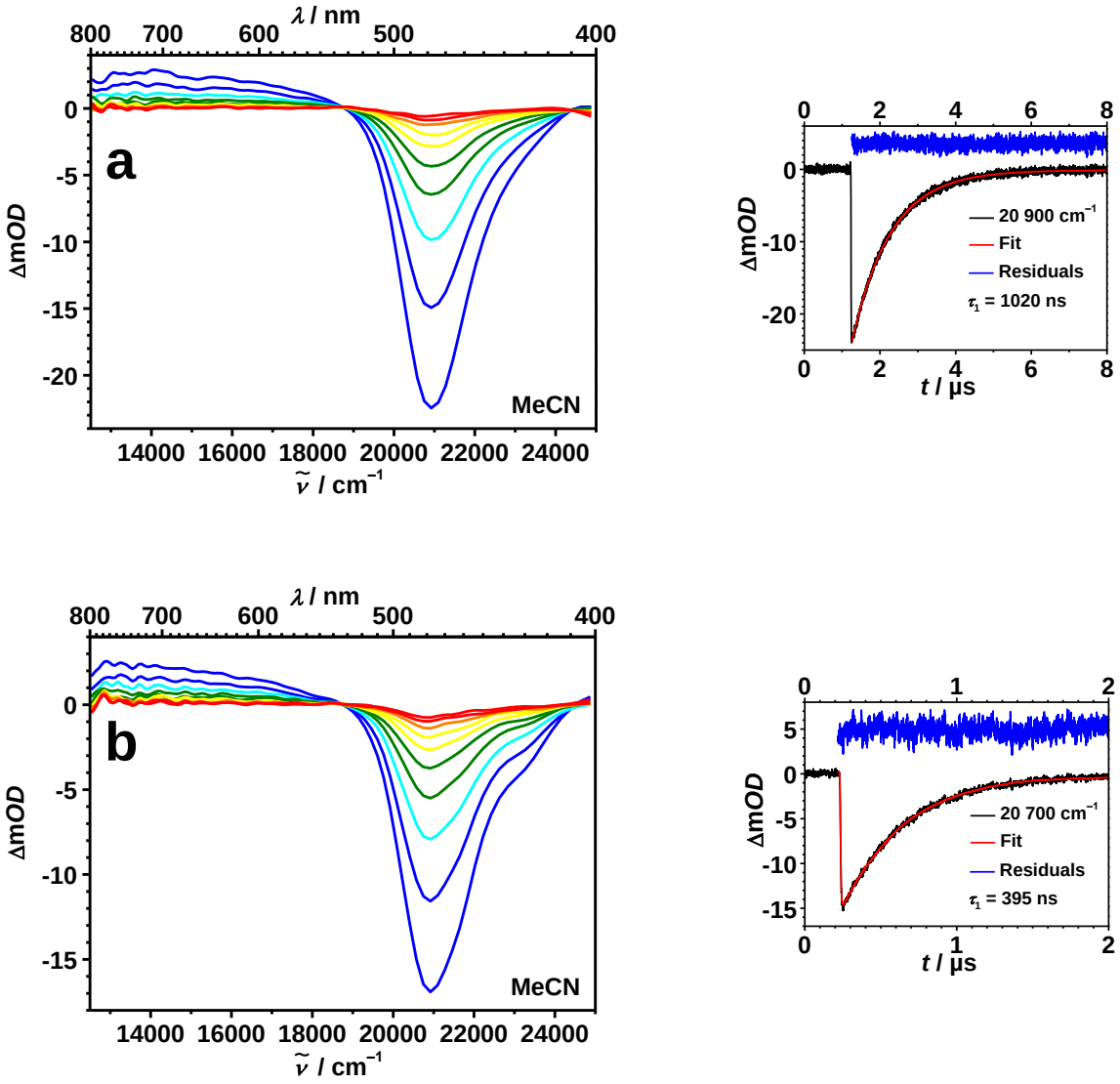

Figure 97 ns-Transient absorption spectra of (a) **Ref2** in MeCN (0–2.8 µs) and (b) **D2** in MeCN (0–1.5 µs) and corresponding time scans and fits at 20 900 cm^{-1} (478 nm) and 20 700 cm^{-1} (482 nm), respectively. Early spectra are shown in blue/green and spectra at later times in yellow/orange/red colours.

Likewise, the **Ref3**-**D3** pair shows only GSB and the lifetime of the ^{3}Ir state is lower in the dyad (τ_1 = 200 ns) than in the reference complex (τ_1 = 311 ns) as it is the case in the two former pairs. Conversely, their bleaching maxima (20 000 cm^{-1} (500 nm)) is located at lower energies due to a shifted absorption band (cf. Figure 93) compared to the first two pairs. The energy difference between the CS state and the emissive LC state is now reduced to ca. 0.06

eV (Table 21) and a more polar solvent may minimise or overcome this energy difference to yield a lower lying CS state.

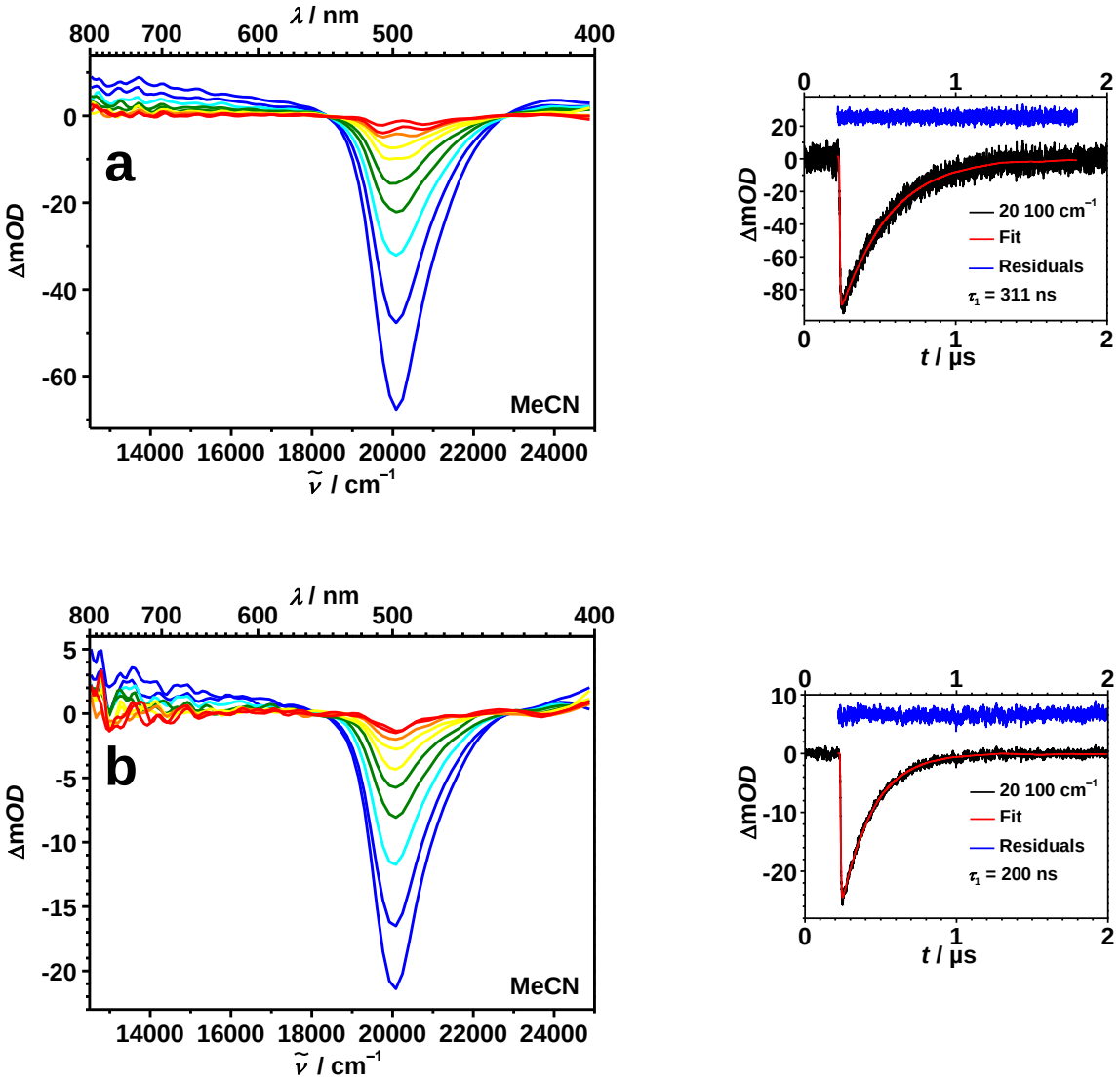

Figure 98 ns-Transient absorption spectra of (a) **Ref3** in MeCN (0–1.0 µs) and (b) **D3** in MeCN (0–0.7 µs) and corresponding time scans and fits at 20 100 cm^{-1} (478 nm). Early spectra are shown in blue/green and spectra at later times in yellow/orange/red colours.

Finally, the **Ref4**-**D4** pair is investigated by fs-pump-probe spectroscopy (details of the set-up and the global analysis can be found in section 3.1.1.6) because with the ns-laser flash set-up no kinetic traces could be recorded. Both complexes were excited at 20 000 cm^{-1} (500 nm) laser energy and the evolution associated difference spectra (EADS) with the

corresponding transient absorption evolution plus decay kinetics at selected wavelengths are shown in Figure 99 and 100.

From the global analysis of **Ref4** two EADS were obtained with τ_1 = 200 ps and τ_2 = 2.6 ns. Both EADS show almost identical GSB at ca. 20 000 cm^{-1} (500 nm) which is in agreement with the absorption spectrum in Figure 93. Similarly, a second bleaching spectrum was already observed for **Ref1** within the fs-transient absorption analysis (cf. Figure 46). On the contrary, the fitted lifetimes for **Ref1** differ significantly from **Ref4** with τ_1 = 51 ps and τ_2 = 1.86 µs. First, the shorter lifetime is by a factor of ca. 4 longer in **Ref4** than in **Ref1**. The first lifetime has been assigned to a conformational change of the phenyl ring in the *meso*-position of the dipyrrin in **Ref1**. For **Ref4** the situation is somewhat different because methyl substituents connected to the core position hamper or block completely the rotation of the phenyl unit in the *meso*-position. If the rotation is still possible in **Ref4** this may explain the longer time constant (200 ps) for the first bleaching spectrum compared to **Ref1** (51 ps).

An important trend is present for the second and longer lifetime of the relaxed ^{3}Ir state. Going from **Ref1** to **Ref4** the lifetime of the lowest excited state decreases subsequently from 1.86 µs to 2.6 ns. The structural change of the dipyrrin framework may be responsible for the drop of the lifetimes. From BODIPY derivatives and zinc dipyrrin complexes it is known that a hindered rotation of the phenyl ring caused by methyl substituents on the *ortho*-positons of the phenyl ring lead to longer lifetimes and higher quantum yields of these compounds. This is attributed to less effective non-radiative deactivation processes related to the hampered rotation of the phenyl group.[141] In addition, *Thompson et al.* determined a higher quantum yield of the phosphorescence with a mesitylene instead of a phenyl group in *meso*-position of the iridium dipyrrin framework.[142] Hence, **Ref4** should show longer lifetimes due to the reduced conformational flexibility due to the methyl groups at the pyrrole cores which is obviously not the case. Moreover, the methyl groups pointing to the iridium complex may distort the dipyrrin π-system compared to the unsubstituted dipyrrins. Thus, non-radiative deactivation pathways are favoured in **Ref4**.

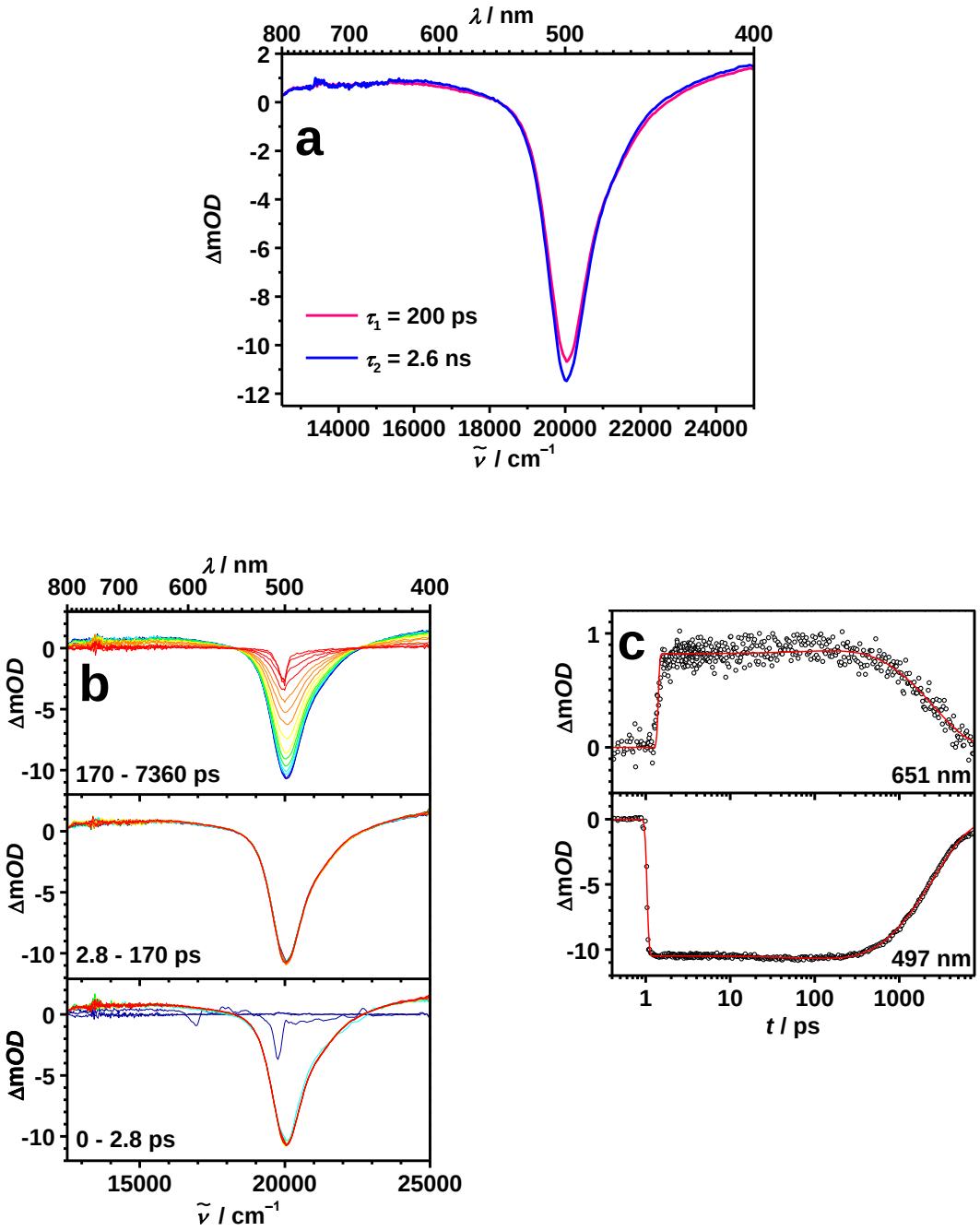

Figure 99 (a) Evolution associated difference spectra (EADS) of **Ref4** from a global analysis of a transient map. (b) fs-Transient absorption data corrected for chirp and scattered pump light. Early spectra are in blue to green and in orange to red colours at later times. (c) Decay profiles at selected wavelengths for which the zero time delay was set arbitrarily. Excitation at 20 800 cm^{-1} (480 nm) in MeCN.

The last transient absorption analysis focuses on the excited state properties of **D4** in which the CS state was postulated to be energetically lower in energy by 0.17 eV than the iridium triplet state. Consequently, a triarylamine radical cation at ca. 13 700 cm^{-1} (730 nm)

and a bleaching signal for an oxidised iridium dipyrrin radical anion are expected in MeCN. The first EADS of the global analysis possesses the same features for the ^{3}Ir state as those for **Ref4** but this time with a reduced lifetime of τ_1 = 60 ps. The following state has a lifetime of τ_2 = 3.9 ns and shows GSB at 20 000 cm^{-1} (500 nm) for the corresponding EADS. In addition, a slightly increased excited-state absorption (ESA) can be seen at 13 700 cm^{-1} (730 nm). Although the TAA cation is expected at around 13 700 cm^{-1} (730 nm), the excited state absorption intensity is relatively low for such a monoradical cation. Additionally, the relatively high noise ratio affects the ESA and increases spectral uncertainties in this spectral region. Moreover, the additional reduction process (cf. CV of **Ref4** and **D4**) may lead to a different follow-up product in **D4** whose origin is not disclosed, yet. However, an ET process which may run simultaneously can in principle generate a CS state with a low concentration. This then would result in a very low ESA of the monoradical cation. The slightly higher lifetime of the second EADS compared to that in **Ref4** (2.6 ns) is in contrast to a pure ^{3}Ir state because the lifetimes for the dyads were always shorter than for the reference complexes. Moreover, the reduced lifetime of the first EADS (60 ps in **D4** and 200 in **Ref4**) points to a faster follow-up reaction in **D4** which may be correlated to an ET.

However, at this moment a final conclusion is not possible until the origin of the additional reduction process is unclear. As already mentioned in the electrochemistry section, the change of the substitution on the phenyl unit of the dipyrrin may help to get an idea of that redox process. The aim should be to switch off the unwanted irreversible reduction process to increase the possibility of an ET from the TAA to the iridium dipyrrin unit.

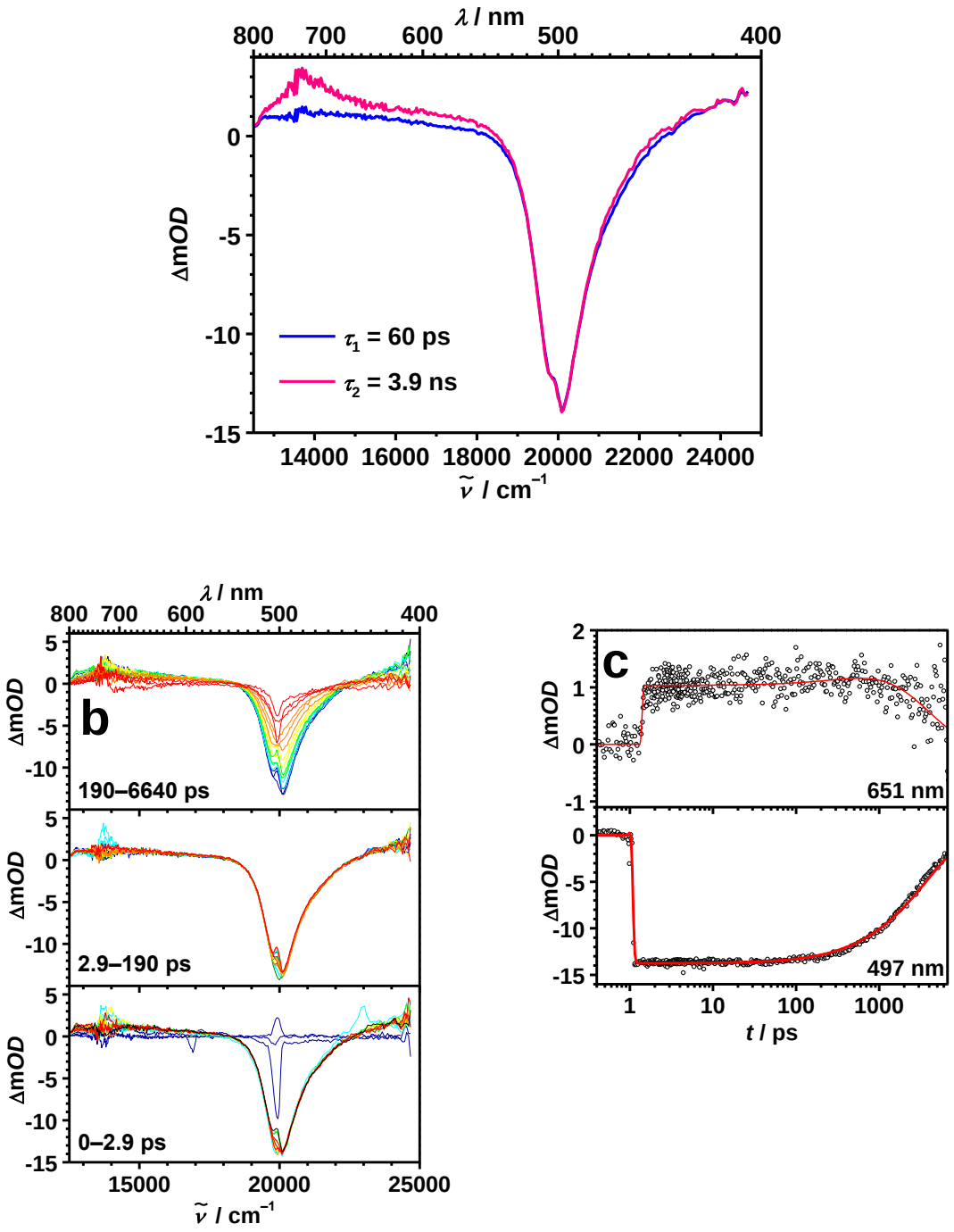

Figure 100 (a) Evolution associated difference spectra (EADS) of **D4** from a global analysis of a transient map. (b) fs-Transient absorption data corrected for chirp and scattered pump light. Early spectra are in blue to green and in orange to red colours at later times. (c) Decay profiles at selected wavelengths for which the zero time delay was set arbitrarily. Excitation at 20 800 cm^{-1} (480 nm) in MeCN.

3.3.6 Conclusion and Future Outlook

In the present chapter the synthesis of four reference-dyad pairs (**Ref1**–**Ref4**, **D1**–**D4**) was reported. Expect for the **Ref4**-**D4** pair acceptable yields were obtained. Unfortunately, the realisation of additional dyads where the phenyl unit in the *meso*-position of the dipyrrin is substituted by a triple bond was not successful. Further synthetic effort is necessary to overcome this problem e.g. a palladium catalysed cross coupling on the iridium complex. Hence, a dipyrromethane with a bromo or iodo functionalisation in the *meso*-position of the dipyrrin ligand is needed. This ligand will coordinate to the iridium metal and a *Sonogashira*-coupling between that complex and an phenylacetylene will result in the desired complex (Scheme 21).[397] Furthermore, the origin of the irreversible reduction has to be clarified. First, the cyano group attached to the phenyl ring should be omitted and second the substitution of the cyano groups in the core position of pyrroles by chloro atoms may be illuminating (Scheme 21).

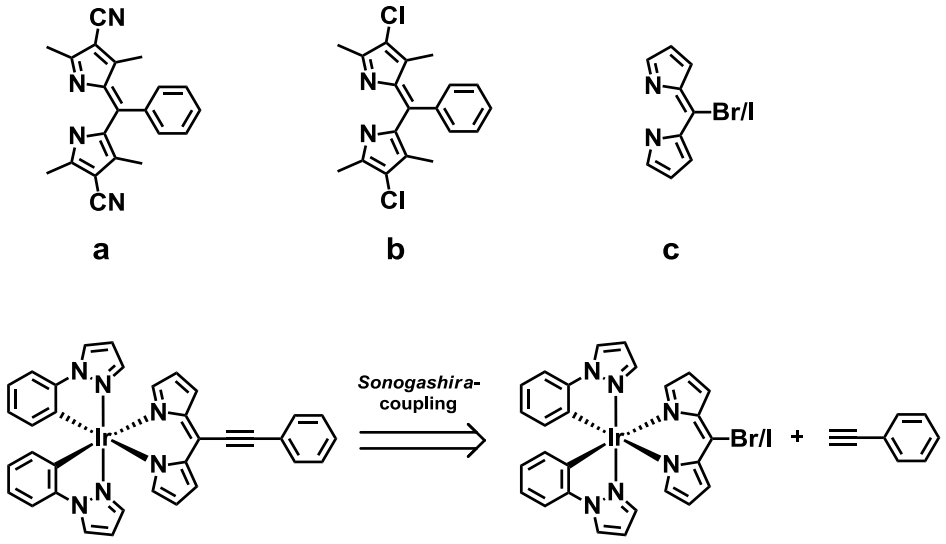

Scheme 21 Future projects to reveal the occurrence of the irreversible reduction in **D4** (with the dipyrrins a and b). Retrosynthetic strategy for a triple bond functionalisation to the dipyrrin framework using dipyrrin c (bottom).

The spectroscopic properties of the complexes revealed a bathochromic shift of the absorption upon substituting the pyrrole core with EWGs. The same is true for the emission except the **Ref4**-**D4** pair is not luminescent at rt. In addition, the LC absorption intensity is

increased significantly in **Ref4** and **D4**, whereas the effect is less pronounced in **Ref3**-**D3**. In a glassy 2-MeTHF matrix all complexes show an intense phosphorescence signal.

The transient absorption spectra show GSB for all complexes with lifetimes ranging from 3 ns to 1.86 µs. The dyads **D1**–**D3** have shorter lifetimes than their reference complexes due to additional non-radiative deactivation processes. The GSB signals for **D1**–**D3** are in agreement with the lower lying energy of the emissive ^{3}Ir states than for the calculated CS states in the dyads.

Ref4 exhibits two EADS with identical bleaching spectra as it was already observed for **Ref1**, whereas for **D4** two slightly different GSB features could be detected. One is identical to the **Ref4** spectra and the other shows little ESA at around 17 300 cm^{-1} (730 nm) where a TAA radical cation is expected. Although the presence of the CS state was predicted by a lower lying CS state, the spectral features are not a sufficient prove for charge separation. The additional redox process whose origin is not yet resolved may be responsible for a different follow-up reaction. Hence, the lifetime of 3.9 ns corresponding to the second EADS of **D4** may be assigned either to the charge recombination of the CS state or to the phosphorescence of the ^{3}Ir state (Figure 101).

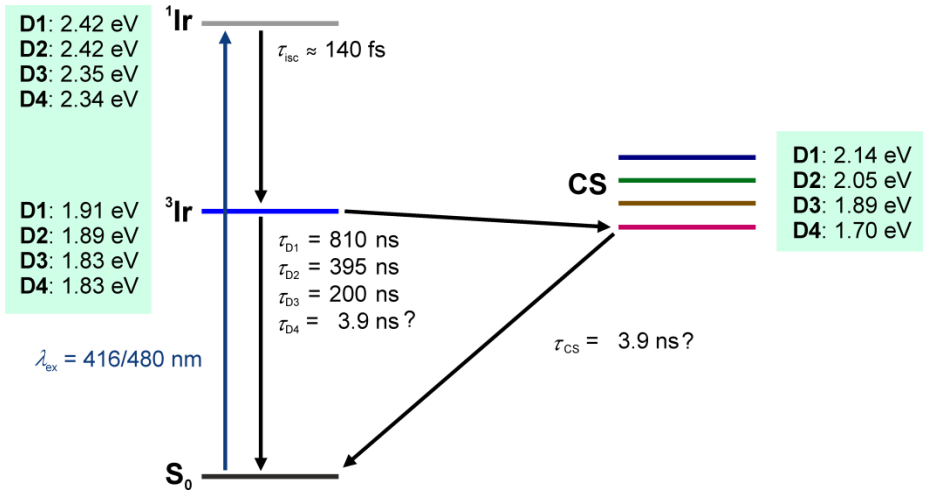

Figure 101 Energy state diagram of dyads **D1**–**D4** in MeCN with singlet and triplet excited and CS state energies.

In conclusion, it was possible to influence the excited state energies by a subsequent change of the ligand architecture of the dipyrrin ligand. The electrochemical properties were changed at the same time with the spectroscopic features. But only in **D4** the CS state energy was below the ^{3}Ir state energy.

4 Summary

The successful synthesis of a family of donor-iridium complex-acceptor triads (**T1–T6**, **pMV1** and **mMV1**) and their electrochemical and photophysical properties were presented in this work. Triarylamines (TAA) were used as donors and naphthalene diimide (NDI) as acceptor. A *bis*-cyclometalated phenylpyrazole iridium dipyrrin complex acts as a photosensitiser. In addition, a molecular structure of **T1** was obtained by single crystal X-ray diffraction.

Transient absorption spectroscopy experiments of these triads resembled that upon excitation a photoinduced electron transfer efficiently generates long-lived, charge-separated (CS) states. Thereby, the electron-transfer mechanism depends on the excitation energy.

The presence of singlet and triplet CS states was clarified by magnetic-field dependent transient-absorption spectroscopy in the nanosecond time regime. It was demonstrated that the magnetic field effect of charge-recombination kinetics showed for the first time a transition from the coherent to the incoherent spin-flip regime.

The lifetime of the CS states could be drastically prolonged by varying the spacer between the iridium complex and the NDI unit by using a biphenyl instead of a phenylene unit in **T4**.

A mixed-valence (MV) state of two TAA donors linked to an iridium metal centre were generated upon photoexcitation of triad **pMV1** and **mMV1**. The mixed-valence character in these triads was proven by the analysis of an intervalence charge-transfer (IV-CT) band in the (near-infrared) NIR spectral region by femtosecond pump-probe experiments. These findings were supported by TD-DFT calculations.

The synthesis of dyads (**D1–D4**) was performed. Thereby the dipyrrin ligand was substituted with electron withdrawing groups. The electrochemical and photophysical characterisation revealed that in one case (**D4**) it was possible to generate a CS state upon photoexcitation.

.

5 Experimental Section[1]

5.1 Analytical Methods

5.1.1 Steady-State Absorption Spectroscopy

- JASCO V-670 UV/Vis/NIR spectrometer (software SpectraManager v. 2.08.04)
- Agilent Technologies Cary 5000 UV-Vis-NIR spectrophotometer (software Agilent Cary WinUV Analysis and Bio v.4.2)

All solvents were spectroscopic grade and were used without further purification, only THF was destilled prior to use. Absorption spectra were recorded in 1 cm quartz cuvettes from Starna (Pfungstadt, Germany) at rt. Aggregation of the samples could be excluded by a concentration independent behaviour (10^{-6}–10^{-5} M).

Singlet energies of the reference complexes were determined by fitting a tangent on the inflexion point of the low energy side of the low energy absorption band and the x-axis.

5.1.2 Steady-State Emission Spectroscopy

- Photon Technology International QuantaMaster™ model QM-2000-4 including a cooled photomultiplier (R928 P), an InGaAs detector and a xenon short-arc lamp (75 W, Ushio UXL-75XE), (software FeliX32™ v. 1.2.0.56)

[1] Reproduced or adapted in part with permission from a) *Stepwise versus pseudo-concerted two-electron-transfer in a triarylamine–iridium dipyrrin–naphthalene diimide triad*, J. H. Klein, T. L. Sunderland, C. Kaufmann, M. Holzapfel, A. Schmiedel, C. Lambert, *Phys. Chem. Chem. Phys.* **2013**, *15*,16024-16030. - Reproduced or adapted in part by permission of the PCCP Owner Societies; b) *A photoinduced mixed-valence state in an organic bis-triarylamine mixed-valence compound with an iridium-metal-bridge*, C. Lambert, R. Wagener, J. H. Klein, G. Grelaud, M. Moos, A. Schmiedel, M. Holzapfel, T. Bruhn, *Chem. Commun.* **2014**, *50*, 11350-11353. - Reproduced by permission of The Royal Society of Chemistry; c) *On the Spin-Chemistry of Charge Separated States in Donor-Iridium Complex-Acceptor Triads,* J. H. Klein, D. Schmidt, U. E. Steiner, C. Lambert, *J. Amer. Chem. Soc.* **2015**, DOI: 10.1021/jacs.5b04868. Copyright 2015 American Chemical Society.

Steady state emission spectra at room temperature were recorded in 1 cm quartz cells from Starna (Pfungstadt, Germany). All solvents were of spectroscopic grade and were used without further purification, only THF was destilled prior to use. The concentration was ca. 10^{-6}–10^{-5} M and oxygen was removed by bubbling inert gas through the solutions for at least 30 min before each measurement.

The luminescence quantum yields were determined by a calibrated integrating sphere (labsphere, North Sutton, NH, USA). For the assignment of the quantum yield two spectra, one with solely the solvent and a second with the soluted dye, were recorded. Both spectra were multiplied by a correction file of the spectrometer and by the the corresponding wavelength at each intensity value. Thereafter, the dye spectra was substracted by the solvent spectra and the resulting difference spectra were integrated in two wavelength regimes. The first integration covers the area under the excitation light (I_{ex} (λ)), which is equal to 100 % and the second integration equals the area under the emission band of the sample (I_{em} (λ)). The ratio between both values (eq. (38))

$$\Phi_{em} = \frac{\int I_{em}(\lambda)}{\int I_{ex}(\lambda)} \qquad (38)$$

is equivalent to the quantum yield of the emission Φ_{em}. If the *Stokes* shift between the absorption and emission band of the sample is large enough, no further correction for self-absorption is necessary, which is the case for the measured complexes (**Ref1** and **D1**).

Emission spectra at 77 K in a 2-MeTHF glassy matrix were measured in EPR quart tubes (5 mm diameter) and were cooled to 77 K in an EPR *Dewar* vessel with liquid nitrogen.

Emission lifetimes were measured with the ns-laser flash spectrometer and analysis was performed with the corresponding software package (*vide infra*).

Excitation spectra were recorded with the same set-up as was used for the emission spectroscopy with a one order of magnitude lower concentration as that used in the emission spectroscopy (10^{-7}–10^{-6} M). The only difference was the fixed wavelength (emission maximum at ca. 14 500 cm^{-1} (690 nm)) of the emission monochromator and the excitation wavelength of the monochromator was successively varied.

5.1.3 Electrochemistry

Electrochemical measurements were either performed in CH_2Cl_2 or in MeCN with tetrabutylammonium hexafluorophosphate [*n*Bu_4N][PF_6] (0.2 M/0.1 M) as supporting electrolyte. CH_2Cl_2 was first dried over calcium chloride, distilled from calcium hydride and stored over activated alumina prior to use. MeCN was distilled from calcium hydride and stored over activated alumina prior to use. [*n*Bu_4N][PF_6] was synthesised according to literature,[398] recrystallised from ethanol/water and dried under high vacuum.

Cyclic Voltammetry (CV)

- BAS CV-50 W electrochemical workstation including corresponding software (v. 2.31) or Gamry Instruments Reference 600 Potentiostat/Galvanostat/ZRA (v. 6.2.2, Warminster, PA, USA)

Cyclic voltammograms were measured under an argon atmosphere. In MeCN the concentration of the solute was lower than 0.5 mM due to weak solubility of many complexes. Conversely, in CH_2Cl_2 1–3 mM concentrations were used. For this reason, some complexes were investigated in both solvents and the CH_2Cl_2 voltammograms were displayed in the Results section. A conventional three electrode set-up consisting of a platinum disc working electrode (Ø = 1 mm), a Ag/AgCl 'LEAK FREE' reference electrode (Warner Instruments, Hamden, CT, USA) and a platinum wire counter electrode was used. The measurement cell was dried in an oven and flushed with argon before use. The reference electrode was first referenced against the ferrocene/ferrocenium (Fc/Fc^+) redox couple. The measurements were performed at a scan rate of 250 mV s^{-1}. Chemical and electrochemical reversability of the redox processes were checked by multi thin layer experiments and measurements at different scan rates (from 10–1000 mV s^{-1}), respectively.

Spectroelectrochemistry (SEC)

UV/Vis/NIR-spectroelectrochemistry was performed at rt in a custom built three electrode quartz-cell sample compartment implemented in a Jasco V-670 spectrometer (*vide supra*).

The cell consists of a platinum disc working electrode (Ø = 6 mm), a gold covered stainless steel (V2A) plate as counter electrode and an AgCl-covered silver wire as pseudo-reference electrode and the cell volume was flushed with argon before use.[399] All experiments were measured in reflexion with a path length of 100 µm. The working electrode potential was controlled by a Princeton Applied Research Model 283 potentiostat (20 or 50 mV steps). The concentrations of the solutes were 10^{-4}–10^{-3} M for **MV1** and **MV2** complexes and NDI (**17**) and 10^{-6} M for triad **T1**. The spectra of "pure" radical anions and dianions were obtained by subtracting the spectra of the neutral species from the spectra at maximum intensity at the first and second reduction process, respectively. If redox processes at positive potentials were overlapping, the cation and dication spectra were deconvoluted with SpecFit Software.[378]

5.1.4 Transient Absorption Spectroscopy

5.1.4.1 fs-Pump-Probe Spectroscopy

- Newport-Spectra-Physics Solstice one box amplified ultrafast Ti:Sapphir laser system with a fundamental wavenumber of 12 500 cm^{-1} (800 nm), a pulse length of 100 fs and a repetition rate of 1 kHz
- Newport-Spectra-Physics TOPAS-C optical parametric amplifier as the source for the pump pulses with a pulse length of 140 fs
- Ultrafast Systems Helios transient absorption spectrometer with a CMOS sensor (1.5 nm intrinsic resolution, 350–800 nm sensitivity range) and an InGaAs sensor (3.5 nm intrinsic resolution, 800–1600 nm sensitivity range)

All experiments were performed in quartz cuvettes from Spectrocell (Oreland, PA) with an optical path length of 2 mm equipped with a micro-stirrer to allow stirring during the measurement. All samples were dissolved in the solvent as indicated, filtered and degassed for at least 15 min before each measurement.

The laser beam from the Solstice amplifier was split into two parts. One part was used to seed an optical parametric amplifier (Newport-Spectra-Physics, TOPAS) as the source for the

pump pulse with an pump energy of 100–250 nJ, and a wavenumber of 20 800 cm^{-1} (480 nm) and 26 500 cm^{-1} (378 nm) with a pulse length of 140 fs. The second fraction of the Ti:sapphire output was focused into a moving calcium fluoride-plate for the Vis or Ti:sapphire crystal for the NIR to produce a white light continuum in the visible between 25 000 cm^{-1} (400 nm) and 11 800 cm^{-1} (850 nm) and in the NIR between 11 800 cm^{-1} (850 nm) and 6820 cm^{-1} (1466 nm), respectively. The resulting white light acted as the probe pulse and was horizontally polarised. The measurements were done under magic angle conditions and the excitation pulse was collimated to a spot, which was at least two times larger than the diameter of the spatially overlapping probe pulse. After passing the sample the probe pulses were detected via a transient absorption spectrometer (Ultrafast Systems, Helios) with a CMOS (1.5 nm intrinsic resolution, 350–860 nm sensitivity range) sensor and an InGaAs (3.5 nm intrinsic resolution, 800–1600 nm sensitivity range) sensor, respectively. A typically instrument response function (IRF) was in the range of 150–350 fs depending on the used solvent and the pump wavelength. Part of the probe light pulse was used to correct for intensity fluctuations of the white light continuum. A mechanical chopper, working at 500 Hz, blocked every second pulse, in order to measure I and I_0. The photoinduced change in optical density can directly be recorded by comparing the transmitted spectral intensity of consecutive pulses [$I(\lambda, \tau)$, $I_0(\lambda)$]:

$$\Delta OD = -\log\left[\frac{I(\lambda,\tau)}{I_0(\lambda)}\right] \tag{39}$$

The relative temporal delay between pump and probe pulses was varied over a maximum range of 8 ns with a motorised, computer-controlled linear stage. The first 4 ps had a delay interval between two consecutive data points of 20 fs and the interval was increased in logarithmic steps up to 200 ps for very large delay times. The stability of the samples was verified by recording the steady-state absorption spectra before and after the time-resolved measurements.

For the dual probe alignment (sample/reference), each pair of laser pulses was normalised to the linear absorption spectra, after acquiring a certain number of transient spectra:

$$\Delta A = \log\left[\left(\frac{I_{ex}(\text{sample})}{I_0(\text{sample})}\right)\left(\frac{I_{ex}(\text{reference})}{I_0(\text{reference})}\right)\right] \tag{40}$$

I_{ex} (sample): intensity of the probe light after the sample when the excitation light was incident on the sample

I_{ex} (reference): intensity of light in the reference channel when the excitation light was incident on the sample

I_0 (sample): intensity of probe light after the sample when the excitation light was blocked by optical chopper

I_0 (reference): intensity of light in the reference channel when the excitation light was blocked by optical chopper

Assuming the splitting ratio between the sample and the reference probe beam to be constant, reflection of the fluctuations in the sample beam by the corresponding fluctuations in the reference beam are not related to the excitation pulse. This method is used mainly with less stable white light.

The time resolved spectra were analysed by global fitting with GLOTARAN (v. 1.2).[321] For this purpose a sequential (i. e. unbranched unidirectional model) or a target model was applied to model the Gaussian type IRF, the coherent artifact at time zero, and to yield the evolution associated difference spectra (EADS) or the species associated difference spectra (SADS). In the case of a target model efficiencies of the different energy or electron transfer events were an additional input parameter. The white light dispersion (chirp) was corrected by fitting a third order polynomial to the crossphase modulation signal of the pure solvent under otherwise identical experimental conditions. Singular value decomposition was used to estimate the number of components and the quality of the fits.

5.1.4.2 ns-Laser Flash Spectroscopy

- Edinburgh LP 920 laser flash spectrometer with a 450 W ozone-free Xe arc lamp including a photomultiplier (Hamamatsu R955), digital storage oscilloscope (Tektronix TD3012B) and software (L900 v. 7.3.5)
- Continuum Minilite II Nd:YAG laser operating at 10 Hz, 3-5 ns pulse duration, pulse energy 25 mJ at 18 800 cm^{-1} (532 nm), 8 mJ at 28 200 cm^{-1} (355 nm)

- H_2-Raman shifter (~50 bar) for generating 24 000 cm^{-1} (416 nm) from 28 200 cm^{-1} (355 nm)

Zero-field (B=0)

ns-Transient absorption spectra were measured with an Edinburgh LP 920 laser flash spectrometer. All solvents were spectroscopic grade and used without further purification. Measurements were carried out in a 1 cm quartz cell (Starna, Pfungstadt, Germany). The samples were degassed by bubbling argon through the solution for at least 30 min. The samples were excited with ca. 5 ns laser pulses at 24 000 cm^{-1} (416 nm) or 28 200 cm^{-1} (355 nm) (see Scheme S1). The excitation pulse was produced by a Continuum Minilite II Nd:YAG laser operating at 10 Hz and the probe pulse was provided by a pulsed Xe flash lamp. For experiments at 24 000 cm^{-1} the THG (third harmonic generation) of the fundamental of 9400 cm^{-1} (1064 nm) was shifted to lower energy by means of a 50 cm Raman shifter which was charged with hydrogen (~50 bar). The corresponding energy was selected by a Pellin-Broca prism. The 24 000 cm^{-1} pump energy was used in order to avoid ionisation of the triarylamine moieties.[279] All measurements were carried out with activated fluorescence correction implemented in the L900 software and the time range was chosen such that the decay profile was completely back to zero. Additionally, transient maps were obtained by measuring temporal decay profiles in 4 nm steps between 12 500 and 25 000 cm^{-1} (800–400 nm) and were at least averaged four times (4 × 16 shots). For selected wavelengths the signals were averaged 10–20 times depending on the signal-to-noise ratio. For all measurements a long pass (LP) filter (> 400 nm) was placed in front of the detector slit to avoid signals of higher order. The instrument response (ca. 8 ns) of the set-up was determined by measuring the scattered light using a LUDOX AS-30 colloidal silica suspension in water. Decay curves with a lifetime shorter than 100 ns were deconvoluted with the IRF using the corresponding spectrometer software. Longer decays were fitted with the Tail-Fit function of the spectrometer software. Residuals and autocorrelation function (without any significant structure) served as the main criteria in the evaluation of the fit.

Measurements were performed at different concentrations (10^{-6}–10^{-5} M) and pulse energies (0.2–1.2 mJ). Within these ranges there is no significant variation of lifetimes or amplitudes which excludes the presence of bimolecular deactivation processes.

The quantum yield of CS state formation was estimated by actinometry at 28 200 cm^{-1} (355 nm) vs. benzophenone[316] (in benzene) and at 24 000 cm^{-1} (416 nm) vs. $Ru(bpy)_3Cl_2$[47] (in H_2O) with the following equation: $\Phi_{CS} = \Phi_{ref} \times ((\Delta OD_{CS} \times \varepsilon_{ref}) / (\Delta OD_{ref} \times \varepsilon_{CS}))$.[260, 317] The value of 7220 L mol^{-1} cm^{-1} [316] was used for ε_{ref} of the benzophenone transient absorption signal at 18 900 cm^{-1} (530 nm) and 11 300 L mol^{-1} cm^{-1} [47] for the $Ru(bpy)_3Cl_2$ transient signal at 22 300 cm^{-1} (448 nm). The triplet state quantum yield for both references are according to literature[318-320] close to unity, therefore $\Phi_{ref} = 1$. The ε_{CS} values for the CS state were extracted from spectroelectrochemistry measurements (Table 7). The ΔOD_{CS} and ΔOD_{ref} values were determined by an average of four different measurements at four different laser intensities. Intensities were adjusted with neutral density (ND) filters. A linear dependence of the ΔOD with laser intensity is crucial for the determination of that value.

Non-zero Field (B>0)

- GMW Associates C-frame electromagnet 5403 (pole diameter = 76 mm, pole face = 38 mm, axial hole in poles 6.35 mm, pole gap = 12 mm), Sorensen (DLM40-75E) power supply
- Hall-Sensor (Single-Axis Magnetic Field Transductor YM12-2-5-5T, SENIS GmbH)

For the field-dependent measurements the aforementioned laser pump-probe set-up (Scheme S1) was equipped with an electromagnet. The pump and probe beams were perpendicular to each other, while the pump beam was focused through the poles and the probe white light was directed through the open faces of the C-frame. The field-dependent transient absorption experiments were performed with 24 000 cm^{-1} (416 nm) pump energy only and the magnetic field strength was controlled by a Hall-sensor which was placed at the side of the pole face. The difference of the measured current at the side of the pole face and at the middle of the cuvette (focus of laser and white light beams) was corrected by a previously determined calibrating curve. For the magnetic field set-up zero-field

measurements were carried out by reversing the current through the magnet to compensate the remanent field of the pole pieces. At low magnetic fields (0–10 mT) the stepsize between different fields was 0.3–0.5 mT and was further increased to 4–5 mT steps (between 10–50 mT), 10 mT steps (between 50–100 mT), 20 mT steps (between 100–200 mT), 50 mT steps (between 200–400 mT) and 200 mT steps (between 400–1800 mT). The error of determining the magnetic field was assigned to ±0.02 mT.

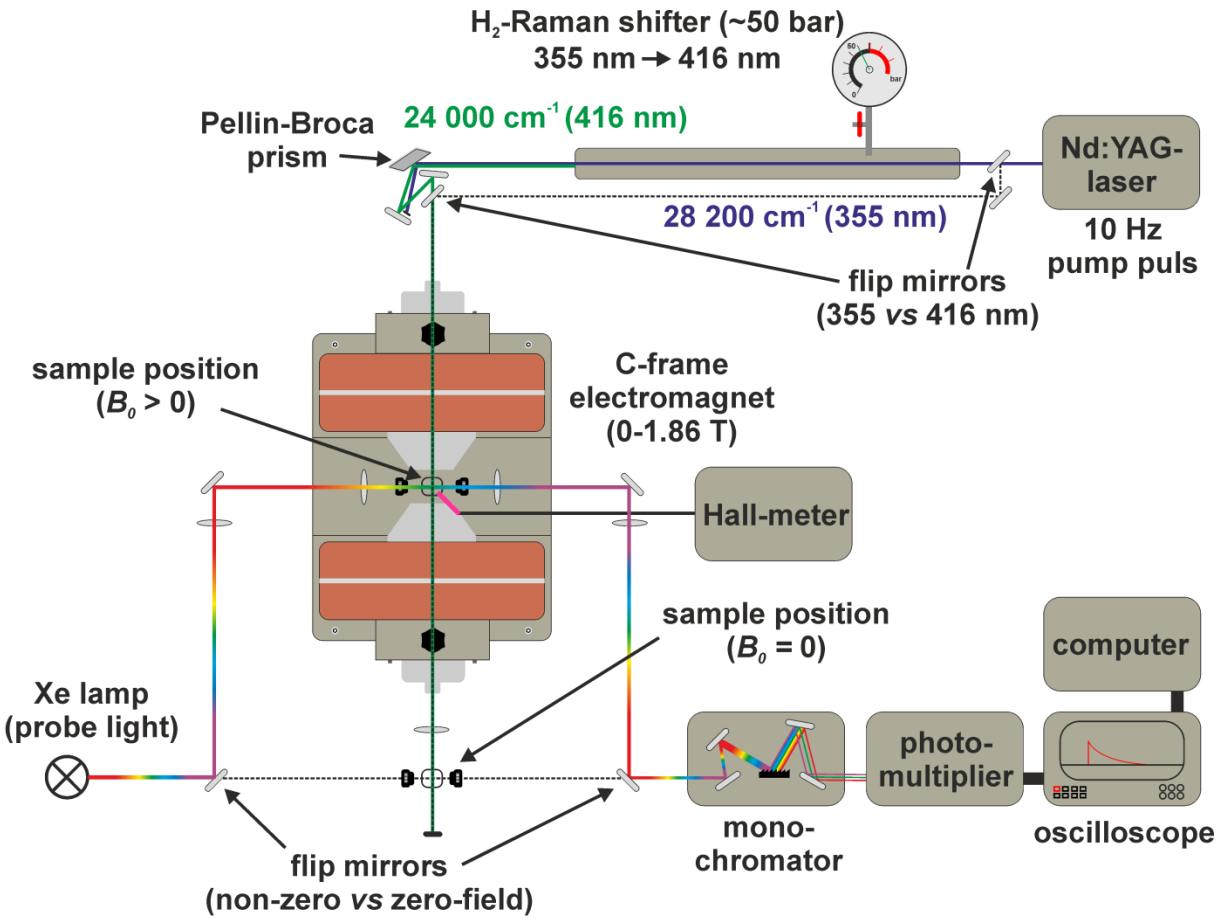

Scheme S1 Pump-probe set-up with flip-mirrors for changing i) excitation wavelengths between 28 200 cm^{-1} (355 nm) and 24 000 cm^{-1} (416 nm) and ii) between zero and non-zero field case.

The magnetic-field set-up was checked by using the following bimolecular system: zinc tetraphenylporphyrine as photosensitiser and 2-methyl-1,4-naphthoquinone as excited state quencher in a 3 : 1 mixture of cyclohexanol and 2-propanol within a field range of 0–1.8 T.[218]

The MFE using the current set-up with the aformentioned bimolecular mixture confirmed the results of the literature.[218]

The samples were carefully deoxygenated because traces of O_2 in the solution minimise the MFE drastically. For that reason, the samples were first degassed by bubbling argon through a septum on top of the optical cuvette for at least 60 min and then the septum was changed to a sealed stopper in a glove box. To make sure that there are no traces of O_2 anymore, this procedure was repeated until the transient signal at selected wavelengths and selected magnetic fields, e.g. 300, 1000 and 1800 mT, stayed constant.

5.1.5 NMR Spectroscopy

- Avance III HD 400 FT-Spectrometer (^{1}H: 400.13 MHz, ^{13}C: 100.61 MHz) with a Bruker Ultrashield magnet
- Avance III HD 400 FT-Spectrometer (^{1}H: 400.03 MHz, ^{13}C: 100.59 MHz) with a Bruker Ascend magnet
- Avance III HD 600 FT-Spectrometer (^{1}H: 600.13 MHz, ^{13}C: 150.90 MHz) with an Oxford Instruments magnet (with cryoprobe unit, CPDCH 13C)
- Avance III HD 600 FT-Spectrometer (^{1}H: 600.43 MHz, ^{13}C: 150.98 MHz) with a Bruker Ascend magnet

^{1}H and ^{13}C NMR spectra were acquired on one of the aforementioned NMR-spectrometers in deuterated solvents as indicated (e. g. acetone-d_6, chloroform-*d* ($CDCl_3$), dichloromethane-d_2 (CD_2Cl_2), tetrahydrofurane-d_8 (THF-d_8) and dimethylsulfoxide-d_6 (DMSO-d_6). The 400 MHz spectrometers run at 300 K and the two 600 MHz spectrometers have different temperatures for each solvent, e. g. 298.8 K for acetone-d_6, 303.6 K for chloroform-*d* or 293.5 K for dichloromethane-d_2. Samples were filtered and placed in frequency-matched 5 mm glass sample tubes. Chemical shifts are given in ppm relative to residual nondeuterated solvent signal (^{1}H in ppm: $CHCl_3$: δ 7.26, acetone: δ 2.05, CH_2Cl_2: 5.32, THF: 3.58, DMSO: 2.50; ^{13}C: $CHCl_3$: δ 77.16, acetone: δ 29.84, CH_2Cl_2: 53.84, THF: 67.21, DMSO: 39.52).[400] Some ^{1}H-decoupled carbon NMR spectra are recorded with a cryoprobe unit (CPDCH 13C) as indicated

to enhance the ^{13}C-sensitivity of the probe, especially for the iridium complexes. Deuterated solvents were used as received. Additionally, the solvent, e.g. CH_2Cl_2 or $CHCl_3$, for acid sensitive compounds was used after rinsing over basic alumina.

The abbreviations used for declaration of the spin multiplicities and C-atom depictions are: s = singlet, d = doublet, t = triplet, q = quartet, m = multiplet, dd = doublet of doublet. ddd = doublet of doublet of doublet, dddd = doublet of doublet of doublet of doublet; CH_3 = primary, CH_2 = secondary, CH = tertiary, C_q = quaternary. Multiplet signals or overlapping signals in proton NMR spectra that could not be assigned to first order couplings are given as (-).

Order of declaration for proton spectra: chemical shift (spin multiplicity, coupling constant, number of protons).

5.1.6 Mass Spectrometry

- Bruker Daltonics microTOF focus (ESI)
- Bruker Daltonics autoflex II (MALDI)

Mass spectra were recorded with a Bruker Daltonics autoflex II (MALDI) in positive mode (POS) using a DCTB (*trans*-2-[3-(4-*tert*-butylphenyl)-2-methyl-2-propenylidene]malononitrile) matrix or with a Bruker Daltonic microTOF focus (ESI). All mass spectrometry peaks are reported as m/z. For calculation of the respective mass values of the isotopic distribution, the software module “Bruker Daltonics IsotopePattern” from the software Compass 1.1 from Bruker Daltonics GmbH, Bremen was used. Calculated (calc.) and measured (found) peak values always correspond to the first peak of the isotopic distribution.

5.1.7 Microanalysis (CHN)

- vario MICRO cube CHNS instrument from Elementar (Hanau, Germany)
- Euro EA CHNSO Elemental Analyser from HEKAtech (Wegberg, Germany)

Elemntal analyses were either performed with a vario MICRO cube CHNS instrument for non-halogenated compounds or with Euro EA for halogenated compounds at the Institut für Anorganische Chemie, Universität Würzburg. $KMnO_4$ was added to some samples to enhance the combustion process.

5.1.8 Microwave Oven

- *µCHEMIST microPREP Microwave Digestion System ATC-FO 300* from MLS (Leutkirch, Germany)

Microwave reactions were performed in a microwave oven with a fibre optical thermometer sensor (ATC-FO, 0–270°C), which controls the reaction temperature by regulation of the output power (0–1200 W) of the microwave oven. The reaction mixture was placed in a pressure quartz vessel (max. 12 bar) or in a round bottom flask with an adapter for the fibre optical thermometer, if reactions under reflux and/or inert gas atmosphere were performed.

5.1.9 Recycling Gel Permeation Chromatography (GPC)

- JASCO Gel Permeation Chromatography System
  - interface box (LC-NetII ADC)
  - intelligent HPLC pump (PU-2080 plus)
  - inline degasser (DG-2080-53)
  - solvent selection valve unit (LV-2080-03)
  - multi wavelength UV/Vis detector 195–700 nm (UV-2077)
  - fraction collector (CHF122SC) with software FraColl (v. 3.0.2)
  - software Chrompass (v. 6.1)

Gel permeation chromatography (GPC) was done using two preparative GPC columns (styrene-divinylbenzene-copolymer, 50 and 500 Å, 600 × 20.8 mm) from PSS, a four channel

UV/Vis-detector (195–700 nm) and a fraction collector. The flow rate was 4 mL·min^{-1} and the used solvent was HPLC grade $CHCl_3$.

5.1.10 DFT-Calculations

Triad complexes

DFT-calculations were performed using *Gaussian09* with *PBE1PBE* functional and a 6-31G* basis set for C, H, N and O and pseudo potentials (SDD) for the Ir atom.[312] The reorganisation energy (λ_v) of $Ir(ppz)_2(dipy)$ was calculated via the NICG (neutral in cation geometry) method: $\lambda_v = (n^+ + c^0) - (n^0 + c^+)$[35, 332-333]

with n^+: energy of the neutral geometry of $Ir(ppz)_2(dipy)$ but positively charged (doublet multiplicity),

c^0: energy of the cationic geometry of $Ir(ppz)_2(dipy)$ with no charge (singlet multiplicity),

n^0: energy of the neutral geometry of $Ir(ppz)_2(dipy)$ but with no charge (singlet multiplicity),

c^+: energy of the cationic geometry of $Ir(ppz)_2(dipy)$ but positively charged (doublet multiplicity).

Orbitals and spin densities of ground or excited states were calculated with Gaussian09. Orbital plots and cube files were visualised with chemcraft and rendered with PovRay.

MV-complexes

Structure optimizations of the single oxidised species were performed analogously to the method described by Kaupp et al. for MV compounds with *bis*(triarylamine) motifs.[381] A preliminary conformational analysis was done with the ORCA software package[401] and the BLYP35 functional (by using the BHandHLYP keyword and subsequently setting the HF part to 35 % in the method block, ACM_A = 0.35, ACM_B = 0.65) in combination with the COSMO[402] solvent model for dichloromethane. As basis sets def2-SVP were used for H, C, O, and N and def2-TZVP for Ir.[403] In addition ECP of the Stuttgart-Dresden group were applied for Ir.[404] Symmetric conformations were used as starting structures but the optimisation was done without any symmetry constraints. To include dispersion corrections in the optimisation the

D3BJ keyword was applied in combination with the following coefficients: D3S6 = 1.000, D3A1 = 0.2793, D3S8 = 1.0354, D3A2 = 4.9615. The coefficients are in fact the values for BHLYP and were not further optimised for BLYP35. To increase calculation speed the chain-of-spheres approximation (RIJCOSX) was used.[405]

Only the energetically lowest conformations found for the complexes were further investigated. TDDFT-calculations for the oxidised complexes were performed with Gaussian09 Revision D.01.[312] All calculations were done using the BLYP35 functional with 35 % HF exchange (BLYP in combination with IOP(3/76=0650003500), IOP(3/77=1000010000), and IOP(3/78=1000010000)) and the above mentioned basis set and ECP combination (taken from the EMSL database).[406] As a solvent model the C-PCM[407] method was applied with dichloromethane as solvent. Spin densities of the ground states of and the electron density difference (EDD) plots were calculated with Gaussian09. The cube files were visualised with Avogadro[408] (isovalue of 0.002 for the spin densities and for the EDD plots) and rendered with PovRay.

5.2 Synthesis

All reactions were carried out under an atmosphere of nitrogen (dried with Sicapent from Merck, oxygen was removed with a cupric oxide catalyst R3-11 from BASF) using standard Schlenk techniques.[409] Solvent for oxygen and/or moisture sensitive reactions were freshly distilled under nitrogen from the appropriate dehydrating agent (sodium/benzophenone "ketyl blue" for THF and dioxane, sodium for toluene, CaH_2 for DMF, CH_2Cl_2, pyridine and MeCN and Mg/I_2 for EtOH and MeOH) and sparged with dry nitrogen before use. Solvents for chromatography and work-up procedures were of technical grade and distilled prior to use. Flash chromatography[410] was performed on silica gel (Macherey-Nagel "Silica 60 M", 40–63 µm) wet-packed in glass columns.

5.2.1 Reagents

$Ir(III)Cl_3 \cdot nH_2O$ was received from Heraeus (Hanau, Germany), pyrazole was recrystallised from ethyl acetate, 1-(*tert*-butyl)-4-iodobenzene[411] and tetraphenylporphyrin[412] (TTP) were synthesised according to literature procedures. *Bis*(*p*-cyanophenyl)amine was gratefully handed out by Mr. Dipl. Chem. A. Heckmann (Universität Würzburg). All other chemicals were obtained commercially and were used without further purification.

5.2.2 General Procedures

5.2.2.1 Ligands

General procedure for the synthesis of the cyclometalating ligands (4–9) by a *Buchwald-Hartwig* coupling reaction according to ref.[262, 279, 283-284] (GP I)

A substituted aryl bromide/iodide (1.0 eq.), the appropriate substituted-arylamine (1.0–1.5 eq.), $Pd_2(dba)_3 \cdot CHCl_3$ (0.08 eq.) and sodium *tert*-butoxide (2.50 eq.) were dissolved in dry toluene under nitrogen atmosphere and degassed for 10 min. A 1.0 M solution of tri-*tert*-butylphosphane in toluene (0.12 eq.) was added and the mixture was stirred at 110°C for 12–48 h. The solvent was removed under reduced pressure and the residue was taken up with CH_2Cl_2 and water, the phases were separated and the aqueous phase was extracted with CH_2Cl_2 (3 × 30 mL). The combined organic layers were washed with water, dried with $MgSO_4$

and the solvent was removed under reduced pressure. The crude product was purified by flash column chromatography on silica gel and dried *in vacuo*.

General procedure for the synthesis of dipyrromethane ligands (11–12, 14 and 23) by a microwave-assisted reaction according to ref.[286] (GP II)

A *p*-substituted benzaldehyde (1.0 eq.), 1*H*-pyrrole (used without further purification) (10 eq.) and iodine (0.10 eq.) were dissolved in CH_2Cl_2 (1*H*-pyrrole : CH_2Cl_2 = 1 : 20 by volume) and the reaction mixture was placed in a round bottom flask (reflux conditions, *vide supra*), irradiated and stirred for 1–5 min in a microwave reactor (80–300 W). Regulation of the fibre optical temperature sensor started at 30°C and finished at 40°C. The solvent was removed under reduced pressure and the resulting brown residue/oil was purified by flash column chromatography on silica gel to obtain the pure desired compound which was then dried *in vacuo*.

5.2.2.2 Complexes

General procedure for the synthesis of the dinuclear cyclometalated *μ*-dichloro bridged iridium(III) dimers (34–40) according to ref.[131] (GP III).

Ir(III)$Cl_3 \cdot n H_2O$ (Hereaus, Hanau, Germany) (1.0 eq.) and the appropiate 1-phenylpyrazole derivative (2.25 eq.) were suspended in a mixture of 2-ethoxyethanol and deionised water (3 : 1) under nitrogen and the resulting suspension was stirred at 100°C for 24 h, the reaction mixture was cooled to rt, diluted with water (15 mL). The grey solid was collected by filtration, washed with water (3 × 10 mL) and hexane (20 mL) and dried *in vacuo*. The dinuclear complexes were used for the next reaction step without further purification.

General procedure for the synthesis of the neutral cyclometalated iridium(III) dipyrrinato complexes according to ref.[142] (GP IV)

To a solution of the appropriate dipyrromethane (1.0 eq.) in THF 2,3-dichloro-5,6-dicyano-1,4-benzoquinone (1.1 eq.) was added under nitrogen and the mixture was stirred at rt for 2–3 h. Potassium carbonate (20 eq.) was added followed by the addition of the dinuclear iridium(III) complex (0.5 eq.) after stirring of 15 min. The mixture was stirred at 66°C for 12 h and, once cooled to rt, CH_2Cl_2 (15 mL) and celite (5–10 g) were added to the reaction mixture. After 15 min of stirring, the heterogeneous mixture was flushed through a plug of celite. The celite plug was rinsed with CH_2Cl_2 until no more red-coloured materials were eluted. The solvents were removed under reduced pressure and the crude product was purified by flash column chromatography on silica gel and if necessary with preparative recycling GPC ($CHCl_3$, 4 mL min^{-1}). Finally, the product was precipitated by dropping a concentrated CH_2Cl_2 solution of the complex into *n*-hexane or *n*-pentane. Satisfactory CHN analysis was obtained after drying the collected red solids under high vacuum (ca. $8 \cdot 10^{-6}$ mbar).

General procedure for the synthesis of neutral cyclometalated iridium(III) dipyrrinato complexes (GP V)

The dipyrromethane ligand (1 eq.) was dissolved in dry CH_2Cl_2 and 2,3-dichloro-5,6-dicyano-1,4-benzoquinone (1.1 eq.) was added under nitrogen atmosphere and the mixture was stirred at rt for 1 h and the solution turned deeply red. The solvent was removed under reduced pressure and was redissolved in dry THF. After stirring for 5 min potassium carbonate (20 eq.) was added and the mixture was stirred again for 15 min, followed by the addition of the dinuclear iridium(III) complex (0.5 eq.). The mixture was stirred at 66°C for 12–48 h. The solids were filtered over a plug of celite and washed with excess of CH_2Cl_2. The solvent was removed under reduced pressure and the crude product was purified by flash column chromatography on silica gel and if necessary with preparative recycling GPC ($CHCl_3$, 4 mL min^{-1}). Finally, the product was precipitated by dropping a concentrated CH_2Cl_2 solution of the complex into *n*-pentane. Satisfactory CHN analysis was obtained after drying the collected pale red solids under high vacuum (ca. $8 \cdot 10^{-6}$ mbar).

5.2.3 Phenylpyrazole Ligand

3,7-Dibromodibenzosuberone (1)

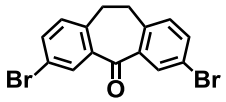

Synthesis adopted from lit.[413]

CA: [226946-20-9]

A suspension of aluminium(III)chloride (14.2 g, 106 mmol) in dry CH_2Cl_2 (20 mL) was cooled to 0°C and a solution of dibenzosuberone (8.70 mL, 10.0 g, 48.0 mmol) in dry CH_2Cl_2 (30 mL) was added. A solution of bromine (5.41 mL, 16.9 g, 106 mmol) in dry CH_2Cl_2 (50 mL) was added over a period of 30 min under an atmosphere of nitrogen. The resulting mixture was stirred for 30 min at 0°C and 3 h at rt and then poured in ice water (200 mL). CH_2Cl_2 (200 mL) was added and, the two layers separated and the aqueous phase was extracted with CH_2Cl_2 (3 × 50 mL). The resulting organic phases were washed with water, dried over $MgSO_4$ and the solvent was evaporated under reduced pressure. The crude product was purified by flash column chromatography on silica gel (eluent: ethyl acetate : petrol ether = 1 : 10) to obtain the product after recrystallization from ethyl acetate and hexane.

Yield: 6.15 g (16.8 mmol, 35 %) as colourless plates.

$C_{15}H_{10}Br_2O$ [366.05]

^{1}H-NMR (400 MHz, $CDCl_3$):

δ [ppm] = 8.12 (d, $^4J_{HH}$ = 2.2 Hz, 2H), 7.55 (dd, $^3J_{HH}$ = 8.1Hz, $^4J_{HH}$ = 2.2 Hz, 2H), 7.11 (d, $^3J_{HH}$ = 8.2 Hz, 2H), 3.14 (s, 4H).

3,7-Dibromo-10,11-dihydro-5*H*-dibenzo[ad][7]annulene (2)

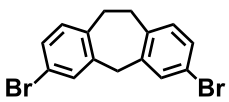

Synthesis according to lit.[279, 414]

CA: [1001909-72-3]

Sodium borohydride (2.30 g, 60.8 mmol) was suspended in trifluoroacetic acid (140 mL) at 0°C under nitrogen. A solution of 3,7-dibromodibenzosuberone (**1**) (2.48 g, 6.78 mmol) in dry CH_2Cl_2 (10 mL) was added dropwise and the mixture was stirred for 24 h at rt. After 24 h additional sodium borohydride (2.30 g, 60.9 mmol) was added to the mixture which was then stirred for further 24 h at rt. The reaction was hydrolysed with ice/water (100 mL), basified with 10 % aqueous NaOH, separated with CH_2Cl_2 (80 mL) and the aqueous phase was extracted with CH_2Cl_2 (3 × 40 mL). The combined organic phases were washed with water, dried with $MgSO_4$ and the solvent was evaporated under reduced pressure. The residue was purified by flash column chromatography on silica gel (eluent: petrol ether : CH_2Cl_2 = 95 : 5) to obtain the product as a colourless solid. If necessary, recrystallisation from an ethanol water mixture (2.5 : 1), cooling the precipitation for 13 h and filtering the solids was executed.

Yield: 2.11 g (5.99 mmol, 89 %) as colourless crystals.

$C_{15}H_{12}Br_2$ [352.06]

^{1}H-NMR (400 MHz, $CDCl_3$):

δ [ppm] = 7.32 (d, $^4J_{HH}$ = 2.1 Hz, 2H), 7.26 (dd, $^3J_{HH}$ = 8.1, $^4J_{HH}$ = 2.1 Hz, 2H), 6.97 (d, $^3J_{HH}$ = 8.1 Hz, 2H), 4.01 (s, 2H), 3.10 (s, 4H).

3-Bromo-7-(1-pyrazolyl)-10,11-dihydro-5*H*-dibenzo[a,d][7]annulene (3)

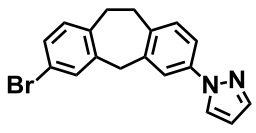

Synthesis adopted from lit.[415]

CA: [1151886-23-5]

3,7-Dibromo-10,11-dihydro-5*H*-dibenzo[a,d]cycloheptene (**2**) (2.00 g, 5.68 mmol), 1-*H*-pyrazole (297 mg, 4.37 mmol), Cu_2O (31.0 mg, 218 µmol), cesium carbonate (2.99 g, 9.18

mmol) and salicylaldoxime (120 mg, 874 µmol) were dissolved in dry MeCN (12 mL) under nitrogen atmosphere and degassed for 10 min. Stirring of the mixture was continued during the process of degassing and was maintained while heating the reaction mixture at 82°C for 3 d. The solvent was removed under reduced pressure and the residue was partitioned between CH_2Cl_2 and water and the aqueous phase was extracted with CH_2Cl_2 (3 × 40 mL). The combined organic extracts were washed with water, dried with $MgSO_4$ and the solvent was removed under reduced pressure. The residue was purified by flash column chromatography on silica gel (eluent: petrol ether : CH_2Cl_2 = 1 : 1 → 2 : 1).

Yield: 730 mg (2.15 mmol, 49 %) of a colourless solid.

$C_{18}H_{15}BrN_2$ [339.23]

^{1}H-NMR (400 MHz, $CDCl_3$):

δ [ppm] = 7.88 (dd, $^3J_{HH}$ = 2.5 Hz, $^4J_{HH}$ = 0.6 Hz, 1H), 7.71 (dd, $^3J_{HH}$ = 1.8 Hz, $^4J_{HH}$ = 0.5 Hz, 1H), 7.56 (d, $^4J_{HH}$ = 2.3 Hz, 1H), 7.42 (dd, $^3J_{HH}$ = 8.2 Hz, $^4J_{HH}$ = 2.4 Hz, 1H), 7.34 (d, $^4J_{HH}$ = 2.0 Hz, 1H), 7.26 (dd, $^3J_{HH}$ = 8.1 Hz, $^4J_{HH}$ = 2.1 Hz, 1H), 7.18 (d, $^3J_{HH}$ = 8.2 Hz, 1H), 6.99 (d, $^3J_{HH}$ = 8.1 Hz, 1H), 6.45 (dd, $^3J_{HH}$ = 2.4 Hz, $^3J_{HH}$ = 1.8 Hz, 1H), 4.12 (s, 2H), 3.16 (-, 4H).

3-*Bis*(*p*-anisyl)amine-7-(1-pyrazolyl)-10,11-dihydro-5*H*-dibenzo[a,d][7]annulene (4)

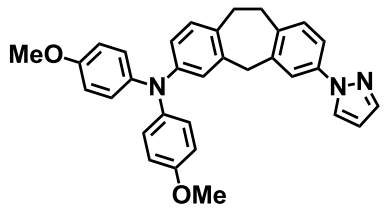

Synthesis according to lit.[160, 279]

CA: [1151886-24-6]

Synthesis according to GP I:

3-Bromo-7-pyrazolyl-10,11-dihydro-5*H*-dibenzo[a,d]cycloheptene (**3**) (1.06 g, 3.12 mmol), *bis*(*p*-anisyl)amine (787 mg, 3.43 mmol), $Pd_2(dba)_3{\cdot}CHCl_3$ (258 mg, 250 µmol), sodium-*tert*-

butoxide (749 mg, 7.80 mmol), tri-*tert*-butylphosphane (374 µL, 374 µmol, 1 M in toluene), toluene: 10 mL; 48 h at 110°C; flash column chromatography (eluent: petrol ether : ethyl acetate = 4 : 1 → 3 : 1).

Additional purification protocol: EtOH (70 mL) was added to the residue obtained after evaporation of the combined fractions and heated to reflux, while stirring, until all solids dissolved. Water (40 mL) was added to the refluxing solution until permanent cloudiness and then stored at −30°C for 16 h. The crystalline solids were collected, washed with 50 % aqueous EtOH (15 mL) and dried *in vacuo*.

Yield: 1.09 g (2.23 mmol, 72 %) of a grey powder.

$C_{32}H_{29}N_3O_2$ [487.59]

^{1}H-NMR (400 MHz, acetone-d_6):

δ [ppm] = 8.24 (dd, $^3J_{HH}$ = 2.4 Hz, $^4J_{HH}$ = 0.6 Hz, 1H), 7.67 (d, $^4J_{HH}$ = 2.4 Hz, 1H), 7.63 (dd, $^3J_{HH}$ = 2.4 Hz, $^4J_{HH}$ = 0.5 Hz, 1H), 7.59 (dd, $^3J_{HH}$ = 8.2 Hz, $^4J_{HH}$ = 2.4 Hz, 1H), 7.23 (d, $^3J_{HH}$ = 8.2 Hz, 1H), 6.98-6.95 (-, 5H), 6.87-6.83 (-, 5H), 6.67 (dd, $^3J_{HH}$ = 8.21 Hz, $^4J_{HH}$ = 2.48 Hz, 1H), 6.45 (dd, $^3J_{HH}$ = 2.5 Hz, $^3J_{HH}$ = 1.8 Hz, 1H), 4.07 (s, 2H), 3.77 (s, 6H, OCH_3), 3.15 (-, 4H).

***Bis*(*p*-*tert*-butylphenyl)amine (5)**

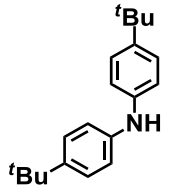

Synthesis follows a slightly modified procedure according to lit.[416]

CA: [4627-22-9]

1-*tert*-Butyl-4-iodobenzene (1.12 mL, 1.63 g, 6.28 mmol), 4-*tert*-butylaniline (1.00 mL, 937 mg, 6.28 mmol), $Pd_2(dba)_3{\cdot}CHCl_3$ (650 mg, 628 µmol), sodium-*tert*-butoxide (1.51 g,

15.7 mmol), tri-*tert*-butylphosphane (942 µl, 942 µmol, 1 M in toluene), toluene: 20 mL; 48 h at 110°C; flash column chromatography (eluent: petrol ether : ethyl acetate = 50 : 1).

Yield: 1.20 g (4.28 mmol, 68 %) of brown solid.

$C_{20}H_{27}N$ [281.44]

^{1}H-NMR (400 MHz, acetone-d_6):
δ [ppm] = 7.27 (AA', 4H), 7.12 (s, 1H, N*H*), 7.04 (BB', 4H), 1.29 (s, 18H, ^{t}Bu).

3-*Bis*(*p*-*tert*-butylphenyl)amine-7-(1-pyrazolyl)-10,11-dihydro-5*H*-dibenzo[a,d][7]annulene (6)

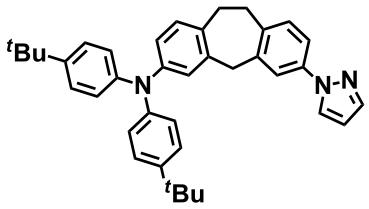

Synthesis according to lit.[160, 279]

CA: [1463527-64-1]

Synthesis according to GP I:

3-Bromo-7-pyrazolyl-10,11-dihydro-5*H*-dibenzo[a,d]cycloheptene (**3**) (595 mg, 1.75 mmol), *bis*(*p*-*tert*-butylphenyl)amine (543 mg, 1.93 mmol), $Pd_2(dba)_3{\cdot}CHCl_3$ (145 mg, 140 µmol), sodium-*tert*-butoxide (421 mg, 4.38 mmol), tri-*tert*-butylphosphane (210 µL, 210 µmol, 1 M in toluene), toluene: 12 mL; 12 h at 110°C; flash column chromatography (eluent: petrol ether : ethyl acetate = 4 : 1).

Yield: 730 mg (1.35 mmol, 77 %) of an orange-brown solid.

$C_{38}H_{41}N_3$ [539.75]

^{1}H-NMR (400 MHz, acetone-d_6):
δ [ppm] = 8.23 (dd, $^3J_{HH}$ = 2.5 Hz, $^4J_{HH}$ = 0.6 Hz, 1H), 7.69 (d, $^3J_{HH}$ = 2.4 Hz, 1H), 7.63 (d, $^3J_{HH}$ = 1.7 Hz, 1H), 7.59 (dd, $^3J_{HH}$ = 8.2 Hz, $^4J_{HH}$ = 2.4 Hz, 1H), 7.29 (AA', 4H), 7.24 (d,

$^3J_{HH}$ = 8.2 Hz, 1H), 7.05 (d, $^3J_{HH}$ = 8.2 Hz, 1H), 6.98 (d, $^3J_{HH}$ = 2.3 Hz, 1H), 6.92 (BB', 4H), 6.78 (dd, $^3J_{HH}$ = 8.1 Hz, $^4J_{HH}$ = 2.4 Hz, 1H), 6.45 (dd, $^3J_{HH}$ = 2.5 Hz, $^4J_{HH}$ = 1.8 Hz, 1H), 4.10 (s, 2H), 3.22–3.13 (-, 4H), 1.30 (s, 18H, ^{t}Bu).

^{13}C-NMR (100 MHz, acetone-d_6):

δ [ppm] = 146.93 (C_q), 146.44 (C_q), 145.93 (C_q), 2 × 141.2 (CH, C_q), 140.6 (C_q), 139.3 (C_q), 138.3 (C_q), 134.5 (C_q), 131.43 (CH), 131.38 (CH), 127.6 (CH), 126.9 (CH), 125.4 (CH), 124.2 (CH), 123.4 (CH), 120.0 (CH), 117.6 (CH), 108.0 (CH), 41.1 (CH_2), 34.8 (C_q), 32.8 (CH_2), 32.5 (CH_2), 31.8 (CH_3).

MALDI-MS (pos.): m/z calc. for $C_{38}H_{41}N_3$ 539.330, found 539.321.

3-(*p*-Chlorophenyl)amine-7-(1-pyrazolyl)-10,11-dihydro-5*H*-dibenzo[a,d][7]annulene (7)

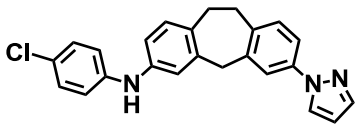

Synthesis according to lit.[160, 279]

CA: [–]

Synthesis according to GP I:

3-Bromo-7-pyrazolyl-10,11-dihydro-5*H*-dibenzo[a,d]cycloheptene (**3**) (466 mg, 1.37 mmol), *p*-chloroaniline (360 mg, 2.82 mmol), $Pd_2(dba)_3{\cdot}CHCl_3$ (114 mg, 110 µmol), sodium-*tert*-butoxide (330 mg, 3.43 mmol), tri-*tert*-butylphosphane (165 µL, 165 µmol, 1 M in toluene), toluene: 12 mL; 12 h at 110°C; flash column chromatography (eluent: petrol ether : ethyl acetate = 15 : 1).

Yield: 104 mg (270 µmol, 20 %) of a grey solid.

$C_{24}H_{20}ClN_3$ [385.89]

^{1}H-NMR (400 MHz, acetone-d_6):

δ [ppm] = 8.24 (dd, $^{3}J_{HH}$ = 2.5 Hz, $^{4}J_{HH}$ = 0.6 Hz, 1H), 7.71 (d, $^{3}J_{HH}$ = 2.3 Hz, 1H), 7.65 (dd, $^{3}J_{HH}$ = 1.7 Hz, $^{4}J_{HH}$ = 0.4 Hz, 1H), 7.57 (dd, $^{3}J_{HH}$ = 8.2 Hz, $^{4}J_{HH}$ = 2.4 Hz, 1H), 7.35 (s(br), 1H, N*H*), 7.24 (d, $^{3}J_{HH}$ = 8.2 Hz, 1H), 7.19 (AA', 2H), 7.08–7.04 (-, 4H), 6.92 (dd, $^{3}J_{HH}$ = 8.1 Hz, $^{4}J_{HH}$ = 2.4 Hz, 1H), 6.46 (dd, $^{3}J_{HH}$ = 2.5 Hz, $^{4}J_{HH}$ = 1.8 Hz, 1H), 4.16 (s, 2H), 3.12–3.21 (-, 4H).

^{13}C-NMR (100 MHz, acetone-d_6):[1]

δ [ppm] = (144.4 (C_q), 144.3 (C_q), Int. 1), (141.9 (C_q), 141.8 (C_q), Int. 1), 141.4 (C_q), 141.2 (CH), 140.6 (C_q), 139.3 (C_q), 138.4 (C_q), 132.7 (C_q), (131.4 (CH), 131.3 (CH), Int. 2), 129.8 (CH), 127.6 (CH), 124.2 (C_q), 120.0 (CH), (119.9 (CH), 119.8 (CH), Int. 1), 118.6 (CH), 118.5 (CH), (117.7 (CH), 117.63 (CH), Int. 1), 117.57 (CH), 108.1 (CH), 41.3 (CH_2), 32.8 (CH_2), 32.4 (CH_2).

MALDI-MS (pos.): m/z calc. for $C_{24}H_{20}ClN_3$ 385.134, found 385.151.

3-*Bis*(*p*-chlorophenyl)amine-7-(1-pyrazolyl)-10,11-dihydro-5*H*-dibenzo[a,d][7]annulene (8)

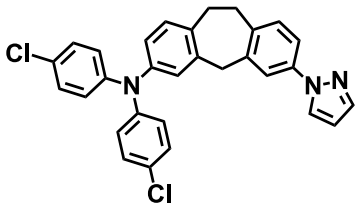

Synthesis according to lit.[160, 279]

CA: [–]

Synthesis according to GP I:

3-(*p*-Chlorophenyl)amine-7-pyrazolyl-10,11-dihydro-5*H*-dibenzo[a,d]cycloheptene (**3**) (460 mg, 1.19 mmol), *p*-chloro-iodobenzene (426 mg, 1.79 mmol), $Pd_2(dba)_3{\cdot}CHCl_3$ (99.0 mg, 95.0 µmol), sodium-*tert*-butoxide (286 mg, 2.98 mmol), tri-*tert*-butylphosphane (143 µL, 143

[1] A deuterium-hydrogen exchange at the secondary amine probably caused a second set of carbon signals of the carbon atoms in the direct vicinity of the amine. Integrals (Int.) indicate which carbon signals belong together.

µmol, 1 M in toluene), toluene: 12 mL; 12 h at 110°C; flash column chromatography (eluent: petrol ether : ethyl acetate = 15 : 1).

Yield: 350 mg (705 µmol, 52 %) of a light yellow solid.

$C_{30}H_{23}Cl_2N_3$ [496.43]

^{1}H-NMR (400 MHz, acetone-d_6):

δ [ppm] = 8.23 (dd, $^3J_{HH}$ = 2.5 Hz, $^4J_{HH}$ = 0.6 Hz, 1H), 7.70 (d, $^3J_{HH}$ = 2.4 Hz, 1H), 7.64 (dd, $^3J_{HH}$ = 1.7 Hz, $^4J_{HH}$ = 0.6 Hz, 1H), 7.60 (dd, $^3J_{HH}$ = 8.2 Hz, $^4J_{HH}$ = 2.4 Hz, 1H), 7.29–7.25 (-, 5H), 7.13 (d, $^3J_{HH}$ = 8.1 Hz, 1H), 7.04 (d, $^4J_{HH}$ = 2.2 Hz, 1H), 7.00 (BB', 4H), 6.87 (dd, $^3J_{HH}$ = 8.1 Hz, $^4J_{HH}$ = 2.4 Hz, 1H), 6.45 (ddd, $^3J_{HH}$ = 2.5 Hz, $^4J_{HH}$ = 1.8 Hz, $^4J_{HH}$ = 1.0 Hz, 1H), 4.14 (s, 2H), 3.16–3.24 (-, 4H).

^{13}C-NMR (100 MHz, acetone-d_6):

δ [ppm] = 147.5 (C_q), 145.8 (C_q), 141.3 (CH), 141.20 (C_q), 141.16 (C_q), 139.4 (C_q), 138.3 (C_q), 136.2 (C_q), 131.9 (CH), 131.4 (CH), 130.2 (CH), 127.9 (CH), 127.6 (C_q), 126.5 (CH), 125.7 (CH), 124.4 (CH), 120.1 (CH), 117.7 (CH), 108.1 (CH), 40.9 (CH_2), 32.6 (CH_2), 32.5 (CH_2).

MALDI-MS (pos.): m/z calc. for $C_{30}H_{23}Cl_2N_3$ 495.126, found 495.132.

3-*Bis*(*p*-cyanophenyl)amine-7-(1-pyrazolyl)-10,11-dihydro-5*H*-dibenzo[a,d][7]annulene (9)

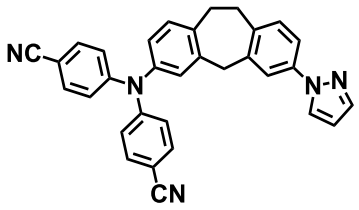

CA: [–]

Synthesis according to GP I:

3-Bromo-7-pyrazolyl-10,11-dihydro-5*H*-dibenzo[a,d]cycloheptene (**3**) (200 mg, 590 µmol), *bis*(*p*-cyanophenyl)amine (142 mg, 649 µmol), $Pd_2(dba)_3{\cdot}CHCl_3$ (49.0 mg, 47.3 µmol), sodium-*tert*-butoxide (142 mg, 1.47 mmol), tri-*tert*-butylphosphane (71.0 µL, 71.0 µmol, 1 M in

toluene), toluene: 12 mL; 12 h at 110°C; flash column chromatography (eluent: petrol ether : ethyl acetate = 4 : 1).

Yield: 160 mg (335 mmol, 57 %) of a yellow solid.

$C_{32}H_{23}N_5$ [477.55]

^{1}H-NMR (400 MHz, acetone-d_6):

δ [ppm] = 8.22 (dd, $^3J_{HH}$ = 2.5 Hz, $^4J_{HH}$ = 0.6, 1H), 7.70 (d, $^3J_{HH}$ = 2.3 Hz, 1H), 7.67–7.62 (-, 5H), 7.61 (dd, $^3J_{HH}$ = 8.2 Hz, $^4J_{HH}$ = 2.4 Hz, 1H), 7.27 (dd, $^3J_{HH}$ = 8.4 Hz, $^3J_{HH}$ = 8.4 Hz, 2H), 7.20–7.16 (-, 5H), 7.02 (dd, $^3J_{HH}$ = 8.0 Hz, $^4J_{HH}$ = 2.3 Hz, 1H), 6.46 (dd, $^3J_{HH}$ = 2.5 Hz, $^4J_{HH}$ = 1.8 Hz, 1H), 4.21 (s, 2H), 3.25 (s, 4H).

^{13}C-NMR (150 MHz, acetone-d_6):

δ [ppm] = 151.3 (C_q), 143.9 (C_q), 142.0 (C_q), 141.3 (CH), 141.0 (C_q), 139.5 (C_q), 138.8 (C_q), 138.2 (C_q), 134.4 (CH), 132.6 (CH), 131.4 (CH), 128.7 (CH), 127.6 (CH), 126.5 (CH), 123.7 (CH), 120.1 (CH). 119.5 (C_q), 117.7 (CH), 108.1 (C_q), 106.3 (CH), 40.5 (CH_2), 32.5 (CH_2), 32.1 (CH_2).

MALDI-MS (pos.): m/z calc. for $C_{32}H_{23}N_5$ 477.195, found 477.194.

3-Pyrazolyl-10,11-dihydro-5H-dibenzo[a,d][7]annulene (10)

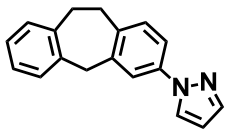

CA: [1463527-65-2]

3-Bromo-7-pyrazolyl-10,11-dihydro-5*H*-dibenzo[a,d]cycloheptene (**3**) (200 mg, 590 µmol) was dissolved in dry THF and the solution was cooled to −78°C. A solution of ^{t}BuLi in pentane (652 µl, 1.24 mmol, 1.9 M) was added dropwise and the mixture was stirred at −40°C for 2–3 h. To the reddish solution 2 N HCl (103 µl, 2.95 mmol) was added during a period of 15 min. The reaction mixture was allowed to warm to rt and was then diluted with additional 2 N HCl (10 mL). The organic solvent was removed under reduced pressure and the residue was taken up

with CH_2Cl_2 and water, the layer were separated and the aqueous layer was extracted with CH_2Cl_2 (3 × 40 mL). The combined organic phases were washed with water, dried with $MgSO_4$ and the solvent was removed under reduced pressure. The residue was purified by flash chromatography on silica gel (eluent: petrol ether : CH_2Cl_2 = 1 : 1 → 1 : 2).

Yield: 100 mg (384 µmol, 65 %) of a colourless solid.

$C_{18}H_{16}N_2$ [260.33]

^{1}H-NMR (400 MHz, $CDCl_3$):

δ [ppm] = 7.88 (dd, $^3J_{HH}$ = 2.4 Hz, $^4J_{HH}$ = 0.6 Hz, 1H), 7.71 (dd, $^3J_{HH}$ = 1.7 Hz, $^4J_{HH}$ = 0.5 Hz, 1H), 7.58 (d, $^4J_{HH}$ = 2.4 Hz, 1H), 7.40 (dd, $^3J_{HH}$ = 8.2 Hz, $^4J_{HH}$ = 2.4 Hz, 1H), 7.20–7.10 (-, 5H), 6.44 (dd, $^3J_{HH}$ = 2.4 Hz, $^3J_{HH}$ = 1.8 Hz, 1H), 4.17 (s, 2H), 3.20 (s, 4H).

^{13}C-NMR (100 MHz, $CDCl_3$):

δ [ppm] = 140.9 (CH), 140.4 (C_q), 139.2 (C_q), 138.6 (C_q), 138.4 (C_q), 137.7 (C_q), 130.7 (CH), 129.7 (CH), 129.2 (CH), 127.0 (CH), 126.8 (CH), 126.3 (CH), 120.1 (CH), 117.3 (CH), 107.4 (CH), 41.1 (CH_2), 32.5 (CH_2), 32.2 (CH_2).

MALDI-S (pos.): m/z calc. for $C_{18}H_{16}N_2$ 216.131, found 216.136.

5.2.4 Dipyrromethane Ligands

***meso*-(Phenyl)dipyrromethane (11)**

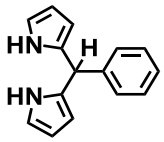

CA: [107798-98-1]

Synthesis according to GP II:

Benzaldehyde (633 mg, 603 µL, 5.96 mmol), 1*H*-pyrrole (4.00 g, 4.12 mL, 59.6 mmol), iodine (151 mg, 596 µmol), CH_2Cl_2: 50 mL; 60 s at 30–40°C (150 W); flash column chromatography (eluent: petrol ether : ethyl acetate = 5 : 1).

Yield: 943 mg (4.24 mmol, 71 %) of a colourless solid.

$C_{15}H_{14}N_2$ [222.29]

^{1}H-NMR (400 MHz, $CDCl_3$):

δ [ppm] = 7.92 (s(br), 2H, N*H*), 7.34–7.21 (-, 5H), 6.71 (ddd, $^3J_{HH}$ = 4.2 Hz, $^3J_{HH}$ = 2.7 Hz, $^4J_{HH}$ = 1.6 Hz, 2H), 6.17 (dd, $^3J_{HH}$ = 2.7 Hz, $^4J_{HH}$ = 2.7 Hz, 2H), 5.93 (dddd, $^3J_{HH}$ = 3.4 Hz, $^3J_{HH}$ = 2.5 Hz, $^4J_{HH}$ = 1.5 Hz, $^5J_{HH}$ = 0.8 Hz, 2H), 5.48 (s, 1H).

***meso*-(*p*-Nitrophenyl)dipyrromethane (12)**

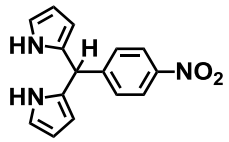

CA: [143859-77-2]

Synthesis according to GP II:

p-Nitrobenzaldehyde (901 mg, 5.96 mmol), 1*H*-pyrrole (4.00 g, 4.12 mL, 59.6 mmol), iodine (151 mg, 596 µmol), CH_2Cl_2: 50 mL; 60 sec at 30–40°C (80 W); flash column chromatography (eluent: petrol ether : ethyl acetate = 8 : 1 → 4 : 1).

Yield: 961 mg (3.60 mmol, 60 %) of a green solid.

$C_{15}H_{13}N_3O_2$ [267.28]

^{1}H-NMR (400 MHz, $CDCl_3$):

δ [ppm] = 7.34 (AA', 2H), 7.98 (s(br), 2H, N*H*), 7.37 (BB', 2H), 6.75 (ddd, $^3J_{HH}$ = 4.2 Hz, $^3J_{HH}$ = 2.7 Hz, $^4J_{HH}$ = 1.6 Hz, 2H), 6.18 (dd, $^3J_{HH}$ = 2.7 Hz, $^4J_{HH}$ = 2.7 Hz, 2H), 5.88 (dddd, $^3J_{HH}$ = 3.4 Hz, $^3J_{HH}$ = 2.5 Hz, $^4J_{HH}$ = 1.5 Hz, $^5J_{HH}$ = 0.8 Hz, 2H), 5.58 (s, 1H).

***meso*-(*p*-Aminophenyl)dipyrromethane (13)**

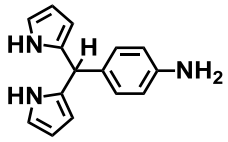

CA: [873955-91-0]

meso-(*p*-Nitrophenyl)dipyrromethane (**12**) (4.64 g, 17.4 mmol) was dissolved in dry THF (70 mL) and 10 % palladium on carbon (1.48 mg, 1.39 µmol) was added. The mixture was degassed 15 min under nitrogen atmosphere and then saturated with hydrogen gas and stirred for 3 d. The solid catalyst was removed by filtration through a plug of celite and the solvent was removed under reduced pressure. The residue was purified by flash column chromatography on silica gel (eluent: petrol ether : ethyl acetate = 2 : 1 → 1 : 1) in no more than 10 min to prevent decomposition of the desired compound and dried in *vacuo*.

Yield: 4.05 g (17.1 mmol, 98 %) of a red-brown solid.

$C_{15}H_{15}N_3$ [237.30]

^{1}H-NMR (400 MHz, acetone-d_6):

δ [ppm] = 9.50 (s(br), 2H, N*H*), 6.88 (AA', 2H), 6.64 (dd, $^3J_{HH}$ = 4.3 Hz, $^4J_{HH}$ = 2.7 Hz, $^4J_{HH}$ = 1.6 Hz, 2H), 6.56 (BB', 2H), 5.95 (dd, $^3J_{HH}$ = 2.6 Hz, $^4J_{HH}$ = 2.8 Hz, 2H), 5.71 (dddd, $^3J_{HH}$ = 4.2 Hz, $^3J_{HH}$ = 2.5 Hz, $^4J_{HH}$ = 1.6 Hz, $^5J_{HH}$ = 0.8 Hz, 2H), 5.26 (s, 1H), 4.44 (s(br), 2H, NH_2).

***meso*-(*p*-Chlorophenyl)dipyrromethane (14)**

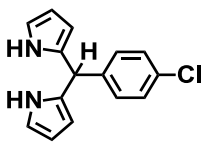

CA: [137018-26-9]

Synthesis according to GP II:

p-Chlorobenzaldehyde (1.26 g, 8.94 mmol), 1*H*-pyrrole (6.00 g, 6.25 mL, 89.4 mmol), iodine (227 mg, 894 µmol), CH_2Cl_2: 100 mL; 90 s at 30–40°C (80 W); flash column chromatography (eluent: petrol ether : ethyl acetate = 10 : 1).

Yield: 957 mg (3.73 mmol, 42 %) of a light brown solid.

$C_{15}H_{13}ClN_2$ [256.73]

^{1}H-NMR (400 MHz, $CDCl_3$):

δ [ppm] = 7.87 (brs, 2H, N*H*), 7.31 (AA', 2H), 7.15 (BB', 2H), 6.70 (ddd, $^3J_{HH}$ = 2.7 Hz, $^3J_{HH}$ = 2.7 Hz, $^4J_{HH}$ = 1.6 Hz, 2H), 6.19 (ddd, $^3J_{HH}$ = 6.0 Hz, $^3J_{HH}$ = 6.0 Hz, $^4J_{HH}$ = 2.7 Hz, 2H), 5.92–5.90 (m, 2H), 5.44 (s, 1H).

1,9-Dichloro-*meso*-(*p*-chlorophenyl)dipyrromethane (15)

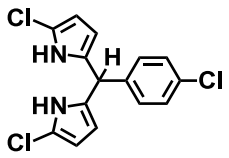

CA: [–]

Synthesis according to lit.[391]

A suspension of *N*-chlorosuccinimide (NCS) (229 mg, 1.71 mmol) in dry THF (2–3 mL) was added to a cooled solution (−78°C) of *meso*-(*p*-chlorophenyl)dipyrromethane (**14**) (200 mg, 779 µmol) in dry THF (16 mL) over a period of 1 h and was stirred for 1.5 h under the exclusion of light. The mixture was brought to rt and stirred for further 3 h. After hydrolysis with water (20 mL), addition of CH_2Cl_2 (50 mL) and extraction with the same solvent (3 × 30 mL), the combined organic phases were dried with $MgSO_4$ and the solvent was removed under reduced pressure. The resulting dark brown oil was purified by flash column chromatography on silica gel (eluent: petrol ether : CH_2Cl_2 = 2 : 1) and dried *in vacuo*.

Yield: 133 mg (408 µmol, 52 %) of a green oil.

$C_{15}H_{11}Cl_3N_2$ [325.62]

^{1}H-NMR (400 MHz, acetone-d_6):

δ [ppm] = 10.32 (s(br), 2H, N*H*), 7.32 (AA', 2H), 7.23 (BB', 2H), 5.69–5.67 (m, 2H), 5.68 (dd, $^3J_{HH}$ = 3.2 Hz, $^4J_{HH}$ = 3.2 Hz, 2H), 5.38 (s, 1H).

MALDI-MS (pos.): m/z calc. for $C_{15}H_{11}Cl_3N_2$ ($M^{+\cdot}$) 323.998 was not observed,
m/z calc. for $C_{15}H_{11}Cl_2N_2$ ($M^{+\cdot}$ -Cl) 289.029, found 289.074.

***meso*-(Phenylethynyl)dipyrromethane (16)**

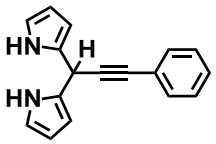

CA: [–]

3-Phenyl-2-propynal (250 µL, 2.04 mmol) and 1*H*-pyrrole (1.37 g, 1.14 mL, 20.4 mmol), freshly filtered over basic alumina, were dissolved in CH_2Cl_2 (8 mL) and the mixture was degassed for 10 min with nitrogen and cooled to 0°C (ice-water bath). 3 drops of TFA were added and after 1 h of stirring, the solution was warmed to rt and was stirred for additional 30 min. The reaction mixture was diluted with CH_2Cl_2 (5 mL) and 0.1 M aqueous NaOH (8 mL). The phases were separated and the aqueous phase was extracted with CH_2Cl_2 (2 × 10 mL) and the combined organic phases were dried with $MgSO_4$. The solvent was removed under reduced pressure and the resulting oil was purified by flash column chromatography on deactivated alumina (activity III) (eluent: petrol ether : ethyl acetate = 40 : 1 → 8 : 1).

Yield: 130 mg (528 µmol, 26 %) of a brownish-green oil.

$C_{17}H_{14}N_2$ [246.31]

^{1}H-NMR (400 MHz, CD_2Cl_2):

δ [ppm] = 8.29 (s(br), 2H, N*H*), 7.49–7.52 (m, 2H), 7.34–7.38 (-, 3H), 6.72–6.73 (m, 2H), 6.17–6.15 (-, 4H), 5.40 (s, 1H).

^{13}C-NMR (100 MHz, CD_2Cl_2):

δ [ppm] = 132.1 (CH), 129.5 (C_q), 128.78 (CH), 128.76 (CH), 123.2 (C_q), 118.0 (CH), 108.8 (CH), 106.6 (CH), 87.5 (C_q), 83.5 (C_q), 31.1 (CH).

MALDI-MS (pos.): m/z calc. for $C_{17}H_{14}N_2$ 246.115 ($M^{+\cdot}$) was not observed,
m/z calc. for $C_{17}H_{13}N_2$ ($M^{+\cdot}$ –H) 245.107, found 245.107.

5.2.5 Naphthalene Diimide Ligands

_N_-(2,5-Di-_tert_-butylphenyl)-_N'_-phenyl-naphthalene-1,4,5,8-tetracarboxylic diimide (17)

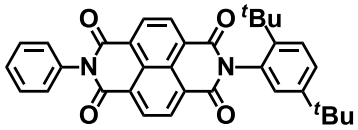

CA: [1463527-66-3]

Naphthalene-1,4,5,8-tetracarboxylic dianhydride (500 mg, 1.86 mmol) and 2,5-di-*tert*-butylaniline (459 mg, 2.24 mmol) and aniline (174 mg, 1.87 mmol) were dissolved in dry DMF (18 mL) in a quartz microwave tube and heated in a microwave oven (300 W, 140°C) for 1 h. The solvent was removed under reduced pressure and the resulting solid was purified by flash column chromatography on silica gel (eluent: petrol ether : ethyl acetate = 10 : 1 → 1 : 1).

Yield: 145 mg (273 µmol, 15 %) of a brown solid.

$C_{34}H_{30}N_2O_4$ [530.61]

^{1}H-NMR (400 MHz, $CDCl_3$):

δ [ppm] = 8.86 (s, 4H), 7.62–7.58 (-, 3H), 7.54 (m, 1H), 7.49 (dd, $^{3}J_{HH}$ = 8.6 Hz, $^{4}J_{HH}$ = 2.2 Hz, 1H), 7.35–7.33 (-, 2H), 7.02 (d, $^{4}J_{HH}$ = 2.2 Hz, 1H), 1.34 (s, 9H, ^{t}Bu), 1.28 (s, 9H, ^{t}Bu).

^{13}C-NMR (100 MHz, $CDCl_3$):

δ [ppm] = 164.0 (C_q), 163.2 (C_q), 150.6 (C_q), 143.9 (C_q), 134.8 (C_q), 132.2 (C_q), 131.62 (CH), 131.60 (CH), 129.8 (CH), 129.4 (CH), 129.2 (CH), 128.6 (CH), 127.7 (CH), 127.51

(C_q), 127.46 (C_q), 127.4 (C_q), 127.2 (C_q), 126.8 (CH), 35.7 (C_q), 34.4 (C_q), 31.9 (CH_3), 31.4 (CH_3).

MALDI-MS (pos.): m/z calc. for $C_{34}H_{30}N_2O_4$ 530.220, found 530.120.

N-(2,5-Di-*tert*-butylphenyl)-*N'*-(4-(dipyrrolylmethyl)phenyl)-naphthalene-1,4,5,8-tetracarboxylic diimide (18)

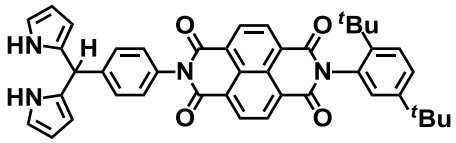

CA: [1463527-67-4]

Naphthalene-1,4,5,8-tetracarboxylic dianhydride (1.12 g, 4.16 mmol) and 2,5-di-*tert*-butylaniline (855 mg, 4.16 mmol) were dissolved in dry DMF (26 mL) in a quartz microwave tube and heated in a microwave oven (300 W, 140°C) for 30 min 5-(4-Aminophenyl)dipyrromethane (**13**) (988 mg, 4.16 mmol) was added and the mixture was heated for another 30 min in the microwave oven under the same conditions. The solvent was removed under reduced pressure and the resulting solid was purified by flash column chromatography on silica gel (eluent: petrol ether : ethyl acetate = 4 : 1 → 1 : 2).

Yield: 484 mg (717 µmol, 17 %) of a brown solid.

$C_{43}H_{38}N_4O_4$ [674.79]

^{1}H-NMR (400 MHz, $CDCl_3$):

δ [ppm] = 8.87–8.81 (-, 4H), 8.11 (br d, $^3J_{HH}$ = 1.7 Hz, 2H, N*H*), 7.63 (d, $^3J_{HH}$ = 8.6 Hz, 1H), 7.51 (dd, $^3J_{HH}$ = 8.6 Hz, $^4J_{HH}$ = 2.2 Hz, 1H), 7.37 (AA', 2H), 7.23 (BB', 2H), 7.04 (d, $^4J_{HH}$ = 2.2 Hz, 1H), 6.67 (ddd, $^3J_{HH}$ = 4.2 Hz, $^3J_{HH}$ = 2.6 Hz, $^4J_{HH}$ = 1.6 Hz, 2H), 6.17 (dd, $^3J_{HH}$ = 2.7 Hz, $^3J_{HH}$ = 2.7 Hz, 2H), 5.98 (dddd, $^3J_{HH}$ = 3.3 Hz, $^3J_{HH}$ = 2.4 Hz, $^4J_{HH}$ = 1.5 Hz, $^4J_{HH}$ = 0.8 Hz, 2H), 5.57 (s, 1H), 1.34 (s, 9H, ^{t}Bu), 1.29 (s, 9H, ^{t}Bu).

^{13}C-NMR (100 MHz, $CDCl_3$):

δ [ppm] = 163.9 (C_q), 163.2 (C_q), 150.6 (C_q), 143.8 (C_q), 143.4 (C_q), 133.4 (C_q), 132.1 (C_q), 132.0 (C_q), 131.6 (2 × CH), 129.7 (CH), 129.2 (CH), 128.8 (CH), 127.7 (CH), 127.5

(C_q), 127.44 (C_q), 127.40 (C_q), 127.1 (C_q), 126.9 (CH), 117.7 (CH), 108.7 (CH), 107.8 (CH), 43.9 (CH), 35.7 (C_q), 34.4 (C_q), 31.9 (CH_3), 31.4 (CH_3).

MALDI-MS (pos.): m/z calc. for $C_{43}H_{38}N_4O_4$ 674.289, found 674.311.

***N,N'-Bis*(4-(di(dipyrrolylmethyl)phenyl)-naphthalene-1,4,5,8-tetracarboxylic diimide (19)**

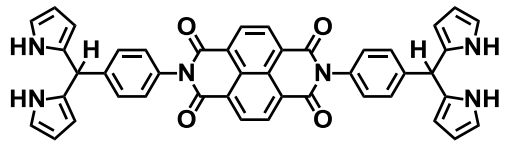

CA: [–]

1,4,5,8-Naphthalenetetracarboxylic dianhydride (200 mg, 746 µmol) and *meso*-(*p*-aminophenyl)dipyrromethane (**13**) (389 mg, 1.64 mmol) were combined in a schlenk tube in dry pyridine (8 mL) and stirred for 20 h at 120°C. Pyridine was distilled under reduced pressure and the resulting crude product was treated with CH_2Cl_2 (20 mL), the insoluble black solid (in CH_2Cl_2) was collected and washed twice with CH_2Cl_2 (10 mL).

Yield: 474 mg (671 µmol, 90 %) of a brown solid.

$C_{44}H_{30}N_6O_4$ [706.75]

^{1}H-NMR (400 MHz, dimethylsulfoxide-d_6):

δ [ppm]= 10.69 (d, $^3J_{HH}$ = 2.1 Hz, 4H, N*H*), 8.69 (s, 4H), 7.36–7.31 (-, 8H), 6.66 (dd, $^3J_{HH}$ = 4.0 Hz, $^3J_{HH}$ = 2.4 Hz, 4H), 5.97 (dd, $^3J_{HH}$ = 2.8 Hz, $^3J_{HH}$ = 2.4 Hz, 4H), 5.79 (dd, $^3J_{HH}$ = 4.0 Hz, $^3J_{HH}$ = 2.4 Hz, 4H), 5.47 (s, 2H).

^{13}C-NMR (100 MHz, dimethylsulfoxide-d_6):

δ [ppm] = 163.4 (C_q), 144.7 (C_q), 133.9 (C_q), 133.3 (C_q), 130.9 (CH), 129.0 (CH), 128.9 (CH), 127.4 (C_q), 127.1 (C_q), 117.4 (CH), 107.5 (CH), 106.7 (CH), 43.7 (CH).

MALDI-MS (pos.): m/z calc. for $C_{44}H_{30}N_6O_4$ 706.232, found 706.249.1

4-Bromobenzaldehyde ethylene acetal (20)

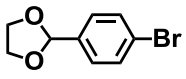

Synthesis according to lit.[288]

[CA: [10602-01-4]

Etyhlene glycol (3.35 mL, 54.0 mmol) and *p*-toluenesulfonic acid (4.70 mg, 270 µmol) were mixed in toluene (30 mL) and heated for 90 min at 120°C. 4-Bromobenzaldehyde (5.00 g, 27.0 mmol) dissolved in toluene (10 mL) was added and the reaction mixture was refluxed for 20 h. After cooling to room temperature saturated $NaHCO_3$-solution (20 mL) was added and the two layers were separated. The aqueous layer was extracted with ethyl acetate (3×40 mL). The combined organic phases were washed with water (40 mL) and brine (50 mL), dried with $MgSO_4$ and the solvent was removed under reduced pressure. The crude product was purified by flash chromatography on silica gel (eluent: petrol ether : Et_2O = 9 : 1).

Yield: 3.93 g (17.2 mmol, 64 %) of a colourless solid.

$C_9H_9BrO_2$ [229.07]

^{1}H-NMR (400 MHz, CDCl3):
δ [ppm] = 7.51 (AA', 2H), 7.35 (BB', 2H), 4.14–3.99 (-, 4H), 5.77 (s, 1H).

4-Formylphenylboronic acid (21)

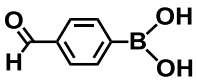

Synthesis according to lit.[289]

CA: [87199-17-5]

4-Bromobenzaldehyde ethylene acetal (**20**) (3.93 g, 17.2 mmol) was dissolved in dry THF and the solution was cooled to −78°C. A solution of *n*BuLi in THF (9.90 mL, 25.7 mmol, 2.6 M) was added dropwise and the mixture was stirred at −78°C for 60 min. To the solution

tri-isopyropyl borate (12.0 mL, 9.68 g, 51.5 mmol) was added dropwise and the reaction mixture was allowed to warm to rt and stirred for 12 h. Then mixture was quenched with 3 N HCl (15 mL) and stirred for additional 3 h. The phases were separated and the aqueous phase was extracted with ethyl acetate (3 × 40 mL). The combined organic phases were washed with water (30 mL) and brine (30 mL), dried with $MgSO_4$ and the solvent was removed under reduced pressure. The residue was purified by flash chromatography on silica gel (eluent: petrol ether : ethyl acetat = 1 : 1 → CH_2Cl_2 : MeOH = 30 : 1).

Yield: 2.00 g (13.3 mmol, 78 %) of a colourless solid.

$C_7H_7BO_3$ [149.94]

^{1}H-NMR (400 MHz, dimethylsulfoxide-d_6):

δ [ppm] = 10.03 (s, 1H, C*H*O), 8.32 (s, 2H, O*H*), 7.98 (AA', 2H), 7.86 (BB', 2H).

4'-Nitrobiphenyl-4-carboxaldehyde (22)

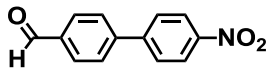

Synthesis follows a slightly modified procedure according to lit.[290]

CA: [98648-23-8]

4-Formylphenylboronic acid (**21**) (2.00 g, 13.3 mmol), 1-iodo-4-nitrobenzene (3.99 g, 16.0 mmol) and $Pd_2(dba)_3{\cdot}CHCl_3$ (276 mg, 267 µmol) were dissolved in abs. THF (20 mL) under nitrogen and a 2 M Na_2CO_3 solution (14 mL) was added. The reaction mixture was degassed for 10 min and stirred for 12 h at 80°C. The solvent was removed under reduced pressure and the residue was partitioned between CH_2Cl_2 (20 mL) and water (20 mL). The phases were separated and the aqueous phase was extracted with CH_2Cl_2 (3 × 30 mL). The combined organic phases were dried with $MgSO_4$ and the solvent was removed under reduced pressure. The crude product was purified by flash chromatography on silica gel (eluent: petrol ether : ethyl acetate = 10 : 1 → 4 : 1).

Yield: 2.04 g (8.98 mmol, 67 %) of a grey solid.

$C_{13}H_9NO_3$ [227.22]

^{1}H-NMR (400 MHz, CDCl3):

δ [ppm] = 10.03 (s, 1H, C*H*O), 8.27 (AA', 2H), 7.95 (BB', 2H), 7.74–7.70 (-, 4H).

***meso*-(4,4´-Nitrobiphenyl)dipyrromethane (23)**

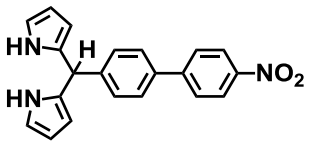

CA: [–]

Synthesis according to GP II:

4'-Nitrobiphenyl-4-carboxaldehyde (**22**) (1.54 g, 6.78 mmol), 1*H*-pyrrole (4.55 g, 4.69 mL, 67.8 mmol), iodine (172 mg, 678 µmol), CH_2Cl_2: 60 mL; 5 min at 30–40°C (150 W); flash column chromatography (eluent: petrol ether : ethyl acetate = 10 : 1 → 5 : 1).

Yield: 1.71 g (4.98 mmol, 74 %) of a brownish-green solid.

$C_{21}H_{17}N_3O_2$ [343.38]

^{1}H-NMR (400 MHz, acetone-d_6):

δ [ppm] = 9.73 (s, 2H, N*H*), 8.31 (AA', 2H), 7.93 (BB', 2H), 7.70 (AA'', 2H), 7.35 (BB'', 2H), 6.71 (ddd, $^3J_{HH}$ = 4.2 Hz, $^3J_{HH}$ = 2.7 Hz, $^4J_{HH}$ = 1.6 Hz, 2H), 6.01 (dd, $^3J_{HH}$ = 5.5 Hz, $^3J_{HH}$ = 2.6 Hz, 2H), 5.98 (dddd, $^3J_{HH}$ = 3.4 Hz, $^3J_{HH}$ = 2.5 Hz, $^4J_{HH}$ = 1.6 Hz, $^4J_{HH}$ = 0.8 Hz, 2H), 5.54 (s, 1H).

^{13}C-NMR (100 MHz, acetone-d_6)[1]:

δ [ppm] = 148.2 (C_q), 148.1 (C_q), 145.9 (C_q), 137.5 (C_q), 133.8 (C_q, rel. Int.: 0.83) together with 133.6 (C_q, rel. Int.: 0.17), 130.3 (CH), 128.7 (CH), 128.1 (CH), 125.0 (CH), 118.1 (CH, rel. Int.: 0.84) together with 118.0 (CH, rel. Int.: 0.16), 108.39 (CH,

[1] Carbon NMRs of some dipyrromethanes, measured in acetone-d_6, give a second set of signals for the pyrrole rings only. This may be due to a hindered conformational rotation of the carbon in *meso*-position. In other solvents, like dimethylsulfoxide-d_6, $CDCl_3$ and CD_2Cl_2, such a behaviour is not observed and excludes impurities.

rel. Int.: 0.79) together with 108.35 (CH, rel. Int.: 0.21), 127.7 (CH, rel. Int.: 0.76) together with 127.51 (CH, rel. Int.: 0.24), 44.7 (CH, rel. Int.: 0.70) together with 44.6 (CH, rel. Int.: 0.30).

MALDI-MS (pos.): m/z calc. for $C_{21}H_{17}N_3O_2$ 343.132 ($M^{+\cdot}$),
m/z calc. for $C_{21}H_{16}N_3O_2$ ($M^{+\cdot}$ –H) 342.124, found 342.120.

***meso*-(4´-Phenyl-4-aniline)dipyrromethane (24)**

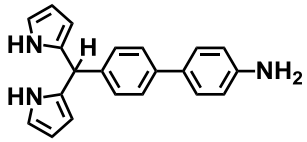

Synthesis according to lit.[287]

CA: [–]

meso-(4,4´-Nitrobiphenyl)dipyrromethane (**23**) (1.71 g, 4.98 mmol) and 10 % palladium on carbon (424 mg, 398 µmol) were suspended in dry THF (50 mL) and saturated with hydrogen gas. The reaction mixture was stirred at rt for 48 h under an atmosphere of nitrogen. After no more hydrogen gas was consumed, the reaction mixture was filtered over celite and the celite plug was washed with THF. The solvent was removed under reduced pressure and the residue was purified by flash column chromatography on silica gel (eluent: petrol ether : ethyl acetate = 2 : 1 → 1 : 1).

Yield: 1.41 g (4.50 mmol, 90 %) of a light brown solid.

$C_{21}H_{19}N_3$ [313.40]

^{1}H-NMR (400 MHz, acetone-d_6):

δ [ppm] = 9.65 (s, 2H, N*H*), 7.45 (AA', 2H), 7.36 (BB', 2H), 7.20 (AA'', 2H), 6.73 (BB'', 2H), 6.68 (ddd, $^3J_{HH}$ = 2.7 Hz, $^3J_{HH}$ = 2.7 Hz, $^4J_{HH}$ = 1.6 Hz, 2H), 5.98 (dd, $^3J_{HH}$ = 2.7 Hz, $^3J_{HH}$ = 2.7 Hz, 2H), 5.77 (dddd, $^3J_{HH}$ = 3.3 Hz and $^3J_{HH}$ = 2.5 Hz, $^4J_{HH}$ = 1.6 Hz and $^4J_{HH}$ = 0.8 Hz, 2H), 5.45 (s, 1H), 4.68 (d, 2H, NH_2).

^{13}C-NMR (100 MHz, acetone-d_6):

δ [ppm] = 149.0 (C_q), 142.3 (C_q), 140.5 (C_q), 134.4 (C_q), 130.2 (C_q), 129.8 (CH), 128.4 (CH), 126.5 (CH), 117.9 (CH), 115.7 (CH), 108.3 (CH), 107.5 (CH), 44.8 (CH).

MALDI-MS (pos.): m/z calc. for $C_{21}H_{19}N_3$ 313.157, found 313.156.

***meso*-(4,4´-(*N*-(2,5-Di-*tert*-butylphenyl)-naphthalene-1,4,5,8-tetracarboxyldiimide)biphenyl)dipyrromethane (25)**

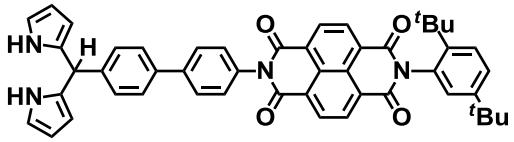

CA: [–]

Naphthalene-1,4,5,8-tetracarboxylic dianhydride (1.00 g, 3.73 mmol), 2,5-di-*tert*-butylaniline (766 mg, 3.73 mmol) and *meso*-(4´-phenyl-4-aniline)dipyrromethane (**24**) (1.17 g, 3.73 mmol) were dissolved in a microwave quartz tube in abs. DMF (20 mL) and heated in a microwave oven (300 W, 150°C) for 1.5 h. The solvent was removed under reduced pressure and the resulting solid was purified by flash column chromatography on silica gel (eluent: petrol ether : ethyl acetate = 4 : 1 → 1 : 2).

Yield: 430 mg (573 mmol, 15 %) of a redish-brown solid.

$C_{49}H_{42}N_4O_4$ [750.88]

^{1}H-NMR (400 MHz, $CDCl_3$):

δ [ppm] = 8.87 (-, 4H), 8.04 (s, 2H, N*H*), 7.77 (AA', 2H), 7.63–7.59 (-, 3H), 7.50 (dd, $^3J_{HH}$ = 8.6 Hz, $^4J_{HH}$ = 2.2 Hz, 1H), 7.40 (AA'', 2H), 7.33 (BB'', 2H), 7.03 (d, $^4J_{HH}$ = 2.2 Hz, 1H), 6.74 (ddd, $^3J_{HH}$ = 4.2 Hz, $^3J_{HH}$ = 2.7 Hz, $^4J_{HH}$ = 1.6 Hz, 2H), 6.19 (dd, $^3J_{HH}$ = 2.7 Hz, $^3J_{HH}$ = 2.7 Hz, 2H), 5.99 (dddd, $^3J_{HH}$ = 3.4 Hz and $^3J_{HH}$ = 2.4 Hz, $^4J_{HH}$ = 1.5 Hz and $^4J_{HH}$ = 0.8 Hz, 2H), 5.56 (s, 1H), 1.34 (s, 9H, ^{t}Bu), 1.29 (s, 9H, ^{t}Bu).

^{13}C-NMR (100 MHz, $CDCl_3$):

δ [ppm] = 164.0 (C_q), 163.3 (C_q), 150.6 (C_q), 143.8 (C_q), 142.0 (C_q), 141.9 (C_q), 139.1 (C_q), 133.8 (C_q), 132.4 (C_q), 132.1 (C_q), 131.68 (CH), 131.65 (CH), 129.2 (CH), 129.1 (CH), 128.9 (CH), 128.4 (CH), 127.73 (CH), 127.68 (CH), 127.49 (C_q), 127.45 (C_q), 127.4 (C_q), 127.1 (C_q), 126.9 (CH), 117.5 (CH), 108.7 (CH), 107.5 (CH), 43.9 (CH), 35.7 (C_q), 34.4 (C_q), 31.9 (CH_3), 31.4 (CH_3).

MALDI-MS (pos.): m/z calc. for $C_{49}H_{42}N_4O_4$ 750.320 ($M^{+\cdot}$) was not observed,
m/z calc. for $C_{49}H_{41}N_4O_4$ 749.312 ($M^{+\cdot}$ -H), found 749.388.

5.2.6 Dipyrromethane Ligands with Substituted Pyrrole Rings

2-(Methoxy(methyl)amino)-2-oxoethanaminiumbromide (26)

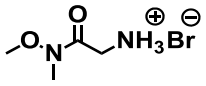

Synthesis according to lit.[393-394]

CA: [154780-67-3]

N-*tert*-Butoxycarbonyl-*N*-methoxy-*N*-methylglycinamide (5.00 g, 22.9 mmol) and HBr (48 %) (4.98 mL, 92.0 mmol) were dissolved in acetic acid (10 mL) and stirred at room temperature for 16 h. Acetic acid was removed by distillation and the residue was partitioned between water and CH_2Cl_2, the two layers separated and the aqueous phase was washed with CH_2Cl_2 (3 × 30 mL). The aqueous phase was taken to dryness under reduced pressure and the resulting colourless solid was used without further purification for the following step.

Yield: 4.50 g (22.6 mmol, 99 %).

$C_4H_{12}BrN_2O_2$ [199.05]

^{1}H-NMR (400 MHz, dimethylsulfoxide-d_6):

δ [ppm] = 8.09 (s, 3H, NH_3), 3.87 (q, $^{3}J_{HH}$ = 5.6 Hz, 2H, CH_2), 3.71 (s, 3H, CH_3), 3.15 (s, 3H, CH_3).

(*E*)-2-((1-Cyanoprop-1-en-2-yl)amino)-*N*-methoxy-*N*-methylacetamide (27)

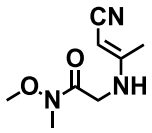

Synthesis according to lit.[393-394]

CA: [231609-57-7]

2-(Methoxy(methyl)amino)-2-oxoethanaminiumbromide (**26**) (2.74 g, 13.8 mmol) was dissolved in dry EtOH (120 mL), 3-aminocrotonitrile (2.37 g, 28.9 mmol) was added and the solution was stirred for 12 h at 50°C. The solid was filtered, the solvent was removed under reduced pressure and the oily residue was treated with CH_2Cl_2 (50 mL). The resulting solid was filtered off and washed with CH_2Cl_2 (100 mL). The organic phases were combined and the solvent was removed under reduced pressure. The crude product was purified by flash column chromatography (eluent: petrol ether : ethyl acetate = 2 : 1 → 1 : 1 → 1 : 2) and the product fractions containing the desired product were evaporated and the resulting residue was recrystallised from ethyl acetate.

Yield: 2.06 g (11.2 mmol, 82 %) of a yellowish solid.

$C_8H_{13}N_3O_2$ [183.21]

^{1}H-NMR (400 MHz, $CDCl_3$):

δ [ppm] = 5.29 (s, 1H, N*H*), 3.80 (d, ^3J = 3.9 Hz, 2H, CH_2), 3.75 (d, ^4J = 0.9 Hz, 1H, C*H*), 3.73 (s, 3H, CH_3), 3.24 (s, 3H, CH_3), 2.16 (s, 3H, CH_3).

(*E*)-3-((2-Oxopropyl)amino)but-2-enenitrile (28)

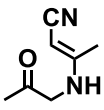

Synthesis according to lit.[393-394]

CA: [910225-64-8]

A solution of (*E*)-2-((1-cyanoprop-1-en-2-yl)amino)-*N*-methoxy-*N*-methylacetamide (**27**) (3.65 g, 19.9 mmol) in THF (25 mL) was added to a solution of MeMgBr (19.9 mL, 59.8 mmol, 3 M in Et_2O) at −10°C. The mixture was stirred at −10°C for 3 h, warmed to rt and stirred for further 12 h. The solvent was removed under reduced pressure and the residue was taken-up in ethyl acetate and washed with brine (30 mL) and water (2 × 30 mL). The combined organic phases were dried over $MgSO_4$, the solvent was removed under reduced pressure and the product was dried and used without further purification.

Yield: 2.54 g (18.4 mmol, 92 %) of a colourless solid.

$C_7H_{10}N_2O$ [138.17]

^{1}H-NMR (400 MHz, $CDCl_3$):

δ [ppm] = 5.18 (s, 1H, N*H*), 3.82 (d, $^3J_{HH}$ = 4.1 Hz, 2H, CH_2), 3.72 (s, 1H, C*H*), 2.25 (s, 3H, CH_3), 2.14 (s, 3H, CH_3).

3-Cyano-2,4-dimethyl-1*H*-pyrrole (29)

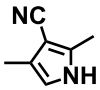

Synthesis according to lit.[392-394]

CA: [26187-28-0]

(*E*)-3-((2-Oxopropyl)amino)but-2-enenitrile (**28**) (2.54 g, 18.4 mmol) was dissolved in dry EtOH (50 mL) and cooled to 0°C (ice-water bath). A freshly prepared solution of NaOEt (from 85.0 mg sodium in 14 mL EtOH, 3.89 mmol) was added dropwise over a period of 10 min. The reaction mixture was stirred for 3 h at 0°C, warmed to room temperature and stirred for 12 h. The solvent was removed under reduced pressure, water (20 mL) was added and the mixture was extracted with ethyl acetate (4 × 30 mL). The combined organic phases were washed with brine and with water (2 × 20 mL) and dried over $MgSO_4$. The solvent was removed under reduced pressure and the solid residue purified by flash column chromatography on silica gel (petroleum ether : ethyl acetate = 2 : 1 → 1 : 1 → 1 : 2).

Yield: 1.77 g (14.7 mmol, 80 %) of a creamy white solid.

$C_7H_8N_2$ [120.15]

^{1}H-NMR (400 MHz, $CDCl_3$):

δ [ppm] = 8.19 (s, 1H, N*H*), 6.37 (q, $^4J_{HH}$ = 1.1 Hz, 1H, C*H*), 2.37 (s, 3H, CH_3), 2.13 (d, $^4J_{HH}$ = 1.1 Hz, 3H, CH_3).

2-Cyano-1*H*-pyrrole (30)

CA: [4513-94-4]

Synthesis according lit:[417]

2-Formyl-1*H*-pyrrole (1.50 g, 15.8 mmol) was dissolved in water (50 mL) and hydroxylamine-*O*-sulfonic acid (6.24 g, 55.2 mmol) was added. The mixture was stirred at rt for 12 h, cooled to 0°C (water-ice bath) and a freshly prepared solution of KOH (6.19 g, 110 mmol) in water (40 mL) was added dropwise over a period of 1 h. After 3 h of stirring at rt, the reaction mixture was extracted with CH_2Cl_2 (3 × 60 mL), the combined organic phases dried with $MgSO_4$ and the solvent removed under reduced pressure. The crude product was used for the following steps without further purification.

Yield: 1.07 g (11.6 mmol, 74 %) of a brown liquid.

$C_5H_4N_2$ [92.10]

^{1}H-NMR (400 MHz, acetone-d_6):

δ [ppm] = 11.24 (s, 1H), 7.10 (d, $^3J_{HH}$ = 1.24, 1H), 6.85 (m, 1H), 6.25 (m, 1H).

2,8-Dicycano-1,3,7,9-tetramethyl-*meso*-(*p*-cyanophenyl)dipyrromethane (31)

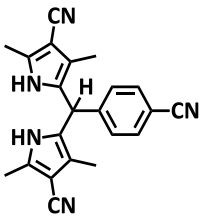

CA: [–]

4-Cyanobenzaldehyde (295 mg, 2.25 mmol) and 3-cyano-2,4-dimethyl-1*H*-pyrrole (**29**) (541 mg, 4.50 mmol) were dissolved in dry CH_2Cl_2 (25 mL) and degassed for 5 min. Three drops of TFA were added and the reaction mixture turned from colourless to pink. After 3 h of stirring at rt, the reaction mixture was filtered and the filtrate taken to dryness. The precipitate was collected and the solvent of the reaction mixture was removed under reduced pressure. The resulting pale red solids were combined and recrystallised from ethyl acetate.

Yield: 728 mg (2.06 mmol, 92 %) of a colourless solid.

$C_{22}H_{19}N_5$ [353.42]

^{1}H-NMR (400 MHz, CD_2Cl_2):

δ [ppm] = 7.80 (s, 2H, N*H*), 6.37 (AA', 2H), 2.21 (BB', 2H), 5.48 (s, 1H), 2.31 (s, 6H, CH_3), 1.87 (s, 6H CH_3).

^{13}C-NMR (100 MHz, CD_2Cl_2):

δ [ppm] = 145.2 (C_q), 136.7 (C_q), 133.4 (CH), 129.4 (CH), 125.0 (C_q), 119.0 (C_q), 118.7 (C_q), 116.5 (C_q), 111.9 (C_q), 94.5 (C_q), 40.5 (CH), 12.6 (CH_3), 9.9 (CH_3).

MALDI-MS (pos.): m/z calc. for $C_{22}H_{19}N_5$ 353.163, found 353.154.

2,8-Dicycano-1,3,7,9-tetramethyl-*meso*-(trimethylsilylethynyl)dipyrromethane (32)

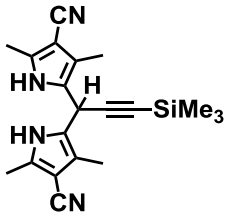

CA: [–]

Iodine (84.0 mg, 330 µmol) and 3-cyano-2,4-dimethyl-1*H*-pyrrole (**29**) (793 mg, 6.60 mmol) were dissolved in dry CH_2Cl_2 (15 mL) under nitrogen. 3-(Trimethylsilyl)-2-propinal (500 mg, 571 µL, 3.69 mmol) was added and the mixture stirred (reflux conditions) in a microwave oven for 30 minutes at 30°C (max. 80 W). The solvent was removed under reduced pressure and the solid residue purified by flash column chromatography on silica gel (petroleum ether : ethyl acetate = 5 : 1 → 3 : 1 → 2 : 1).

Yield: 774 mg (2.22 mmol, 67 %) of a pale red solid.

$C_{20}H_{24}N_4Si$ [348.52]

^{1}H-NMR (400 MHz, CD_2Cl_2):

δ [ppm] = 8.29 (s, 2H, N*H*), 5.07 (s, 1H), 2.34 (s, 6H, CH_3), 2.00 (s, 6H, CH_3), 0.20 (s, 9H, Si(CH_3)$_3$).

^{13}C-NMR (100 MHz, CD_2Cl_2):

δ [ppm] = 136.2 (C_q), 122.9 (C_q), 117.9 (C_q), 116.6 (C_q), 101.4 (C_q), 94.1 (C_q), 89.8 (C_q), 28.0 (CH), 12.5 (CH_3), 9.7 (CH_3), -0.1 (Si(CH_3)$_3$).

MALDI-MS (pos.): m/z calc. for $C_{20}H_{24}N_4Si$ 348.176, found 348.155.

2,8-Dicycano-1,3,7,9-tetramethyl-*meso*-(ethynyl)dipyrromethane (33)

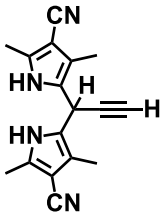

CA: [–]

2,8-Dicycano-1,3,7,9-tetramethyl-*meso*-(trimethylsilylethynyl)dipyrromethane (**32**) (75.0 mg, 215 µmol) was dissolved in a mixture of dry THF (2 mL) and dry methanol (4 mL) and potassium fluoride (50.0 mg, 861 µmol) was added. The mixture was stirred at rt for 12 h, CH_2Cl_2 (5 mL) and water (5 mL) were added and stirred for 5 min. The layers were separated and the aqueous layer was extracted with CH_2Cl_2 (2 × 10 mL) and the combined organic phases were dried with $MgSO_4$. The solvent was removed under reduced pressure and the solid residue purified by flash column chromatography on silica gel (petroleum ether : ethyl acetate = 2 : 1).

Yield: 55.0 mg (199 µmol, 92 %) of a beige solid.

$C_{17}H_{16}N_4$ [276.34]

^{1}H-NMR (400 MHz, CD_2Cl_2):

δ [ppm] = 8.32 (s, 2H, N*H*), 5.06 (s, $^4J_{HH}$ = 2.6 Hz, 1H, C*H*), 2.56 (d, $^4J_{HH}$ = 2.6 Hz, 1H, CH_3), 2.34 (s, 6H, CH_3), 1.98 (d, $^5J_{HH}$ = 0.3 Hz, 6H, CH_3).

^{13}C-NMR (100 MHz, CD_2Cl_2):

δ [ppm] = 136.3 (C_q), 122.6 (C_q), 118.1 (C_q), 116.5 (C_q), 94.2 (C_q), 80.2 (C_q), 73.3 (C_q), 26.8 (CH), 12.5 (CH_3), 9.6 (CH_3).

MALDI-MS (pos.): m/z calc. for $C_{17}H_{16}N_4$ 276.137, found 276.093.

5.2.7 Dinuclear Cyclometalated μ-Chloro Bridged Iridium(III) Complexes

***Tetrakis*(1-phenylpyrazolyl)(μ-dichloro) diiridium(III) (34)**

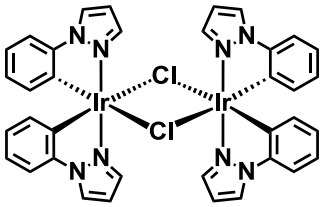

CA: [57175-14-1]

Synthesis according to GP IV

Ir(III)$Cl_3 \cdot n H_2O$ (1.20 g, 3.40 mmol), 1-phenylpyrazole (1.03 g, 945 µL, 7.15 mmol) in a 3 : 1 mixture of 2-ethoxyethanol and deionised water (30 mL), 100°C for 24 h.

Yield: 1.57 g (1.70 mmol, 90 %) of a grey solid.

$C_{36}H_{28}Cl_2Ir_2N_8$ [1028.00]

Compound (35)

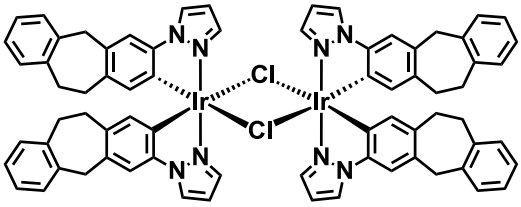

CA: [1465025-41-5]

Synthesis according to GP IV

Ir(III)$Cl_3 \cdot n H_2O$ (139 mg, 393 µmol), 3-(1-pyrazolyl)-10,11-dihydro-5*H*-dibenzo[a,d][7]annulene (**10**) (215 mg, 826 µmol) in a 3 : 1 mixture of 2-ethoxyethanol water (20 mL), 100°C, 12 h.

Yield: 280 mg (188 µmol, 95 %) of a grey solid.

$C_{72}H_{60}Cl_2Ir_2N_8$ [1492.64]

MALDI-MS (pos.): m/z calc. for $C_{72}H_{60}Cl_2Ir_2N_8$ 1488.352, found 1488.313,
m/z calc. for $C_{36}H_{30}ClIrN_4$ 744.176, found 744.162.

Compound (36)

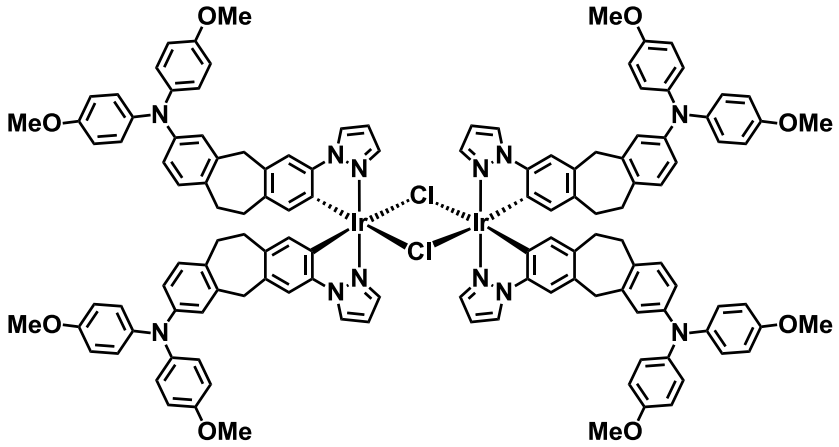

CA: [1151886-25-7]

Synthesis according to GP IV

Ir(III)Cl_3·*n*H_2O (100 mg, 284 µmol), 3-*bis*(*p*-anisyl)amine-7-(1-pyrazolyl)-10,11-dihydro-5*H*-dibenzo[a,d][7]annulene (**4**) (311 mg, 638 µmol) in a 3 : 1 mixture of 2-ethoxyethanol water (15 mL), 100°C, 12 h.

Yield: 337 mg (140 µmol, 99 %) of a grey solid.

$C_{128}H_{112}Cl_2Ir_2N_{12}O_8$ [2401.67]

MALDI-MS (pos.): m/z calc. for $C_{64}H_{56}ClIrN_6O_4$ 1198.365, found 1198.327,
m/z calc. for $C_{64}H_{56}IrN_6O_4$ 1163.396, found 1163.319.

Compound (37)

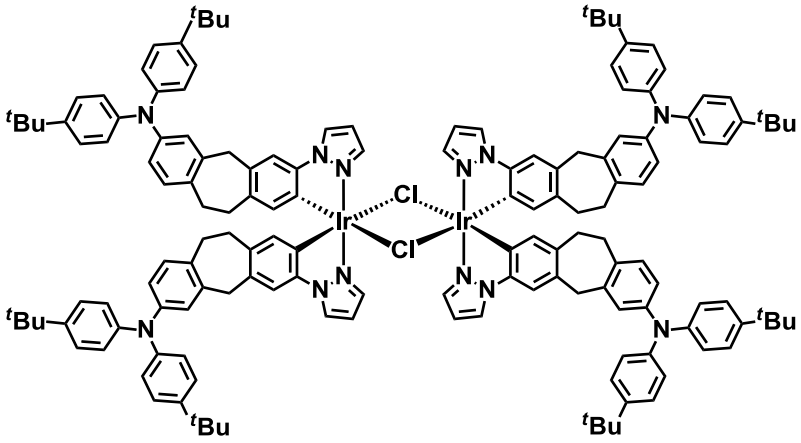

CA: [1465025-43-7]

Synthesis according to GP IV

Ir(III)Cl_3·*n*H_2O (131 mg, 371 µmol), 3-*bis*(*p*-*tert*-butylphenyl)amine-7-(1-pyrazolyl)-10,11-dihydro-5*H*-dibenzo[a,d][7]annulene (**6**) (400 mg, 741 µmol) in a 3 : 1 mixture of 2-ethoxyethanol water (15 mL), 100°C, 12 h.

Yield: 414 mg (159 µmol, 86 %) of a grey solid.

$C_{152}H_{160}Cl_2Ir_2N_{12}$ [2610.31]

MALDI-MS (pos.): m/z calc. for $C_{76}H_{80}ClIrN_6$ 1304.576, found 1304.592,
m/z calc. for $C_{76}H_{80}IrN_6$ 1269.608, found 1269.630.

Compound (38)

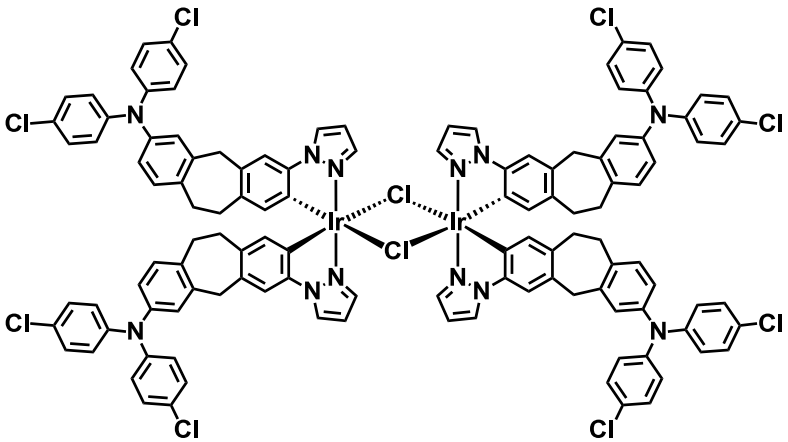

CA: [–]

Synthesis according to GP IV

Ir(III)Cl_3·*n*H_2O (115 mg, 326 µmol), 3-*bis*(*p*-chlorophenyl)amine-7-(1-pyrazolyl)-10,11-dihydro-5*H*-dibenzo[a,d][7]annulene (**8**) (340 mg, 685 µmol) in a 3 : 1 mixture of 2-ethoxyethanol water (15 mL), 100°C, 12 h.

Yield: 378 mg (155 µmol, 95 %) of a grey solid.

$C_{120}H_{88}Cl_{10}Ir_2N_{12}$ [2437.03]

MALDI-MS (pos.): m/z calc. for $C_{60}H_{44}Cl_5IrN_6$ 1214.167, found 1214.061,
m/z calc. for $C_{60}H_{44}Cl_4IrN_6$ 1179.198, found 1179.086.

Compound (39)

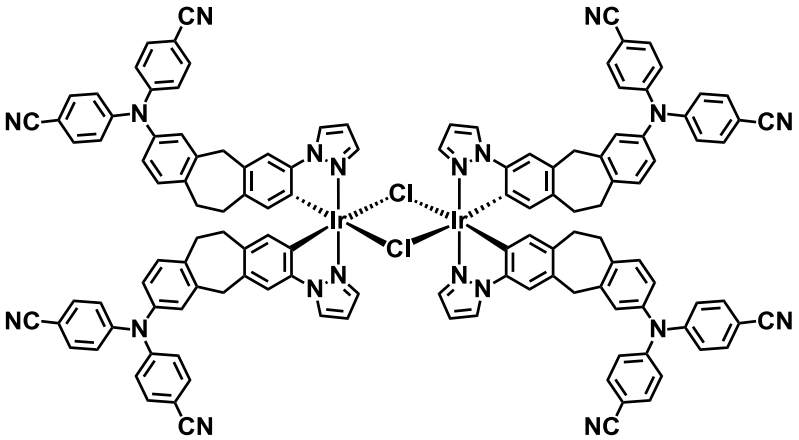

CA: [–]

Synthesis according to GP IV

Ir(III)Cl_3·*n*H_2O (118 mg, 335 µmol), 3-*bis*(*p*-cyanophenyl)amine-7-(1-pyrazolyl)-10,11-dihydro-5*H*-dibenzo[a,d][7]annulene (**9**) (320 mg, 670 µmol) in a 3 : 1 mixture of 2-ethoxyethanol water (15 mL), 100°C, 12 h.

Yield: 270 mg (114 µmol, 68 %) of a yellow solid.

$C_{128}H_{88}Cl_2Ir_2N_{20}$ [2361.55]

MALDI-MS (pos.): m/z calc. for $C_{64}H_{44}ClIrN_{10}$ 1178.304, found 1178.273,
m/z calc. for $C_{64}H_{44}IrN_{10}$ 1143.335, found 1143.299.

Compound (40)

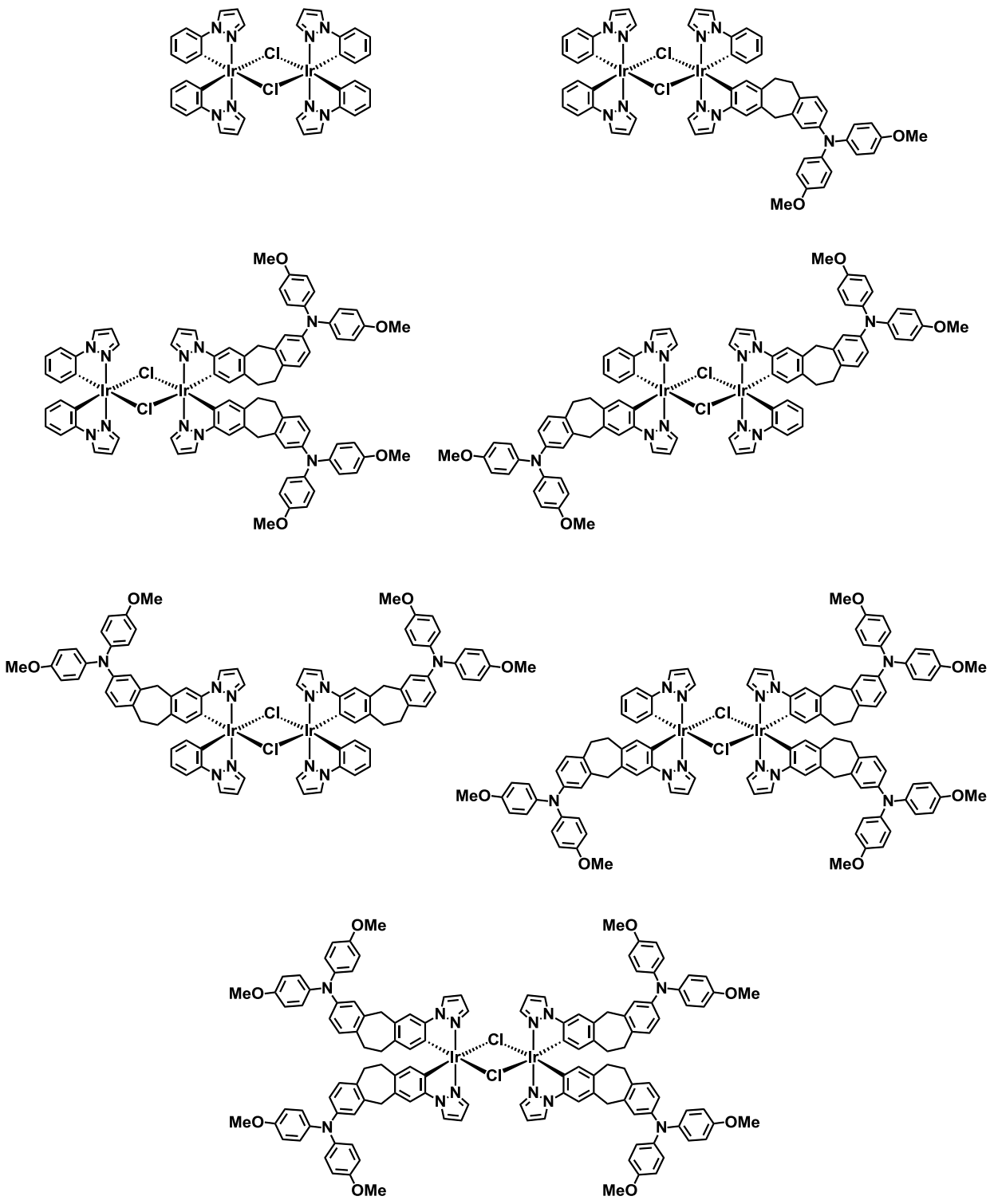

CA: [–]

Synthesis according to GP IV

Ir(III)Cl_3·*n*H_2O (120 mg, 340 µmol), 3-*bis*(*p*-anisyl)amine-7-(1-pyrazolyl)-10,11-dihydro-5*H*-dibenzo[a,d][7]annulene (**4**) (199 mg, 408 µmol), 1-phenylpyrazole (49.0 mg, 340 µmol) in a 3 : 1 mixture of 2-ethoxyethanol-water (15 mL), 100°C, 12 h.

Yield: 360 mg of a grey solid as a mixture of five different complexes, some present as a mixture of different stereoisomers/diastereisomers.

$C_{36}H_{28}Cl_2Ir_2N_8$ [1028.00], $C_{59}H_{49}Cl_2Ir_2N_9O_2$ [1371.42], $C_{82}H_{70}Cl_2Ir_2N_{10}O_4$ [1714.84], $C_{105}H_{91}Cl_2Ir_2N_{11}O_6$ [2058.26], $C_{128}H_{112}Cl_2Ir_2N_{12}O_8$ [2401.67]

MALDI-MS (pos.): m/z calc. for $C_{18}H_{14}ClIrN_4$ 512.051, found 512.071,
m/z calc. for $C_{18}H_{14}IrN_4$ 477.082, found 477.116.

m/z calc. for $C_{41}H_{35}ClIrN_5O_2$ 855.208, found 855.021,
m/z calc. for $C_{41}H_{35}IrN_5O_2$, 820.239, found 820.047.

m/z calc. for $C_{64}H_{56}ClIrN_6O_4$ 1198.365, found 1198.191,
m/z calc. for $C_{64}H_{56}IrN_6O_4$ 1163.396, found 1163.216.

5.2.8 Neutral Cyclometalated Iridium(III) Dipyrrinato Complexes

5.2.8.1 Reference Complexes

Ref1

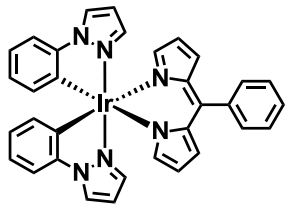

CA: [1012047-85-6]

Synthesis following GP V:

Meso-(phenyl)dipyrromethane (**11**) (90.0 mg, 405 µmol), 2,3-dichloro-5,6-dicyano-1,4-benzoquinone (DDQ) (101 mg, 445 µmol), potassium carbonate (1.12 g, 8.10 mmol), compound (**34**) (208 mg, 202 µmol) in THF (15 mL), 66°C, 12 h, flash column chromatography (eluent: petrol ether : ethyl acetate = 5 : 2 → 7 : 3).

Yield: 253 mg (363 µmol, 90 %) of a red solid.

$C_{33}H_{25}IrN_6$ [697.81]

^{1}H-NMR (400 MHz, acetone-d_6):

δ [ppm]= 8.54 (dd, $^{3}J_{HH}$ = 2.9 Hz, $^{3}J_{HH}$ = 0.8 Hz, 2H), 7.52–7.43 (-, 7H), 7.05 (dd, $^{3}J_{HH}$ = 2.2 Hz, $^{3}J_{HH}$ = 0.7 Hz, 2H), 6.99 (dd, $^{3}J_{HH}$ = 1.4 Hz, $^{3}J_{HH}$ = 1.4 Hz, 2H), 6.92 (ddd, $^{3}J_{HH}$ = 7.9 Hz, $^{3}J_{HH}$ = 7.3 Hz, $^{4}J_{HH}$ = 1.4 Hz, 2H), 6.75 (ddd, $^{3}J_{HH}$ = 7.4 Hz, $^{3}J_{HH}$ = 7.4 Hz, $^{4}J_{HH}$ = 1.2 Hz, 2H), 6.65 (dd, $^{3}J_{HH}$ = 2.8 Hz, $^{3}J_{HH}$ = 2.2 Hz, 2H) 6.43 (dd, $^{3}J_{HH}$ = 4.3 Hz, $^{3}J_{HH}$ = 1.4 Hz, 2H), 6.39 (ddd, $^{3}J_{HH}$ = 7.4 Hz, $^{3}J_{HH}$ = 1.4 Hz, $^{3}J_{HH}$ = 0.4 Hz, 2H), 6.23 (dd, $^{3}J_{HH}$ = 4.3 Hz, $^{3}J_{HH}$ = 1.4 Hz, 2H).

^{13}C-NMR (100 MHz, acetone-d_6):

δ [ppm] = 152.6 (CH), 149.3 (C_q), 145.3 (C_q), 140.6 (C_q), 138.7 (C_q), 138.5 (CH), 135.9 (C_q), 134.9 (CH), 131.6 (CH), 131.2 (CH), 128.9 (CH), 127.9 (CH), 127.4 (CH), 126.4 (CH), 122.4 (CH), 117.4 (CH), 111.8 (CH), 108.3 (CH).

Ref2

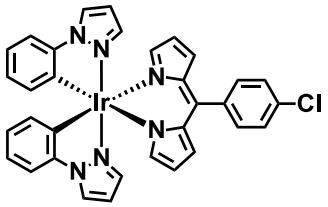

CA: [–]

Synthesis following GP V:

meso-(*p*-Chlorophenyl)dipyrromethane (**14**) (41.0 mg, 160 µmol), 2,3-dichloro-5,6-dicyano-1,4-benzoquinone (DDQ) (40.0 mg, 176 µmol), potassium carbonate (442 mg, 3.20 mmol), compound (**34**) (82.0 mg, 80.0 µmol) in THF (15 mL), 66°C, 12 h, flash column chromatography (eluent: petrol ether : CH_2Cl_2 = 5 : 1 → 1 : 1).

Yield: 73.5 mg (100 µmol, 63 %) of a red solid.

$C_{33}H_{24}ClIrN_6$ [732.25]

^{1}H-NMR (400 MHz, acetone-d_6):

δ [ppm]= 8.54 (dd, $^3J_{HH}$ = 2.9 Hz, $^4J_{HH}$ = 0.6 Hz, 2H), 7.48 (-, 6H), 7.04 (dd, $^3J_{HH}$ = 2.2 Hz, $^4J_{HH}$ = 0.7 Hz, 2H), 7.00 (dd, $^3J_{HH}$ = 1.3 Hz, $^4J_{HH}$ = 1.3 Hz, 2H), 6.92 (ddd, $^3J_{HH}$ = 7.9 Hz, $^3J_{HH}$ = 7.4 Hz, $^4J_{HH}$ = 1.4 Hz, 2H), 6.75 (ddd, $^3J_{HH}$ = 7.4 Hz, $^3J_{HH}$ = 7.4 Hz, $^4J_{HH}$ = 1.2 Hz, 2H), 6.64 (dd, $^3J_{HH}$ = 2.8 Hz, $^3J_{HH}$ = 2.2 Hz, 2H), 6.44 (dd, $^3J_{HH}$ = 4.3 Hz, $^4J_{HH}$ = 1.4 Hz, 2H), 6.38 (dd, $^3J_{HH}$ = 7.4 Hz, $^4J_{HH}$= 2.2 Hz, 2H), 6.25 (dd, $^3J_{HH}$ = 4.3 Hz, $^3J_{HH}$ = 1.4 Hz, 2H).

^{13}C-NMR (100 MHz, acetone-d_6):

δ [ppm] = 153.1 (CH), 147.9 (C_q), 145.4 (C_q), 139.5 (C_q), 138.7 (C_q), 138.7 (CH), 135.8 (C_q), 135.0 (CH), 134.7 (C_q), 133.0 (CH), 131.7 (CH), 128.3 (CH), 127.5 (CH), 126.6 (CH), 122.6 (CH), 117.8 (CH), 112.0 (CH), 108.4 (CH).

Microanalysis (CHN): calc. for $C_{33}H_{24}ClIrN_6$ C-%: 54.13, H-%: 3.30, N-%: 11.48

found for $C_{33}H_{24}ClIrN_6$ C-%: 54.15, H-%: 3.12, N-%: 11.09

ESI-MS (pos., high res.): m/z calc. for $C_{33}H_{24}ClIrN_6$ 731.14296, found 731.14247

Δ = 0.67 ppm.

Ref3

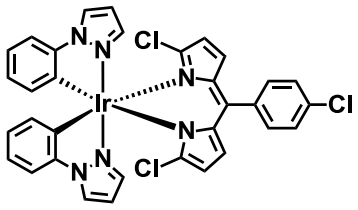

CA: [–]

Synthesis following GP V:

1,9-Dichloro-*meso*-(*p*-chlorophenyl)dipyrromethane (**15**) (64.0 mg, 197 µmol), 2,3-dichloro-5,6-dicyano-1,4-benzoquinone (DDQ) (49.0 mg, 216 µmol), potassium carbonate (543 mg, 3.93 mmol), compound (**34**) (101 mg, 98.0 µmol) in THF (15 mL), 66°C, 12 h, flash column chromatography (eluent: petrol ether : ethyl acetate = 5 : 1 → 3 : 1).

Yield: 76.0 mg (95.0 µmol, 48 %) of a red solid.

$C_{33}H_{22}Cl_3IrN_6$ [801.14]

^{1}H-NMR (400 MHz, acetone-d_6):

δ [ppm]= 8.58 (dd, $^3J_{HH}$ = 2.9 Hz, $^4J_{HH}$ = 0.7 Hz, 2H), 7.68 (dd, $^3J_{HH}$ = 2.2 Hz, $^4J_{HH}$ = 0.7 Hz, 2H), 7.53 (AA', 2H), 7.43 (BB', 2H), 7.33 (dd, $^3J_{HH}$ = 8.0 Hz, $^4J_{HH}$ = 1.0 Hz, 2H), 6.80 (dd, $^3J_{HH}$ = 2.9 Hz, $^3J_{HH}$ = 2.2 Hz, 2H), 6.76 (ddd, $^3J_{HH}$ = 7.9 Hz, $^3J_{HH}$ = 7.3 Hz, $^4J_{HH}$ =1.4 Hz, 2H), 6.53 (ddd, $^3J_{HH}$ = 7.4 Hz, $^3J_{HH}$ = 7.4 Hz, $^4J_{HH}$ = 1.2 Hz, 2H), 6.48 (d, $^3J_{HH}$ = 4.3 Hz, 2H), 6.13 (dd, $^3J_{HH}$ = 7.5 Hz, $^4J_{HH}$ = 1.0 Hz, 2H), 6.12 (d, $^3J_{HH}$ = 4.3 Hz, 2H).

^{13}C-NMR (100 MHz, acetone-d_6):

δ [ppm] = 151.6 (C_q), 146.2 (C_q), 145.2 (C_q), 141.2 (CH), 138.0 (C_q), 137.7 (C_q), 135.9 (CH), 134.9 (C_q), 133.6 (C_q), 133.0 (CH), 133.0 (CH), 128.5 (CH), 127.6 (CH), 125.2 (CH), 122.2 (CH), 117.9 (CH), 111.3 (CH), 108.1 (CH).

Microanalysis (CHN): calc. for $C_{33}H_{22}Cl_3IrN_6$ C-%: 49.47, H-%: 2.71, N-%: 7.53,
found for $C_{33}H_{22}Cl_3IrN_6$ C-%: 50.00, H-%: 2.59, N-%: 7.34.

ESI-MS (pos., high res.): m/z calc. for $C_{33}H_{22}Cl_3IrN_6$ 799.06502, found 799.06548
Δ = 0.58 ppm.

Ref4

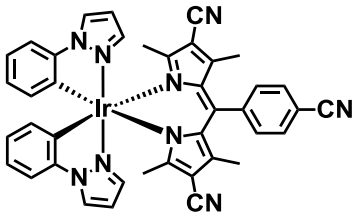

CA: [–]

Synthesis following GP VI:

2,8-Dicyano-1,3,7,9-tetramethl-*meso*-(*p*-cyanophenyl)dipyrromethane (**31**) (50.0 mg, 141 µmol), 2,3-dichloro-5,6-dicyano-1,4-benzoquinone (DDQ) (39.0 mg, 170 µmol), potassium carbonate (391 mg, 2.83 mmol), compound (**34**) (73.0 mg, 71.0 µmol) first in CH_2Cl_2 (5 mL) thereafter in THF (8 mL), 66°C, 24 h, flash column chromatography on aluminium oxide (eluent: petrol ether : CH_2Cl_2 : NEt_3 = 6 : 4 : 0.1 → 6 : 4 : 0.1).

Yield: 10.9 mg (13.0 µmol, 9 %) of a pale red solid.

$C_{40}H_{30}IrN_9$ [828.94]

^{1}H-NMR (600 MHz, CD_2Cl_2):

δ [ppm]= 8.17 (dd, $^3J_{HH}$ = 3.7 Hz, $^4J_{HH}$ = 0.7 Hz, 2H), 7.85 (AA', 2H), 7.62 (dd, $^3J_{HH}$ = 2.2 Hz, $^4J_{HH}$ = 0.7 Hz, 2H), 7.38 (BB', 2H), 7.18 (dd, $^3J_{HH}$ = 7.9 Hz, $^4J_{HH}$ = 1.0 Hz, 2H), 6.88 (ddd, $^3J_{HH}$ = 7.9 Hz, $^3J_{HH}$ = 7.3 Hz, $^4J_{HH}$ =1.3 Hz, 2H), 6.73 (dd, $^3J_{HH}$ = 2.9 Hz, $^3J_{HH}$ =

2.2 Hz, 2H), 6.63 (ddd, $^3J_{HH}$ = 8.7 Hz, $^3J_{HH}$ = 7.5 Hz, $^4J_{HH}$ =1.2 Hz, 2H), 6.12 (dd, $^3J_{HH}$ = 7.6 Hz, $^4J_{HH}$ = 1.0 Hz, 2H), 1.52 (s, 6H, CH_3), 1.34 (s, 6H, CH_3).

^{13}C-NMR (150 MHz, CD_2Cl_2):

δ [ppm] = 164.2 (C_q), 149.4 (C_q), 147.1 (C_q), 143.8 (C_q), 143.1 (C_q), 140.5 (CH), 135.7 (C_q), 135.0 (CH), 133.6 (CH), 133.5 (C_q), 130.7 (CH), 127.0 (CH), 125.5 (CH), 122.3 (CH), 118.6 (C_q), 116.3 (C_q), 113.8 (C_q), 111.2 (CH), 107.9 (CH), 106.9 (C_q), 16.9 (CH_3), 16.3 (CH_3).

Microanalysis (CHN): calc. for $C_{40}H_{30}IrN_9$ C-%: 57.96, H-%: 4.65, N-%: 15.21,
found for $C_{40}H_{30}IrN_9$: C-%: 57.73, H-%: 4.67, N-%: 15.01.

ESI-MS (pos., high res.): m/z calc. for $C_{40}H_{30}IrN_9$ 827.22246, found 827.22171
Δ = -0.91 ppm.

Ref_{NDI}

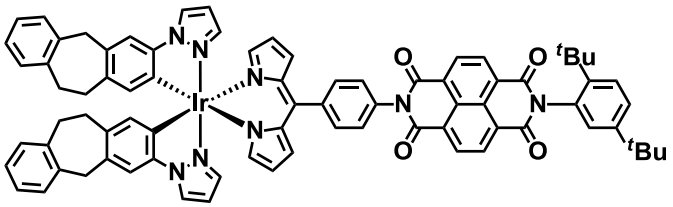

CA: [1465025-46-0]

Synthesis following GP V:

Compound (**18**) (77.0 mg, 114 µmol), 2,3-dichloro-5,6-dicyano-1,4-benzoquinone (DDQ) (28.0 mg, 124 µmol), potassium carbonate (286 mg, 2.07 mmol), compound (**35**) (80.0 mg, 52.0 µmol) in THF (15 mL), 66°C, 12 h, flash column chromatography (eluent: CH_2Cl_2 : MeOH = 99.5 : 0.5) and GPC.

Yield: 40.0 mg (28.9 µmol, 28 %) of a red solid.

$C_{79}H_{65}IrN_8O_4$ [1382.63]

^{1}H-NMR (600 MHz, $CDCl_3$):

δ [ppm] = 8.84 (s, 4H), 7.97 (d, $^{3}J_{HH}$ = 2.3 Hz, 2H), 7.67 (AA', 2H), 7.62 (d, $^{3}J_{HH}$ = 8.6 Hz, 1H), 7.50 (dd, $^{3}J_{HH}$ = 8.6 Hz, $^{4}J_{HH}$ = 2.2 Hz, 1H), 7.37 (BB', 2H), 7.15 (dd, $^{3}J_{HH}$ = 6.2 Hz, $^{4}J_{HH}$ = 2.6 Hz, 2H), 7.09–7.02 (-, 9H), 7.00 (dd, $^{3}J_{HH}$ = 1.3 Hz, $^{4}J_{HH}$ = 1.2 Hz, 2H), 6.97 (dd, $^{3}J_{HH}$ = 2.2 Hz, $^{4}J_{HH}$ = 0.5 Hz, 2H), 6.62 (dd, $^{3}J_{HH}$ = 4.3 Hz, $^{4}J_{HH}$ = 1.3 Hz, 2H), 6.43 (dd, $^{3}J_{HH}$ = 2.7 Hz, $^{3}J_{HH}$ = 2.3 Hz, 2H), 6.25 (dd, $^{3}J_{HH}$ = 4.3 Hz, $^{3}J_{HH}$ = 1.3 Hz, 2H), 6.09 (s, 2H), 4.02 (s, 4H), 3.10–2.88 (-, 8H), 1.34 (s, 9H), 1.29 (s, 9H).

^{13}C-NMR (150 MHz, CPDCH 13C, $CDCl_3$):

δ [ppm] = 164.0 (C_q), 163.1 (C_q), 152.6 (CH), 150.6 (C_q), 146.9 (C_q), 143.8 (C_q), 142.3 (C_q), 140.8 (C_q), 140.0 (C_q), 139.4 (C_q), 137.4 (CH), 137.0 (C_q), 135.3 (CH), 135.0 (C_q), 134.9 (C_q), 134.3 (C_q), 132.2 (C_q), 131.80 (C_q), 131.78 (CH), 131.7 (CH), 131.6 (CH), 131.1 (CH), 129.7 (CH), 129.2 (CH), 129.0 (CH), 127.7 (CH), 127.5 (C_q), 127.4 (C_q), 127.33 (C_q), 127.30 (CH), 127.1 (C_q), 126.9 (CH), 126.5 (CH), 126.0 (CH), 124.9 (CH), 116.9 (CH), 111.3 (CH), 106.8 (CH), 41.0 (CH_2), 35.7 (C_q), 34.5 (C_q), 33.1 (CH_2), 32.5 (CH_2), 31.9 (CH_3), 31.4 (CH_3).

Microanalysis (CHN): calc. for $C_{79}H_{65}IrN_8O_4$ C-%: 68.63, H-%: 4.74, N-%: 8.10,
found for $C_{79}H_{65}IrN_8O_4$ C-%: 68.44, H-%: 5.05, N-%: 7.80.

ESI-MS (pos., high res.): m/z calc. for $C_{79}H_{65}IrN_8O_4$ 1380.47292, found 1380.47390
Δ = -0.71 ppm.

5.2.8.2 Triad Complexes

T1

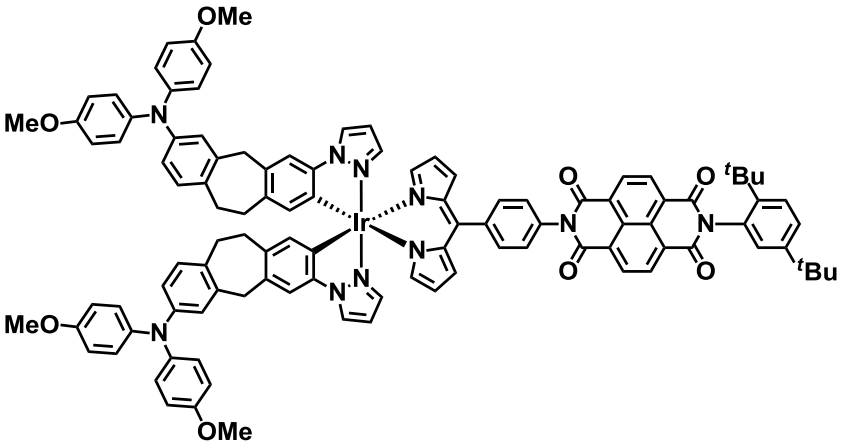

CA: [1465025-48-2]

Synthesis following GP V:

Compound (**18**) (150 mg, 222 µmol), 2,3-dichloro-5,6-dicyano-1,4-benzoquinone (DDQ) (56.0 mg, 245 µmol), potassium carbonate (614 mg, 4.45 mmol), compound (**36**) (294 mg, 122 µmol) in THF (20 mL), 66°C, 12 h, flash column chromatography (eluent: CH_2Cl_2 : MeOH = 99.5 : 0.5) and GPC.

Yield: 52.0 mg (28.3 µmol, 13 %) of a red solid.

$C_{107}H_{91}IrN_{10}O_8$ [1837.15]

^{1}H-NMR (600 MHz, acetone-d_6):

δ [ppm]= 8.86 (d, $^3J_{HH}$ = 3.3 Hz, 4H), 8.47 (d, $^3J_{HH}$ = 2.5 Hz, 2H), 7.65–7.62 (-, 3H), 7.59 (BB‘, 2H), 7.51 (dd, $^3J_{HH}$ = 8.6 Hz, $^4J_{HH}$ = 2.3 Hz, 1H), 7.39 (d, $^4J_{HH}$ = 2.3 Hz, 1H), 7.32 (s, 2H), 7.09 (dd, $^3J_{HH}$ = 1.3 Hz, $^4J_{HH}$ = 1.3 Hz, 2H), 7.03 (dd, $^3J_{HH}$ = 2.2 Hz, $^4J_{HH}$ = 0.5 Hz, 2H), 6.95 (AA‘‘, 8H), 6.88 (d, $^3J_{HH}$ = 8.3 Hz, 2H), 6.85 (BB‘‘, 8H), 6.70 (d, $^4J_{HH}$ = 2.4 Hz, 2H), 6.61 (dd, $^3J_{HH}$ = 8.2 Hz, $^4J_{HH}$ = 2.4 Hz, 2H), 6.59 (dd, $^3J_{HH}$ = 2.7 Hz, $^3J_{HH}$ = 2.3 Hz, 2H), 6.57 (dd, $^3J_{HH}$ = 4.3 Hz, $^4J_{HH}$ = 1.3 Hz, 2H), 6.27 (dd, $^3J_{HH}$ = 4.3 Hz, $^3J_{HH}$ = 1.3 Hz, 2H), 6.13 (s, 2H), 3.84 (m, 4H), 3.76 (s, 12H, OMe), 3.00–2.78 (-, 8H), 1.32 (s, 9H, ^{t}Bu), 1.28 (s, 9H, ^{t}Bu).

^{13}C-NMR (150 MHz, CPDCH 13C, acetone-d_6):

δ [ppm] = 164.8 (C_q), 163.8 (C_q), 156.6 (C_q), 152.9 (CH), 150.6 (C_q), 148.3 (C_q), 147.6 (C_q), 144.6 (C_q), 143.4 (C_q), 142.1 (C_q), 140.9 (C_q), 140.7 (C_q), 138.1 (CH), 137.4 (C_q), 136.6 (C_q), 135.8 (C_q), 135.7 (CH), 135.6 (C_q), 134.1 (C_q), 132.9 (C_q), 132.8 (C_q), 131.7 (CH), 131.6 (CH), 131.5 (2 × CH), 131.0 (CH), 129.4 (CH), 129.1 (CH), 128.8 (CH), 128.5 (CH), 128.3 (C_q), 128.2 (C_q), 128.1 (C_q), 127.0 (C_q), 126.8 (CH), 126.7 (CH), 122.2 (CH), 120.0 (CH), 117.5 (CH), 115.4 (CH), 112.4 (CH), 108.0 (CH), 55.6 (OCH_3), 41.3 (CH_2), 36.0 (C_q), 34.8 (C_q), 33.3 (CH_2), 32.7 (CH_2), 32.0 (CH_3), 31.5 (CH_3).

Microanalysis (CHN): calc. for $C_{107}H_{91}IrN_{10}O_8$ C-%: 69.95, H-%: 4.99, N-%: 7.62

found for $C_{107}H_{91}IrN_{10}O_8$ C-%: 69.42, H-%: 4.89, N-%: 7.64.

ESI-MS (pos., high res.): m/z calc. for $C_{107}H_{91}IrN_{10}O_8$ ($M^{+\cdot}$) 1834.66218, found 1834.65979

Δ = -1.30 ppm (6 %),

m/z calc. for $C_{107}H_{91}IrN_{10}O_8$ ($M^{2+\cdot}$) 917.33109, found 917.33235,

Δ = 1.37 ppm (100 %).

T2

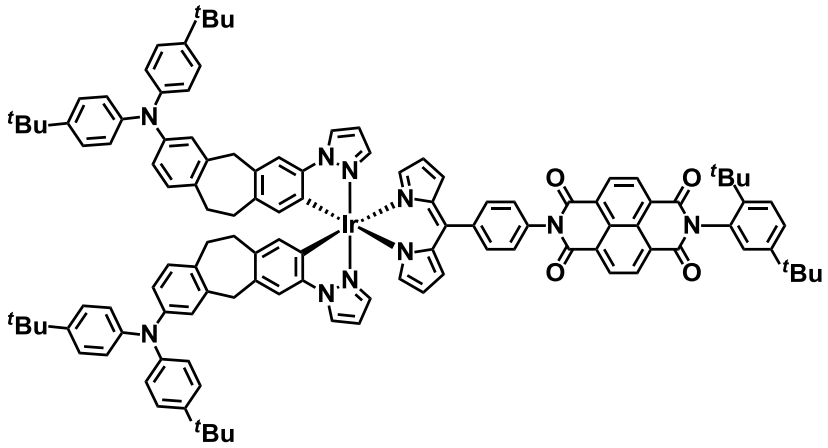

CA: [1465025-50-6]

Synthesis following GP V:

Compound (**18**) (109 mg, 161 µmol), 2,3-dichloro-5,6-dicyano-1,4-benzoquinone (DDQ) (40.0 mg, 177 µmol), potassium carbonate (445 mg, 3.22 mmol), compound (**37**) (210 mg, 80.4 µmol) in THF (15 mL), 66°C, 12 h, flash column chromatography (eluent: CH_2Cl_2 : petrol ether = 3 : 2) and GPC.

Yield: 79.0 mg (40.7 µmol, 25 %) of a red solid.

$C_{119}H_{115}IrN_{10}O_4$ [1941.47]

^{1}H-NMR (600 MHz, acetone-d_6):

δ [ppm]= 8.86 (s, 4H), 8.40 (d, $^3J_{HH}$ = 2.7 Hz, 2H), 7.64–7.62 (-, 3H), 7.58 (BB‘, 2H), 7.51 (dd, $^3J_{HH}$ = 8.6 Hz, $^4J_{HH}$ = 2.3 Hz, 1H), 7.38 (d, $^3J_{HH}$ = 2.2 Hz, 1H), 7.29 (s, 2H), 7.27 (AA‘‘, 8H), 7.09 (dd, $^3J_{HH}$ = 1.3 Hz, $^3J_{HH}$ = 1.3 Hz, 2H), 7.02 (dd, $^3J_{HH}$ = 2.1 Hz, $^4J_{HH}$ = 0.5 Hz, 2H), 6.94 (d, $^3J_{HH}$ = 8.24 Hz, 2H), 6.90 (BB‘‘, 8H), 6.87 (d, $^3J_{HH}$ = 2.3 Hz, 2H), 6.73 (dd, $^3J_{HH}$ = 8.1 Hz, $^4J_{HH}$ = 2.4 Hz, 2H), 6.57–6.56 (–, 4H), 6.24 (dd, $^3J_{HH}$ = 4.3 Hz, $^4J_{HH}$ = 1.3 Hz, 2H), 6.16 (s, 2H), 3.92–3.82 (m, 4H), 3.00–2.81 (m, 8H), 1.33 (s, 9H, ^{t}Bu), 1.29 (s, 36H, ^{t}Bu), 1.28 (s, 9H, ^{t}Bu).

^{13}C-NMR (150 MHz, CPDCH 13C, acetone-d_6):

δ [ppm] = 164.8 (C_q), 163.8 (C_q), 152.9 (CH), 150.6 (C_q), 148.2 (C_q), 146.6 (C_q), 146.3 (C_q), 145.7 (C_q), 144.6 (C_q), 143.4 (C_q), 141.1 (C_q), 140.8 (C_q), 138.1 (CH), 137.5 (C_q), 136.5 (C_q), 135.9 (C_q), 135.64 (C_q), 135.57 (CH), 134.7 (C_q), 134.1 (C_q), 132.9 (C_q), 131.8 (CH), 131.7 (CH), 131.52 (CH), 131.49 (CH), 131.3 (CH), 129.4 (C_q), 129.1 (CH), 128.8 (CH), 128.5 (CH), 128.3 (C_q), 128.2 (C_q), 128.1 (C_q), 126.8 (CH), 126.74 (CH), 126.69 (CH), 125.1 (CH), 124.2 (CH), 122.9 (CH), 117.6 (CH), 112.4 (CH), 108.0 (CH), 41.2 (CH_2), 36.1 (C_q), 34.8 (C_q), 34.7 (C_q), 33.1 (CH_2), 32.9 (CH_2), 32.0 (CH_3), 31.7 (CH_3), 31.5 (CH_3).

Microanalysis (CHN): calc. for $C_{119}H_{115}IrN_{10}O_8$ C-%: 73.62, H-%: 5.97, N-%: 7.21,
found for $C_{119}H_{115}IrN_{10}O_8$ C-%: 73.35, H-%: 6.03, N-%: 7.37.

ESI-MS (pos., high res.): m/z calc. for $C_{119}H_{115}IrN_{10}O_4$ 1938.870320, found 1938.87120, Δ = 0.45 ppm.

T3

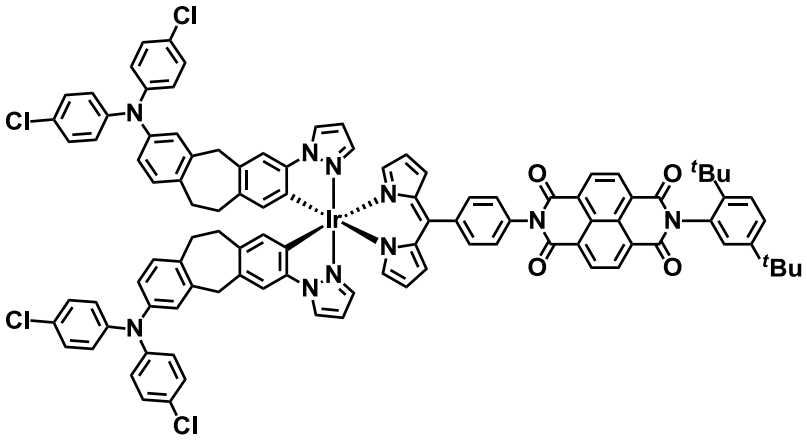

CA: [–]

Synthesis following GP V:

Compound (**18**) (74.0 mg, 109 µmol), 2,3-dichloro-5,6-dicyano-1,4-benzoquinone (DDQ) (27.0 mg, 120 µmol), potassium carbonate (301 mg, 2.18 mmol), compound **(38)** (146 mg, 59.9 µmol) in THF (12 mL), 66°C, 12 h, flash column chromatography (eluent: CH_2Cl_2 : MeOH = 99.5 : 0.5) and GPC.

Yield: 75.2 mg (40.5 µmol, 37 %) of a red solid.

$C_{103}H_{79}Cl_4IrN_{10}O_4$ [1854.82]

^{1}H-NMR (400 MHz, CD_2Cl_2):

δ [ppm]= 8.86 (s, 4H), 8.02 (dd, $^3J_{HH}$ = 2.9 Hz, $^4J_{HH}$ = 0.6 Hz, 2H), 7.67 (AA‘, 2H), 7.64 (d, $^3J_{HH}$ = 8.6 Hz, 1H), 7.53 (dd, $^3J_{HH}$ = 8.6 Hz, $^4J_{HH}$ = 2.3 Hz, 1H), 7.42 (BB‘, 2H), 7.15 (AA‘‘, 8H), 7.06–7.03 (-, 7H), 7.01 (d, $^3J_{HH}$ = 8.2 Hz, 2H), 6.93 (BB‘, 8H), 6.90 (d, $^4J_{HH}$ = 2.3 Hz, 2H), 6.81 (dd, $^3J_{HH}$ = 8.1 Hz, $^4J_{HH}$ = 2.3 Hz, 2H), 6.62 (dd, $^3J_{HH}$ = 4.3 Hz, $^4J_{HH}$ = 1.3 Hz, 2H), 6.59 (dd, $^3J_{HH}$ = 2.7 Hz, $^3J_{HH}$ = 2.3 Hz, 2H), 6.29 (dd, $^3J_{HH}$ = 4.3 Hz, $^4J_{HH}$ = 1.3 Hz, 2H), 6.14 (s, 2H), 4.08–3.80 (m, 4H), 3.16–2.87 (-, 8H), 1.34 (s, 9H, ^{t}Bu), 1.27 (s, 9H, ^{t}Bu).

^{13}C-NMR (100 MHz, CD_2Cl_2):

δ [ppm] = 164.3 (C_q), 163.4 (C_q), 152.6 (CH), 151.0 (C_q), 147.5 (C_q), 146.7 (C_q), 145.0 (C_q), 144.6 (C_q), 142.6 (C_q), 141.0 (C_q), 140.7 (C_q), 137.9 (CH), 137.3 (C_q), 135.9 (C_q), 135.4 (C_q), 135.3 (CH), 135.13 (C_q), 135.11 (C_q), 133.0 (C_q), 132.4 (C_q), 131.8 (CH), 131.73 (CH), 131.68 (CH), 131.4 (CH), 131.3 (CH), 129.6 (CH), 129.5 (CH), 128.0 (CH), 127.78 (CH), 127.75 (C_q), 127.7 (C_q), 127.6 (C_q), 127.51 (C_q), 127.48 (C_q), 126.9 (CH), 125.7 (2×CH), 125.1 (CH), 123.6 (CH), 117.2 (CH), 111.7 (CH), 107.3 (CH), 41.1 (CH_2), 35.9 (C_q), 34.6 (C_q), 32.6 (CH_2), 31.8 (CH_3), 31.3 (CH_3), 30.9 (CH_2).

Microanalysis (CHN): calc. for $C_{103}H_{79}Cl_4IrN_{10}O_4$ C-%: 66.70, H-%: 4.29, N-%: 7.55,
found for $C_{103}H_{79}Cl_4IrN_{10}O_4$ C-%: 67.05, H-%: 4.72, N-%: 7.43.

ESI-MS (pos., high res.): m/z calc. for $C_{103}H_{79}Cl_4IrN_{10}O_4$ 1850.46403, found 1850.47110, Δ = 3.82 ppm.

T4

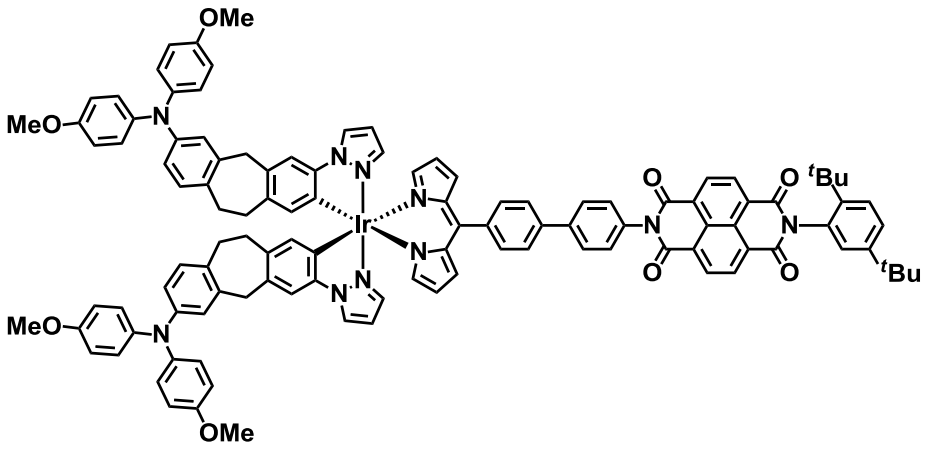

CA: [–]

Synthesis following GP V:

Compound (**25**) (75.0 mg, 99.9 µmol), 2,3-dichloro-5,6-dicyano-1,4-benzoquinone (DDQ) (25.0 mg, 109 µmol), potassium carbonate (251 mg, 1.82 mmol), compound (**36**) (109 mg,

45.4 µmol) in THF (15 mL), 66°C, 12 h, flash column chromatography (eluent: CH_2Cl_2 : MeOH = 99.5 : 0.5) and GPC.

Yield: 50.0 mg (26.1 µmol, 29 %) of a red solid.

$C_{113}H_{95}IrN_{10}O_8$ [1913.24]

^{1}H-NMR (600 MHz, CD_2Cl_2):

δ [ppm]= 8.88–8.85 (-, 4H), 8.01 (d, $^4J_{HH}$ = 2.9 Hz, $^5J_{HH}$ = 0.5 Hz, 2H), 7.91 (AA', 2H), 7.76 (BB', 2H), 7.64 (d, $^3J_{HH}$ = 8.6 Hz, 1H), 7.59 (AA'', 2H), 7.53 (dd, $^3J_{HH}$ = 8.6 Hz, $^4J_{HH}$ = 2.2 Hz, 1H), 7.65 (BB'', 2H), 7.06 (d, $^4J_{HH}$ = 2.3 Hz, 1H), 7.03–7.02 (-, 4H), 7.01 (dd, $^3J_{HH}$ = 2.2 Hz, $^4J_{HH}$ = 0.5 Hz, 2H), 6.97 (AA'', 8H), 6.89 (d, $^3J_{HH}$ = 8.3 Hz, 2H), 6.95 (BB'', 8H), 6.77 (d, $^4J_{HH}$ = 2.5 Hz, 2H), 6.67 (dd, $^3J_{HH}$ = 8.2 Hz, $^4J_{HH}$ = 2.4 Hz, 2H), 6.59 (dd, $^3J_{HH}$ = 4.3 Hz, $^4J_{HH}$ = 1.3 Hz, 2H), 6.50 (dd, $^3J_{HH}$ = 2.7 Hz, $^3J_{HH}$ = 2.3 Hz, 2H), 6.26 (dd, $^3J_{HH}$ = 4.3 Hz, $^4J_{HH}$ = 1.4 Hz, 2H), 6.11 (s, 2H), 3.92–3.86 (m, 4H), 3.76 (s, 12H, OMe), 3.04–2.88 (-, 8H), 1.34 (s, 9H, ^{t}Bu), 1.28 (s, 9H, ^{t}Bu).

^{13}C-NMR (150 MHz, CPDCH 13C, CD_2Cl_2):

δ [ppm] = 164.3 (C_q), 163.5 (C_q), 155.8 (C_q), 152.5 (CH), 151.0 (C_q), 148.2 (C_q), 146.9 (C_q), 144.5 (C_q), 142.5 (C_q), 141.9 (C_q), 141.8 (C_q), 140.3 (C_q), 140.1 (C_q), 139.6 (C_q), 137.8 (CH), 137.4 (C_q), 135.3 (C_q), 2 × 135.2 (CH + C_q), 134.7 (C_q), 133.0 (C_q), 132.6 (C_q), 132.5 (C_q), 131.71 (CH), 131.68 (CH), 131.5 (CH), 131.2 (CH), 130.6 (CH), 129.5 (CH), 129.4 (CH), 128.5 (CH), 128.0 (CH), 127.73 (C_q), 127.71 (C_q), 127.6 (C_q), 127.5 (C_q), 126.9 (CH), 126.34 (CH), 126.27 (CH), 125.6 (CH), 122.1 (CH), 120.1 (CH), 117.0 (CH), 114.8 (CH), 111.6 (CH), 107.2 (CH), 55.8 (OCH_3), 41.2 (CH_2), 35.9 (C_q), 34.6 (C_q), 32.8 (CH_2), 32.4 (CH_2), 31.8 (CH_3), 31.3 (CH_3).

Microanalysis (CHN): calc. for $C_{113}H_{95}IrN_{10}O_8$ C-%: 70.94, H-%: 5.00, N-%: 7.32,
found for $C_{113}H_{95}IrN_{10}O_8$ C-%: 70.54, H-%: 5.19, N-%: 7.46.

ESI-MS (pos., high res.): m/z calc. for $C_{113}H_{95}IrN_{10}O_8$ 1910.69348, found 1910.69313
Δ = -0.18 ppm.

T5

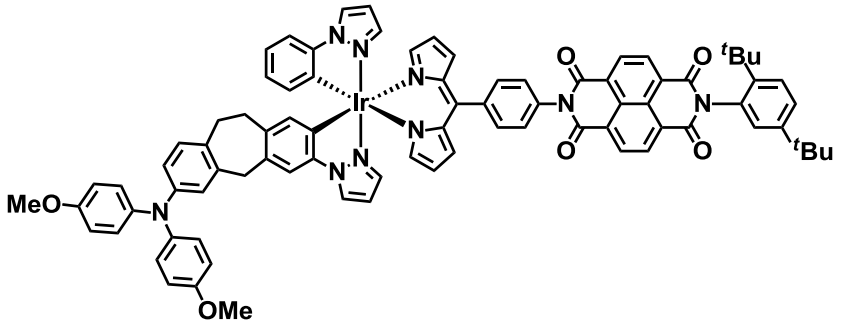

CA: [–]

Synthesis following GP V:

Compound (**18**) (150 mg, 222 µmol), 2,3-dichloro-5,6-dicyano-1,4-benzoquinone (DDQ) (56.0 mg, 245 µmol), potassium carbonate (614 mg, 4.45 mmol), compound mixture (**40**) (229 mg) in THF (15 mL), 66°C, 12 h, flash column chromatography (eluent: CH_2Cl_2 : MeOH = 99.5 : 0.5) and GPC.

Yield: 38.0 mg (25.4 µmol, 11 %) of a red solid and two other red complexes (**T1** and **T5b**). The ratio of the three complexes was roughly estimated by GPC to **T1** : **T5** : **T5b** = 0.36 : 0.21 : 0.43.

T1 : $C_{107}H_{91}IrN_{10}O_8$ [1837.15], **T5**: $C_{84}H_{70}IrN_9O_6$ [1493.73], **T5b**: $C_{61}H_{49}IrN_8O_4$ [1150.31]

^{1}H-NMR (600 MHz, CD_2Cl_2):

δ [ppm]= 8.88–8.85 (m, 4H), 8.09 (d, $^4J_{HH}$ = 2.5 Hz, 1H), 8.02 (d, $^4J_{HH}$ = 2.5 Hz, 1H), 7.78 (AA', 2H), 7.64 (d, $^3J_{HH}$ = 8.6 Hz, 1H), 7.53 (dd, $^3J_{HH}$ = 8.6 Hz, $^4J_{HH}$ = 2.2 Hz, 1H), 7.42 (BB', 2H), 7.27 (d, $^3J_{HH}$ = 7.3 Hz, 1H), 7.09 (-, 1H), 7.07 (d, $^3J_{HH}$ = 1.86 Hz, 1H), 7.06 (d, $^3J_{HH}$ = 2.2 Hz, 1H), 7.05 (s, 1H), 7.02 (d, $^3J_{HH}$ = 2.04 Hz, 1H), 6.99–6.96 (-, 5H), 6.89 (d, $^3J_{HH}$ = 8.2 Hz, 1H), 6.82–6.78 (-, 5H), 6.77 (d, $^3J_{HH}$ = 2.4 Hz, 2H), 6.67 (dd, $^3J_{HH}$ = 8.2 Hz, $^4J_{HH}$ = 2.4 Hz, 1H), 6.63–6.61 (-, 2H), 6.55 (dd, $^3J_{HH}$ = 2.6 Hz, $^3J_{HH}$ = 2.4 Hz, 1H), 6.51 (dd, $^3J_{HH}$ = 2.6 Hz, $^3J_{HH}$ = 2.5 Hz, 1H), 6.36 (dd, $^3J_{HH}$ = 7.4 Hz, $^4J_{HH}$ = 1.1 Hz, 1H), 6.30 (dd, $^3J_{HH}$ = 4.3 Hz, $^3J_{HH}$ = 1.2 Hz, 1H), 6.28 (dd, $^3J_{HH}$ = 4.3 Hz, $^4J_{HH}$ = 1.3 Hz, 1H), 6.17 (s, 1H), 3.92–3.87 (m, 2H), 3.77 (s, 6H, OMe), 3.05–2.90 (-, 4H), 1.34 (s, 9H, ^{t}Bu), 1.27 (s, 9H, ^{t}Bu).

^{13}C-NMR (150 MHz, CD_2Cl_2):

δ [ppm] = 164.3 (C_q), 163.4 (C_q), 155.9 (C_q), 152.9 (CH), 152.6 (CH), 151.0 (C_q), 147.5 (C_q), 147.0 (C_q), 144.5 (C_q), 144.4 (C_q), 142.5 (C_q), 141.8 (C_q), 140.7 (C_q), 140.2 (C_q), 138.4 (C_q), 138.1 (CH), 137.8 (CH), 137.5 (C_q), 135.3 (CH), 135.2 (C_q), 135.11 (C_q), 135.10 (C_q), 134.9 (C_q), 134.4 (CH), 133.0 (C_q), 132.8 (C_q), 132.5 (C_q), 131.81 (CH), 131.72 (CH), 131.67 (CH), 131.4 (CH), 131.3 (CH), 130.6 (CH), 129.4 (CH), 128.0 (CH), 127.8 (CH), 127.74 (C_q), 127.71 (C_q), 127.6 (C_q), 127.5 (C_q), 126.9 (CH), 126.4 (CH), 126.14 (CH), 125.05 (CH), 125.7 (CH), 122.1 (CH), 121.9 (CH), 120.0 (CH), 117.3 (CH), 117.2 (CH), 114.9 (CH), 111.6 (CH), 111.2 (CH), 107.5 (CH), 107.4 (CH), 55.8 (OCH_3), 41.2 (CH_2), 35.9 (C_q), 34.6 (C_q), 32.8 (CH_2), 32.4 (CH_2), 31.8 (CH_3), 31.3 (CH_3).

Microanalysis (CHN): calc. for $C_{84}H_{70}IrN_9O_6$ C-%: 67.54, H-%: 4.72, N-%: 8.44,
found for $C_{84}H_{70}IrN_9O_6$ C-%: 67.08, H-%: 5.18, N-%: 8.14.

ESI-MS (pos., high res.): m/z calc. for $C_{84}H_{70}IrN_9O_6^+$ 1491.50495, found 1491.50451
Δ = -0.30 ppm.

T6

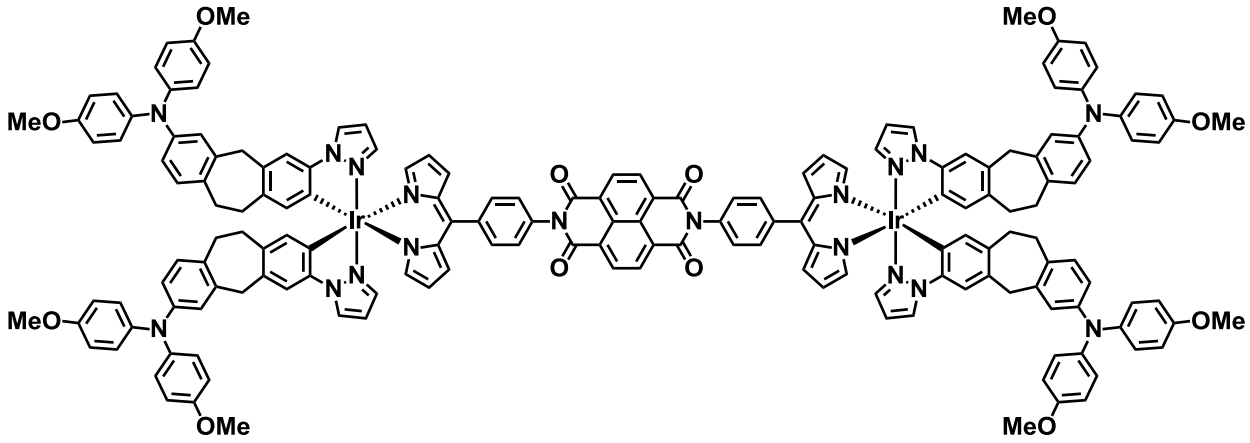

CA: [–]

Synthesis following GP V:

Compound (**19**) (106 mg, 150 µmol), 2,3-dichloro-5,6-dicyano-1,4-benzoquinone (DDQ) (82.0 mg, 360 µmol), potassium carbonate (622 mg, 4.50 mmol), compound (**36**) (901 mg, 375 µmol) in THF (20 mL), 66°C, 48 h, flash column chromatography (eluent: CH_2Cl_2 : MeOH = 99.5 : 0.5) and GPC.

Yield: 75.0 mg (25.0 µmol, 17 %) of a red solid.

$C_{172}H_{136}Ir_2N_{18}O_{12}$ [3031.47]

^{1}H-NMR (600 MHz, CD_2Cl_2):

δ [ppm]= 8.87–8.86 (-, 4H), 8.00 (d, $^4J_{HH}$ = 2.5 Hz, 2H), 7.98 (d, $^4J_{HH}$ = 2.2 Hz, 2H), 7.68 (AA', 4H), 7.42 (BB', 4H), 7.04–7.02 (-, 12H), 6.98 (AA'',16H), 6.89 (d, $^3J_{HH}$ = 8.4 Hz, 4H), 6.80–6.77 (-, 20H), 6.68 (dd, $^3J_{HH}$ = 8.2 Hz, $^4J_{HH}$ = 2.3 Hz, 4H), 6.62–6.60 (-, 4H), 6.49 (dd, $^3J_{HH}$ = 2.8 Hz, $^3J_{HH}$ = 2.3 Hz, 4H), 6.29–6.27 (-, 4H), 6.12 (2×s, 2×2H), 3.92–3.86 (m, 8H), 3.76 (s, 12H, OMe), 3.75 (s, 12H, OMe), 3.08–2.89 (-, 16H).

^{13}C-NMR (150 MHz, CD_2Cl_2):

δ [ppm] = 163.4 (C_q), 155.9 (C_q), 152.7 (CH), 147.41 (C_q), 147.39 (C_q), 147.0 (C_q), 142.5 (C_q), 141.8 (C_q), 140.7 (C_q), 140.3 (C_q), 140.2 (C_q), 137.8 (CH), 137.4 (C_q), 135.2 (C_q + CH), 135.10 (C_q), 135.09 (C_q), 135.07 (C_q), 132.63 (C_q), 132.62 (C_q), 132.55 (C_q), 131.8 (CH), 131.7 (CH), 131.3 (CH), 130.6 (CH), 127.8 (CH), 127.6 (C_q), 127.5 (C_q), 126.4 (CH), 125.6 (CH), 122.17 (CH), 122.15 (CH), 120.1 (CH), 117.2 (CH), 114.9 (CH), 111.7 (CH), 107.3 (CH), 55.78 (OCH_3), 55.77 (OCH_3), 41.2 (CH_2), 32.8 (CH_2), 32.4 (CH_2).

Microanalysis (CHN): calc. for $C_{172}H_{136}Ir_2N_{18}O_{12}$ C-%: 68.15, H-%: 4.52, N-%: 8.32,
found for $C_{172}H_{136}Ir_2N_{18}O_{12}$ C-%: 67.57, H-%: 4.74, N-%: 8.14.

ESI-MS (pos., high res.): m/z calc. for $C_{172}H_{136}Ir_2N_{18}O_{12}$ ($M^{2+\cdot}$) 1513.48930,
found 1513.49086
Δ = -1.03 ppm.

5.2.8.3 Dyad Complexes

D1

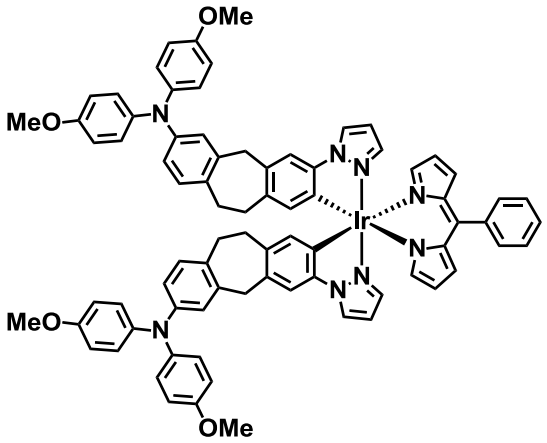

CA: [–]

Synthesis following GP V:

Compound (**11**) (50.0 mg, 225 µmol), 2,3-dichloro-5,6-dicyano-1,4-benzoquinone (DDQ) (56.0 mg, 247 µmol), potassium carbonate (622 mg, 4.50 mmol), compound (**36**) (270 mg, 112 µmol) in THF (15 mL), 66°C, 12 h, flash column chromatography (eluent: CH_2Cl_2 : petrol ether = 3 : 2 → 2 : 1 → 6 : 1).

Yield: 200 mg (144.0 µmol, 64 %) of a red solid.

$C_{79}H_{67}IrN_8O_4$ [1384.65]

^{1}H-NMR (400 MHz, acetone-d_6):

δ[ppm]= 8.44 (d, ^3J = 2.4 Hz, 2H), 7.49–7.41 (-, 5H), 7.30 (s, 2 H), 7.04 (dd, ^3J = 1.4 Hz, ^4J = 1.4 Hz, 2H), 6.98 (dd, ^3J = 2.2 Hz, ^4J = 0.6 Hz, 2H), 6.95 (AA', 8H), 6.88–6.82 (-, 10H), 6.70 (d, ^4J = 2.4 Hz, 2H), 6.61 (dd, ^3J = 8.2 Hz, ^4J = 2.5 Hz, 2H), 6.57 (dd, ^3J = 2.8 Hz, ^3J = 2.3 Hz, 2H), 6.41 (dd, ^3J = 4.3 Hz, ^4J = 1.3 Hz, 2H) 6.19 (dd, ^3J = 4.3 Hz, ^3J = 1.4 Hz, 2H), 6.12 (s, 2H), 3.88–3.80 (m, 4H, CH_2), 3.77 (s, 12H, OCH_3), 2.96–2.82 (-, 8H, CH_2-CH_2).

^{13}C-NMR (100 MHz, acetone-d_6):

δ [ppm] = 156.8 (C_q), 152.8 (CH), 149.3 (C_q), 147.7 (C_q), 143.6 (C_q), 142.4 (C_q), 141.0 (C_q), 140.8 (C_q), 138.2 (CH), 137.6 (C_q), 136.1 (C_q), 135.88 (C_q), 135.86 (CH), 133.1 (C_q), 133.0 (C_q), 131.6 (CH), 131.3 (CH), 131.1 (CH), 129.0 (CH), 128.0 (CH), 127.1 (CH), 126.9 (CH), 122.5 (CH), 120.3 (CH), 117.4 (CH), 115.6 (CH), 112.5 (CH), 108.1 (CH), 55.8 (OCH_3), 41.5 (CH_2), 33.5 (CH_2), 32.9 (CH_2).

Microanalysis (CHN): calc. for $C_{79}H_{67}IrN_8O_4$ C-%: 68.53, H-%: 4.88, N-%: 8.09,
found for $C_{79}H_{67}IrN_8O_4$ C-%: 68.71, H-%: 4.85, N-%: 8.22.

ESI-MS (pos., high res.): m/z calc. for $C_{79}H_{67}IrN_8O_4$ 1382.48857, found 1382.48829
Δ = -0.20 ppm.

D2

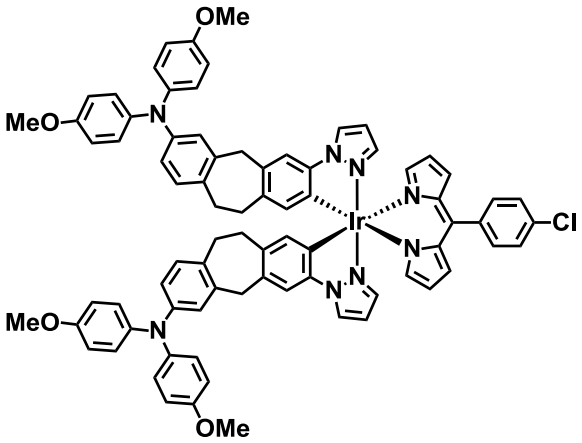

CA: [–]

Synthesis following GP V:

meso-(*p*-Chlorophenyl)dipyrromethane (**14**) (32.0 mg, 125 µmol), 2,3-dichloro-5,6-dicyano-1,4-benzoquinone (DDQ) (31.0 mg, 147 µmol), potassium carbonate (345 mg, 2.50 mmol), compound (**36**) (150 mg, 62.0 µmol) in THF (8 mL), 66°C, 12 h, flash column chromatography (eluent: petrol ether : CH_2Cl_2 = 2 : 3 → 1 : 3).

Yield: 89.0 mg (62.7 µmol, 50 %) of a red solid.

$C_{79}H_{66}ClIrN_8O_4$ [1419.09]

^{1}H-NMR (400 MHz, acetone-d_6):

δ [ppm] = 8.38 (dd, $^3J_{HH}$ = 2.9 Hz, $^4J_{HH}$ = 0.6 Hz, 2H), 7.48 (AA', 2H), 7.43 (BB', 2H), 7.27 (s, 2H), 7.04 (dd, $^3J_{HH}$ = 1.3 Hz, $^4J_{HH}$ = 1.3 Hz, 2H), 6.96 (dd, $^3J_{HH}$ = 2.2 Hz, $^3J_{HH}$ = 0.6 Hz, 2H), 6.93 (AA', 8H), 6.86–6.81 (-,10H), 6.69 (d, $^4J_{HH}$ = 2.4 Hz, 2H), 6.60 (dd, $^3J_{HH}$ = 8.2 Hz, $^4J_{HH}$ = 2.5 Hz, 2H), 6.53 (dd, $^3J_{HH}$ = 2.8 Hz, $^3J_{HH}$ = 2.3 Hz, 2H), 6.40 (dd, $^3J_{HH}$ = 4.3 Hz, $^3J_{HH}$ = 1.3 Hz, 2H), 6.18 (dd, $^3J_{HH}$ = 4.3 Hz, $^3J_{HH}$ =1.4 Hz, 2H), 6.11 (s, 2H), 3.81 (-, 4H), 3.85–3.76 (s, 12H, OCH_3), 2.92-2.75 (-, 8H).

^{13}C-NMR (100 MHz, acetone-d_6):

δ [ppm] = 156.7 (C_q), 153.0 (CH), 147.7 (C_q), 147.5 (C_q), 143.4 (C_q), 142.3 (C_q), 140.9 (C_q), 139.4 (C_q), 138.1 (CH), 137.5 (C_q), 135.8 (C_q), 135.7 (CH), 135.5 (C_q), 134.5 (C_q), 133.0 (C_q), 132.9 (C_q), 132.8 (CH), 131.3(CH), 131.0 (CH), 128.1 (CH), 127.0 (CH), 126.8 (CH), 122.4 (CH), 120.1 (CH), 117.6 (CH), 115.5 (CH), 112.4 (CH), 108.0 (CH), 55.7 (OCH_3) 41.4 (CH_2), 33.4 (CH_2), 32.8 (CH_2).

Microanalysis (CHN): calc. for $C_{79}H_{66}ClIrN_8O_4$ C-%: 66.98, H-%: 4.76, N-%: 7.70,
found for $C_{79}H_{66}ClIrN_8O_4$ C-%: 66.86, H-%: 4.69, N-%: 7.90.

ESI-MS (pos., high res.): m/z calc. for $C_{79}H_{66}ClIrN_8O_8$ 1416.44960, found 1416.45064,
Δ = 0.73 ppm.

D3

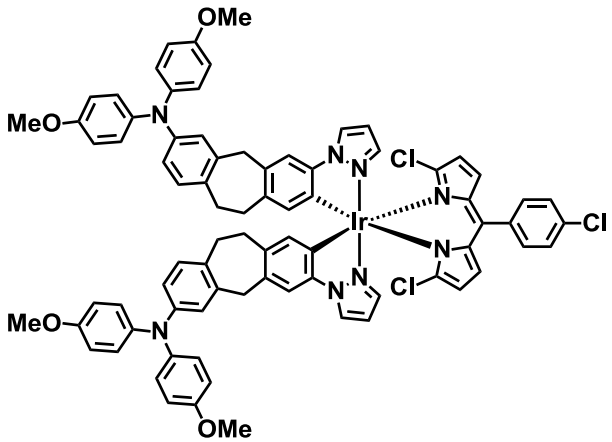

CA: [–]

Synthesis following GP V:

1,9-Dichloro-*meso*-(*p*-chlorophenyl)dipyrromethane (**15**) (33.0 mg, 101 µmol), 2,3-dichloro-5,6-dicyano-1,4-benzoquinone (DDQ) (25.0 mg, 111 µmol), potassium carbonate (280 mg, 2.03 mmol), compound (**36**) (122 mg, 50.8 µmol) in THF (8 mL), 66°C, 12 h, flash column chromatography (eluent: petrol ether : CH_2Cl_2 = 1 : 1 → 3 : 1).

Yield: 83.0 mg (55.8 µmol, 55 %) of a red solid.

$C_{79}H_{64}Cl_3IrN_8O_4$ [1487.98]

^{1}H-NMR (400 MHz, THF-d_8):

δ [ppm] = 8.29 (dd, $^3J_{HH}$ = 2.9 Hz, $^4J_{HH}$ = 0.6 Hz, 2H), 7.56 (dd, $^3J_{HH}$ = 2.2 Hz, $^4J_{HH}$ = 0.6 Hz, 2H), 7.42 (AA', 2H), 7.33 (BB', 2H), 6.99 (s, 2H), 6.91 (AA', 8H), 6.78–6.73 (-, 10H), 6.68 (d, $^3J_{HH}$ = 2.4 Hz, 2H), 6.61–6.57 (-, 4H), 6.38 (d, $^3J_{HH}$ = 4.3 Hz, 2H), 5.98 (d, $^3J_{HH}$ = 4.3 Hz, 2H), 5.87 (s, 2H), 3.85–3.72 (m, 4H), 3.71 (s, 12H, OCH_3), 2.84–2.69 (-, 8H).

^{13}C-NMR (100 MHz, THF-d_8):

δ [ppm] = 156.5 (C_q), 151.4 (C_q), 147.4 (C_q), 145.6 (C_q), 143.4 (C_q), 142.3 (C_q), 140.5 (CH), 140.5 (C_q), 137.9 (C_q), 137.8 (C_q), 136.7 (CH), 136.3 (C_q), 134.7 (C_q), 133.1 (C_q), 132.8 (CH), 132.3 (C_q), 132.2 (CH), 130.6 (CH), 130.2 (C_q), 128.1 (CH), 126.5 (CH), 126.4 (CH), 122.7 (CH), 120.2 (CH), 117.4 (CH), 115,1 (CH), 111.6 (CH), 107.0 (CH), 55.3 (OCH_3) 41.6 (CH_2), 33.4 (CH_2), 33.1 (CH_2).

Microanalysis (CHN): calc. for $C_{79}H_{64}Cl_3IrN_8O_4$ C-%: 63.77, H-%: 4.34, N-%: 7.53,
found for $C_{79}H_{64}Cl_3IrN_8O_4$ C-%: 63.84, H-%: 4.65, N-%: 7.26.

ESI-MS (pos., high res.): m/z calc. for $C_{79}H_{64}Cl_3IrN_8O_4$ 1484.37165, found 1484.37273,
Δ = 0.73 ppm.

D4

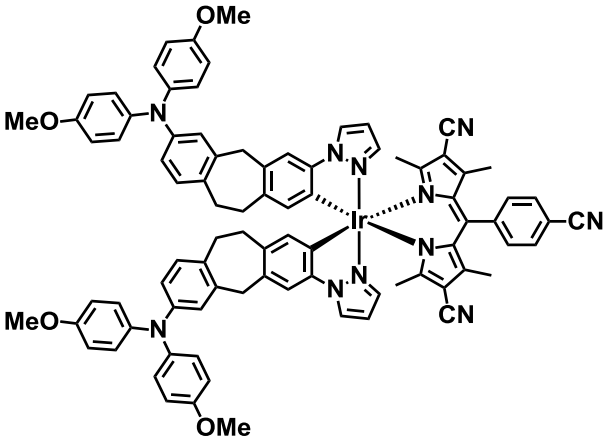

CA: [–]

Synthesis following GP VI:

2,8-Dicyano-1,3,7,9-tetramethyl-*meso*-(*p*-cyanophenyl)dipyrromethane (**31**) (177 mg, 500 µmol), 2,3-dichloro-5,6-dicyano-1,4-benzoquinone (DDQ) (125 mg, 550 µmol), potassium carbonate (1.38 g, 10.0 mmol), compound (**36**) (600 mg, 250 µmol) first in CH_2Cl_2 (7 mL) thereafter in THF (10 mL), 66°C, 72 h, flash column chromatography on alumina oxide (eluent: petrol ether : ethyl acetate : NEt_3 = 7 : 3 : 0.1).

Yield: 43.2 mg (28.5 µmol, 6 %) of a pale red solid.

$C_{86}H_{72}IrN_{11}O_4$ [1515.78]

^{1}H-NMR (600 MHz, CD_2Cl_2):

δ [ppm] = 8.07 (d, $^3J_{HH}$ = 2.8 Hz, 2H), 7.83 (AA', 2H), 7.57 (d, $^3J_{HH}$ = 2.2 Hz, 2H), 7.36 (BB', 2H), 6.95 (AA'', 8H), 6.93 (s, 2H), 6.85 (d, $^3J_{HH}$ = 8.3 Hz, 2H), 6.77 (BB'', 8H), 6.71 (d, $^4J_{HH}$ = 2.3 Hz, 2H), 6.68 (dd, $^3J_{HH}$ = 2.8 Hz, $^4J_{HH}$ = 2.3 Hz, 2H), 6.65 (dd, $^3J_{HH}$ = 8.2 Hz, $^4J_{HH}$ = 2.4 Hz, 2H), 5.83 (s, 2H), 3.87–3.80 (-, 4H), 3.75 (s, 12H, OCH_3), 2.96–2.79 (-, 8H), 1.49 (s, 6H, CH_3), 1.32 (s, 6H, CH_3).

^{13}C-NMR (150 MHz, CD_2Cl_2):

δ [ppm] = 164.1 (C_q), 155.9 (C_q), 149.3 (C_q), 147.01 (C_q), 146.99 (C_q), 143.1 (C_q), 142.0 (C_q), 141.8 (C_q), 140.2 (CH), 140.0 (C_q), 137.1 (C_q), 135.9 (CH), 135.7 (C_q), 133.5 (CH), 133.0 (C_q), 132.4 (C_q), 130.7 (CH), 130.6 (CH), 130.3 (C_q), 126.5 (CH), 126.4 (CH),

122.1 (CH), 120.1 (CH), 118.6 (C_q), 116.4 (C_q), 114.9 (CH), 113.7 (C_q), 111.8 (CH), 107.6 (CH), 106.8 (C_q), 55.8 (OCH_3) 41.1 (CH_2), 32.9 (CH_2), 32.3 (CH_2), 17.0 (CH_3), 16.3 (CH_3).

Microanalysis (CHN): calc. for $C_{86}H_{72}IrN_{11}O_4$ C-%: 68.14, H-%: 4.79, N-%: 10.16,
found for $C_{86}H_{72}IrN_{11}O_4$ C-%: 68.09, H-%: 4.95, N-%: 10.19.

ESI-MS (pos., high res.): m/z calc. for $C_{86}H_{72}IrN_{11}O_4$ 1513.53692, found 1513.53549,
Δ = -0.94 ppm.

D5

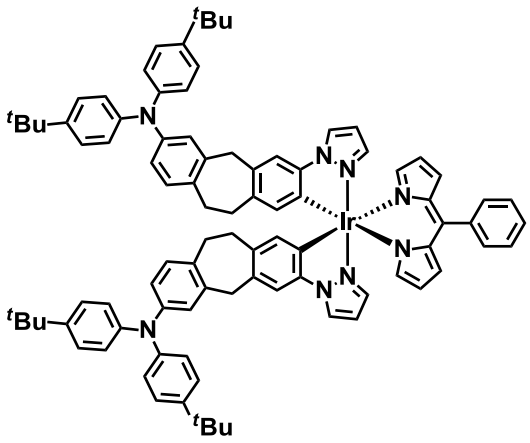

CA: [–]

Synthesis following GP V:

meso-Phenyldipyrromethane (**11**) (26.0 mg, 115 µmol), 2,3-dichloro-5,6-dicyano-1,4-benzoquinone (DDQ) (29.0 mg, 126 µmol), potassium carbonate (318 mg, 2.30 mmol), compound (**37**) (150 mg, 57.5 µmol) in THF (15 mL), 66°C, 12 h, flash column chromatography (eluent: CH_2Cl_2 : MeOH = 99 : 1) and GPC.

Yield: 100 mg (67.2 µmol, 58 %) of a red solid.

$C_{91}H_{91}IrN_8$ [1488.97]

^{1}H-NMR (600 MHz, acetone-d_6):

δ [ppm] = 8.41 (dd, $^{3}J_{HH}$ = 3.6 Hz, $^{4}J_{HH}$ = 0.6 Hz, 2H), 7.50–7.41 (-, 5H), 7.31 (s, 2H), 7.28 (AA', 8H), 7.04 (dd, $^{3}J_{HH}$ = 1.7 Hz, $^{3}J_{HH}$ = 1.7 Hz, 2H), 6.98 (dd, $^{3}J_{HH}$ = 2.2 Hz, $^{4}J_{HH}$ = 0.6 Hz, 2H), 6.94 (d, $^{3}J_{HH}$ = 8.2 Hz, 2H), 6.90 (BB', 8H), 6.86 (d, $^{3}J_{HH}$ = 2.4 Hz, 2H), 6.72 (dd, $^{3}J_{HH}$ = 8.1 Hz, $^{4}J_{HH}$ = 2.4 Hz, 2H), 6.56 (dd, $^{3}J_{HH}$ = 2.8 Hz,$^{4}J_{HH}$ = 2.2 Hz, 2H), 6.41 (dd, $^{3}J_{HH}$ = 4.3 Hz, $^{4}J_{HH}$ = 1.4 Hz, 2H), 6.18 (dd, $^{3}J_{HH}$ = 4.3 Hz, $^{4}J_{HH}$ = 1.4 Hz, 2H), 6.13 (s, 2H), 3.88 (d, $^{3}J_{HH}$ = 4.4 Hz, 4H), 2.99–2.81 (m, 8H), 1.29 (s, 36H, CH_3).

^{13}C-NMR (150 MHz, CPDCH 13C, acetone-d_6):

δ [ppm] = 152.6 (CH), 149.1 (C_q), 146.7 (C_q), 146.4 (C_q), 145.8 (C_q), 143.5 (C_q), 141.2 (C_q), 140.6 (C_q), 138.1 (C_q), 137.4 (CH), 136.0 (C_q), 135.73 (CH), 135.72 (C_q), 134.8 (C_q), 132.8 (C_q), 131.5 (CH), 131.3 (CH), 131.2 (CH), 128.9 (CH), 127.9 (CH), 126.9 (CH), 126.8 (CH), 125.0 (CH), 124.2 (CH), 122.9 (CH), 117.3 (CH), 112.5 (CH), 108.0 (CH), 41.0 (CH_2), 34.8 (C_q), 33.2 (CH_2), 32.9 (CH_2), 31.7 (CH_3).

Microanalysis (CHN): calc. for $C_{91}H_{91}IrN_8$ C-%: 73.40, H-%: 6.16, N-%: 7.53,
found for $C_{91}H_{91}IrN_8$ C-%: 72.58, H-%: 6.06, N-%: 7.50.

ESI-MS (pos., high res.): m/z calc. for $C_{91}H_{91}IrN_8$ 1486.69671, found 1486.69587,
Δ = 0.57 ppm.

6 Literature

[1] D. O. Hall, K. K. Rao, *Photosynthesis*, Cambridge University Press, Boca Raton, FL, **1994**.

[2] H. Kazuhito, I. Hiroshi, F. Akira, *Jpn. J. Appl. Phys.* **2005**, *44*, 8269-8285.

[3] A. Fujishima, K. Honda, *Nature* **1972**, *238*, 37-38.

[4] J. J. Concepcion, R. L. House, J. M. Papanikolas, T. J. Meyer, *Proc. Natl. Acad. Sci. U. S. A.* **2012**, *109*, 15560-15564.

[5] D. Gust, T. A. Moore, A. L. Moore, *Acc. Chem. Res.* **2009**, *42*, 1890-1898.

[6] T. A. Moore, D. Gust, P. Mathis, J. C. Mialocq, C. Chachaty, R. V. Bensasson, E. J. Land, D. Doizi, P. A. Liddell, W. R. Lehman, G. A. Nemeth, A. L. Moore, *Nature* **1984**, *307*, 630-632.

[7] A. Magnuson, M. Anderlund, O. Johansson, P. Lindblad, R. Lomoth, T. Polivka, S. Ott, K. Stensjo, S. Styring, V. Sundstrom, L. Hammarstrom, *Acc. Chem. Res.* **2009**, *42*, 1899-1909.

[8] E. Baranoff, J. P. Collin, L. Flamigni, J. P. Sauvage, *Chem. Soc. Rev.* **2004**, *33*, 147-155.

[9] M. R. Wasielewski, M. P. Niemczyk, W. A. Svec, E. B. Pewitt, *J. Am. Chem. Soc.* **1985**, *107*, 5562-5563.

[10] M. R. Wasielewski, *J. Org. Chem.* **2006**, *71*, 5051-5066.

[11] O. S. Wenger, *Coord. Chem. Rev.* **2009**, *253*, 1439-1457.

[12] H. Durr, S. Bossmann, *Acc. Chem. Res.* **2001**, *34*, 905-917.

[13] L. Flamigni, J. P. Collin, J. P. Sauvage, *Acc. Chem. Res.* **2008**, *41*, 857-871.

[14] V. Balzani, A. Credi, M. Venturi, *ChemSusChem* **2008**, *1*, 26-58.

[15] P. P. Laine, S. Campagna, F. Loiseau, *Coord. Chem. Rev.* **2008**, *252*, 2552-2571.

[16] V. Balzani, F. Barigelletti, L. Decola, *Top. Curr. Chem.* **1990**, *158*, 31-71.

[17] C. R. Bock, T. J. Meyer, D. G. Whitten, *J. Am. Chem. Soc.* **1974**, *96*, 4710-4712.

[18] M. Falkenstrom, O. Johansson, L. Hammarstrom, *Inorg. Chim. Acta* **2007**, *360*, 741-750.

[19] E. S. Andreiadis, M. Chavarot-Kerlidou, M. Fontecave, V. Artero, *Photochem. Photobiol.* **2011**, *87*, 946-964.

[20] M. R. Wasielewski, *Chem. Rev.* **1992**, *92*, 435-461.

[21] J. W. Verhoeven, H. J. van Ramesdonk, M. M. Groeneveld, A. C. Benniston, A. Harriman, *ChemPhysChem* **2005**, *6*, 2251-2260.

[22] J. W. Verhoeven, *J. Photochem. Photobiol., C* **2006**, *7*, 40-60.

[23] P. F. Barbara, T. J. Meyer, M. A. Ratner, *J. Phys. Chem.* **1996**, *100*, 13148-13168.

[24] A. Arrigo, A. Santoro, M. T. Indelli, M. Natali, F. Scandola, S. Campagna, *Phys. Chem. Chem. Phys.* **2014**, *16*, 818-826.

[25] P. P. Edwards, H. B. Gray, M. T. J. Lodge, R. J. P. Williams, *Angew. Chem. Int. Ed.* **2008**, *47*, 6758-6765.

[26] M. Natali, S. Campagna, F. Scandola, *Chem. Soc. Rev.* **2014**, *43*, 4005-4018.

[27] M. N. Paddon-Row, *Aust. J. Chem.* **2003**, *56*, 729-748.

[28] O. S. Wenger, *Acc. Chem. Res.* **2011**, *44*, 25-35.

[29] D. Gust, T. A. Moore, *Multistep Electron and Energy Transfer in Artificial Photosynthesis,* in *The Photosynthetic Reaction Center, Vol. II* (Eds.: J. Deisenhofer, J. R. Norris), Academic Press, London, **1993**.

[30] V. Balzani, A. Credi, M. Venturi, *Molecular Devices and Machines*, Wiley-VCH, Weinheim, **2008**.

[31] V. Balzani, G. Bergamini, S. Campagna, F. Puntoriero, *Photochemistry and photophysics of coordination compounds: Overview and general concepts,* in *Photochemistry and Photophysics of Coordination Compounds I, Vol. 280* (Eds.: V. Balzani, S. Campagna), Springer-Verlag Berlin, Berlin, **2007**, pp. 1-36.

[32] T. J. Meyer, *Acc. Chem. Res.* **1989**, *22*, 163-170.

[33] D. Gust, T. A. Moore, A. L. Moore, *Acc. Chem. Res.* **2001**, *34*, 40-48.

[34] M. D. Kärkäs, O. Verho, E. V. Johnston, B. Åkermark, *Chem. Rev.* **2014**, *114*, 11863-12001.

[35] A. Heckmann, C. Lambert, *Angew. Chem. Int. Ed.* **2012**, *51*, 326-392.

[36] H. Heitele, *Angew. Chem. Int. Ed.* **1993**, *32*, 359-377.

[37] R. A. Marcus, *J. Chem. Phys.* **1956**, *24*, 966-978.

[38] R. A. Marcus, N. Sutin, *Biochim. Biophys. Acta* **1985**, *811*, 265-322.

[39] P. Y. Chen, T. J. Meyer, *Chem. Rev.* **1998**, *98*, 1439-1477.

[40] J. Jortner, M. Bixon, *J. Chem. Phys.* **1988**, *88*, 167-170.

[41] J. Gierschner, J. Cornil, H. J. Egelhaaf, *Adv. Mater.* **2007**, *19*, 173-191.

[42] D. Rehm, A. Weller, *Isr. J. Chem.* **1970**, *8*, 259-271.

[43] A. Weller, *Z. Phys. Chem. Neue Fol.* **1982**, *133*, 93-98.

[44] S. Campagna, F. Puntoriero, F. Nastasi, G. Bergamini, V. Balzani, *Photochemistry and photophysics of coordination compounds: Ruthenium,* in *Photochemistry and Photophysics of Coordination Compounds I, Vol. 280* (Eds.: V. Balzani, S. Campagna), Springer-Verlag Berlin, Berlin, **2007**, pp. 117-214.

[45] A. Juris, V. Balzani, F. Barigelletti, S. Campagna, P. Belser, A. Vonzelewsky, *Coord. Chem. Rev.* **1988**, *84*, 85-277.

[46] D. W. Thompson, A. Ito, T. J. Meyer, *Pure Appl. Chem.* **2013**, *85*, 1257-1305.

[47] P. Muller, K. Brettel, *Photochem. Photobiol. Sci.* **2012**, *11*, 632-636.

[48] S. L. Mecklenburg, D. G. McCafferty, J. R. Schoonover, B. M. Peek, B. W. Erickson, T. J. Meyer, *Inorg. Chem.* **1994**, *33*, 2974-2983.

[49] S. L. Mecklenburg, B. M. Peek, B. W. Erickson, T. J. Meyer, *J. Am. Chem. Soc.* **1991**, *113*, 8540-8542.

[50] M. H. V. Huynh, D. M. Dattelbaum, T. J. Meyer, *Coord. Chem. Rev.* **2005**, *249*, 457-483.

[51] E. Danielson, C. M. Elliott, J. W. Merkert, T. J. Meyer, *J. Am. Chem. Soc.* **1987**, *109*, 2519-2520.

[52] D. R. Striplin, S. Y. Reece, D. G. McCafferty, C. G. Wall, D. A. Friesen, B. W. Erickson, T. J. Meyer, *J. Am. Chem. Soc.* **2004**, *126*, 5282-5291.

[53] J. H. Alstrum-Acevedo, M. K. Brennaman, T. J. Meyer, *Inorg. Chem.* **2005**, *44*, 6802-6827.

[54] M. Borgstrom, N. Shaikh, O. Johansson, M. F. Anderlund, S. Styring, B. Akermark, A. Magnuson, L. Hammarstrom, *J. Am. Chem. Soc.* **2005**, *127*, 17504-17515.

[55] J. Hankache, O. S. Wenger, *Chem. Commun.* **2011**, *47*, 10145-10147.

[56] J. Hankache, M. Niemi, H. Lemmetyinen, O. S. Wenger, *J. Phys. Chem. A* **2012**, *116*, 8159-8168.

[57] J. Hankache, M. Niemi, H. Lemmetyinen, O. S. Wenger, *Inorg. Chem.* **2012**, *51*, 6333-6344.

[58] I. V. Sazanovich, M. A. H. Alamiry, A. Meijer, M. Towrie, E. S. Davies, R. D. Bennett, J. A. Weinstein, *Pure Appl. Chem.* **2013**, *85*, 1331-1348.

[59] I. V. Sazanovich, J. Best, P. A. Scattergood, M. Towrie, S. A. Tikhomirov, O. V. Bouganov, A. Meijer, J. A. Weinstein, *Phys. Chem. Chem. Phys.* **2014**, *16*, 25775-25788.

[60] S. Chakraborty, T. J. Wadas, H. Hester, C. Flaschenreim, R. Schmehl, R. Eisenberg, *Inorg. Chem.* **2005**, *44*, 6284-6293.

[61] S. Chakraborty, T. J. Wadas, H. Hester, R. Schmehl, R. Eisenberg, *Inorg. Chem.* **2005**, *44*, 6865-6878.

[62] J. E. McGarrah, Y. J. Kim, M. Hissler, R. Eisenberg, *Inorg. Chem.* **2001**, *40*, 4510-4511.

[63] S. Suzuki, Y. Matsumoto, M. Tsubamoto, R. Sugimura, M. Kozaki, K. Kimoto, M. Iwamura, K. Nozaki, N. Senju, C. Uragami, H. Hashimoto, Y. Muramatsu, A. Konno, K. Okada, *Phys. Chem. Chem. Phys.* **2013**, *15*, 8088-8094.

[64] S. Suzuki, R. Sugimura, M. Kozaki, K. Keyaki, K. Nozaki, N. Ikeda, K. Akiyama, K. Okada, *J. Am. Chem. Soc.* **2009**, *131*, 10374-10375.

[65] J. Hankache, O. S. Wenger, *Chem. Eur. J.* **2012**, *18*, 6443-6447.

[66] L. Flamigni, E. Baranoff, J. P. Collin, J. P. Sauvage, *Chem. Eur. J.* **2006**, *12*, 6592-6606.

[67] L. Flamigni, E. Baranoff, J. P. Collin, J. P. Sauvage, B. Ventura, *ChemPhysChem* **2007**, *8*, 1943-1949.

[68] R. Lopez, A. M. Leiva, F. Zuloaga, B. Loeb, E. Norambuena, K. M. Omberg, J. R. Schoonover, D. Striplin, M. Devenney, T. J. Meyer, *Inorg. Chem.* **1999**, *38*, 2924-2930.

[69] A. J. Bard, M. A. Fox, *Acc. Chem. Res.* **1995**, *28*, 141-145.

[70] S. Karlsson, J. Boixel, Y. Pellegrin, E. Blart, H. C. Becker, F. Odobel, L. Hammarstrom, *J. Am. Chem. Soc.* **2010**, *132*, 17977-17979.

[71] S. E. Miller, A. S. Lukas, E. Marsh, P. Bushard, M. R. Wasielewski, *J. Am. Chem. Soc.* **2000**, *122*, 7802-7810.

[72] P. Connolly, J. H. Espenson, *Inorg. Chem.* **1986**, *25*, 2684-2688.

[73] V. Artero, M. Chavarot-Kerlidou, M. Fontecave, *Angew. Chem. Int. Ed.* **2011**, *50*, 7238-7266.

[74] G. A. N. Felton, C. A. Mebi, B. J. Petro, A. K. Vannucci, D. H. Evans, R. S. Glass, D. L. Lichtenberger, *J. Organomet. Chem.* **2009**, *694*, 2681-2699.

[75] F. Gartner, B. Sundararaju, A. E. Surkus, A. Boddien, B. Loges, H. Junge, P. H. Dixneuf, M. Beller, *Angew. Chem. Int. Ed.* **2009**, *48*, 9962-9965.

[76] I. Ganesh, *Renew. Sust. Energ. Rev.* **2014**, *31*, 221-257.

[77] I. Ganesh, *Renew. Sust. Energ. Rev.* **2015**, *44*, 904-932.

[78] J. Hawecker, J. M. Lehn, R. Ziessel, *Helv. Chim. Acta* **1986**, *69*, 1990-2012.

[79] S. Sato, T. Arai, T. Morikawa, *Inorg. Chem.* **2015**.

[80] M. S. Lowry, S. Bernhard, *Chem. Eur. J.* **2006**, *12*, 7970-7977.

[81] S. Ladouceur, E. Zysman-Colman, *Eur. J. Inorg. Chem.* **2013**, *2013*, 2985-3007.

[82] Y. Chi, P. T. Chou, *Chem. Soc. Rev.* **2010**, *39*, 638-655.

[83] S. Lamansky, P. Djurovich, D. Murphy, F. Abdel-Razzaq, H. E. Lee, C. Adachi, P. E. Burrows, S. R. Forrest, M. E. Thompson, *J. Am. Chem. Soc.* **2001**, *123*, 4304-4312.

[84] L. Flamigni, A. Barbieri, C. Sabatini, B. Ventura, F. Barigelletti, *Photochemistry and photophysics of coordination compounds: Iridium,* in *Photochemistry and Photophysics of Coordination Compounds II, Vol. 281*, Springer-Verlag Berlin, Berlin, **2007**, pp. 143-203.

[85] Y. You, W. Nam, *Chem. Soc. Rev.* **2012**, *41*, 7061-7084.

[86] Y. You, S. Y. Park, *Dalton Trans.* **2009**, 1267-1282.

[87] P. I. Djurovich, M. E. Thompson, *Cyclometallated Organoiridium Complexes as Emitters in Electrophosphorescent Devices,* in *Highly Efficient OLEDs with Phosphorescent Materials* (Ed.: H. Yersin), Wiley-VCH, Weinheim, **2007**, pp. 131-162.

[88] P. T. Chou, Y. Chi, *Chem. Eur. J.* **2007**, *13*, 380-395.

[89] H. Yersin, *Triplet emitters for OLED applications. Mechanisms of exciton trapping and control of emission properties,* in *Transition Metal and Rare Earth Compounds III, Vol. 241*, **2004**, pp. 1-26.

[90] M. A. Baldo, S. Lamansky, P. E. Burrows, M. E. Thompson, S. R. Forrest, *Appl. Phys. Lett.* **1999**, *75*, 4-6.

[91] C. Adachi, R. C. Kwong, P. Djurovich, V. Adamovich, M. A. Baldo, M. E. Thompson, S. R. Forrest, *Appl. Phys. Lett.* **2001**, *79*, 2082-2084.

[92] C. Adachi, M. A. Baldo, M. E. Thompson, S. R. Forrest, *J. Appl. Phys.* **2001**, *90*, 5048-5051.

[93] S. Jung, Y. Kang, H.-S. Kim, Y.-H. Kim, C.-L. Lee, J.-J. Kim, S.-K. Lee, S.-K. Kwon, *Eur. J. Inorg. Chem.* **2004**, *2004*, 3415-3423.

[94] D. Hanss, J. C. Freys, G. Bernardinelli, O. S. Wenger, *Eur. J. Inorg. Chem.* **2009**, *2009*, 4850-4859.

[95] J. Jayabharathi, R. Sathishkumar, V. Thanikachalam, *J. Phys. Org. Chem.* **2014**, *27*, 504-511.

[96] E. Baranoff, J.-H. Yum, M. Graetzel, M. K. Nazeeruddin, *J. Organomet. Chem.* **2009**, *694*, 2661-2670.

[97] W. C. H. Choy, W. K. Chan, Y. Yuan, *Adv. Mater.* **2014**, *26*, 5368-5399.

[98] G. M. Farinola, R. Ragni, *Chem. Soc. Rev.* **2011**, *40*, 3467-3482.

[99] E. Holder, B. M. W. Langeveld, U. S. Schubert, *Adv. Mater.* **2005**, *17*, 1109-1121.

[100] M. K. Nazeeruddin, R. Humphry-Baker, D. Berner, S. Rivier, L. Zuppiroli, M. Graetzel, *J. Am. Chem. Soc.* **2003**, *125*, 8790-8797.

[101] M. A. Baldo, D. F. O'Brien, Y. You, A. Shoustikov, S. Sibley, M. E. Thompson, S. R. Forrest, *Nature* **1998**, *395*, 151-154.

[102] M. K. Nazeeruddin, M. Gratzel, *Transition metal complexes for photovoltaic and light emitting applications,* in *Photofunctional Transition Metals Complexes, Vol. 123* (Ed.: V. W. W. Yam), Springer-Verlag Berlin, Berlin, **2007**, pp. 113-175.

[103] H. Yersin, A. F. Rausch, R. Czerwieniec, T. Hofbeck, T. Fischer, *Coord. Chem. Rev.* **2011**, *255*, 2622-2652.

[104] R. D. Costa, E. Orti, H. J. Bolink, F. Monti, G. Accorsi, N. Armaroli, *Angew. Chem. Int. Ed.* **2012**, *51*, 8178-8211.

[105] M. S. Lowry, W. R. Hudson, R. A. Pascal, S. Bernhard, *J. Am. Chem. Soc.* **2004**, *126*, 14129-14135.

[106] S. Lamansky, P. Djurovich, D. Murphy, F. Abdel-Razzaq, R. Kwong, I. Tsyba, M. Bortz, B. Mui, R. Bau, M. E. Thompson, *Inorg. Chem.* **2001**, *40*, 1704-1711.

[107] A. B. Tamayo, S. Garon, T. Sajoto, P. I. Djurovich, I. M. Tsyba, R. Bau, M. E. Thompson, *Inorg. Chem.* **2005**, *44*, 8723-8732.

[108] F. I. Wu, H. J. Su, C. F. Shu, L. Y. Luo, W. G. Diau, C. H. Cheng, J. P. Duan, G. H. Lee, *J. Mater. Chem.* **2005**, *15*, 1035-1042.

[109] E. D. Cline, S. Bernhard, *Chimia* **2009**, *63*, 709-713.

[110] J. I. Goldsmith, W. R. Hudson, M. S. Lowry, T. H. Anderson, S. Bernhard, *J. Am. Chem. Soc.* **2005**, *127*, 7502-7510.

[111] M. Wang, Y. Na, M. Gorlov, L. C. Sun, *Dalton Trans.* **2009**, 6458-6467.

[112] L. L. Tinker, N. D. McDaniel, P. N. Curtin, C. K. Smith, M. J. Ireland, S. Bernhard, *Chem. Eur. J.* **2007**, *13*, 8726-8732.

[113] P. N. Curtin, L. L. Tinker, C. M. Burgess, E. D. Cline, S. Bernhard, *Inorg. Chem.* **2009**, *48*, 10498-10506.

[114] T. S. Teets, D. G. Nocera, *Chem. Commun.* **2011**, *47*, 9268-9274.

[115] K. K. W. Lo, C. K. Chung, T. K. M. Lee, L. H. Lui, K. H. K. Tsang, N. Y. Zhu, *Inorg. Chem.* **2003**, *42*, 6886-6897.

[116] Y. You, S. Cho, W. Nam, *Inorg. Chem.* **2013**, *53*, 1804-1815.

[117] Y. You, *Curr. Opin. Chem. Biol.* **2013**, *17*, 699-707.

[118] C. Dragonetti, S. Righetto, D. Roberto, R. Ugo, A. Valore, S. Fantacci, A. Sgamellotti, F. De Angelis, *Chem. Commun.* **2007**, 4116-4118.

[119] K. Y. Kim, R. T. Farley, K. S. Schanze, *J. Phys. Chem. B* **2006**, *110*, 17302-17304.

[120] A. Valore, E. Cariati, C. Dragonetti, S. Righetto, D. Roberto, R. Ugo, F. De Angelis, S. Fantacci, A. Sgamellotti, A. Macchioni, D. Zuccaccia, *Chem. Eur. J.* **2010**, *16*, 4814-4825.

[121] A. Valore, A. Colombo, C. Dragonetti, S. Righetto, D. Roberto, R. Ugo, F. De Angelis, S. Fantacci, *Chem. Commun.* **2010**, *46*, 2414-2416.

[122] V. Aubert, L. Ordronneau, M. Escadeillas, J. A. G. Williams, A. Boucekkine, E. Coulaud, C. Dragonetti, S. Righetto, D. Roberto, R. Ugo, A. Valore, A. Singh, J. Zyss, I. Ledoux-Rak, H. Le Bozec, V. Guerchais, *Inorg. Chem.* **2011**, *50*, 5027-5038.

[123] A. Singh, K. Teegardin, M. Kelly, K. S. Prasad, S. Krishnan, J. D. Weaver, *J. Organomet. Chem.* **2015**, *776*, 51-59.

[124] K. Dedeian, P. I. Djurovich, F. O. Garces, G. Carlson, R. J. Watts, *Inorg. Chem.* **1991**, *30*, 1685-1687.

[125] C. M. Flynn, J. N. Demas, *J. Am. Chem. Soc.* **1974**, *96*, 1959-1960.

[126] E. C. Constable, *Adv. Inorg. Chem.* **1989**, *34*, 1-63.

[127] I. M. Dixon, J. P. Collin, J. P. Sauvage, L. Flamigni, S. Encinas, F. Barigelletti, *Chem. Soc. Rev.* **2000**, *29*, 385-391.

[128] A. C. Hazell, R. G. Hazell, *Acta Crystallogr. Sect. C-Cryst. Struct. Commun.* **1984**, *40*, 806-811.

[129] R. J. Watts, *Comments Inorg. Chem.* **1991**, *11*, 303-337.

[130] B. P. Sullivan, T. J. Meyer, *J. Chem. Soc.-Chem. Commun.* **1984**, 403-405.

[131] M. Nonoyama, *Bull. Chem. Soc. Jpn.* **1974**, *47*, 767-768.

[132] E. Baranoff, H. J. Bolink, E. C. Constable, M. Delgado, D. Haussinger, C. E. Housecroft, M. K. Nazeeruddin, M. Neuburger, E. Orti, G. E. Schneider, D. Tordera, R. M. Walliser, J. A. Zampese, *Dalton Trans.* **2013**, *42*, 1073-1087.

[133] F. O. Garces, K. A. King, R. J. Watts, *Inorg. Chem.* **1988**, *27*, 3464-3471.

[134] A. B. Tamayo, B. D. Alleyne, P. I. Djurovich, S. Lamansky, I. Tsyba, N. N. Ho, R. Bau, M. E. Thompson, *J. Am. Chem. Soc.* **2003**, *125*, 7377-7387.

[135] K. A. King, P. J. Spellane, R. J. Watts, *J. Am. Chem. Soc.* **1985**, *107*, 1431-1432.

[136] K. Dedeian, J. M. Shi, N. Shepherd, E. Forsythe, D. C. Morton, *Inorg. Chem.* **2005**, *44*, 4445-4447.

[137] F. De Angelis, S. Fantacci, N. Evans, C. Klein, S. M. Zakeeruddin, J. E. Moser, K. Kalyanasundaram, H. J. Bolink, M. Gratzel, M. K. Nazeeruddin, *Inorg. Chem.* **2007**, *46*, 5989-6001.

[138] T. Sajoto, P. I. Djurovich, A. B. Tamayo, J. Oxgaard, W. A. Goddard, M. E. Thompson, *J. Am. Chem. Soc.* **2009**, *131*, 9813-9822.

[139] G. J. Zhou, C. L. Ho, W. Y. Wong, Q. Wang, D. G. Ma, L. X. Wang, Z. Y. Lin, T. B. Marder, A. Beeby, *Adv. Funct. Mater.* **2008**, *18*, 499-511.

[140] Y. H. Song, Y. C. Chiu, Y. Chi, Y. M. Cheng, C. H. Lai, P. T. Chou, K. T. Wong, M. H. Tsai, C. C. Wu, *Chem. Eur. J.* **2008**, *14*, 5423-5434.

[141] C. Bronner, M. Veiga, A. Guenet, L. De Cola, M. W. Hosseini, C. A. Strassert, S. A. Baudron, *Chem. Eur. J.* **2012**, *18*, 4041-4050.

[142] K. Hanson, A. Tamayo, V. V. Diev, M. T. Whited, P. I. Djurovich, M. E. Thompson, *Inorg. Chem.* **2010**, *49*, 6077-6084.

[143] D. Ramlot, M. Rebarz, L. Volker, M. Ovaere, D. Beljonne, W. Dehaen, L. Van Meervelt, C. Moucheron, A. Kirsch-De Mesmaeker, *Eur. J. Inorg. Chem.* **2013**, 2031-2040.

[144] C. Bronner, S. A. Baudron, M. W. Hosseini, *Inorg. Chem.* **2010**, *49*, 8659-8661.

[145] J. Li, P. I. Djurovich, B. D. Alleyne, M. Yousufuddin, N. N. Ho, J. C. Thomas, J. C. Peters, R. Bau, M. E. Thompson, *Inorg. Chem.* **2005**, *44*, 1713-1727.

[146] L. Q. Chen, H. You, C. L. Yang, X. W. Zhang, J. G. Qin, D. G. Ma, *J. Mater. Chem.* **2006**, *16*, 3332-3339.

[147] E. Baranoff, I. M. Dixon, J. P. Collin, J. P. Sauvage, B. Ventura, L. Flamigni, *Inorg. Chem.* **2004**, *43*, 3057-3066.

[148] L. Flamigni, B. Ventura, E. Baranoff, J. P. Collin, J. P. Sauvage, *Eur. J. Inorg. Chem.* **2007**, 5189-5198.

[149] L. Flamigni, B. Ventura, F. Barigelletti, E. Baranoff, J. P. Collin, J. P. Sauvage, *Eur. J. Inorg. Chem.* **2005**, 1312-1318.

[150] M. Polson, M. Ravaglia, S. Fracasso, M. Garavelli, F. Scandola, *Inorg. Chem.* **2005**, *44*, 1282-1289.

[151] M. Polson, S. Fracasso, V. Bertolasi, M. Ravaglia, F. Scandola, *Inorg. Chem.* **2004**, *43*, 1950-1956.

[152] Y. Koga, M. Kamo, Y. Yamada, T. Matsumoto, K. Matsubara, *Eur. J. Inorg. Chem.* **2011**, 2869-2878.

[153] A. J. Wilkinson, H. Puschmann, J. A. K. Howard, C. E. Foster, J. A. G. Williams, *Inorg. Chem.* **2006**, *45*, 8685-8699.

[154] K. R. Lee, M. S. Eum, C. S. Chin, S. C. Lee, I. J. Kim, Y. S. Kim, Y. Kim, S. J. Kim, N. H. Hur, *Dalton Trans.* **2009**, 3650-3652.

[155] G. Gritzner, J. Kùta, *Pure Appl. Chem.* **1984**, *56*, 461-466.

[156] J. L. Kahl, K. W. Hanck, K. Dearmond, *J. Phys. Chem.* **1978**, *82*, 540-545.

[157] M. Montalti, A. Credi, L. Prodi, M. T. Gandolfi, *Handbook of Photochemistry*, III ed., CRC/Taylor & Francis, Boca Raton, **2006**.

[158] K. A. King, R. J. Watts, *J. Am. Chem. Soc.* **1987**, *109*, 1589-1590.

[159] M. S. Lowry, J. I. Goldsmith, J. D. Slinker, R. Rohl, R. A. Pascal, G. G. Malliaras, S. Bernhard, *Chem. Mater.* **2005**, *17*, 5712-5719.

[160] B. Geiss, PhD thesis, Julius-Maximilians-Universität Würzburg (Würzburg), **2009**.

[161] M. K. Nazeeruddin, R. T. Wegh, Z. Zhou, C. Klein, Q. Wang, F. De Angelis, S. Fantacci, M. Grätzel, *Inorg. Chem.* **2006**, *45*, 9245-9250.

[162] B. Minaev, H. Agren, F. De Angelis, *Chem. Phys.* **2009**, *358*, 245-257.

[163] A. R. G. Smith, P. L. Burn, B. J. Powell, *ChemPhysChem* **2011**, *12*, 2428-2437.

[164] X. Li, B. Minaev, H. Agren, H. Tian, *Eur. J. Inorg. Chem.* **2011**, 2517-2524.

[165] Y. Yang, F. Q. Bai, H. X. Zhang, X. Zhou, C. C. Sun, *Comput. Theor. Chem.* **2011**, *963*, 298-305.

[166] F. De Angelis, L. Belpassi, S. Fantacci, *Theochem-J. Mol. Struct.* **2009**, *914*, 74-86.

[167] P. J. Hay, *J. Phys. Chem. A* **2002**, *106*, 1634-1641.

[168] R. Terki, L. P. Simoneau, A. Rochefort, *J. Phys. Chem. A* **2009**, *113*, 534-541.

[169] D. Tordera, J. J. Serrano-Perez, A. Pertegas, E. Orti, H. J. Bolink, E. Baranoff, M. K. Nazeeruddin, J. Frey, *Chem. Mater.* **2013**, *25*, 3391-3397.

[170] S. Ladouceur, K. N. Swanick, S. Gallagher-Duval, Z. Ding, E. Zysman-Colman, *Eur. J. Inorg. Chem.* **2013**, *2013*, 5329-5343.

[171] P. S. Wagenknecht, P. C. Ford, *Coord. Chem. Rev.* **2011**, *255*, 591-616.

[172] B. Schmid, F. O. Garces, R. J. Watts, *Inorg. Chem.* **1994**, *33*, 9-14.

[173] M. G. Colombo, A. Hauser, H. U. Gudel, *Competition between Ligand Centered and Charge-Transfer Lowest Excited-States in Bis Cyclometalated Rh^{3+} and Ir^{3+} Complexes,* in *Electronic and Vibronic Spectra of Transition Metal Complexes I, Vol. 171*, **1994**, pp. 143-171.

[174] J. V. Caspar, T. J. Meyer, *Inorg. Chem.* **1983**, *22*, 2444-2453.

[175] A. Tsuboyama, H. Iwawaki, M. Furugori, T. Mukaide, J. Kamatani, S. Igawa, T. Moriyama, S. Miura, T. Takiguchi, S. Okada, M. Hoshino, K. Ueno, *J. Am. Chem. Soc.* **2003**, *125*, 12971-12979.

[176] A. P. Wilde, K. A. King, R. J. Watts, *J. Phys. Chem.* **1991**, *95*, 629-634.

[177] M. G. Colombo, A. Hauser, H. U. Gudel, *Inorg. Chem.* **1993**, *32*, 3088-3092.

[178] H. Yersin, W. J. Finzenzeller, *Triplet Emitters for Organic Light-Emitting Diodes: Basic Poperties,* in *Highly Efficient OLEDs with Phosphorescent Materials* (Ed.: H. Yersin), Wiley-VCH, Weinheim, **2007**, pp. 1-98.

[179] Y. Komada, S. Yamauchi, N. Hirota, *J. Phys. Chem.* **1986**, *90*, 6425-6430.

[180] H. Riesen, E. Krausz, *J. Lumines.* **1992**, *53*, 263-265.

[181] W. J. Finkenzeller, H. Yersin, *Chem. Phys. Lett.* **2003**, *377*, 299-305.

[182] C. Haken, H. C. Wolf, *Molekülphysik und Quantenchemie*, Springer, Berlin, Heidelberg, New York, **2003**.

[183] J. Franck, E. G. Dymond, *Trans. Faraday Soc.* **1926**, *21*, 536-542.

[184] E. U. Condon, *Phys. Rev.* **1928**, *32*, 858-872.

[185] E. U. Condon, *Phys. Rev.* **1926**, *28*, 1182-1201.

[186] K. C. Tang, K. L. Liu, I. C. Chen, *Chem. Phys. Lett.* **2004**, *386*, 437-441.

[187] M. Chergui, *Acc. Chem. Res.* **2015**.

[188] G. J. Hedley, A. Ruseckas, I. D. W. Samuel, *J. Phys. Chem. A* **2010**, *114*, 8961-8968.

[189] G. J. Hedley, A. Ruseckas, Z. H. Liu, S. C. Lo, P. L. Burn, I. D. W. Samuel, *J. Am. Chem. Soc.* **2008**, *130*, 11842-11843.

[190] G. J. Hedley, A. Ruseckas, I. D. W. Samuel, *Chem. Phys. Lett.* **2008**, *450*, 292-296.

[191] T. Sajoto, P. I. Djurovich, A. Tamayo, M. Yousufuddin, R. Bau, M. E. Thompson, R. J. Holmes, S. R. Forrest, *Inorg. Chem.* **2005**, *44*, 7992-8003.

[192] M. Bixon, J. Jortner, J. Cortes, H. Heitele, M. E. Michel-Beyerle, *J. Phys. Chem.* **1994**, *98*, 7289-7299.

[193] J. V. Caspar, T. J. Meyer, *J. Phys. Chem.* **1983**, *87*, 952-957.

[194] C. S. K. Mak, A. Hayer, S. I. Pascu, S. E. Watkins, A. B. Holmes, A. Kohler, R. H. Friend, *Chem. Commun.* **2005**, 4708-4710.

[195] P. Coppo, E. A. Plummer, L. De Cola, *Chem. Commun.* **2004**, 1774-1775.

[196] A. J. Lees, *Comments Inorg. Chem.* **1995**, *17*, 319-346.

[197] H. Yersin, J. Strasser, *Coord. Chem. Rev.* **2000**, *208*, 331-364.

[198] H. Hayashi, *Introduction to Dynamic Spin Chemistry, Vol. 8*, World Scientific Publishing, Singapore, **2004**.

[199] T. Klumpp, M. Linsenmann, S. L. Larson, B. R. Limoges, D. Burssner, E. B. Krissinel, C. M. Elliott, U. E. Steiner, *J. Am. Chem. Soc.* **1999**, *121*, 1076-1087.

[200] D. Kuciauskas, P. A. Liddell, A. L. Moore, T. A. Moore, D. Gust, *J. Am. Chem. Soc.* **1998**, *120*, 10880-10886.

[201] U. Werner, Y. Sakaguchi, H. Hayashi, G. Nohya, R. Yoneshima, S. Nakajima, A. Osuka, *J. Phys. Chem.* **1995**, *99*, 13930-13937.

[202] B. vanDijk, P. Gast, A. J. Hoff, *Phys. Rev. Lett.* **1996**, *77*, 4478-4481.

[203] A. M. Lewis, D. E. Manolopoulos, P. J. Hore, *J. Chem. Phys.* **2014**, *141*, 044111.

[204] Y. Tanimoto, M. Takashima, K. Hasegawa, M. Itoh, *Chem. Phys. Lett.* **1987**, *137*, 330-335.

[205] A. Weller, H. Staerk, R. Treichel, *Farad. Discuss,* **1984**, *78*, 271-278.

[206] M. T. Colvin, A. B. Ricks, A. M. Scott, A. L. Smeigh, R. Carmieli, T. Miura, M. R. Wasielewski, *J. Am. Chem. Soc.* **2011**, *133*, 1240-1243.

[207] Z. E. X. Dance, Q. X. Mi, D. W. McCamant, M. J. Ahrens, M. A. Ratner, M. R. Wasielewski, *J. Phys. Chem. B* **2006**, *110*, 25163-25173.

[208] A. S. Lukas, P. J. Bushard, E. A. Weiss, M. R. Wasielewski, *J. Am. Chem. Soc.* **2003**, *125*, 3921-3930.

[209] E. A. Weiss, E. T. Chernick, M. R. Wasielewski, *J. Am. Chem. Soc.* **2004**, *126*, 2326-2327.

[210] E. A. Weiss, M. A. Ratner, M. R. Wasielewski, *J. Phys. Chem. A* **2003**, *107*, 3639-3647.

[211] E. A. Weiss, M. J. Tauber, M. A. Ratner, M. R. Wasielewski, *J. Am. Chem. Soc.* **2005**, *127*, 6052-6061.

[212] E. A. Weiss, M. J. Ahrens, L. E. Sinks, A. V. Gusev, M. A. Ratner, M. R. Wasielewski, *J. Am. Chem. Soc.* **2004**, *126*, 5577-5584.

[213] Y. Mori, Y. Sakaguchi, H. Hayashi, *J. Phys. Chem. A* **2002**, *106*, 4453-4467.

[214] M. T. Rawls, G. Kollmannsberger, C. M. Elliott, U. E. Steiner, *J. Phys. Chem. A* **2007**, *111*, 3485-3496.

[215] Y. Sakaguchi, H. Hayashi, *J. Phys. Chem.* **1984**, *88*, 1437-1440.

[216] M. Wakasa, K. Nishizawa, H. Abe, G. Kido, H. Hayashi, *J. Am. Chem. Soc.* **1999**, *121*, 9191-9197.

[217] N. J. Turro, B. Kraeutler, *Acc. Chem. Res.* **1980**, *13*, 369-377.

[218] M. Gohdo, Y. Kitahama, Y. Sakaguchi, M. Wakasa, *J. Photochem. Photobiol., A* **2008**, *199*, 130-135.

[219] L. Fodor, A. Horvath, K. A. Hotzer, S. Walbert, U. E. Steiner, *Chem. Phys. Lett.* **2000**, *316*, 411-418.

[220] W. Schlenker, T. Ulrich, U. E. Steiner, *Chem. Phys. Lett.* **1983**, *103*, 118-123.

[221] T. von Feilitzsch, P. Harter, O. Schiemann, M. E. Michel-Beyerle, U. E. Steiner, P. Gilch, *J. Am. Chem. Soc.* **2005**, *127*, 15228-15235.

[222] J. Q. Wu, D. Baumann, U. E. Steiner, *Mol. Phys.* **1995**, *84*, 981-994.

[223] U. E. Steiner, H. J. Wolff, *Magnetic Field Effects in Photochemistry,* in *Photochemistry and Photophysics, Vol. IV* (Eds.: J. J. Rabek, G. W. Scott), CRC Press, Boca Raton, FL, **1991**, pp. 1-130.

[224] U. E. Steiner, T. Ulrich, *Chem. Rev.* **1989**, *89*, 51-147.

[225] P. Desai, P. Shakya, T. Kreouzis, W. P. Gillin, *J. Appl. Phys.* **2007**, *102*, 073710.

[226] E. Ehrenfreund, Z. V. Vardeny, *Isr. J. Chem.* **2012**, *52*, 552-562.

[227] Y. Goto, T. Noguchi, U. Takeuchi, K. Hatabayashi, Y. Hirose, T. Uchida, T. Sasaki, T. Hasegawa, T. Shimada, *Org. Electron.* **2010**, *11*, 1212-1216.

[228] J. P. Wang, A. Chepelianskii, F. Gao, N. C. Greenham, *Nat. Commun.* **2012**, *3*, 1191.

[229] B. Ehrler, B. J. Walker, M. L. Bohm, M. W. B. Wilson, Y. Vaynzof, R. H. Friend, N. C. Greenham, *Nat. Commun.* **2012**, *3*, 1019.

[230] M. C. Hanna, A. J. Nozik, *J. Appl. Phys.* **2006**, *100*, 074510.

[231] P. J. Jadhav, A. Mohanty, J. Sussman, J. Lee, M. A. Baldo, *Nano Lett.* **2011**, *11*, 1495-1498.

[232] M. B. Smith, J. Michl, *Chem. Rev.* **2010**, *110*, 6891-6936.

[233] M. B. Smith, J. Michl, *Annu. Rev. Phys. Chem.* **2013**, *64*, 361-386.

[234] M. W. B. Wilson, A. Rao, B. Ehrler, R. H. Friends, *Acc. Chem. Res.* **2013**, *46*, 1330-1338.

[235] C. B. Grissom, *Chem. Rev.* **1995**, *95*, 3-24.

[236] C. A. Dodson, P. J. Hore, M. I. Wallace, *Trends Biochem. Sci.* **2013**, *38*, 435-446.

[237] P. J. Hore, *Proc. Natl. Acad. Sci. U. S. A.* **2012**, *109*, 1357-1358.

[238] N. Lambert, Y. N. Chen, Y. C. Cheng, C. M. Li, G. Y. Chen, F. Nori, *Nat. Phys.* **2013**, *9*, 10-18.

[239] T. Ritz, S. Adem, K. Schulten, *Biophys. J.* **2000**, *78*, 707-718.

[240] C. T. Rodgers, P. J. Hore, *Proc. Natl. Acad. Sci. U. S. A.* **2009**, *106*, 353-360.

[241] K. Maeda, A. J. Robinson, K. B. Henbest, H. J. Hogben, T. Biskup, M. Ahmad, E. Schleicher, S. Weber, C. R. Timmel, P. J. Hore, *Proc. Natl. Acad. Sci. U. S. A.* **2012**, *109*, 4774-4779.

[242] K. Maeda, C. J. Wedge, J. G. Storey, K. B. Henbest, P. A. Liddell, G. Kodis, D. Gust, P. J. Hore, C. R. Timmel, *Chem. Commun.* **2011**, *47*, 6563-6565.

[243] K. Maeda, K. B. Henbest, F. Cintolesi, I. Kuprov, C. T. Rodgers, P. A. Liddell, D. Gust, C. R. Timmel, P. J. Hore, *Nature* **2008**, *453*, 387-391.

[244] B. Brocklehurst, *Chem. Soc. Rev.* **2002**, *31*, 301-311.

[245] S. G. Boxer, C. E. D. Chidsey, M. G. Roelofs, *Annu. Rev. Phys. Chem.* **1983**, *34*, 389-417.

[246] A. J. Hoff, *Q. Rev. Biophys.* **1981**, *14*, 599-665.

[247] B. Brocklehurst, K. A. McLauchlan, *Int. J. Radiat. Biol.* **1996**, *69*, 3-24.

[248] P. W. Atkins, *Quanten - Begriffe und Konzepte für Chemiker*, VCH Weinheim, **1993**.

[249] B. Brocklehurst, *Nature* **1969**, *221*, 921-923.

[250] K. M. Salikhov, Y. N. Molin, R. Z. Sagdeev, A. L. Buchachenko, *Spin Polarization and Magnetic Effects in Radical Reactions*, elsevier, Amsterdam, **1984**.

[251] G. L. Closs, C. E. Doubleday, *J. Am. Chem. Soc.* **1973**, *95*, 2735-2736.

[252] H. Hayashi, S. Nagakura, *Bull. Chem. Soc. Jpn.* **1984**, *57*, 322-328.

[253] R. Haberkorn, M. E. Michel-Beyerle, *Biophys. J.* **1979**, *26*, 489-498.

[254] R. Kaptein, *J. Am. Chem. Soc.* **1972**, *94*, 6251-6262.

[255] K. Schulten, A. Weller, *Biophys. J.* **1978**, *24*, 295-305.

[256] A. Weller, *Z. Phys. Chem. Neue Fol.* **1982**, *130*, 129-138.

[257] H. J. Werner, K. Schulten, A. Weller, *Biochim. Biophys. Acta* **1978**, *502*, 255-268.

[258] H. J. Werner, Z. Schulten, K. Schulten, *J. Chem. Phys.* **1977**, *67*, 646-663.

[259] K. Schulten, P. G. Wolynes, *J. Chem. Phys.* **1978**, *68*, 3292-3297.

[260] C. Kaiser, A. Schmiedel, M. Holzapfel, C. Lambert, *J. Phys. Chem. C* **2012**, *116*, 15265-15280.

[261] F. Zieschang, M. H. Schreck, A. Schmiedel, M. Holzapfel, J. H. Klein, C. Walter, B. Engels, C. Lambert, *J. Phys. Chem. C* **2014**, *118*, 27698-27714.

[262] B. Geiss, C. Lambert, *Chem. Commun.* **2009**, 1670-1672.

[263] I. V. Khudyakov, Y. A. Serebrennikov, N. J. Turro, *Chem. Rev.* **1993**, *93*, 537-570.

[264] H. J. Wolff, U. E. Steiner, *Z. Phys. Chem. Neue Fol.* **1990**, *169*, 147-158.

[265] H. Hayashi, K. Itoh, S. Nagakura, *Bull. Chem. Soc. Jpn.* **1966**, *39*, 199.

[266] G. L. Closs, *J. Am. Chem. Soc.* **1969**, *91*, 4552-4554.

[267] R. Kaptein, L. J. Oosterhoff, *Chem. Phys. Lett.* **1969**, *4*, 214-216.

[268] C. R. Timmel, U. Till, B. Brocklehurst, K. A. McLauchlan, P. J. Hore, *Mol. Phys.* **1998**, *95*, 71-89.

[269] H. Staerk, W. Kuhnle, R. Treichel, A. Weller, *Chem. Phys. Lett.* **1985**, *118*, 19-24.

[270] A. Weller, F. Nolting, H. Staerk, *Chem. Phys. Lett.* **1983**, *96*, 24-27.

[271] E. W. Knapp, K. Schulten, *J. Chem. Phys.* **1979**, *71*, 1878-1883.

[272] I. K. Kominis, *Phys. Rev. E* **2009**, *80*, 056115.

[273] K. Schulten, *J. Chem. Phys.* **1985**, *82*, 1312-1316.

[274] K. Schulten, I. R. Epstein, *J. Chem. Phys.* **1979**, *71*, 309-316.

[275] L. Banci, L. Bertini, C. Luchinat, *Nuclear and Electron Relaxation*, VCH, Weinheim, New York, Basel, Cambridge, **1991**.

[276] K. Luders, K. M. Salikhov, *Chem. Phys.* **1987**, *117*, 113-131.

[277] C. Mailer, R. D. Nielsen, B. H. Robinson, *J. Phys. Chem. A* **2005**, *109*, 4049-4061.

[278] M. Holzapfel, PhD thesis, Julius-Maximilians-Universität Würzburg (Würzburg), **2007**.

[279] M. Holzapfel, C. Lambert, *J. Phys. Chem. C* **2008**, *112*, 1227-1243.

[280] I. P. Beletskaya, A. V. Cheprakov, *Coord. Chem. Rev.* **2004**, *248*, 2337-2364.

[281] J. Hassan, M. Sevignon, C. Gozzi, E. Schulz, M. Lemaire, *Chem. Rev.* **2002**, *102*, 1359-1469.

[282] F. Monnier, M. Taillefer, *Angew. Chem. Int. Ed.* **2009**, *48*, 6954-6971.

[283] A. R. Muci, S. L. Buchwald, *Top. Curr. Chem.* **2002**, *219*, 131-209.

[284] D. S. Surry, S. L. Buchwald, *Chem. Sci.* **2011**, *2*, 27-50.

[285] C. H. Lee, J. S. Lindsey, *Tetrahedron* **1994**, *50*, 11427-11440.

[286] P. A. Faugeras, B. Boens, P. H. Elchinger, J. Vergnaud, K. Teste, R. Zerrouki, *Tetrahedron Lett.* **2010**, *51*, 4630-4632.

[287] N. Malatesti, R. Hudson, K. Smith, H. Savoie, K. Rix, K. Welham, R. W. Boyle, *Photochem. Photobiol.* **2006**, *82*, 746-749.

[288] Y. Kuramochi, A. S. D. Sandanayaka, A. Satake, Y. Araki, K. Ogawa, O. Ito, Y. Kobuke, *Chem. Eur. J.* **2009**, *15*, 2317-2327.

[289] D. Cousin, J. Mann, M. Nieuwenhuyzen, H. van den Berg, *Org. Biomol. Chem.* **2006**, *4*, 54-62.

[290] A. Beeby, S. Bettington, I. J. S. Fairlamb, A. E. Goeta, A. R. Kapdi, E. H. Niemela, A. L. Thompson, *New J. Chem.* **2004**, *28*, 600-605.

[291] S. Amthor, B. Noller, C. Lambert, *Chem. Phys.* **2005**, *316*, 141-152.

[292] T. C. Barros, S. Brochsztain, V. G. Toscano, P. Berci, M. J. Politi, *J. Photochem. Photobiol., A* **1997**, *111*, 97-104.

[293] S. V. Bhosale, C. H. Jani, S. J. Langford, *Chem. Soc. Rev.* **2008**, *37*, 331-342.

[294] G. Andric, J. F. Boas, A. M. Bond, G. D. Fallon, K. P. Ghiggino, C. F. Hogan, J. A. Hutchison, M. A. P. Lee, S. J. Langford, J. R. Pilbrow, G. J. Troup, C. P. Woodward, *Aust. J. Chem.* **2004**, *57*, 1011-1019.

[295] J. Föller, Master thesis, Heinrich-Heine-Universität Düsseldorf (Düsseldorf), **2014**.

[296] E. Pomarico, M. Chergui, personal communication, Swiss Federal Institute of Technology (Lausanne), **2015**.

[297] P. Gawrys, D. Djurado, J. R. Rimarcik, A. Kornet, D. Boudinet, J. M. Verilhac, V. Lukes, I. Wielgus, M. Zagorska, A. Pron, *J. Phys. Chem. B* **2010**, *114*, 1803-1809.

[298] J. E. Bullock, M. T. Vagnini, C. Ramanan, D. T. Co, T. M. Wilson, J. W. Dicke, T. J. Marks, M. R. Wasielewski, *J. Phys. Chem. B* **2010**, *114*, 1794-1802.

[299] G. J. Hedley, A. Ruseckas, A. Harriman, I. D. W. Samuel, *Angew. Chem. Int. Ed.* **2011**, *50*, 6634-6637.

[300] R. W. Wagner, J. S. Lindsey, *Pure Appl. Chem.* **1996**, *68*, 1373-1380.

[301] H. L. Kee, C. Kirmaier, L. Yu, P. Thamyongkit, W. J. Youngblood, M. E. Calder, L. Ramos, B. C. Noll, D. F. Bocian, W. R. Scheidt, R. R. Birge, J. S. Lindsey, D. Holten, *J. Phys. Chem. B* **2005**, *109*, 20433-20443.

[302] D. L. Dexter, *J. Chem. Phys.* **1953**, *21*, 836-850.

[303] T. Forster, *Naturwiss.* **1946**, *33*, 166-175.

[304] S. Speiser, *Chem. Rev.* **1996**, *96*, 1953-1976.

[305] P. Ganesan, J. Baggerman, H. Zhang, E. J. R. Sudholter, H. Zuilhof, *J. Phys. Chem. A* **2007**, *111*, 6151-6156.

[306] J. E. Rogers, L. A. Kelly, *J. Am. Chem. Soc.* **1999**, *121*, 3854-3861.

[307] D. D. Bao, B. Millare, W. Xia, B. G. Steyer, A. A. Gerasimenko, A. Ferreira, A. Contreras, V. I. Vullev, *J. Phys. Chem. A* **2009**, *113*, 1259-1267.

[308] S. Green, M. A. Fox, *J. Phys. Chem.* **1995**, *99*, 14752-14757.

[309] S. L. Suraru, F. Wurthner, *Angew. Chem. Int. Ed.* **2014**, *53*, 7428-7448.

[310] S. R. Greenfield, W. A. Svec, D. Gosztola, M. R. Wasielewski, *J. Am. Chem. Soc.* **1996**, *118*, 6767-6777.

[311] G. P. Wiederrecht, M. P. Niemczyk, W. A. Svec, M. R. Wasielewski, *J. Am. Chem. Soc.* **1996**, *118*, 81-88.

[312] Gaussian 09, Revision D.01, M. J. Frisch, G. W. Trucks, H. B. Schlegel, G. E. Scuseria, M. A. Robb, J. R. Cheeseman, G. Scalmani, V. Barone, B. Mennucci, G. A. Petersson, H. Nakatsuji, M. Caricato, X. Li, H. P. Hratchian, A. F. Izmaylov, J. Bloino, G. Zheng, J. L. Sonnenberg, M. Hada, M. Ehara, K. Toyota, R. Fukuda, J. Hasegawa, M. Ishida, T. Nakajima, Y. Honda, O. Kitao, H. Nakai, T. Vreven, J. A. Montgomery, Jr., J. E. Peralta, F. Ogliaro, M. Bearpark, J. J. Heyd, E. Brothers, K. N. Kudin, V. N. Staroverov, R. Kobayashi, J. Normand, K. Raghavachari, A. Rendell, J. C. Burant, S. S. Iyengar, J. Tomasi, M. Cossi, N. Rega, J. M. Millam, M. Klene, J. E. Knox, J. B. Cross, V. Bakken, C. Adamo, J. Jaramillo, R. Gomperts, R. E. Stratmann, O. Yazyev, A. J. Austin, R. Cammi, C. Pomelli, J. W. Ochterski, R. L. Martin, K. Morokuma, V. G. Zakrzewski, G. A. Voth, P. Salvador, J. J. Dannenberg, S. Dapprich, A. D. Daniels, Ö. Farkas, J. B. Foresman, J. V. Ortiz, J. Cioslowski, and D. J. Fox, Gaussian, Inc., Wallingford CT, **2009**.

[313] R. T. Hayes, M. R. Wasielewski, D. Gosztola, *J. Am. Chem. Soc.* **2000**, *122*, 5563-5567.

[314] G. P. Wiederrecht, W. A. Svec, M. R. Wasielewski, *J. Am. Chem. Soc.* **1999**, *121*, 7726-7727.

[315] M. P. Debreczeny, W. A. Svec, E. M. Marsh, M. R. Wasielewski, *J. Am. Chem. Soc.* **1996**, *118*, 8174-8175.

[316] J. K. Hurley, N. Sinai, H. Linschitz, *Photochem. Photobiol.* **1983**, *38*, 9-14.

[317] C. V. Suneesh, K. R. Gopidas, *J. Phys. Chem. C* **2009**, *113*, 1606-1614.

[318] I. Carmichael, G. L. Hug, *J. Phys. Chem. Ref. Data* **1986**, *15*, 1-250.

[319] A. N. Tarnovsky, W. Gawelda, M. Johnson, C. Bressler, M. Chergui, *J. Phys. Chem. B* **2006**, *110*, 26497-26505.

[320] J. N. Demas, G. A. Crosby, *J. Am. Chem. Soc.* **1970**, *92*, 7262-7270.

[321] I. H. M. van Stokkum, D. S. Larsen, R. van Grondelle, *Biochim. Biophys. Acta, Bioenerg.* **2004**, *1657*, 82-104.

[322] M. Maroncelli, *J. Mol. Liq.* **1993**, *57*, 1-37.

[323] J. Petersson, M. Eklund, J. Davidsson, L. Hammarstrom, *J. Phys. Chem. B* **2010**, *114*, 14329-14338.

[324] A. Pigliucci, G. Duvanel, L. M. L. Daku, E. Vauthey, *J. Phys. Chem. A* **2007**, *111*, 6135-6145.

[325] T. Elsaesser, W. Kaiser, *Annu. Rev. Phys. Chem.* **1991**, *42*, 83-107.

[326] A. Pigliucci, E. Vauthey, *Chimia* **2003**, *57*, 200-203.

[327] M. Licchelli, L. Linati, A. O. Biroli, E. Perani, A. Poggi, D. Sacchi, *Chem. Eur. J.* **2002**, *8*, 5161-5169.

[328] B. M. Aveline, S. Matsugo, R. W. Redmond, *J. Am. Chem. Soc.* **1997**, *119*, 11785-11795.

[329] P. M. Hare, C. E. Crespo-Hernández, B. Kohler, *J. Phys. Chem. B* **2006**, *110*, 18641-18650.

[330] Y. Geng, S. X. Wu, H. B. Li, X. D. Tang, Y. Wu, Z. M. Su, Y. Liao, *J. Mater. Chem.* **2011**, *21*, 15558-15566.

[331] M. Malagoli, J. L. Bredas, *Chem. Phys. Lett.* **2000**, *327*, 13-17.

[332] S. F. Nelsen, S. C. Blackstock, Y. Kim, *J. Am. Chem. Soc.* **1987**, *109*, 677-682.

[333] S. F. Nelsen, H. Chang, J. J. Wolff, J. Adamus, *J. Am. Chem. Soc.* **1993**, *115*, 12276-12289.

[334] B. S. Brunschwig, S. Ehrenson, N. Sutin, *J. Phys. Chem.* **1986**, *90*, 3657-3668.

[335] T. B. Truong, *J. Phys. Chem.* **1984**, *88*, 3906-3913.

[336] M. D. Newton, *Chem. Rev.* **1991**, *91*, 767-792.

[337] L. D. Zusman, D. N. Beratan, *J. Phys. Chem. A* **1997**, *101*, 4136-4141.

[338] M. Akiyama, T. Watanabe, M. Kakihana, *J. Phys. Chem.* **1986**, *90*, 1752-1755.

[339] E. A. Aleman, C. D. Shreiner, C. S. Rajesh, T. Smith, S. A. Garrison, D. A. Modarelli, *Dalton Trans.* **2009**, 6562-6577.

[340] S. Arulmozhiraja, T. Fujii, *J. Chem. Phys.* **2001**, *115*, 10589-10594.

[341] M. W. Holman, P. Yan, K. C. Ching, R. C. Liu, F. I. Ishak, D. M. Adams, *Chem. Phys. Lett.* **2005**, *413*, 501-505.

[342] R. Siebert, A. Winter, U. S. Schubert, B. Dietzek, J. Popp, *J. Phys. Chem. C* **2010**, *114*, 6841-6848.

[343] E. A. Weiss, M. J. Tauber, R. F. Kelley, M. J. Ahrens, M. A. Ratner, M. R. Wasielewski, *J. Am. Chem. Soc.* **2005**, *127*, 11842-11850.

[344] V. Markovic, D. Villamaina, I. Barabanov, L. M. L. Daku, E. Vauthey, *Angew. Chem. Int. Ed.* **2011**, *50*, 7596-7598.

[345] E. Vauthey, *ChemPhysChem* **2012**, *13*, 2001-2011.

[346] F. Steiner, S. Bange, J. Vogelsang, J. M. Lupton, *J. Phys. Chem. Lett.* **2015**, *6*, 999-1004.

[347] M. E. Moret, I. Tavernelli, M. Chergui, U. Rothlisberger, *Chem. Eur. J.* **2010**, *16*, 5889-5894.

[348] A. T. Yeh, C. V. Shank, J. K. McCusker, *Science* **2000**, *289*, 935-938.

[349] N. Banerji, A. Furstenberg, S. Bhosale, A. L. Sisson, N. Sakai, S. Matile, E. Vauthey, *J. Phys. Chem. B* **2008**, *112*, 8912-8922.

[350] J. E. Bullock, R. Carmieli, S. M. Mickley, J. Vura-Weis, M. R. Wasielewski, *J. Am. Chem. Soc.* **2009**, *131*, 11919-11929.

[351] R. Stahl, C. Lambert, C. Kaiser, R. Wortmann, R. Jakober, *Chem. Eur. J.* **2006**, *12*, 2358-2370.

[352] M. R. Wasielewski, *Acc. Chem. Res.* **2009**, *42*, 1910-1921.

[353] G. Feher, J. P. Allen, M. Y. Okamura, D. C. Rees, *Nature* **1989**, *339*, 111-116.

[354] M. J. Fuller, A. V. Gusev, M. R. Wasielewski, *Isr. J. Chem.* **2004**, *44*, 101-108.

[355] J. M. Giaimo, A. V. Gusev, M. R. Wasielewski, *J. Am. Chem. Soc.* **2002**, *124*, 8530-8531.

[356] H. Khandelwal, A. R. Mallia, R. T. Cheriya, M. Hariharan, *Phys. Chem. Chem. Phys.* **2012**, *14*, 15282-15285.

[357] M. L. Horng, J. A. Gardecki, A. Papazyan, M. Maroncelli, *J. Phys. Chem.* **1995**, *99*, 17311-17337.

[358] K. J. Reszka, M. Takayama, R. H. Sik, C. F. Chignell, I. Saito, *Photochem. Photobiol.* **2005**, *81*, 573-580.

[359] D. R. Kattnig, B. Mladenova, G. Grampp, C. Kaiser, A. Heckmann, C. Lambert, *J. Phys. Chem. C* **2009**, *113*, 2983-2995.

[360] R. Bakova, M. Chergui, C. Daniel, A. Vlcek, S. Zalis, *Coord. Chem. Rev.* **2011**, *255*, 975-989.

[361] G. A. Crosby, K. W. Hipps, W. H. Elfring, *J. Am. Chem. Soc.* **1974**, *96*, 629-630.

[362] P. Gilch, F. Pollinger-Dammer, C. Musewald, M. E. Michel-Beyerle, U. E. Steiner, *Science* **1998**, *281*, 982-984.

[363] K. A. Hötzer, A. Klingert, T. Klumpp, E. Krissinel, D. Bürßner, U. E. Steiner, *J. Phys. Chem. A* **2002**, *106*, 2207 -2217.

[364] G. Grampp, P. J. Hore, M. Justinek, S. Landgraf, N. N. Lukzen, *Res. Chem. Intermed.* **2005**, *31*, 567-573.

[365] M. Justinek, G. Grampp, S. Landgraf, P. J. Hore, N. N. Lukzen, *J. Am. Chem. Soc.* **2004**, *126*, 5635-5646.

[366] B. Mladenova, D. R. Kattnig, C. Kaiser, J. Schäfer, C. Lambert, G. Grampp, *J. Phys. Chem. C* **2015**, *119*, 8547-8553.

[367] M. T. Rawls, I. Kuprov, C. M. Elliott, U. E. Steiner, *Spin Relaxation in Ru-Chromophore-Linked Azine/Diquat Radical Pairs,* in *Carbon-Centered Free Radicals and Radical Cations* (Ed.: M. D. E. Forbes), John Wiley & Sons, Hoboken, New Jersey, **2010**.

[368] A. A. Carrington, A. D. McLachlan, *Introduction to magnetic resonance*, Chapman and Hall, **1967**.

[369] S. Gückel, M. Kaupp, Technische Universität Berlin (Berlin), **2015**.

[370] V. Meyer, S. S. Eaton, G. R. Eaton, *Appl. Magn. Reson.* **2014**, *45*, 993-1007.

[371] L. Yong, J. Harbridge, R. W. Quine, G. A. Rinard, S. S. Eaton, G. R. Eaton, C. Mailer, E. Barth, H. J. Halpern, *J. Magn. Reson.* **2001**, *152*, 156-161.

[372] K. Tsujimoto, R. Ogasawara, T. Nakagawa, H. Fujiwara, *Eur. J. Inorg. Chem.* **2014**, *2014*, 3960-3972.

[373] R. Wagener, Master thesis, Julius-Maximilians-Universität Würzburg (Würzburg), **2013**.

[374] S. F. Nelsen, *Chem. Eur. J.* **2000**, *6*, 581-588.

[375] S. F. Nelsen, R. F. Ismagilov, D. A. Trieber, *Science* **1997**, *278*, 846-849.

[376] J. Hankache, O. S. Wenger, *Chem. Rev.* **2011**, *111*, 5138-5178.

[377] C. Lambert, G. Noll, *Angew. Chem. Int. Ed.* **1998**, *37*, 2107-2110.

[378] Specfit/32^{TM} V3.0.23, Program for Multivariate Data Analysis, Spectrum Software Associates, Marlborough (USA), 1993.

[379] J. Bonvoisin, J. P. Launay, M. Van der Auweraer, F. C. De Schryver, *J. Phys. Chem.* **1994**, *98*, 5052-5057.

[380] S. Barlow, C. Risko, S. A. Odom, S. J. Zheng, V. Coropceanu, L. Beverina, J. L. Brédas, S. R. Marder, *J. Am. Chem. Soc.* **2012**, *134*, 10146-10155.

[381] M. Kaupp, M. Renz, M. Parthey, M. Stolte, F. Würthner, C. Lambert, *Phys. Chem. Chem. Phys.* **2011**, *13*, 16973-16986.

[382] M. Parthey, K. B. Vincent, M. Renz, P. A. Schauer, D. S. Yufit, J. A. K. Howard, M. Kaupp, P. J. Low, *Inorg. Chem.* **2014**, *53*, 1544-1554.

[383] A. D. Becke, *J. Chem. Phys.* **1993**, *98*, 1372-1377.

[384] N. Sutin, *Prog. Inorg. Chem.* **1983**, *30*, 441-498.

[385] C. Creutz, M. D. Newton, N. Sutin, *J. Photochem. Photobiol., A* **1994**, *82*, 47-59.

[386] B. S. Brunschwig, C. Creutz, N. Sutin, *Chem. Soc. Rev.* **2002**, *31*, 168-184.

[387] *Mixed-Valence Compounds*, D. Reidel Publishers, Dordrecht, Boston, London, **1980**.

[388] C. Lambert, S. Amthor, J. Schelter, *J. Phys. Chem. A* **2004**, *108*, 6474-6486.

[389] S. C. Jones, V. Coropceanu, S. Barlow, T. Kinnibrugh, T. Timofeeva, J. L. Bredas, S. R. Marder, *J. Am. Chem. Soc.* **2004**, *126*, 11782-11783.

[390] C. J. Yao, J. N. A. Yao, Y. W. Zhong, *Inorg. Chem.* **2011**, *50*, 6847-6849.

[391] D. W. Domaille, L. Zeng, C. J. Chang, *J. Am. Chem. Soc.* **2010**, *132*, 1194-1195.

[392] A. Alberola, A. G. Ortega, M. L. Sadaba, C. Sanudo, *Tetrahedron* **1999**, *55*, 6555-6566.

[393] K. Krumova, G. Cosa, *J. Am. Chem. Soc.* **2010**, *132*, 17560-17569.

[394] T. Ueno, Y. Urano, H. Kojima, T. Nagano, *J. Am. Chem. Soc.* **2006**, *128*, 10640-10641.

[395] S. Riese, Lehramt Staatsexamen (teacher apprenticeship), Julius-Maximilians-Universität Würzburg (Würzburg), **2012**.

[396] A. B. Nepomnyashchii, A. J. Bard, *Acc. Chem. Res.* **2012**, *45*, 1844-1853.

[397] V. Leen, P. Yuan, L. Wang, N. Boens, W. Dehaen, *Org. Lett.* **2012**, *14*, 6150-6153.

[398] S. E. Dummling, E.; Schneider, S.; Speiser, B.; Wuerde, M., *Curr. Sep. Drug Dev.* **1996**, *15*, 53-56.

[399] S. Amthor, C. Lambert, *J. Phys. Chem. A* **2006**, *110*, 1177-1189.

[400] G. R. Fulmer, A. J. M. Miller, N. H. Sherden, H. E. Gottlieb, A. Nudelman, B. M. Stoltz, J. E. Bercaw, K. I. Goldberg, *Organometallics* **2010**, *29*, 2176-2179.

[401] F. Neese, F. Wennmohs, U. Becker, D. Bykov, D. Ganyushin, A. Hansen, R. Izsák, D. G. Liakos, C. Kollmar, S. Kossmann, D. A. Pantazis, T. Petrenko, C. Reimann, C. Riplinger, M. Roemelt, B. Sandhöfer, I. Schapiro, K. Sivalingam, B. Wezisla, version 3.0.2 ed., Max Planck Institute for Chemical EnergyConversion, Germany, **2014**.

[402] A. Klamt, *Wiley Interdiscip. Rev.-Comput. Mol. Sci.* **2011**, *1*, 699-709.

[403] F. Weigend, R. Ahlrichs, *Phys. Chem. Chem. Phys.* **2005**, *7*, 3297-3305.

[404] D. Andrae, U. Häußermann, M. Dolg, H. Stoll, H. Preuß, *Theor. Chim. Acta* **1990**, *77*, 123-141.

[405] F. Neese, F. Wennmohs, A. Hansen, U. Becker, *Chem. Phys.* **2009**, *356*, 98-109.

[406] K. L. Schuchardt, B. T. Didier, T. Elsethagen, L. Sun, V. Gurumoorthi, J. Chase, J. Li, T. L. Windus, *J. Chem. Inf. Model.* **2007**, *47*, 1045-1052.

[407] M. Cossi, N. Rega, G. Scalmani, V. Barone, *J. Comput. Chem.* **2003**, *24*, 669-681.

[408] M. Hanwell, D. Curtis, D. Lonie, T. Vandermeersch, E. Zurek, G. Hutchison, *J. Cheminform.* **2012**, *4*, 17.

[409] D. F. Shriver, Drezdon M. A. , *The manipulation of air-sensitive compounds*, John Wiley & Sons, New York, **1986**.

[410] W. C. Still, M. Kahn, A. Mitra, *J. Org. Chem.* **1978**, *43*, 2923-2925.

[411] Y. Q. Xiang, P. Y. Caron, B. M. Lillie, R. Vaidyanathan, *Org. Process Res. Dev.* **2008**, *12*, 116-119.

[412] M. E. El-Khouly, J. B. Ryu, K. Y. Kay, O. Ito, S. Fukuzumi, *J. Phys. Chem. C* **2009**, *113*, 15444-15453.

[413] I. Cepanec, G. Karminski-Zamola, M. Litvic, Z. Mikotic-Mihun **1999**, *PCT Int. Appl.* WO1999028284 A1.

[414] G. W. Gribble, W. J. Kelly, S. E. Emery, *Synthesis Stuttgart* **1978**, 763-765.

[415] H. J. Cristau, P. P. Cellier, J. F. Spindler, M. Taillefer, *Eur. J. Org. Chem.* **2004**, 695-709.

[416] K. C. Moss, K. N. Bourdakos, V. Bhalla, K. T. Kamtekar, M. R. Bryce, M. A. Fox, H. L. Vaughan, F. B. Dias, A. P. Monkman, *J. Org. Chem.* **2010**, *75*, 6771-6781.

[417] K. A. Simmen, T.-I. Lin, O. Lenz, D. L. N. G. Surleraux, P. J.-M. B. Raboisson **2006**, *PCT Int. Appl.* WO2006/035061 A1.

7 Table of Formulas

Phenylpyrazole Ligands

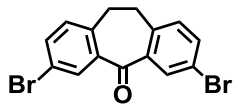

1

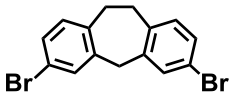

2

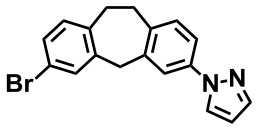

3

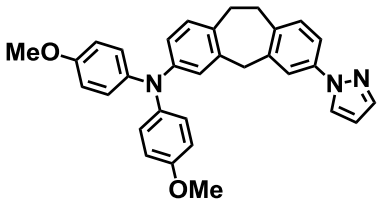

4

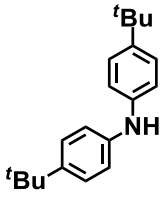

5

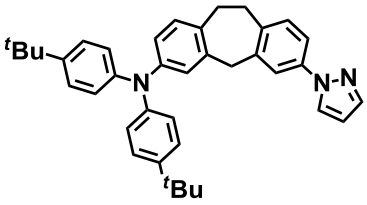

6

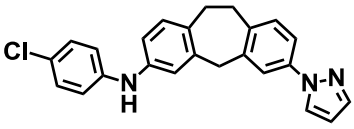

7

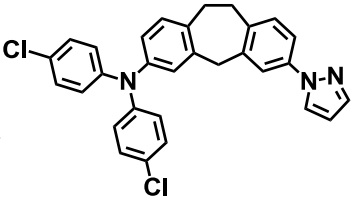

8

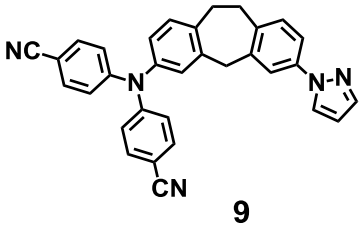

9

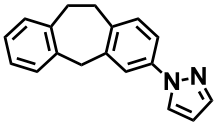

10

Dipyrromethane Ligands

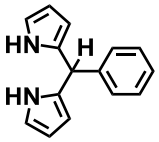

11

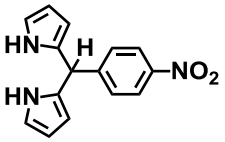

12

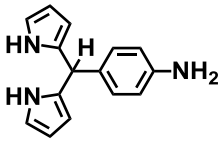

13

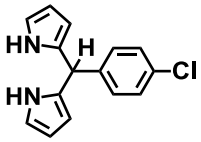

14

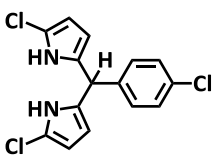

15

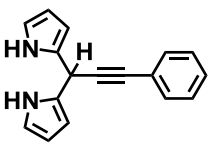

16

Naphthalene Diimide Ligands

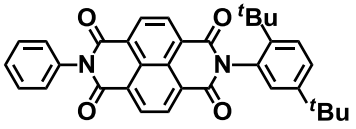

17

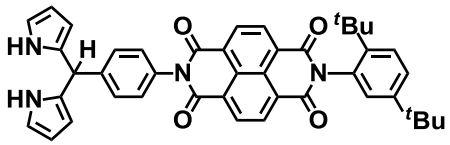

18

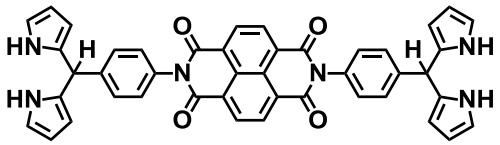

19

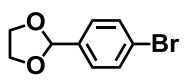

20

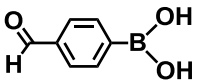

21

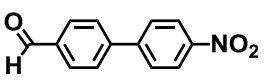

22

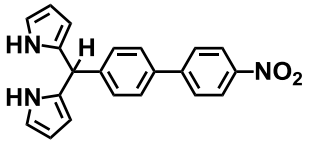

23

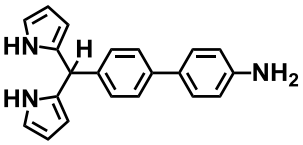

24

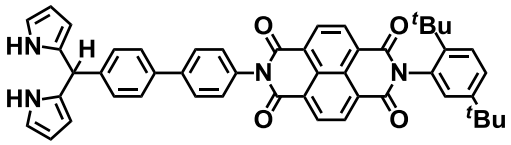

25

Dipyrromethane Ligands with Substituted Pyrrole Rings

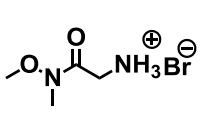

26

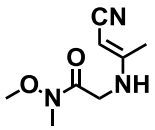

27

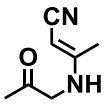

28

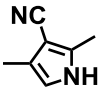

29

30

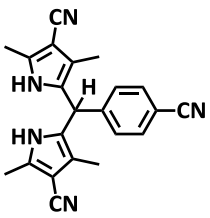

31

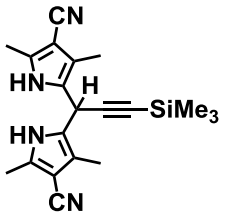

32

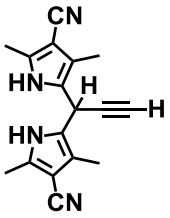

33

Dinuclear Cyclometalated μ-Chloro Bridged Dimers

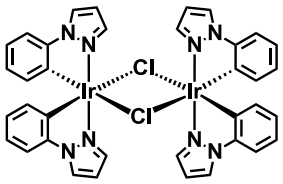

34

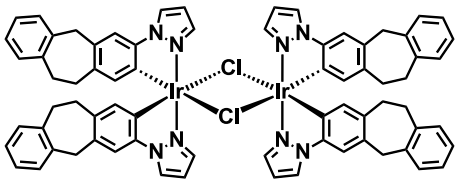

35

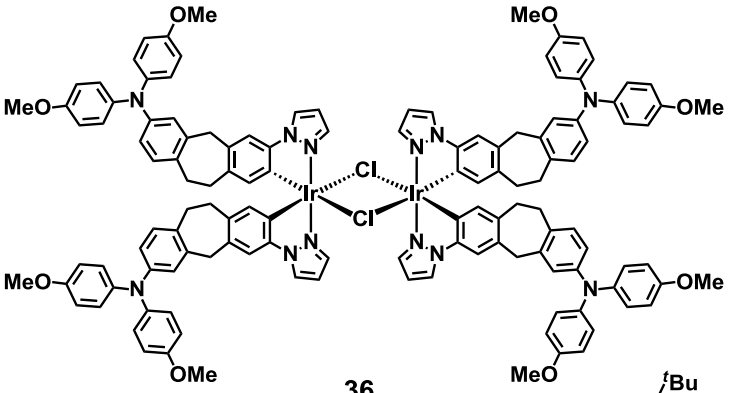

36

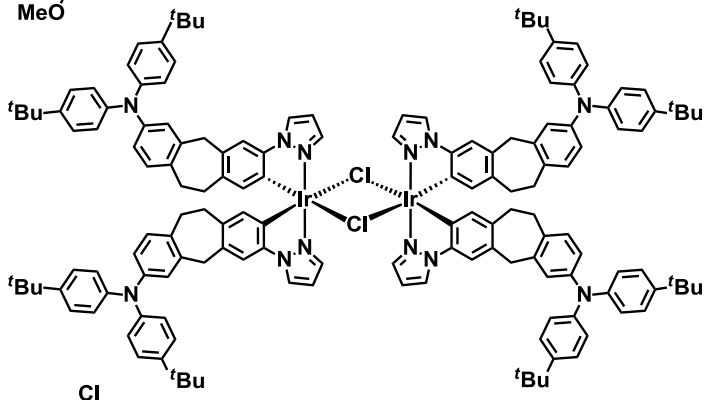

37

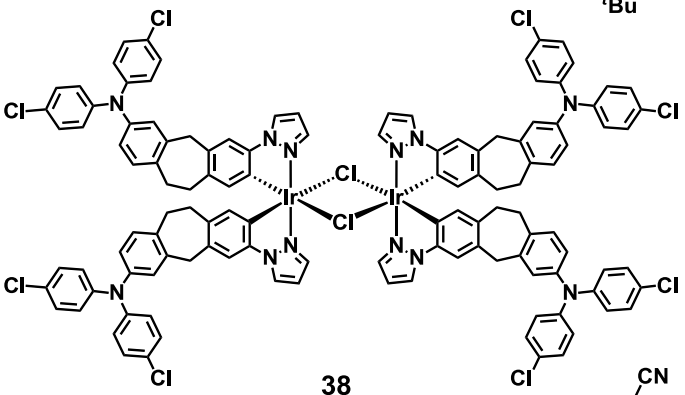

38

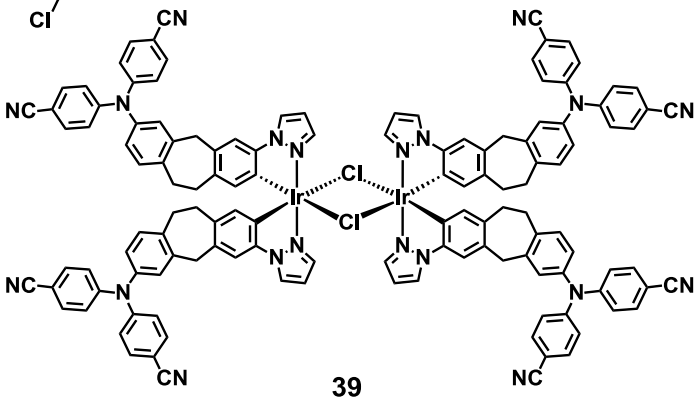

39

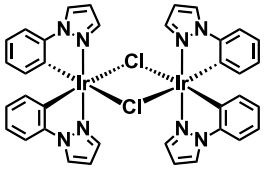

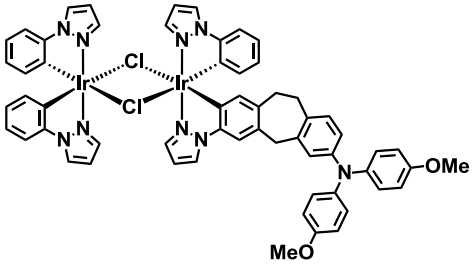

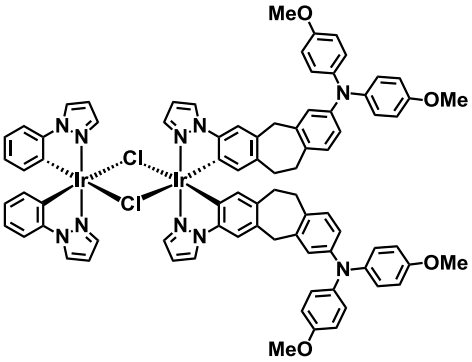

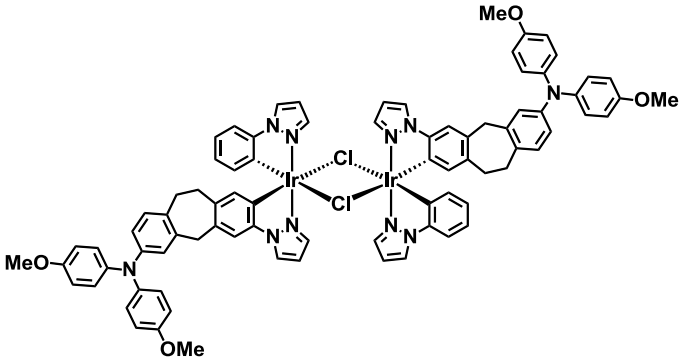

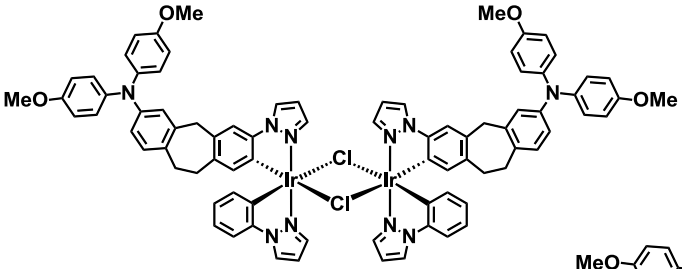

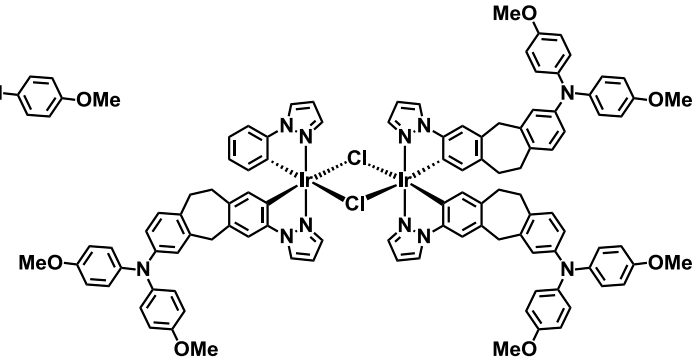

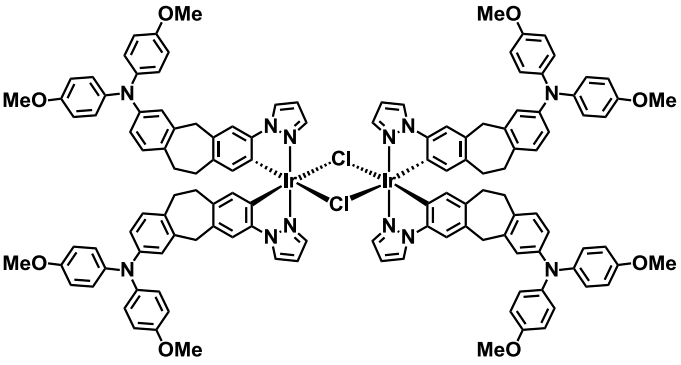

40

Neutral Cyclometalated Complexes

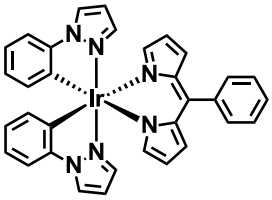

Ref1

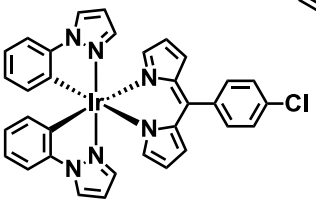

Ref2

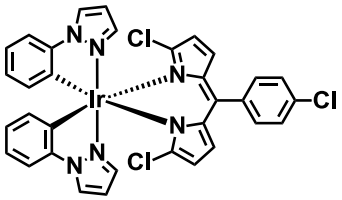

Ref3

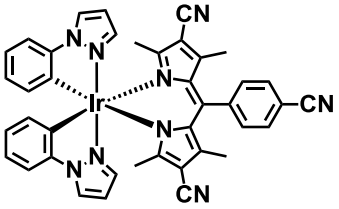

Ref4

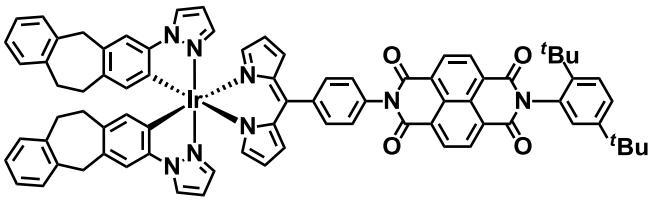

Ref_{NDI}

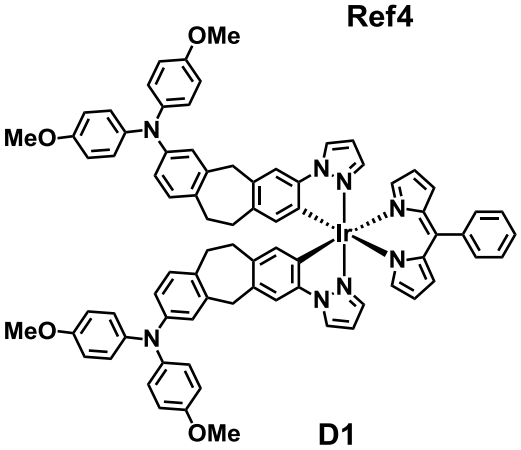

D1

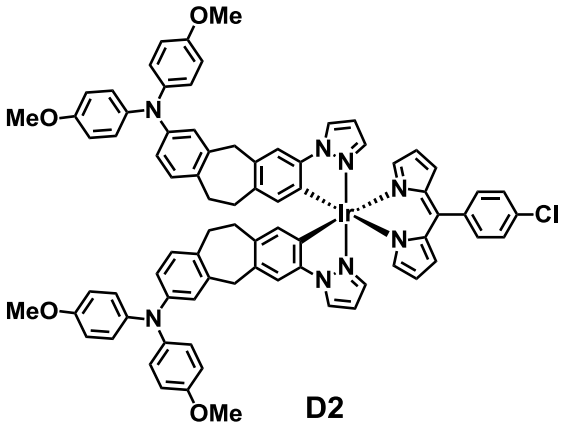

D2

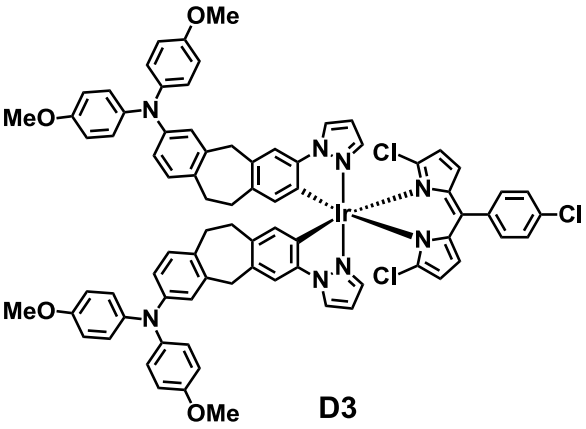

D3

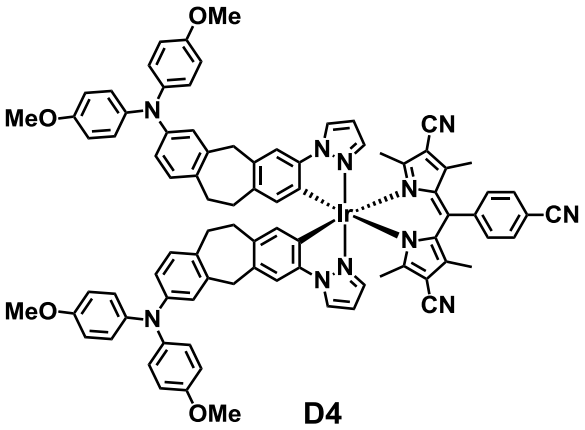

D4

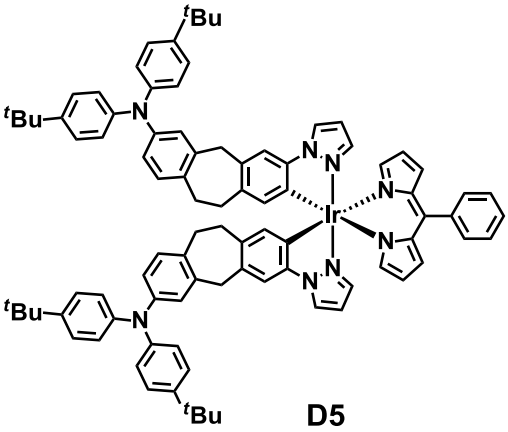

D5

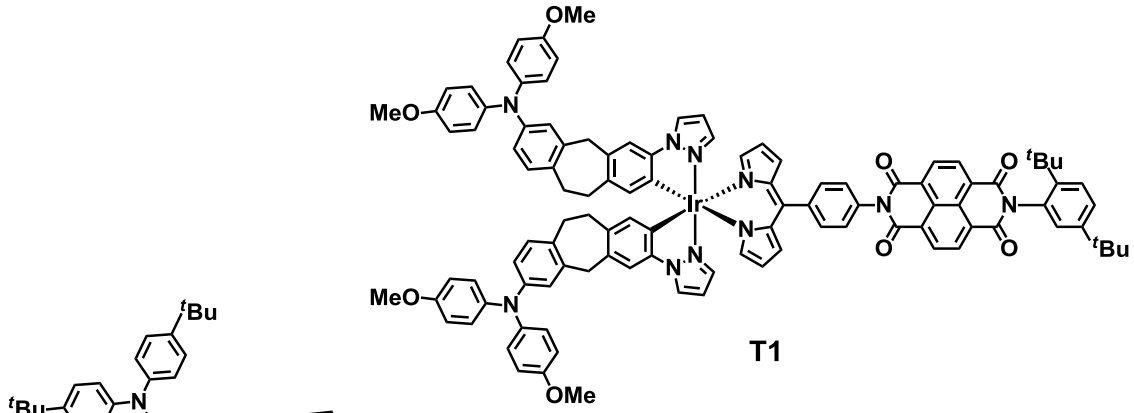

T1

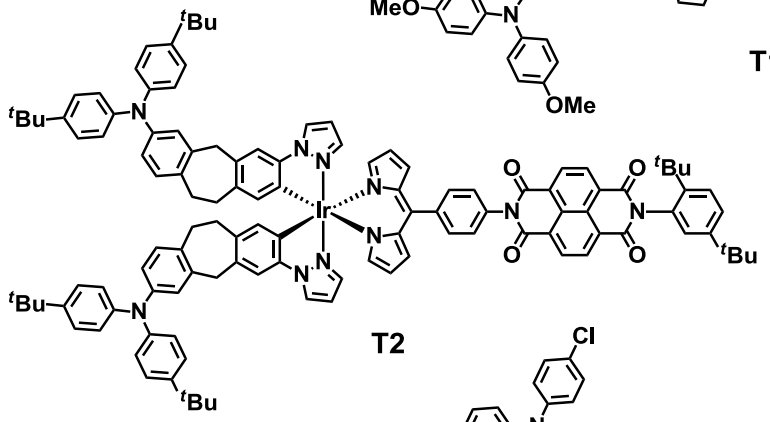

T2

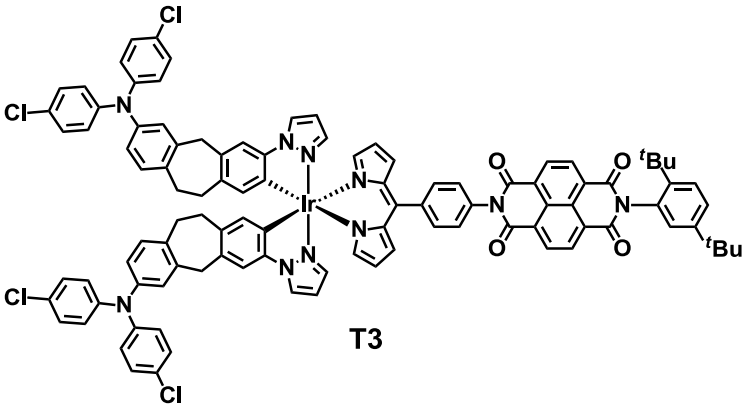

T3

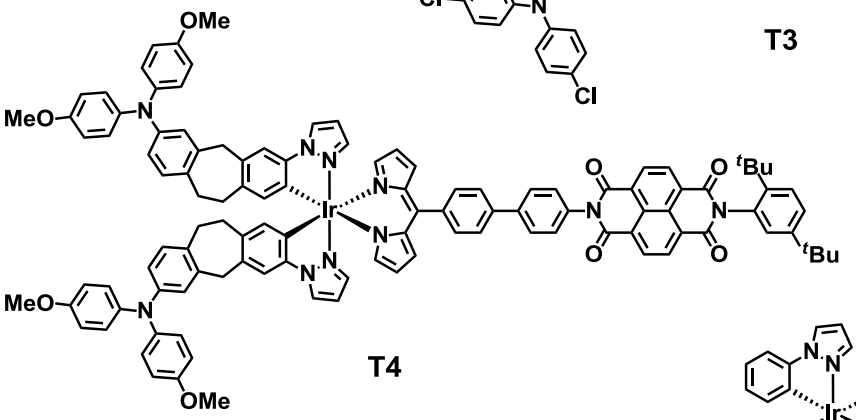

T4

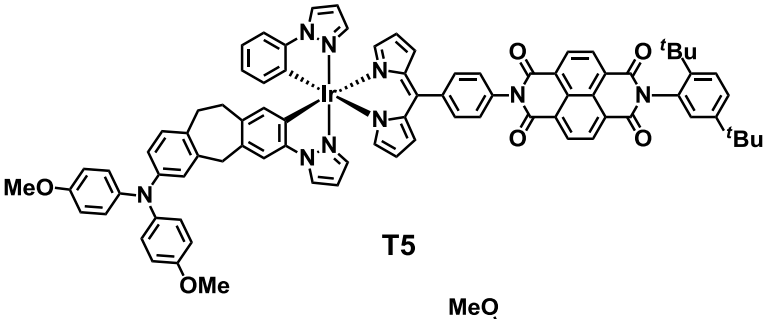

T5

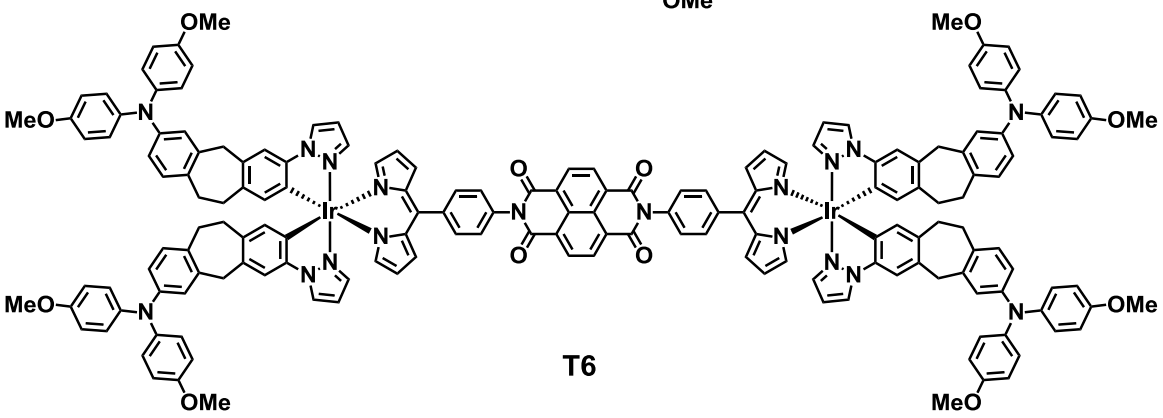

T6

8 Zusammenfassung

In dieser Arbeit wurden die erfolgreiche Synthese einer Donor-Iridiumkomplex-Akzeptor-Familie (Triaden **T1**–**T6**, **pMV1** und **mMV1**) und deren elektrochemischen und photophyiskalischen Eigenschaften vorgestellt. Als Donor wurden Triarylamine (TAA) verwendet, als Akzeptoreinheit diente ein Naphthalin-Diimid (NDI). Ein *bis*-cyclometallierter Phenylpyrazol-Iridium-Dipyrrin-Komplex übernahm die Aufgabe des Photosensibilisators. Die synthetischen Arbeiten konnten mit einer molekularen Struktur von **T1** mittels Röntgenbeugung eines Einkristalls ergänzt werden.

Bei Photoanregung der Triaden mit transienter Absorptions-Spektroskopie wurde die sehr effiziente Bildung von langlebigen, ladungsgetrennten (CS) Zuständen beobachtet. Es wurde zudem herausgefunden, dass der Elektronentransfer (ET)-Mechanismus von der verwendeten Anregungswellenlänge abhängt.

Der Nachweis von Singulett und Triplett CS-Zuständen wurde mittels magnetfeldabhängiger, transienter Absorptions-Spektroskopie erbracht. Eine Analyse des Magnetfeldeffekts der Ladungsrekombinations-Kinetik zeigte zum ersten Mal einen Übergang von einem kohärenten zu einem inkohärenten Spinumkehrprozess.

Die Lebenszeit des CS-Zustandes ließ sich dramatisch verlängern indem die Phenylen- durch eine Biphenyl-Brückeneinheit zwischen dem Iridiumkomplex und dem NDI ersetzt wurde.

Gemischvalente Zustände konnten mittels photinduziertem Elektronentransfer in den Triaden **pMV1** und **mMV1** erzeugt werden. Im Fall von **pMV1** wurde eine intensive Intervalenz-Ladungstransfer (IV-CT) Bande im nahinfraroten Spektralbereich mittels Femtosekunden transienter Anregungs-Abfrage-Spektroskopie beobachtet werden. Die Analyse dieser IV-CT Bande wurde mit TD-DFT Rechnungen vervollständigt.

Die Synthese von Dyaden (**D1**–**D4**) wurde erfolgreich durchgeführt, dabei wurde der Dipyrrin-Ligand mit elektronenziehenden Subsituenten versehen. Die spektroskopische und

elektrochemische Analyse erbrachte nach erfolgter Lichtanregung in einem Fall (**D4**) ebenfalls einen CS-Zustand.

9 APPENDIX

9.1 List of Publications

1. *Stepwise versus pseudo-concerted two-electron-transfer in a triarylamine–iridium dipyrrin–naphthalene diimide triad*, J. H. Klein, T. L. Sunderland, C. Kaufmann, M. Holzapfel, A. Schmiedel, C. Lambert, *Phys. Chem. Chem. Phys.* **2013**, *15*, 16024–16030.

2. *Multiple Reduction of 2,5-Bis(borolyl)thiophene: Isolation of a Negative Bipolaron by Comproportionation*, H. Braunschweig, V. Dyakonov, B. Engels, Z. Falk, C. Hörl, J. H. Klein, T. Kramer, H. Kraus, I. Krummenacher, C. Lambert, C. Walter, *Angew. Chem. Int. Ed.* **2013**, *52*, 12852–12855; *Angew. Chem.* **2013**, *125*, 13088–13092.

3. *A photoinduced mixed-valence state in an organic bis-triarylamine mixed-valence compound with an iridium-metal-bridge*, C. Lambert, R. Wagener, J. H. Klein, G. Grelaud, M. Moos, A. Schmiedel, M. Holzapfel, T. Bruhn, *Chem. Commun.* **2014**, *50*, 11350–11353.

4. *Photoinduced Electron Transfer Dynamics in Triarylamine-Naphthalene Diimide Cascades*, F, Zieschang, M. H. Schreck¸ A. Schmiedel, M. Holzapfel, J. H. Klein, C. Walter, B. Engels, C. Lambert, *J. Phys. Chem. C.* **2014**, 27698–27714.

5. *A Combined Experimental and Theoretical Study on the Isomers of 2,3,4,5.Tetracarba-nido-Hexaborane(6) Derivatives and Their Photophysical Properties*, H. Braunschweig, S. Ghosh, J. O. C. Jimenez-Halla, J. H. Klein, C. Lambert, K. Radacki, A. Steffen, A. Vargas, J. Wahler, *Chem. - Eur. J.* **2015**, *21*, 210-218.

6. *Photoluminescent One-dimensional Coordination Polymers from Versatile Pyridine Antenna and $LnCl_3$ for Visible and NIR Emission*, P. R. Matthes, J. Eyley, J. H. Klein, C. Lambert, K. Müller-Buschbaum, *Eur. J. Inorg. Chem.* **2015**, 826–836.

7. *Complete Monitoring of Coherent and Incoherent Spin Flip Domains in the Recombination of Charge-Separated States of Donor-Iridium Complex-Acceptor Triads*, J. H. Klein, D. Schmidt, U. E. Steiner, C. Lambert, *J. Amer. Chem. Soc.* **2015**, DOI: 10.1021/jacs.5b04868.

9.2 Conference Contributions

1. Oral presentations:

1.1 Workshop of the Research Training School 1221 (GRK 1221), October **2012**, Schöntal, Germany.

1.2 Workshop of the DFG Forschergruppe 1809, March **2013**, Niederstetten, Germany.

1.3 Solar Technologies Go Hybrid Workshop, April **2013**, Kloster Banz, Bad Staffelstein, Germany.

1.4 Conference of the Research Training School 1221 (GRK 1221), March **2015**, Würzburg, Germany.

2. Posters:

2.1 XXIII IUPAC Symposium on Photochemistry, July **2010**, Ferrara, Italy.

2.2 22nd GDCh-Fachgruppentagung für Photochemie, September **2010**, Erlangen, Germany.

2.3 Workshop of the Research Training School 1221 (GRK 1221), October **2010**, Zeilitzheim, Germany.

2.4 19th International Symposium on the Photochemistry and Photophysics of Coordination Compounds (ISPPCC), July **2011**, Strasbourg, Frankreich. **Best poster prize winner**.

2.5 Conference of the Research Training School 1221 (GRK 1221), September **2011**, Würzburg, Germany.

2.6 10th International Symposium on Functional π-Electron Systems, October 2011, Beijing, China.

2.7 XXIV IUPAC Symposium on Photochemistry, July **2012**, Coimbra, Portugal.

2.8 SolTech Kick-off Workshop of Solar Technologies Go Hybrid, October **2012**, München, Germany.

2.9 Molecules, Light and Life – Manfred-Eigen-Gespräche, November **2012**, Jena, Germany.

2.10 Solar Technologies Go Hybrid Workshop, April **2014**, Wildbad Kreuth, Germany.

2.11 COST Action CM1202 - PERSPECT-H2O Meeting, November **2014**, Lund, Sweden.

9.3 Rate Constants

Table A1 Rate constants for singlet and triplet NDI (^{1,3}NDI), charge transfer (hot-CT, CT and CT_{biph}), charge separation (CS_1 and CS_2), phosphorescence (^3Ir_i, ^3Ir and $^3Ir_{biph}$) and charge recombination (S_0) of the different complexes (**T1**–**T4**) and of **17** at different excitation wavelengths (λ_{ex}) in MeCN or THF.

Compound	λ_{ex} / nm	k ($^1NDI \longrightarrow CT_{hot}$) [($^1NDI \longrightarrow CT$)] / ps^{-1}	k ($^1NDI \longrightarrow {}^3NDI$) / ps^{-1}	k ($^3NDI \longrightarrow S_0$) / ns^{-1}	k ($CT_{hot} \longrightarrow CT$) / ps^{-1}	k ($CT \longrightarrow CS_1$) / ns^{-1}	k ($CS_1 \longrightarrow CS_2$) / ns^{-1}	k ($CS_1 \longrightarrow S_0$) [($Int2 \longrightarrow S_0$)] / ns^{-1}	k ($CT \longrightarrow S_0$) [($CT \longrightarrow Int1$)] / ns^{-1}	k ($Int1 \longrightarrow Int2$)] / ns^{-1}	k ($^3Ir \longrightarrow CS_1$) / ns^{-1}	k ($^3Ir \longrightarrow S_0$) / μs^{-1}	k ($^3Ir_i \longrightarrow {}^3Ir$) / ns^{-1}	k ($CS_2 \longrightarrow S_0$) / μs^{-1}
Ref1[1]	480	-	-	-	-	-	-	-	-	-	-	0.538	19.6	-
17[1]	378	10.1	1.1	0.1	4.6	-	-	[1.9]	[71.4]	25.6	-	-	-	-
Ref_{NDI}[1]	378	7.5	0.833	0.1	1.4	32.9	-	5.9	38.6	-	-	13.9	-	-
	480	-	-	-	-	-		9.1	-		1.4	11.2		
T1[1]	378	9.1	-	-	1.6	30.8	> 200	-	46.2	-	1.2	11.8	-	1.7
	480	-			-	-	-	-	-		1.1	10.8	-	1.7
T2[1]	378	11.9	-	-	4.0	40.5	17.1	7.3	36.2	-	1.0	10.2	-	31.3
	480	-			-	-	5.1	6.3	-		1.1	11.5		31.3
T3[2]	378	4.0	1.7	0.17	-	208	-	1.0	-	-	-	-	-	-
	480	-	-	-		-		1.7			1.4	14.2		

Compound	λ_{ex} / nm	k ($^1NDI \longrightarrow CT_{hot}$) / ps^{-1}	k ($CT_{hot} \longrightarrow CT$) / ps^{-1}	k ($CT \longrightarrow CT_{biph}$) / ns^{-1}	k ($CT \longrightarrow CS_1$) / ns^{-1}	k ($CT \longrightarrow S_0$) / ns^{-1}	k ($CT_{biph} \longrightarrow CS_1$) / ns^{-1}	k ($CT_{biph} \longrightarrow S_0$) / ns^{-1}	k ($CS_1 \longrightarrow CS_2$) / ns^{-1}	k ($CS_1 \longrightarrow S_0$) / ns^{-1}	k ($^3Ir \longrightarrow {}^3Ir_{biph}$) / ns^{-1}	k ($^3Ir_{biph} \longrightarrow CS_1$) / ns^{-1}	k ($^3Ir \longrightarrow S_0$) / μs^{-1}	k ($CS_2 \longrightarrow S_0$) / μs^{-1}
T4[1]	378	10.1	0.357	18.8	0.536	6.3	0.889	0.222	> 536	179	-	-	-	0.059/0.014
	480	-	-	-	-	-	-	-	-	-	3.6	1.1	10.8	0.081/0.012

[1] in MeCN, [2] in THF.

Table A2 Rate constants for singlet and triplet NDI (^{1}NDI), charge transfer (CT_{hot}, CT), charge separation (CS_1 and CS_2), phosphorescence (^{3}Ir) and charge recombination (S_0) of the different complexes (**T1**, **T5** and **T6**) at different excitation wavelengths (λ_{ex}) in THF.

Compound	λ_{ex} / nm	k ($^1NDI \longrightarrow CT_{hot}$) / ps^{-1}	k ($CT_{hot} \longrightarrow CT$) / ps^{-1}	k ($CT_{hot} \longrightarrow S_0$) / ps^{-1}	k ($CT \longrightarrow CS_1$) / ns^{-1}	k ($CT \longrightarrow CS_2$) / ns^{-1}	k ($CS_1 \longrightarrow CS_2$) / ns^{-1}	k ($CS_1 \longrightarrow S_0$) / ns^{-1}	k ($CT \longrightarrow S_0$) / ns^{-1}	k ($^3Ir \longrightarrow CS_1$) / ns^{-1}	k ($^3Ir \longrightarrow S_0$) / μs^{-1}	k ($CS_2 \longrightarrow S_0$) / μs^{-1}
T5	378	6.9	0.111	0.259	30.6	0.323	85.0	15	1.3	1.2	12.6	6.3
	480	-	-	-	-	-	-	-	-	1.3	13.0	6.3
T1	378	5.1	0.090	0.243	31.7	0.333	142	25	1.3	2.0	19.7	6-3
	480	-	-	-	-	-	-	-	-	2.1	20.2	6.3
T6	378	7.6	0.238	-	36.5	0.385	495	5.0	1.5	1.7	17.0	6.5
	480	-	-		-	-	-	-	-	2.0	20.0	6.5

9.4 MatLab-Script

```
function [x,resnorm,residual,exitflag,output] = Difg(xo,Mx,My)
options      =      optimset('Display',      'iter','TolFun',2E-30,'TolX',2E-
30,'Algorithm',{'levenberg-
marquardt',.001},'MaxIter',1000,'MaxFunEvals',10000);
[x,resnorm,residual,exitflag,output]                                          =
lsqcurvefit(@nestedfun1,xo,Mx,My,[],[],options);
    function output = nestedfun1(x,Mx)

        x(1:16,2)=4e7;
        x(1:16,3)= x(1,3);
        x(1:16,4)=0;

        k=x;

        o=length(Mx(1,:));

        for b=1:o
            l(b) = find(Mx(:,b)>0,1,'last');
        end

        function dy = ode1(t,y)
        dy =zeros(4,1);
dy(1)=-k(1,3)*y(1)-k(1,1)*y(1)+k(1,1)*y(4)+k(1,1)*y(3)-k(1,1)*y(1)-
k(1,2)*y(1)+k(1,2)*y(2);
dy(2)=-k(1,4)*y(2)-k(1,1)*y(2)-k(1,1)*y(2)+k(1,1)*y(3)+k(1,1)*y(4)-
k(1,2)*y(2)+k(1,2)*y(1);
dy(3)=-k(1,4)*y(3)-k(1,1)*y(3)-k(1,1)*y(3)+k(1,1)*y(2)+k(1,1)*y(1);
dy(4)=-k(1,4)*y(4)-k(1,1)*y(4)-k(1,1)*y(4)+k(1,1)*y(2)+k(1,1)*y(1);
        end
        function dy = ode2(t,y)
            dy =zeros(4,1);
dy(1)=-k(2,3)*y(1)-k(2,1)*y(1)+k(2,1)*y(4)+k(2,1)*y(3)-k(2,1)*y(1)-
k(2,2)*y(1)+k(2,2)*y(2);
dy(2)=-k(2,4)*y(2)-k(2,1)*y(2)-k(2,1)*y(2)+k(2,1)*y(3)+k(2,1)*y(4)-
k(2,2)*y(2)+k(2,2)*y(1);
dy(3)=-k(2,4)*y(3)-k(2,1)*y(3)-k(2,1)*y(3)+k(2,1)*y(2)+k(2,1)*y(1);
dy(4)=-k(2,4)*y(4)-k(2,1)*y(4)-k(2,1)*y(4)+k(2,1)*y(2)+k(2,1)*y(1);
        end
        function dy = ode3(t,y)
            dy =zeros(4,1);
dy(1)=-k(3,3)*y(1)-k(3,1)*y(1)+k(3,1)*y(4)+k(3,1)*y(3)-k(3,1)*y(1)-
k(3,2)*y(1)+k(3,2)*y(2);
dy(2)=-k(3,4)*y(2)-k(3,1)*y(2)-k(3,1)*y(2)+k(3,1)*y(3)+k(3,1)*y(4)-
k(3,2)*y(2)+k(3,2)*y(1);
dy(3)=-k(3,4)*y(3)-k(3,1)*y(3)-k(3,1)*y(3)+k(3,1)*y(2)+k(3,1)*y(1);
dy(4)=-k(3,4)*y(4)-k(3,1)*y(4)-k(3,1)*y(4)+k(3,1)*y(2)+k(3,1)*y(1);
        end
        function dy = ode4(t,y)
            dy =zeros(4,1);
dy(1)=-k(4,3)*y(1)-k(4,1)*y(1)+k(4,1)*y(4)+k(4,1)*y(3)-k(4,1)*y(1)-
k(4,2)*y(1)+k(4,2)*y(2);
dy(2)=-k(4,4)*y(2)-k(4,1)*y(2)-k(4,1)*y(2)+k(4,1)*y(3)+k(4,1)*y(4)-
k(4,2)*y(2)+k(4,2)*y(1);
dy(3)=-k(4,4)*y(3)-k(4,1)*y(3)-k(4,1)*y(3)+k(4,1)*y(2)+k(4,1)*y(1);
dy(4)=-k(4,4)*y(4)-k(4,1)*y(4)-k(4,1)*y(4)+k(4,1)*y(2)+k(4,1)*y(1);
        end
        function dy = ode5(t,y)
```

```
            dy =zeros(4,1);
dy(1)=-k(5,3)*y(1)-k(5,1)*y(1)+k(5,1)*y(4)+k(5,1)*y(3)-k(5,1)*y(1)-
k(5,2)*y(1)+k(5,2)*y(2);
dy(2)=-k(5,4)*y(2)-k(5,1)*y(2)-k(5,1)*y(2)+k(5,1)*y(3)+k(5,1)*y(4)-
k(5,2)*y(2)+k(5,2)*y(1);
dy(3)=-k(5,4)*y(3)-k(5,1)*y(3)-k(5,1)*y(3)+k(5,1)*y(2)+k(5,1)*y(1);
dy(4)=-k(5,4)*y(4)-k(5,1)*y(4)-k(5,1)*y(4)+k(5,1)*y(2)+k(5,1)*y(1);
        end
        function dy = ode6(t,y)
            dy =zeros(4,1);
dy(1)=-k(6,3)*y(1)-k(6,1)*y(1)+k(6,1)*y(4)+k(6,1)*y(3)-k(6,1)*y(1)-
k(6,2)*y(1)+k(6,2)*y(2);
dy(2)=-k(6,4)*y(2)-k(5,1)*y(2)-k(6,1)*y(2)+k(6,1)*y(3)+k(6,1)*y(4)-
k(6,2)*y(2)+k(6,2)*y(1);
dy(3)=-k(6,4)*y(3)-k(6,1)*y(3)-k(6,1)*y(3)+k(6,1)*y(2)+k(6,1)*y(1);
dy(4)=-k(6,4)*y(4)-k(6,1)*y(4)-k(6,1)*y(4)+k(6,1)*y(2)+k(6,1)*y(1);
        end
        function dy = ode7(t,y)
            dy =zeros(4,1);
dy(1)=-k(7,3)*y(1)-k(7,1)*y(1)+k(7,1)*y(4)+k(7,1)*y(3)-k(7,1)*y(1)-
k(7,2)*y(1)+k(7,2)*y(2);
dy(2)=-k(7,4)*y(2)-k(7,1)*y(2)-k(7,1)*y(2)+k(7,1)*y(3)+k(7,1)*y(4)-
k(7,2)*y(2)+k(7,2)*y(1);
dy(3)=-k(7,4)*y(3)-k(7,1)*y(3)-k(7,1)*y(3)+k(7,1)*y(2)+k(7,1)*y(1);
dy(4)=-k(7,4)*y(4)-k(7,1)*y(4)-k(7,1)*y(4)+k(7,1)*y(2)+k(7,1)*y(1);
        end
        function dy = ode8(t,y)
            dy =zeros(4,1);
dy(1)=-k(8,3)*y(1)-k(8,1)*y(1)+k(8,1)*y(4)+k(8,1)*y(3)-k(8,1)*y(1)-
k(8,2)*y(1)+k(8,2)*y(2);
dy(2)=-k(8,4)*y(2)-k(8,1)*y(2)-k(8,1)*y(2)+k(8,1)*y(3)+k(8,1)*y(4)-
k(8,2)*y(2)+k(8,2)*y(1);
dy(3)=-k(8,4)*y(3)-k(8,1)*y(3)-k(8,1)*y(3)+k(8,1)*y(2)+k(8,1)*y(1);
dy(4)=-k(8,4)*y(4)-k(8,1)*y(4)-k(8,1)*y(4)+k(8,1)*y(2)+k(8,1)*y(1);
        end
        function dy = ode9(t,y)
            dy =zeros(4,1);
dy(1)=-k(9,3)*y(1)-k(9,1)*y(1)+k(9,1)*y(4)+k(9,1)*y(3)-k(9,1)*y(1)-
k(9,2)*y(1)+k(9,2)*y(2);
dy(2)=-k(9,4)*y(2)-k(9,1)*y(2)-k(9,1)*y(2)+k(9,1)*y(3)+k(9,1)*y(4)-
k(9,2)*y(2)+k(9,2)*y(1);
dy(3)=-k(9,4)*y(3)-k(9,1)*y(3)-k(9,1)*y(3)+k(9,1)*y(2)+k(9,1)*y(1);
dy(4)=-k(9,4)*y(4)-k(9,1)*y(4)-k(9,1)*y(4)+k(9,1)*y(2)+k(9,1)*y(1);
        end
        function dy = ode10(t,y)
            dy =zeros(4,1);
dy(1)=-k(10,3)*y(1)-k(10,1)*y(1)+k(10,1)*y(4)+k(10,1)*y(3)-k(10,1)*y(1)-
k(10,2)*y(1)+k(10,2)*y(2);
dy(2)=-k(10,4)*y(2)-k(10,1)*y(2)-k(10,1)*y(2)+k(10,1)*y(3)+k(10,1)*y(4)-
k(10,2)*y(2)+k(10,2)*y(1);
dy(3)=-k(10,4)*y(3)-k(10,1)*y(3)-k(10,1)*y(3)+k(10,1)*y(2)+k(10,1)*y(1);
dy(4)=-k(10,4)*y(4)-k(10,1)*y(4)-k(10,1)*y(4)+k(10,1)*y(2)+k(10,1)*y(1);
        end
        function dy = ode11(t,y)
            dy =zeros(4,1);
dy(1)=-k(11,3)*y(1)-k(11,1)*y(1)+k(11,1)*y(4)+k(11,1)*y(3)-k(11,1)*y(1)-
k(11,2)*y(1)+k(11,2)*y(2);
dy(2)=-k(11,4)*y(2)-k(11,1)*y(2)-k(11,1)*y(2)+k(11,1)*y(3)+k(11,1)*y(4)-
k(11,2)*y(2)+k(11,2)*y(1);
dy(3)=-k(11,4)*y(3)-k(11,1)*y(3)-k(11,1)*y(3)+k(11,1)*y(2)+k(11,1)*y(1);
dy(4)=-k(11,4)*y(4)-k(11,1)*y(4)-k(11,1)*y(4)+k(11,1)*y(2)+k(11,1)*y(1);
        end
```

```
        function dy = ode12(t,y)
            dy =zeros(4,1);
dy(1)=-k(12,3)*y(1)-k(12,1)*y(1)+k(12,1)*y(4)+k(12,1)*y(3)-k(12,1)*y(1)-
k(12,2)*y(1)+k(12,2)*y(2);
dy(2)=-k(12,4)*y(2)-k(12,1)*y(2)-k(12,1)*y(2)+k(12,1)*y(3)+k(12,1)*y(4)-
k(12,2)*y(2)+k(12,2)*y(1);
dy(3)=-k(12,4)*y(3)-k(12,1)*y(3)-k(12,1)*y(3)+k(12,1)*y(2)+k(12,1)*y(1);
dy(4)=-k(12,4)*y(4)-k(12,1)*y(4)-k(12,1)*y(4)+k(12,1)*y(2)+k(12,1)*y(1);
        end
        function dy = ode13(t,y)
            dy =zeros(4,1);
dy(1)=-k(13,3)*y(1)-k(13,1)*y(1)+k(13,1)*y(4)+k(13,1)*y(3)-k(13,1)*y(1)-
k(13,2)*y(1)+k(13,2)*y(2);
dy(2)=-k(13,4)*y(2)-k(13,1)*y(2)-k(13,1)*y(2)+k(13,1)*y(3)+k(13,1)*y(4)-
k(13,2)*y(2)+k(13,2)*y(1);
dy(3)=-k(13,4)*y(3)-k(13,1)*y(3)-k(13,1)*y(3)+k(13,1)*y(2)+k(13,1)*y(1);
dy(4)=-k(13,4)*y(4)-k(13,1)*y(4)-k(13,1)*y(4)+k(13,1)*y(2)+k(13,1)*y(1);
        end
              function dy = ode14(t,y)
            dy =zeros(4,1);
dy(1)=-k(14,3)*y(1)-k(14,1)*y(1)+k(14,1)*y(4)+k(14,1)*y(3)-k(14,1)*y(1)-
k(14,2)*y(1)+k(14,2)*y(2);
dy(2)=-k(14,4)*y(2)-k(14,1)*y(2)-k(14,1)*y(2)+k(14,1)*y(3)+k(14,1)*y(4)-
k(14,2)*y(2)+k(14,2)*y(1);
dy(3)=-k(14,4)*y(3)-k(14,1)*y(3)-k(14,1)*y(3)+k(14,1)*y(2)+k(14,1)*y(1);
dy(4)=-k(14,4)*y(4)-k(14,1)*y(4)-k(14,1)*y(4)+k(14,1)*y(2)+k(14,1)*y(1);
        end
        function dy = ode15(t,y)
            dy =zeros(4,1);
dy(1)=-k(15,3)*y(1)-k(15,1)*y(1)+k(15,1)*y(4)+k(15,1)*y(3)-k(15,1)*y(1)-
k(15,2)*y(1)+k(15,2)*y(2);
dy(2)=-k(15,4)*y(2)-k(15,1)*y(2)-k(15,1)*y(2)+k(15,1)*y(3)+k(15,1)*y(4)-
k(15,2)*y(2)+k(15,2)*y(1);
dy(3)=-k(15,4)*y(3)-k(15,1)*y(3)-k(15,1)*y(3)+k(15,1)*y(2)+k(15,1)*y(1);
dy(4)=-k(15,4)*y(4)-k(15,1)*y(4)-k(15,1)*y(4)+k(15,1)*y(2)+k(15,1)*y(1);
        end
        function dy = ode16(t,y)
            dy =zeros(4,1);
dy(1)=-k(16,3)*y(1)-k(16,1)*y(1)+k(16,1)*y(4)+k(16,1)*y(3)-k(16,1)*y(1)-
k(16,2)*y(1)+k(16,2)*y(2);
dy(2)=-k(16,4)*y(2)-k(16,1)*y(2)-k(16,1)*y(2)+k(16,1)*y(3)+k(16,1)*y(4)-
k(16,2)*y(2)+k(16,2)*y(1);
dy(3)=-k(16,4)*y(3)-k(16,1)*y(3)-k(16,1)*y(3)+k(16,1)*y(2)+k(16,1)*y(1);
dy(4)=-k(16,4)*y(4)-k(16,1)*y(4)-k(16,1)*y(4)+k(16,1)*y(2)+k(16,1)*y(1);
        end


        ode_options = odeset('OutputFcn',@odeplot,'Stats', 'on');
        odes = {@ode1, @ode2, @ode3, @ode4, @ode5, @ode6, @ode7, @ode8,
@ode9, @ode10, @ode11, @ode12, @ode13, @ode14, @ode15, @ode16};
        output = zeros(size(Mx));
        parfor a = 1:length(odes)
            [t,y] = ode23(odes{a},Mx(:,a),[0.25 0.25 0.25 0.25]);
            output(:,a) = sum(y, 2);
        end

    end

Eo=nestedfun1(x,Mx);
for q=1:16
p(q)=length(Eo(:,q));
```

```
end
display(p)
display(l)

figure
cmap=colormap(jet(o))
for w=1:16
plot(Mx(:,w),My(:,w),'color',cmap(w,:),'LineStyle','.');
hold on
plot(Mx(:,w),Eo(:,w),'color',cmap(w,:),'LineWidth',1);

end
xlabel('t/s')
ylabel('intensity a.u.')
axis([0 1E-5 0 1])
hold off


for u=1:16
    AusgabeD(:,u*2-1)=Mx(:,u);
    AusgabeD(:,u*2)=My(:,u);
end

for u=1:16
    AusgabeF(:,u*2-1)=Mx(:,u);
    AusgabeF(:,u*2)=Eo(:,u);
end


dlmwrite('xo.txt',x,',')
dlmwrite('Datensatz.txt',AusgabeD,',')
dlmwrite('Fit.txt',AusgabeF,',')

display(resnorm)
display(output)



end
```

9.5 Fit Parameters ($k_{\pm}$ Values)

Table A3 The $k_{\pm}$ parameters were obtained by fitting the decay curve of CS_2 for triad **T1** at all applied magnetic fields. Global parameters are: $k_S = 6.71 \cdot 10^6\ s^{-1}$, $k_{ST_0} = 4.0 \cdot 10^7\ s^{-1}$ and $p_S = 25$. $k_{\pm}$ is freely chosen. The zero-field data point is plotted at 0.02 mT, because a logarithmic scale is used.

B / mT	$k_{\pm}$ / s^{-1}	B / mT	$k_{\pm}$ / s^{-1}	B / mT	$k_{\pm}$ / s^{-1}
0.02	$4.59 \cdot 10^7$	9.00	$3.36 \cdot 10^6$	160	$3.60 \cdot 10^5$
0.30	$3.48 \cdot 10^7$	9.50	$3.44 \cdot 10^6$	180	$3.53 \cdot 10^5$
0.70	$3.24 \cdot 10^7$	10.0	$3.47 \cdot 10^6$	200	$3.39 \cdot 10^5$
1.00	$2.26 \cdot 10^7$	12.0	$2.90 \cdot 10^6$	250	$3.29 \cdot 10^5$
1.50	$1.10 \cdot 10^7$	16.0	$2.04 \cdot 10^6$	350	$3.21 \cdot 10^5$
2.00	$8.06 \cdot 10^6$	20.0	$1.52 \cdot 10^6$	400	$3.08 \cdot 10^5$
2.50	$6.3 \cdot 10^6$	25.0	$1.18 \cdot 10^6$	600	$2.77 \cdot 10^5$
3.00	$5.67 \cdot 10^6$	30.0	$9.58 \cdot 10^5$	800	$3.07 \cdot 10^5$
3.50	$4.54 \cdot 10^6$	35.0	$8.38 \cdot 10^5$	1000	$2.81 \cdot 10^5$
4.00	$4.03 \cdot 10^6$	40.0	$7.49 \cdot 10^5$	1200	$2.98 \cdot 10^5$
4.50	$3.89 \cdot 10^6$	45.0	$6.73 \cdot 10^5$	1400	$2.98 \cdot 10^5$
5.00	$3.49 \cdot 10^6$	50.0	$6.23 \cdot 10^5$	1600	$3.04 \cdot 10^5$
5.50	$3.78 \cdot 10^6$	60.0	$5.49 \cdot 10^5$	1800	$2.78 \cdot 10^5$
6.00	$4.62 \cdot 10^6$	70.0	$4.99 \cdot 10^5$	1800	$2.80 \cdot 10^5$
6.50	$5.73 \cdot 10^6$	80.0	$4.69 \cdot 10^5$		
7.00	$3.36 \cdot 10^6$	90.0	$4.44 \cdot 10^5$		
7.50	$3.60 \cdot 10^6$	100	$4.24 \cdot 10^5$		
8.00	$3.95 \cdot 10^6$	120	$3.95 \cdot 10^5$		
8.50	$3.92 \cdot 10^6$	140	$3.71 \cdot 10^5$		

Table A4 The $k_{\pm}$ parameters were obtained by fitting the decay curve of CS_2 for triad **T3** at all applied magnetic fields. Global parameters are: $k_S = 6.97 \cdot 10^6\ s^{-1}$, $k_{ST_0} = 4.0 \cdot 10^7\ s^{-1}$ and $p_S = 25$. $k_{\pm}$ is freely chosen. The zero-field data point is plotted at 0.02 mT, because a logarithmic scale is used.

B / mT	$k_{\pm}$ / s^{-1}	B / mT	$k_{\pm}$ / s^{-1}	B / mT	$k_{\pm}$ / s^{-1}
0.02	$4.00 \cdot 10^7$	7.51	$2.03 \cdot 10^6$	79.9	$3.28 \cdot 10^5$
0.27	$1.25 \cdot 10^8$	7.99	$1.94 \cdot 10^6$	89.8	$2.99 \cdot 10^5$
0.48	$4.76 \cdot 10^7$	8.50	$1.85 \cdot 10^6$	100	$2.80 \cdot 10^5$
0.61	$3.83 \cdot 10^7$	8.99	$1.81 \cdot 10^6$	120	$2.52 \cdot 10^5$
0.79	$2.25 \cdot 10^7$	9.47	$1.81 \cdot 10^6$	140	$2.37 \cdot 10^5$
0.85	$1.91 \cdot 10^7$	9.98	$1.61 \cdot 10^6$	160	$2.20 \cdot 10^5$
1.02	$1.29 \cdot 10^7$	11.9	$1.34 \cdot 10^6$	180	$2.11 \cdot 10^5$
1.22	$8.62 \cdot 10^6$	14.0	$1.40 \cdot 10^6$	200	$2.01 \cdot 10^5$
1.36	$7.71 \cdot 10^6$	16.3	$1.28 \cdot 10^6$	250	$1.89 \cdot 10^5$
1.68	$5.39 \cdot 10^6$	18.1	$1.17 \cdot 10^6$	300	$1.82 \cdot 10^5$
1.86	$5.25 \cdot 10^6$	19.9	$1.08 \cdot 10^6$	350	$1.70 \cdot 10^5$
1.98	$4.71 \cdot 10^6$	24.9	$8.75 \cdot 10^5$	400	$1.64 \cdot 10^5$
2.50	$3.66 \cdot 10^6$	30.4	$7.45 \cdot 10^5$	600	$1.59 \cdot 10^5$
2.91	$3.35 \cdot 10^6$	35.0	$6.62 \cdot 10^5$	800	$1.59 \cdot 10^5$
3.47	$3.04 \cdot 10^6$	39.8	$5.71 \cdot 10^5$	1000	$1.54 \cdot 10^5$
4.01	$2.55 \cdot 10^6$	44.8	$5.25 \cdot 10^5$	1200	$1.51 \cdot 10^5$
4.49	$2.66 \cdot 10^6$	50.0	$5.64 \cdot 10^5$	1400	$1.54 \cdot 10^5$
4.97	$2.57 \cdot 10^6$	55.1	$4.36 \cdot 10^5$	1600	$1.52 \cdot 10^5$
5.47	$2.33 \cdot 10^6$	60.0	$4.05 \cdot 10^5$	1800	$1.51 \cdot 10^5$
6.00	$2.18 \cdot 10^6$	65	$3.80 \cdot 10^5$		
6.51	$2.17 \cdot 10^6$	70	$3.57 \cdot 10^5$		
6.95	$2.01 \cdot 10^6$	75.1	$3.37 \cdot 10^5$		

9.6 Single-Crystal Structure Analysis

Single-crystal X-ray diffraction data for compound **T1** were collected at 100 K on a Bruker D8 Quest Kappa diffractometer with a Photon100 CMOS detector and multi-layered mirror monochromated $Cu_{K\alpha}$ radiation. The structure was solved using direct methods, expanded with Fourier techniques and refined with the Shelx software package. All non-hydrogen atoms were refined anisotropically. Hydrogen atoms were included in the structure factor calculation on geometrically idealised positions.

Crystal data for compound **T1** ($C_{107}H_{91}IrN_{10}O_8 \cdot 1.5\ C_6H_{14}$): *M*r = 1966.35, 0.140 × 0.034 × 0.018 mm^3, monoclinic space group C2/c, *a* = 28.3226(15) Å, α = 90°, *b* = 33.5643(15) Å, β = 100.806(2)° *c* = 21.4252(9) Å, γ = 90°, *V* = 20006.2(16) $Å^3$, *Z* = 8, ρ(*calcd)* = 1.306 $g \cdot cm^{-3}$, μ = 3.082 mm^{-1}, $F_{(000)}$ = 8152, *GooF*(F^2) = 1.017, R_1 = 0.0615, wR^2 = 0.1276 for I>2σ(I), R_1 = 0.1136, wR^2 = 0.1495 for all data, 19353 unique reflections [2θ ≤ 72.588°] with a completeness of 98.8 % and 1201 parameters, 36 restraints.

Table A5 Atomic coordinates (·10^4) and equivalent isotropic displacement parameters ($Å^2 \cdot 10^3$) for **T1**. U_{eq} is defined as 1/3 of the trace of the orthogonalised U^{ij} tensor.

atom	x	y	z	U_{eq}
Ir(1)	3661(1)	2466(1)	6370(1)	26(1)
O(1)	5255(2)	4962(1)	6324(2)	34(1)
O(2)	3930(2)	5276(1)	7161(2)	39(1)
O(3)	5735(2)	6995(1)	6023(2)	42(1)
O(4)	4391(2)	7318(1)	6792(2)	43(1)
O(5)	493(2)	-1223(1)	4904(2)	47(1)
O(6)	2952(2)	290(2)	3201(3)	60(2)
O(7)	6673(2)	669(2)	9327(3)	64(2)
O(8)	8104(3)	1549(3)	6013(4)	110(3)
N(1)	4325(2)	2780(1)	6515(2)	27(1)
N(2)	3324(2)	3023(1)	6512(2)	27(1)
N(3)	3787(2)	2310(1)	7293(2)	29(1)
N(4)	4032(2)	1966(2)	7430(2)	32(1)
N(5)	3533(2)	2502(2)	5406(2)	29(1)
N(6)	3168(2)	2261(1)	5114(2)	27(1)
N(7)	4578(2)	5115(1)	6715(2)	30(1)
N(8)	5076(2)	7160(1)	6435(2)	30(1)
N(9)	1793(2)	46(2)	5008(3)	45(1)
N(10)	6518(2)	801(2)	6699(4)	59(2)
C(1)	4765(2)	2621(2)	6592(3)	33(1)
C(2)	5128(2)	2916(2)	6683(3)	37(2)
C(3)	4898(2)	3274(2)	6663(3)	34(1)
C(4)	4389(2)	3191(2)	6557(3)	26(1)
C(5)	4023(2)	3472(2)	6544(3)	28(1)
C(6)	3531(2)	3399(2)	6525(3)	28(1)
C(7)	3176(2)	3691(2)	6574(3)	35(2)
C(8)	2761(2)	3482(2)	6622(3)	37(2)
C(9)	2873(2)	3076(2)	6582(3)	35(2)

C(10)	4172(2)	3897(2)	6593(3)	28(1)
C(11)	4222(2)	4112(2)	6055(3)	29(1)
C(12)	4350(2)	4510(2)	6094(3)	32(1)
C(13)	4444(2)	4694(2)	6680(3)	33(1)
C(14)	4395(2)	4490(2)	7227(3)	30(1)
C(15)	4259(2)	4092(2)	7178(3)	34(1)
C(16)	4275(2)	5388(2)	6947(3)	33(1)
C(17)	4395(2)	5817(2)	6904(3)	28(1)
C(18)	4097(2)	6102(2)	7083(3)	32(1)
C(19)	4186(2)	6509(2)	7013(3)	32(1)
C(20)	4581(2)	6630(2)	6765(3)	28(1)
C(21)	4667(2)	7060(2)	6679(3)	34(1)
C(22)	5402(2)	6881(2)	6255(3)	31(1)
C(23)	5308(2)	6456(2)	6359(3)	30(1)
C(24)	5617(2)	6172(2)	6203(3)	31(1)
C(25)	5527(2)	5767(2)	6259(3)	31(1)
C(26)	5118(2)	5645(2)	6473(3)	27(1)
C(27)	5004(2)	5215(2)	6491(3)	30(1)
C(28)	4806(2)	5936(2)	6658(3)	27(1)
C(29)	4897(2)	6342(2)	6597(3)	28(1)
C(30)	5186(2)	7582(2)	6387(3)	31(1)
C(31)	4942(2)	7831(2)	5899(3)	41(2)
C(32)	5071(3)	8235(2)	5965(3)	46(2)
C(33)	5423(3)	8374(2)	6442(3)	48(2)
C(34)	5687(3)	8124(2)	6892(3)	41(2)
C(35)	5548(2)	7726(2)	6859(3)	37(2)
C(36)	4589(3)	7710(2)	5294(3)	45(2)
C(37)	4527(3)	7267(3)	5164(4)	70(3)
C(38)	4095(3)	7888(3)	5312(4)	70(2)
C(39)	4773(3)	7886(3)	4709(4)	73(3)
C(40)	6090(3)	8281(2)	7421(3)	53(2)
C(41)	6442(3)	7953(3)	7659(5)	92(3)
C(42)	5866(4)	8419(4)	7967(5)	106(4)
C(43)	6373(4)	8606(3)	7162(5)	112(5)
C(44)	3786(2)	2599(2)	4956(3)	31(1)
C(45)	3587(2)	2422(2)	4384(3)	35(1)
C(46)	3198(2)	2209(2)	4499(3)	32(1)
C(47)	2869(2)	2097(2)	5515(3)	28(1)
C(48)	3020(2)	2177(2)	6163(3)	27(1)
C(49)	2711(2)	2044(2)	6557(3)	28(1)
C(50)	2283(2)	1845(2)	6323(3)	32(1)
C(51)	2170(2)	1748(2)	5677(3)	29(1)
C(52)	2456(2)	1885(2)	5265(3)	27(1)
C(53)	1943(2)	1724(2)	6750(3)	35(1)
C(54)	1941(2)	1283(2)	6891(3)	34(1)
C(55)	1869(2)	978(2)	6354(3)	31(1)
C(56)	1793(2)	1063(2)	5697(3)	28(1)
C(57)	1735(2)	1490(2)	5436(3)	27(1)
C(58)	1900(2)	581(2)	6535(3)	38(2)
C(59)	1873(2)	271(2)	6110(3)	40(2)
C(60)	1809(2)	357(2)	5463(3)	38(2)
C(61)	1774(2)	750(2)	5272(3)	32(1)
C(62)	1449(2)	-267(2)	4977(3)	38(2)
C(63)	1513(2)	-623(2)	4664(3)	38(2)
C(64)	1180(2)	-928(2)	4637(3)	40(2)
C(65)	793(3)	-893(2)	4941(3)	38(2)
C(66)	723(2)	-540(2)	5253(3)	37(2)
C(67)	1051(2)	-229(2)	5261(3)	37(2)
C(68)	120(3)	-1199(2)	5269(3)	58(2)
C(69)	2078(2)	90(2)	4528(3)	37(2)
C(70)	1871(3)	132(2)	3889(3)	43(2)
C(71)	2151(3)	194(2)	3437(3)	45(2)
C(72)	2646(3)	218(2)	3615(4)	46(2)
C(73)	2858(3)	167(2)	4244(4)	51(2)
C(74)	2579(3)	101(2)	4700(4)	46(2)
C(75)	2736(4)	370(3)	2549(5)	83(3)
C(76)	3656(2)	2440(2)	7824(3)	34(1)
C(77)	3834(3)	2172(2)	8321(3)	46(2)
C(78)	4068(2)	1879(2)	8055(3)	40(2)

C(79)	4155(2)	1755(2)	6903(3)	30(1)
C(80)	4403(2)	1402(2)	6972(3)	36(2)
C(81)	4480(2)	1194(2)	6434(3)	35(1)
C(82)	4315(2)	1355(2)	5830(3)	34(1)
C(83)	4087(2)	1723(2)	5796(3)	35(2)
C(84)	3995(2)	1930(2)	6316(3)	26(1)
C(85)	4740(2)	789(2)	6532(4)	44(2)
C(86)	5178(3)	773(2)	6229(4)	44(2)
C(87)	5120(3)	766(2)	5568(4)	54(2)
C(88)	4618(3)	763(2)	5176(4)	57(2)
C(89)	4362(3)	1165(2)	5198(3)	46(2)
C(90)	5641(3)	780(2)	6592(4)	48(2)
C(91)	6051(3)	789(2)	6318(4)	55(2)
C(92)	5989(3)	768(3)	5659(5)	69(2)
C(93)	5528(3)	757(3)	5294(4)	68(2)
C(94)	6576(3)	767(2)	7371(4)	55(2)
C(95)	6740(2)	1092(2)	7763(4)	51(2)
C(96)	6786(3)	1066(2)	8412(4)	51(2)
C(97)	6655(3)	718(2)	8692(4)	51(2)
C(98)	6498(3)	395(2)	8308(5)	64(2)
C(99)	6464(3)	420(3)	7659(5)	72(3)
C(100)	6897(3)	983(2)	9746(4)	62(2)
C(101)	6894(3)	998(3)	6463(4)	59(2)
C(102)	7356(3)	827(3)	6610(4)	62(2)
C(103)	7734(3)	1021(4)	6437(4)	73(3)
C(104)	7694(3)	1382(4)	6146(5)	83(3)
C(105)	7230(4)	1550(3)	5973(6)	86(3)
C(106)	6846(3)	1361(3)	6152(5)	80(3)
C(107)	8064(5)	1944(5)	5723(8)	159(8)
C(206)	3685(4)	6480(3)	3515(5)	79(3)
C(205)	3295(4)	6530(3)	3886(5)	74(3)
C(204)	2953(3)	6181(3)	3793(4)	66(2)
C(203)	2557(3)	6186(3)	4181(5)	75(3)
C(202)	2230(4)	5836(4)	4105(5)	93(3)
C(201)	1837(4)	5840(4)	4492(6)	107(4)
C(301)	-439(15)	5375(13)	3434(18)	290(11)
C(302)	47(14)	5376(14)	3220(16)	290(11)
C(303)	1(11)	5353(7)	2497(15)	290(11)
C(304)	485(11)	5355(10)	2277(15)	290(11)
C(305)	440(11)	5331(14)	1554(15)	290(11)
C(306)	925(12)	5333(15)	1339(17)	290(11)

Crystallographic data have been deposited with the Cambridge Crystallographic Data Center as supplementary publication no. *CCDC 1063988*. These data can be obtained free of charge from The Cambridge Crystallographic Data Centre via www.ccdc.cam.ac.uk/data_request/cif.

9.7 Emission Decay Profiles Ref1–Ref4 and T1

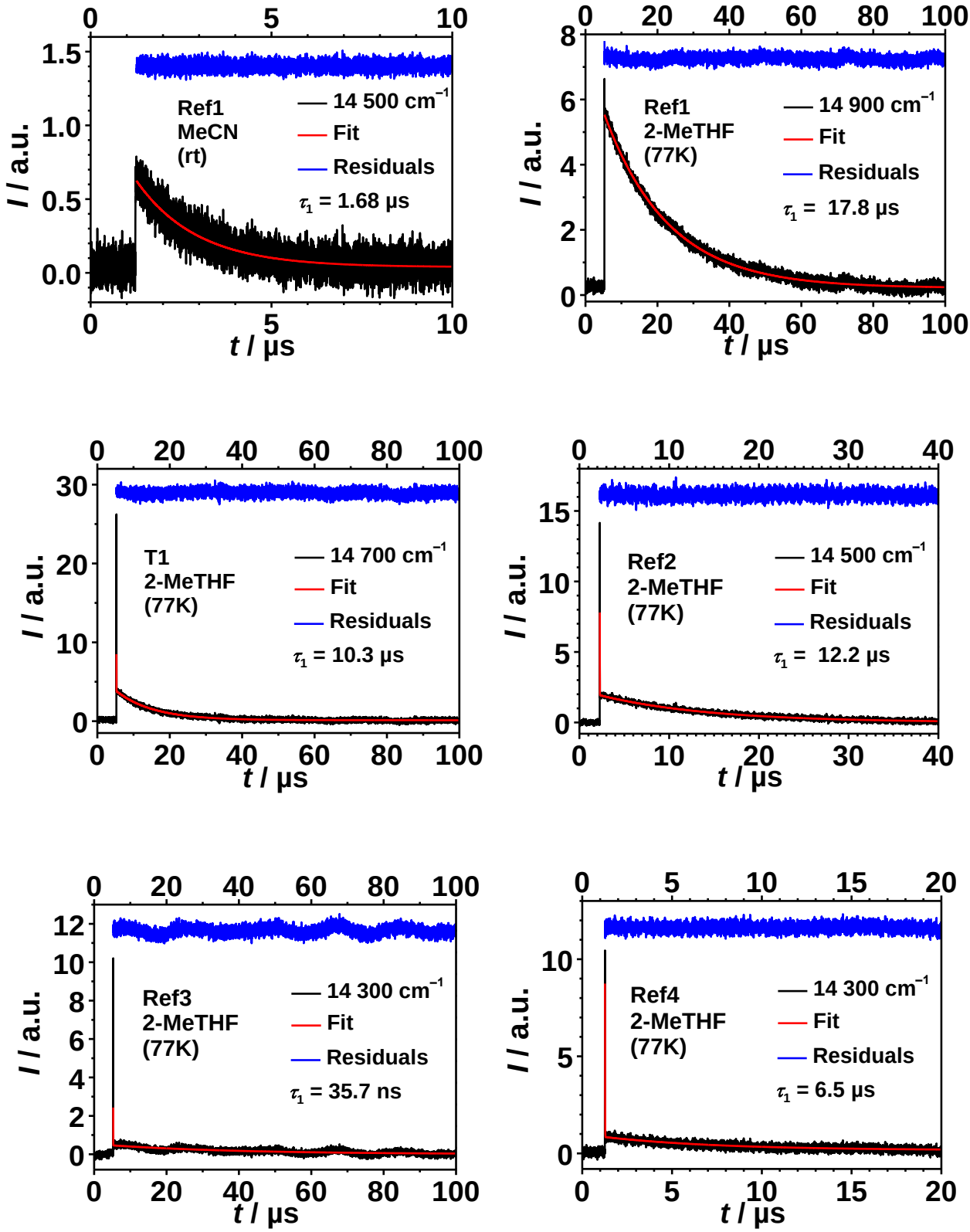

Figure A1 Emission decay profiles of **Ref1–Ref4** and **T1** in 2-MeTHF at 77K and of **Ref1** in MeCN at rt.